New Inorganic and Hybrid Framework Materials

Thesis submitted in accordance with the requirements of the University of Liverpool for the degree of Doctor in Philosophy by Jennifer Lindsay Nicholls

March 2012

Abstract

This thesis describes the formation of new inorganic and hybrid framework materials, from cationic layered structures through to three-dimensional frameworks, with potential applications in catalysis, gas storage and anion exchange. A study of the formation of a number of these materials is also discussed within this thesis.

Chapter 1 presents a review of literature covering the area of hybrid and also cationic materials. This includes a discussion of hybrid materials such as coordination polymers and metal organic frameworks (MOFs), and also cationic materials such as layered double hydroxides (LDHs) and three recently reported cationic inorganic frameworks.

Chapter 2 describes the hydrothermal synthesis of six new pillared layered lanthanide molybdate and tungstate phases. Five of these phases have a general composition of $[Ln(H_2O)MO_4]_2[A]$ (Ln= La-Nd, M = MoO_4 or WO_4, A = 1,5-NDS or 2,6-NDS) with the sixth phase, being pillared by fumarate, having the composition $[Ce(H_2O)MoO_4]_2[Fumarate]$. Each phase consists of two-dimensional cationic inorganic layers comprising of a bilayer of polyhedra and are pillared by charge-balancing organic dianions. The catalytic and anion exchange capabilities of the NDS materials were tested. It was discovered that these materials are able to undergo successful anion exchange of the NDS anions, with dicarboxylates such as fumarate, terephthalate and 2,6-NDC. The tungstate containing phases were also tested for their catalytic properties and proved to be successful catalysts for the oxidative bromination of phenol red to bromophenol blue.

Chapter 3 describes the hydrothermal synthesis of three new lanthanide phosphonoacetate coordination polymers, two having a general formula of $[Ln(H_2O)_2][C_2H_2O_5P]$ (where Ln = Er, Ho and Tb or Yb and Lu), which have infinite three-dimensional structures containing discrete LnO_7 polyhedra connected together via O-P-O bridges, and the remaining phase having a composition of $[YbC_2H_2O_5P]$ consisting of one-dimensional chains of LnO_7 polyhedra which are held together via pillaring phosphonoacetate anions to form a three-dimensional network. Porosity measurements confirmed each phase to be non-porous. Also hydrothermally synthesised are two organosulfonate coordination polymers with compositions of $[Ln(H_2O)_5]_2[2,6\text{-}AQDS]_3{\cdot}2H_2O$ (Ln = La - Nd) and $[Ln(H_2O)_5][C_8H_{17}SO_3]_3.2H_2O$ (Ln = La and Nd). The former phase consists of layers of monomeric Nd polyhedra which are linked by 2,6-AQDS anions forming a three-dimensional network and the latter phase consists of two-dimensional layers of monomeric lanthanum cations which are bridged together by octanesulfonate anions to form a two-dimensional layered structure.

Chapter 4 describes the study of the formation of pillared layered lanthanide molybdate and tungstate phases and also the dehydration of $[Yb(H_2O)_2][C_2H_2O_5P]$ to $[YbC_2H_2O_5P]$ using the *in-situ* energy dispersive X-ray diffraction technique. *In-situ* measurements of the formation of neodymium/molybdate/NDS phases allowed the observation and successful isolation of an intermediate phase which was detected during the formation of the required phase. Kinetic analysis, including calculation of the activation energy, was achieved for the formation of $[La(H_2O)WO_4]_2[1,5\text{-}NDS]$. Also observed by *in-situ* measurements was the dehydration of $[Yb(H_2O)_2][C_2H_2O_5P]$ forming $[YbC_2H_2O_5P]$, which occurs via a dissolution/re-precipitation mechanism.

Chapter 5 describes the boric acid flux preparation of lanthanide borate compounds with compositions $[Ln(NO_3)(H_2O)_2][B_6O_{10}(OH_2)]$ (**1**) (Ln = La and Ce), $[Ln(NO_3)(H_2O)_2][B_5O_9(OH_2)]$ (**2**) (Ln = Pr and Ce), and $[Ln(B_6O_{13}H_3)][BO_3H_2]$ (**3**) (Ln = Sm, Eu and Gd). **1** and **2** are found to have infinite three-dimensional structures consisting of either hexaborate clusters as found in **1** or pentaborate clusters as found in **2**, with one dimensional channels being present in both structures. **3** differs to **1** and **2** as a two-dimensional layered structure is formed consisting of positively charged layers of gadolinium cations coordinated to unique hexaborate clusters, which are charge balanced by non-coordinating borate anions residing in the interlayer gallery. The anion exchange capabilities have been tested for **3** although this proved largely unsuccessful.

Chapter 6 gives details of the syntheses of all the phases prepared during the course of this study and the analytical techniques used to characterise them.

Acknowledgements

I would like to thank my supervisor Dr Andrew Fogg, firstly for allowing me to join his research group, secondly for all the support, encouragement and guidance he has given me throughout my Ph.D, and finally for giving me the opportunity to discover new places such as china- an experience I will never forget.

To the past members of the Fogg research group, Laura and Richard, thank you for being so helpful to me during my first year of study, you allowed me to settle in well and also to understand the research area much quicker. Also a mention has to go to our past undergraduate students Maxine and Helen; I thoroughly enjoyed working with you both, thank you for making the endless amount of hydrothermal reactions more fun and also working within the laboratory.

Also a special mention to Emma who has worked alongside me during our entire, and what feels like a, never ending student lifetime. You have helped me a lot with our endless discussions about research and also given me many ideas and most importantly made group meetings slightly more bearable!

A big thank you has to go to my mum and dad, for firstly allowing me to stay at home rent free during my degree and Ph.D; you have allowed me to not be stressed with my finances as I, unlike many, have come out of University debt free. Also for believing in me and making me feel that I am able to achieve what I set out to achieve. A special thank you has to be said to my Dad for the endless conversations about Chemistry, you seem to know the answer to everything! Thanks also to my siblings Vicki, Gemma and Craig you have all been there for me during the course of my education making me believe that I am capable of gaining my Ph.D and going on to further my career. I could not have done this without the help and support form you all, you really spurred me on and made me believe in myself.

Last but by no means least, thank you to Danny for being there for me through the toughest, stressful and most challenging time of my life. You have been my rock and supported me all the way through my Ph.D. and University lifetime. You have put up with me during all the challenging aspects, thank you again; I truly don't know how you have put up with me!

Abbreviations

BET	Brunner, Emmet, Teller
SEM	Scanning electron microscopy
NMR	Nuclear magnetic resonance
TGA	Thermogravimetric analysis
XRD	X-ray diffraction
PXRD	Powder X-ray diffraction
EDXRD	Energy-dispersive X-ray diffraction
IGA	Intelligent gravimetric analyser
FTIR	Fourier transform infrared spectroscopy
AQDS	Anthraquinone disulfonate
BDC	Benzene dicarboxylate
BTB	Benzene tribenzoate
DMF	Dimethylformamide
NDS	Naphthalene disulfonate
NDC	Naphthalene dicarboxylate
PDC	Pyridine dicarboxylate
Bpy	Bipyridine
Phen	Phenathroline
TBDC	Tetramethylbenzene dicarboxylate
LDH	Layered double hydroxide
LRH	Layered rare-earth hydroxide
MOF	Metal-organic framework
IRMOF	Iso-reticular metal-organic framework

SBU	Secondary building unit
FBB	Fundamental building blocks
NDTB	Notre Dame thorium borate

Contents

Chapter Two - Synthesis, Structure and Characterisation of Pillared Lanthanide Molybdates and Tungstates with Framework Layers

Chapter Three - Synthesis and Crystal Structures of Lanthanide Coordination Polymers

Chapter Four - *In-Situ* Energy Dispersive X-ray Diffraction Studies

Chapter Five – Synthesis, Structure and Characterisation of Lanthanide Borates

Chapter Six – Experimental Details

Chapter One
Introduction

1.0 Hybrid Materials

Hybrid materials are classed as materials which contain metal ions in-conjunction with other molecular species. Materials which fit into the class of hybrid inorganic-organic materials can be split into two categories; firstly are the coordination polymers, and metal organic frameworks (MOFs), and secondly extended inorganic hybrids, which contain infinite metal-oxygen-metal (M-O-M) arrays leading to extended inorganic connectivity. This classification excludes materials in which the organic components are guests within the cavities as in zeolites, and hybrid composites in which the inorganic and the organic components are present as separate phases.[1, 2, 3]

Hybrid inorganic-organic materials have been described by Cheetham *et al.,* as compounds that contain both inorganic and organic moieties as integral parts of a network with infinite bonding connectivity in at least one dimension.[2] They are crystalline materials in which the organic and inorganic components co-exist within a single phase, therefore allowing the properties of the two components to be expressed within a single material.[4, 5] Cheetham *et al.*, also proposed a system for the range of possible dimensions an inorganic-organic hybrid material may possess, which depends on the organic connectivity between metal centres, metal-ligand-metal (M-L-M), or the extended inorganic dimensionalities of the connections, metal-oxygen-metal (M-O-M), or a combination of both, Figure 1.[2] The metal-organic-metal connectivity is also denoted as O^n, where *n* represents the dimensionality of the bridging ligand and the inorganic metal-oxygen-metal connectivity is denoted as I^n, where *n* represents the dimensionality of the inorganic connectivity, the sum of the values of *n* gives the overall dimensionality of the material.

Dimensionality of inorganic connectivity, I^n (n = 0–3)

Metal–organic–metal connectivity, O^n (n = 0–3)	0	1	2	3
0	Molecular complexes I^0O^0	Hybrid inorg. chains I^1O^0	Hybrid inorg. layers I^2O^0	3-D Inorg. hybrids I^3O^0
1	Chain coordination polymers I^0O^1	Mixed inorg.–organic layers I^1O^1	Mixed inorg.–organic 3-D framework I^2O^1	—
2	Layered coordination polymers I^0O^2	Mixed inorg.–organic 3-D framework I^1O^2	—	—
3	3-D Coordination polymers I^0O^3	—	—	—

Figure 1 Classification of inorganic-organic hybrid materials.[2]

Hybrid inorganic-organic materials have become an important class of materials due to their potential applications in gas storage, separation and catalysis. There are many synthetic methods utilised in the formation of crystalline hybrid materials such as diffusion based crystallisation and hydro-, solvo- and ionothermal synthesis. Many factors have to be accounted for in the formation of these materials such as synthetic conditions for example reaction temperature, time, concentrations of reagents, pH, and the solvent employed and also the choice of building units such as the metal ion, organic linker, and counter ions (if required).

1.1 Coordination Polymers

Coordination polymers, as a whole, describe the formation of extended structures based on metals and organic ligands.[6] Compounds of this class are found to have infinite structures from one to three dimensional, although it is noted that if a porous three-dimensional framework is formed this becomes part of the sub-class of metal-organic frameworks (MOFs), as discussed in the next section. The components or building blocks of coordination polymers, metals and organic ligands, are connected through coordination bonds and other weak chemical bonds such as van der Waals and hydrogen bonding interactions. The metal ions act as 'nodes' and the organic ligands act as the 'linkers'. The nodes are often transition metal ions and depending on which metal is employed a variety of coordination numbers may be achieved ranging from 2 – 7, leading to various metal coordination geometries such as linear, T or Y- shaped, tetrahedral, square planar, square- pyramidal, trigonal bi-pyramidal, octahedral and their corresponding distorted forms, Figure 2.[7, 8]

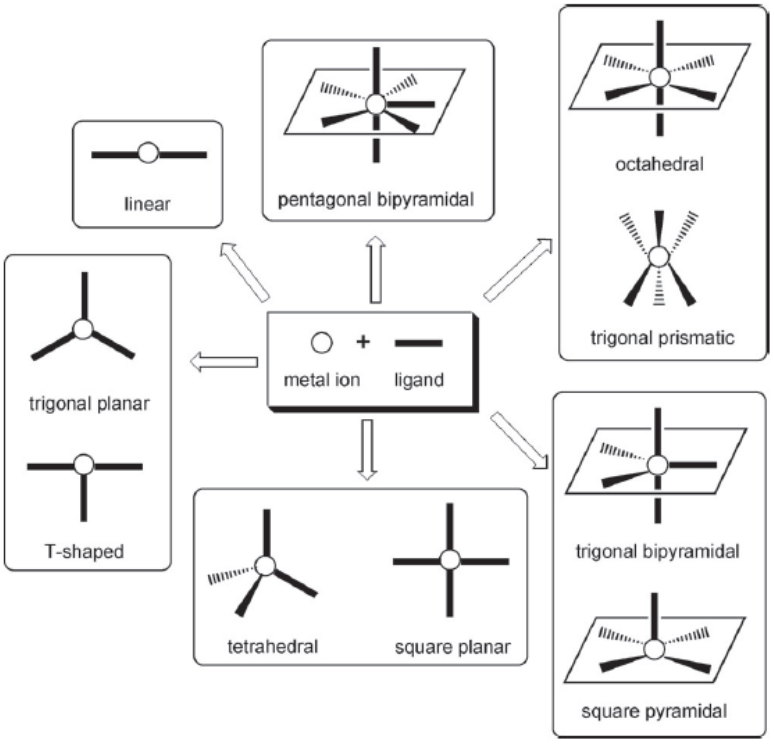

Figure 2 Coordination geometries of transition metal ions found in coordination polymers.[8]

A variety of structures, one,[9, 10] two[11, 12] and three-dimensional,[13, 14] may be formed from the synthesis of coordination polymers by reacting a metal ion, which has more than one vacant coordination site and also a specific coordination geometry, with a potential bridging ligand, as shown in Figure 3.[6]

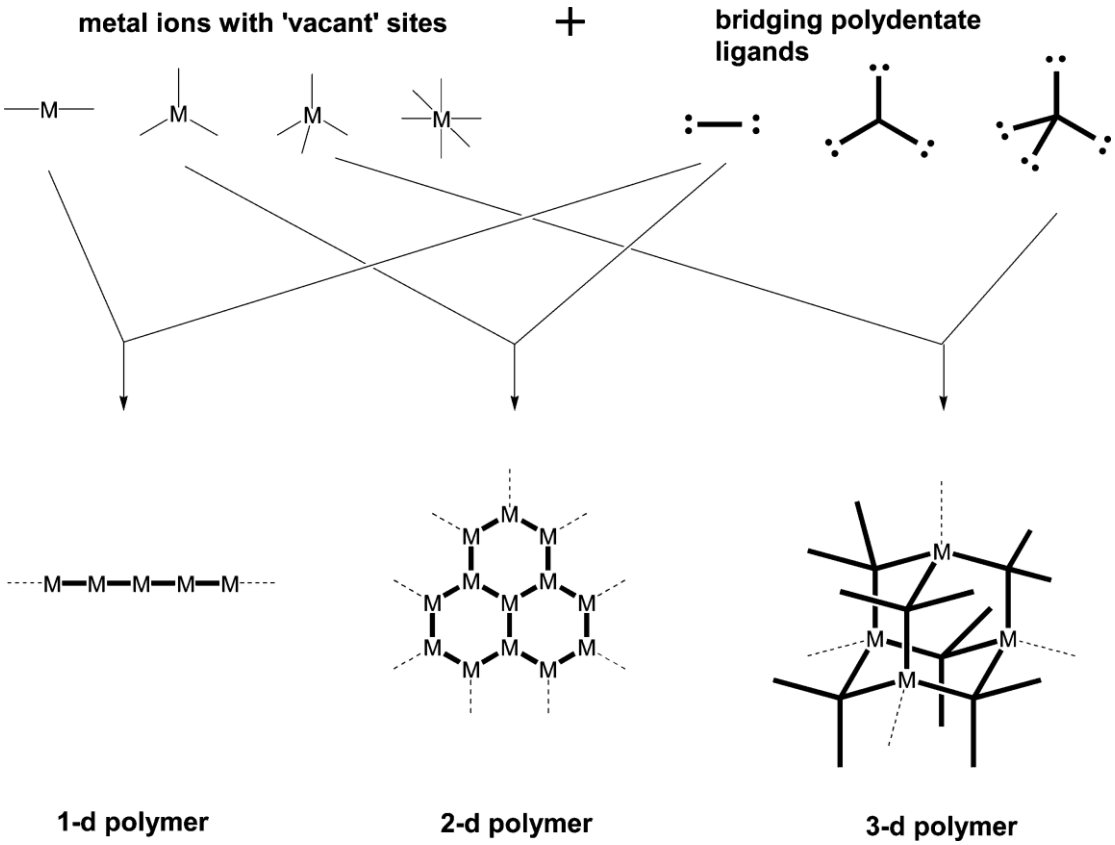

Figure 3 The building block principle behind the formation of coordination polymers.[6]

Prediction of the network topology, although not the prediction of the cell parameters, and the dimensionality of these materials may be achieved by the choice of metal ion and organic linker, and also by other more subtle conditions such as choice of solvent and counterions included within a synthesis.[15, 16] Supplementary components such as counterions, template molecules and non-bonding guests can also form part of coordination polymers. Counterions are needed within a synthesis when using neutral ligands so that the positive charge associated with the metal centre is balanced. Counter anions such as ClO_4^-, BF_4^-, NO_3^-, $CF_3SO_3^-$, SiF_6^{2-} and

PF_6^- have been employed in this way acting as either free guests, hydrogen-bond acceptors or coordination units.[8] An example is $[Cu(4,4'\text{-bpy})_2(H_2O)_2].SiF_6$, which consists of two-dimensional layers of $[Cu(4,4'\text{-bpy})_2(H_2O)_2]$ which interpenetrate forming one-dimensional channels in which the charge balancing SiF_6^{2-} anions reside and also interact with the coordinated water molecules through hydrogen bonding interactions.[8, 17]

Solvent molecules act as the reaction medium but may also control the topology of the resulting framework as they can co-crystallise into the final structure and also act as guest molecules filling any void space. These guest solvent molecules may be removed once the network has formed allowing porosity to be achieved, only if the network does not collapse on de-solvation, therefore demonstrating that the solvent can act as a template in the formation of porous phases. Examples of this phenomenon are found in Section 1.2.1.1.

Synthesis of coordination polymers is aimed towards the formation of single crystals so that the crystal structure of the resulting compound can be determined. Some crystallisation methods which have been adopted to obtain highly crystalline coordination polymers with good quality single crystals include the slow diffusion of two solutions, one solution containing the metal ion and the other containing the organic ligand, which are diffused together in a layered effect. Various devices for this crystallisation method are known such as straight cell, H cell or Y cells. Also the use of hydro- and solvothermal methods allows for the formation of crystalline materials.[8] Re-crystallisation, as used in organic synthesis, is not available for the crystallisation of coordination polymers, due to their low solubility in most solvents, therefore other methods, as mentioned above, have to be utilized in order to synthesise large single crystals for structure determination.

1.2 Metal Organic Frameworks

Metal organic frameworks (MOFs) are a well known sub-class of coordination polymers. Rowsell *et al.*, have recently defined metal-organic frameworks as materials which have strong bonding providing robustness, linking units which may

be modified by organic synthesis and also geometrically well-defined structures, hence they must be crystalline.[1] The term metal organic framework is applied mainly to structures which exhibit porosity, therefore two- or three-dimensional structures, and also to structures in which their organic linkers may be modified by organic synthesis to increase porosity. The metal ions and organic linkers, also known as bridging ligands, link together through metal-ligand-metal (M-L-M) connectivity,[2] in turn forming two and three-dimensional structures. Depending on the specific application desired the structure may be fine tuned in accordance with the application. This may be achieved by modifying the linking ligands by organic synthesis using either post synthetic modification[18] or by pre-designing the material before synthesis which is known as reticular synthesis[19] and allows a structure to be predicted. The resultant network topology, as discussed above in coordination polymers, is dependent mainly on the coordination environment and the geometry of the metal ion 'node' as the linker is usually found to act as a linear connection between adjacent nodes, therefore the topology is not deemed to be reliant on this.[20] It is therefore not only important which building blocks are employed, as there are a vast variety of metal ions and organic ligands which can be incorporated within the synthesis, but also the connectivity they retain.

Secondary building units (SBUs) are often found to be formed within a MOFs structure, and are defined as the inorganic clusters or coordination spheres formed in the synthesis, linked together by the organic components. SBUs are not introduced directly within a synthesis but are formed *in-situ* under specific reaction conditions. Some examples of SBUs that are found within MOFs are shown in Figure 4. Branched organic linkers, with more than two coordinating functionalities, for example square tetrakis(4-carboxyphenyl)porphyrin, Figure 5(a), tetrahedral adamantine-1,3,5,7-tetracarboxylic acid, Figure 5(b) and trigonal 1,3,5-tris(4-carboxyphenyl)benzene, Figure 5(c), are also known SBUs but they are pre-formed before synthesis.[1] The catalogue of SBUs which have been formed in the synthesis of MOFs enables one to predict if certain SBUs will be formed using specific metals and organic ligands within the synthesis. Therefore one may be able to predict or pre-determine the outcome of the topology of the final structure formed, and in turn use the predicted SBUs to fine-tune the properties of MOFs.

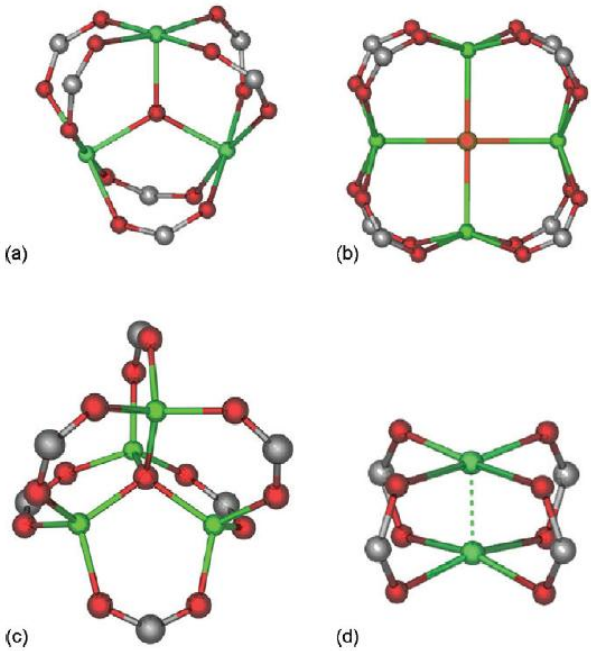

Figure 4 Structural representation of SBUs commonly occurring in the formation of metal-organic frameworks including (a) trigonal planar, (b) square planar, (c) tetrahedral and (d) tetragonal paddlewheel.[6]

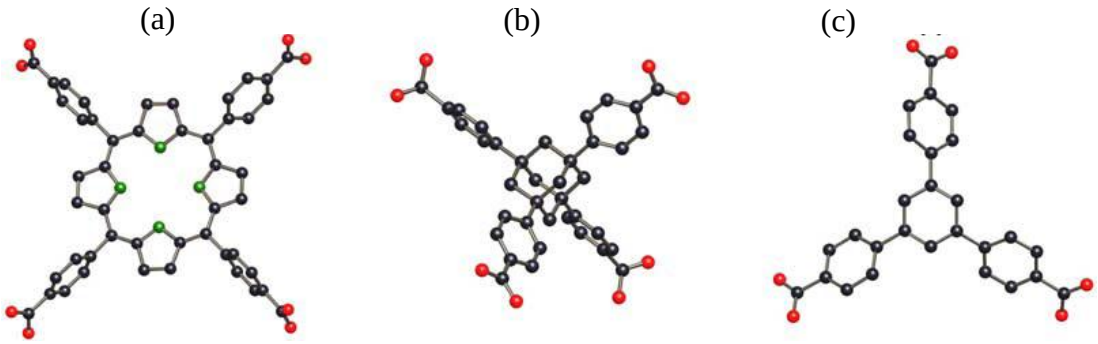

Figure 5 Some carboxylate SBUs which are pre-formed before synthesis of MOFs
(a) square tetrakis(4-carboxyphenyl)porphyrin
(b) tetrahedral adamantine-1,3,5,7-tetracarboxylic acid and
(c) trigonal 1,3,5-tris(4-carboxyphenyl)benzene.
(Adapted from *Microporous Mesoporous Mat.* **2004**, *73*, 3.)[1]

Reticular synthesis of MOFs has allowed the design and assembly of target frameworks to become possible. The network connectivity of the building units within a MOF are found to determine the properties the compound may exhibit for example porosity. Reticular synthesis is a strategy which exploits SBUs which have previously been formed.[20] Some examples exploiting reticular synthesis include the formation of carboxylate MOFs derived using MOF-5 as a prototype. These MOFs are known as iso-reticular metal organic frameworks (IRMOFs), in which they are based on the same net and topology as MOF-5, Figure 6. The pore size and functionality has been altered but without changing the original topology found in MOF-5. The organic linkers are found to differ in functionality of the pendant groups in IRMOFs 1- 7, as they have the addition of bromo (2), amino (3), n-propoxy (4), n-pentaoxy (5), cyclobutyl (6) and fused benzene functional groups (7), and in length by substituting 1,4-benzenedicarboxylate producing IRMOFs 8 – 16, using 2,6-naphthalenedicarboxyalate (8), biphenyl-4,4'-dicarboxylate (10), pyrene-2,7-dicarboxylate (14) and terphenyl-4''-dicarboxylate (16), Figure 6.[1, 21] Each structure contains the SBUs $Zn_4O(CO_2)_6$ as found in MOF-5, therefore the topology of the structure remains unchanged, although the size of the pores and their functionalities now differ.

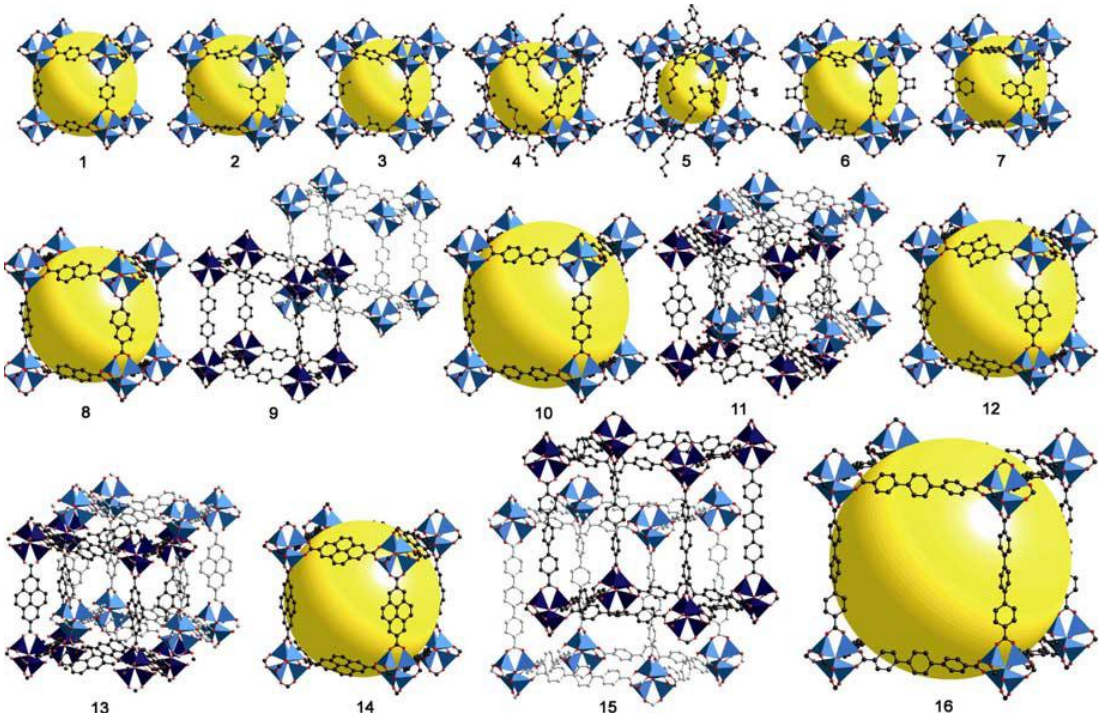

Figure 6 Structures of iso-reticular MOFs (IRMOFs 1 – 16) using MOF-5 as the prototype.[1]

Synthesis of MOFs is achieved using soluble salts of the metal component usually with mono-, di-, tri- and tetracarboxylic acids in an organic solvent typically an amine, triethylamine or amide, diethylformamide or dimethylformamide. The metal-organic structures are then formed by self-assembly at temperatures from room temperature up to solvothermal conditions of 200 °C typically for a few hours.[22] The filtering and drying process of MOFs may become problematic, due to the high porosity MOFs possess, therefore during the drying process incorporation of the solvent may occur.

The organic linkers are found to also play an important role in the formation of porous MOFs, for example the use of long bridging ligands. Ligands of this type may introduce some problems within a framework such as interpenetration, whereby large voids are produced when using longer ligands which allows a second polymer network to interpenetrate the first formed network, thus filling up potential cavities and reducing or removing potential porosity.[6] Counter balancing anions and also the use of bulky bridging ligands may be used to avoid the problem of interpenetration

when synthesising porous MOFs. The choice of metal ion and organic ligand are known to affect the framework topology and hence the size and shape of the pores.

The pores within MOFs may be modified by pre-functionalisation of the organic ligand in order to enhance and modify their host-guest interaction ability. There are two ways of functionalising MOFs, firstly by functionalising the ligand pre-synthesis, Figure 7. This is found to be a limited approach due to many functional groups not being compatible or stable to solvothermal conditions in which most MOFs are synthesised, and also due to the formation of unwanted frameworks which may occur.[23]

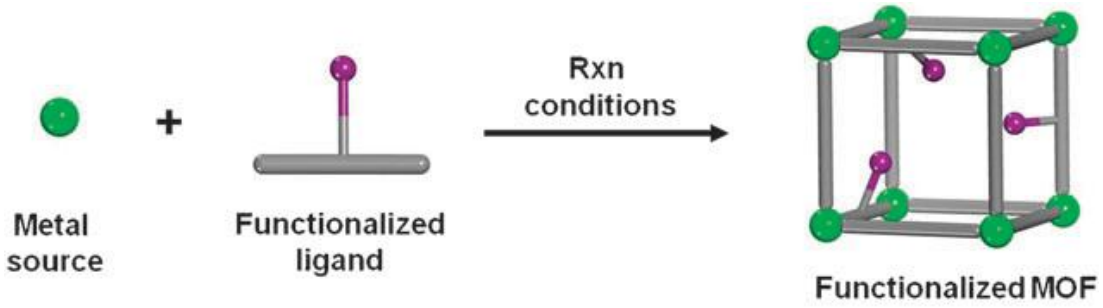

Figure 7 Schematic preparation of a functionalized MOF using direct synthesis[23]

As discovered occasionally the use of a functionalised ligand pre-synthesis may not form the required topology, therefore an alternative to this approach is needed. This approach is that of post-synthetic modification, which is defined as the chemical modification of a framework after it has been synthesised, Figure 8.[18, 23] It is necessary to first form the MOF of required topology then add the functional group to the MOF post synthetically. The metal and organic components of the framework are able to be modified without disrupting the stability or topology of the structure, leading to applications in catalysis and gas storage.

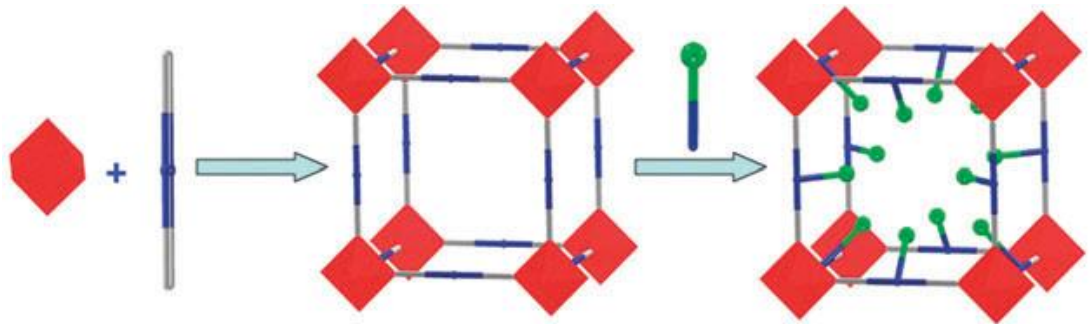

Figure 8 A general schematic for the post-synthetic modification of MOFs.[18]

Generally MOFs have been formed using organic carboxylates as the most common linkers. Formation of MOFs using non-carboxylate linkers such as phosphonates and sulfonates is less well studied.[24, 25] In the synthesis of MOFs it has been discovered that subtle changes in reaction conditions, such as changes in concentrations,[26, 27] temperature,[28] reaction time[26] and also pH,[26, 27] may reduce crystallinity, yield or form phases which were not predicted. Therefore it may be said that reaction conditions play a vital role in determining the final structure formed. An example of how varying the reaction temperature, whilst all other reaction conditions remain identical, can affect the final outcome of the structure, can be shown in formation of cobalt succinate MOFs as synthesised by Cheetham *et al*. Cobalt succinates were synthesised over a range of reaction temperatures, from 60 – 250 °C, their compositions and dimensionalities are shown in Table 1. The results of varying the synthesis temperature shows some clear trends, for example at the lowest temperature of 60 °C the tetra-aquo phase of $Co(H_2O)_4(C_4H_4O_4)_2$ is favoured which has previously been formed by Livage *et al.*, at room temperature.[29] Increasing the reaction temperature leads to fewer coordinated water molecules per cobalt atom, and also higher coordination numbers of the carboxylate groups. Above 100 °C hydroxide is found to incorporate into the phases although no general trend is found on the amount of hydroxide incorporated into the structures.

Table 1 Cobalt succinates synthesised over various reaction temperatures[28]

Synthesis temperature °C	Phase	Dimensionality[†]
60	$Co(H_2O)_4(C_4H_4O_4)_2$	1(0)
100	$Co(H_2O)_2(C_4H_4O_4)_2$	1(0)
150	$Co_4(H_2O)_2(OH)_2(C_4H_4O_4)_3.2H_2O$	2(2)
190	$Co_6(OH)_2(C_4H_4O_4)_5.2H_2O$	3(2)
250	$Co_5(OH)_2(C_4H_4O_4)_4$	3(2)

[†]Note: In the dimensionality column of Table 1 the first number refers to the total dimensionality of the phase with the second number referring to the M-O-M inorganic dimensionality.

Another trend is in the of dimensionality of the structures, which is found to increase with an increase of reaction temperature with one-dimensional chains observed up to 100 °C, two-dimensional sheets at 150 °C and three-dimensional materials at 190 °C and above, as show in Figure 9.

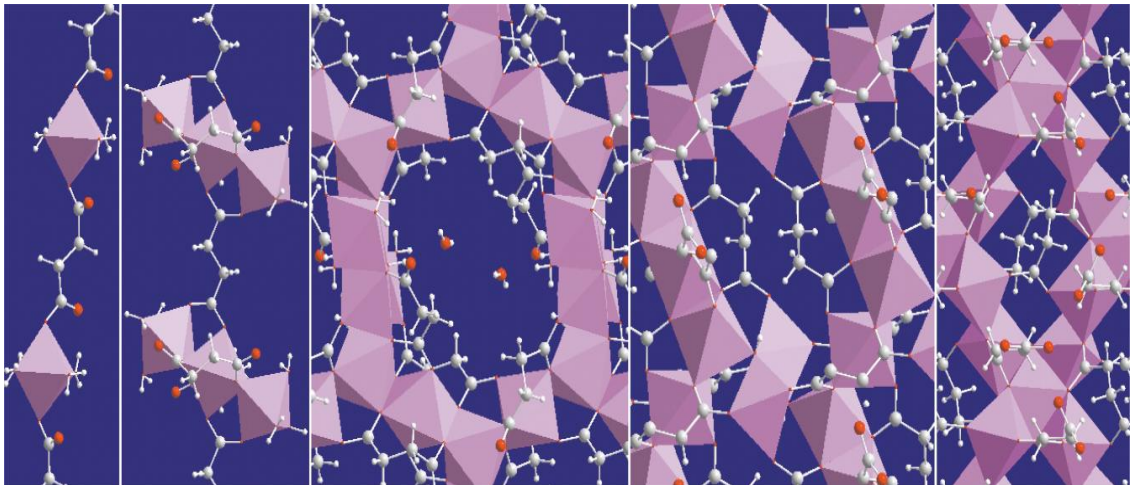

Figure 9 Structures of cobalt succinates produced from low temperature synthesis (left) and high temperature synthesis (right).[28]

1.2.1 Applications of MOFs

Metal organic frameworks are found to have various potential applications such as use in catalysis, gas storage, gas separation and purification. Due to their ability to be fine tuned for example using reticular synthesis or post-synthetic modification MOFs can be applied in a diverse range of fields. Many reviews have been published on the applications of MOFs and their industrial applications.[1, 22, 30, 31]

1.2.1.1 Gas Storage

Until the mid 1990s there were only two classes of porous inorganic materials, such as zeolites and carbon based materials, including activated carbons.[8] MOFs are now a well known area of porous materials and are found to have perfectly regular pores, as found in zeolites, and also high porosity as found in carbon based materials.[8] The structure of the building units may be maintained throughout the synthesis of MOFs allowing certain molecular building units to be chosen in order to form a desired network. This is known as the 'bottom-up' method. Porosity foreknowledge to which topology will be observed by a given set of building blocks is relevant for the production of porous materials. To increase the pore sizes in MOFs extending the length of the organic linker may be viable, in conjunction with using other previously synthesised MOFs that are porous as the prototype; however, formation of larger pores may lead to interpenetration. Interpenetration will itself therefore play a key role into whether a porous MOF will form; the networks may either become maximally displaced from one another, therefore blocking access to the pores, or interweave whereby they are minimally displaced.[1] Interpenetration is found to be a major obstacle to overcome in the formation of porous MOFs, although there is a strategy in place of using ligands containing hindrance groups to block interpenetration leading to the formation of porous MOFs which possess excellent gas storage capability and/or selectivity.[32] The metal ion used in the synthesis of MOFs also plays a key role in the formation of porous frameworks as the metals coordination preferences will influence how many ligands may coordinate to the metal centre and also in which orientation they will bind therefore affecting the size and shapes of the pores. A porous metal organic framework is defined by having

open channels in which guest species are able to be removed and re-introduced reversibly without collapse of the framework.[33]

Yaghi's group is one of the leading research groups in the area of porous metal organic frameworks. This group uses polycarboxylates in their synthesis such as benzenedicarboxylates and benzenetricarboxylates to form porous metal organic frameworks. An example of an exceptionally stable and porous metal organic framework is that of $Zn_4(O)(BDC)_3.(DMF)_8C_6H_5Cl$ (MOF-5)[34] (BDC = 1,4-benzendicarboxylate, DMF = dimethylformamide) which was reported in 1999. This structure consists of $Zn_4(O)O_{12}C_6$ clusters, which are formed from a core consisting of an oxide centered cluster of a single oxygen atom bound to four Zn atoms, creating a Zn_4O tetrahedron. Each of these Zn_4O tetrahedron edges are capped by carboxylate groups to form the $Zn_4(O)O_{12}C_6$ clusters. These clusters link together forming the three-dimensional metal-organic framework of $Zn_4(O)(BDC)_3$ as shown in Figure 10. This framework is found to remain crystalline when de-solvating the phase in air at 300°C for 24 hrs, showing incredible stability with no loss of crystallinity or morphology. Post de-solvation MOF-5 is found to have a high Langmuir surface area of 2900 m^2/g, assuming monolayer coverage of N_2 although to note this may not be entirely correct due to the large cavities present in MOF-5. The same reversible sorption behaviour was also observed for organic vapours such as dichloromethane, chloroform, carbon tetrachloride, benzene and hexane. The guest molecules present in this structure can be fully exchanged with chloroform guests which can then be easily evacuated from the pores to create the porous framework.[34, 35] The iso-reticular MOFs IRMOF-1, 3 and 6, discussed in Section 1.2, are also found to uptake methane, with IRMOF-6 having a higher uptake of methane of 240 cm^3 adsorbed per gram of material compared to that of zeolite A (87 cm^3/g)[21] and other coordination frameworks[21] such as $[CuSiF_6(4,4'\text{-bipyridine})_2.8H_2O)]$[36] and $[Cu(O_2RCO_2).(TED)_{1/2}]$ (R = 4,4'-$C_6H_4C_6H_4$ (212 cm^3/g) or *trans* – $C_6H_4CH{=}CH$ (213 cm^3/g), TED = triethylenediamine).[37]

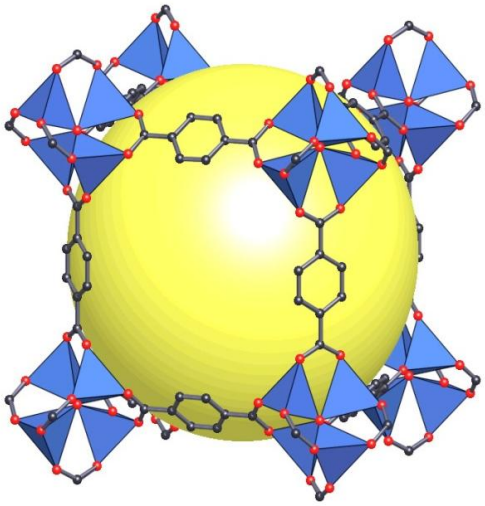

Figure 10 Framework structure of $Zn_4(O)(BDC)_3$ MOF-5, large cavity is indicated by the yellow sphere of diameter 18.5 Å.[34]

By substituting 1,4-benzenedicarboxylate with a larger organic linker of benzenetribenzoate (BTB) results in a higher surface area compared to that of MOF-5. This resulted in the formation of MOF-177, shown in Figure 11, and is found to have estimated Langmuir surface area of 4500 m^2/g.[38] MOF-177 has the composition Zn_4O-(1,3,5-benzentribenzoate)$_2$, and is an ordered structure that has extra large pores. The structure consists of $OZn_4(CO_2)_6$ clusters, as seen in MOF-5, linked together via 1,3,5-benzentribenzoate into a three-dimensional framework.

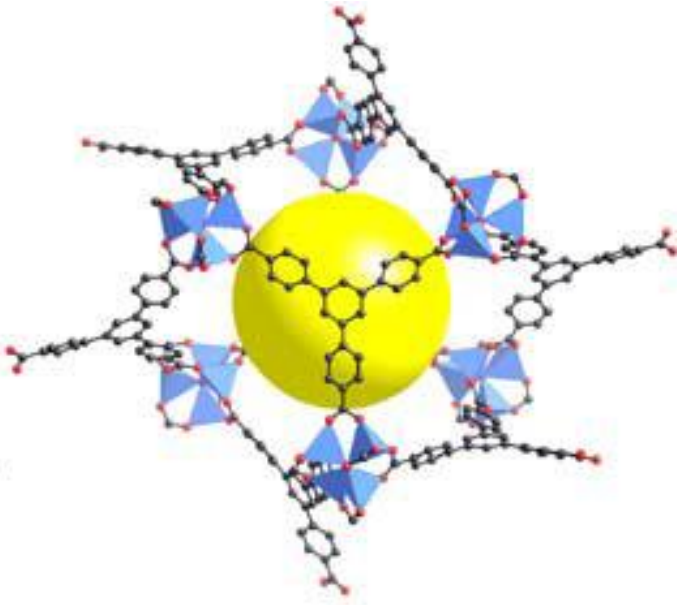

Figure 11 Structure of Zn_4O-(1,3,5-benzentribenzoate)$_2$, MOF-177. (adapted from *Microporous Mesoporous Mat.* **2004**, *73*, 3)[1, 38]

1.2.1.2 Catalysis

Interest in MOFs as catalytically active species has increased over the years for a few potential reasons. Firstly it is possible to further functionalise the pores found within MOFs in order to make the material catalytically active,[21] secondly the pores may also be fine tuned in their chemical characteristics[39] and thirdly MOFs are able to form large and crystalline pores quite easily, allowing catalytic reactions to take place within them.[3] MOFs are also deemed to be increasingly good catalysts as they contain 'single-site' active species in which every active site is in an identical environment due to the crystalline nature of MOFs.[40]

MOFs can be used as catalytic supports, whereby the MOF is used as a carrier for an active site,[22] an example of this includes MOF-5. This MOF is able to be utilized as a catalytic support in many catalytic reactions such as use in the epoxidation of propylene with molecular oxygen by incorporating Ag onto MOF-5, H_2O_2 synthesis from the elements utilizing Pt on MOF-5, the synthesis of methanol from synthesis gas utilizing Cu on MOF-5, and also in the hydrogenation of cycloctene by incorporating Pd onto MOF-5.[22]

Many components of MOFs can be used within a catalytic reaction such as using the SBU as the active centre and also having the active centre being introduced to the MOF by post-synthesis modification. An example of a SBU as the active centre includes $Cu(bpy)(H_2O)_2(BF_4)_2(bpy)$ (bpy = 4,4'-bipyridine) which is a highly effective and selective heterogeneous catalyst in the alcoholysis of epoxides which is the ring opening of epoxides by methanol at room temperature, for example the ring opening of styrene oxide with methanol, shown in Figure 12.[40] The structure of the Cu-MOF consists of two-dimensional sheets of active octahedral Cu sites which are bridged together by 4,4'-bipyridine (bpy) linkers, these sheets are connected by BF_4^- anions forming a three-dimensional structure. The catalytic activity of this MOF is found to be comparable to that of the corresponding homogeneous catalyst of $Cu(BF_4)_2.H_2O$.[40, 41]

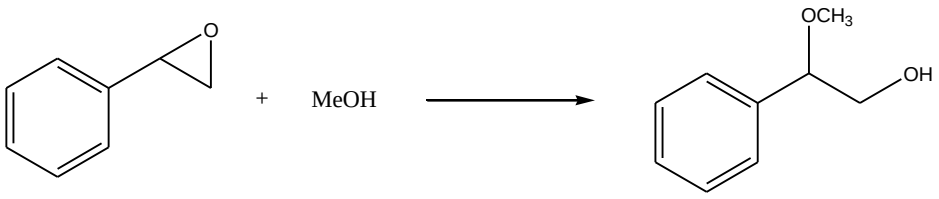

Figure 12 Reaction scheme of the alcoholysis reaction of the ring-opening of the epoxide, styrene oxide, by methanol to form 2-methoxy-2-phenylethanol.[40]

An example of the active centre of a MOF being introduced by post-synthetic modification is that of $Cr_3(F,OH)(en)_2O(BDC)_3$ (ED-MIL-101) (en = ethylenediamine, BDC = 1,4-benzenedicarboxylate).[42] This involved the post synthetic modification of MIL-101 by ethylenediamine to yield a MOF which is then able catalyse the Knoevenagel condensation of benzaldehyde and ethyl cyanoacetate. $Cr_3F(H_2O)_2O(O_2C\text{-}C_6H_4\text{-}CO_2)_3.nH_2O$ (n ~ 25) (MIL-101)[43] was originally synthesised in 2005 by Ferey *et al*., and consists of trimers of inorganic Cr octahedral units which are linked together by 1,4-benzenedicarboxylate anions in turn forming a three dimensional framework with cages present which accommodate water molecules. It was discovered on dehydrating this phase one could graft the dehydrated product with a multifunctional ligand such as ethylenediamine; coordination of this ligand allowed the formation of a grafted $Cr_3(F,OH)(en)_2O(BDC)_3$ (ED-MIL-101) compound.[42] The amine group present was then able to play the role of an immobilised base catalyst in the Knoevenagel condensation of benzaldehyde and ethyl cyanoacetate, Figure 13, therefore also determining that the reaction takes place within the amine-grafted pores.

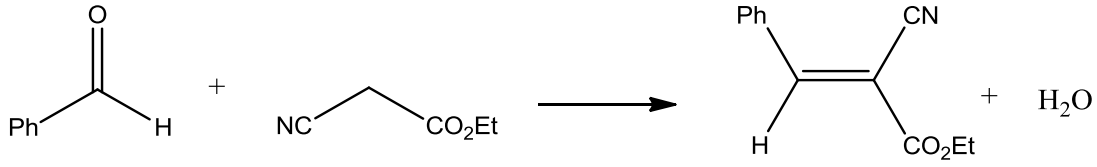

Figure 13 Knoevenagel condensation of benzaldehyde and ethyl cyanoacetate forming ethyl-2-cyano-3-phenylacrylate.[42]

1.3 Lanthanide Coordination Polymers

Coordination polymers incorporating lanthanides, also known as lanthanide coordination polymers, is also an established area of research albeit less well established than the corresponding metal-organic framework area. The use of lanthanide cations in compounds of this type allows for larger coordination numbers of 7 – 12 to be achieved, which leads to new and unusual network topologies.[8] Lanthanide containing coordination polymers are found to be less investigated compared to their d-block analogues. There are a few simple reasons as to why this may be the case such as the coordination preferences of lanthanides. These preferences differ to d-block metals, as lanthanides have a larger coordination sphere, allowing high and variable coordination numbers, which is believed to be a disadvantage as this leads to their coordination spheres being difficult to control, therefore design of these materials with specific structures for use in certain applications is rendered hard.[16, 44] However this can also be an advantage of using lanthanides in comparison to transition metals as their greater coordination flexibility leads to structures which would not be formed when using the more predictable d-block metals. Forming metal-organic frameworks with the lanthanides also leads to potential applications in a variety of fields such as catalysis, luminescence and gas storage.

Despite the high coordination numbers available to lanthanides, as discussed above, three-dimensional coordination polymers are found to be less common, with the choice of the organic bridging ligand being key to the dimensionality of the product formed.[45] Lanthanide coordination polymers of various dimensions have been formed using carboxylates,[46, 47, 48, 49] phosphonates[50, 51] and also sulfonates.[52, 53]

Recently attention has been focused on the formation of lanthanide coordination polymers which exhibit porosity. Three-dimensional coordination frameworks are needed for this purpose and have been recently reported mainly with the incorporation of carboxylate ligands for example $Tb(BDC)NO_3.2DMF$ (BDC = 1,4-benzenedicarboxylate and DMF = *N*,*N*-dimethylformamide),[54] and $Eu_2(BDC)_3(DMF)_2.(DMF)_{1.7}$ (BDC = 1,3-benzenedicarboxylate).[55] The latter phase displays a three dimensional framework which has one-dimensional channels running through the framework, Figure 14. The structure consists of zigzag chains of

EuO_9 polyhedra which are linked together through shared oxygen atoms from the carboxylate anions generating the three dimensional open framework. The free and capping DMF molecules occupy the one-dimensional channels. This framework is stable up to 460 °C and displays a BET surface area of 502 m^2/g after removal of the guest and coordinated solvent molecules.

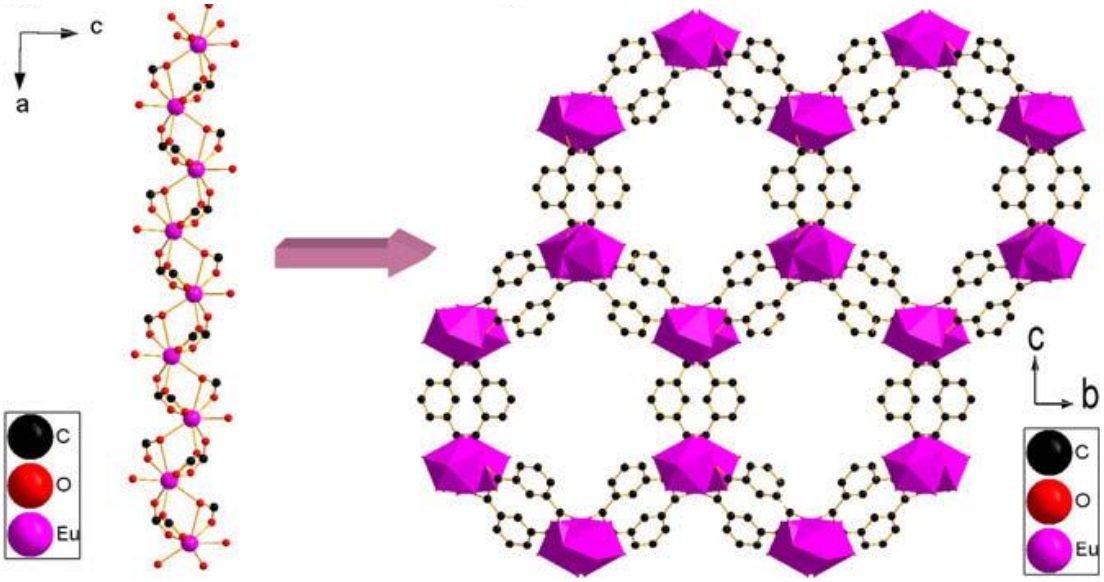

Figure 14 Crystal structure of $Eu_2(BDC)_3(DMF)_2.(DMF)_{1.7}$ showing the zigzag connections of the Er^{3+} centres and the one-dimensional hexagonal channels running through the three-dimensional framework. Hydrogen atoms, uncoordinated DMF molecules and solvent molecules have been omitted for clarity.[55]

He *et al*., produced lanthanide coordination polymers of $Ln(BDC)_{1.5}(DMF)(H_2O)$ (Ln = Er or Tm, BDC = 1,3- benzenedicarboxylate) in the hope of forming porous frameworks. This group found that this compound was interpenetrated, due to the existence of large channels, therefore lacked porosity, forming a three-dimensional non-porous framework. Due to interpenetration this group formed a new strategy in which to develop frameworks with the same topology of the interpenetrated material, but with control to form non-penetrating networks so that porosity could be achieved. To control interpenetration in this compound they firstly thought to replace the coordinated solvates with other chelating ligands such as phenanthroline (phen), and secondly to add hindrance groups to a ligand similar to 1,3-benzenedicarboxylate

(BDC) for example 2,3,5,6-tetramethyl-1,4-benzenedicarboxylate (TBDC), or to employ a combination of both these ideas. This lead to the formation of three new porous lanthanide organic frameworks of compositions $Er_2(BDC)_3(phen)_2.3H_2O$, by replacing coordinated DMF and water in the synthesis with chelating phen ligands, $Tm_2(TBDC)_3(DMF)_2(H_2O)_2.4H_2O$, synthesised by replacement of 1,3-benzenedicarboxylate (BDC) with 2,3,5,6-tetramethyl-1,4-benzenedicarboxylate (TBDC) with the coordinated solvent remaining unchanged, and $Er_2(TBDC)_3(phen)_2.4DMF.2H_2O$, in which both the coordinated solvent and ligand is substituted in the synthesis for TBDC and phen.[32] The use of ligands containing hindrance groups, as in the latter phase, has allowed for the formation of a porous lanthanide-organic open framework by controlling interpenetration without changing the original topology. The framework of $Er_2(TBDC)_3(phen)_2.4DMF.2H_2O$, shown in Figure 15, consists of two Er cations bridged together by two carboxylate groups to generate a binuclear SBU which is further bridged by TBDC ligands in different directions to form a three-dimensional porous framework containing channels. The methyl groups of TBDC and the coordinated phen ligands point towards the pores partly blocking the channels thus preventing interpenetration.

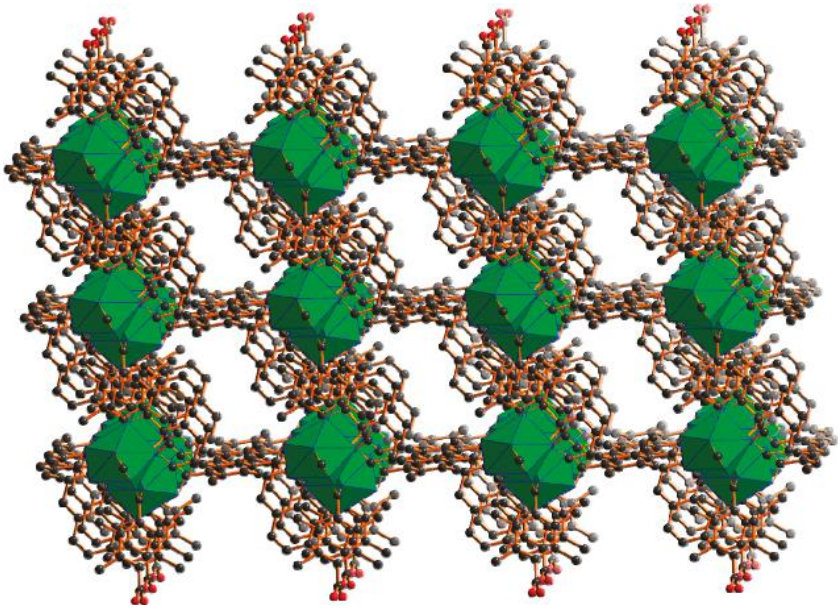

Figure 15 Crystal structure of $Er_2(TBDC)_3(phen)_2.4DMF.2H_2O$.[32]

1.4 Extended Inorganic Hybrids

Extended inorganic hybrid metal oxides contain infinite metal-oxygen-metal (M-O-M) arrays as part of their structure leading to extended inorganic connectivity. A schematic example, shown in Figure 16, represents inorganic connectivity which has formed in two-dimensions and is connected into the third dimension by organic linkers, therefore classing this material as an extended inorganic hybrid.

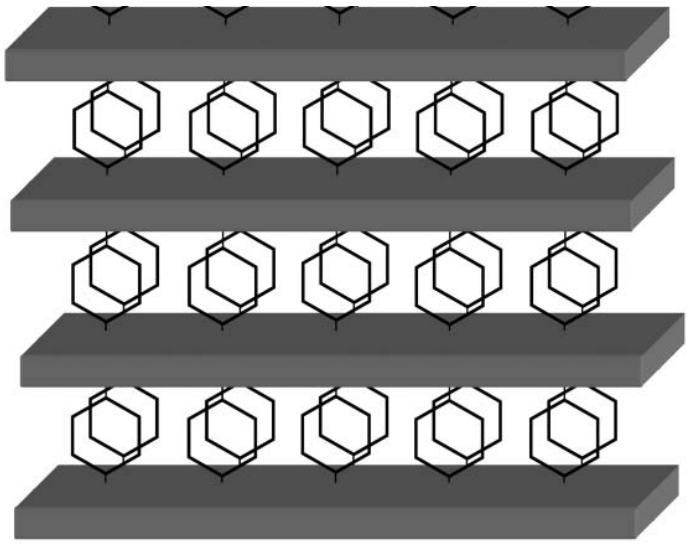

Figure 16 Schematic representation of a system in that has inorganic connectivity in two dimensions which is connected in the third dimension by organic linkers. (adapted from *Chem. Commun*, **2006**, 4780)[2]

One-dimensional through to three-dimensional networks are known for extended inorganic hybrids. An example of a one-dimensional network is $Zn(O_2P(OC_2H_5)_2)_2$[56] which consists of one-dimensional inorganic chains in which the organophosphonate ligands decorate the chains instead of cross linking them. Layered structures are also known in which one-dimensional inorganic chains are cross linked, instead of being decorated, by organic linkers for example $Ni_7(OH)_6(H_2O)_3(C_4H_4O_4)_4.7H_2O$.[57] Also three-dimensional networks are known, examples include a family of transition-metal gallates of composition $M(C_7O_5H_4).2H_2O$ (M = Fe, Mn, Co or Ni).[58] This structure consists of chains of MO_6 octahedra, having their oxygen atoms supplied from the gallate anions, cross linked by gallate anions forming a three-dimensional

network with one-dimensional channels present in which water molecules reside, as shown in Figure 17.

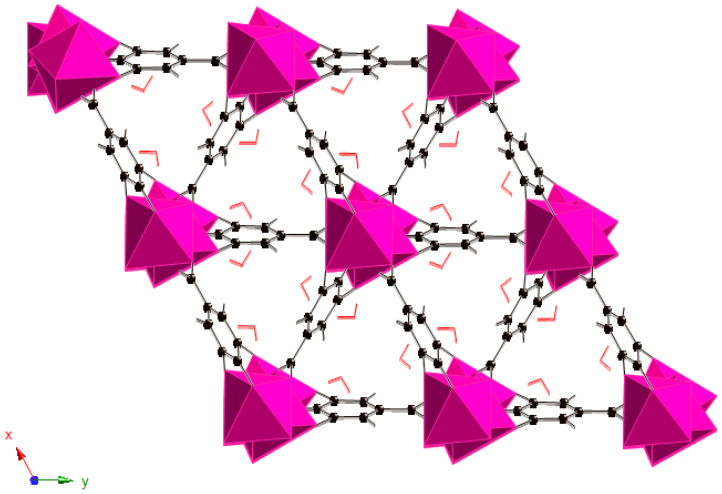

Figure 17 Crystal structure of $Mn(C_7O_5H_4).2H_2O$ (Colour key; Mn – pink, H_2O – red and C – black)[58]

1.5 Cationic Materials

Materials with extended structures are typically based on a neutral structure or an anionic one whose charge is balanced by cations, such as in zeolites, alumino and gallophosphates and in a number of metal-organic frameworks. Alternatively materials which are based on a cationic structure in which the pillar or template species is anionic are much rarer and are the subject of a recent review.[59] Cationic materials have potential to be applied in a variety of applications such as in anion exchange and catalysis. The most widely studied cationic materials are those consisting of a layered structure such as layered double hydroxides, and more recently lanthanide hydroxysalts, along with the less studied materials which adopt the structure of francisite $Cu_3BiSeO_8[X^-]$ and also layered structures of heavy p-block elements. Some examples of cationic metal or lanthanide-organic frameworks are also known.

1.5.1 Layered Double Hydroxides

Layered double hydroxides are a well known and studied class of inorganic materials due to their anion exchange properties. The layer structure of these materials is typically based on brucite ($Mg(OH)_2$), Figure 18(a), where the infinite two-dimensional layers consist of edge-sharing metal hydroxide octahedra. Substitution of a number of the divalent cations in the brucite lattice by trivalent cations leads to these layers becoming positively charged.[60] This leads to layered double hydroxides with the general formula $[M^{2+}_{1-x}\ M^{3+}_{x}(OH)_2]^{x+}A^{n-}_{x/n}.mH_2O$ (M^{2+} = Mg, Mn, Fe, Zn, Co, Cu & Ni, M^{3+} = Al, Cr, Fe & Ga),[59, 61] a schematic representation is shown in Figure 18(b). The now cationic layers are charge balanced by interlayer anions and stack together via hydrogen bonding interactions between the interlayer anion and water molecules, which are also found in the interlayer gallery, with the hydroxide groups present within the layer. Materials of this kind are found to have vast compositional flexibility due to the different metals and intercalated anions which can be incorporated. The charge balancing anions can be either inorganic or organic such as carbonate, nitrate, sulfate, halides, and polyoxometalate anions and also functionalized organic molecules e.g. amino acids.

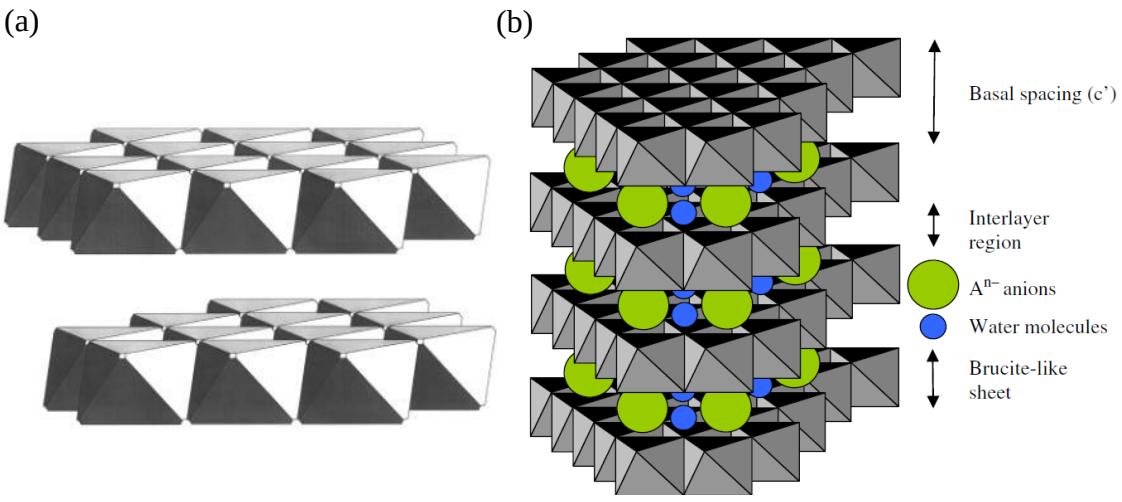

Figure 18 (a) The layer structure of brucite[62] and (b) Schematic representation of the layered double hydroxide structure.[63]

Layered double hydroxides are a well known class of materials which undergo anion exchange quite freely, by substitution of interlayer anions with either inorganic or organic anions, due to the flexibility of the interlayer region and also the nature of the interactions of the counterbalancing anions with the layers. This allows materials of this type to be applied to a diverse range of fields for example in pharmaceuticals,[64, 65, 66] catalysis[67, 68] and separation technologies.[69, 70, 71, 72]

Studies of the intercalation and controlled release of pharmaceutically active compounds, which takes advantage of LDHs biocompatibility, variable chemical composition and also their ability to intercalate anionic drugs, is an area of recent interest for LDHs.[73] Khan *et al*., have successfully intercalated pharmaceutically active compounds into the host material $[LiAl_2(OH)_6]Cl.H_2O$, by exchanging the charge balancing chloride anions with pharmaceutically active compounds including diclofenac, gemfibrozil, ibuprofen, naproxen, 2-propylpentanoic acid, 4-biphenylacetic acid and tolfenamic acid. De-intercalation of the drugs was achieved by placing the intercalated phase into a phosphate buffer solution, showing the use of LDHs as a feasible approach for the storage and controlled release of bioactive agents.[64]

In the area of separation technologies Millange *et al.*, has shown the layered double hydroxide $[Ca_2Al(OH)_6]NO_3.2H_2O$, to be an efficient host in the selective intercalation of terephthalate and phthalate anions. Time resolved *in-situ* energy dispersive X-ray diffraction studies of the competitive exchange reaction showed initially both 1,2- and 1,4-benzenedicarboxylates to intercalate into the host material followed by replacement of the 1,2- isomer with 1,4- as the reaction proceeds to give a final product of $[Ca_2Al(OH)_6][1,4\text{-}C_8H_4O_4]_{0.5}.xH_2O$. This anion exchange reaction is found to be useful as benzendicarboxylates are important starting materials in the synthesis of polyester polymers, therefore the possibility of the separation of these geometric isomers would be advantageous.[70]

1.5.2 Layered Rare-Earth Hydroxides

Layered rare-earth hydroxides, (LRHs) can be split into two sub-classes of lanthanide hydroxyhalides and lanthanide hydroxynitrates. These compounds consist of positively charged layers with charge balancing halide or nitrate anions located

within the interlayer gallery. These materials may be formed with halide anions such as chloride and bromide and have been recently reported with the general composition $Ln_2(OH)_5X.1.5H_2O$ (Ln = Y, Dy, Er and Yb, X = Cl, Br). These materials show facile anion exchange with organodicarboxylates.[74] Anhydrous lanthanide hydroxychloride materials have also been previously formed with the composition $Ln(OH)_2Cl$ (Ln = Y, Pr, Nd, Sm or Gd),[75, 76, 77] although in these phases the chloride anion is found to be bound to the lanthanide centre. Anion exchange for the anhydrous phases has not been performed.

Lanthanide hydroxynitrates have a general formula of $Ln_2(OH)_{6-m}(NO_3)_m.mH_2O$. In these materials, where m = 1, the nitrate anions are found to reside in the interlayer gallery balancing the charge associated with the layers. The use of smaller lanthanides allows the formation of lanthanide hydroxynitrates, m = 1, such as $Ln_2(OH)_5(NO_3).xH_2O$ (Ln = Y, Gd- Lu, $x \approx 1$ or 1.5).[78, 79] This phase shows successful anion exchange with a variety of organic carboxylate and sulfonate anions; some examples include succinate, suberate and 2,6-naphthalenedisulfonate leading to an elemental composition of $Ln_2(OH)_5(A)_{0.5}.xH_2O$ ($x \approx 1$, 1.5).[79] Larger lanthanides are found to form phases, m = 2, with a general composition of $Ln(OH)_2(NO_3).xH_2O$ (Ln = La, Pr, Nd and Gd, x = 0 or 1).[80,81,82,83] In these materials the nitrate anion is bound to the lanthanide centre. The La phase is able to successfully anion exchange with carboxylates such as acetate, benzoate and terephthalate, although the anion exchange proves harder than in the above materials, containing non-coordinating nitrate anions, as prolonged heating is needed at 65 °C for one week.[84] The incorporation of lanthanides within these hydroxyhalide and hydroxynitrate materials allows the added bonus of applications for use in catalysis and luminescence.

Gandara *et al.*, reported a lanthanide phase in which the interlayer anions, other than nitrate or halides, were incorporated during the synthesis. This phase has the composition of $[Ln_4(OH)_{10}(H_2O)_4]A$ (Ln = Y, Dy, Ho or Yb, A = 2,6-naphthalenedisulfonate or 2,6-anthraquinonedisulfonate)[85] and consists of $[Ln_4(OH)_{10}(H_2O)_4]^{2+}$ cationic layers of eight and nine coordinate lanthanide cations which are linked through hydroxyl groups, with each lanthanide cation having one water molecule coordinated, Figure 19. The cationic layers are charge balanced by the disulfonate anions forming a two-dimensional layered structure. This material

proves interesting due to the properties of the anion and the lanthanide being incorporated into one material. The phase containing Yb and 2,6-anthraquinonedisulfonate is found to be an effective catalyst for the hydrodesulfurization of thiophene under mild conditions.

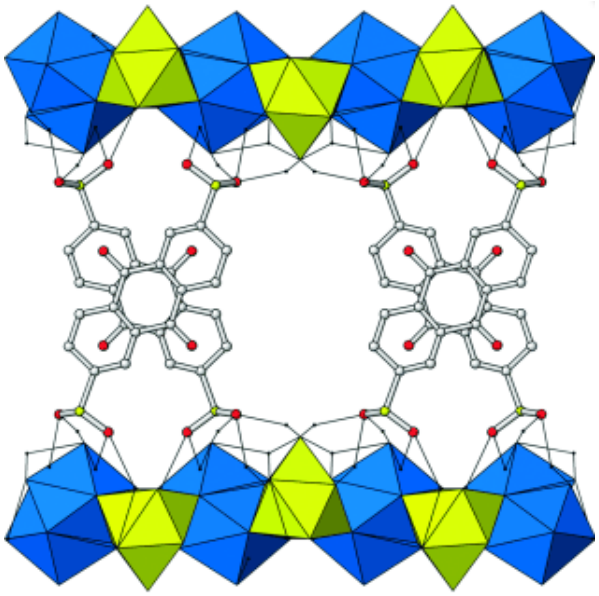

Figure 19 Crystal structure of $[Yb_4(OH)_{10}(H_2O)_4][2,6\text{-AQDS}]$[85]
(Colour key; blue - $Yb(OH)_7H_2O$, green - $Yb(OH)_6H_2O$)

1.5.3 Cationic Structures based on Francisite

The mineral francisite, $Cu_3BiSeO_8[Cl^-]$, shown in Figure 20, was first discovered in 1990 at Iron Monarch, South Australia, where Pring *et al*., described its structure.[86] The structure of this copper bismuth oxy-chloro selenite was firstly thought to be a three-dimensional framework, although long metal-oxygen contacts along one crystallographic plane deemed the structure to be a two-dimensional cationic framework.[59, 87] This structure comprises of eight-coordinate Bi^{3+}, four coordinate Cu^{2+} and three coordinate Se^{4+} ions. Chloride ions and the lone pair of electrons of Se occupy the channels within the framework.

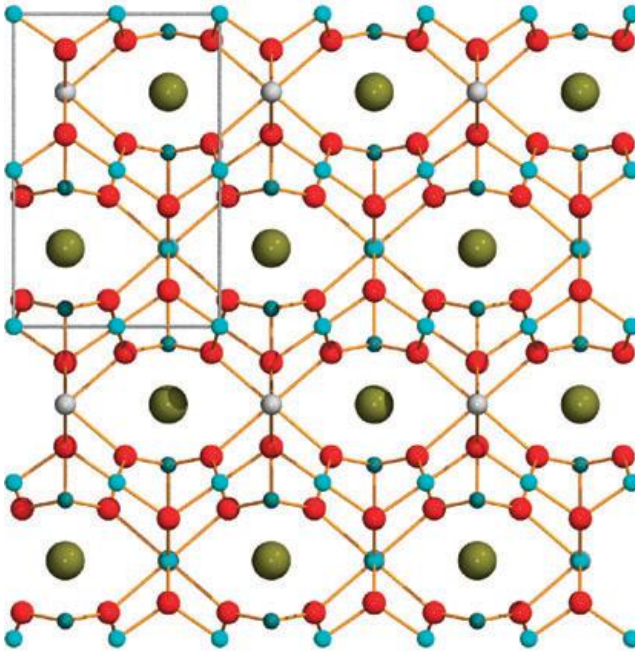

Figure 20 Crystal structure of Francisite, $Cu_3BiSe_2O_8[X^-]$ (X^- = halide, Colour key; Cu – blue, Bi – grey, Se – dark blue, O – red and halide – gold).[59]

Synthetic analogues of francisite, $Cu_3BiSe_2O_8[X^-]$ (X^- = Cl, Br and I), have recently been reported. Each phase, incorporating different halides, is found to be iso-structural to one another forming a two-dimensional cationic framework. The structure consists of layers of Cu(II)-O connections which are linked together by Bi(III)-O bonds. The Bi-O bond lengths are found to increase when substituting Cl^- with the larger halides of Br^- and I^-. The Se atoms are three-fold coordinate to three Cu-O square planes of the same Cu-O layer.[87] X^- reside within the channels and are discovered to be truly extra-framework as they do not covalently bind to any of the framework metal atoms. Anion exchange of these materials has not been investigated.

Using alternative metals such as Nb, Ta and Te[88] has allowed iso-structural analogues with the same overall three-dimensional channel topology of francisite to be formed with the composition $Te_4M_3O_{15}Cl$ (M = Ta^{5+} or Nb^{5+}), Figure 21. These analogues have been synthesised by Ok *et al.*, and are found to have a three-dimensional structure consisting of MO_6 octahedra linked to TeO_3 polyhedra. Charge balancing chloride anions reside in the centre of the positively charged channels, which are formed by eight membered rings of MO_6 octahedra and TeO_3 polyhedra,

with the rings being connected through corner linked MO_6 octahedra in turn forming cationic channels. Anion exchange reactions have been performed on these materials although it has been discovered that exchange of the chloride anions proved difficult. This is thought to be due to the lone pairs present on Te^{4+} which point into the channels where the chloride anions reside and prevent any mobility of the anion thus the chloride anions are locked into place within the channels so exchange is unlikely to occur.[88]

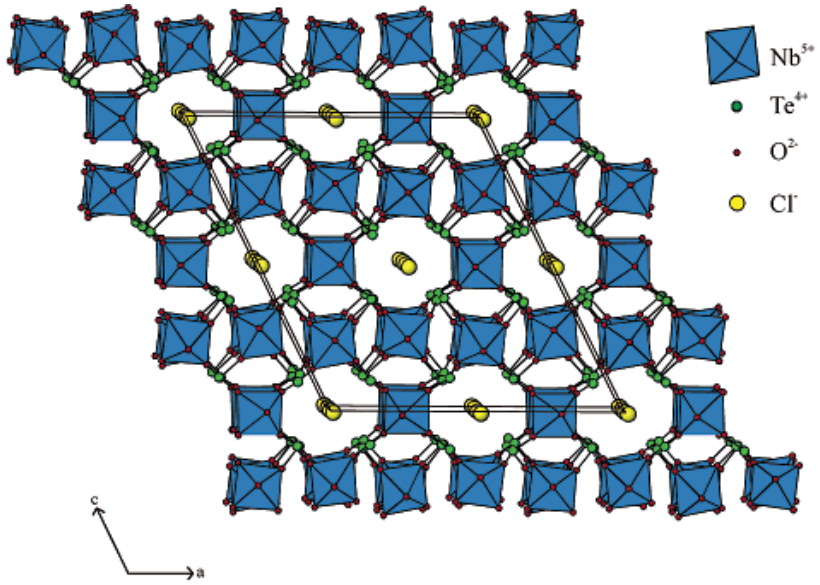

Figure 21 Crystal structure of $Te_4Nb_3O_{15}Cl$.[88]

1.5.4 Cationic Structures Based on Heavy p-block Elements

Cationic inorganic layers are known for heavy p-block elements with examples including $[Pb_3F_5][NO_3]$ (BING-5),[59] shown in Figure 22(a), consisting of three-dimensional cationic layers of lead fluoride, $[Pb_3F_5]^+$, and charge balancing nitrates residing in the interlamellar region. The layers consist of an inner neutral layer which is capped by two outer, Pb_2F_3, cationic layers. The lead centres are eight coordinate in the neutral centre layer and five coordinate in the outer cationic layers. The nitrate anions interact with the lead centres in the outer cationic layers via their oxygen atoms. The nitrate anions charge balance and also fill the empty space within the structure in turn stabilising the structure. The properties of this material include anion

exchange where the interlamellar anions have been successfully exchanged with dichromate anions.[89]

Another example is that of $[Sb_4O_4(OH)_2][O_3S(CH_2)_2SO_3].H_2O$ (SLUG-5)[90], shown in Figure 22(b), as synthesised by Swanson *et al*. This phase is defined as a two-dimensional antimony oxide hydroxide templated by the anion ethanedisulfonate.[59] The layers consist of Sb-O-Sb covalent bonds of pyramidal SbO_3 units whereby a free electron pair is pointed into the lamellar region. 1,2-ethanedisulfonate anions, reside in the interlayer gallery and balance the charge associated with the cationic layers via electrostatic bonding interactions. This allows the formation of a two-dimensional cationic material. Water is located in the channels between the charge balancing ethanedisulfonate anions. This material is found to be a good heterogeneous catalyst, for the formation of a ketal from a ketone. This reaction was tested by reacting 2-butanone with 1,2-ethanediol to produce 2-ethyl-2-methyl-[1,3]-dioxolane, showing a conversion of 53% of 2-butanone.[90]

Using ethanedisulfonate as a linker also allowed the discovery of a three-dimensional metal-organic framework of $[Pb_2F_2][O_3S(CH_2)_2SO_3]$ (SLUG-6), shown in Figure 22(c). The cationic layers present in this framework are found to be embedded within the structure therefore this phase is deemed a metal-organic framework. The layer topology is $[Pb_2F_2SO_4]$ with the layers directly bonded together through Pb-O-Pb bonds.[59]

Currently Oliver *et al*. are studying the effect of the template shape, i.e. controlling the shape and also size of the R group within sulfonates in the hope to discover new three-dimensional cationic materials of composition $[Pb_2F_2][O_3S\mathbf{R}SO_3]$ (SLUG-11).[59]

(a) (b) (c)

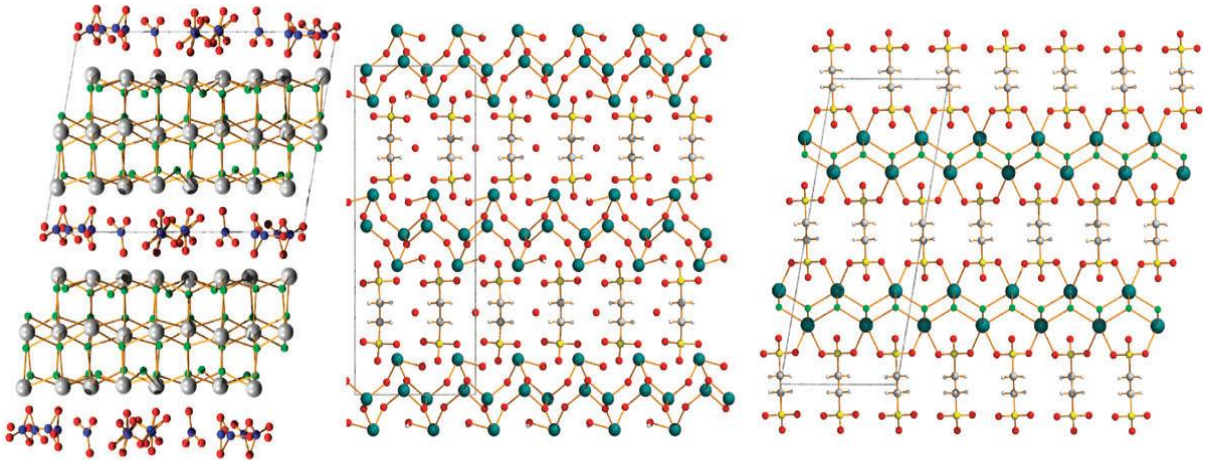

Figure 22 Crystal structure of (a) $[Pb_3F_5]^+[NO_3]^-$ (BING-5) (Colour key; Pb – grey, F – green, N – blue and O- red)[59] (b) $[Sb_4O_4(OH)_2]^{2+}[O_3S(CH_2)_2SO_3]^{2-}.H_2O$ (SLUG-5) (Colour key; Sb – green-blue, S – yellow, C – grey, O- red and H - white)[90] and (c) $[Pb_2F_2]^{2+}[O_3S(CH_2)_2SO_3]^{2-}$(SLUG-6) (Colour key; Pb – green-blue, F- green, S – yellow, C – grey, O- red and H - white).[59]

1.5.5 Cationic Metal and Lanthanide-Organic Frameworks

Most metal and lanthanide organic frameworks are found to be neutral or anionic although there are known examples of MOFs with a cationic framework[91, 92, 93] whereby the positive charge associated with the metal ion outweighs any negative charge on the organic linker. The resulting net positive charge is balanced by charge balancing extra framework anions, which reside in either the channels or pockets present in the structure. Some examples include Ag_2(4,4'-bipy)$_2$($O_3SCH_2CH_2SO_3$)$_2$.$4H_2O$ (SLUG-21),[94] shown in Figure 23, and Cu_2(4,4'-bipy)$_2$($O_3SCH_2CH_2SO_3$)$_2$.$3H_2O$ (SLUG-22).[95] These structures consist of 4,4'-bipyridine linkers and 1,2-ethanedisulfonate as the charge balancing template, these features along with the metal ion forms a one-dimensional cationic MOF. Infinite chains of metal centres and 4,4'-bipyridine organic linkers interact through π-π stacking between adjacent chains. The alkane disulfonate anions reside in the interlayer gallery, balancing the layers, and weakly interact with them through one

sulfonate oxygen. The remaining oxygen atoms on the sulfonate group are involved in a hydrogen bonding network with interlamellar waters.

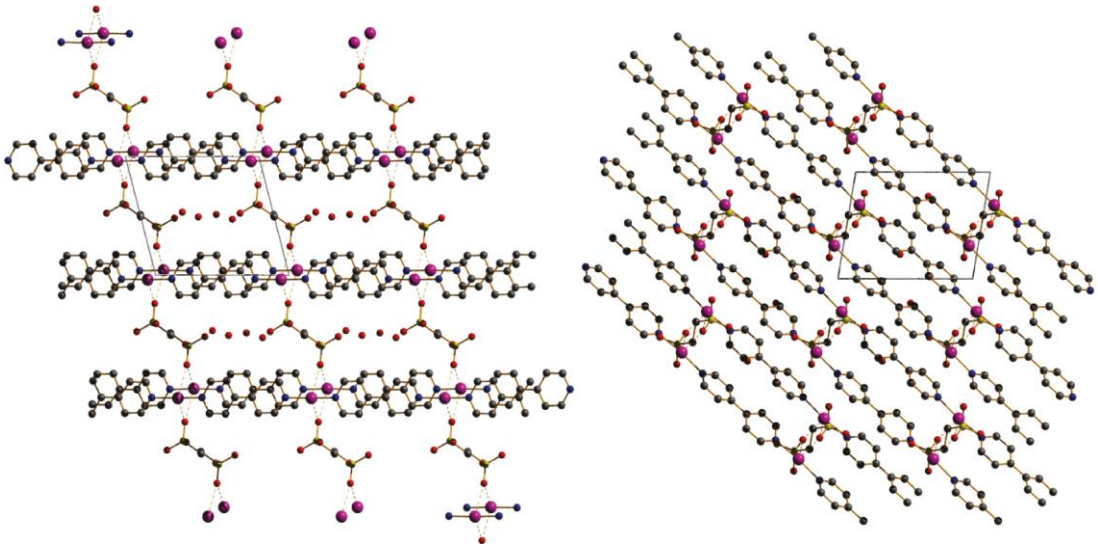

Figure 23 Crystal structure of $Ag_2(4,4'\text{-bipy})_2(O_3SCH_2CH_2SO_3)_2.4H_2O$ (SLUG-21), view along (a) the *a* axis and (b) view along the *b* axis. Hydrogen atoms have been omitted for clarity (Colour key; Ag – purple, C – grey, S – yellow, O – red and N – blue)[94]

Both materials show reversible anion exchange behaviour between the organosulfonate and a variety of inorganic species. SLUG-21 is able to reversibly exchange the ethanedisulfonate anions with NO_3^-, MnO_4^- and ReO_4^-, which is a model for pertechnetate; a radioactive pollutant.[96] SLUG-22 is able to reversibly exchange the ethanedisulfonate anions with NO_3^- and ClO_4^-.[95]

SLUG-21 and SLUG-22 also have the added advantage of being strongly active and reusable catalysts in the formation of a ketal between 2-butanone and ethylene glycol.[94, 95] Ketalisation of aldehydes and ketones is important for the protection of carbonyl groups in preparative organic synthesis and drug design.[97]

Lanthanide organic cationic coordination polymers are also known such as $[Ln(H_2O)_4(PDC)]_4[XMo_{12}O_{40}].2H_2O$ (Ln = La, Ce or Nd, X = Si or Ge, and PDC = pyridine-2,6-dicarboxylate), shown in Figure 24.[98] This structure comprises of a four-connected three-dimensional framework of $[Ln(H_2O)_4(PDC)]_4^{4+}$ cations and

non-coordinated $[XMo_{12}O_{40}]^{4-}$ ball shaped keggin type anionic templates. The keggin type template has a central tetrahedral XO_4 (X = Si or Ge) unit surrounded by 12 MoO_6 octahedra units, which themselves are arranged in four groups of three edge-sharing octahedral subunits of Mo_3O_{13}. The nine-coordinate lanthanide centres are linked by the carboxylate groups of four pyridinedicarboxylate ligands to form the tetranuclear cyclic unit $[Ln(H_2O)_4(PDC)]_4^{4+}$. Two of these Ln_4 clusters chelate the $[XMo_{12}O_{40}]^{4-}$ templates via hydrogen bonding interactions overall forming a three-dimensional framework.

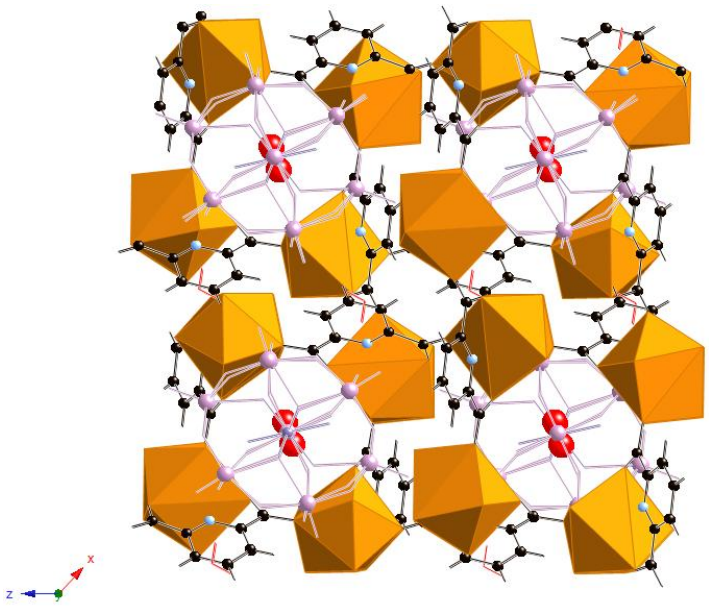

Figure 24 Crystal structure of $[Nd(H_2O)_4(PDC)]_4[GeMo_{12}O_{40}].2H_2O$ (PDC = pyridine-2,6-dicarboxylate).[98]

A new and novel cationic material containing lanthanide ions has been recently reported. This material is a pillared lanthanide molybdate framework which has a composition of $[Ln(H_2O)MoO_4]_2[\lambda\text{-}Mo_2O_4EDTA]$ (Ln=Y, Eu, Gd, or Tb), shown in Figure 25. This structure consists of cationic two-dimensional layers which are pillared by covalently bound anions in turn forming a three-dimensional framework.[99] This material will be discussed further in the introduction to Chapter 2.

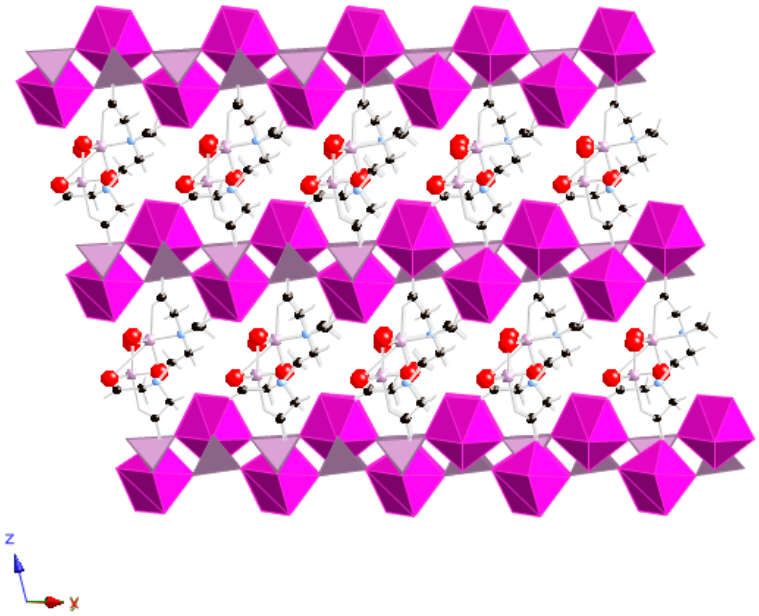

Figure 25 Crystal structure of $[Eu(H_2O)MoO_4]_2[\lambda\text{-}Mo_2O_4EDTA]$ (Ln=Y, Gd, & Tb).[99]

To date only three cationic inorganic three-dimensional frameworks are known, with only two of the structures capable of anion exchange. Two are Yb oxyhydroxide phases with compositions of $Yb_3O(OH)_6Cl.2H_2O$[100] shown in Figure 26(a), and $Yb_4O(OH)_9NO_3$[101] shown in Figure 26(b). Both phases consist of a three-dimensional cationic Ytterbium oxyhydroxide framework which is based on oxide centered Yb_4 tetrahedra which are linked together by bridging hydroxide anions to form a cationic framework. One-dimensional channels run through both structures in which chloride anions and water or nitrate anions are located.

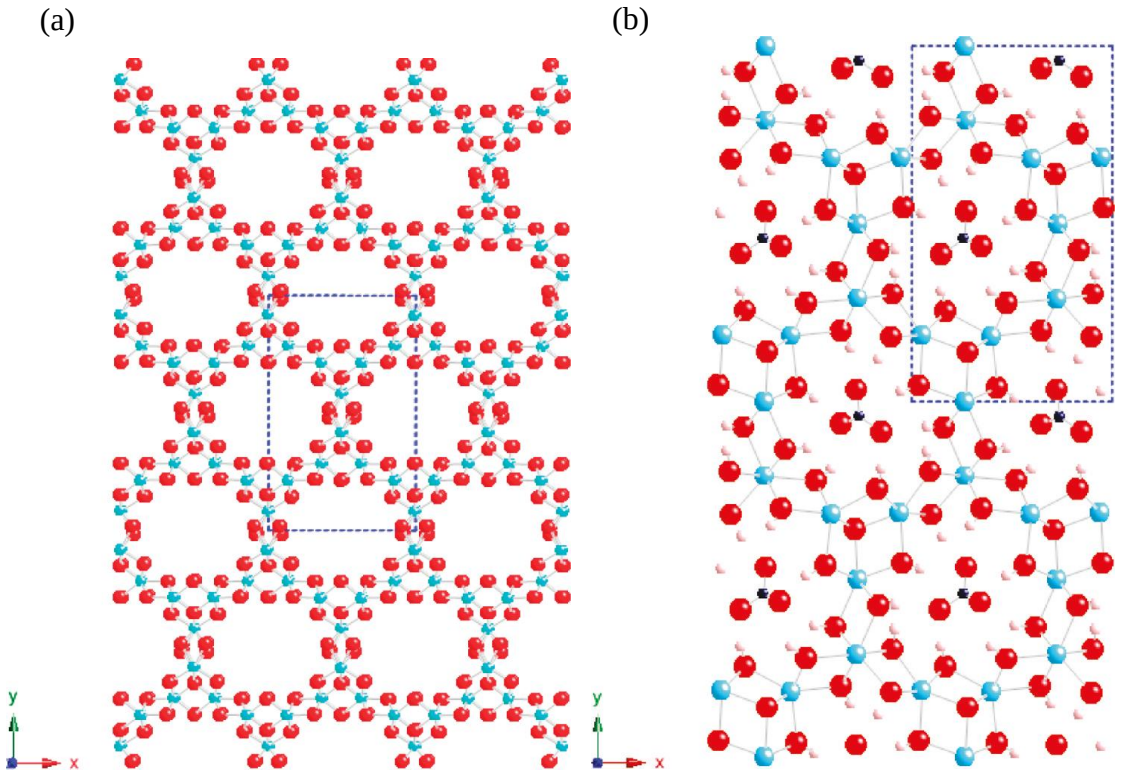

Figure 26 Crystal structures of (a) $Yb_3O(OH)_6Cl.2H_2O$. The Cl^- and water molecules are found to reside in the channels but have been omitted for clarity[100] and (b) $Yb_4O(OH)_9NO_3$, nitrate anions are located within the channels.[101] (Colour key; Yb – blue, O – red, N – dark blue, H – pink)

The third cationic inorganic framework is of a thorium borate phase, $[ThB_5O_6(OH_6)][BO(OH)_2].2.5H_2O$ (NDTB-1)[102] shown in Figure 27, which consists of a three-dimensional cationic thorium borate framework with one dimensional channels running through the structure in which borate anions are found to reside. These phases will be discussed in depth within the introduction to Chapter 5, with two of the phases, $Yb_3O(OH)_6Cl.2H_2O$ and $[ThB_5O_6(OH_6)][BO(OH)_2].2.5H_2O$, having potential applications in anion exchange.

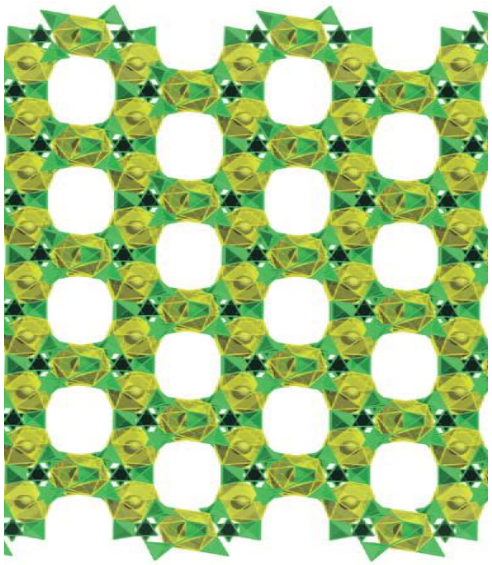

Figure 27 Crystal structure of $[ThB_5O_6(OH_6)][BO(OH)_2].2.5H_2O$ (NDTB-1), borate, BO_3, anions and water reside within the channels and have been omitted for clarity[102]

1.6 Hydrothermal Synthesis

Hydrothermal synthesis is found to be a powerful technique for the preparation of crystalline inorganic-organic hybrid materials due to water having reduced viscosity under hydrothermal conditions. Typically reactions using this technique are carried out in the temperature range of 100 – 260 °C. The reduced viscosity of water under these conditions enhances diffusion processes so that crystal growth from solution is favoured allowing retention of the structural elements of the reactants in the final product.[103] The autoclave is a thick walled sealed steel reaction vessel with a Teflon-lined insert in which the temperature of the reaction media is able to increase above the boiling point of the solvent used. A schematic of a Teflon-lined autoclave is shown in Figure 28. Under these conditions autogenous pressure is developed, whereby the pressure within the reaction vessel is self-developed and not externally applied, allowing the formation of new products which may not necessarily be able to be produced under other reaction techniques such as high temperature solid state reactions. The pressure within the reaction vessel increases dramatically with increasing temperature although is dependent on the fill of the vessel and also the

amount of reagents used within the reaction.[104] The increased pressure and temperature allows the dissolution of reagents which would otherwise be insoluble under ambient conditions.[105] Other solvents are able to be utilized within this reaction technique changing the synthesis to solvothermal synthesis. The hydrothermal and solvothermal techniques have been utilized to synthesise new materials, for the development of new processes for the preparation of new functional materials and also in the shaping of new materials i.e. crystal growth.[106] There are advantages of the hydrothermal technique such as the ability to synthesise large stable crystals and also to have good control over their compositions, although a major disadvantage would be that it may be impossible to watch the crystal growth. However it is possible to deduce the mechanism of formation of crystalline phases produced via the use of the *in-situ* energy dispersive X-ray diffraction technique.[107]

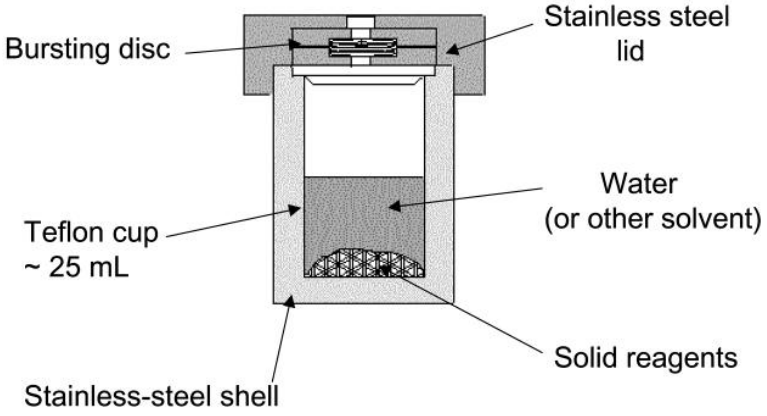

Figure 28 Teflon-lined stainless steel autoclave used for hydrothermal synthesis.[104]

1.7 Aims

The key aim of this thesis is to use exploratory hydrothermal synthesis in order to synthesise new three-dimensional cationic hybrid materials. The combination of lanthanide cations, along with tetrahedral anionic building blocks and also anionic organic linkers, which themselves can act as templates, will hopefully allow the formation of hybrid frameworks.

The inclusion of lanthanides in conjunction with organic compounds into these materials will allow the properties of both components to be expressed in a single material therefore allowing enhancement of the potential applications such as use in catalysis, gas storage, anion exchange and also luminescence.

As discussed, the formation of three-dimensional cationic materials is rare, therefore formation of these materials will allow for potentially new and novel structures to be generated.

Use of the hydrothermal technique for synthesising these materials will allow the dissolution of reagents, which may otherwise be insoluble under ambient conditions, and also potentially allow the formation of crystalline phases in which their structures may be determined by single crystal X-ray diffraction.

The synthesis, characterisation and potential applications of phases synthesised will be discussed within this thesis.

1.8 References

(1) Rowsell, J. L. C.; Yaghi, O. M. *Microporous Mesoporous Mat.* **2004**, *73*, 3.

(2) Cheetham, A. K.; Rao, C. N. R.; Feller, R. K. *Chem. Commun.* **2006**, 4780.

(3) Forster, P. M.; Cheetham, A. K. *Top. Catal.* **2003**, *24*, 79.

(4) Rao, C. N. R.; Cheetham, A. K.; Thirumurugan, A. *J. Phys.-Condes. Matter* **2008**, *20*.

(5) Jose, N. M.; Prado, L. *Quim. Nova* **2005**, *28*, 281.

(6) James, S. L. *Chem. Soc. Rev.* **2003**, *32*, 276.

(7) Kitagawa, S.; Kitaura, R.; Noro, S. *Angew. Chem.-Int. Edit.* **2004**, *43*, 2334.

(8) Noro, S.; Kitagawa, S.; Akutagawa, T.; Nakamura, T. *Prog. Polym. Sci.* **2009**, *34*, 240.

(9) Fu, A. H.; Lu, J. Y.; Huang, X. Y.; Li, J. *J. Alloy. Compd.* **2001**, *319*, 89.

(10) Huh, H. S.; Min, D.; Lee, Y. K.; Lee, S. W. *Bull. Korean Chem. Soc.* **2002**, *23*, 619.

(11) Zhang, L. Z.; Cheng, P.; Shi, W.; Liao, D. Z.; Xiong, Y.; Tang, G. Q. *Inorg. Chem. Commun.* **2002**, *5*, 361.

(12) Min, D. W.; Yoon, S. S.; Lee, S. W. *Inorg. Chem. Commun.* **2002**, *5*, 143.

(13) Guo, J. Y.; Zhang, T. L.; Zhang, J. G. *Chin. J. Chem.* **2006**, *24*, 745.

(14) Prior, T. J.; Rosseinsky, M. J. *Chem. Commun.* **2001**, 495.

(15) Batten, S. R. *Curr. Opin. Solid State Mat. Sci.* **2001**, *5*, 107.

(16) Robin, A. Y.; Fromm, K. M. *Coord. Chem. Rev.* **2006**, *250*, 2127.

(17) Noro, S.; Kitaura, R.; Kondo, M.; Kitagawa, S.; Ishii, T.; Matsuzaka, H.; Yamashita, M. *J. Am. Chem. Soc.* **2002**, *124*, 2568.

(18) Wang, Z. Q.; Cohen, S. M. *Chem. Soc. Rev.* **2009**, *38*, 1315.

(19) Yaghi, O. M.; O'Keeffe, M.; Ockwig, N. W.; Chae, H. K.; Eddaoudi, M.; Kim, J. *Nature* **2003**, *423*, 705.

(20) Perry, J. J.; Perman, J. A.; Zaworotko, M. J. *Chem. Soc. Rev.* **2009**, *38*, 1400.

(21) Eddaoudi, M.; Kim, J.; Rosi, N.; Vodak, D.; Wachter, J.; O'Keeffe, M.; Yaghi, O. M. *Science* **2002**, *295*, 469.

(22) Czaja, A. U.; Trukhan, N.; Muller, U. *Chem. Soc. Rev.* **2009**, *38*, 1284.

(23) Tanabe, K. K.; Cohen, S. M. *Chem. Soc. Rev.* **2011**, *40*, 498.

(24) Natarajan, S.; Mahata, P. *Curr. Opin. Solid State Mat. Sci.* **2009**, *13*, 46.

(25) Tran, D. T.; Chernova, N. A.; Chu, D.; Oliver, A. G.; Oliver, S. R. J. *Cryst. Growth Des.* **2010**, *10*, 874.

(26) Forster, P. M.; Stock, N.; Cheetham, A. K. *Angew. Chem.-Int. Edit.* **2005**, *44*, 7608.

(27) Stock, N.; Bein, T. *J. Mater. Chem.* **2005**, *15*, 1384.

(28) Forster, P. M.; Burbank, A. R.; Livage, C.; Ferey, G.; Cheetham, A. K. *Chem. Commun.* **2004**, 368.

(29) Livage, C.; Egger, C.; Ferey, G. *Chem. Mat.* **2001**, *13*, 410.

(30) Kuppler, R. J.; Timmons, D. J.; Fang, Q. R.; Li, J. R.; Makal, T. A.; Young, M. D.; Yuan, D. Q.; Zhao, D.; Zhuang, W. J.; Zhou, H. C. *Coord. Chem. Rev.* **2009**, *253*, 3042.

(31) Isaeva, V. I.; Kustov, L. M. *Pet. Chem.* **2010**, *50*, 167.

(32) He, H., Yuan, D. *Inorg. Chem. Commun.* **2010**, *49*, 7605

(33) Rosseinsky, M. J. *Microporous Mesoporous Mat.* **2004**, *73*, 15.

(34) Li, H.; Eddaoudi, M.; O'Keeffe, M.; Yaghi, O. M. *Nature* **1999**, *402*, 276.

(35) Eddaoudi, M.; Li, H. L.; Yaghi, O. M. *J. Am. Chem. Soc.* **2000**, *122*, 1391.

(36) Noro, S.; Kitagawa, S.; Kondo, M.; Seki, K. *Angew. Chem.-Int. Edit.* **2000**, *39*, 2082.

(37) Seki, K. *Chem. Commun.* **2001**, 1496.

(38) Chae, H. K.; Siberio-Perez, D. Y.; Kim, J.; Go, Y.; Eddaoudi, M.; Matzger, A. J.; O'Keeffe, M.; Yaghi, O. M. *Nature* **2004**, *427*, 523.

(39) Chui, S. S. Y.; Lo, S. M. F.; Charmant, J. P. H.; Orpen, A. G.; Williams, I. D. *Science* **1999**, *283*, 1148.

(40) Jiang, D., Mallat, T., Krumeich, F., and Baike, A. *Journal of Catalysis* **2008**, *257*, 390

(41) Barluenga, J.; Vazquez-Villa, H.; Ballesteros, A.; Gonzalez, J. M. *Org. Lett.* **2002**, *4*, 2817.

(42) Hwang, Y., Hong, H-Y., Chang, J-S., Jhung, S., Seo, Y.K., Kim, J., Vimont, A., Dautri, M., Serre, C. and Ferey, G. *Angewandte Chemie* **2008**, *120*, 4212.

(43) Ferey, G.; Mellot-Draznieks, C.; Serre, C.; Millange, F.; Dutour, J.; Surble, S.; Margiolaki, I. *Science* **2005**, *309*, 2040.

(44) Hill, R. J.; Long, D. L.; Hubberstey, P.; Schroder, M.; Champness, N. R. *J. Solid State Chem.* **2005**, *178*, 2414.

(45) Daiguebonne, C.; Kerbellec, N.; Bernot, K.; Gerault, Y.; Deluzet, A.; Guillou, O. *Inorg. Chem.* **2006**, *45*, 5399.

(46) Pan, L.; Woodlock, E. B.; Wang, X. T.; Zheng, C. *Inorg. Chem.* **2000**, *39*, 4174.

(47) Millange, F.; Serre, C.; Marrot, J.; Gardant, N.; Pelle, F.; Ferey, G. *J. Mater. Chem.* **2004**, *14*, 642.

(48) Serpaggi, F.; Ferey, G. *J. Mater. Chem.* **1998**, *8*, 2737.

(49) Serpaggi, F.; Ferey, G. *Microporous Mesoporous Mat.* **1999**, *32*, 311.

(50) Serpaggi, F.; Ferey, G. *Inorg. Chem.* **1999**, *38*, 4741.

(51) Li, J. T.; Zheng, L. M. *Inorg. Chim. Acta* **2009**, *362*, 1739.

(52) Snejko, N.; Cascales, C.; Gomez-Lor, B.; Gutierrez-Puebla, E.; Iglesias, M.; Ruiz-Valero, C.; Monge, M. A. *Chem. Commun.* **2002**, 1366.

(53) Gandara, F.; Garcia-Cortes, A.; Cascales, C.; Gomez-Lor, B.; Gutierrez-Puebla, E.; Iglesias, M.; Monge, A.; Snejko, N. *Inorg. Chem.* **2007**, *46*, 3475.

(54) Reineke, T. M.; Eddaoudi, M.; O'Keeffe, M.; Yaghi, O. M. *Angew. Chem.-Int. Edit.* **1999**, *38*, 2590.

(55) Wang, G.; Song, T. Y.; Fan, Y.; Xu, J. N.; Wang, M.; Wang, L. P.; Zhang, L. R.; Wang, L. *Inorg. Chem. Commun.* **2010**, *13*, 95.

(56) Harrison, W. T. A.; Nenoff, T. M.; Gier, T. E.; Stucky, G. D. *Inorg. Chem.* **1992**, *31*, 5395.

(57) Guillou, N.; Livage, C.; van Beek, W.; Nogues, M.; Ferey, G. *Angew. Chem.-Int. Edit.* **2003**, *42*, 644.

(58) Feller, R. K.; Cheetham, A. K. *Solid State Sci.* **2006**, *8*, 1121.

(59) Oliver, S. R. J. *Chem. Soc. Rev.* **2009**, *38*, 1868.

(60) Evans, D. G.; Slade, R. C. T. In *Layered Double Hydroxides*; Duan, X., Evans, D. G., Eds.; Springer-Verlag Berlin: Berlin, 2006; Vol. 119.

(61) Cavani, F.; Trifiro, F.; Vaccari, A. *Catal. Today* **1991**, *11*, 173.

(62) Rajamathi, M.; Thomas, G. S.; Kamath, P. V. *Proc. Indian Acad. Sci.-Chem. Sci.* **2001**, *113*, 671.

(63) Goh, K. H.; Lim, T. T.; Dong, Z. *Water Res.* **2008**, *42*, 1343.

(64) Khan, A. I.; Lei, L. X.; Norquist, A. J.; O'Hare, D. *Chem. Commun.* **2001**, 2342.

(65) Li, B. X.; He, J.; Evans, D. G.; Duan, X. *Int. J. Pharm.* **2004**, *287*, 89.

(66) Nalawade, P.; Aware, B.; Kadam, V. J.; Hirlekar, R. S. *J. Sci. Ind. Res.* **2009**, *68*, 267.

(67) Sels, B.; De Vos, D.; Buntinx, M.; Pierard, F.; Kirsch-De Mesmaeker, A.; Jacobs, P. *Nature* **1999**, *400*, 855.

(68) Kwon, T.; Pinnavaia, T. J. *Journal of Molecular Catalysis* **1992**, *74*, 23.

(69) Li, L.; Zhang, N.; Liu, S. J.; Chen, D. Z. *J. Phys. Chem. Solids* **2005**, *66*, 1844.

(70) Millange, F.; Walton, R. I.; Lei, L. X.; O'Hare, D. *Chem. Mat.* **2000**, *12*, 1990.

(71) Fogg, A. M.; Dunn, J. S.; Shyu, S. G.; Cary, D. R.; O'Hare, D. *Chem. Mat.* **1998**, *10*, 351.

(72) Williams, G. R.; Dunbar, T. G.; Beer, A. J.; Fogg, A. M.; O'Hare, D. *J. Mater. Chem.* **2006**, *16*, 1231.

(73) Li, F., Duan, X. *in Layered double hydroxides*; Springer: Berlin, 2006.

(74) Poudret, L.; Prior, T. J.; McIntyre, L. J.; Fogg, A. M. *Chem. Mat.* **2008**, *20*, 7447.

(75) Klevtsova, R. F., Klevtsov, P. V. *J. Struct. Chem* **1966**, *7*, 524.

(76) Klevtsova, R. F., Glinskaya, L. A. *J. Struct. Chem* **1969**, *10*, 408.

(77) Bukin, V. I. *Doklady Akademii Nauk Sssr* **1972**, *207*, 1332.

(78) McIntyre, L. J.; Jackson, L. K.; Fogg, A. M. *J. Phys. Chem. Solids* **2008**, *69*, 1070.

(79) McIntyre, L. J.; Jackson, L. K.; Fogg, A. M. *Chem. Mat.* **2008**, *20*, 335.

(80) Louer, D.; Louer, M. *J. Solid State Chem.* **1987**, *68*, 292.

(81) Lundberg, M.; Skarnulis, A. J. *Acta Crystallogr. Sect. B-Struct. Commun.* **1976**, *32*, 2944.

(82) Louer, M.; Louer, D.; Delgado, A. L.; Martinez, O. G. *Eur. J. Solid State Inorg. Chem.* **1989**, *26*, 241.

(83) Mullica, D. F.; Sappenfield, E. L.; Grossie, D. A. *J. Solid State Chem.* **1986**, *63*, 231.

(84) Newman, S. P.; Jones, W. *J. Solid State Chem.* **1999**, *148*, 26.

(85) Gandara, F.; Perles, J.; Snejko, N.; Iglesias, M.; Gomez-Lor, B.; Gutierrez-Puebla, E.; Monge, M. A. *Angew. Chem.-Int. Edit.* **2006**, *45*, 7998.

(86) Pring, A.; Gatehouse, B. M.; Birch, W. D. *Am. Miner.* **1990**, *75*, 1421.

(87) Millet, P.; Bastide, B.; Pashchenko, V.; Gnatchenko, S.; Gapon, V.; Ksari, Y.; Stepanov, A. *J. Mater. Chem.* **2001**, *11*, 1152.

(88) Ok, K. M.; Halasyamani, P. S. *Inorg. Chem.* **2002**, *41*, 3805.

(89) Tran, D. T.; Zavalij, P. Y.; Oliver, S. R. J. *J. Am. Chem. Soc.* **2002**, *124*, 3966.

(90) Swanson, C. H.; Shaikh, H. A.; Rogow, D. L.; Oliver, A. G.; Campana, C. F.; Oliver, S. R. J. *J. Am. Chem. Soc.* **2008**, *130*, 11737.

(91) Sudik, A. C.; Cote, A. P.; Yaghi, O. M. *Inorg. Chem.* **2005**, *44*, 2998.

(92) Chen, X. D.; Wan, C. Q.; Sung, H. H. Y.; Williams, I. D.; Mak, T. C. W. *Chem.-Eur. J.* **2009**, *15*, 6518.

(93) Custelcean, R.; Gorbunova, M. G. *J. Am. Chem. Soc.* **2005**, *127*, 16362.

(94) Fei, H. H.; Paw, L.; Rogow, D. L.; Bresler, M. R.; Abdollahian, Y. A.; Oliver, S. R. J. *Chem. Mat.* **2010**, *22*, 2027.

(95) Fei, H. H.; Rogow, D. L.; Oliver, S. R. J. *J. Am. Chem. Soc.* **2010**, *132*, 7202.

(96) Wang, Y., Guo, H. *Journal of Colloid and Interface Science* **2006**, *301*, 19

(97) Banik, B. K.; Chapa, M.; Marquez, J.; Cardona, M. *Tetrahedron Lett.* **2005**, *46*, 2341.

(98) Li, C. H.; Huang, K. L.; Chi, Y. N.; Liu, X.; Han, Z. G.; Shen, L.; Hu, C. W. *Inorg. Chem.* **2009**, *48*, 2010.

(99) Luo, J. J.; Xu, L. *Inorg. Chem.* **2006**, *45*, 11030.

(100) Goulding, H. V.; Hulse, S. E.; Clegg, W.; Harrington, R. W.; Playford, H. Y.; Walton, R. I.; Fogg, A. M. *J. Am. Chem. Soc.* **2010**, *132*, 13618.

(101) McIntyre, L. J.; Prior, T. J.; Fogg, A. M. *Chem. Mat.* **2010**, *22*, 2635.

(102) Wang, S. A.; Alekseev, E. V.; Juan, D. W.; Casey, W. H.; Phillips, B. L.; Depmeier, W.; Albrecht-Schmitt, T. E. *Angew. Chem.-Int. Edit.* **2010**, *49*, 1057.

(103) Hagrman, P. J.; Hagrman, D.; Zubieta, J. *Angew. Chem.-Int. Edit.* **1999**, *38*, 2639.

(104) Walton, R. I. *Chem. Soc. Rev.* **2002**, *31*, 230.

(105) Rabenau, A. *Angew. Chem.-Int. Edit. Engl.* **1985**, *24*, 1026.

(106) Demazeau, G. *J. Mater. Chem.* **1999**, *9*, 15.

(107) Evans, J. S. O.; Francis, R. J.; Ohare, D.; Price, S. J.; Clark, S. M.; Flaherty, J.; Gordon, J.; Nield, A.; Tang, C. C. *Rev. Sci. Instrum.* **1995**, *66*, 2442.

Chapter Two

Synthesis, Structure and Characterisation of Pillared Lanthanide Molybdates and Tungstates with Framework Layers

2.0 Introduction

Molybdate, MoO_4^{2-}, and tungstate, WO_4^{2-}, are tetrahedral oxo-anions and are used as anionic building blocks in the formation of a variety of compounds, including simple metal molybdates ($MMoO_4$) and tungstates (MWO_4), templated molybdates with or without the incorporation of a second metal, and metal molybdate compounds without the incorporation of a template species. Molybdate containing compounds are more commonly reported compared to tungstate compounds although both anions are found to behave in a similar manner. Molybdate and tungstate compounds are an important and interesting research area due to their structural diversity and potential applications in a variety of fields such as such as catalysis,[1] magnetic properties,[2] and photoluminescence.[3] They adopt a variety of structures from one dimensional through to three dimensional, depending on the metal and any structure directing agents employed. In ternary compounds the anionic units are able to coordinate to either large bivalent cations where the ionic radius > 0.99 Å, for example Ca, Ba and Sr, or small bivalent cations with an ionic radius < 0.77 Å, e.g. Fe, Mn, Co, Ni, Mg and Zn, generally leading to either a scheelite ($CaWO_4$), Figure 1(a), in which molybdenum or tungsten adopts a tetrahedral coordination, or wolframite ($Mn_{1-x,}Fe_xWO_4$) structure, Figure 1(b), where molybdenum or tungsten adopt a six-fold coordination, depending on the size of the metal cation.[4, 5]

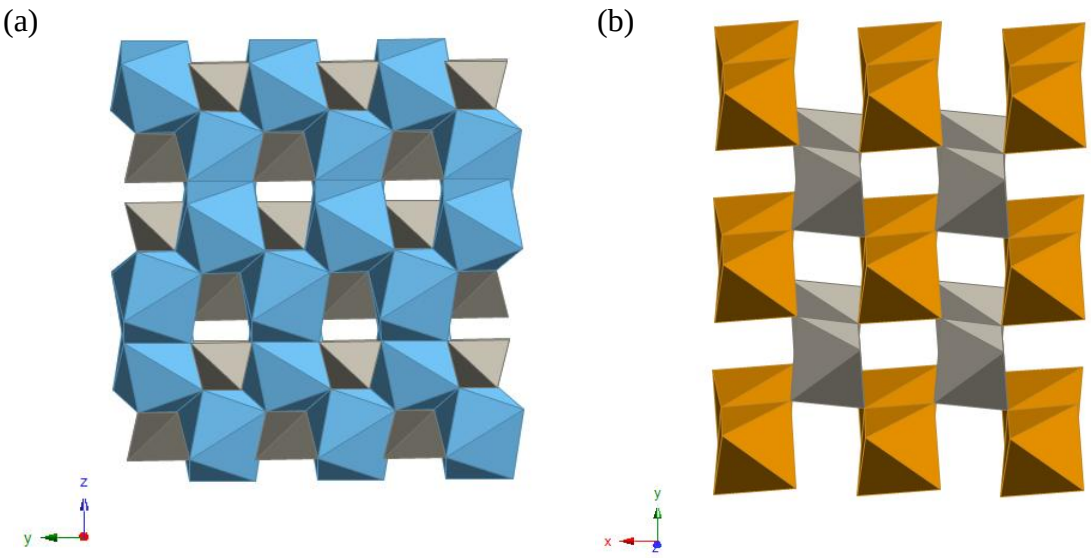

Figure 1 Crystal structure of (a) Scheelite ($CaWO_4$) and (b) Wolframite ($FeWO_4$). (Colour key; Ca polyhedra – blue, Fe polyhedra - orange and WO_4 – grey)[6, 7]

Formation of metal molybdate and tungstates, without a structure directing agent, has previously been performed under harsh reaction conditions including solid state high temperature synthesis[8], high pressure synthesis[9] or via a sol-gel method.[10] Recently Ding *et al.* and Yu *et al.* reported a softer approach via use of the hydrothermal method to produce a family of molybdate and tungstate nanorods and 3D structures, for example MWO_4 (M= Zn, Mn & Fe) and $MMoO_4.nH_2O$ (M= Co, Ni & Mn).[11,12] The addition of a templating species, generally an amine or an ammonium cation, within the synthesis leads to the formation of a range of complex structures from one through to three-dimensional. The template may adopt a variety of roles in the formation of these compounds, for example as charge compensation cations, which are able to bridge to the negatively charged molybdate centres or stitch smaller molybdate units together in turn forming large assemblies, as a ligand coordinated to the molybdenum oxide skeleton or as a ligand bonding directly to the second metal centre.[13] Examples include $[H_3N(CH_2)_6NH_3][Mo_4O_{13}]$[14] in which the organic subunit is incorporated as the organoammonium cation forming a one-dimensional chain structure, $[MoO_3(4,4'\text{-bipy})_{0.5}]$ MOXI-8[15] where the organodiammine present acts as a ligand coordinated to the Mo oxide skeleton forming a three-dimensional covalent framework and $[(Cu(en)_2)_2Mo_8O_{26})]$ MOXI-11[16] whereby the organodiamine coordinates directly to the metal centre forming a two-dimensional structure.

A review of recent literature has revealed that there are relatively few molybdate compounds reported which contain discrete monomeric MoO_4^{2-} units.[13] The compounds that do contain these discrete anions typically adopt structures in which the inorganic component forms either chains or layers. Examples include [MoO_4{FeCl(2,2'-bipy)] (MOXI-21), Figure 2,[17] which comprises 1D chains of {$FeClN_2O_3$} octahedra and molybdate tetrahedra, and [$Cu(bpa)_{0.5}MoO_4$] (MOXI-24), Figure 3,[18] consisting of two-dimensional {$CuMoO_4$} bimetallic oxide layers covalently linked by 4,4'-bipyridylamine (bpa) ligands forming a three-dimensional framework. In both compounds the template is coordinated to the metal centre rather than Mo or the molybdate skeleton.

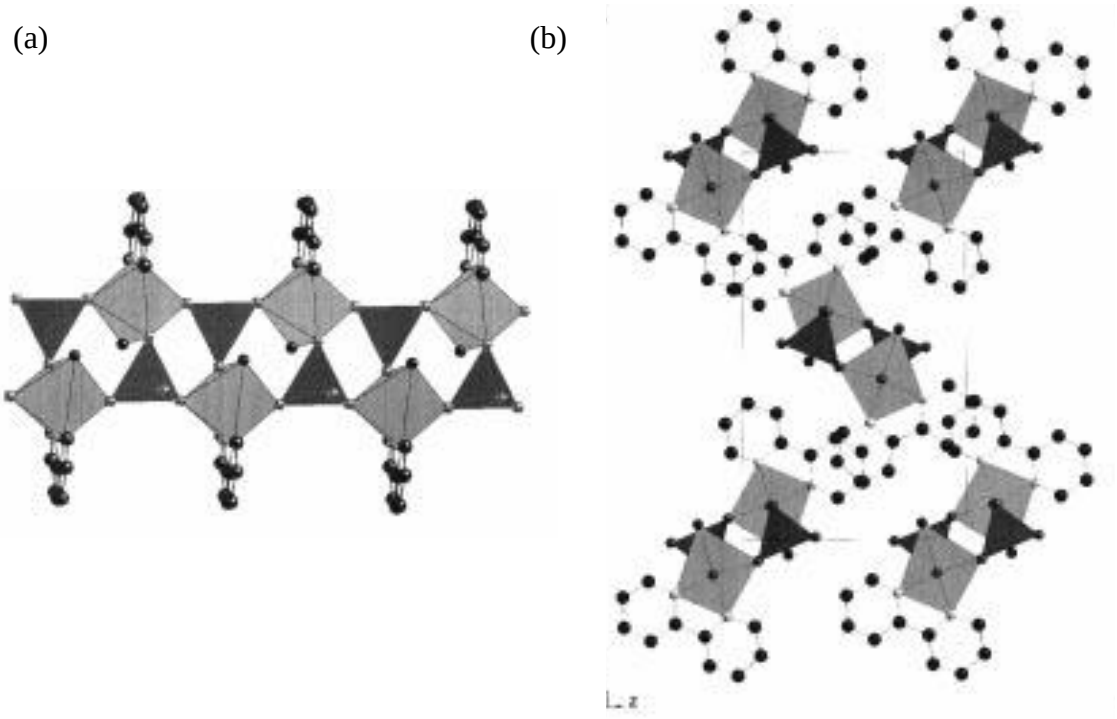

Figure 2 (a) Layer structure and (b) The unit cell packing of adjacent symmetry-related chains of [MoO_4{FeCl(2,2'-bipy)] (MOXI-21).[13, 17]

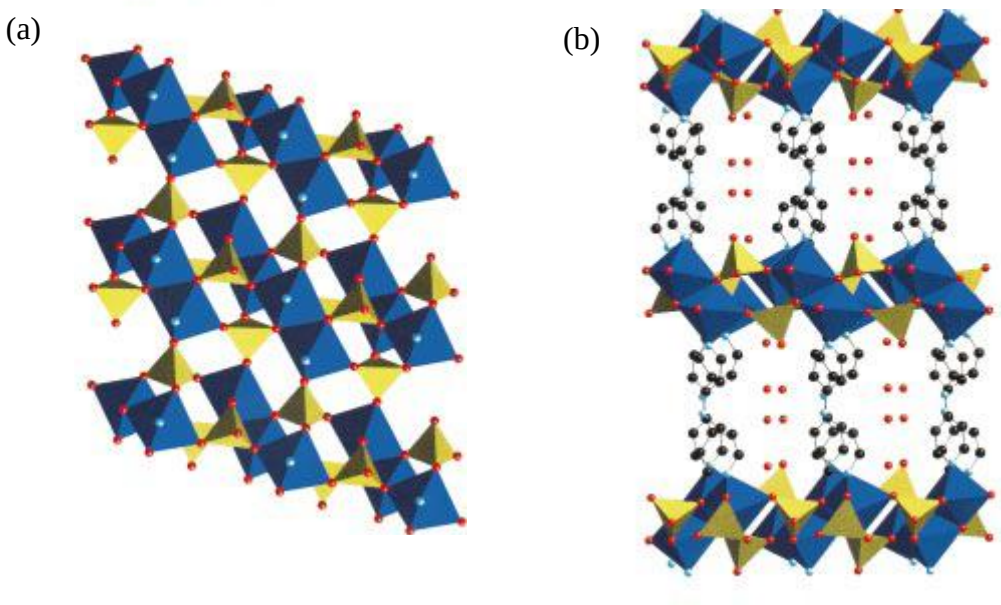

Figure 3 (a) Crystal structure and (b) layer structure of $[Cu(bpa)_{0.5}MoO_4]$ (MOXI-24) (Colour key; Cu – blue, Mo – yellow, O – red and C – black).[13]

The formation of polymeric units of molybdate within these compounds is more common. These units are formed either as, metal oxide clusters, chains, or layers which are separated by amines or ammonium cations and formed either with or without a second metal, commonly a transition metal, present. Examples include $Mo_8O_{26}^{4-}$ clusters, which are commonly seen to form 1D chain structures through to 2D networks. For example $[H_2N(CH_2)_6NH_3][Mo_4O_{13}]$,[14] contains clusters of $Mo_8O_{26}^{4-}$ which are linked together into 1D chains, and $[\{Ni(4,4'\text{-bipy})_2(H_2O)_2\}_2Mo_8O_{26}]$ (MOXI 14),[19] which comprises of $Mo_8O_{26}^{4-}$ clusters linked to 1D $\{Ni(4,4'\text{-bipy})_2\}^{2+}$ chains, forming a 2D network. $[Mo_3O_{10}]_n^{2n-}$ chains and $[Mo_5O_{16}]_n^{2n-}$ layers are also commonly seen in pure molybdate materials and also mixed metal oxide compounds.

The formation of molybdate phases with the incorporation of organic moieties is found to be rare and usually these ligands are restricted to organonitrogen compounds. Recently a material which incorporates a carboxylate and an amine, allowing the properties of the two components to be combined and expressed in a single material, has been reported; $[\{Cu(2,2'\text{-bipy})\}_2(tp)(Mo_4O_{13})]$ (tp = terephthalate). This system is found to be the first hybrid molybdate compound containing both organodiamine and dicarboxylate ligands.[20] Incorporating ligands,

containing carboxylate, into molybdate materials is found to be rare, due to the carboxylate group possessing negative charges. The presence of these negative charges makes it difficult for the charge associated with the molybdate skeleton to become balanced, therefore in turn making it a great challenge to incorporate ligands of this type into these materials.[21]

The pillaring or templating species, in the materials mentioned above, is either neutral or cationic. Phases in which the pillar or template species is anionic are much rarer and are the subject of a recent review.[22] The materials reported, were the extended inorganic material carries a positive charge, are predominantly layered materials such as layered double hydroxides[23] and more recently lanthanide hydroxysalts.[24,25] These materials contain positively charged layers with the charge balancing anions occupying the interlayer gallery with no covalent links to the cationic layer. Formation of materials with the incorporation of molybdate and tungstate and also lanthanides is rare, with a pillared lanthanide molybdate with cationic layers being reported recently; $[Ln(H_2O)MoO_4]_2[\lambda\text{-}Mo_2O_4EDTA]$ (Ln=Y, Gd, Eu and Tb), Figure 4.[26]

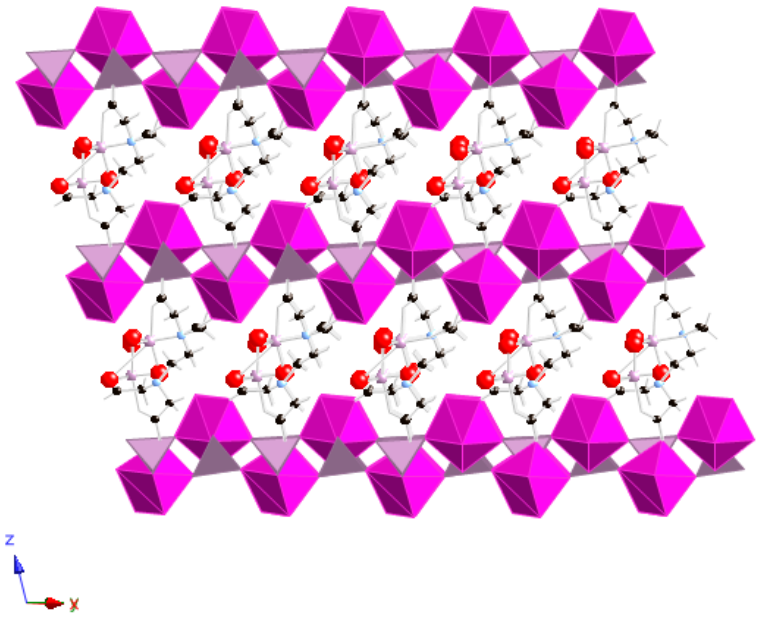

Figure 4 Crystal structure of $[Eu(H_2O)MoO_4]_2[\lambda\text{-}Mo_2O_4EDTA]$ (Ln=Y, Gd, & Tb) (Colour key; Eu – pink, Mo – purple, O – red and C – black).[26]

These materials have high thermal stability and adopt a 3D chiral framework structure resulting from coordination of the $[\lambda\text{-}Mo_2O_4EDTA]^{2-}$ complex to the lanthanide cation, in turn pillaring the 2D bimetallic oxide layers. The organic anionic ligand/template present acts as a structure-directing agent completing the coordination geometry of Ln^{3+}, producing a layered inorganic-organic hybrid material.

Incorporation of lanthanide cations into these materials may potentially allow the interesting properties of lanthanides to be exploited, such as catalytic and optical properties. Lanthanides also have great structural flexibility due to their high and variable coordination numbers, therefore potentially allowing a variety of interesting structures to be formed.

2.1 Scope of Chapter

The hydrothermal preparation, crystal structures and characterisation of six new pillared layered lanthanide molybdate and tungstate phases is described. Five of these phases have the general composition $[Ln(H_2O)MO_4]_2[A]$ (Ln= La- Nd, M= MoO_4 or WO_4, A= 1,5-NDS or 2,6-NDS, NDS = naphthalenedisulfonate) with the sixth phase, being pillared by fumarate, having the composition $[Ce(H_2O)MoO_4]_2$[Fumarate]. These phases have a closely related cationic inorganic layer structure comprising of a bilayer of polyhedra leading to the formation of a framework layer containing small, inaccessible pores. The layers are pillared by the organic anions which also bridge between the lanthanide cations within the layers.

2.2 Pillared Lanthanide Molybdate and Tungstates with Framework Layers

2.2.1 General Synthesis

Six new phases, with compositions $[Nd(H_2O)MoO_4]_2$[2,6-NDS] (**1**), $[Nd(H_2O)MoO_4]_2$[1,5-NDS] (**2**), $[La(H_2O)WO_4]_2$[1,5-NDS] (**3**), $[La(H_2O)WO_4]_2$[2,6-NDS] (**4**), $[La(H_2O)W_2O_8]$[2,6-NDS] (**5**), and $[Ce(H_2O)MoO_4]_2$[Fumarate] (**6**) have been synthesised via a hydrothermal route from $LnCl_3.xH_2O$, Na_2MoO_4 or Na_2WO_4, and disodium 1,5-naphthalenedisulfonate, disodium 2,6-naphthalenedisulfonate or sodium fumarate. Crystallographic data for each phase is provided in Appendix A. The reactions were heated at 165°C (**1-5**) or 145°C (**6**) for 14 h before being cooled slowly back to room temperature at a rate of 0.1°C/min producing single crystals. The yields of the reactions lie in the range of 35-60% with respect to the Ln^{3+} cation. A variety of reaction conditions were screened, for example change in reaction temperature, concentration and the use of different solvent systems, to obtain phase pure materials. The optimal conditions found are those stated above with others leading to either less pure or less crystalline samples.

2.2.2 Characterisation of $[Nd(H_2O)MoO_4]_2$[2,6-NDS] (1)

$[Nd(H_2O)MoO_4]_2$[2,6-NDS] (**1**) has been synthesised via a hydrothermal route. Single crystal X-ray diffraction data has shown that it adopts a monoclinic crystal system with the space group *C*2/*c*, shown in Figure 5 with the main crystallographic and refinement data summarised in Table 1. Detailed bond lengths are provided in Appendix A. This phase has also been successfully synthesised with Ln = La, Ce and Pr, powder XRD patterns are shown in Figure 6 and characterising data are provided in the appendices. Attempts to synthesise this phase using smaller lanthanides, such as Ln=Dy & Yb, proved unsuccessful, with different poorly crystalline phases being produced under these conditions.

The structure comprises of two-dimensional inorganic mixed-metal oxide layers which are pillared by the 2,6-NDS organic anions. The inorganic sheet contains a bilayer of neodymium and molybdate polyhedra leading to the formation of a framework with very small pores within the layer. There is one crystallographically distinct Nd atom in this structure with is eight coordinate. Nd^{3+} coordinates to one water molecule, two 2,6-NDS anions and five molybdate anions. The Nd-OH_2 bond distance is 2.481(9) Å and Nd-$OMoO_3$ distances lie in the range of 2.364(8)-2.632(9) Å and Nd-OSO_2 distances are 2.473(9) Å. The organic sulfonate anions bridge two adjacent neodymium atoms in the mixed metal oxide sheet and also pillar the layers such that each 2,6-NDS anion coordinates to four Nd atoms through four of its six O atoms. There are also two crystallographically distinct Mo atoms in this structure. Each molybdate is coordinated to five Nd^{3+} cations via oxygen bridges; one O atom is triply coordinated to one molybdenum and two adjacent neodymium ions while the remaining three O atoms bridge Mo and one Nd^{3+} becoming doubly coordinated. This in turn forms the two-dimensional inorganic layer in the *xy* plane, also creating pores within these layers. The small pores present in the inorganic layer of this phase have window sizes of 4.50Å in diameter, measuring the distance between the O6 atoms across the pore window in the *yz* plane. This window diameter suggests that the pores are inaccessible to even the smallest species. This assumption has been confirmed by CO_2 sorption measurements following activation of the sample, initially at 120 °C and subsequently at 250 °C, which corresponds to the removal of the coordinated water. In both cases, the sample showed type II behaviour with a similar level of uptake of approximately 1.15 mass %, indicative of a nonporous material. Powder XRD patterns of the samples from the gas sorption experiments indicate that there is a reduction in the lattice parameters on dehydration but show that they retain their crystallinity. Sorption data is provided in the appendix.

.

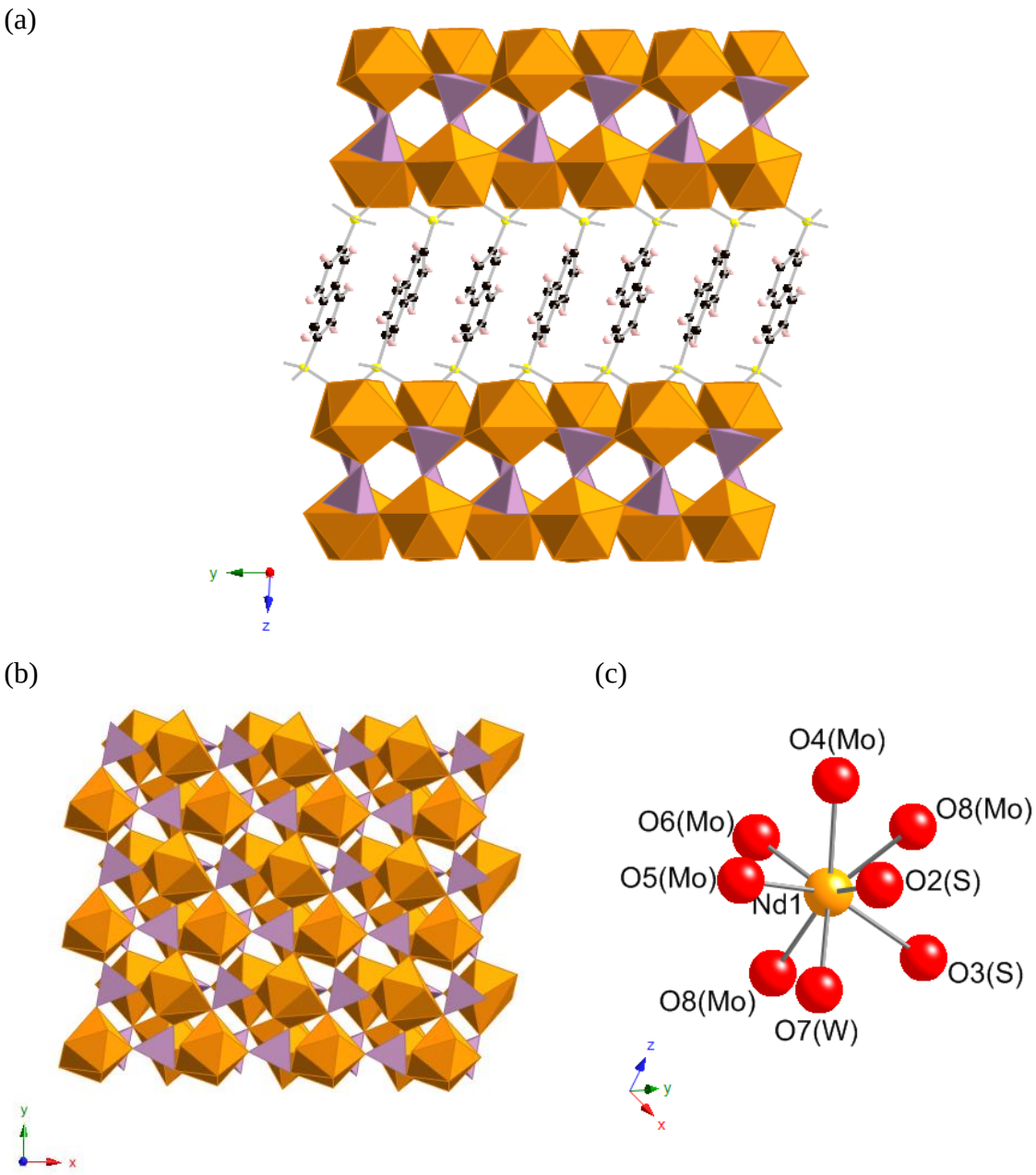

Figure 5 (a) Crystal structure and (b) layer structure of $[Nd(H_2O)MoO_4]_2[2,6\text{-NDS}]$ (**1**) and (c) coordination sphere of neodymium in (**1**)
(Colour key: Orange - Nd^{3+}, Purple - MoO_4^{2-})

Table 1 Crystallographic data and refinement parameters for phases (**1 - 3**).

	(1)	**(2)**	**(3)**
Empirical formula	$C_5H_3MoNdO_8S$	$C_{10}H_5Mo_2Nd_2O_{14}S_2$	$C_{10}H_{10}La_2O_{16}S_2W_2$
Formula weight	463.31	893.62	1095.82
Temperature	120(2) K	120(2) K	120(2) K
Wavelength	0.71073Å	0.71073Å	0.71073Å
Crystal system	Monoclinic	Monoclinic	Monoclinic
Space group	*C*2/*c*	$P2_1/c$	$P2_1/c$
Unit cell dimensions	a = 35.6918(18) Å	a = 16.9552(9) Å	a = 17.1242(11) Å
	b = 7.2951(4) Å	b = 7.3924(4) Å	b = 7.4638(5) Å
	c = 7.4407(4) Å	c = 7.5290(4) Å	c = 7.6228(5) Å
	α = 90 º	α = 90 º	α = 90 º
	β = 93.730(3) º	β = 91.079(3) º	β = 91.048 º
	γ = 90 º	γ = 90 º	γ = 90 º
Volume ($Å^3$)	1933.27(18)	943.51(9)	974.12(11)
Z	8	2	2
Density (calculated) (Mg/m^3)	3.184	3.262	3.736
Absorption coefficient(mm^{-1})	6.849	7.017	16.365
Crystal	needle; light purple	fragment; purple	plate; colourless
Crystal Size (mm^3)	0.14x0.02x0.01	0.04x0.02x0.002	0.10x0.04x0.01
θ range for data collection (deg)	3.28-27.48	3.0-27.5	3.0-27.5
Reflections collected	15260	16145	10570
Independent reflections collected	2220 [R_{int}= 0.1351]	2157 [R_{int}= 0.0800]	2214 [R_{int}= 0.0782]
Max. and min. transmission	0.935 and 0.447	0.986 and 0.767	0.0854 and 0.291
Goodness of fit on F^2	1.151	1.093	1.121
R [F, $F^2 > 2\sigma$]	0.0685	0.0418	0.0595
R_w (F, all data)	0.1468	0.0839	0.1255
Diff. map extremes (e $Å^{-3}$)	2.09 and -1.78	1.29 and -1.17	2.08 and -2.51

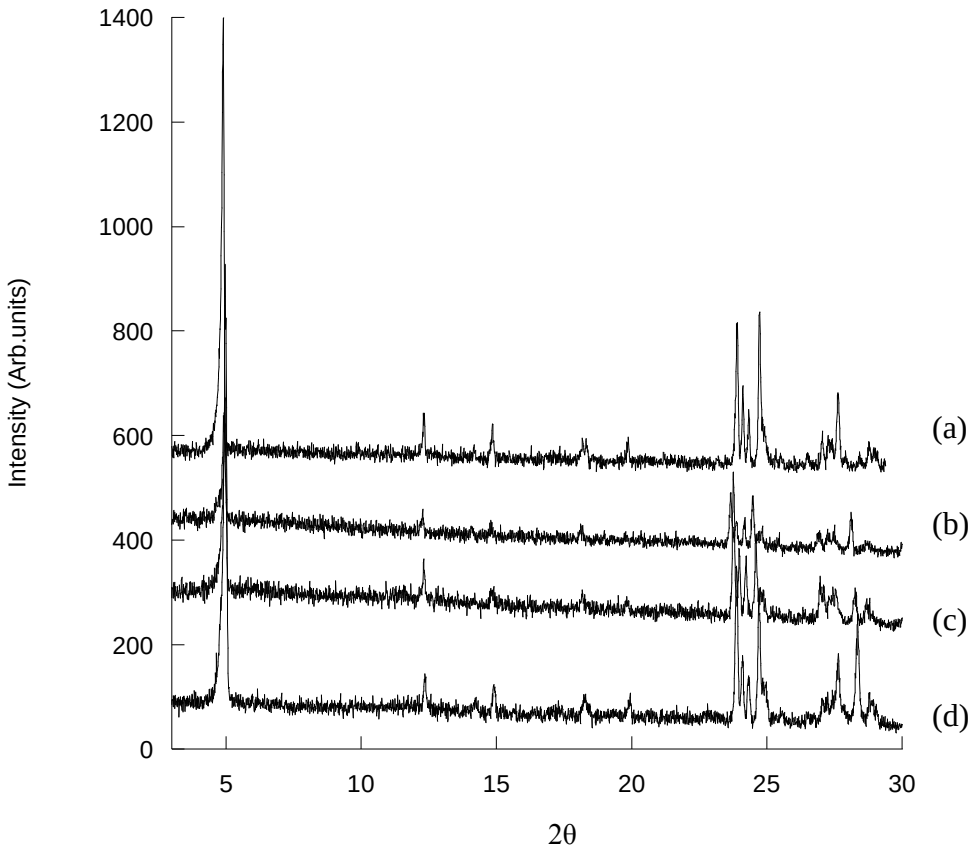

Figure 6 Powder XRD patterns (Cu K_α radiation) of iso-structural phases of (a) $[Nd(H_2O)MoO_4]_2$[2,6-NDS], (b) $[La(H_2O)MoO_4]_2$[2,6-NDS], (c) $[Ce(H_2O)MoO_4]_2$[2,6-NDS] and (d) $[Pr(H_2O)MoO_4]_2$[2,6-NDS].

A range of analytical techniques were used to determine the composition and phase purity of this material. Elemental analysis indicated that the sample contains 12.34 % C (calc 12.91 %) and 0.92 % H (1.08 %), which is consistent with the composition obtained from the crystal structure and the absence of crystalline impurities in the PXRD pattern. The powder XRD pattern of **1** is shown in Figure 7, where it is compared to one calculated from the crystal structure. No crystalline impurities are evident in the experimental data, and good agreement between the two patterns is apparent, suggesting that the crystal structure of **1** is representative of the bulk phase.

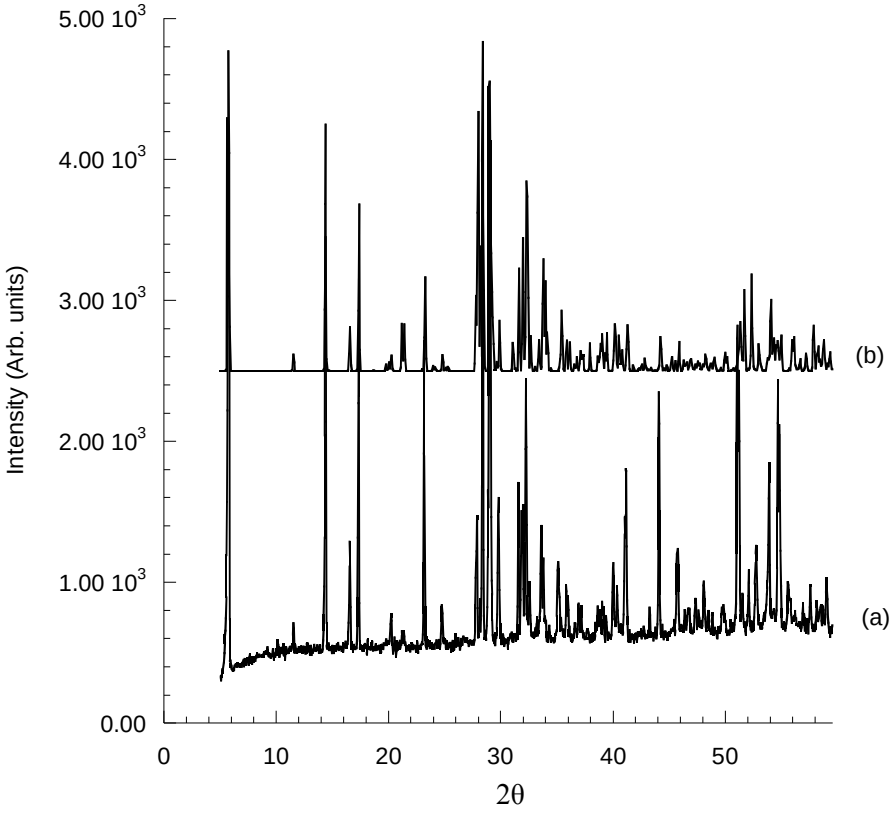

Figure 7 (a) Powder XRD pattern (Cu K_α radiation) of $[Nd(H_2O)MoO_4]_2$[2,6-NDS] and (b) diffraction pattern calculated from the crystal structure.

The TGA trace of $[Nd(H_2O)MoO_4]_2$[2,6-NDS] is shown in Figure 8 and displays two distinct mass losses below 650 °C. The first mass loss of 3.5 % below 350 °C corresponds to the dehydration of the material to $[NdMoO_4]_2$[2,6-NDS] and compares well to the calculated value of 3.9 %. The decomposition of the phase is complete by 650 °C following an additional mass loss of 26.5 %, which corresponds to decomposition of the organic anion. Powder X-ray diffraction showed the residue to be a mixture of Nd_2MoSO_9 and $Nd_2Mo_3O_9$.

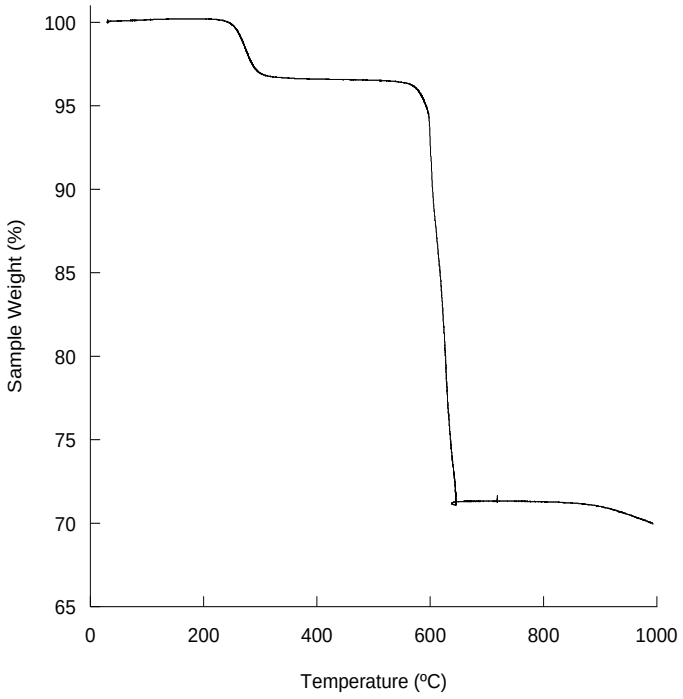

Figure 8 TGA trace of $[Nd(H_2O)MoO_4]_2[2,6\text{-NDS}]$.

The FTIR spectrum, shown in Figure 9, has a weak band due to an O-H stretch at approximately 3390 cm^{-1}. The other features of the spectrum are due to molybdate and 2,6-NDS anions present in the structure. Frequencies characteristic of the S-O stretching modes, antisymmetric and symmetric stretches, are observed at 1177 and 1055 cm^{-1}. The 2,6-NDS stretches have reduced in frequency in comparison to the starting disodium salt of 2,6-NDS, which is consistent with coordination to the Nd cations. The sulfonate frequencies detected are found to be consistent with compounds containing NDS anions reported in the recent literature.[27] This is also true for the molybdate stretching frequency, which is observed at 760 cm^{-1}.

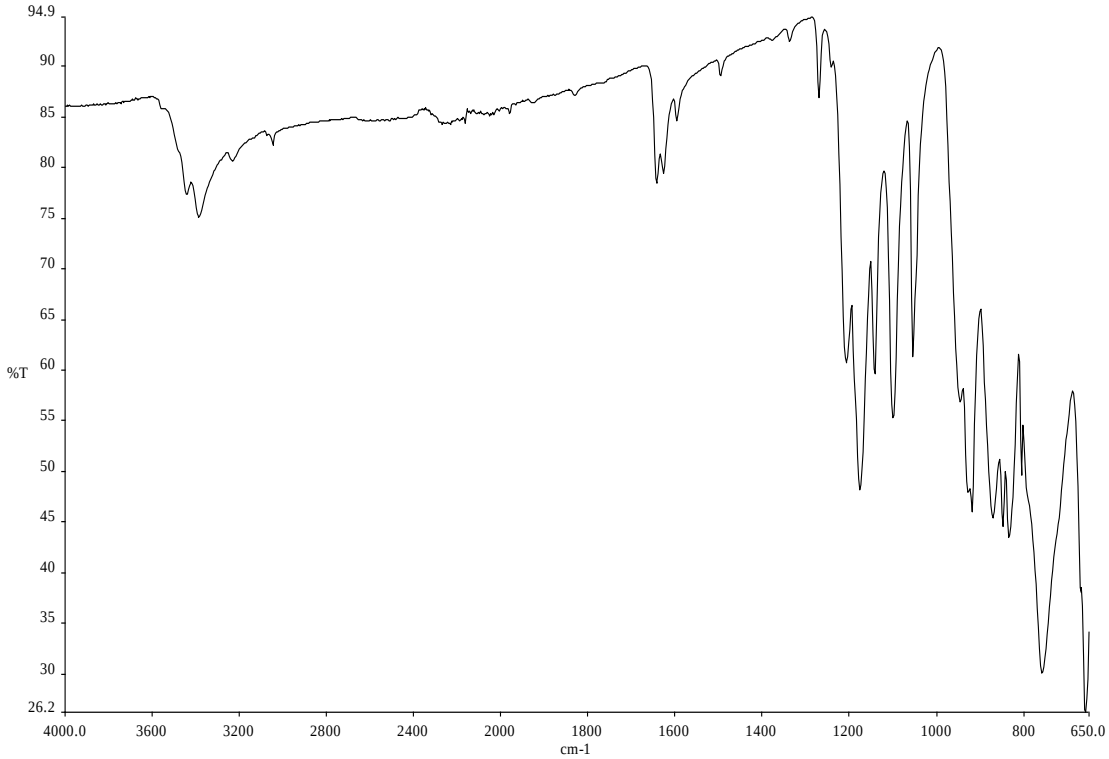

Figure 9 FTIR spectrum of $[Nd(H_2O)MoO_4]_2$[2,6-NDS].

The SEM image, Figure 10, shows $[Nd(H_2O)MoO_4]_2$[2,6-NDS] to exist as a microcrystalline powder, exhibiting needle-like morphology.

Figure 10 SEM image of $[Nd(H_2O)MoO_4]_2$[2,6-NDS]

2.2.3 Characterisation of $[Nd(H_2O)MoO_4]_2$[1,5-NDS] (2)

Following the successful synthesis of **1** with 2,6-naphthalenedisulfonate, the reaction was repeated with the 1,5-naphthalenedisulfonate isomer. A similar structure to **1** was obtained, with the same composition of $[Nd(H_2O)MoO_4]_2$[1,5-NDS]. Single crystal X-ray diffraction confirmed that an analogous phase had formed. The structure is shown in Figure 11, with the main crystallographic and refinement data is summarised in Table 1**,** and detailed bond lengths are provided in the appendix. The single crystal X-ray diffraction data shows that the structure adopts a monoclinic unit cell with the space group $P2_1/c$. This phase has also been successfully synthesised with Ln = La, Ce and Pr, showing a decrease in d-spacing on going across the lanthanide series from La - Pr, characterising data for these phases are provided in the appendix. Attempts to synthesise this material using smaller lanthanides Ln = Dy and Yb proved unsuccessful.

(a)

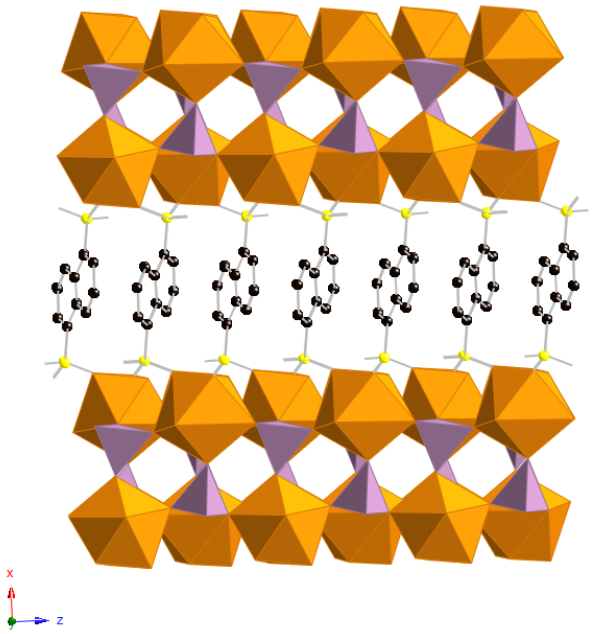

(b) (c)

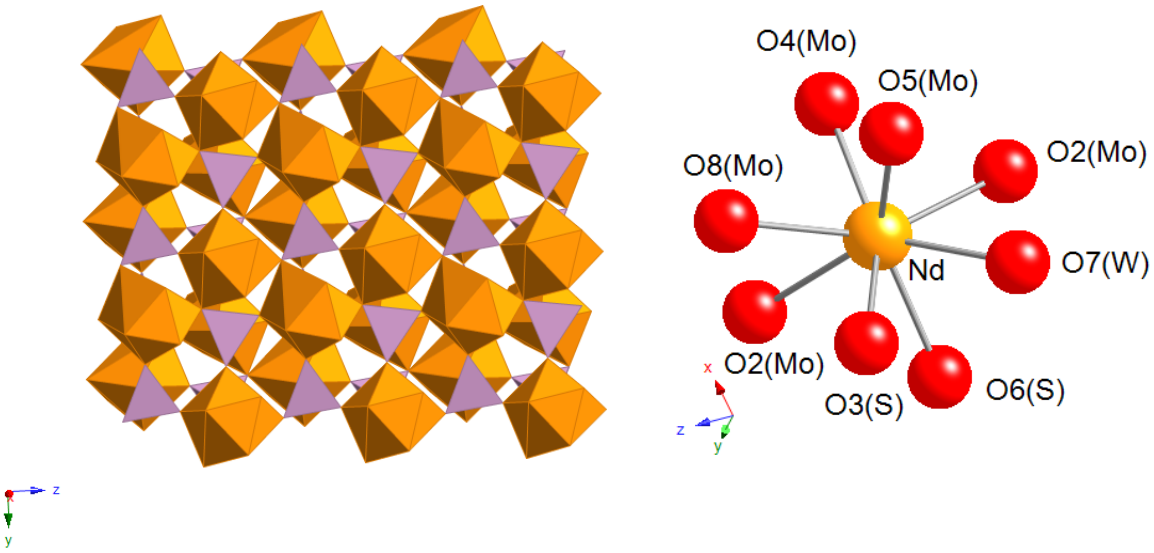

Figure 11 (a) Crystal structure and (b) layer structure of $[Nd(H_2O)MoO_4]_2[1,5\text{-NDS}]$ (**2**) and (c) coordination sphere of neodymium in (**2**) (Colour key: Orange - Nd^{3+}, Purple - MoO_4^{2-}).

The structure consists of two-dimensional inorganic mixed metal oxide layers, of composition $[Nd(H_2O)MoO_4]^+$, in the *yz* plane which are charge balanced by pillaring 1,5-NDS organic anions. The inorganic layer is found to have the same connectivity and composition as in **1**, with only subtle differences resulting from the symmetry of the structure. There is one crystallographically distinct Nd atom in this structure which is eight coordinate, coordinating to one water molecule, two 1,5-NDS anions and five molybdate anions. The Nd-OH_2 bond distance is 2.453(6) Å and the Nd-$OMoO_3$ distances lie in the range of 2.354(5) - 2.653(5) Å and Nd-OSO_2 distances are 2.433(6) and 2.509(5) Å, these bond distances compare well to those observed in **1**. The organic sulfonate anions bridge two adjacent neodymium atoms in the mixed metal oxide sheet and also pillar the layers, via the same coordination, such that each 1,5-NDS anion coordinates to four Nd atoms through four of its six O atoms. There is one crystallographically distinct Mo atom in this structure, coordinating to five Nd cations via oxygen bridges; one O atom is triply coordinated to molybdenum and to two adjacent neodymium ions while the remaining three O atoms bridge Mo and one Nd^{3+}. This in turn forms the two-dimensional inorganic layer in the *yz* plane, also creating pores within these layers. The small pores present

in the inorganic layer of this phase have window sizes of 4.51Å, in diameter, measuring the distance between the oxygen atoms across the pore window.

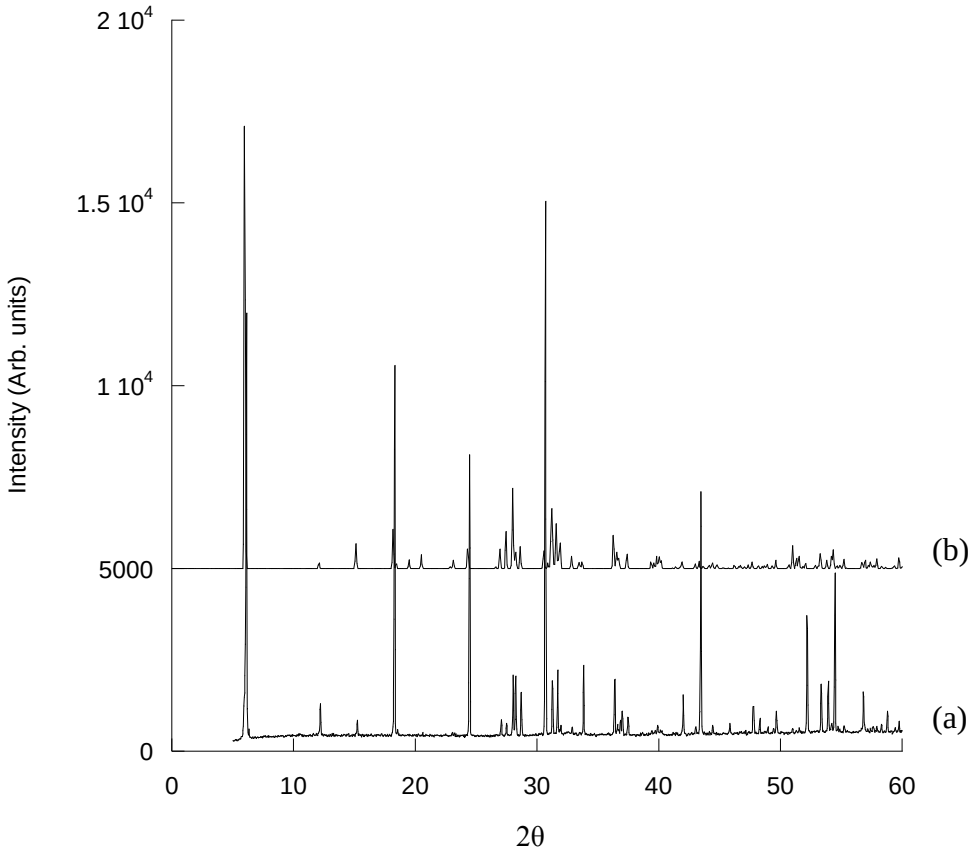

Figure 12 (a) Powder XRD pattern (Cu K_α radiation) of $[Nd(H_2O)MoO_4]_2[1,5\text{-NDS}]$ (**2**) and (b) diffraction pattern calculated from the crystal structure.

A range of analytical techniques were used to determine the composition and phase purity of this material. From the analysis obtained this material is found to be phase pure. Elemental analysis indicated that the sample contains 9.57 % C (calc 12.91 %) and 0.81 % H (calc 1.08 %), which suggests an amorphous inorganic impurity may be present within the sample. The powder XRD pattern of **2** is shown in Figure 12, where it is compared to one calculated from the crystal structure. No crystalline impurities are evident in the experimental data, and good agreement between the two patterns is apparent, suggesting that the crystal structure of **2** is representative of the bulk phase.

The TGA trace of $[Nd(H_2O)MoO_4]_2$[1,5-NDS] is shown in Figure 13 displays two mass losses below 995 °C. The first mass loss of 3.2 % below 325 °C corresponds to the dehydration of the material and compares well to the calculated value of 3.9 %. The decomposition of the phase is complete by 995 °C following an additional mass loss of 25.3 %, which corresponds to decomposition of the organic anion. Powder X-ray diffraction showed the residue to be a mixture of $Nd_2Mo_2O_7$ and $Nd_2Mo_3O_9$.

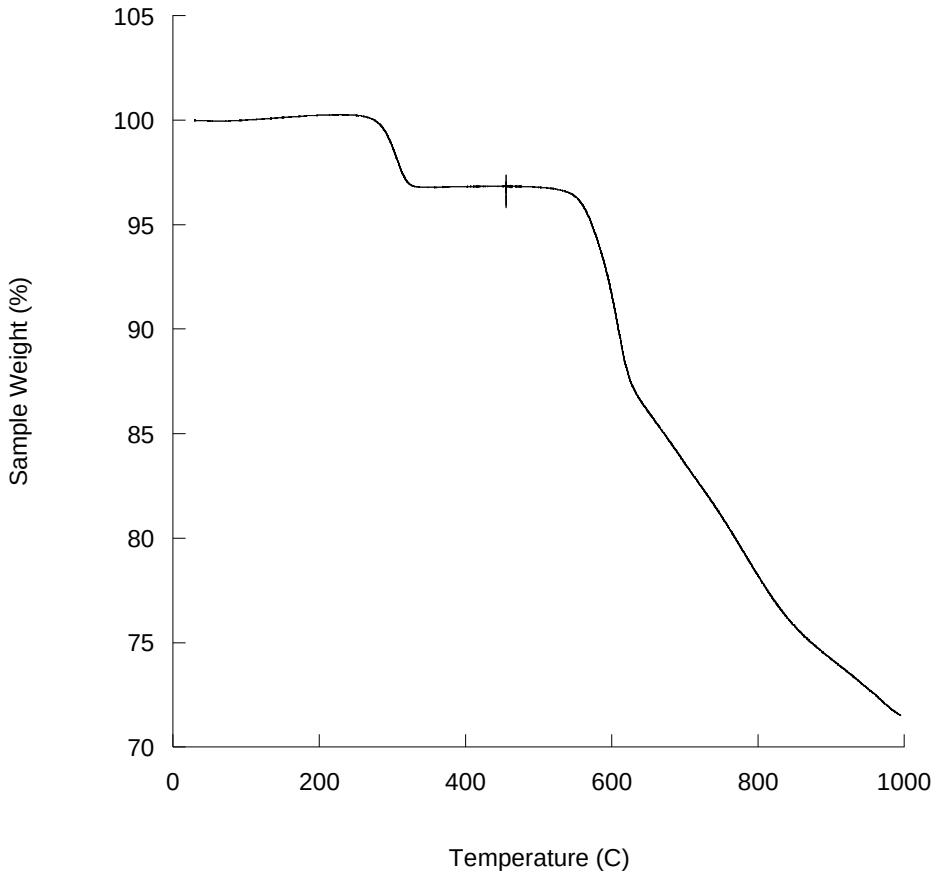

Figure 13 TGA trace of $[Nd(H_2O)MoO_4]_2$[1,5-NDS].

The FTIR spectrum is shown in Figure 14. There is a weak band present due to an O-H stretch at approximately 3368 cm^{-1}. The other features of the spectrum are due to molybdate and 1,5-NDS anions present in the structure. Frequencies characteristic of the S-O stretching modes, antisymmetric and symmetric stretches, are observed at 1184 and 1073 cm^{-1}. The 1,5-NDS stretches have reduced in frequency in comparison to the starting disodium salt of 1,5-NDS, which is consistent with

coordination to the Nd cations. This is also true for the molybdate stretching frequency, which is observed at 756 cm^{-1}.

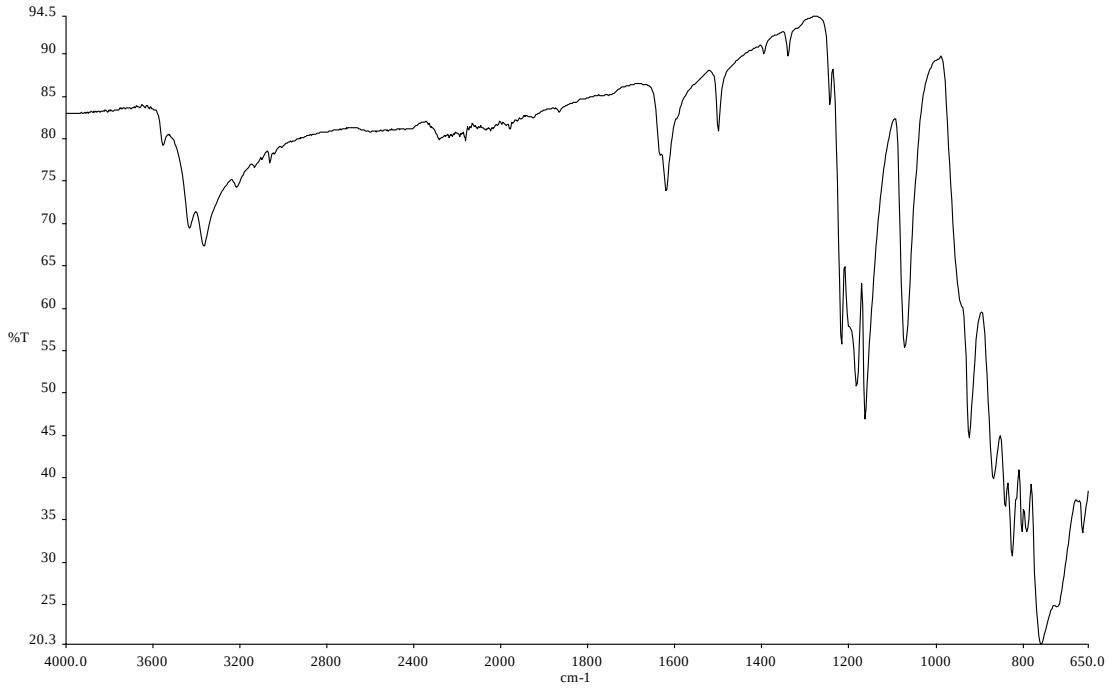

Figure 14 FTIR spectra of $[Nd(H_2O)MoO_4]_2$[1,5-NDS]

The SEM image, Figure 15, shows $[Nd(H_2O)MoO_4]_2$[1,5-NDS] exists as a microcrystalline powder and exhibits plate-like morphology.

Figure 15 SEM image of $[Nd(H_2O)MoO_4]_2[1,5\text{-NDS}]$

2.2.4 Characterisation of $[La(H_2O)WO_4]_2[1,5\text{-NDS}]$ (3)

Following the successful synthesis of **2** the reaction was repeated with the substitution of MoO_4^{2-} with WO_4^{2-} leading to the successful formation of $[La(H_2O)WO_4]_2[1,5\text{-NDS}]$ (**3**). Single crystal X-ray diffraction measurements have confirmed this phase to be iso-structural to **2**, adopting a monoclinic crystal system with space group $P2_1/c$. The structure comprises of two-dimensional inorganic mixed metal oxide layers of composition $[La(H_2O)WO_4]^+$ which are charge balanced by pillaring 1,5-NDS organic anions. The structure is shown in Figure 16 and the main crystallographic and refinement data is summarised in Table 1, detailed bond lengths are provided in the appendix. This phase can also be prepared with Ln = Ce and Pr, although a significant amount of an unknown second phase is present within the samples, characterising data for each phase is provided in the appendix. Attempts to synthesise this phase using smaller lanthanides Ln = Nd - Lu proved unsuccessful. PXRD, FTIR and elemental analysis confirmed that no organic was present in these phases.

(a)

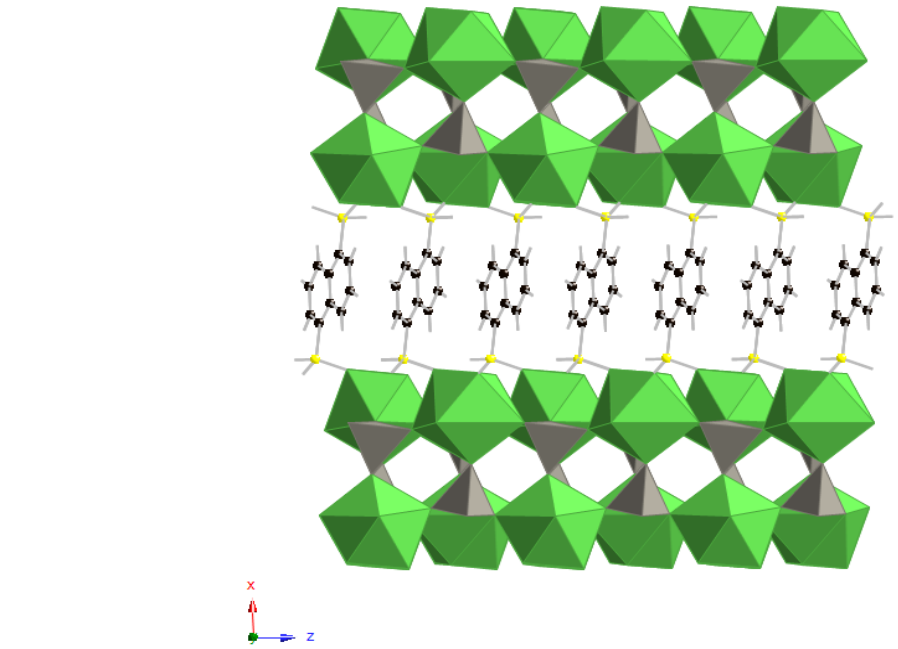

(b)

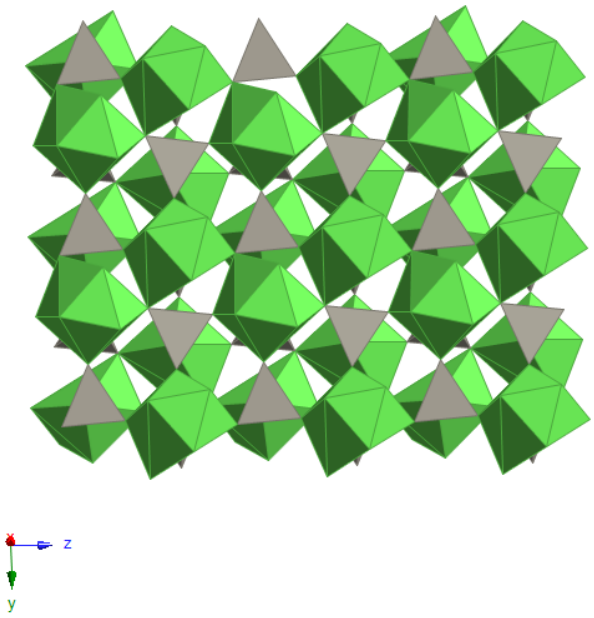

(c)

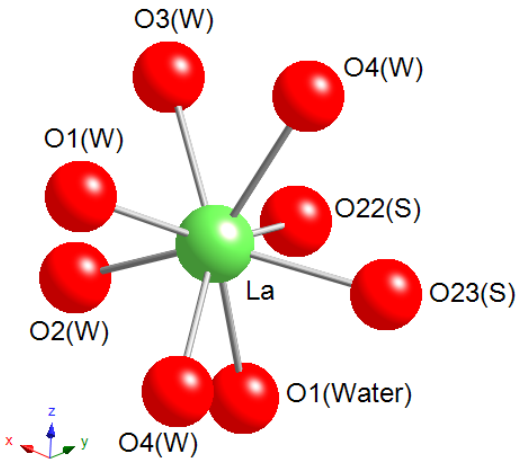

Figure 16 (a) Crystal structure and (b) layer structure of $[La(H_2O)WO_4]_2[1,5\text{-NDS}]$ (**3**) and (c) coordination sphere of lanthanum in (**3**)
(Colour key: Green - La^{3+}, Grey - WO_4^{2-})

The structure contains one crystallographically distinct La^{3+} cation which is found to be eight coordinate to one water molecule, five molybdate and two 1,5-NDS anions. The 1,5-NDS anions pillar the layers with both sulfonates bridging between two adjacent La cations. The La-OH_2 bond distance is 2.518(11) Å and the La-OWO_3 distances lie in the range of 2.423(12)- 2.729(11) Å and La-OSO_2 distance are 2.480 (11) and 2.575(12) Å. The small pores present in the inorganic layer of this phase have window sizes of 4.57 Å in diameter, measuring the O-O distance across the window in the *yz* plane. However, following treatment under vacuum at 120 °C, the material showed a BET surface area of 4 m^2/g which indicates that this material is non-porous.

As this phase is found to be iso-structural to **2**, the crystal structure will not be discussed in any further detail.

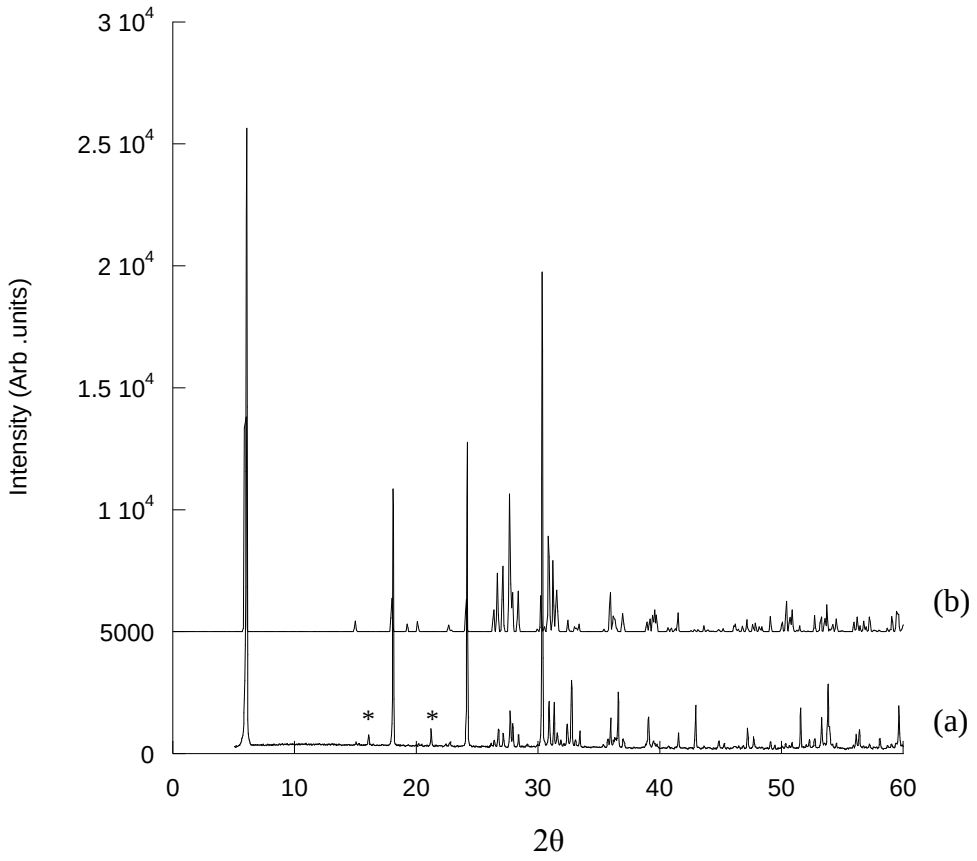

Figure 17 (a) Powder XRD pattern (Cu K_α radiation) of $[La(H_2O)WO_4]_2[1,5\text{-NDS}]$ (**3**) and (b) diffraction pattern calculated from the crystal structure.
(*- unknown impurity)

A range of analytical techniques were used to determine the composition and phase purity of this material. Elemental analysis indicated that the sample contains 8.46 % C (calc 10.95 %) and 0.77 % H (calc 0.91 %), these results suggest an impurity is present within the sample. The powder XRD pattern of **3** is shown in Figure 17, where it is compared to one calculated from the crystal structure. A small amount of an unknown crystalline impurity is evident in the experimental data. Despite this both PXRD patterns are in good agreement with one another, therefore suggesting that the crystal structure of **3** is representative of the bulk phase.

The TGA trace is shown in Figure 18. Two distinct mass losses are observed below 600 °C. The first mass loss of 3.4 % below 300 °C, corresponds to the dehydration of the material, and compares well to the calculated value of 3.3 %. Decomposition of the phase is complete by 600 °C following an additional mass loss of 20.3 % which corresponds to decomposition of the organic anion (calculated mass loss is 24.7 %). This mass loss is found to be lower than that of the calculated value, which is consistent with the presence of an inorganic impurity. Powder X-ray diffraction showed the residue to be a mixture of $La_2W_2O_9$ and La_2O_3.

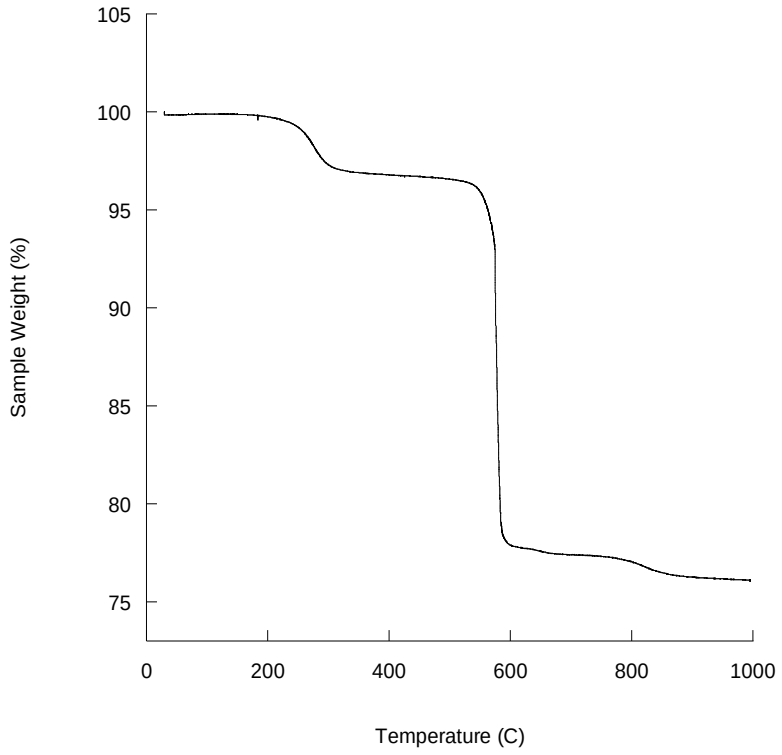

Figure 18 TGA trace of $[La(H_2O)WO_4]_2[1,5\text{-NDS}]$.

The FTIR spectrum is shown in Figure 19 and has a weak band due to an O-H stretch at approximately 3382 cm^{-1}. The other features of the spectrum are due to tungstate and 1,5-NDS anions being present in the structure. Frequencies characteristic of the S-O stretching modes are observed at 1181 cm^{-1} (anti-symmetric) and 1072 cm^{-1} (symmetric) respectively. The 1,5-NDS bands have become weaker and have reduced in frequency in comparison to the original reagent which is consistent with coordination of the anion to the La^{3+} centre . This is also true for the tungstate stretching frequency, which is observed at 771 cm^{-1}.

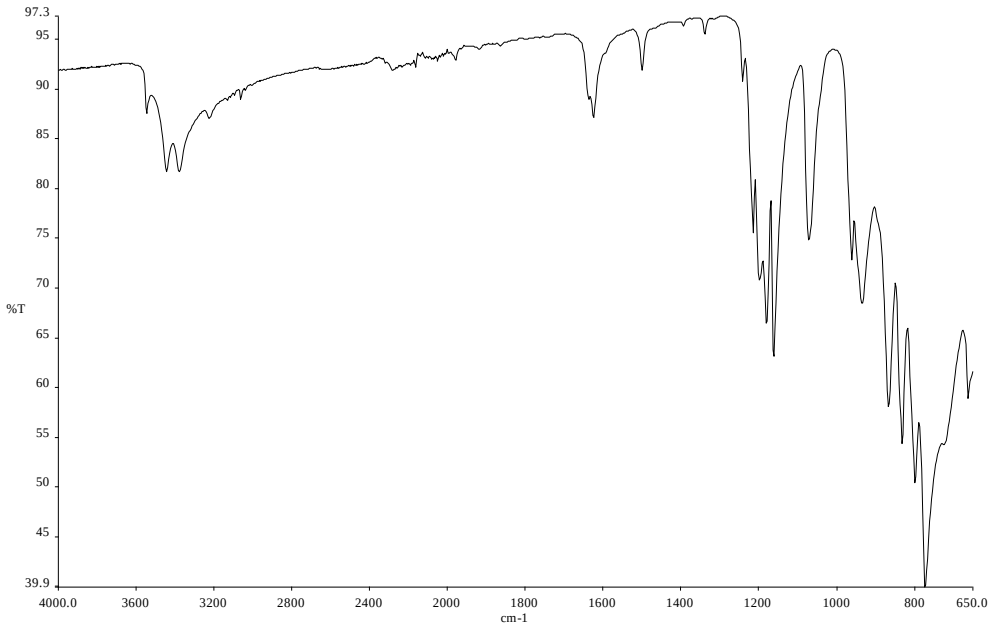

Figure 19 FTIR spectra of $[La(H_2O)WO_4]_2[1,5\text{-NDS}]$.

The SEM image, Figure 20, shows $[La(H_2O)WO_4]_2[1,5\text{-NDS}]$ exists as a microcrystalline powder and exhibits plate-like morphology, similar to that observed in $[Nd(H_2O)MoO_4]_2[1,5\text{-NDS}]$.

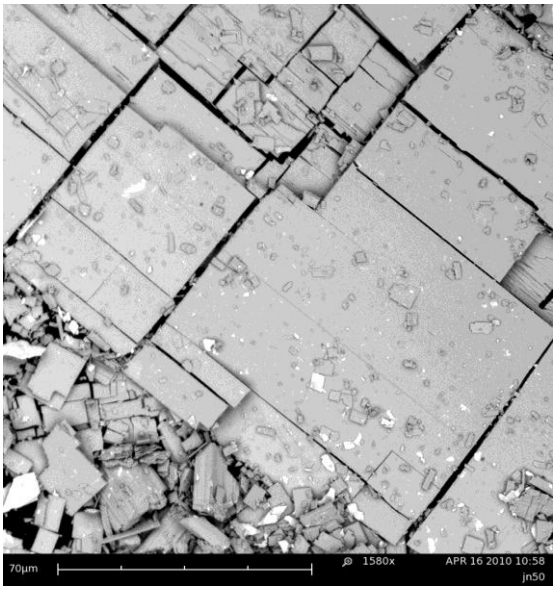

Figure 20 SEM image of $[La(H_2O)WO_4]_2[1,5\text{-NDS}]$ (**3**)

2.2.5 Characterisation of $[La(H_2O)WO_4]_2$[2,6-NDS] & $[La_2(H_2O)_2W_2O_8]$[2,6-NDS]

Following the successful synthesis of **3** the reaction was repeated with the 2,6-naphthalenedisulfonate isomer to see if an analogous phase could be formed. PXRD data has shown the La/W/2,6-NDS system to be much more complex, and despite extensive screening of the experimental conditions it has not proved possible to obtain a phase pure material. It is found that the samples are biphasic with two layered phases present with interlayer separations of 17.90 and 16.38 Å, together with a small amount of $La_2W_2O_9$ (~27 ° 2θ) as an impurity. The 17.90 Å material is always the major phase produced and from the data shown in Figure 21 and comprises approximately 66% of the sample on the basis of peak area of the strongest reflections.

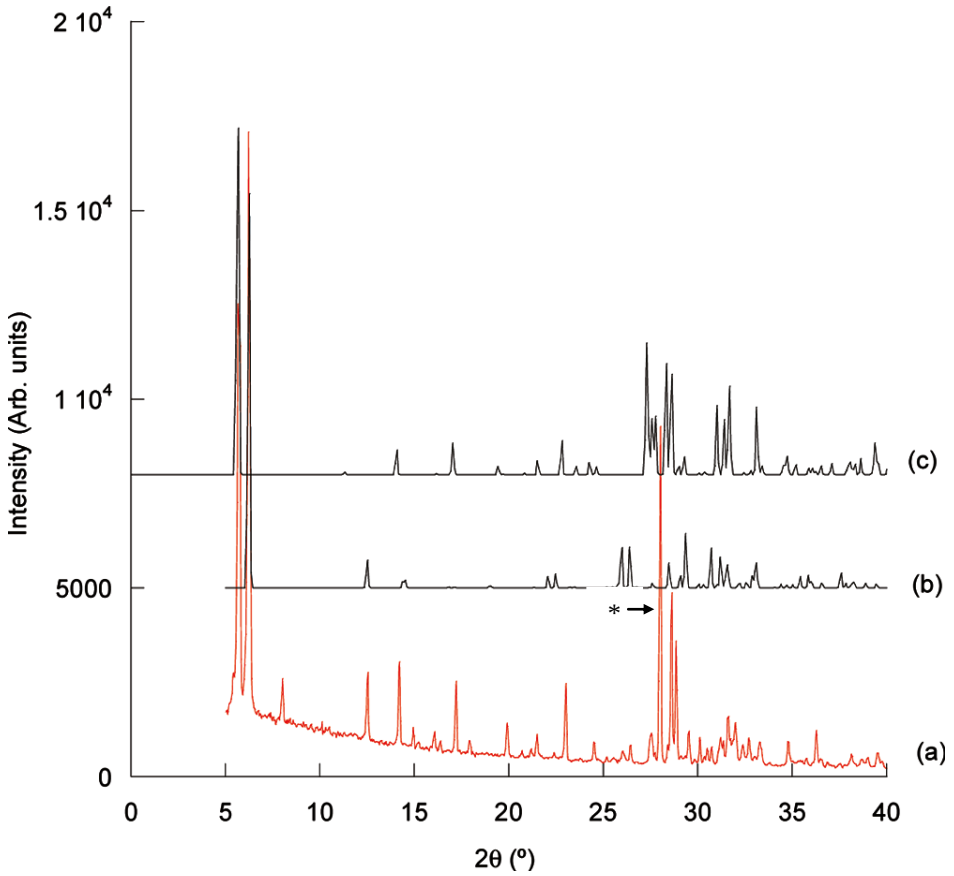

Figure 21 Comparison between (a) experimental powder XRD data (Co K_α radiation) and calculated patterns for (b) $[La_2(H_2O)_2W_2O_8][2,6\text{-NDS}]$ (**5**) and (c) $[La(H_2O)WO_4]_2[2,6\text{-NDS}]$ (**4**).

Small single crystals were present within the sample and single crystal X-ray diffraction measurements allowed for the structures of both phases to be determined. The phase with the larger interlayer separation of 17.90 Å was found to be $[La(H_2O)WO_4]_2[2,6\text{-NDS}]$ (**4**) and is iso-structural with **1**. The structure is shown in Figure 22 and the main crystallographic and refinement data is summarised in Table 2 with detailed bond lengths provided in Appendix A. This phase has also been synthesised were Ln = Ce and Pr, although from elemental analysis results it has been noted that there is a decrease in carbon content when using these lanthanides due to an unknown inorganic impurity being present, characterising data of these phases are provided in the appendix.

(a)

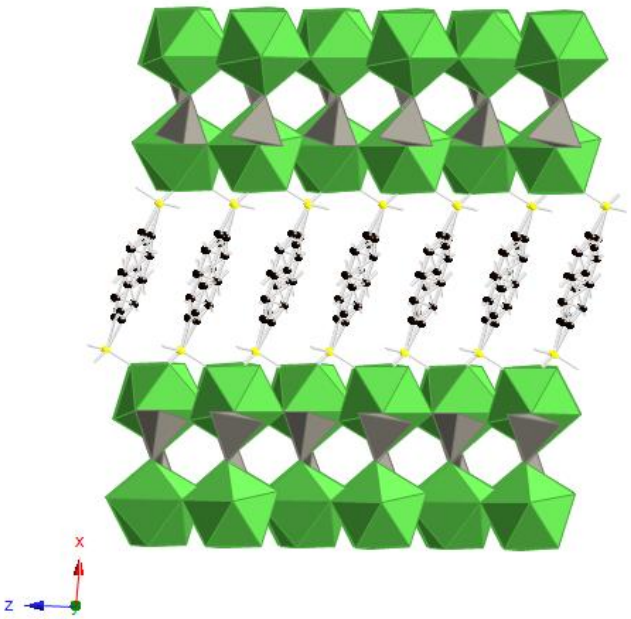

(b)

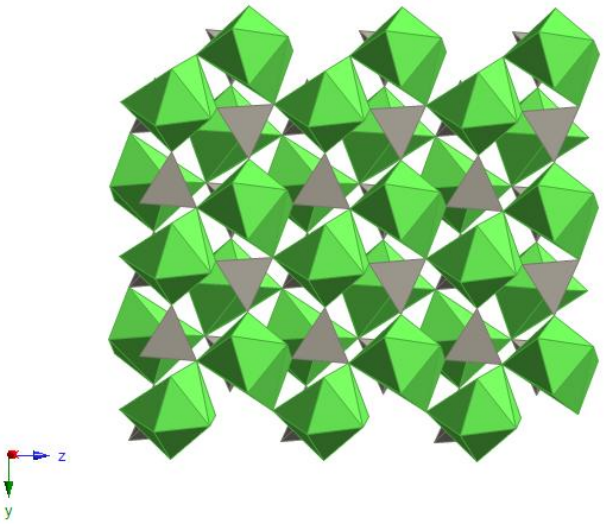

(c)

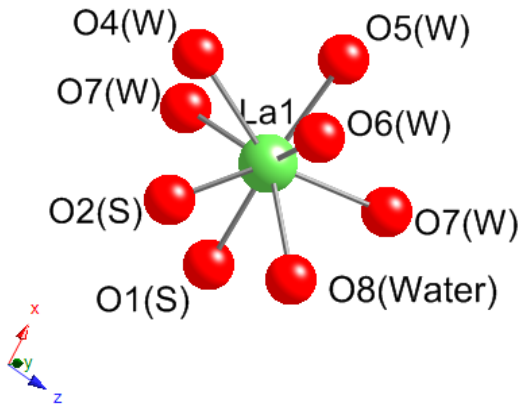

Figure 22 (a) Crystal structure and (b) layer structure of $[La(H_2O)WO_4]_2[2,6\text{-NDS}]$ (**4**) and (c) coordination sphere of lanthanum in (**4**)
(Colour key: Green - La^{3+}, Grey - WO_4^{2-})

Table 2 Crystallographic data and refinement parameters for phases (**4 - 6**).

	(4)	**(5)**	**(6)**
Empirical formula	$C_5H_3WLaO_8S$	$C_{20}H_{20}W_4La_4O_{32}S_4$	$C_4H_6Ce_2O_{14}Mo_2$
Formula weight	545.89	2191.64	750.21
Temperature	120(2) K	120(2) K	120(2) K
Wavelength	0.71073Å	0.71073Å	Synchrotron, 0.6889Å
Crystal system	Monoclinic	Triclinic	Triclinic
Space group	*C*2/*c*	$P\bar{1}$	$P\bar{1}$
Unit cell dimensions	a = 36.204(6) Å	a = 7.2550(2) Å	a = 7.2307(9) Å
	b = 7.4451(10) Å	b = 8.1110(2) Å	b = 7.4798(9) Å
	c = 7.5711(9) Å	c = 16.9310(4) Å	c = 13.5668(7) Å
	α = 90 º	α = 80.408(1)º	α = 78.671(6) º
	β = 93.731(10) º	β = 78.681(1) º	β = 85.649(7) º
	γ = 90 º	γ = 89.674(1) º	γ = 87.288(11) º
Volume ($Å^3$)	2036.4(5)	962.90(4)	716.98(13)
Z	8	1	2
Density (calculated) (Mg/m^3)	3.561	3.780	3.475
Absorption coefficient(mm^{-1})	15.656	16.555	8.007
Crystal	plate; colourless	colourless	block; yellow
Crystal Size (mm^3)	0.10x0.07x0.02	0.14x0.03x0.001	0.05x0.04x0.02
θ range for data collection (deg)	3.22-27.48	3.0-27.5	4.1-30.0
Reflections collected	14611	19673	4475
Independent reflections collected	2326 [R_{int}= 0.0895]	4394 [R_{int}= 0.0598]	4475(twinning prevents merging of equivalents)
Max. and min. transmission	0.745 and 0.304	0.852 and 0.205	0.690 and 0.897
Goodness of fit on F^2	1.137	1.119	1.098
R [F, $F^2 > 2\sigma$]	0.0513	0.0387	0.0714
R_w (F, all data)	0.1260	0.0827	0.2096
Diff. map extremes (e $Å^{-3}$)	1.90 and -2.65	2.12 and -1.76	3.02 and -2.70

The structure contains one crystallographically distinct La^{3+} cation which is found to be eight coordinate to one water molecule, five tungstate and two 2,6-NDS anions. The 2,6-NDS anions pillar the layers with both sulfonates bridging between two adjacent La cations. The La-OH_2 bond distance is 2.560(9) Å, and the La-OWO_3 distances lie in the range of 2.462(9) - 2.715(9) Å and La-OSO_2 distance are 2.533 (10) and 2.548(9) Å. The small pores present in the inorganic layer of this phase have window sizes of 4.49 Å in diameter, measuring the O-O distance across the window in the *yz* plane.

The second crystalline phase found to be present, with an interlayer separation of 16.38 Å, was found to have the composition $[La_2(H_2O)_2W_2O_8][2,6\text{-NDS}]$ (**5**) and is only formed when Ln = La. This phase is still a pillared tungstate with the same empirical formula as **1** - **4**, but the layer structure is significantly different as a result of the dimerization of the tungstate, to $W_2O_8^{4-}$, in the mixed metal oxide layer, during the course of the reaction. Single crystal X-ray diffraction data has shown that it adopts a triclinic structure with the space group $P\bar{1}$ comprising of two-dimensional inorganic mixed metal oxide layers which are pillared by 2,6-NDS organic anions. The structure is shown in Figure 23 the main crystallographic and refinement data is summarised in Table 1, detailed bond lengths are summarised in the appendix.

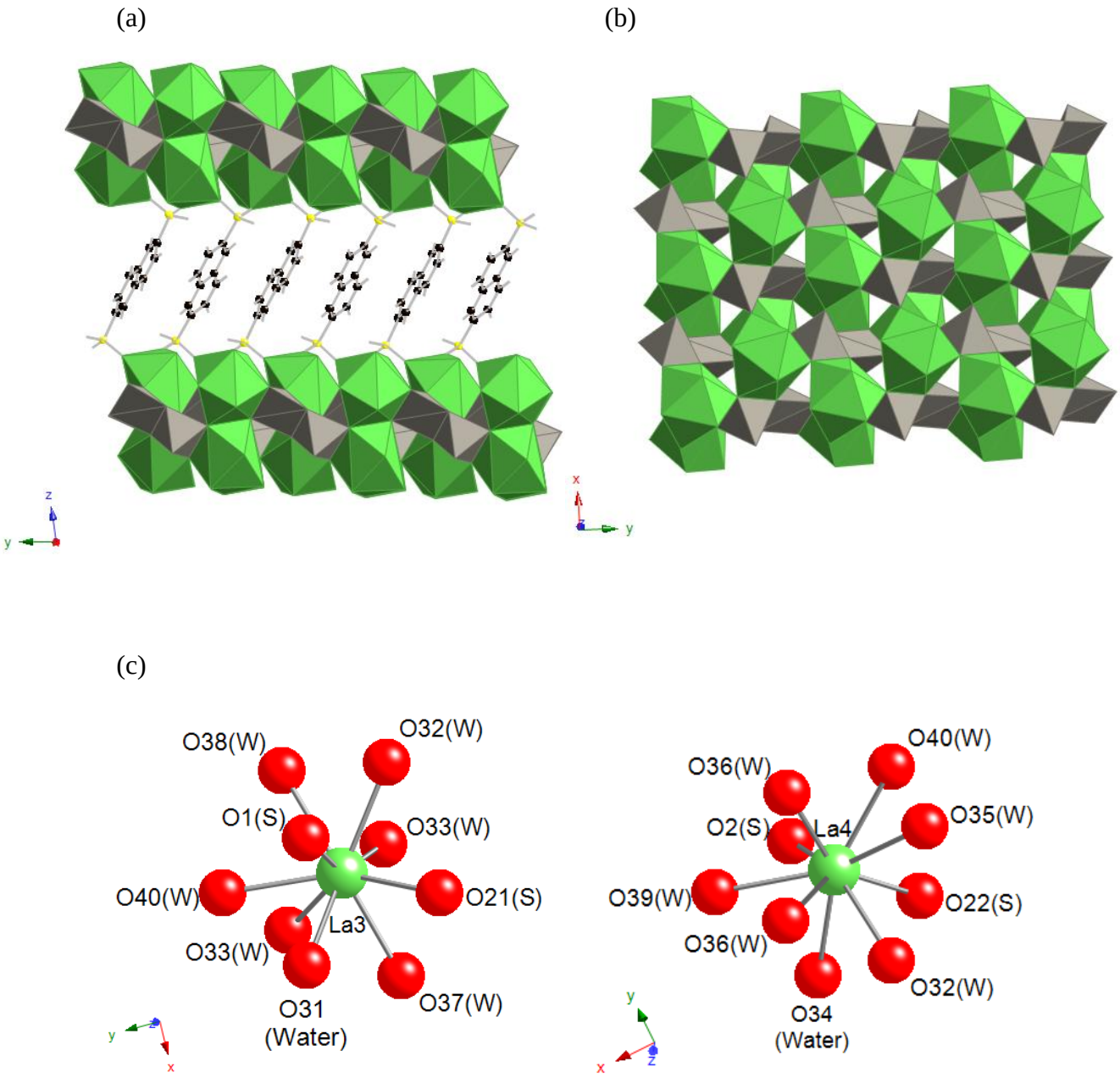

Figure 23 (a) Crystal structure and (b) layer structure of $[La_2(H_2O)_2W_2O_8][2,6\text{-NDS}]$ (**5**) and (c) coordination environments of lanthanum in (**5**)
(Colour key: Green - La^{3+}, Grey - $W_2O_8^{4-}$)

Two crystallographically distinct La cations are present in this structure which are nine coordinate, coordinating to one water molecule, two 2,6-NDS anions and four tungstate dimers, two of which are bidentate to the lanthanum centres. The disulfonate anions pillar the inorganic layers by bridging between adjacent lanthanum cations within each layer such that each 2,6-NDS anion is coordinated to four La cations. The average La-OH_2 bond distance is 2.545 Å and the La-OW_2O_7 distances lie in the range of 2.514-2.718 Å, and La-OSO_2 distances lie in the range of 2.421-2.549 Å, these ranges are comparable to those seen in phases **1** - **4**.

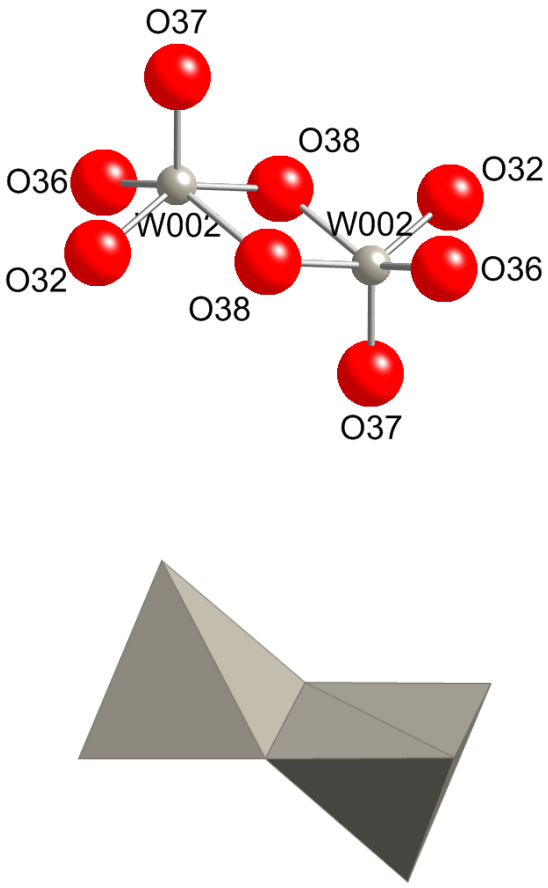

Figure 24 Structure of the $W_2O_8^{4-}$ dimer found in $[La_2(H_2O)_2W_2O_8][2,6\text{-NDS}]$ (**5**).

Differing to phases **1 - 4**, the channel resulting from the presence of the pores within the inorganic layer is not present in this material, having been blocked by the presence of the tungstate dimer. There are two independent $W_2O_8^{4-}$ units present in the structure (though each is itself centrosymmetric), the structure of the tungstate dimer is shown in Figure 24, comprising of two five-coordinate tungsten centres which have a square-based pyramidal geometry and are edge sharing and opposed to each other, making it unique. Dimeric $W_2O_8^{4-}$ units have been previously seen, for example, in Li_2WO_4; however, in that case, the two square-based pyramids are oriented in the same direction.[28] The two tungstate polyhedra have τ factors of 0.05 and 0.04 for W1 and W2, respectively, indicating that they are close to the ideal square-based pyramidal geometry.[29] $W_2O_8^{4-}$ coordinates to eight La cations, with four of the O atoms bridging between pairs of La atoms, while the remaining four bind to a single metal centre. The effect of this is to form a two-dimensional inorganic layer in the *xy* plane.

A range of analytical techniques were used to determine the composition and phase purity of this material. Analysis of the bulk sample, for example, by TGA, indicates that the expected composition of $[La(H_2O)WO_4]_2$[2,6-NDS] is a reasonable fit to the data, as expected due to the polymorphism found in this system.

The TGA trace of the system La/W/2,6-NDS, containing phases **4** and **5**, is shown in Figure 25. There are two distinct mass losses below 610 °C. The first mass loss of 3.8 % below 300 °C corresponds to the dehydration of the material this mass loss compares well to the calculated value of 3.3 %. The decomposition of the phase is complete by 610 °C following an additional mass loss of 20.6 % which corresponds to decomposition of the organic anion (calculated mass loss is 24.6 %). Powder X-ray diffraction showed the residue to be a mixture of $La_2W_2O_9$ and $La_2(WO_4)_3$. Phases **4** and **5** are found to have the same empirical formula, with TGA measurements confirming both phases to have the same thermal behaviour, as no noticeable separation of decompositions is observed.

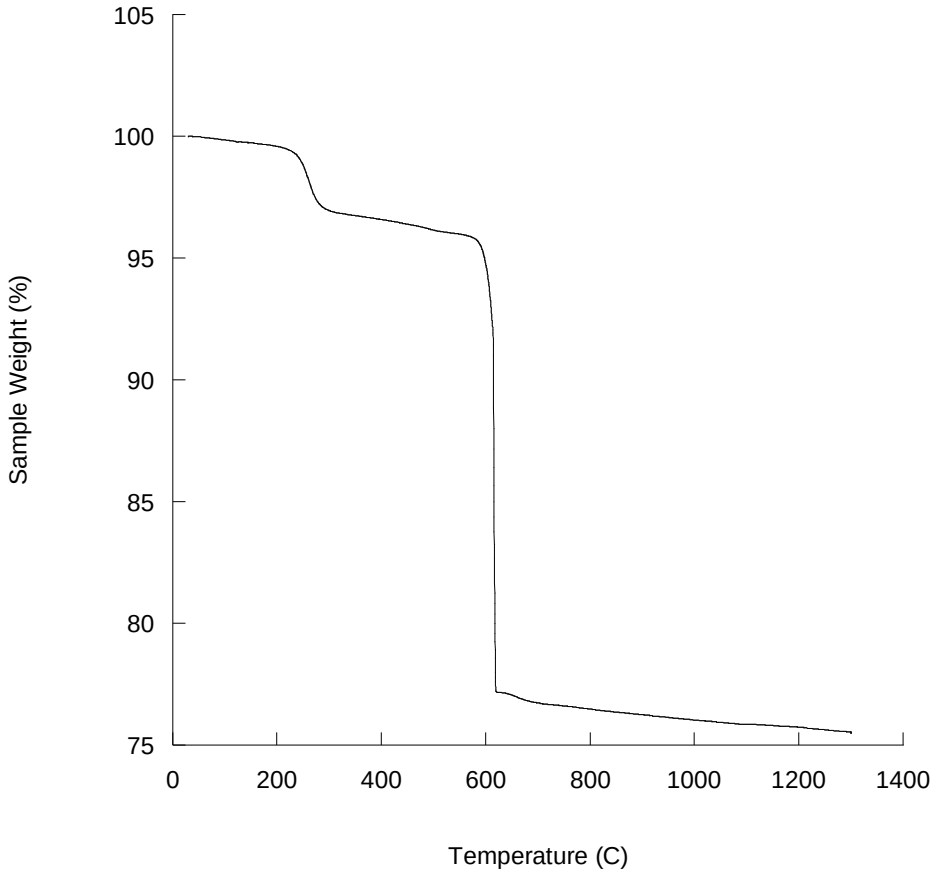

Figure 25 TGA trace of the polymorph system of La/W/2,6-NDS, containing phases **4** and **5**.

The FTIR spectrum is shown in Figure 26 and has a weak band due to an O-H stretch at approximately 3399 cm^{-1}. The other features of the spectrum are due to the tungstate and 2,6-NDS anions being present in the structure. Frequencies characteristic of the S-O stretching modes, antisymmetric and symmetric, are observed in at 1173 and 1052 cm^{-1}. The 2,6-NDS stretches have become weaker and have shifted to lower frequencies in comparison to the original disodium 2,6-naphthalenedisulfonate reagent, which is consistent with coordination to the lanthanide centre. This is also true for the tungstate stretching frequency, which is observed at 776 cm^{-1}.

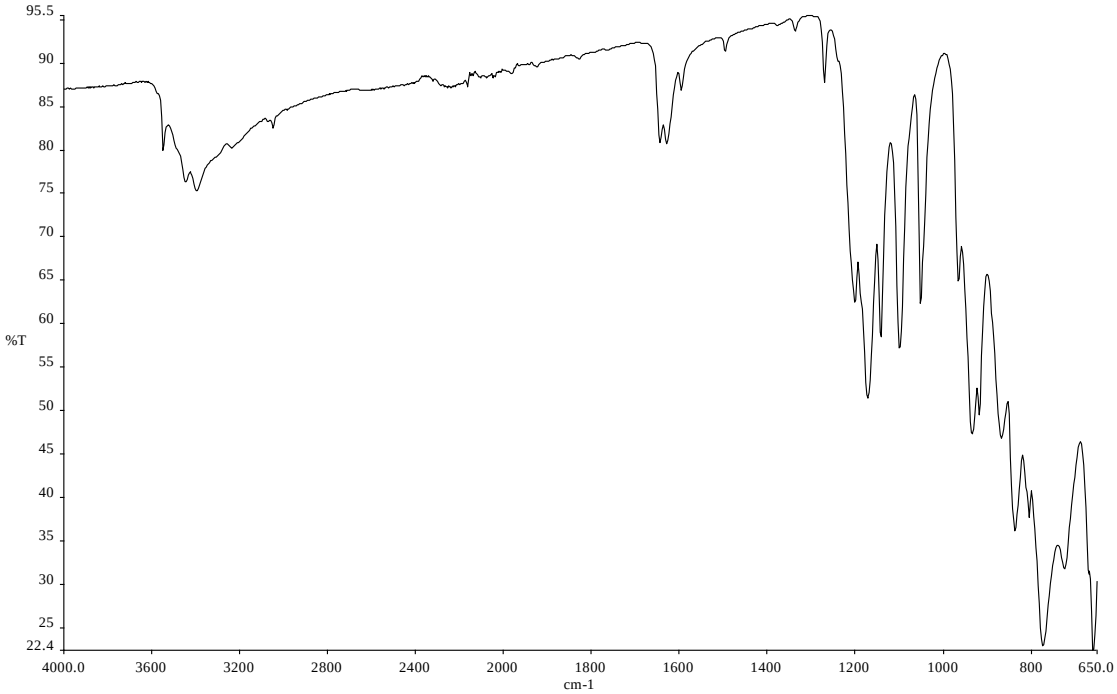

Figure 26 FTIR spectra of the polymorph system of La/W/2,6-NDS, containing phases **4** and **5**.

The SEM image, shown in Figure 27, confirms the simultaneous presence of **4** and **5**. This biphasic system exists as a microcrystalline powder and exhibits needle-like morphology, comparable to that seen in $[Nd(H_2O)MoO_4]_2$[2,6-NDS]. Agglomerates as well as needles are found to be present in the sample, were it may be concluded that these are representative of the dimerised phase.

Figure 27 SEM image of the polymorph system of La/W/2,6-NDS, containing phases **4** and **5**.

2.2.6 Characterisation of $[Ce(H_2O)MoO_4]_2$[Fumarate] (6)

Phases **1 - 5** were successfully synthesised using sulfonate as the anionic functional group, switching this anionic functional group with carboxylate proved to be largely unsuccessful, although one phase, $[Ce(H_2O)MoO_4]_2$[Fumarate] (**6**), was successfully synthesised by an undergraduate project student Sarah Hulse. The main crystallographic details of **6** are summarised in Table 2, and the structure is shown in Figure 28, from which it can be seen that it adopts a layered structure similar to that seen for **1 - 4**.

(a)

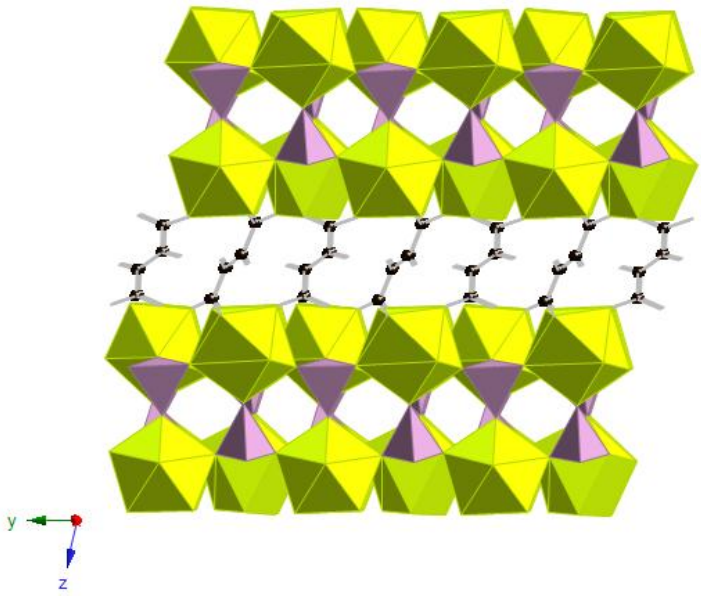

(b)

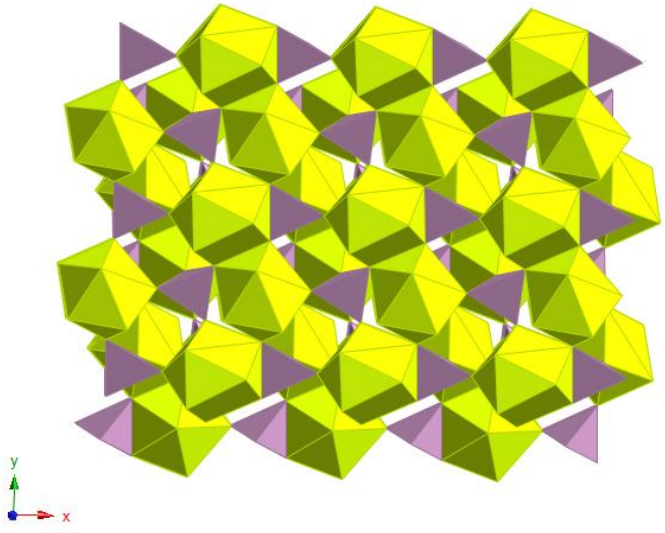

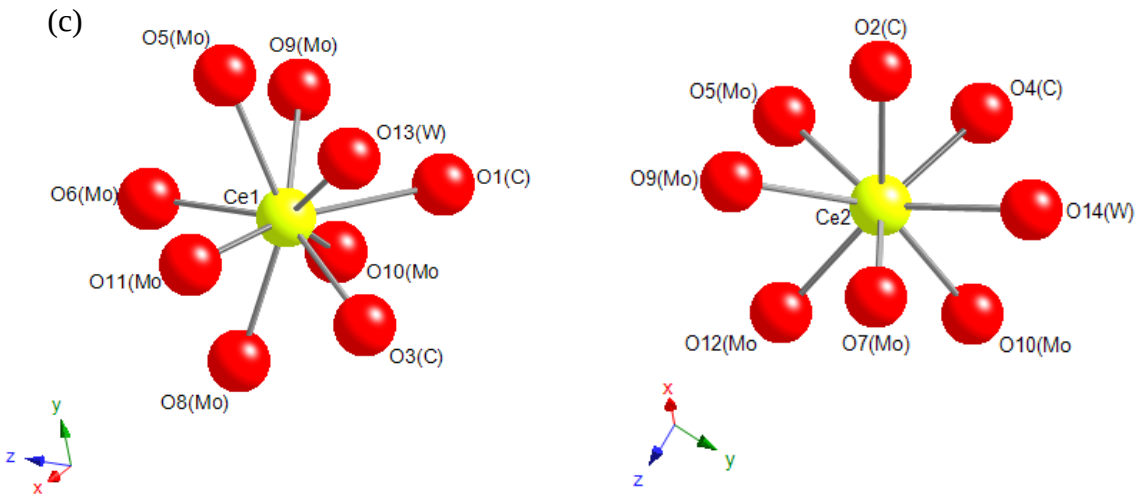

Figure 28 (a) Crystal structure and (b) layer structure of $[Ce(H_2O)MoO_4]_2[Fumarate]$ (**6**) and (c) coordination spheres of cerium in (**6**).
(Colour key; Yellow - Ce^{3+}, Purple - MoO_4^{2-})

In this material, there are two crystallographically independent Ce atoms, one of which is eight-coordinated by five different molybdate anions, two carboxylates, and one terminal water molecule and the other is nine-coordinate with the difference in the coordination number resulting from one molybdate anion being bidentate. The presence of the bidentate molybdate anion in this material creates subtle differences in the layer structure (see Figure 28b) in comparison to **1** - **4** but does not affect the framework nature of the layer, and the carboxylate anions remain bridging between Ce atoms within the layer and pillaring between adjacent ones. In **6**, the pore windows are slightly smaller than for **1** - **4** and measure 4.23 Å from O atom to O atom across the largest dimension.

A range of analytical techniques were used to determine the composition and phase purity of this material The TGA trace of the system $[Ce(H_2O)MoO_4]_2[Fumarate]$ is shown in Figure 29. There are three distinct mass losses below 610 °C. The first two mass losses of 1.8 % below 250 °C, correspond to the dehydration of the material. The decomposition of the phase is complete by 610 °C following an additional mass loss of 17.6 %, corresponding to decomposition of the organic anion. Powder X-ray diffraction showed the residue to be a mixture of $Ce_2Mo_3O_{12}$ and CeO_2.

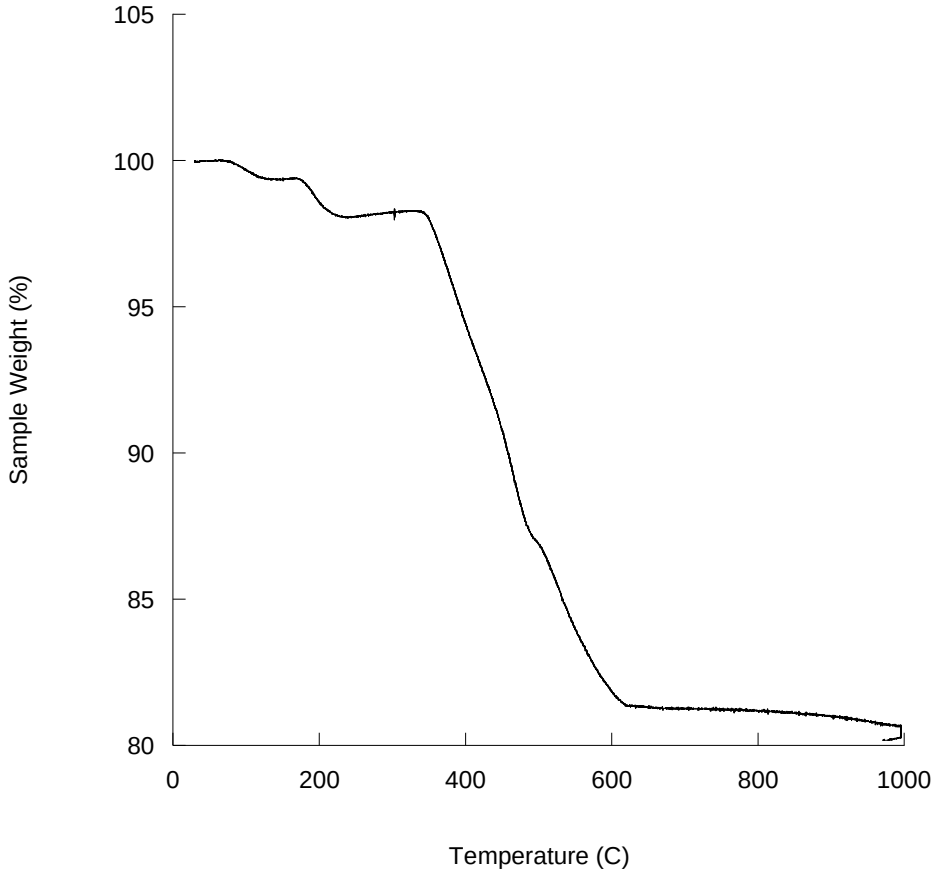

Figure 29 TGA trace of $[Ce(H_2O)MoO_4]_2$[Fumarate].

The FTIR spectrum is shown in Figure 30 and has a weak band due to an O-H stretch at approximately 3500 cm^{-1}. The other features of the spectrum are due to the molybdate and fumarate anions being present in the structure. Frequencies characteristic of the C-O stretching modes, antisymmetric and symmetric, are observed in at 1520 and 1408 cm^{-1}, these frequencies are consistent with literature reports.[30] The molybdate stretching frequency is observed at 763 cm^{-1}.

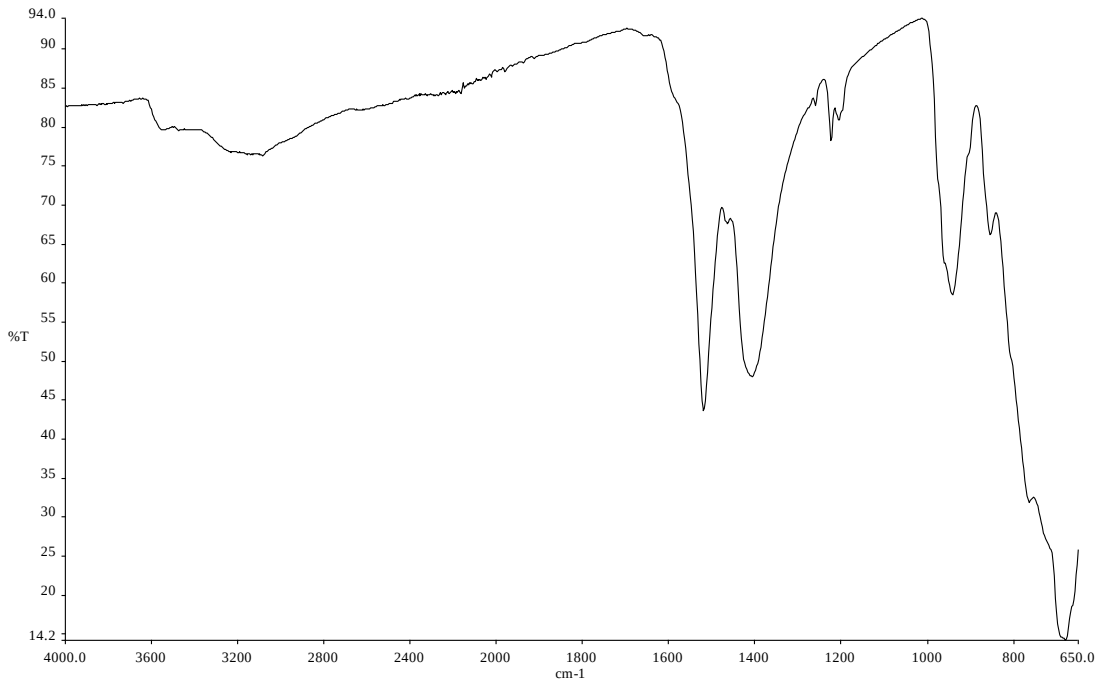

Figure 30 FTIR spectra of $[Ce(H_2O)MoO_4]_2$[Fumarate].

2.3 Properties of $[Ln(H_2O)MO_4]_2[A]$ (Ln= La- Nd, M= MoO_4 or WO_4, A= 1,5-NDS or 2,6-NDS)

2.3.1 Anion Exchange

A property which may be applicable to the molybdate and tungstate layered materials is that of anion exchange. Anion exchange of pillared layered materials is a useful property as it has many potential applications, for example use in, pharmaceuticals,[31, 32, 33] catalysis,[34, 35] and separation technologies.[36, 37, 38, 39] Layered double hydroxides, having the general formula $[M^{2+}_{1-x}\ M^{3+}_{x}(OH)_2]^{x+}A^{n-}_{x/n}.mH_2O$ (M^{2+} = Mg, Zn, Co & Ni, M^{3+} = Al, Cr, Fe & Ga),[40] are a well known class of materials which undergo anion exchange quite freely, due to the flexibility of the interlayer region and also the nature of the interactions of the counterbalancing anions with the layers. These interactions are known to be either; hydrogen bonding interactions between hydroxyl groups present within the layer and interlayer anions and water molecules, or coulombic forces- between the positively charged layers and the interlayer anions.[41] This in turn makes the interlayer anions more accessible to anion exchange due to

their weak interaction with the layers. In the pillared molybdate and tungstate phases reported above the interlayer NDS anions are found to be covalently bound to the lanthanide centers within the layers, therefore making anion exchange less probable, although still achievable. A recently reported layered lanthanide hydroxynitrate, $La(OH)_2NO_3.H_2O$,[42] is able to undergo anion exchange even though the nitrate anions are directly coordinated to the lanthanum centre. The nitrate anions are able to exchange with acetate, benzoate and terephthalate although they need harsher reaction conditions, of 65 °C for one week, than that of the normal anion exchange of layered materials. Exchange is also able to occur under shorter reaction times for this material, although this gives incomplete exchange. Layered lanthanide hydroxyhalide and lanthanide hydroxynitrate materials, with hydrogen bonding interactions between the anion and the layers, are also known to undergo facile anion exchange for example $Ln_2(OH)_5X.1.5H_2O$ (Ln = Dy, Er, Yb and Y , X = Cl or Br)[25] and $Ln_2(OH)_5(NO_3).1.5H_2O$ (Ln = Y, Gd - Lu).[24, 43] These compounds are able to exchange at room temperature with a variety of organic dicarboxylates such as maleate, phthalate, terephthalate and succinate and disulfonates, under soft reaction conditions. These materials are closely related to that of LDHs although metal species of the same charge are present within the layers of hydroxynitrate/halide phases whereas LDHs contain two metals of differing charge within the layers.

There are two main mechanisms of anion uptake from solution, firstly the topotactic mechanism[44] whereby during anion exchange bonding within the layers remains intact and the symmetry is conserved, and the interlayer distance is modified depending only on the size of the incoming anion. Secondly the dissolution re-precipitation mechanism,[41] where anion exchange becomes a two step process in which the host material dissolves and re-precipitates with the inclusion of the incoming anion. It is difficult to distinguish between these two mechanisms due to the rate of anion exchange, which is generally high for these materials, so it is not easy to study the kinetics. Any intermediate phases formed during reactions will be unstable and react quickly to form the anion exchanged phase and are therefore difficult to observe, isolate and characterise to determine the reaction mechanism. To possibly distinguish between these two mechanisms *in-situ* energy dispersive XRD technique may prove viable, whereby to distinguish and isolate any intermediates formed within the exchange reaction. To note, the use of the energy dispersive *in-situ*

technique proved not possible for the molybdate and tungstate compounds discussed, due to time constraints.

The anion exchange capabilities of layered molybdate and tungstates were tested, with anion exchange being confirmed by PXRD where the absence of the reflections characteristic of the host material is notable, and also by FTIR spectroscopy whereby the presence of the new organic anion within the product is observed. Anion exchange reactions were performed using dicarboxylates as the exchanging anion as they have an equivalent charge to NDS, and as it becomes easy to establish when exchange has occurred using elemental analysis and FTIR. Terephthalate, fumarate and 2,6-naphthalenedicarboxylate dianions were found to exchange well for these materials, although when using isomers of terephthalate and fumarate, either no exchange or decomposition of the host material occurred. Decomposition of the host also occurred when using oxalate, dibasic phosphate HPO_4^{2-} and succinate. Anion exchange reactions typically commenced at either room temperature overnight, or if anion exchange did not occur the temperature was increased to 90°C or the reaction proceeded hydrothermally. Details of successful syntheses are given below. To give reactions an additional push some were left for a longer reaction time of typically up to four days. The synthesis of each host material and also anion exchanged material is discussed in Chapter six.

2.3.1.1 Anion Exchange Properties of $[Nd(H_2O)MoO_4]_2$[2,6-NDS] (1)

Phase **1** is found to anion exchange successfully with terephthalate, fumarate and 2,6-NDC. All exchange reactions were successful under room temperature reaction conditions with overnight stirring, with the exception of 2,6-NDC where the reactions were successful only at 90°C over four days, or hydrothermally at 165°C for 14h, producing the same product although with the latter producing a less crystalline phase. Terephthalate and fumarate anion exchange reactions were also attempted hydrothermally, although it was discovered that either decomposition occurred or a less crystalline phase was produced. Several other organic dicarboxylates were used within the reactions where it was discovered that either no exchange occurred, or the host material decomposed post anion exchange reaction.

This was also true when using isomers of the anions which performed exchange successfully; phthalate, an isomer of terephthalate, and maleate an isomer of fumarate. As anion exchange proved unsuccessful using organic isomers, it is assumed that these materials may be successful for use within separation technologies. Details of anion exchange reactions performed are found in Chapter 6.

PXRD patterns of the anion exchange products in comparison to the host material, **1**, are shown in Figure 31 and characterising data in Table 3. Characterising data of anion exchange reactions using terephthalate and 2,6-NDC is provided in the appendix. The same study was performed using **2** as the host material, where the same products were observed with the same interlayer separations to those produced when using **1** as the host, powder X-ray diffraction patterns shown in Figure 32, and the remaining characterising data, of anion exchange product of **2**, provided in the appendix.

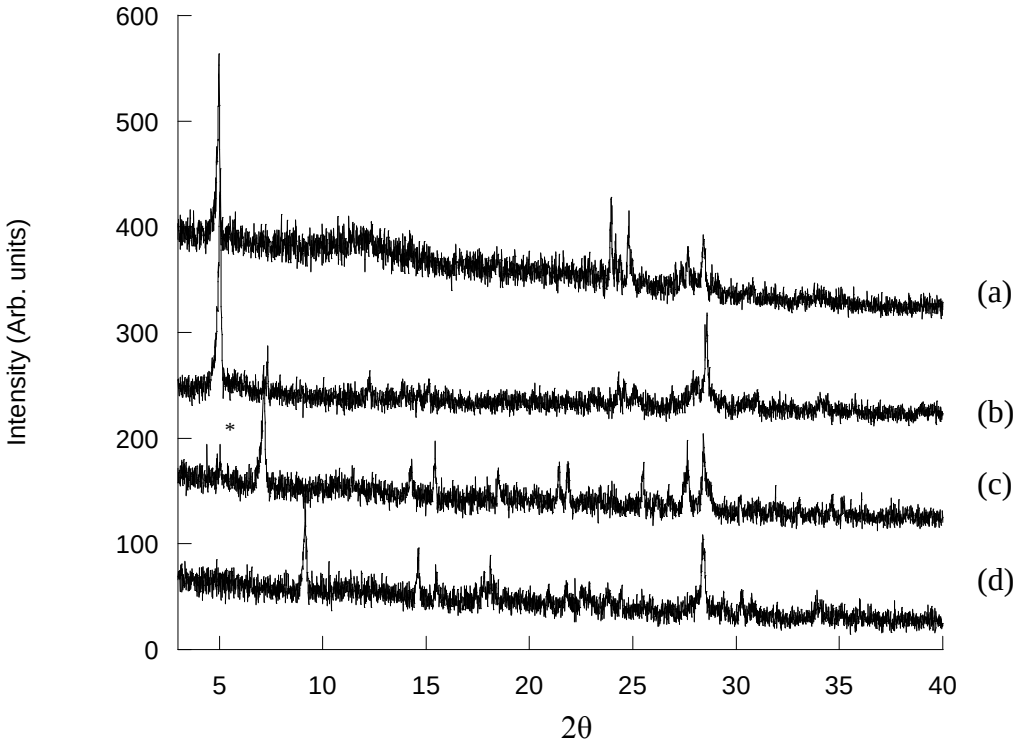

Figure 31 (a) Powder XRD pattern (Cu K_α radiation) of $[Nd(H_2O)MoO_4]_2$[2,6-NDS] (**1**) with anion exchange products (b) $[Nd(H_2O)MoO_4]_2$[2,6-NDC] (90 °C, 4 days), (c) $[Nd(H_2O)MoO_4]_2$[Fumarate] (Room temperature, overnight, * denotes reflection present of host material) and (d) $[Nd(H_2O)MoO_4]_2$[Terephthalate] (Room temperature, overnight).

Table 3 Characterising data for anion exchange reactions using the host material $[Nd(H_2O)MoO_4]_2$[2,6-NDS] (**1**)

Anion	Interlayer Separation (Å)	Elemental Analysis	
		Observed (%)	Calculated (%)
Fumarate	12.4	C-5.06	C-6.19
		H-1.48	H-1.04
Terephthalate	9.7	C-21.08	C-11.88
		H-1.75	H-1.00
2,6-NDC	17.6	C-14.42	C-16.79
(90°C, 4days)		H-1.00	H-1.17
2,6-NDC	17.6	C-16.13	C-16.79
(hydrothermal)		H-1.08	H-1.17

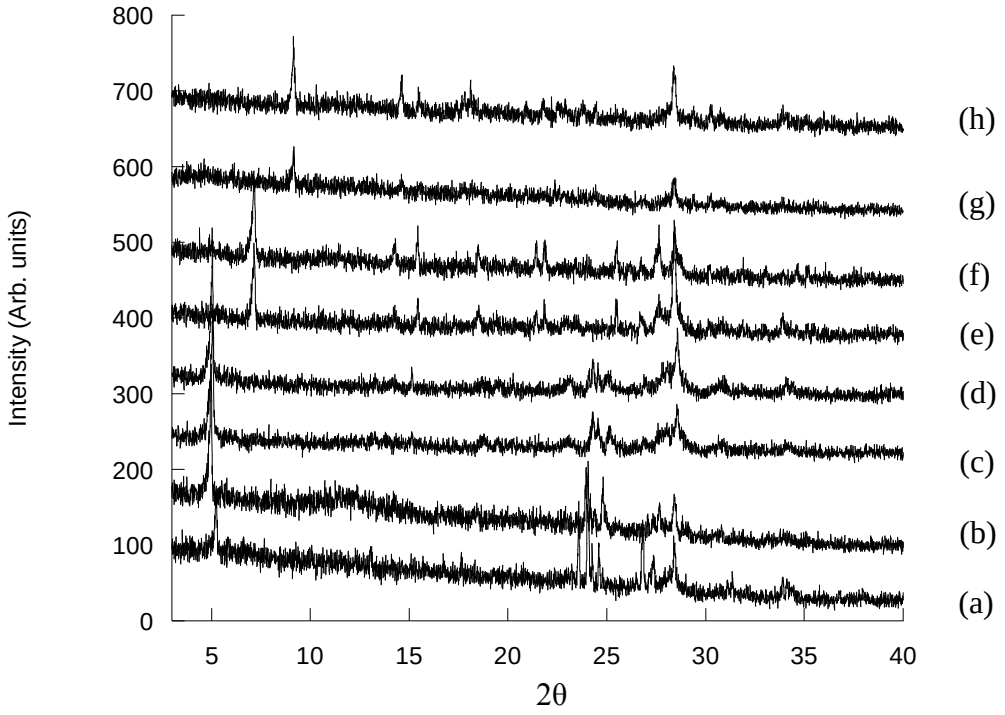

Figure 32 Powder X-ray diffraction patterns (a) $[Nd(H_2O)MoO_4]_2$[1,5-NDS], (b) $[Nd(H_2O)MoO_4]_2$[2,6-NDS], and iso-structural anion exchange products (c) $[Nd(H_2O)MoO_4]_2$[2,6-NDC] synthesised from **2** (90 °C, 4 days), (d) $[Nd(H_2O)MoO_4]_2$[2,6-NDC] synthesised from **1** (hydrothermal), (e) $[Nd(H_2O)MoO_4]_2$[Fumarate] synthesised from **1** (Room temperature, overnight), (f) $[Nd(H_2O)MoO_4]_2$[Fumarate] synthesised from **2**, (Room temperature, overnight), (g) $[Nd(H_2O)MoO_4]_2$[Terephthalate] synthesised from **1** (Room temperature, overnight), and (h) $[Nd(H_2O)MoO_4]_2$[Terephthalate] synthesised from **2** (Room temperature, overnight).

The anion exchange reaction, using fumarate, proved successful at room temperature, overnight. Under hydrothermal conditions a less crystalline phase was produced, with decomposition of the host material commencing. It has been observed from PXRD measurements that a small amount of the host material may still be present post anion exchange, Figure 31 (c), and also inorganic impurity of $Nd_2Mo_3O_9$ (~28 ° 2θ). This is confirmed by elemental analysis and FTIR measurements, as the observed carbon content differs to that of the calculated value, due to a small amount of host material and impurity, and also sulfonate stretches characteristic of 2,6-NDS are observed.

The FTIR spectrum, shown in Figure 33, and confirms the presence of fumarate in the product. There is a strong band present due to an O-H stretch at approximately 3226 cm^{-1}. The other features of the spectrum are due to molybdate and fumarate anions now being present in the structure. Frequencies characteristic of the C-O stretching modes are observed at 1536 cm^{-1} (anti-symmetric) and 1408 cm^{-1} (symmetric) respectively, and the molybdate stretching frequency is observed at 771 cm^{-1}. Frequencies characteristic of the S-O stretching modes are present in the region 1054 - 1230 cm^{-1}, therefore suggesting that trace amounts of 2,6-NDS are present in the product. From these results it may be concluded that only partial exchange has taken place under these conditions.

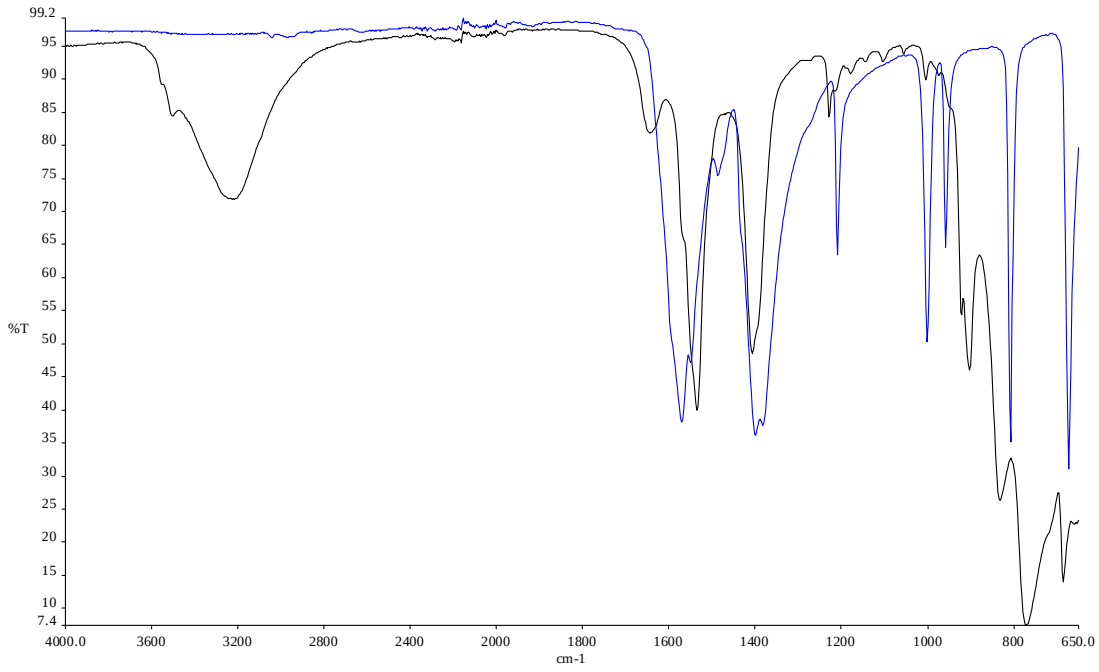

Figure 33 FTIR spectrum of $[Nd(H_2O)MoO_4]_2[Fumarate].H_2O$ (black) and sodium fumarate (blue).

The TGA trace of the anion exchange product $[Nd(H_2O)MoO_4]_2[Fumarate]\ .H_2O$ is shown in Figure 34, and shows two distinct mass losses below 600 °C. The first mass loss of 7.7 % below 200 °C corresponds to the dehydration of the material, calculated mass loss of 7.0 %. Decomposition of the phase is complete by 600 °C following an additional mass loss of 16.2 % which corresponds to decomposition of the organic anion comparing well to the calculated mass loss of 16.8 %. Powder X-ray

diffraction showed the residue to be a mixture of $Nd_2Mo_2O_7$ and $Nd_2Mo_3O_9$. Thermogravimetric analysis of the above phase compares well to the $[Ce(H_2O)MoO_4]_2$[Fumarate] analogue, discussed in Section 2.2.6. The temperature at which the material dehydrates and decomposes is found to be comparable.

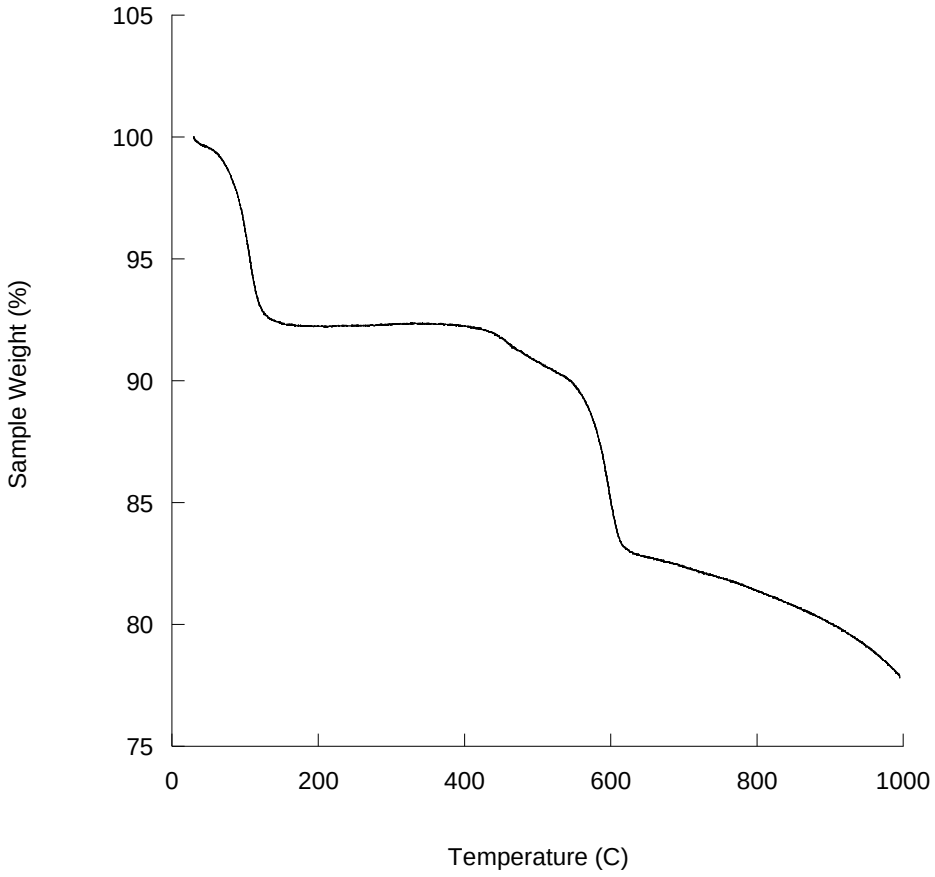

Figure 34 TGA trace of $[Nd(H_2O)MoO_4]_2$[Fumarate].H_2O

It has been calculated from TGA results that there are now three water molecules present in this material. The TGA trace compared to that of the host material now shows a loss of water at a lower temperature, confirming that the extra water maybe that of a lattice water molecule and not directly bound to the Nd^{3+} centre. The calculation of an extra water molecule is also in agreement with a now broader and stronger O-H band seen in the FTIR spectrum compared to that of the host material.

On comparison of $[Nd(H_2O)MoO_4]_2$[Fumarate].H_2O to $[Ce(H_2O)MoO_4]_2$[Fumarate], as discussed in Section 2.2.6, it is noted from powder X-ray diffraction measurements that a similar phase has formed. The interlayer separations are found

to have different values, with the Ce phase having a larger interlayer separation at 13.4 Å and the Nd phase at 12.3 Å. The difference in interlayer separation firstly is due to the difference in size of the lanthanide present and also secondly may be due to the orientation of fumarate, whereby it may reside at a different angle w.r.t the inorganic layers in the exchange phase, due to the position of the sulfonate groups present in the host material. Also to note the X-ray diffraction patterns show the phases to be non-isostructural, which may be accounted for by the differences of the molybdate coordination in the inorganic layers in either material, although some similarities are observed.

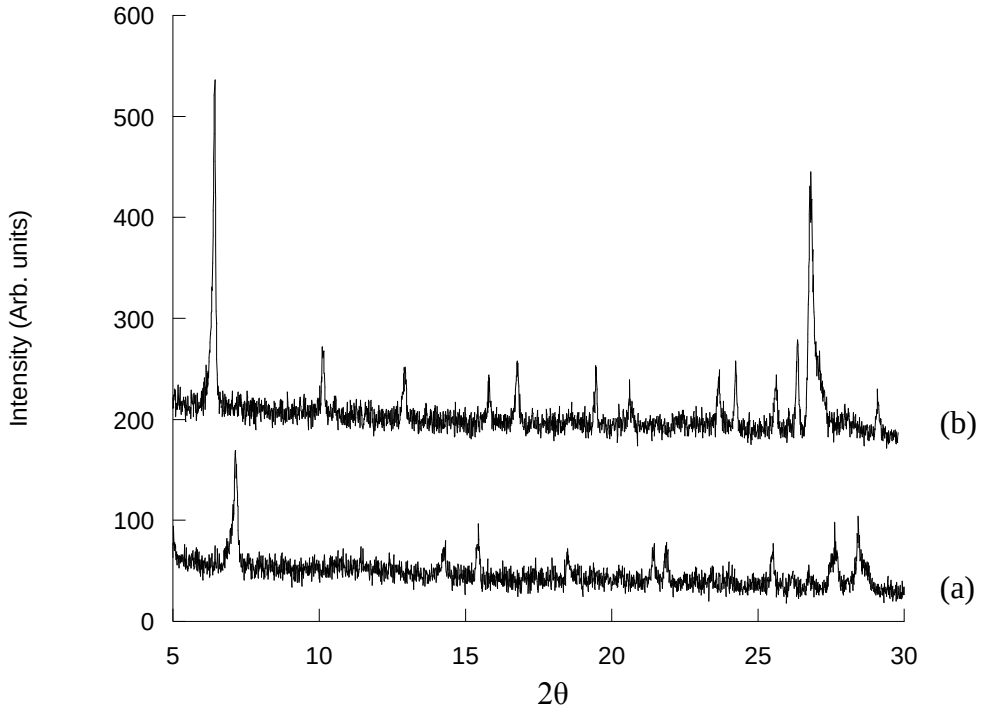

Figure 35 Powder X-ray diffraction patterns (Cu K_α radiation) of (a) $[Nd(H_2O)MoO_4]_2[Fumarate].H_2O$ and (b) $[Ce(H_2O)MoO_4]_2[Fumarate]$.

From TGA measurements it has been confirmed that the anion exchange phases have similar thermal behavior to that of the host material, with the exception of $[Nd(H_2O)MoO_4]_2$[2,6-NDC] (hydrothermal), Figure 36. The TGA of this product shows three distinct mass losses, the first two mass losses correspond to dehydration of the material. Calculations confirm four water molecules are now present in this phase, where it is predicted that two new lattice water molecules are present along

with the typical two water molecules coordinated to the Nd centre. It is therefore suggested that the lattice water molecules are removed first followed by the bound water, leading to two observed mass losses. The final mass loss corresponds to decomposition of the organic. This differs to the host material as there are only two water molecules present here which are coordinated to the Nd centre, therefore only one dehydration step is observed. Dehydration also occurs at a higher temperature in the host material at 250 °C, whereas in the 2,6-NDC exchanged material dehydration occurs at 175 °C, which again suggests the presence of two lattice water molecules. The FTIR spectra of all the anion exchange phases show the presence of the new guest anion, therefore concluding that anion exchange has taken place successfully, although some of the elemental analysis results are found to be inconsistent with these measurements, due to the presence of the inorganic impurity $Nd_2Mo_3O_9$.

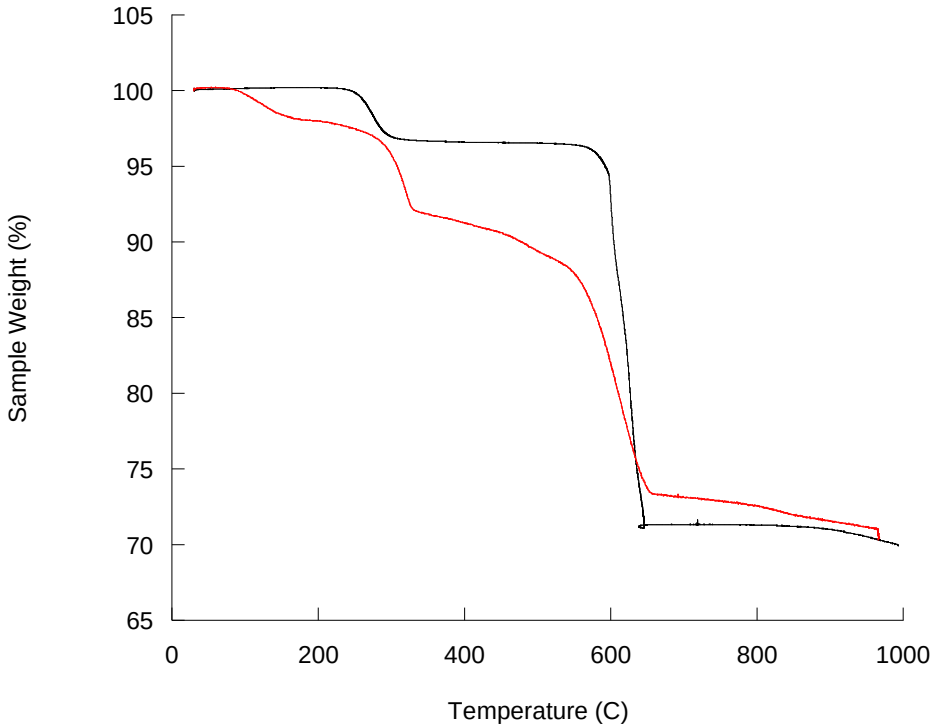

Figure 36 TGA trace of $[Nd(H_2O)MoO_4]_2[2,6\text{-NDS}]$ (black) and $[Nd(H_2O)MoO_4]_2[2,6\text{-NDC}]$ (red)

2.3.1.2 Anion Exchange properties of $[La(H_2O)WO_4]_2$[1,5-NDS] (3)

Phase **3** as well as a biphasic mixture of **4** and **5,** is found to anion exchange successfully with terephthalate, fumarate and 2,6-NDC. All exchange reactions were successful under hydrothermal conditions with the exception of terephthalate and 2,6-NDC where the reactions were also successful at 90 °C overnight. When performing the reactions at room temperature it was found that no exchange took place and the host material remained intact.

PXRD patterns of the anion exchange products in comparison to the host material, **3**, are shown in Figure 37 and characterising data in Table 3. Characterising data of terephthalate and fumarate anion exchange products are provided in the appendix as well as data for the anion exchange reactions using biphasic **4** & **5** as the host material. The anion exchange products from both host materials, **3**, **4** & **5**, are found to be iso-structural to one another.

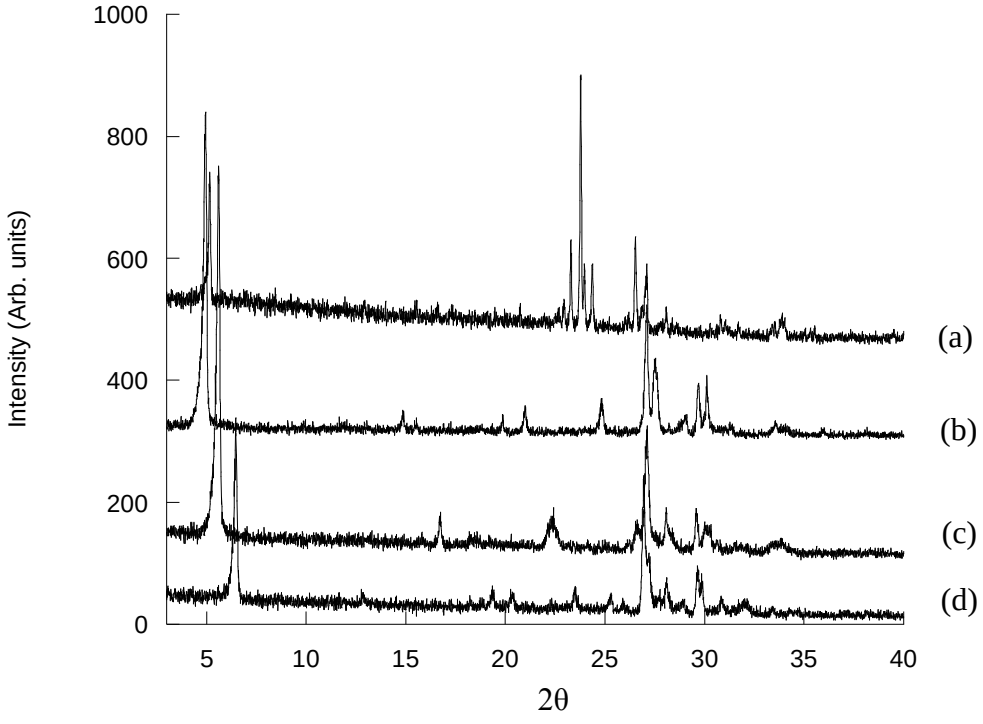

Figure 37 Powder XRD pattern (Cu K_α radiation) of (a) $[La(H_2O)WO_4]_2$[1,5-NDS] (**3**), with anion exchange products (b) $[La(H_2O)WO_4]_2$[2,6-NDC] (hydrothermal), (c) $[La(H_2O)WO_4]_2$[Terephthalate] (90 °C overnight) and (d) $[La(H_2O)WO_4]_2$[fumarate] (hydrothermal).

Table 3 Characterising data for anion exchange reactions using the host material $[La(H_2O)WO_4]_2[1,5\text{-NDS}]$ (**3**)

Anion	Interlayer Separation (Å)	Elemental Analysis Observed (%)	Calculated (%)
Fumarate	13.7	C - 3.31	C - 5.20
		H - 0.84	H - 0.65
Terephthalate	15.9	C - 8.35	C - 9.87
(90°C)		H - 0.64	H - 0.83
Terephthalate	15.8	C - 8.66	C - 9.87
(Hydrothermal)		H - 0.98	H - 0.83
2,6-NDC (90°C)	18.0	C - 12.87	C - 14.08
		H - 0.84	H - 0.98
2,6-NDC	17.9	C - 13.95	C - 14.08
(hydrothermal)		H - 0.89	H - 0.98

Anion exchange using 2,6-NDC proved successful at 90 °C overnight or when the reaction was performed hydrothermally. The hydrothermal results will be discussed in detail as this reaction condition gave the best characterising data results, suggesting that full anion exchange had occurred.

The FTIR spectrum, shown in Figure 38, confirms the presence of 2,6-NDC and the absence of 1,5-NDS in the anion exchanged material. There is a weak band present due to an O-H stretch at approximately 3287 cm^{-1}. The other features of the spectrum are due to tungstate and 2,6-NDC anions now being present in the structure. Frequencies characteristic of the C-O stretching modes are observed at 1530 cm^{-1} (anti-symmetric) and 1425 cm^{-1} (symmetric) respectively, and the tungstate stretching frequency is observed at 804 cm^{-1}. Frequencies characteristic of the S-O stretching modes are now absent.

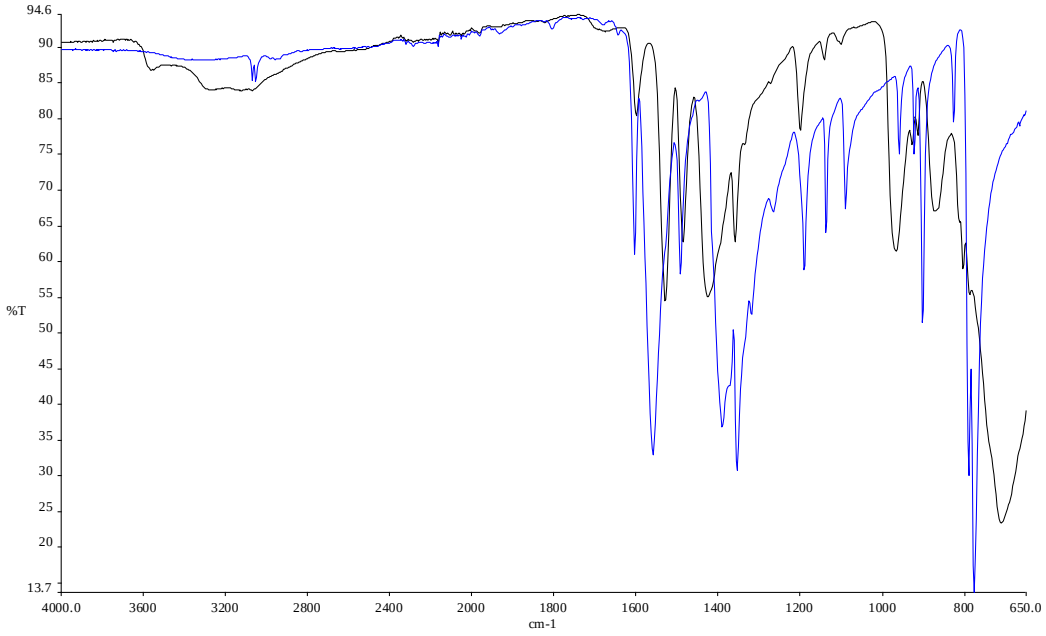

Figure 38 FTIR spectra of $[La(H_2O)WO_4]_2[2,6\text{-NDC}]$ hydrothermal (black) and 2,6-NDC (blue).

The TGA trace of the anion exchange product $[La(H_2O)WO_4]_2[2,6\text{-NDC}]$ synthesised hydrothermally is shown in Figure 39. Two distinct mass losses are observed below 800 °C with the first mass loss of 3.7 % below 200 °C corresponding to the dehydration of the material, comparing well to the calculated value of 3.5 %. Decomposition of the phase is complete by 800 °C following an additional mass loss of 20.4 % which corresponds to decomposition of the organic anion comparing well to the calculated mass loss of 19.4 %. Powder X-ray diffraction showed the residue to be $La_2W_2O_9$. The TGA is found to have a similar thermal behaviour and also mass loss to that of the host material, which is expected.

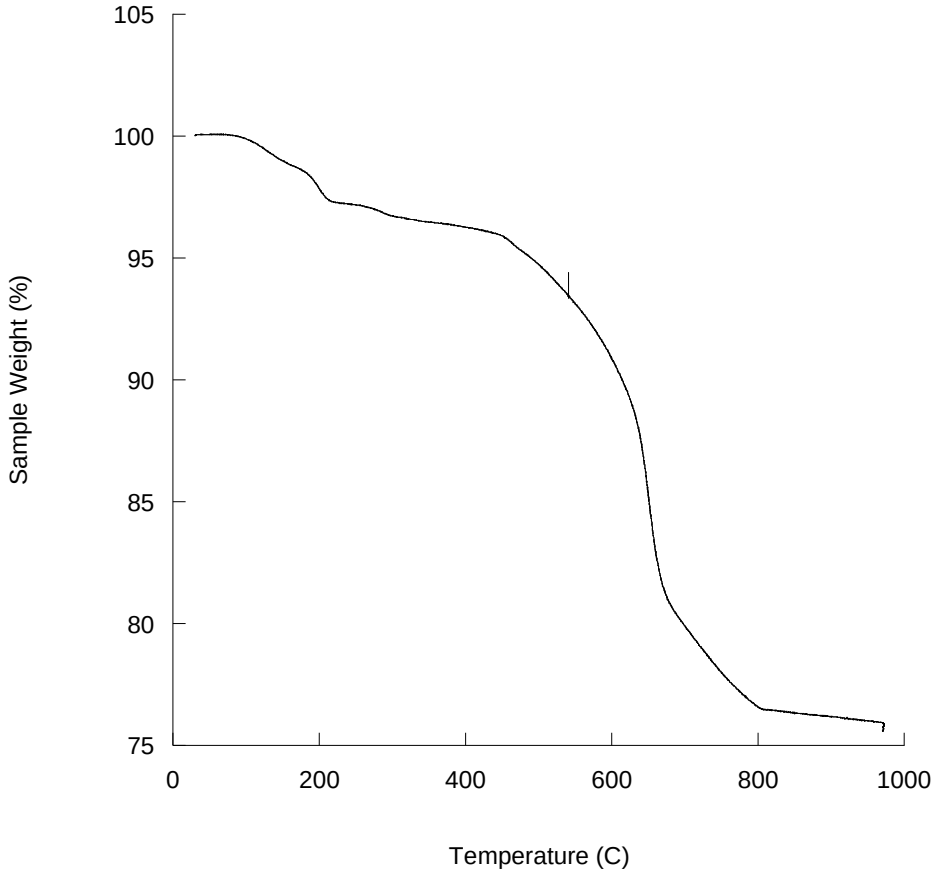

Figure 39 TGA trace of $[La(H_2O)WO_4]_2$[2,6-NDC] hydrothermally.

From TGA measurements it has been confirmed that the anion exchange phases have a similar thermal behavior to that of the host material. FTIR spectra show the presence of the new anion, therefore concluding that anion exchange has taken place successfully, although some elemental analysis results are found to be inconsistent with these measurements, suggesting that an amorphous impurity may be present in some of the anion exchange products.

In general anion exchange is found to occur successfully when the carboxylate groups are orientated in a position where they are able to successfully bind to the lanthanide centers within the inorganic layers, in turn pillaring the layers together.

2.3.2 Orientation of the Guests Anions

The orientation angle of guest anions with respect to the layers in the anion exchange products can be estimated, according to Equation 1, using the interlayer separation determined from PXRD measurements, the layer thickness determined from the crystal structure of the host material and also the anion length, taken from crystal structures previously reported containing the same organic anion.[45, 46, 47] Figure 40 depicts the angle at which 1,5-NDS is orientated with respect to the layers in **3**, calculated using Equation 1, with this estimated value being consistent with that found from the crystal structure of 68 °. As the predicted value is close to the value determined from the crystal structure Equation 1 may be utilized to predict the orientation of the new coordinated anions with respect to the inorganic layers.

$$\theta = \sin^{-1}\left(\frac{d_{gallery}}{d_{anion}}\right)$$

Equation 1

Where $d_{gallery}$ is equal to the interlayer separation ($d_{interlayer}$) minus the layer thickness (d_{layer}) and d_{anion} which is equal to the end-to-end length of the anion.

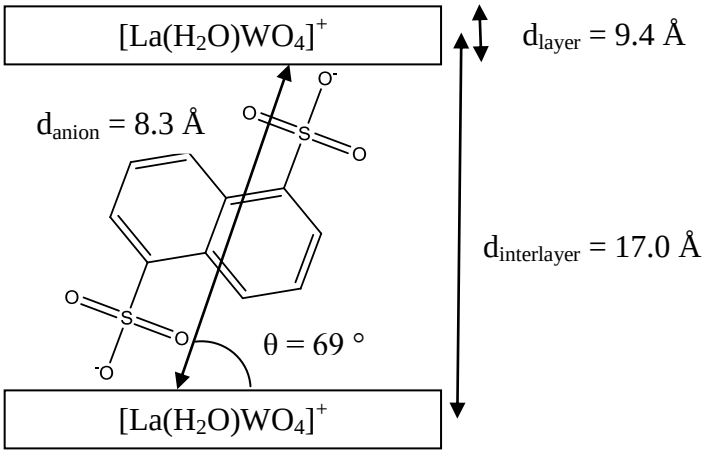

Figure 40 Schematic representation of the orientation angle of the 1,5-NDS anion with respect to the layers in phase **3**.

The tilt angles for guest anions exchanged with host material **1** are summarised in Table 4. The anion exchange reaction of **1** with terephthalate produces an orientation angle of 4 °, indicating that terephthalate lies flat between the layers, other angles lie between 34 & 67 °. The tilt angle is found to increase with the increase in the size of the guest anion, from fumarate to 2,6-NDC, this occurs so that the guest anion is able to mimic the position of the sulfonate group previously bound to the lanthanide centre, in order to complete the coordination arrangement in the same manner. The angle at which 2,6-NDC is tilted with respect to the layers is found to be very similar to that of 1,5-NDS in the host material. Both NDS anion exchanged phases are found to give similar tilt angles of the guest anions, therefore it can be concluded that the phases produced are iso-structural to one another. Tilt angles for **2** are provided in the appendix.

Table 4 Orientation of guest anions using host material $[Nd(H_2O)MoO_4]_2$[2,6-NDS], with a layer thickness of 9.1 Å

Anion	Interlayer separation (Å)	Organic length (Å)	Orientation of anion (°)
Fumarate	12.4	5.9	34
Terephthalate	9.7	8.0	4
2,6-NDC	17.6	9.2	67
2,6-NDS (host)	17.8	10.5	56

The tilt angles for guest anions exchanged with host material **3** are summarised in Table 5. As seen with phases **1** and **2,** similar tilt angles are seen for guest anions exchanged with both NDS phases **3** and **4**, hence iso-structural exchange products are produced. It is noticeable that the 2,6-NDC guest anion is orientated at a similar angle to that of the host material containing 1,5-NDS. Angles lie between 48 & 69 ° showing that decreasing the carbon chain length leads to a smaller tilt angle. The host

material 1,5-NDS is found to have a larger tilt angle than 2,6-NDS which is expected, due to the position of the sulfonate groups. It is also noted that the tilt angles of the NDS host anions in **3** & **4,** are found to be similar to the host anions found in **1** & **2.** Tilt angles for **4** are provided in the appendix.

Table 5 Orientation of guest anions using host material $[La(H_2O)WO_4]_2[1,5\text{-NDS}]$ with a layer thickness of 9.3 Å

Anion	Interlayer separation (Å)	Organic length (Å)	Orientation of anion (°)
Fumarate	13.7	5.9	48
Terephthalate	15.8	8.0	55
2,6-NDC	18.0	9.2	70, 68
1,5-NDS (host)	17.0	8.3	69

2.3.3 Catalysis

Tungstate exchanged LDHs have previously been used as biomimetic catalysts for mild oxidative bromination,[34,48] for example of aromatic olefins and aliphatic alkenes, and bromide assisted selective epoxidation reactions, such as olefin, allylic alcohols and styrene epoxidation.[48] The low cost of this heterogeneous catalytic system allows the development of a clean, mild, and efficient industrial route to important brominated chemicals and epoxide intermediates.[49] Bromination is involved in the manufacture of a range of chemicals from flame retardants through to disinfectants and antiviral drugs.

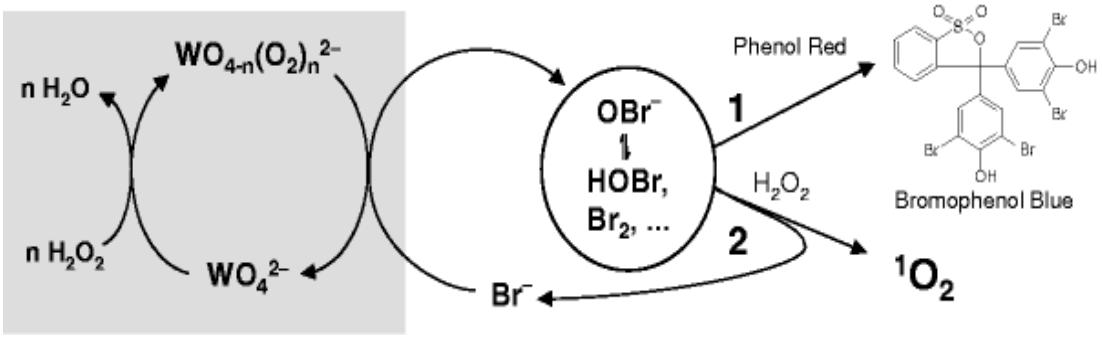

Figure 41 Schematic representation of the catalytic cycle in bromination with WO_4^{2-} LDH.[34]

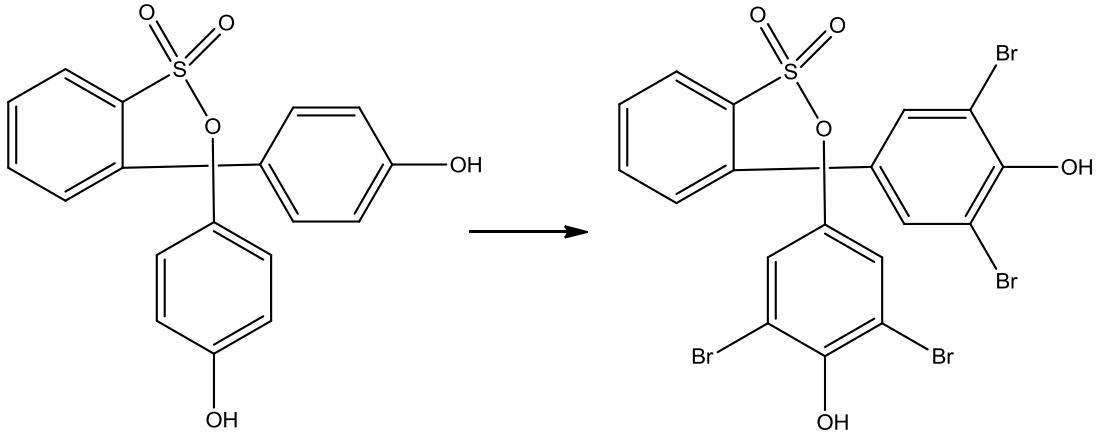

Phenol red Bromophenol blue

Figure 42 Schematic of phenol red and bromophenol blue.

A test for bromoperoxidase activity is the conversion of phenol red (phenolsulphonphthalein) into Bromophenol blue (tetrabromophenolsulphonphthalein). This reaction was found to go to completion within 32 minutes in the presence of WO_4^{2-}(MgAl)LDH.[34]

Within the catalytic reaction it is presumed that the reaction proceeds with coordination of H_2O_2 onto the metal centre forming a peroxo tungstate species. When Br^- is added it reacts with the peroxo tungstate species facilitating transfer of oxygen to Br^- creating Br^+, with reformation of tungstate, allowing the oxidized bromine species to brominate phenol red to bromophenol blue, see Figure 41 & 42. As strong

acid is not needed in the generation of Br^+ within the catalytic reaction, this leads to a mild and environmentally friendly reaction.

As phase **3** incorporates tungstate within the inorganic layers, the catalytic capabilities of this material were tested. As discussed in section 2.3.1, LDHs have charge balancing anions residing in the interlayer gallery and have hydrogen bond interactions between the anion and the layers. However in **3**, tungstate is coordinated to lanthanum into the mixed metal oxide layers, therefore the question is posed as to whether tungstate will be easily accessible to the catalytic reaction, as it is in tungstate exchanged LDHs. **3** may act as an improved catalyst compared to the corresponding LDH as it may be utilized for an increased amount of catalytic cycles, although on the other hand tungstate may be more sheltered within the inorganic layers therefore not available to take part as readily in the catalytic reaction.

The catalytic reaction, details in Section 6.2.3, was found to proceed for ~ 24 hrs until the reaction was deemed complete and a dark blue solution observed. PXRD of $[La(H_2O)WO_4]_2$[1,5-NDS] post catalytic reaction confirmed that the catalyst had successfully remained intact during the reaction, Figure 43. The ^{1}H NMR spectra of the blue residue formed from this reaction are shown in Figures 44 – 46. The NMR shows successful formation of Bromophenol blue, with resonances corresponding to aromatic CH and also OH observed.

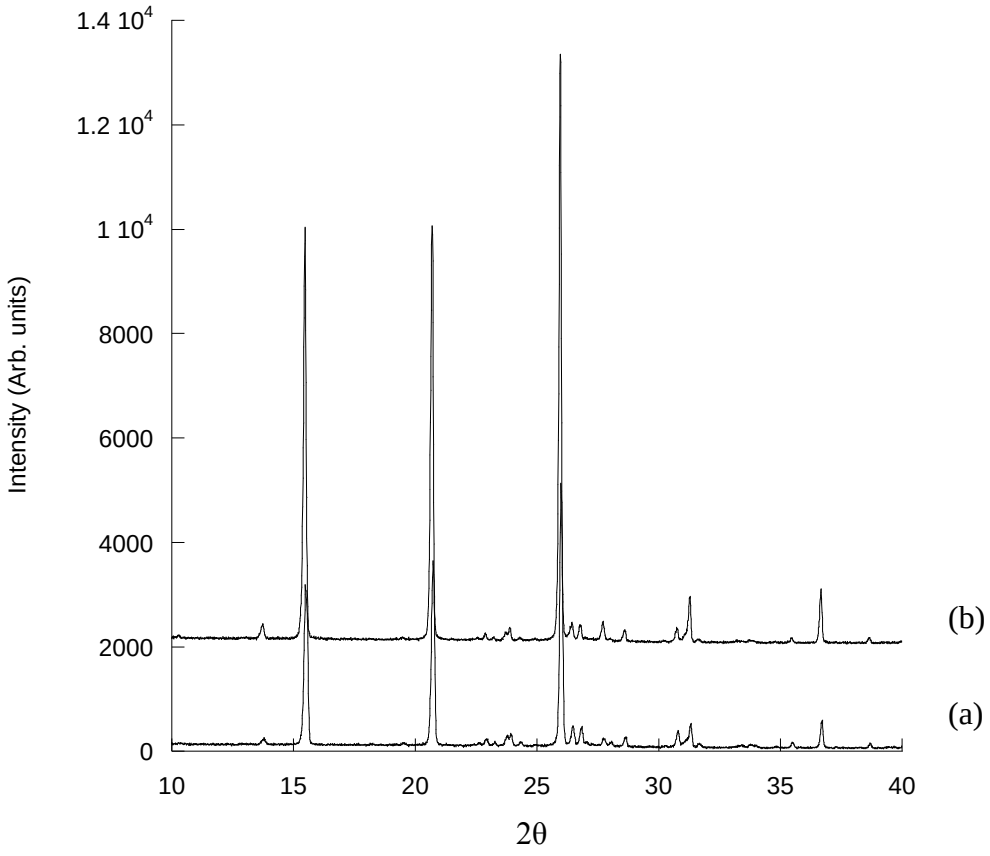

Figure 43 Powder X-ray diffraction patterns (Cu K_α radiation) of (a) $[La(H_2O)WO_4]_2$[1,5-NDS] post catalysis and (b) pre-catalysis.

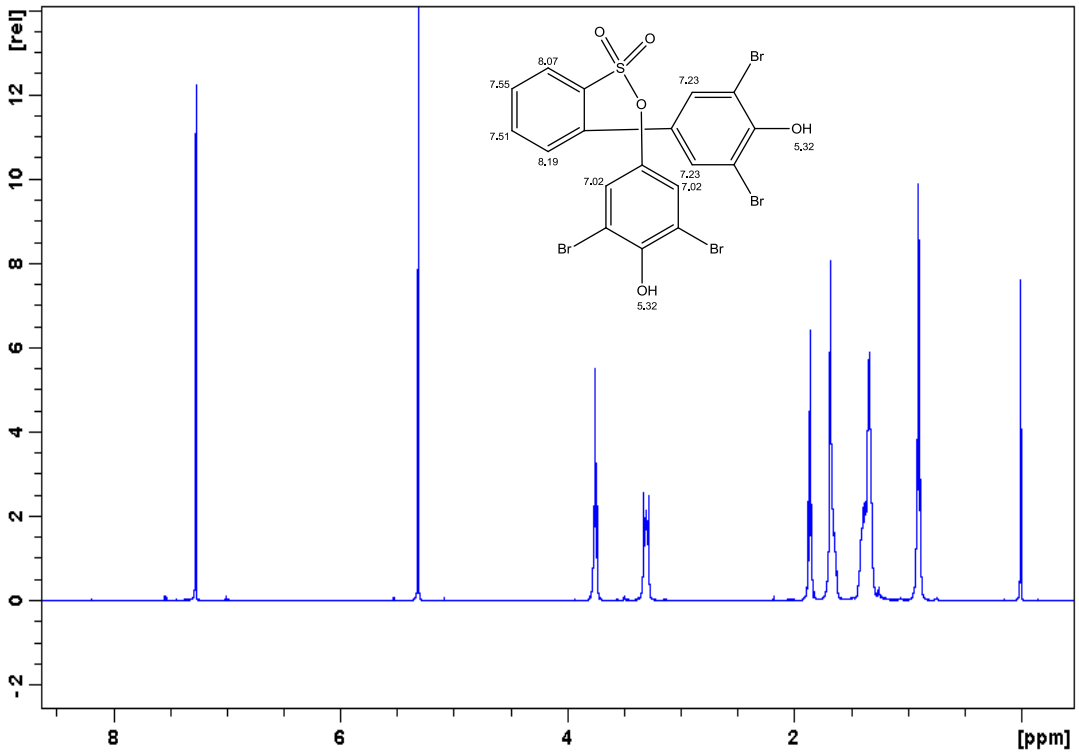

Figure 44 ^{1}H NMR spectrum of bromophenol blue produced from the catalytic reaction using the catalyst $[La(H_2O)WO_4]_2[1,5\text{-NDS}]$ (400 MHz, $CDCl_3$). (Resonances between 0.5 – 4.0 ppm are due to tetrahexyl ammonium chloride being present in the end product)

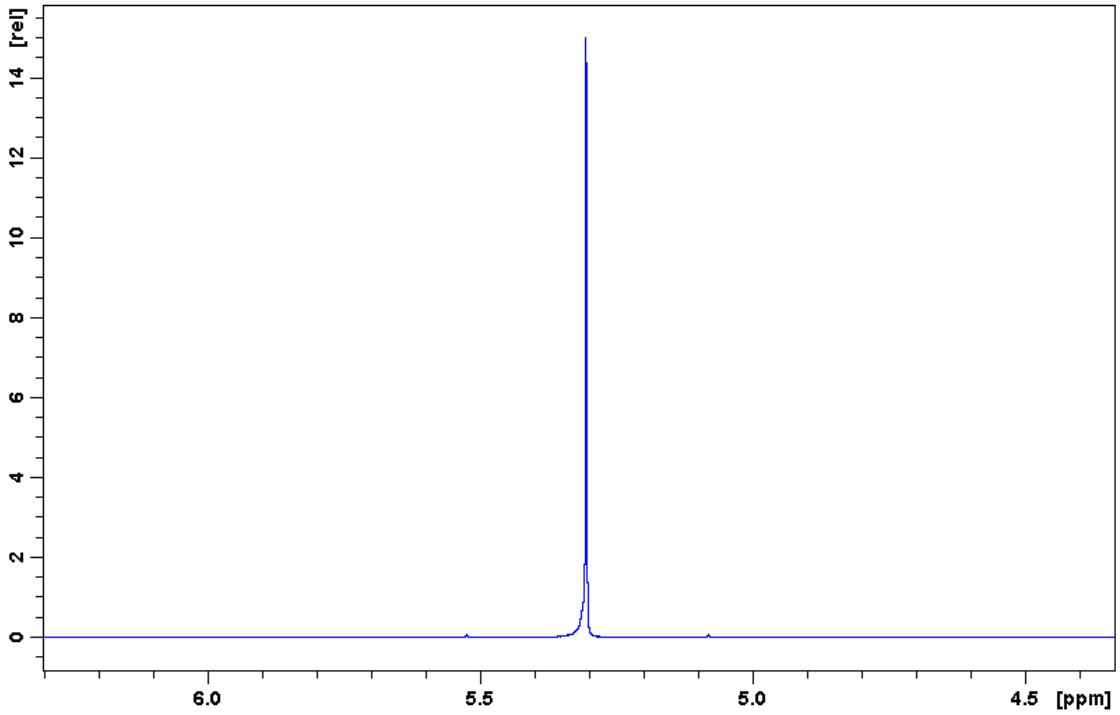

Figure 45 ^{1}H NMR spectrum showing the OH resonance, at 5.32ppm, present in bromophenol blue (400 MHz, $CDCl_3$)

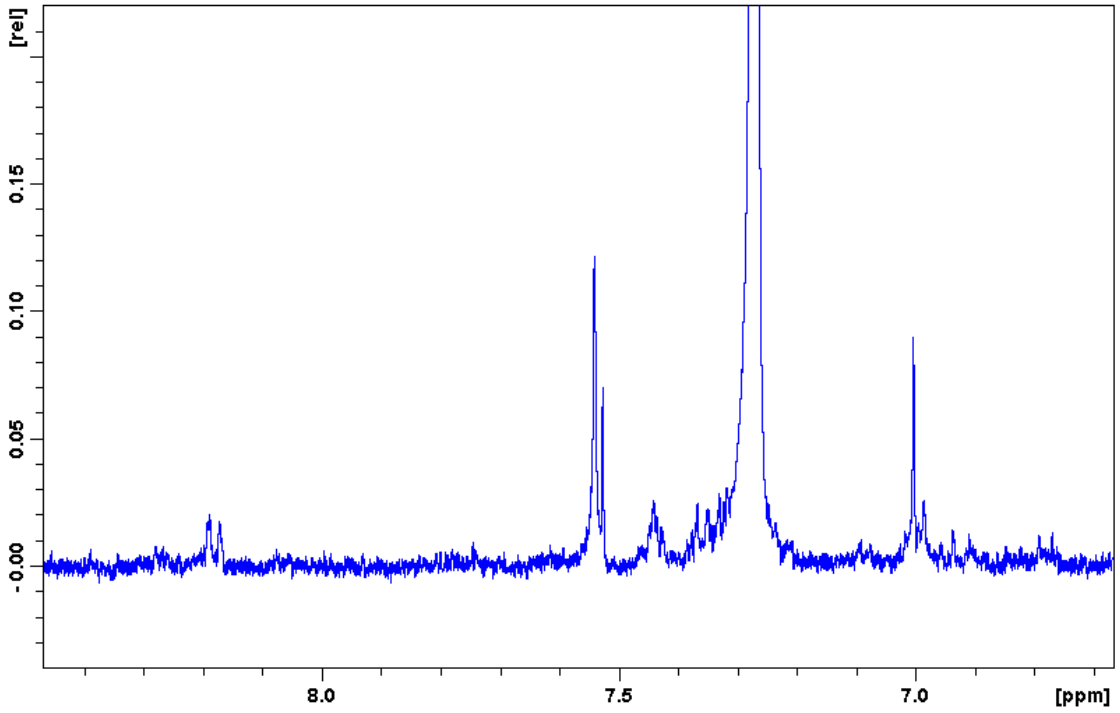

Figure 46 ^{1}H NMR spectrum showing the aromatic CH resonances, at 7.02, 7.23, 7.51, 7.56, 8.07 and 8.18 ppm, present in bromophenol blue (400 MHz, $CDCl_3$)

2.4 Conclusions

Six new inorganic-organic hybrid materials, $[Nd(H_2O)MoO_4]_2$[2,6-NDS](**1**), $[Nd(H_2O)MoO_4]_2$[1,5-NDS](**2**), $[La(H_2O)WO_4]_2$[1,5-NDS](**3**), $[La(H_2O)WO_4]_2$[2,6-NDS](**4**), $[La_2(H_2O)_2W_2O_8]$[2,6-NDS](**5**), and $[Ce(H_2O)MoO_4]_2$[Fumarate](**6**), have been successfully synthesized via a hydrothermal route, under similar reaction conditions, with their crystal structures determined by single-crystal X-ray diffraction.

Each of these lanthanide molybdate or tungstate phases contain positively charged two-dimensional inorganic mixed-metal oxide layers which are charge-balanced by pillaring organic dianions. Phases **1**-**4** contain framework layers which have a bilayer of polyhedra resulting in the formation of small cages in the lanthanide molybdate or tungstate layer. Gas sorption measurements, however, show that these materials are not porous. **5** has a different layer structure resulting from the formation of tungstate dimers, $W_2O_8^{4-}$, in the inorganic layer. These dimers, which have not previously been observed in other structures, block the pore windows, thus removing the channels that created the open framework layer in **1**-**4**. A dicarboxylate pillared structure, **6**, closely related to **1**-**4**, has also been synthesised. In this case, the layers maintain a framework structure, but subtle differences result from the presence of a bidentate molybdate anion in comparison to **1**-**4**.

Re-producing the above phases using a variety of mono, di and tri-sulfonates proved unsuccessful.

The properties of phases **1**-**5** were investigated where it was found that these materials are able to undergo anion exchange, of the NDS anions, with dicarboxylates fumarate, terephthalate and 2,6-NDC. The catalytic properties of the tungstate phases were also tested and proved that catalysis was indeed successful, although the reactions proceeded for a longer time than is expected for the compound to be classified as a good catalyst.

2.5 References

(1) Madeira, L. M.; Portela, M. F.; Mazzocchia, C. *Catal. Rev.-Sci. Eng.* **2004**, *46*, 53.

(2) Livage, C.; Hynaux, A.; Marrot, J.; Nogues, M.; Ferey, G. *J. Mater. Chem.* **2002**, *12*, 1423.

(3) Liu, B.; Yu, S. H.; Li, L. J.; Zhang, Q.; Zhang, F.; Jiang, K. *Angew. Chem.-Int. Edit.* **2004**, *43*, 4745.

(4) Ingham, B.; Chong, S. V.; Tallon, J. L. *Curr. Appl. Phys.* **2006**, *6*, 553.

(5) Ding, Y.; Wan, Y.; Min, Y. L.; Zhang, W.; Yu, S. H. *Inorg. Chem.* **2008**, *47*, 7813.

(6) Hazen, R. M.; Finger, L. W.; Mariathasan, J. W. E. *J. Phys. Chem. Solids* **1985**, *46*, 253.

(7) Escobar, C.; Ciddresd.H; Kittl, P.; Dumler, I. *Am. Miner.* **1971**, *56*, 489.

(8) Sleight, A. W.; Chamberl.Bl *Inorg. Chem.* **1968**, *7*, 1672.

(9) Young, A. P.; Schwartz, C. M. *Science* **1963**, *141*, 348.

(10) Bonanni, M.; Spanhel, L.; Lerch, M.; Fuglein, E.; Muller, G.; Jermann, F. *Chem. Mat.* **1998**, *10*, 304.

(11) Yu, S. H.; Liu, B.; Mo, M. S.; Huang, J. H.; Liu, X. M.; Qian, Y. T. *Adv. Funct. Mater.* **2003**, *13*, 639.

(12) Ding, Y.; Yu, S. H.; Liu, C.; Zang, Z. A. *Chem.-Eur. J.* **2007**, *13*, 746.

(13) Hagrman, P. J.; Hagrman, D.; Zubieta, J. *Angew. Chem.-Int. Edit.* **1999**, *38*, 2639.

(14) Xu, Y.; An, L. H.; Koh, L. L. *Chem. Mat.* **1996**, *8*, 814.

(15) Hagrman, P. J.; LaDuca, R. L.; Koo, H. J.; Rarig, R.; Haushalter, R. C.; Whangbo, M. H.; Zubieta, J. *Inorg. Chem.* **2000**, *39*, 4311.

(16) DeBord, J. R. D.; Haushalter, R. C.; Meyer, L. M.; Rose, D. J.; Zapf, P. J.; Zubieta, J. *Inorg. Chim. Acta* **1997**, *256*, 165.

(17) Zapf, P. J.; Hammond, R. P.; Haushalter, R. C.; Zubieta, J. *Chem. Mat.* **1998**, *10*, 1366.

(18) Hagrman, D.; Warren, C. J.; Haushalter, R. C.; Seip, C.; O'Connor, C. J.; Rarig, R. S.; Johnson, K. M.; LaDuca, R. L.; Zubieta, J. *Chem. Mat.* **1998**, *10*, 3294.

(19) Hagrman, D.; Zubieta, C.; Rose, D. J.; Zubieta, J.; Haushalter, R. C. *Angew. Chem.-Int. Edit. Engl.* **1997**, *36*, 873.

(20) Lu, J.; Li, Y. G.; Shen, E. H.; Yuan, M.; Wang, E.; Hu, C. W.; Xu, L. *J. Solid State Chem.* **2004**, *177*, 1771.

(21) Tao, J.; Zhang, X. M.; Tong, M. L.; Chen, X. M. *J. Chem. Soc.-Dalton Trans.* **2001**, 770.

(22) Oliver, S. R. J. *Chem. Soc. Rev.* **2009**, *38*, 1868.

(23) Evans, D. G.; Slade, R. C. T. In *Layered Double Hydroxides*; Duan, X., Evans, D. G., Eds.; Springer-Verlag Berlin: Berlin, 2006; Vol. 119.

(24) McIntyre, L. J.; Jackson, L. K.; Fogg, A. M. *Chem. Mat.* **2008**, *20*, 335.

(25) Poudret, L.; Prior, T. J.; McIntyre, L. J.; Fogg, A. M. *Chem. Mat.* **2008**, *20*, 7447.

(26) Luo, J. J.; Xu, L. *Inorg. Chem.* **2006**, *45*, 11030.

(27) Kanezaki, E. *Mater. Res. Bull.* **1999**, *34*, 1435.

(28) Horiuchi, H.; Morimoto, N.; Yamaoka, S. *J. Solid State Chem.* **1979**, *30*, 129.

(29) Addison, A. W.; Rao, T. N.; Reedijk, J.; Vanrijn, J.; Verschoor, G. C. *J. Chem. Soc.-Dalton Trans.* **1984**, 1349.

(30) Baddiel, C. B.; Cavendis, C. D.; George, W. O. *J. Mol. Struct.* **1970**, *5*, 263.

(31) Khan, A. I.; Lei, L. X.; Norquist, A. J.; O'Hare, D. *Chem. Commun.* **2001**, 2342.

(32) Li, B. X.; He, J.; Evans, D. G.; Duan, X. *Int. J. Pharm.* **2004**, *287*, 89.

(33) Nalawade, P.; Aware, B.; Kadam, V. J.; Hirlekar, R. S. *J. Sci. Ind. Res.* **2009**, *68*, 267.

(34) Sels, B.; De Vos, D.; Buntinx, M.; Pierard, F.; Kirsch-De Mesmaeker, A.; Jacobs, P. *Nature* **1999**, *400*, 855.

(35) Kwon, T.; Pinnavaia, T. J. *Journal of Molecular Catalysis* **1992**, *74*, 23.

(36) Li, L.; Zhang, N.; Liu, S. J.; Chen, D. Z. *J. Phys. Chem. Solids* **2005**, *66*, 1844.

(37) Millange, F.; Walton, R. I.; Lei, L. X.; O'Hare, D. *Chem. Mat.* **2000**, *12*, 1990.

(38) Fogg, A. M.; Dunn, J. S.; Shyu, S. G.; Cary, D. R.; O'Hare, D. *Chem. Mat.* **1998**, *10*, 351.

(39) Williams, G. R.; Dunbar, T. G.; Beer, A. J.; Fogg, A. M.; O'Hare, D. *J. Mater. Chem.* **2006**, *16*, 1231.

(40) Cavani, F.; Trifiro, F.; Vaccari, A. *Catal. Today* **1991**, *11*, 173.

(41) Radha, A. V.; Kamath, P. V.; Shivakumara, C. *Solid State Sci.* **2005**, *7*, 1180.

(42) Newman, S. P.; Jones, W. *J. Solid State Chem.* **1999**, *148*, 26.

(43) McIntyre, L. J.; Jackson, L. K.; Fogg, A. M. *J. Phys. Chem. Solids* **2008**, *69*, 1070.

(44) Figlarz, M.; Gerand, B.; Delahayevidal, A.; Dumont, B.; Harb, F.; Coucou, A.; Fievet, F. *Solid State Ion.* **1990**, *43*, 143.

(45) Banerjee, S.; Lassahn, P. G.; Janiak, C.; Ghosh, A. *Polyhedron* **2005**, *24*, 2963.

(46) Beko, S. L.; Bats, J. W.; Schmidt, M. U. *Acta Crystallogr. Sect. C-Cryst. Struct. Commun.* **2009**, *65*, M347.

(47) Kaduk, J. A.; Golab, J. T. *Acta Crystallogr. Sect. B-Struct. Sci.* **1999**, *55*, 85.

(48) Sels, B. F.; De Vos, D. E.; Jacobs, P. A. *J. Am. Chem. Soc.* **2001**, *123*, 8350.

(49) Sels, B. F.; De Vos, D. E.; Buntinx, M.; Jacobs, P. A. *J. Catal.* **2003**, *216*, 288.

Chapter Three

Synthesis and Crystal Structures of Lanthanide Coordination Polymers

3.0 Introduction

The preparation of metal phosphonates and more recently lanthanide phosphonates is of great interest owing to their potential ability to be applied in a diverse range of fields such as catalysis, ion-exchange and gas sorption and also their ability to form a variety of framework structures.[1, 2, 3, 4] Phosphonic acids, RPO_3H_2, have two deprotonated forms; RPO_3H^- and RPO_3^{2-}. The phosphonate group is deemed to be a strong anionic moeity and due to this is able to form strong bonds to a variety of metal cations.[5]

The past two decades of research into metal phosphonates has shown that the structures produced depend on a variety of variables such as the nature of the metal used; oxidation state and coordination number, and the presence of additional organic functional groups on the phosphonate backbone. In the preparation of these materials there are many alternative organic phosphonate building blocks which can be incorporated such as monophosphonates,[3] diphosphonates,[6] amino phosphonates,[7, 8, 9] sulfonate phosphonates[10, 11] and carboxylate phosphonates.[12, 13] Depending on the type of organic phosphonate employed within the synthesis, and also the reaction conditions utilized e.g. reaction temperature, reactant ratios and concentrations, a variety of structures may be formed including layered, pillared layered and three-dimensional.[7, 14] The structures formed are also found to be dependant on the coordination chemistry of the phosphonate used, which is itself determined by cation size and the temperature of the reaction media, although this is found to be unpredictable owing to the different available coordination modes of the phosphonate, for example monodentate, bidentate, multidentate and bridging.[4] Rational design of these materials, for highly specific functions, is possible due to the wide choice of metals (transition metals, alkali metals and lanthanides) and organic moieties available.[14, 15, 16]

Metal phosphonates have been the largest area of phosphonate research over recent years and have been formed using first row transition metals, zirconium (IV) and main group metals such as Al(III), Ga(III) and Pd(II).[2, 4, 7, 13, 17, 18, 19, 20, 21, 22] Open framework,

microporous and layered structures are known[23] with the vast majority defined as coordination polymers. Alberti and co-workers reported the first metal phosphonate in 1978, $Zr(C_6H_5PO_3)_2$, which consists of chains of six coordinated Zr cations which are pillared together via the phosphonate groups leading to a two-dimensional layered structure with the benzyl groups orientated into the interlayer gallery. This group also successfully synthesised a compound with an added hydroxyl functionality onto the phosphonate backbone, forming $Zr(HOCH_2PO_3)_2.H_2O$; both phases were synthesised via a precipitation method and are believed to have a layered structure which has been inferred from powder X-ray diffraction measurements and also from the lamellar shape, hexagonal platelets, of the crystals produced.[24] Another example using the same phosphonate as Alberti is that of $Cu(O_3PC_6H_5).H_2O$[25] which also comprises of a layered structure, with the layers consisting of five coordinated copper atoms bridged together via phosphonate groups with the phenyl rings orientated into the interlamellar region. Three-dimensional pillared layered structures have also been reported such as $M(H_2O)(HO_3P(CH_2)_2PO_3)$ (M = Fe, Al, Ga) consisting of inorganic sheets of MO_6 octahedra connected through PO_3C tetrahedra and pillared via the organic diphosphonate [18] and $M_2(O_3PCH_2C_6H_4CH_2PO_3).2H_2O$ (M=Mn, Ni, Cd) which has a similar structure as it is built up from corner linked MO_6 octahedra forming inorganic mixed oxide layers which are linked together via the diphosphonate pillars.[26] Examples of three dimensional open frameworks are rare compared to the layered and pillared layered structures, with the first open framework of β-$Cu(O_3PCH_3)$, reported by LeBideau *et al.* Figure 1.[27] The structure consists of Cu atoms, with distorted tetragonal pyramidal coordination, forming infinite zigzag chains linked together via O-P-O bridges in turn forming hexagonal tunnels of 5.7 Å in diameter (measuring methyl to methyl carbons and omiting hydrogen atoms) across the tunnels, with the methyl groups extending into these tunnels.

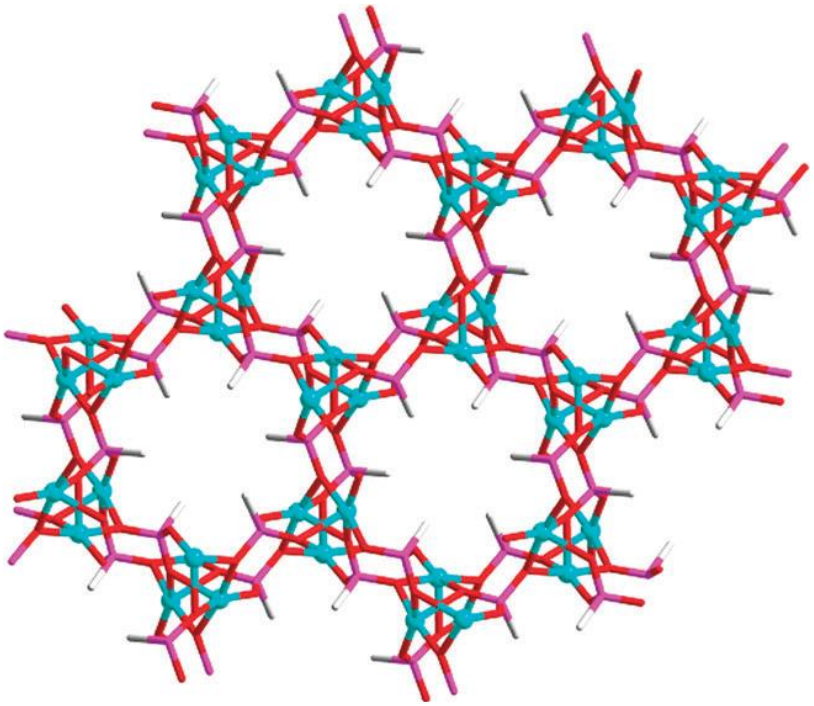

Figure 1 Three-dimensional framework of β-Cu(O_3PCH_3) (Colour key: Cu cyan, P purple, O red and C grey)[4, 27]

Secondary ligands have also been introduced into the preparation of metal phosphonates, and are often amine based, having bidentate coordination preferences, and are able to act as templates and/or bridging species for the formation of new structures. Some secondary ligands incorporated include 2,2'-bipyridine, 4,4'-bipyridine and 1,10-phenanthroline. The latter has been used to synthesise $Mn(HO_3P(CH_2)_2PO_3H)(H_2O)_2(C_{12}H_8N_2)$ forming a one-dimensional chain structure consisting of $MnO_2(H_2O)_2N_2$ octahedra, Figure 2.[20] The use of 4,4'-bipyridine has also produced some interesting structures such as $[Co_3(4,4'\text{-bipy})(H_2O)_2(L)_2].(4,4'\text{-bipy})_{0.5}$ and $[Mn_3(4,4'\text{-bipy})(H_2O)_2(L)_2].(4,4'\text{-bipy})_{0.5}$ (where L = $O_3PCH(OH)CO_2$).[28] Mn (II) and Co(II) are found have octahedral coordination in these complexes and are bridged together by 2-hydroxylphosphonoacetate into a hybrid layer; the layers are further pillared into a three-dimensional neutral framework via coordinating 4,4'-bipyridyl, generating one-dimensional channels which are occupied by isolated 4,4'-bipyridyl molecules.

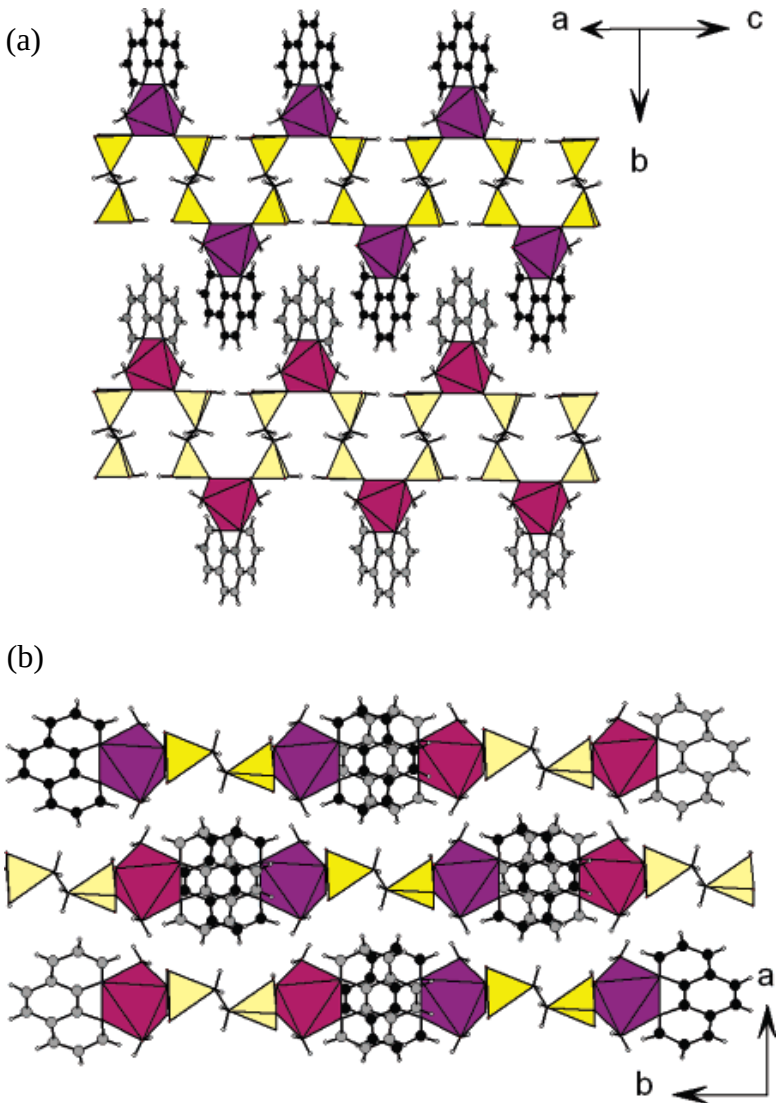

Figure 2 (a) Crystal structure of $Mn(HO_3P(CH_2)_2PO_3H)(H_2O)_2(C_{12}H_8N_2)$ and (b) view of the layers which are perpendicular to the c axis(Colour key; Mn – purple, P – yellow, C – grey or black).[20]

Formation of lanthanide phosphonates however has, until recently, been less extensively researched. Lanthanide containing phosphonates, compared to transition metal phosphonates, are found to have greater coordination flexibility of the metal centre, due to their high and variable coordination numbers.[17] Compounds of this type were first reported by Mallouk and coworkers in 1990 who prepared layered lanthanide phenyl phosphonates with a composition of $Ln(O_3PC_6H_5)(HO_3PC_6H_5)$ and a series of layered lanthanide alkyl phosphonates with a composition of $Ln(O_3PMe)(HO_3PMe)$ (Ln=La,Ce,Sm).[3] Three-dimensional lanthanide organo-diphosphonate structures have also been reported, for example $LnH[O_3P(CH_2)_nPO_3]$ (n=1-3; Ln= Pr, Nd, Eu, Gd),

which has a framework structure consisting of inorganic Ln-P-O sheets joined together by organic groups.[6] It has been suggested that reports of lanthanide phosphonates are found to be quite limited due to their low solubility in water and organic solvents and also their poor crystallinity, with a number of structures being based on X-ray powder diffraction.[1, 17, 29] Their solubility and crystallinity is found to be improved by addition of further functional groups such as carboxylate, sulfonate, hydroxyl and amine groups attached to the phosphonic acid backbone.[6, 12, 30, 28] Addition of further functional groups, for example carboxylate, are found to give products which are structurally related to the lanthanide diphosphonates. An example includes $Ln[O_3P(CH_2)_2CO_2]$ (Ln= La-Lu), which forms a pillared layered structure consisting of inorganic Ln/O/P/C layers connected by the organic groups. Addition of the carboxylate group leads to differences in the lanthanide coordination environment and also in the connectivity of the inorganic layer, for example where Ln = Pr, the praseodymium centre is found to be seven coordinate[12] whereas in the diphosphonate analogue $LnH[O_3P(CH_2)PO_3]$ (Ln = Pr, Gd) it is found to be eight coordinate.[6] Ferey *et al.* recently reported the first lanthanide phosphonate with an open framework with the incorporation of a carboxylate phosphonate, giving a composition of $[Ln_4(H_2O)_7(O_2CC_5H_{10}NCH_2PO_3)_4].(H_2O)_5$ (Ln = Pr and Y).[31] This structure consists of one-dimensional subunits built up of chains of edge sharing rare-earth polyhedra interconnected via carboxyphosphonate anions creating an open three-dimensional framework structure containing small channels occupied by non-coordinated water molecules, Figure 3.

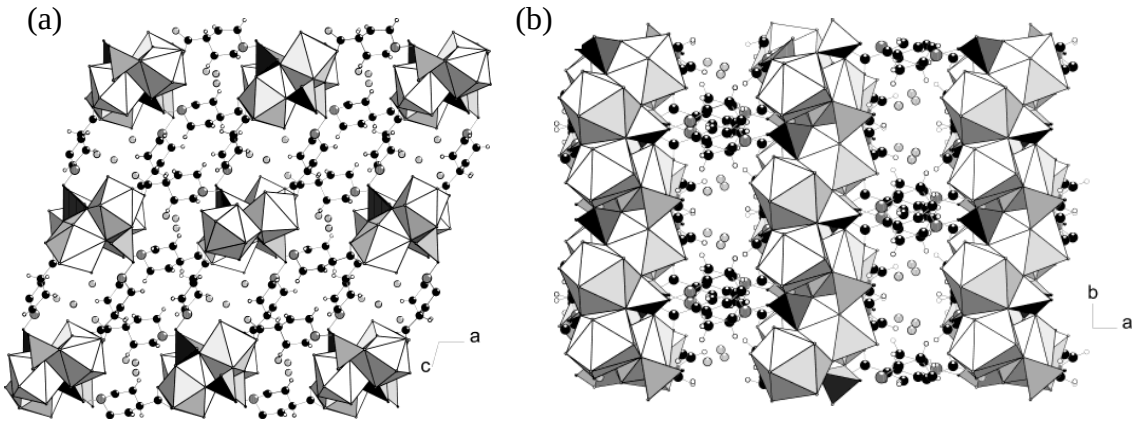

Figure 3 Crystal structure of $[Pr_4(H_2O)_7(O_2CC_5H_{10}NCH_2PO_3)_4].(H_2O)$ (a) view along the *b* axis and (b) view along the *c* axis.[31]

Sulfonate anionic groups may also be an additional functional group of phosphonates allowing the formation of three-dimensional layered structures e.g. $Ln(O_3PC_2H_4SO_3)(H_2O)$ (Ln=La-Dy),[10] which consists of chains of edge-sharing LnO_8 polyhedra connected by the phosphonate and sulfonate groups to form layers which are linked together via the CH_2CH_2 groups forming the three-dimensional framework.

From a review of the literature it may be generalised that both metal and lanthanide phosphonates containing non-functionalised monophosphonates will tend to form layered compounds whereas the diphosphonate or functionalised monophosphonate analogues may lead to the formation of three-dimensional structures.[6]

Lanthanide coordination polymers are more commonly formed using carboxylate anions as the organic component. Carboxylates differ from phosphonates in their charge and also shape, therefore allowing the formation of different structures due to their different coordination preferences. Some examples of lanthanide carboxylate coordination polymers include lanthanide glutarates, with the general formula $[Ln(H_2O)]_2[O_2C(CH_2)_3CO_2]_3.4H_2O$ (Ln= Pr, Sm, Eu, Gd, Ho)[32] and a structure consisting of chains of edge-sharing $LnO_8(H_2O)$ polyhedra linked together by carbon chains forming an inorganic-organic three-dimensional open

framework with channels in which weakly bonded water molecules are incorporated. By varying the carbon chain length, a similar structure has been observed for $[Pr(H_2O)]_2[O_2C(CH_2)_2CO_2]_3.4H_2O$.[33] This phase incorporates succinate which has a smaller chain length compared to glutarate, with the stucture consisting of edge-shared $LnO_8(H_2O)$ polyhedral chains linked together by carbon chains, forming an organic-inorganic three-dimensonal network. This is a relatively open framework compared to the glutarate version, due to the formation of smaller tunnels, which allow the incorporation of one weakly bonded water. These examples show that the size of these channels is directly related to the length of the carbon chain, therefore suggesting that this may be a new strategy to synthesise open framework compounds using a non-template method.

The combination of lanthanide cations with sulfonate anions has also yielded a variety of coordination polymers. Organosulfonates, RSO_3^-, bear a strong structural analogy to that of RPO_3^{2-} as they are both trioxy anionic units containing an organic component. Phosphonates are found to have a greater anionic charge associated with the unit, therefore allowing the unit to bind to a metal centre in a somewhat stronger manner compared to that of analogous sulfonates. Sulfonates are therefore known as poorer ligands compared to phosphonates, and in turn bind in a weaker fashion to metal centres. The formation of lanthanide sulfonate compounds has been less extensively studied due to this weaker binding nature, although it may be noted that a wide variety of structures may form due to the possible coordination modes of the sulfonate group, such as monodentate, bidentate and bridging.[34] Chain, layer and three-dimensional structures are known for compounds containing organosulfonates with examples including $Ln(OH)(1,5\text{-NDS})\cdot H_2O$ (Ln = La, Nd, Pr, Sm, Eu; 1,5-NDS = 1,5-naphthalenedisulfonate)[35, 36] and $[Ln_5(2,6\text{-NDS})_3(OH)_9(H_2O)_4]\cdot 2H_2O$ (Ln = Nd, Eu) both having infinite chain three-dimensional structures and a second form of $Nd(OH)(1,5\text{-NDS})\cdot H_2O$ which has a layered structure.[36] These structures typically contain eight and/or nine coordinate lanthanide cations which are found either as discrete units or as small clusters containing two to five lanthanide cations.

3.1 Objective

Chapter 2 described the successful formation of new inorganic-organic hybrid materials consisting of lanthanide cations and molybdate or tungstate tetrahedral anionic building blocks in conjunction with sulfonate or carboxylate anions, which led to the formation of three-dimensional pillared layered structures. Exploratory synthesis into the substitution of Mo and W in these complexes for phosphate tetrahedral anionic building blocks, such as $H_2PO_4^-$, HPO_4^{2-} or PO_4^{3-}, was explored leading to the unwanted formation of lanthanide phosphates with no incorporation of organic sulfonate anions. Using alternative anionic functional groups to that of sulfonate and carboxylate was also explored, by substitution of these groups for organophosphonates, to identify if analogous materials to those found in Chapter 2 could be produced. Lanthanide coordination polymers, with no incorporation of MoO_4^{2-} and WO_4^{2-} were rapidly discovered.

Varying the organic backbone of the sulfonates reported in Chapter 2 was also explored by substituting naphthalenedisulfonate for anthraquinonedisulfonate and a monosulfonate; octanesulfonate. This investigative synthesis allowed the discovery of the formation of different frameworks compared to the NDS phases, although unfortunately with no incorporation of molybdate or tungstate.

3.2 Scope of Chapter

Three new lanthanide phosphonoacetate coordination polymers, with similar chemical compositions, $[Er(H_2O)_2][C_2H_2O_5P]$ (**1**), $[Yb(H_2O)_2][C_2H_2O_5P]$ (**2**) and $[YbC_2H_2O_5P]$ (**3**), have been synthesised via a hydrothermal route from lanthanide chloride and phosphonoacetic acid. **1** & **2** are found to have infinite three-dimensional structures containing discrete LnO_7 polyhedra connected together via O-P-O bridges, whilst **3** contains one-dimensional chains of LnO_7 polyhedra which are held together via pillaring phosphonoacetate anions in turn forming a three-dimensional network. **1** & **2** have the same chemical composition with different structures, each determined by single crystal X-ray diffraction. The entire lanthanide series was screened allowing the formation of a layered phase to also be discovered

when using larger lanthanides La – Sm, Figure 4 where Ln = Nd. This phase was found to have an elemental composition of **[**$Ln_2(H_2O)_3(C_2H_2O_5P)_2].H_2O$, consisting of lanthanide cations bridged and charge balanced by phosphonoacetate anions forming two-dimensional layers. The layers are found to bind together via hydrogen bonding interactions with unbound interlayer lattice water molecules. This phase has not been described within this chapter due to iso-structural phases being recently reported by Li *et al.* [37]

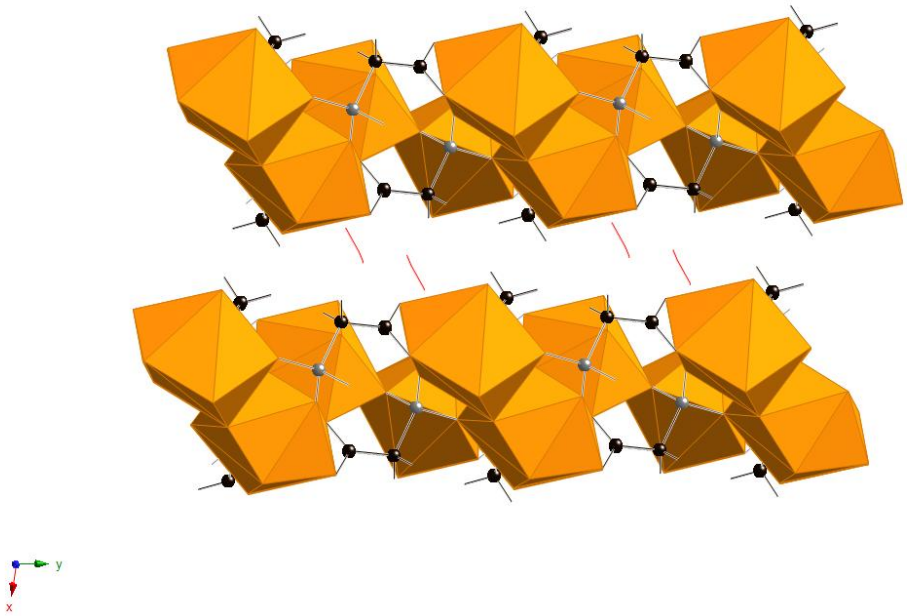

Figure 4 Crystal structure of **[**$Nd_2(H_2O)_3(C_2H_2O_5P)_2].H_2O$
(Colour key; Nd – orange, C - black, P – grey, H_2O – red)

Also synthesised via a hydrothermal route is the coordination polymer, $[(Nd(H_2O)_5)_2(2,6\text{-AQDS})_3]\cdot 2H_2O$ (**4**) where 2,6-AQDS = 2,6-anthraquinonedisulfonate. Structurally, it consists of layers of monomeric Nd polyhedra which are linked by 2,6-AQDS anions forming a polymeric, three-dimensional network. Each Nd atom is nine coordinate, bonding to five water molecules and to four oxygen atoms from four 2,6-AQDS anions which in turn pillar the layers by bridging two Nd atoms in one layer, and coordinating to a single Nd in the other.

A similar phase to be synthesised is that of $[La(H_2O)_5][C_8H_{17}SO_3]_3.2H_2O$ (**5**), where this phase consists of two-dimensional layers of monomeric lanthanum cations which are bridged together by octanesulfonate anions, which themselves are orientated downwards into the interlayer gallery, forming a two-dimensional layered structure.

Each La cation is nine coordinate, bonding to five water molecules and to four oxygen atoms from four octanesulfonate anions which in turn bridge two La cations together forming a layered structure.

3.3 Lanthanide Phosphonoacetate Coordination Polymers

3.3.1 General Synthesis

Three new phases with compositions $[Er(H_2O)_2][C_2H_2O_5P]$ (**1**), $[Yb(H_2O)_2][C_2H_2O_5P]$ (**2**) and $[Yb][C_2H_2O_5P]$ (**3**) have been synthesised via a hydrothermal route from $LnCl_3.xH_2O$ and Phosphonoacetic acid. Crystallographic data for each phase is provided in Appendix B and summarised in Table 1. The reactions were heated at 150°C for 14h (**1**), 165°C for 14h (**2**) and 220°C for 14h (**3**) before being cooled slowly back to room temperature at a rate of 0.1°C/min producing single crystals. The yields of the reactions were calculated at 25% with respect to Er^{3+} in **1**, 46% with respect to Yb^{3+} in **2** and 18% with respect to Yb^{3+} in **3**. A variety of reaction conditions were screened, for example change in reaction temperature and reagent concentrations to obtain a phase pure materials. The optimal conditions found are those stated above with others leading to either less pure or less crystalline samples.

3.3.2 Characterisation of $[Er(H_2O)_2][C_2H_2O_5P]$ (1)

$[Er(H_2O)_2][C_2H_2O_5P]$ (**1**) has been synthesised via a hydrothermal route. Single crystal X-ray diffraction data have shown that it adopts an orthorhombic crystal system with the space group *P*nma, shown in Figure 5, with the main crystallographic and refinement data summarised in Table 1, and detailed bond lengths provided in Appendix B. This phase has also been successfully synthesized with Ln = Ho and Tm, as shown by the powder X-ray diffraction patterns in Figure 6, further characterising data of the Ho and Tm phases are provided in the appendix.
This structure comprises an infinite three-dimensional network containing isolated Er^{3+} cations which are bridged by charge balancing phosphonoacetate anions. There is one crystallographically distinct Er^{3+} cation present in this structure which is seven

coordinate, with the coordination sphere being filled by three phosphate oxygen atoms from three separate phosphonoacetate anions (O1, O2 & O2), two carboxylate oxygen atoms, binding in a bidentate manner from one phosphonoacetate ligand (O3 & O3) and two water molecules (O4 & O5), as shown in Figure 7(a).

There is also one crystallographically distinct phosphonoacetate anion within the structure binding in a monodentate fashion to three separate Er centres via three phosphate oxygen atoms (O1, O2 & O2) with the carboxylate oxygen atoms (O3 & O3) binding in a bidentate manner to a fourth Er centre, leading to one phosphonoacetate anion linking four Er centres together, Figure 7(b). The Er-OH_2 bond distances are 2.284(8) and 2.326(9) Å, Er-OPO_2 distances lie in the range of 2.226(6) - 2.421(6) Å and the Er-OCO bond distance is 2.182(8) Å, these bond lengths are comparable to other compounds containing Er-O bonds.[38, 39]

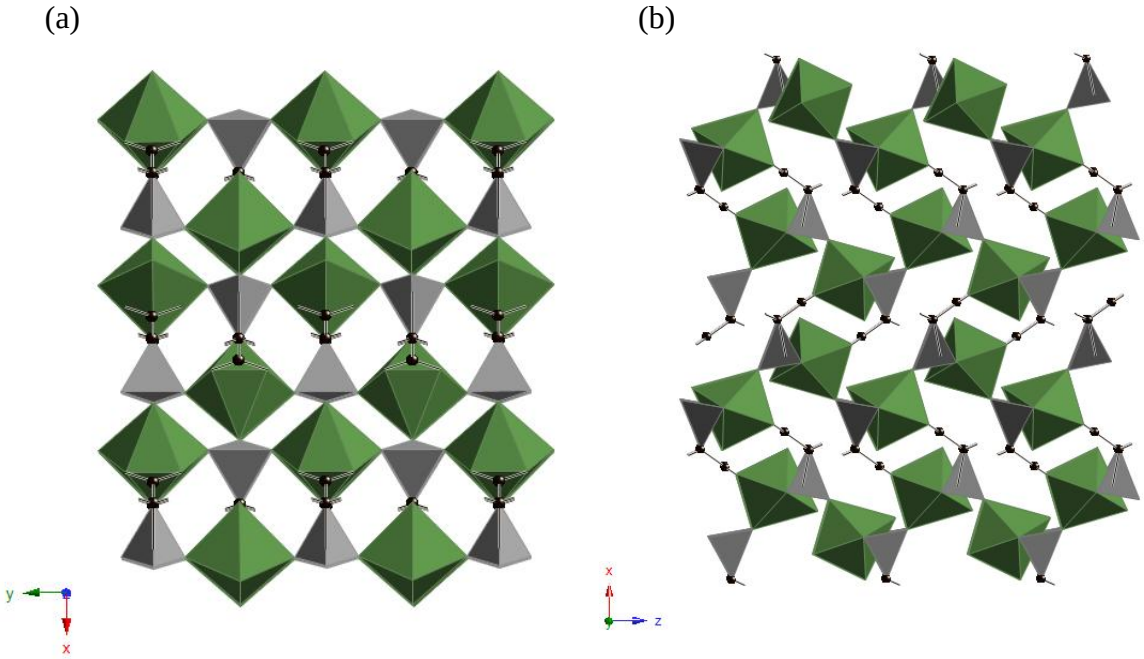

Figure 5 Crystal structure of $[Er(H_2O)_2][C_2H_2O_5P]$ (**1**) (Colour key: Green = Er^{3+}, Black = C , Grey = P) (a) view along the *z* axis and (b) view along the *y* axis

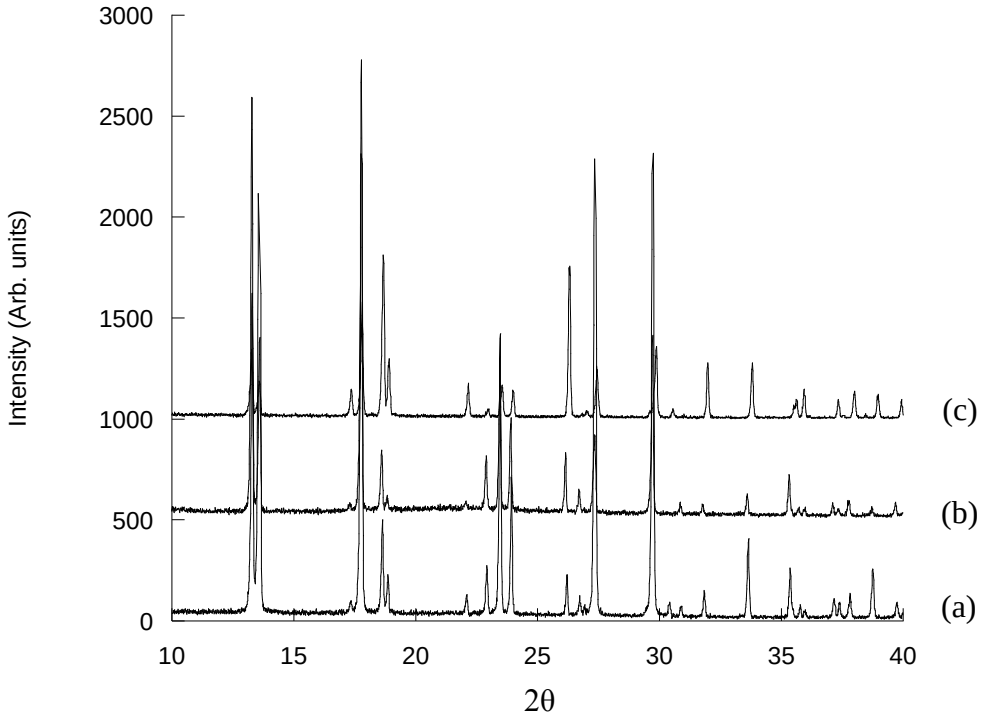

Figure 6 Powder X-ray diffraction patterns (Cu K_α radiation) of iso-structural phases (a) $[Er(H_2O)_2][C_2H_2O_5P]$ (**1**), (b) $[Ho(H_2O)_2][C_2H_2O_5P]$ and (c) $[Tm(H_2O)_2][C_2H_2O_5P]$.

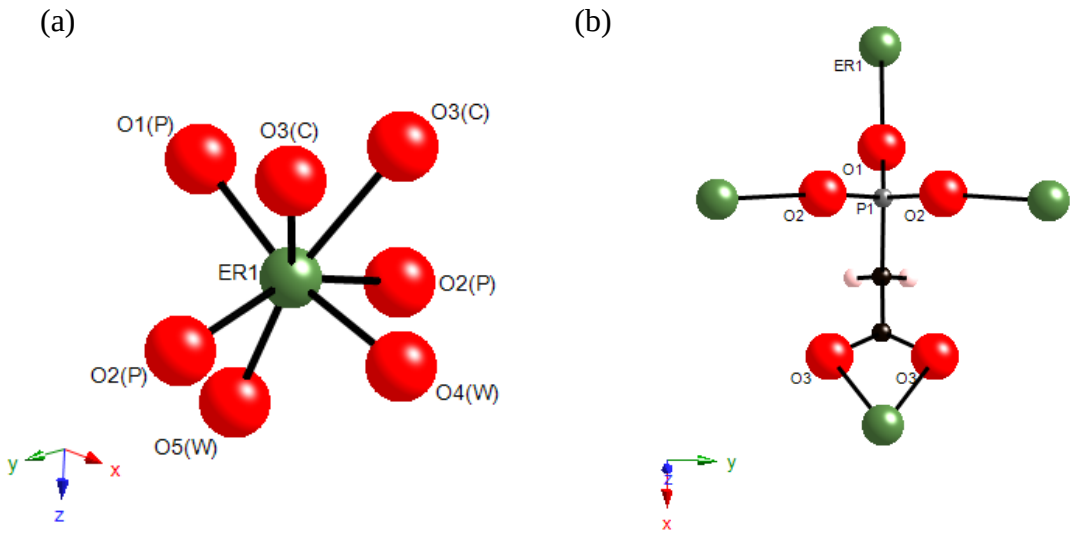

Figure 7 (a) Coordination sphere of Erbium and (b) the coordination arrangement of phosphonoacetate in $[Er(H_2O)_2][C_2H_2O_5P]$ (**1**)

Table 1 Crystallographic data and refinement parameters for phases **1- 3**.

	(1)	**(2)**	**(3)**
Empirical formula	$C_2H_6ErO_7P$	$C_8H_{24}Yb_4O_{28}P_4$	$C_2H_2O_5PYb$
Formula weight	339.29	1384.31	310.05
Temperature (K)	100(2)	120(2)	120(2)
Wavelength (Å)	0.71073	0.71073	0.71073
Crystal system	Orthorhombic	Monoclinic	Monoclinic
Space group	*P*nma	$P\ 2_1/n$	$P\ 2_1/n$
a (Å)	12.933(6)	6.7557(5)	6.4798(5)
b (Å)	6.790(3)	15.1624(13)	6.7979(6)
c (Å)	7.734(4)	7.0945(6)	6.5084(5)
α (º)	90	90	90
β (º)	90	90.44	99.277(4)
γ (º)	90	90	90
Volume ($Å^3$)	679.2(6)	726.69(10)	282.98(4)
Z	4	1	2
Density (calculated) (Mg/m^3)	3.318	3.163	3.639
Absorption coefficient (mm^{-1})	12.582	13.081	16.748
Crystal	pink; prism	colourless; plate	colourless; needle
Crystal size (mm^3)	0.55 x 0.10 x 0.08	0.10 x 0.05 x 0.01	0.04 x 0.01 x 0.01
θ range for data collection (º)	3.07 - 27.46	3.02 - 27.48	3.17 - 27.48
Reflections collected	3126	8376	699
Independent reflections	811[R(int)= 0.0483]	1664 [R_{int} = 0.0442]	699 [R_{int} = 0.0000]

Max. and min. transmission	0.4364 and 0.0549	0.8803 and 0.3546	0.8504 and 0.5539
Goodness of fit on F^2	1.131	1.071	1.254
R [F, $F^2 > 2\sigma$]	0.0348	0.0383	0.0429
R_w *(F, all data)*	0.0844	0.0848	0.1095
Diff. map extremes (e Å^{-3})	2.219 and-2.117	1.727 and-2.474	2.511 and-3.272

A range of analytical techniques have been used to confirm the composition and phase purity of this material. Elemental analysis indicated that the sample contains 6.44 % C (calc - 7.06 %) and 1.66 % H (calc - 1.78 %) which is consistent with the composition obtained from the crystal structure and the absence of crystalline impurities in the powder XRD pattern, although as shown by the elemental analysis results, a small amount of amorphous material may be present. The powder XRD pattern of **1** is shown in Figure 8 where it is compared to one calculated from the crystal structure. No crystalline impurities are evident in the experimental data and good agreement between the two patterns is apparent suggesting that the crystal structure of **1** is representative of the bulk phase.

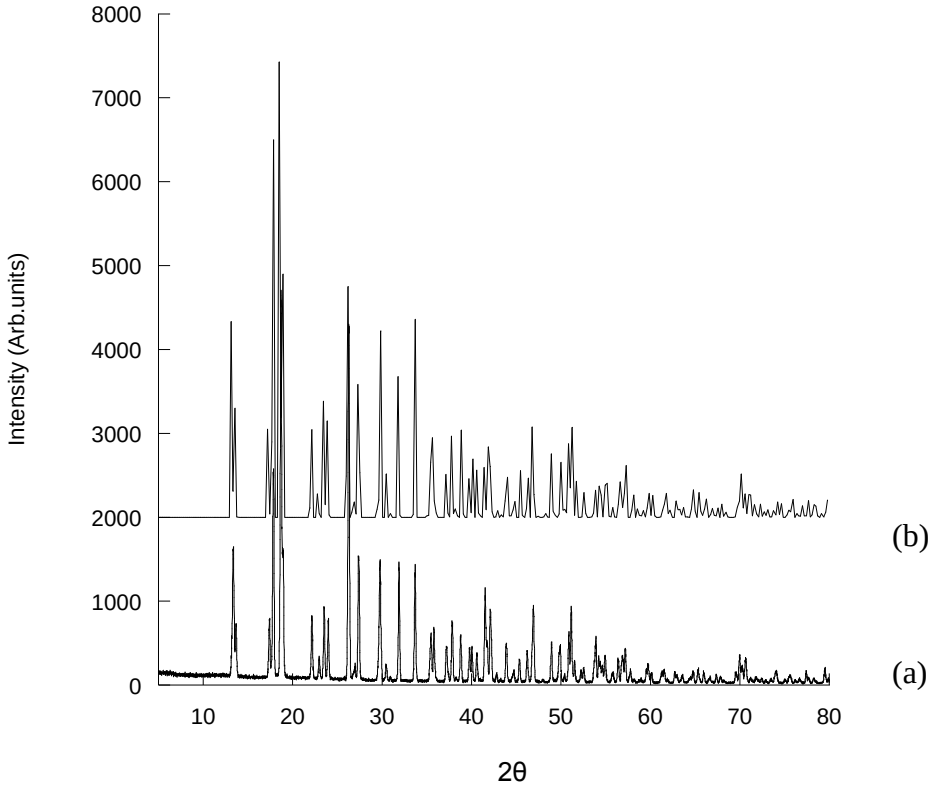

Figure 8 Powder XRD pattern (Cu K_α radiation) of (a) $[Er(H_2O)_2][C_2H_2O_5P]$ (**1**) and (b) diffraction pattern calculated from the crystal structure.

The TGA trace, shown in Figure 9, shows three distinct mass losses below 995 °C, with the first two mass losses corresponding to dehydration of the material, as well as the initial decomposition of the organic, with a total mass loss of 11.6 % (calc – 10.6 %), and the final mass loss of 8.1 % corresponding to the total decomposition of organic (calculated mass loss of 10.0 %). Powder X-ray diffraction showed the residue to be $ErPO_4$.

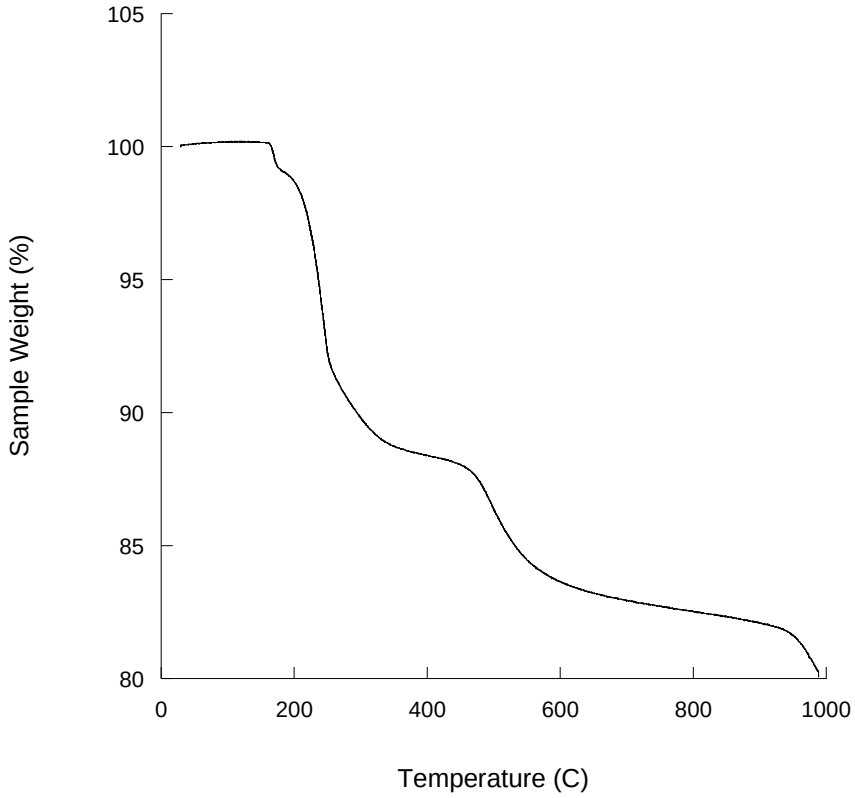

Figure 9 TGA trace of $[Er(H_2O)_2][C_2H_2O_5P]$ (**1**)

The FTIR spectrum, shown in Figure 10, has a broad band due to an O-H stretch at approximately 3065 cm^{-1} and a sharp peak at 1613 cm^{-1} corresponding to the bending mode of water. The other features of the spectrum are due to the phosphonoacetate anion being present in the structure. Frequencies characteristic of the P=O and P-O stretching modes are observed at 1206 cm^{-1}, found to be 1295 cm^{-1} in the free ligand therefore indicating coordination of the phosphoryl oxygen atom, and 1019 cm^{-1} and the C=O, C-O modes at 1614 cm^{-1} and 1128 cm^{-1}, these frequencies are consistent with literature reports.[13, 40, 41, 42, 43] The phosphonoacetate bands have shifted to lower frequencies in comparison to the original reagent, phosphonoacetic acid, which is consistent with coordination to the metal centre. The (O=P)-OH stretch, at approximately 2638 cm^{-1}, in the original reagent is not observed after complexation indicating that all the phosphate oxygen atoms are deprotonated in the product.

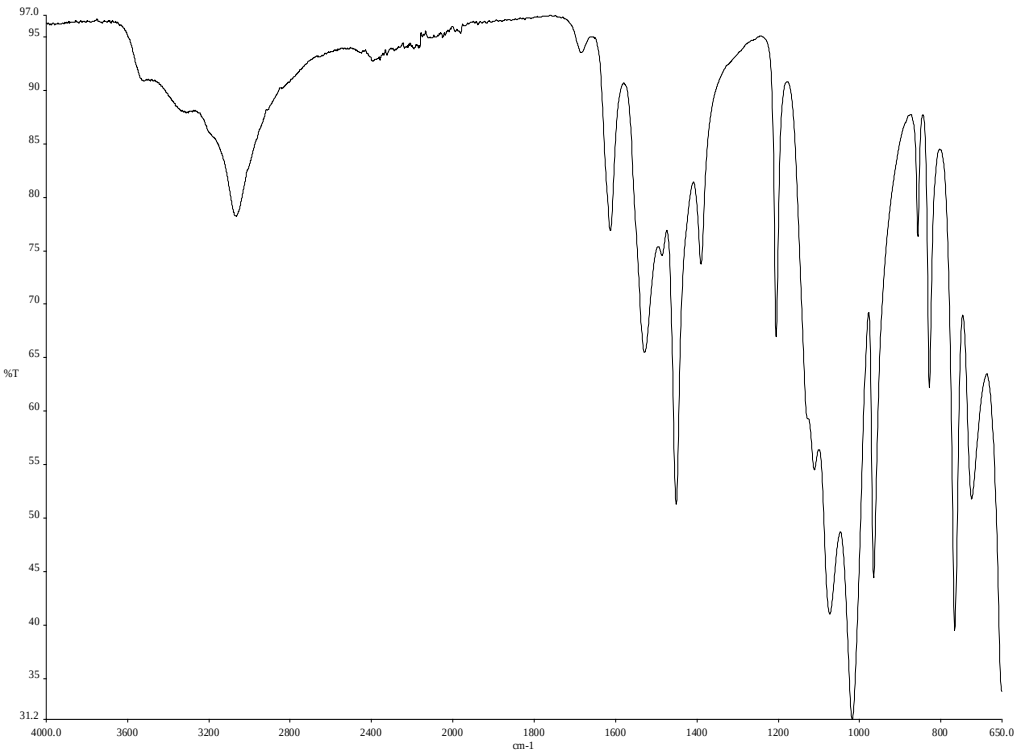

Figure 10 FTIR spectrum of $[Er(H_2O)_2][C_2H_2O_5P]$(**1**)

Channels are found in this phase, along the *y* axis as shown in Figure 5(b), with dimensions of 4.1 x 9.5 Å, measuring the C - C and Er - Er distance across the channel in the *yz* plane, the size of these channels suggest that they are inaccessible. This was confirmed by treatment of the material under vacuum at 120 °C, showing a BET surface area of 2.12 m^2/g with a type II isotherm, indicating that this material does not take up any N_2, therefore is found to be non-porous to N_2, data is provided in the appendices.

The SEM image, Figure 11, shows $[Er(H_2O)_2][C_2H_2O_5P]$ (**1**) to exist as a microcrystalline powder, exhibiting block-like morphology.

Figure 11 SEM image of $[Er(H_2O)_2][C_2H_2O_5P]$ (**1**)

3.3.3 Characterisation of $[Yb(H_2O)_2][C_2H_2O_5P]$ (2)

$[Yb(H_2O)_2][C_2H_2O_5P]$ (**2**) is found have the same chemical composition as **1** although single crystal X-ray diffraction and powder X-ray diffraction measurements, Figure 12, have confirmed that they are not iso-structural. Single crystal X-ray diffraction data has shown that it adopts a monoclinic crystal system in the $P2_1/n$ space group, shown in Figure 13, with the main crystallographic and refinement data summarised in Table 1 and detailed bond lengths provided in Appendix B. This phase has also been successfully synthesized with Ln = Lu, characterising data of this phase is provided in the appendices.

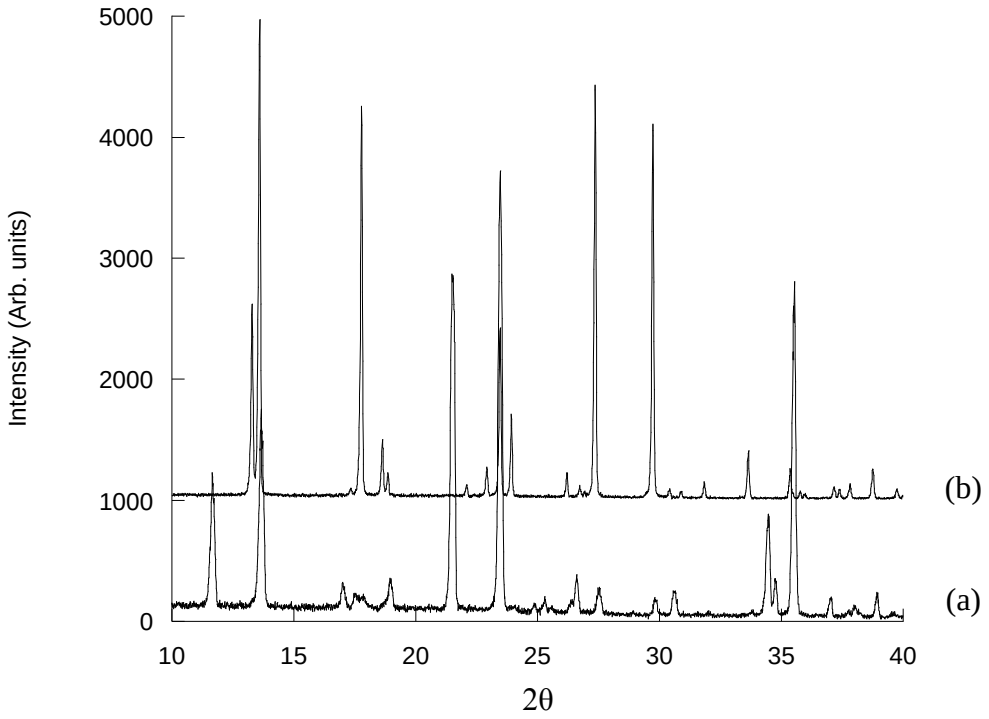

Figure 12 Powder X-ray diffraction patterns of (Cu K_α radiation) (a) $[Yb(H_2O)_2][C_2H_2O_5P]$ (**2**) and (b) $[Er(H_2O)_2][C_2H_2O_5P]$ (**1**)

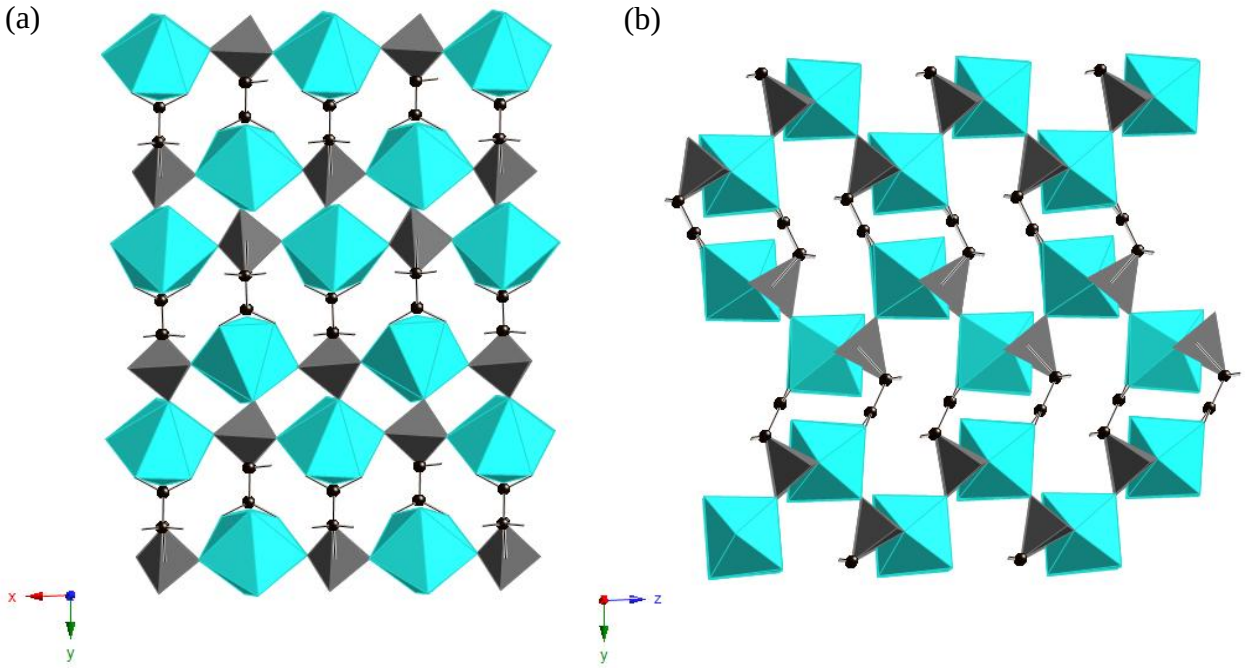

Figure 13 Crystal structure of $[Yb(H_2O)_2][C_2H_2O_5P]$ (**2**) (Colour key: Blue = Yb^{3+}, Black = C, Grey = P) (a) view along the *z* axis and (b) view along the *x* axis

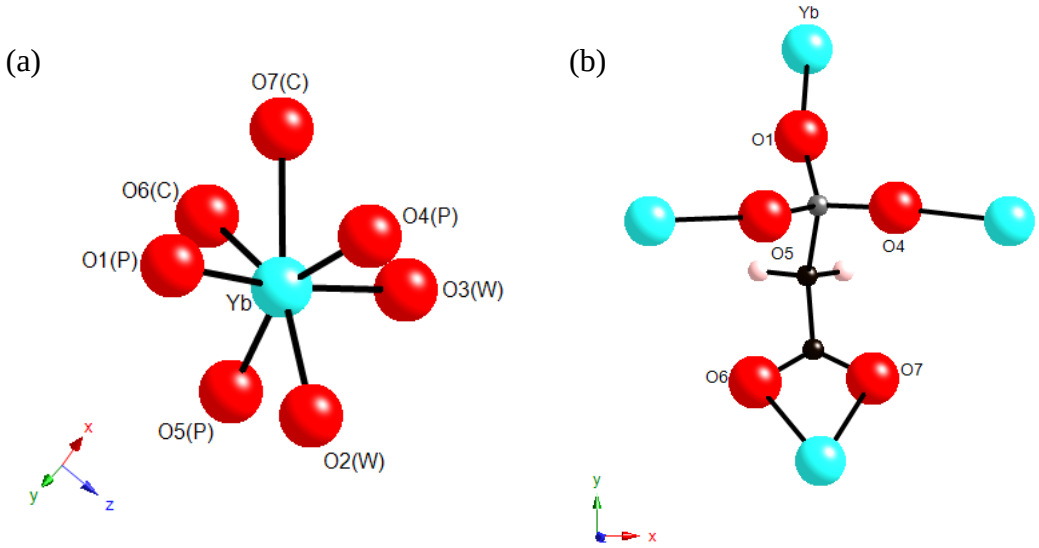

Figure 14 (a) Coordination sphere of Ytterbium and (b) the coordination arrangement of phosphonoacetate in $[Yb(H_2O)_2][C_2H_2O_5P]$ (**2**)

This structure comprises of an infinite three-dimensional network containing isolated Yb^{3+} cations bridged by charge balancing phosphonoacetate anions. There is one crystallographically distinct Yb^{3+} cation which is found to be seven coordinate to two water molecules, three phosphate oxygen atoms from three separate phosphonoacetate ligands, and two carboxylate oxygens which bind in a bidentate manner from one phosphonoacetate ligand to one Yb centre, as shown in Figure 14(a). The ytterbium coordination environment is found to be identical to that of erbium in **1**, although the crystal structures differ due to the orientation of the tetrahedral phosphonate groups located between adjacent lanthanide centres, as shown in Figure 15(a) and (b). In **2**, when looking perpendicular to the *xy* plane a bilayer of phosphonate groups are observed which are oriented in an identical fashion with respect to each other, whereby the phosphonate oxygens are orientated upwards with respect to phosphorus, the adjacent bilayers are found to have opposed orientation of the phosphonate groups with respect to the first bilayer, whereby the phosphonate oxygen atoms point downwards with respect to phosphorus. The orientation of the phosphonate groups in **1** differ to **2**, whereby **1** consists of alternating monolayers of phosphonate polyhedra which are opposed to each other in the *xy* plane. This difference in the orientation of the phosphonate groups in phases **1**

and **2** alters the symmetry observed within each phase, therefore different space groups are observed for each crystal structure.

There is one crystallographically distinct phosphonoacetate anion present in this structure which binds in a multidentate fashion to four Yb centres, shown in Figure 14(b). The anion binds to an Yb centre in a monodentate manner via one phosphate oxygen (O1) and to a second Yb centre directly above in a bidentate fashion via carboxylate oxygen atoms (O6 & O7). The two remaining phosphonate oxygen atoms (O4 & O5) bind in a monodentate manner to two separate Yb^{3+} centres. As in **1** two adjacent Yb centres are bound together via an O-P-O bridge and allows the formation of a three-dimensional coordination polymer. The Yb-OH_2 bond distances are 2.329(8) and 2.255(7) Å, Yb-OPO_2 distances lie in the range of 2.148(7) - 2.220(7) Å and the Yb-OCO distances are 2.399(8) and 2.432(9) Å, and are comparable to other compounds containing Yb-O bonds.[38, 44, 45]

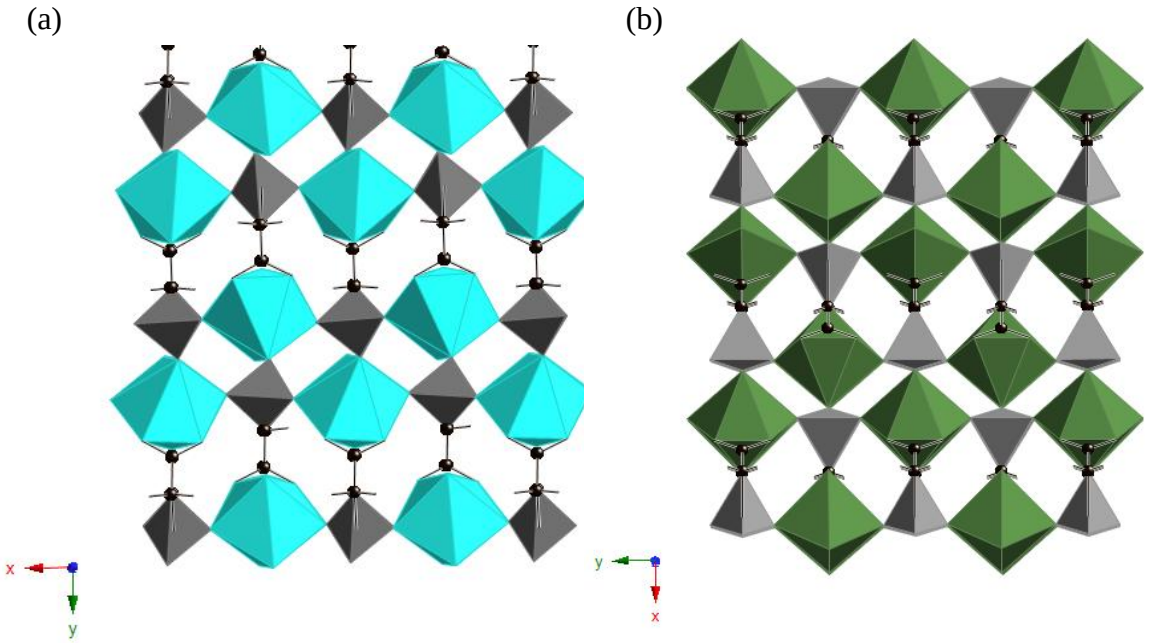

Figure 15 Crystal structures of (a) $[Yb(H_2O)_2][C_2H_2O_5P]$ (**2**) and (b) $[Er(H_2O)_2][C_2H_2O_5P]$ (**1**) showing the orientation of the phosphonate groups when looking perpendicular to the *xy* plane

A range of analytical techniques have been used to confirm the composition and phase purity of this material. Elemental analysis indicated that the sample contains 7.39 % C (calc - 6.94 %) and 1.88 % H (calc - 1.75 %) which is consistent with the composition obtained from the crystal structure and the absence of crystalline impurities in the powder XRD pattern. The powder XRD pattern of **2** is shown in Figure 16, where it is compared to one calculated from the crystal structure. No crystalline impurities are evident in the experimental data and good agreement between the two patterns is apparent suggesting that crystal structure of **2** is representative of the bulk phase.

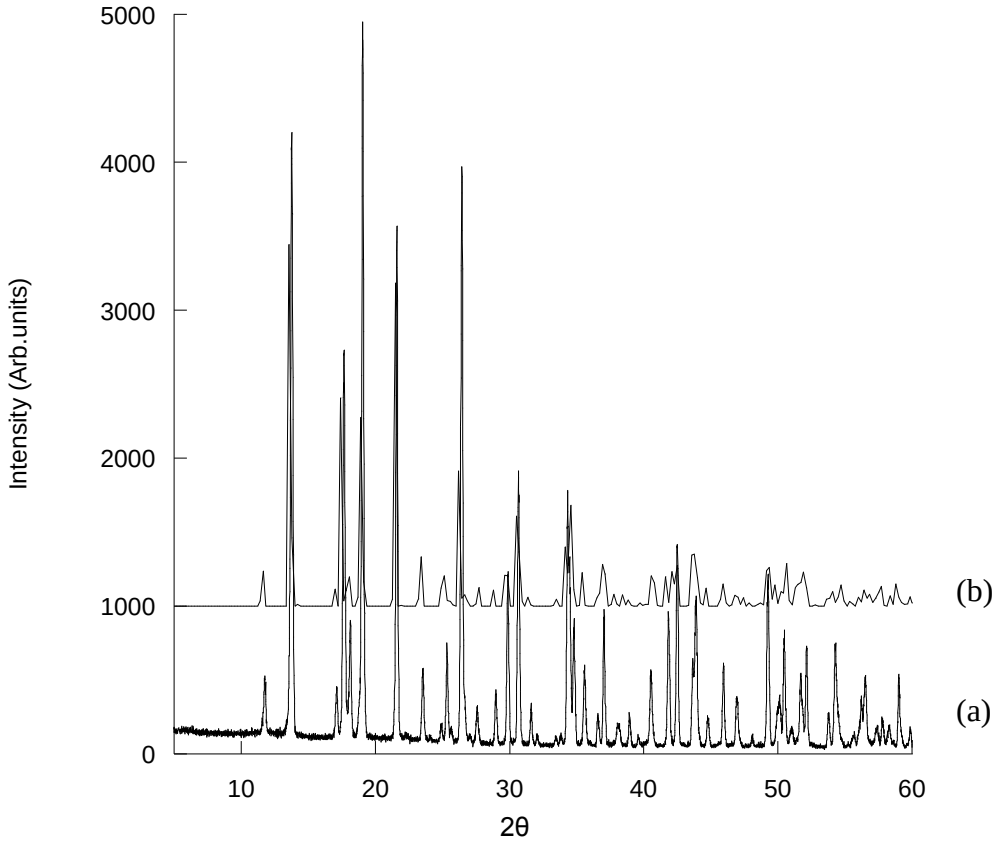

Figure 16 Powder XRD pattern (Cu K_α radiation) of (a) $[Yb(H_2O)_2][C_2H_5O_5P]$ **(2)** and (b) diffraction pattern calculated from the crystal structure.

The TGA trace, shown in Figure 17, shows three distinct mass losses below 1000 °C. The first mass loss of 10.4 %, below 375 °C, corresponds to the dehydration of the material and compares well to the calculated value of 10.4 %. The decomposition of the phase is complete by 995 °C following two additional mass losses of a total of

13.9 % which corresponds to decomposition of the organic anion (calculated mass loss of 12.2 %). Powder X-ray diffraction showed the residue to be $YbPO_4$.

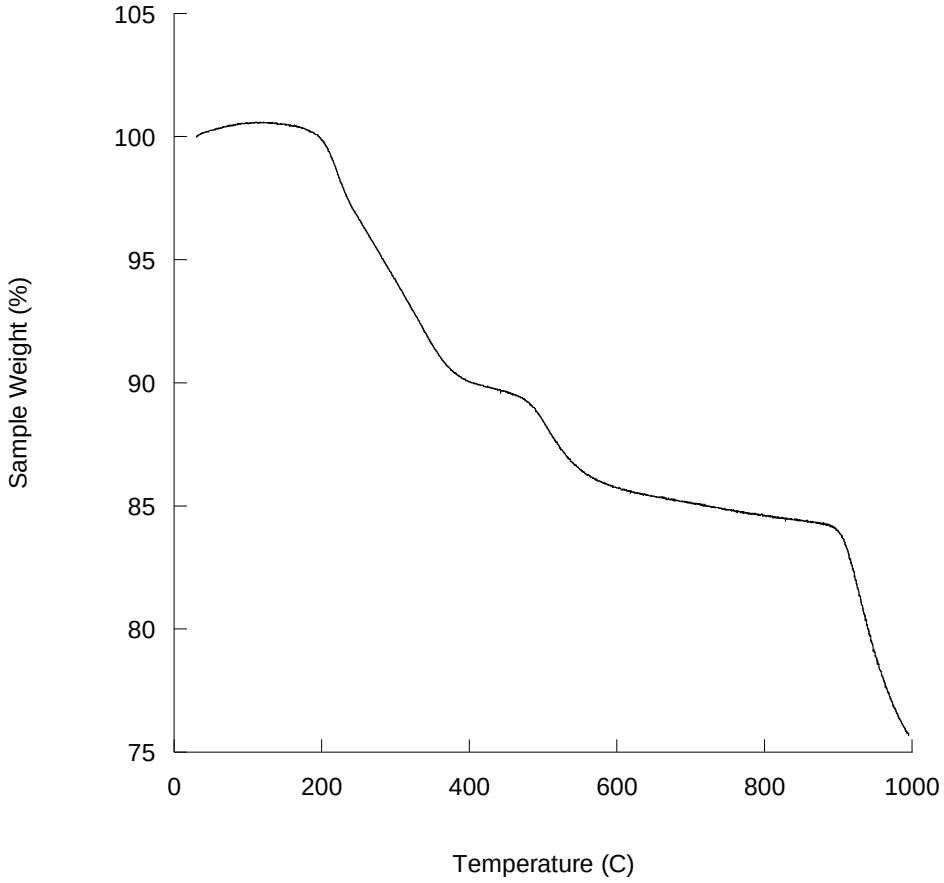

Figure 17 TGA trace of $[Yb(H_2O)_2][C_2H_5O_5P]$ **(2)**

The FTIR spectrum, shown in Figure 18, is found to be similar to that of **1,** having a broad band due to an O-H stretch at approximately 3041 cm^{-1} and a sharp peak at 1697 cm^{-1} corresponding to the bending mode of water. The other features of the spectrum are due to the phosphonoacetate anion being present in the structure. Frequencies characteristic of the P=O modes are observed at 1206 cm^{-1} and 1024 cm^{-1} and the C-O asymmetric and symmetric modes at 1612 cm^{-1} and 1118 cm^{-1}, these frequencies are consistent with literature reports.[13, 40, 41, 42, 43]

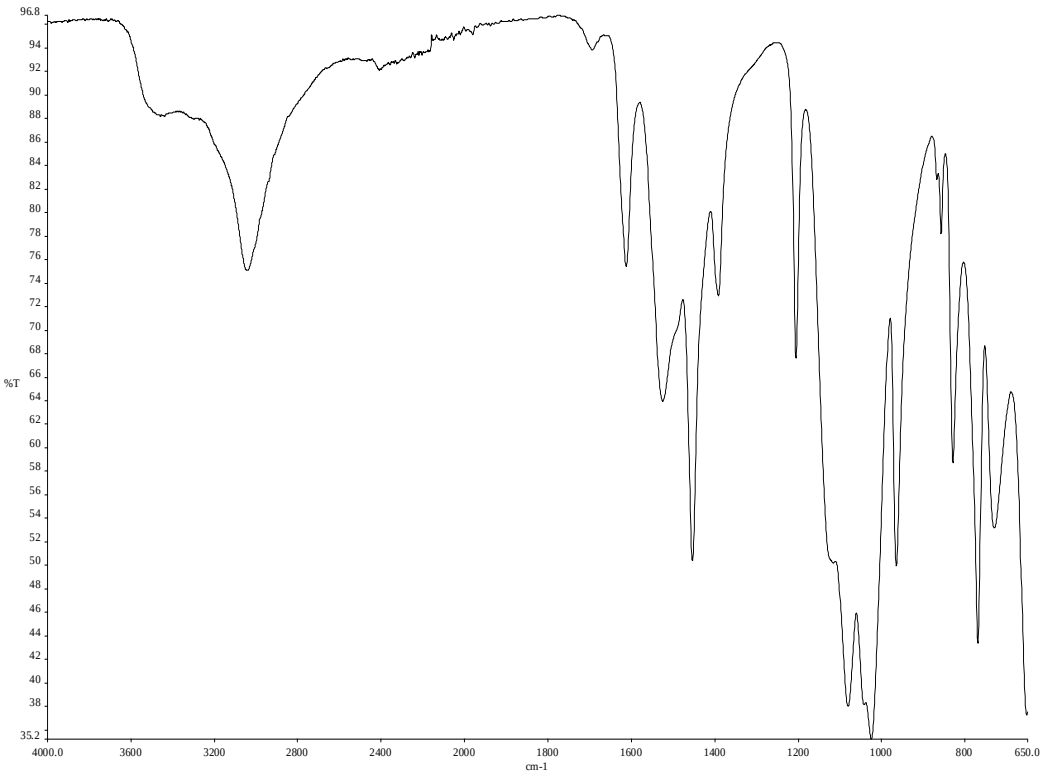

Figure 18 FTIR spectrum of $[Yb(H_2O)_2][C_2H_5O_5P]$ **(2)**

Channels are found in this phase along the *x* axis as shown in Figure 13(b), with dimensions of 4.4 x 11.2 Å, measuring the C - C and Yb - Yb distance across the channel in the *yz* plane. Treatment of this material under vacuum at 120 °C, showed a BET surface area of 1.48 m^2/g and a type II isotherm, indicating that this material is non-porous to N_2. Data is provided in the appendices.

The SEM image of $[Yb(H_2O)_2][C_2H_5O_5P]$ (**2**), shown in Figure 19, shows this compound to exist as a microcrystalline powder consisting of agglomerates with plate-like morphology. This material is found to have a different morphology to that seen in $[Er(H_2O)_2][C_2H_5O_5P]$ (**1**) therefore confirming that phases **1** and **2** are not iso-structural to one another.

Figure 19 SEM image of $[Yb(H_2O)_2][C_2H_5O_5P]$

From varying the reaction temperature of the formation of **1** & **2** it has been found that each phase is formed within a temperature range of 60 - 180 °C, with the purest phases being formed at temperatures stated in Chapter 6. From powder X-ray diffraction measurements it has been discovered that when performing the reactions at a temperature of 200 °C **2** becomes biphasic, with the second phase observed being iso-structural to that of **1**, Figure 20. A reaction temperature of 220 °C produces a new phase as discussed in the next section.

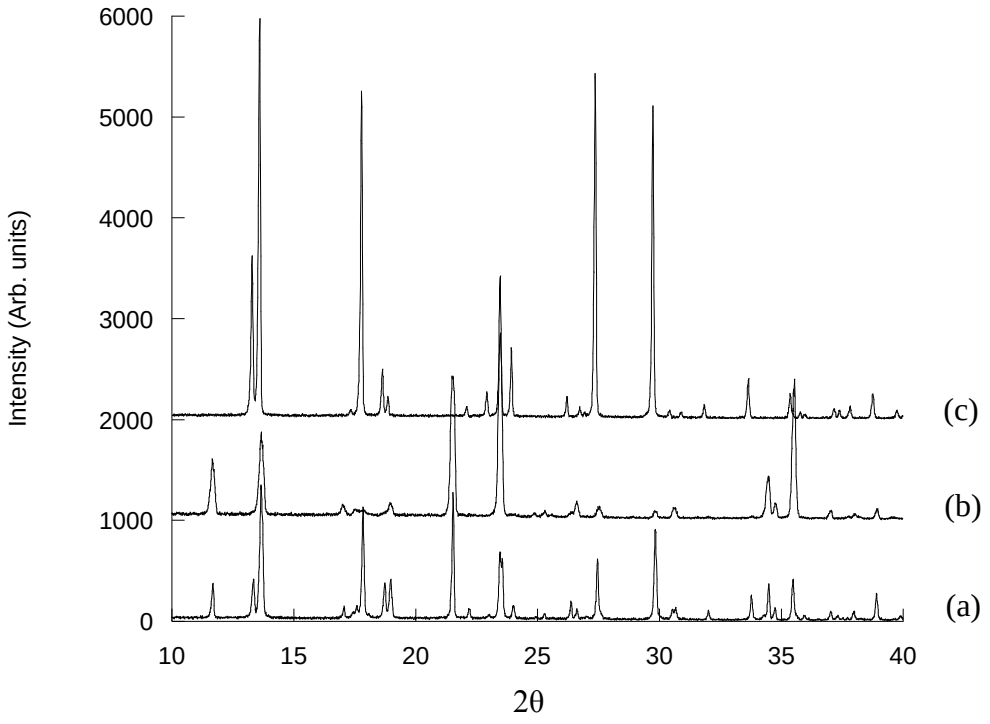

Figure 20 Powder XRD pattern (Cu K_α radiation) of (a) biphasic $[Yb(H_2O)_2][C_2H_5O_5P]$ at 200 °C, (b) $[Yb(H_2O)_2][C_2H_5O_5P]$ at 165 °C and (c) $[Er(H_2O)_2][C_2H_5O_5P]$ at 150 °C

3.3.4 Characterisation of $[Yb][C_2H_2O_5P]$ (3)

$[Yb][C_2H_2O_5P]$ (**3**) has been synthesised via a hydrothermal route at 220 °C, and is found to have a dehydrated chemical composition compared to **1** and **2**. Single crystal X-ray diffraction data has shown that it adopts a monoclinic crystal system with the space group $P2_1/n$, shown in Figure 21, with the main crystallographic and refinement data summarised in Table 1 and detailed bond lengths provided in Appendix B.

This structure comprises of an infinite three-dimensional pillared layered network containing chains of Yb^{3+} cations which are linked together by charge balancing phosphonoacetate anions. There is one crystallographically distinct Yb cation and phosphonoacetate ligand present. Each Yb centre is found to be seven coordinate, as shown in Figure 22(a), to five phosphonate oxygen atoms, from four phosphonoacetate anions, and two carboxylate oxygen atoms, which bind in a

monodentate fashion from two separate phosphonoacetate anions. One of the phosphonoacetate anions bound to the Yb centre is found to bind in a tridentate manner, through the carboxylate oxygen (O4) and two phosphonate oxygen atoms (O2), with the remaining coordinated phosphonoacetate anions binding in a monodentate manner, via a single oxygen atom. Infinite chains of Yb^{3+} polyhedra are found to form along the *y* axis, shown in Figure 23, and are linked together into the *x* plane, forming a layer, by a phosphonate group (PO3). This phosphonate group in turn links four Yb centres together, one Yb centre in the first chain via (O1) and three Yb centres in the adjacent chain via the two remaining phosphate oxygen atoms (O2). The layers in the *xy* plane are also linked together, parallel to the *z* axis, via carboxylate oxygen atoms (O3 & O4), with each oxygen binding in a monodentate manner to an Yb centre in the chain above and in the chain below.

There is one crystallographically distinct phosphonoacetate anion within the structure, shown in Figure 22(b). The anion binds in a monodentate fashion to two separate Yb centres via a phosphonate oxygen atom (O1) and carboxylate oxygen (O3). The remaining two phosphonate oxygen atoms (O2) are bound in a bidentate manner bridging three Yb centres together, forming an infinite chain in the *xy* plane. The remaining carboxylate oxygen (O4) binds to an Yb centre, which has also been coordinated in a bidentate fashion by the two phosphate oxygen atoms (O2) discussed above. This in turn leads to one phosphonoacetate anion linking five Yb centres together. The Yb-OPO_2 bond distances lie in the range of 2.186(16) - 2.406(9) Å and the Yb-OCO bond distances are 2.151(15) and 2.267(14) Å, which are comparable to other compounds containing Yb-O bonds.[44, 45]

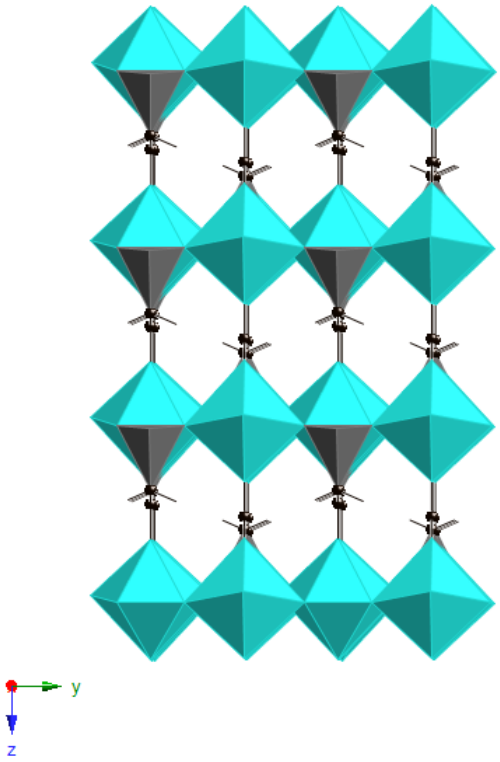

Figure 21 Crystal structure of [Yb][$C_2H_2O_5P$] (**3**) (Colour key: Blue = Yb^{3+}, Black = C, Grey = P)

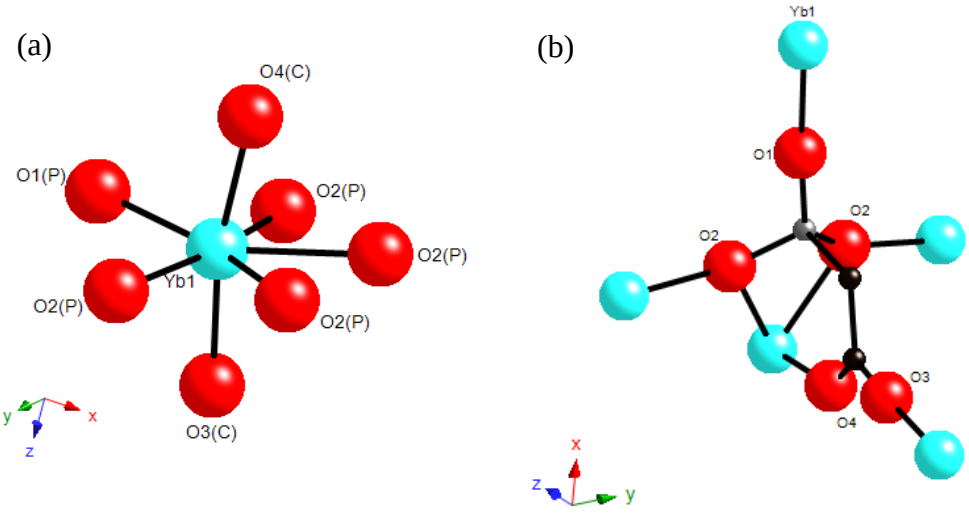

Figure 22 (a) Coordination sphere of Ytterbium and (b) the coordination arrangement of phosphonoacetate in [Yb][$C_2H_2O_5P$] (**3**)

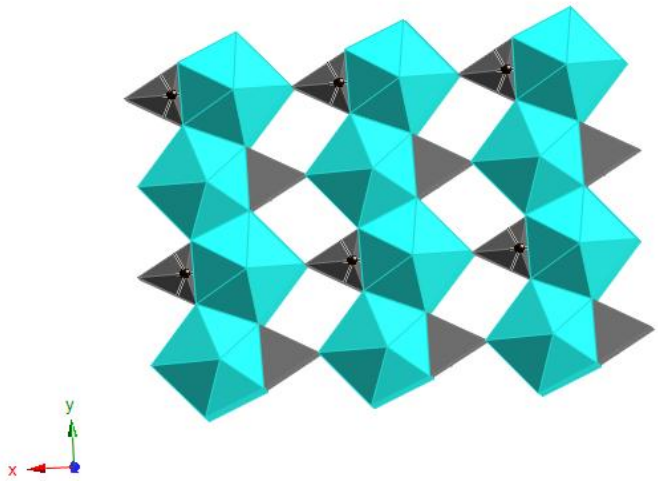

Figure 23 One-dimensional chains of Yb polyhedra, formed along the *y* axis.

A range of analytical techniques have been used to confirm the composition and phase purity of this material. Elemental analysis indicated that the sample contains 7.71 % C (calc - 7.75 %) and 0.63 % H (calc - 0.65 %) which is consistent with the composition obtained from the crystal structure and the absence of crystalline impurities in the powder XRD pattern. The powder XRD pattern of **3** is shown in Figure 24, where it is compared to one calculated from the crystal structure. No crystalline impurities are evident in the experimental data and good agreement between the two patterns is apparent suggesting that crystal structure of **3** is representative of the bulk phase.

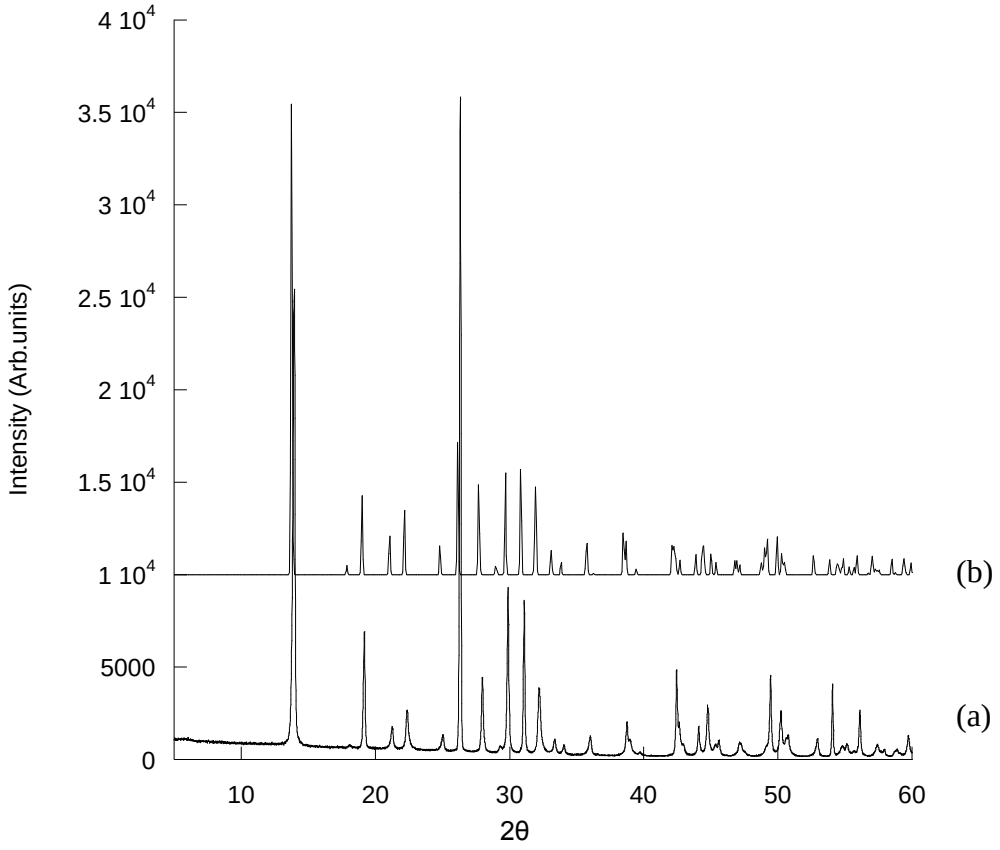

Figure 24 Powder XRD pattern (Cu K_α radiation) of (a) [Yb][$C_2H_2O_5P$] (**3**) and (b) diffraction pattern calculated from the crystal structure.

The TGA trace, shown in Figure 25, shows one distinct mass loss below 995 °C. This mass loss of 14.2 % corresponds to decomposition of the organic anion and compares well to the calculated value of 13.6 %. This data confirms that no water is present in this phase therefore dehydration has occurred using a higher temperature synthesis. The decomposition of the phase is complete by 995 °C with powder X-ray diffraction showing the residue to be $YbPO_4$.

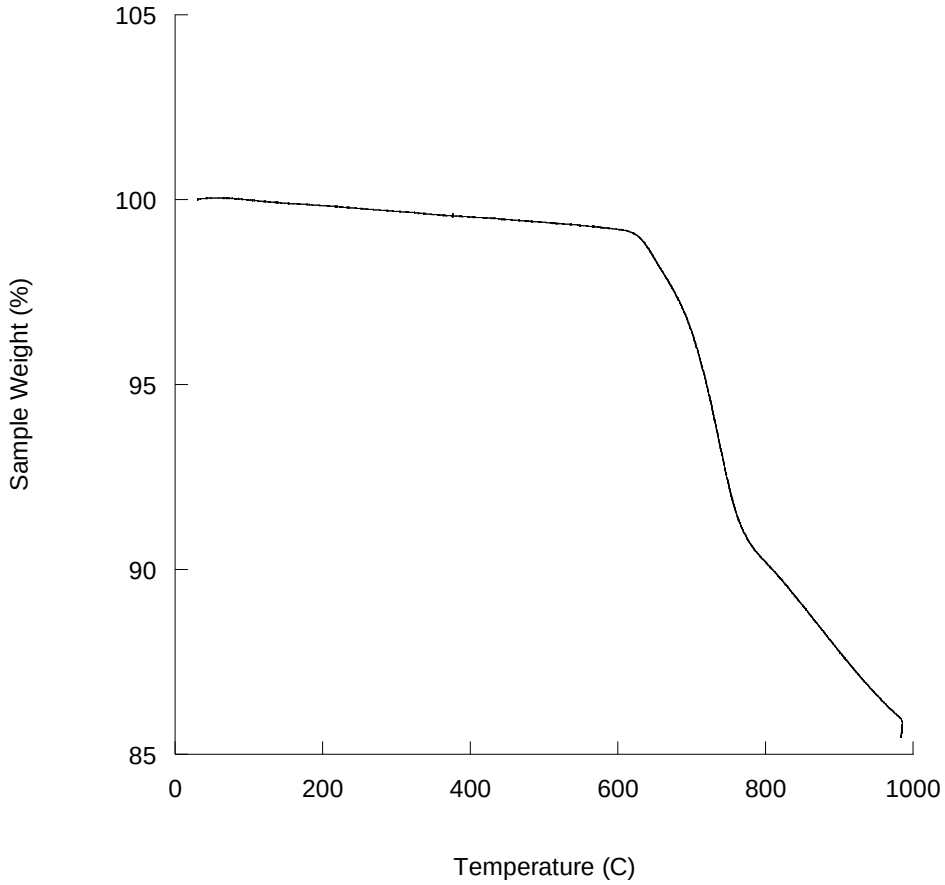

Figure 25 TGA trace of [Yb][$C_2H_5O_5P$] **(3)**

The FTIR spectrum, shown in Figure 26, has bands characteristic of the P-O modes at 1188 cm^{-1} and 999 cm^{-1} and the C=O, C-O modes at 1582 cm^{-1} and 1247 cm^{-1}, which are in agreement with those found in previous literature reports.[13, 40, 41, 42, 43] The (O=P)-OH stretch at approximately 2638 cm^{-1} in the original reagent is now absent after complexation which indicates that all the phosphate oxygen atoms are deprotonated in the product. The spectrum also shows that no water is present in this sample therefore dehydration has occurred on an increase of reaction temperature.

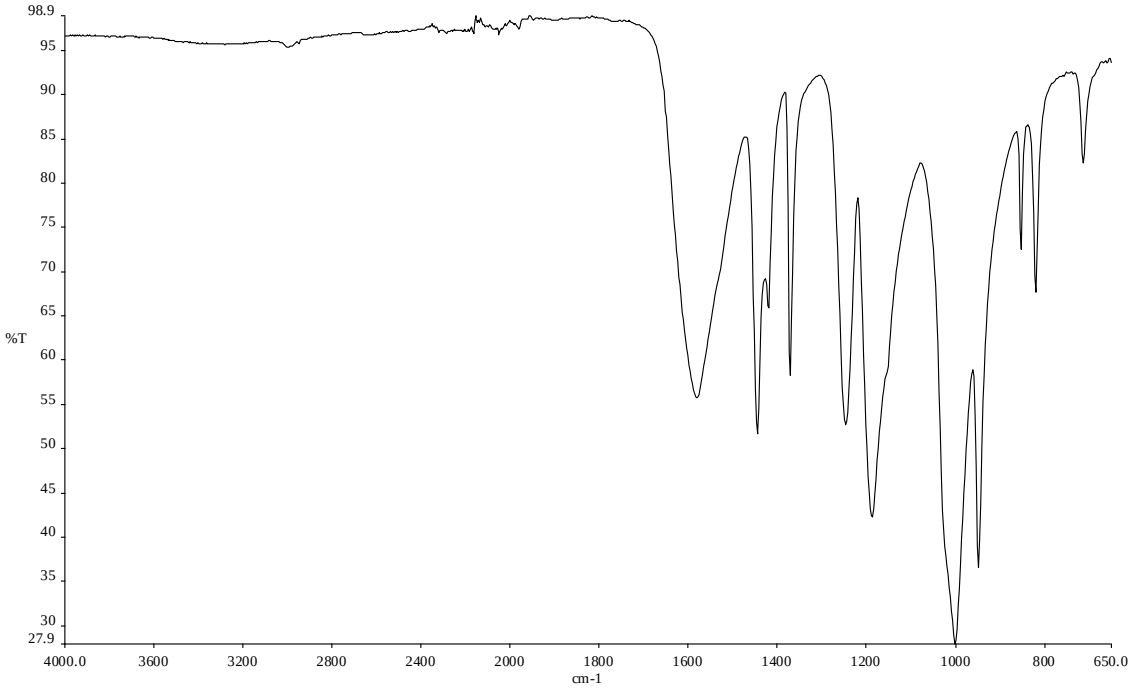

Figure 26 FTIR spectrum of [Yb][$C_2H_5O_5P$] **(3)**

Screening of the lanthanide series has allowed the observation of different structures. It has been discovered that larger lanthanides are able to produce layered structures, when using phosphonoacetate as a ligand, whereas the smaller lanthanides are able to produce three-dimensional frameworks. This may be explained by the coordination numbers of the lanthanide cations employed within these phases, for example when incorporating La – Sm, larger lanthanides, into the synthesis, phases with lanthanide coordination number of nine are seen, whereas when incorporating smaller lanthanides, i.e. Er – Yb, the coordination numbers decrease to seven, allowing three-dimensional frameworks to form. The decrease in coordination numbers from La - Yb are observed due to the lanthanide contraction effect whereby across the lanthanide series the lanthanide ionic radii decrease therefore the available coordination number also decreases.

3.4 Attempted Templating Reactions

As discussed in the introduction the formation of templated phosphonate phases has been achieved using amines such as 4,4'-bipyridyl and 1,10-phenanthrolene resulting in the formation of one-dimensional and three-dimensional frameworks with channels present. Due to these results exploratory synthesis was undertaken in an attempt to template the phases discussed above, using a variety of amines and organics, to determine whether incorporation of a template could be achieved, with the hope to form porous frameworks.

3.4.1 Synthesis

The attempted synthesis to template phases $[Ln_2(H_2O)_3][Phosphonoacetate]_2.H_2O$ (Ln = La - Sm) and $[Ln(H_2O)_2][Phosphonoacetate]$ (Ln = Ho - Tm and Yb - Lu) was via a hydrothermal route, see Chapter 6, Section 6.4.4 for all experimental details. A range of templates were incorporated into the synthesis of these materials such as 2,2'- and 4,4'-bipyridine, aniline, tetrahydrofuran, urea and pyridine. Reaction temperature and also template concentrations were screened in order to obtain new templated phases. However screening proved unsuccessful, with the formation of either the original phase or amorphous phases produced.

3.4.2 Results

When using templates, 2,2'- and 4,4'-bipyridine, tetrahydrofuran, and urea within the template synthesis no incorporation into the lanthanide phases was achieved. On the other hand when using templates aniline and pyridine within the synthesis, this resulted in an amorphous product being formed.

An example of a template reaction using urea within the synthesis, of each phase discussed above, showed no incorporation at 150 °C for 14 hrs for each phase. The powder XRD pattern when using Erbium, urea and phosphonoacetic acid is shown in Figure 27, showing the phase produced is iso-structural to **1** with no incorporation of the template.

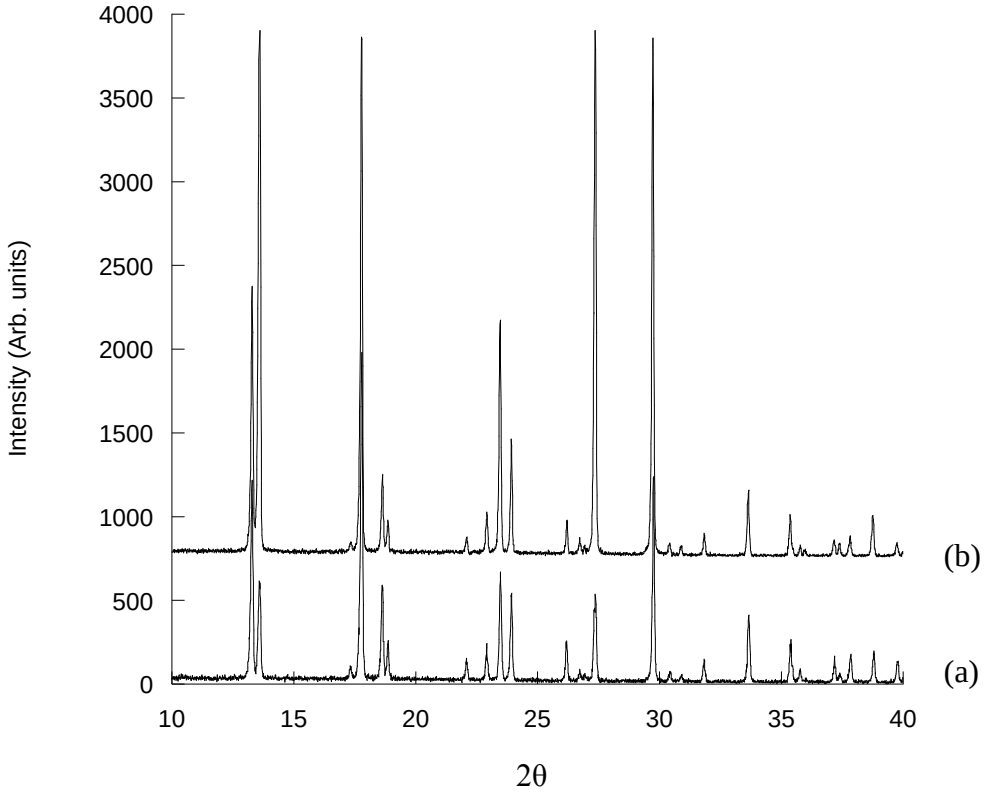

Figure 27 Powder X-ray diffraction patterns (Cu K_α radiation) of (a) Er/phosphonoacetate post synthesis with urea and (b) **[**$Er(H_2O)_2(C_2H_2O_5P)$] (**1**)

3.5 Layered Lanthanide Anthraquinonedisulfonate Coordination Polymer

Chapter 2 described the successful formation of layered hybrid materials consisting of lanthanides and molybdate/tungstate in conjunction with naphthalenedisulfonates. This synthesis was explored using alternative organosulfonates to that of NDS, such as 2,6-anthraquinonedisulfonate and octanesulfonate. This lead to the discovery of two new lanthanide coordination polymers, although unfortunately without the incorporation of molybdate or tungstate.

3.5.1 Synthesis

$[Ln(H_2O)_5]_2[2,6\text{-AQDS}]_3 \cdot 2H_2O$ (Ln = La- Nd) was successfully prepared via a hydrothermal route from $LnCl_3 \cdot xH_2O$ and disodium 2,6-anthraquinonedisulfonate (2,6-AQDS). The reaction was then heated at 165 °C for 14 h before being cooled slowly back to room temperature. This synthesis was also attempted using the isomer 1,5-AQDS, which resulted in no single crystals being formed.

3.5.2 Characterisation of $[Nd(H_2O)_5]_2[2,6\text{-AQDS}]_3 \cdot 2H_2O$ (4)

$[Nd(H_2O)_5]_2[2,6\text{-AQDS}]_3 \cdot 2H_2O$ (**4**) was synthesised via a hydrothermal route. Single crystal X-ray diffraction data showed that it adopts a monoclinic crystal system with the space group $P2_1/m$, shown in Figure 28 with the main crystallographic and refinement data summarised in Table 2, and detailed bond lengths provided in the appendix. This phase has also been successfully synthesised with Ln = La, Ce and Pr, powder XRD patterns are shown in Figure 30, and characterising data is provided in the appendices. Attempts to synthesise this phase using smaller lanthanides, such as Ln = Sm - Lu, proved unsuccessful with different poorly crystalline phases being produced under these conditions.

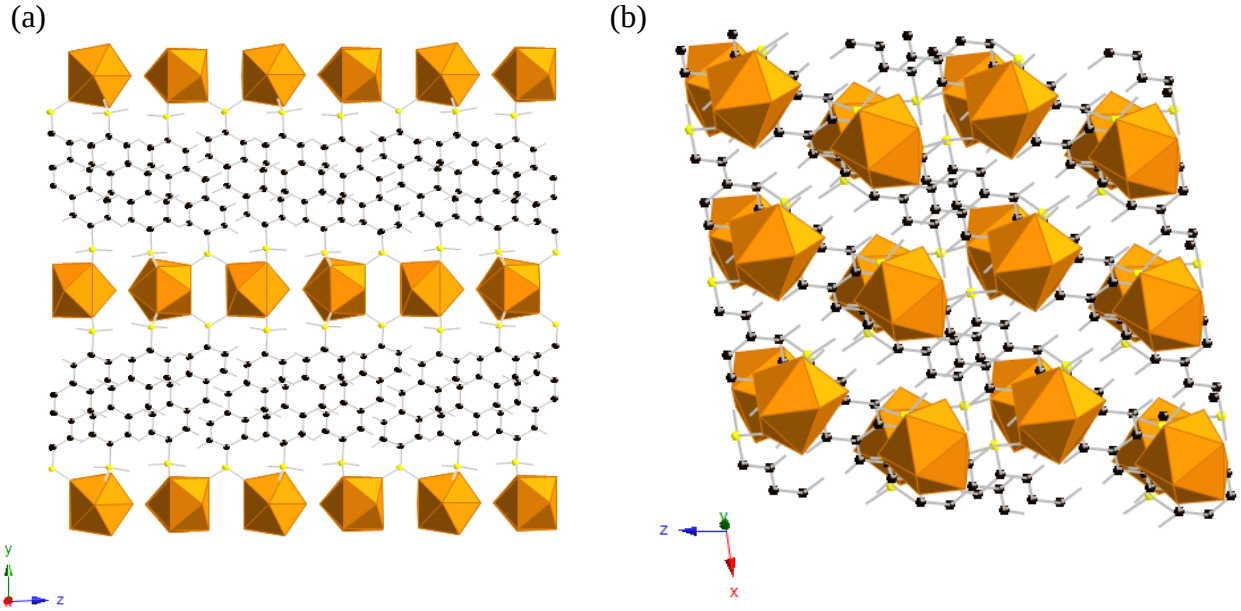

Figure 28 (a) Crystal structure and (b) perpendicular view of $[Nd(H_2O)_5]_2[2,6\text{-AQDS}]_3 \cdot 2H_2O$ (**4**)
(Colour key; Nd – orange, S – yellow and C – black)

This structure comprises of layers of monomeric Nd polyhedra which are linked by 2,6-AQDS anions forming a polymeric, three-dimensional network. There are two crystallographically distinct Nd cations, shown in Figure 29, in this structure, each is isolated, monomeric and nine coordinate, forming layers in the *xz* plane. Each Nd cation is coordinated to five water molecules and four 2,6-AQDS molecules of which two are bridging between adjacent Nd centres and two are singly coordinated. The Nd–OH_2 distances lie in the range 2.425(4) - 2.557(4) Å and the Nd-OSO_2 distance lie in the range of 2.457(3) - 2.509(3) Å, which are comparable to those seen in other lanthanide/sulfonate coordination polymers.[36]

There are three crystallographically distinct 2,6-AQDS anions present in this structure with one bridging between two neodymium centres within the layer, via two of its oxygen atoms with the remaining oxygen atom unbound and interacting with the lattice water molecules present via hydrogen bonding interactions, and the remaining two 2,6-AQDS anions binding in a monodentate manner to a single neodymium centres within the layers, leaving their remaining two oxygen atoms unbound and interacting with the water molecules coordinated to adjacent neodymium centres. The 2,6-AQDS anions pillar the layers with one sulfonate group bridging between two Nd cations and the other coordinating to a single metal centre in the adjacent layer and the remaining 2,6-AQDS anion pillar the layers via one oxygen atom from both sulfonate groups. The effect of this is to create an extended three-dimensional coordination polymer structure. In addition to the five water molecules bound to each Nd cation there are two additional water molecules in the structure. These water molecules are uncoordinated and located between pairs of the bridging sulfonate groups with the O atom at distance of 3.61 Å from one S atom and 3.93 Å from the other.

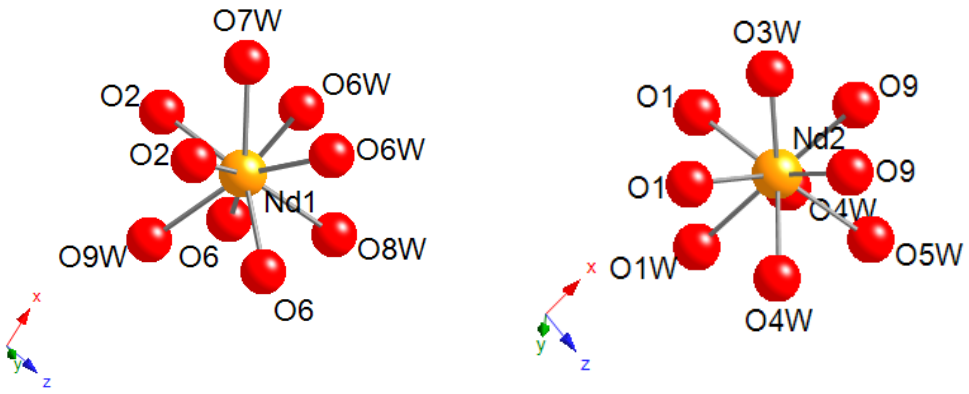

Figure 29 (a) Coordination environment of Neodymium (1) and (b) Neodymium (2) in $[Nd(H_2O)_5]_2[2,6\text{-AQDS}]_3\cdot 2H_2O$ (**4**)

Table 2 Crystallographic data and refinement parameters for $[Nd(H_2O)_5]_2[2,6\text{-AQDS}]_3\cdot 2H_2O$ (**4**)

Empirical formula	$C_{42}H_{42}Nd_2O_{36}S_6$
Formula weight	1597.55
Temperature (K)	100(2)
Wavelength (Å)	0.71073
Crystal system	Monoclinic
Space group	$P2_1/m$
a (Å)	7.4571(12)
b (Å)	29.029(5)
c (Å)	12.046(2)
α (º)	90
β (º)	101.404(4)
γ (º)	90
Volume ($Å^3$)	2556.1(7)
Z	2
Density (calculated) (Mg/m^3)	2.073

Absorption coefficient (mm^{-1})	2.368
Crystal	colourless; prism
Crystal size (mm^3)	0.50 x 0.30 x 0.10
θ range for data collection (º)	2.72 - 25.35
Reflections collected	13055
Independent reflections	4747[R(int)= 0.0259]
Max. and min. transmission	0.7976 and 0.3839
Goodness of fit on F^2	1.181
R [F, $F^2 > 2\sigma$]	0.0341
R_w (F, all data)	0.0784
Diff. map extremes (e $Å^{-3}$)	0.936 and -1.003

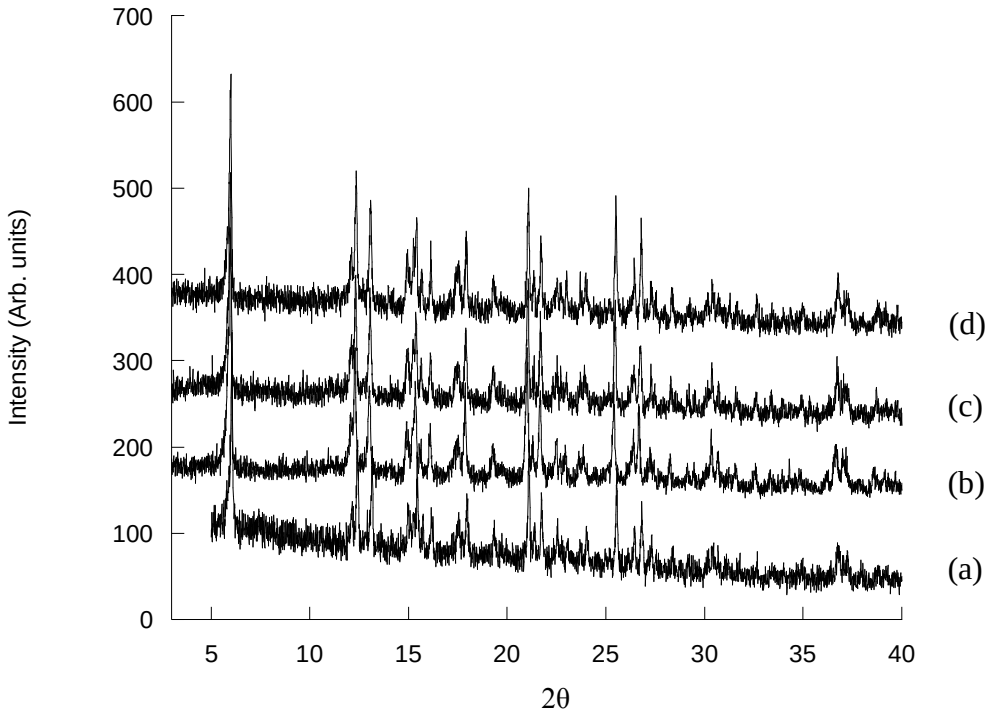

Figure 30 PXRD patterns (Cu K_α radiation) of iso-structural phases (a) $[Nd(H_2O)_5]_2[2,6\text{-AQDS}]_3.2H_2O$, (b) $[La(H_2O)_5]_2[2,6\text{-AQDS}]_3.2H_2O$, (c) $[Ce(H_2O)_5]_2[2,6\text{-AQDS}]_3.2H_2O$ and (d) $[Pr(H_2O)_5]_2[2,6\text{-AQDS}]_3.2H_2O$.

The composition and phase purity of $[Nd(H_2O)_5]_2[2,6\text{-}AQDS]_3 \cdot 2H_2O$ was confirmed by a range of analytical techniques including elemental analysis and Thermogravimetric analysis. A typical sample gave observed analyses of 31.79 % C (calc - 31.46 %) and 2.45 % H (calc - 2.64 %), which is consistent with the composition obtained from the crystal structure and the absence of crystalline impurities in the PXRD pattern. The powder XRD pattern of $[Nd(H_2O)_5]_2[2,6\text{-}AQDS]_3 \cdot 2H_2O$ is shown in Figure 31, where it is compared to one calculated from the crystal structure. No crystalline impurities are evident in the experimental data, and good agreement between the two patterns is apparent, suggesting that the crystal structure is representative of the bulk phase.

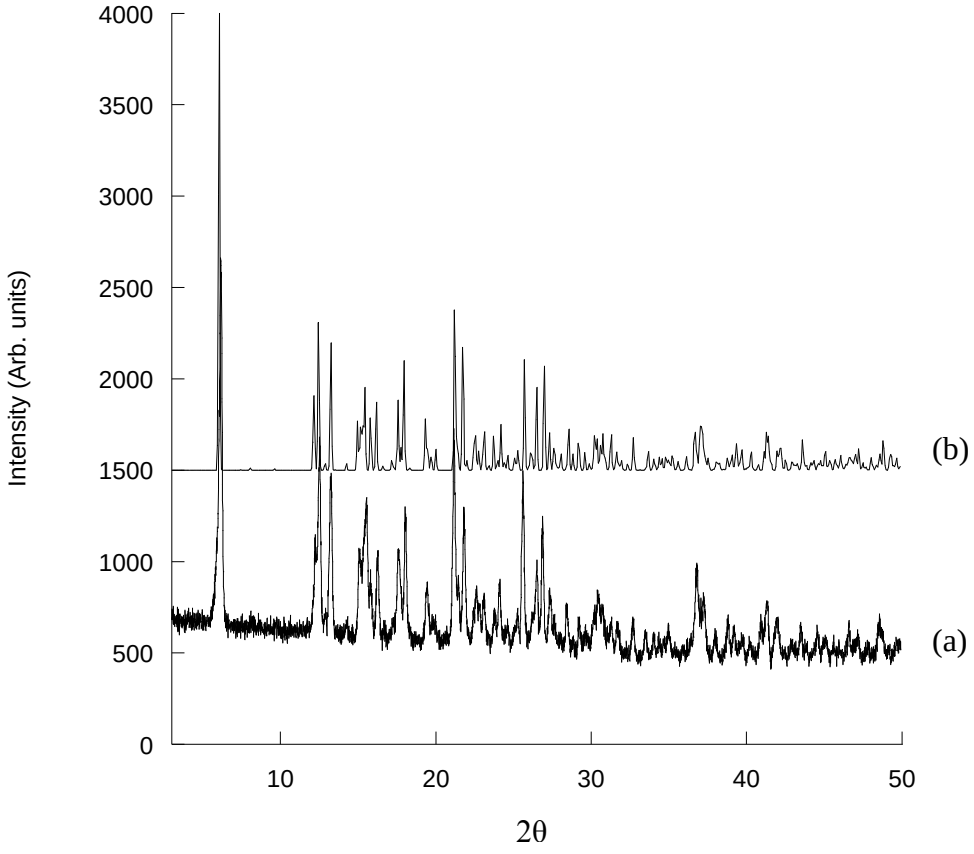

Figure 31 Powder XRD pattern (Cu K_α radiation) of (a) $[Nd(H_2O)_5]_2[2,6\text{-}AQDS]_3 \cdot 2H_2O$ and (b) diffraction pattern calculated from the crystal structure.

The TGA trace is shown in Figure 32, from which it can be seen that there are three distinct mass losses below 600 °C. The first two, with a combined mass loss of 12.0

%, correspond to the dehydration of the material and the mass loss compares well with a calculated value of 13.5 %. The decomposition of the phase is complete by 600 °C following an additional mass loss of 59.4 % (the calculated mass loss is 60.5 %). Powder X-ray diffraction revealed that the residue is $Nd_2O_2SO_4$ and no further mass loss is observed below 1000 °C.

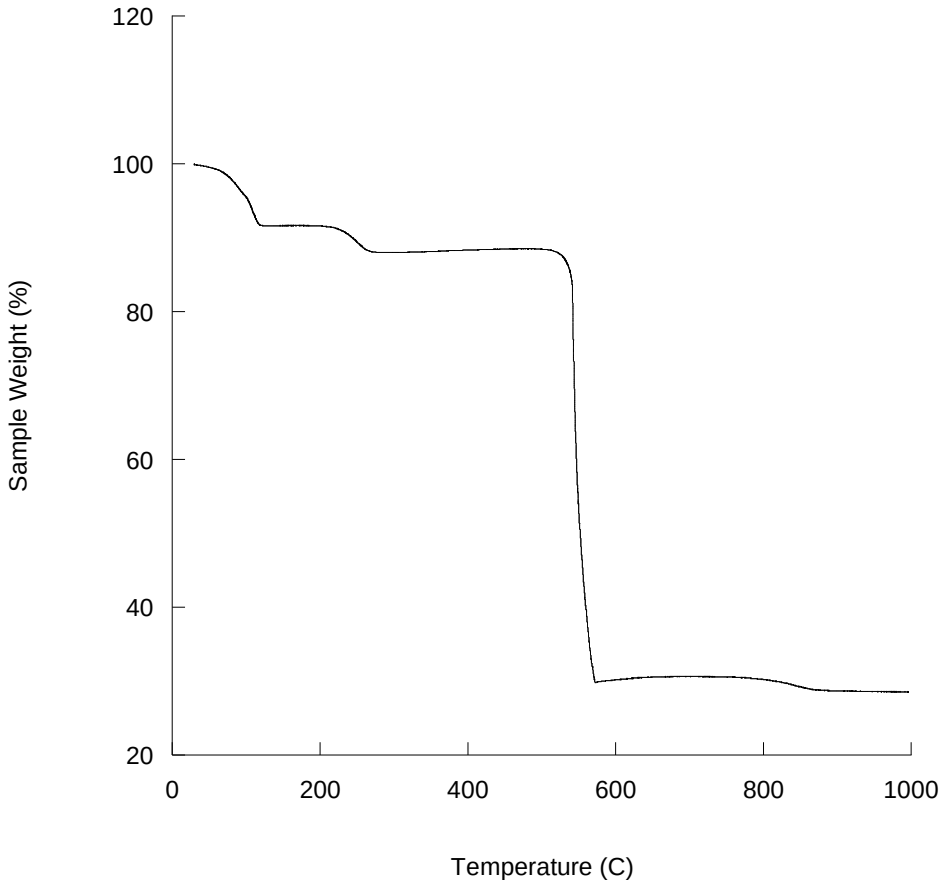

Figure 32 TGA trace of $[Nd(H_2O)_5]_2[2,6\text{-AQDS}]_3 \cdot 2H_2O$

The TGA data suggest that it may be possible to partially dehydrate the material creating a porous phase. However, following treatment under vacuum at 130 °C, the material showed a CO_2 uptake of only 0.27 mmol/g, indicating that a porous material was not formed under these conditions, Figure 33. Powder XRD of the sample following adsorption measurements showed that it was poorly crystalline suggesting that the structure collapses on partial dehydration, Figure 34.

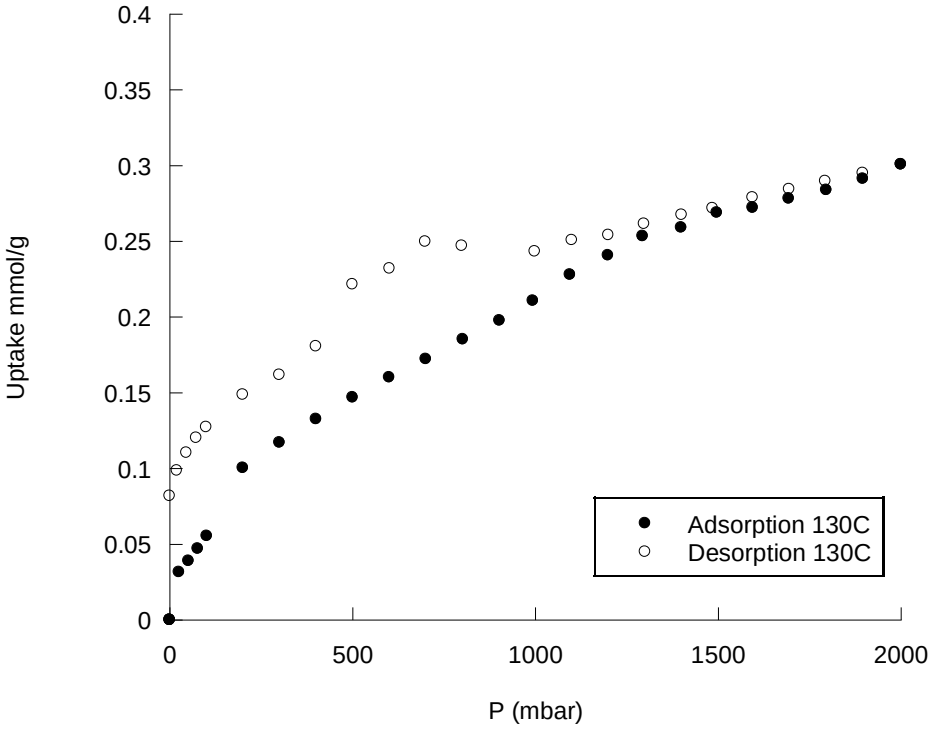

Figure 33 Adsorption and desorption isotherms CO_2 (195 K) for $[Nd(H_2O)_5]_2[2,6\text{-AQDS}]_3 \cdot 2H_2O$ activated at 130 °C.

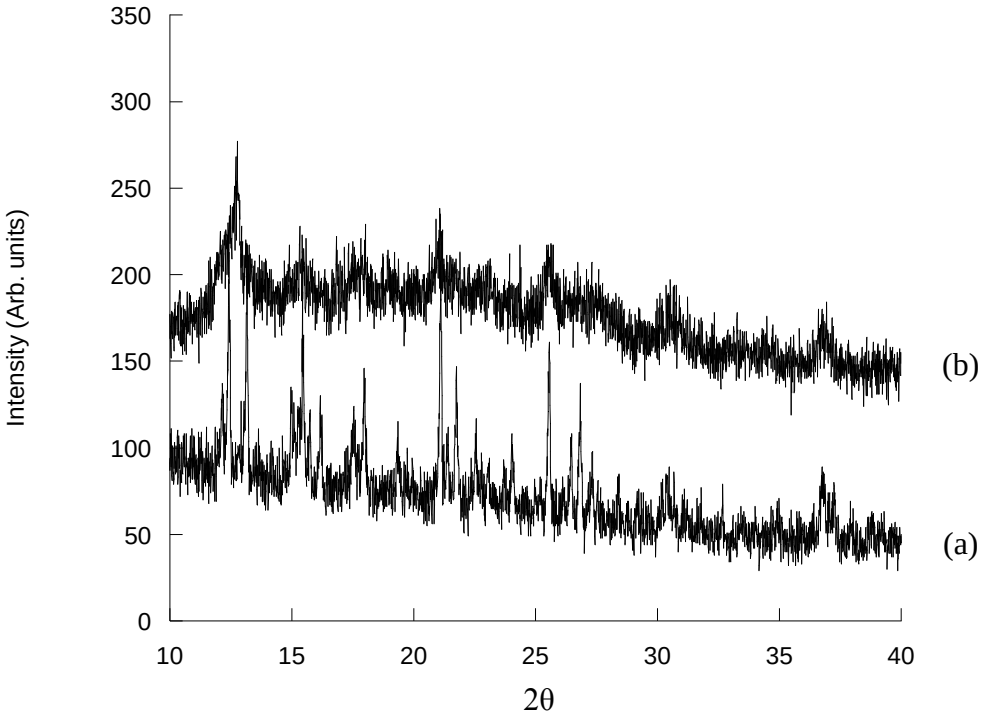

Figure 34 Powder X-ray diffraction pattern (Cu K_α radiation) of $[Nd(H_2O)_5]_2[2,6\text{-AQDS}]_3 \cdot 2H_2O$ (a) pre-IGA measurement and (b) post-IGA measurement

The FTIR spectrum is shown in Figure 35 and has a broad band due to the O–H stretch centred at approximately 3425 cm^{-1}. The bending vibration of water, expected at approximately 1650 cm^{-1}, is largely masked by the 2,6-AQDS bands. The other features of the spectrum are due to the 2,6-AQDS anions and are essentially unchanged in comparison to the original reagent. These include the C=O stretch at approximately 1675 cm^{-1} and the symmetric and asymmetric stretches of the sulfonate groups at approximately 1040 cm^{-1} and 1170 cm^{-1} respectively.

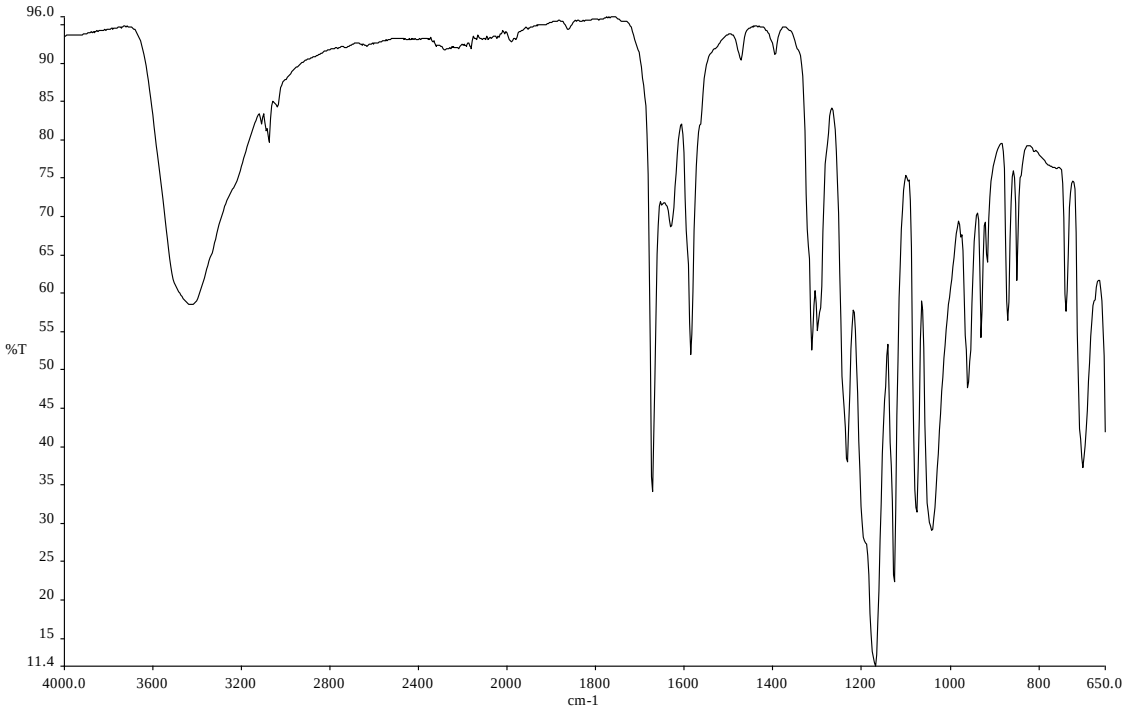

Figure 35 FTIR spectra of $[Nd(H_2O)_5]_2[2,6\text{-AQDS}]_3 \cdot 2H_2O$

3.6 Layered Lanthanide Octanesulfonate Coordination Polymer

3.6.1 Synthesis

$[Ln(H_2O)_5][C_8H_{17}SO_3]_3.2H_2O$ (Ln = La and Nd) was initially prepared via a hydrothermal route from $LnCl_3 \cdot 6H_2O$ and sodium octane-1-sulfonate monohydrate. This was then heated at 165 °C for 14 h before being cooled slowly back to room temperature at a rate of 0.1 °C/min. No product was produced post-synthesis so the solution was left for slow evaporation crystallisation yielding plate like crystals.

3.6.2 Characterisation of $[La(H_2O)_5][C_8H_{17}SO_3]_3.2H_2O$ (5)

$[La(H_2O)_5][C_8H_{17}SO_3]_3.2H_2O$ (**5**) was initially synthesised via a hydrothermal route. However no powder was produced so the solution was left for slow evaporation crystallisation. Single crystal X-ray diffraction data showed that it adopts a triclinic crystal system with the space group $P\bar{1}$, shown in Figure 36 with the main crystallographic and refinement data summarised in Table 3, and detailed bond lengths provided in Appendix B. This phase has also been successfully synthesised with Ln = Nd, with the crystallographic and refinement data provided in the appendices. Attempts to synthesise this phase using smaller lanthanides, such as Ln = Sm - Lu, has proved unsuccessful with the reagents remaining in solution post hydrothermal synthesis and slow evaporation crystallisation.

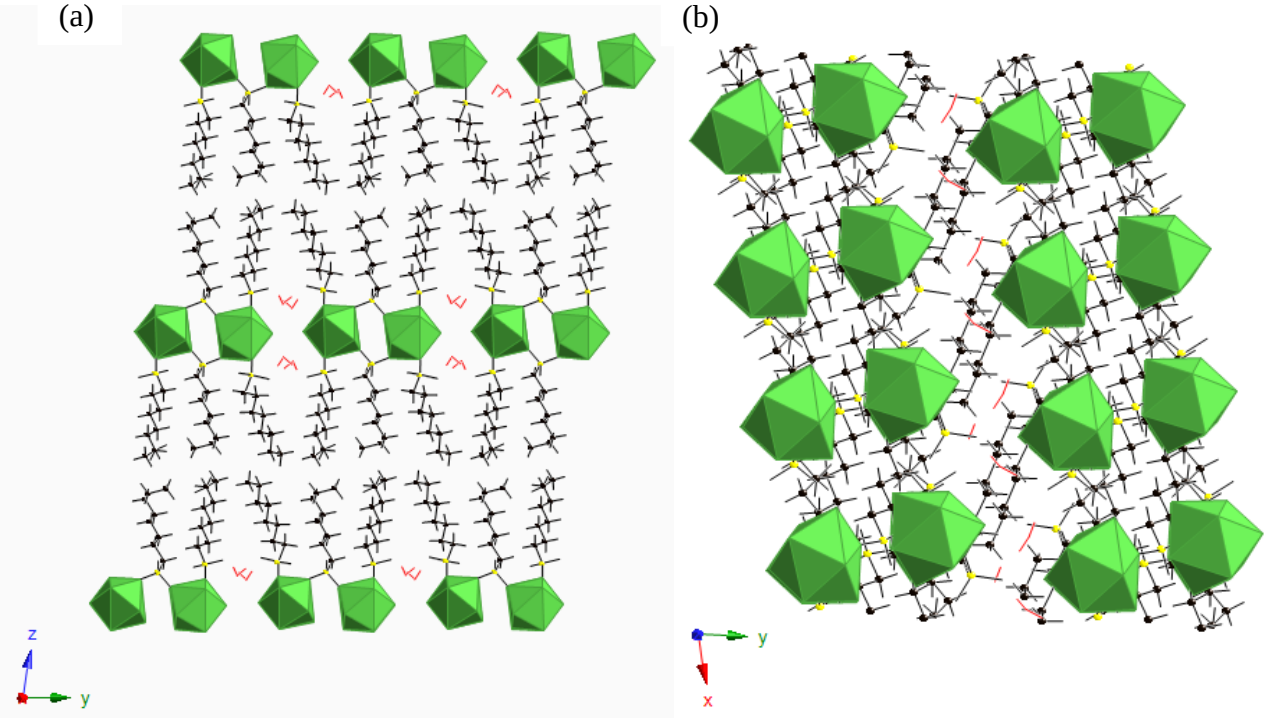

Figure 36 (a) Crystal structure and (b) perpendicular view of $[La(H_2O)_5][C_8H_{17}SO_3]_3.2H_2O$ (**5**)
(Colour key; La – green, S – yellow, C – black and H_2O – red)

This structure comprises of discrete, monomeric La polyhedra which are linked by octanesulfonate anions forming a layered two-dimensional structure. There is one crystallographically distinct La cation in this structure, shown in Figure 37, which is isolated, monomeric, and nine coordinate to five water molecules and four octanesulfonate anions of which two are bridging between adjacent La centres forming one-dimensional chains along the *y* axis, and two are singly coordinated to each lanthanum centre. The octanesulfonate anions are found to be orientated into the interlayer gallery creating a two-dimensional layered coordination polymer, with van der Waals interactions between the methyl groups present at the chain end of octane sulfonate. In addition to the five water molecules bound to each La centre there are two additional water molecules in the structure, located between the pairs of La cations which are bridged by sulfonate anions. These water molecules are found to be hydrogen bound to the water molecules coordinated to each La centre at distances in the range of 2.721 – 2.816 Å and to the unbound sulfonate oxygen atom at distances in the range of 2.749 – 2.848 Å, this leads to layers forming in the *xy* plane. There are three crystallographically distinct octanesulfonate anions present within

this structure with one bridging between two lanthanum centres via two of its oxygen atoms with the remaining oxygen unbound, and the remaining two octanesulfonate anions binding in a monodentate manner to a single lanthanum centre leaving its remaining two oxygen atoms unbound interacting via hydrogen bonds to the lattice water present.

The binding preferences of the sulfonate group within this structure is found to be similar to that of the neodymium phase containing 2,6-AQDS, discussed above, with the difference that in this structure a monosulfonate is incorporated instead of a disulfonate as in 2,6-AQDS, therefore the monosulfonate present is unable to pillar the layers due to the lack of the second sulfonate group, hence only a two-dimensional layered phase is formed unlike the three-dimensional phase formed with 2,6-AQDS. The La–OH_2 distances lie in the range 2.5044(4) – 2.7544(3) Å and the La-OSO_2 bond distances lie in the range of 2.4604(4) – 2.5097(4) Å.

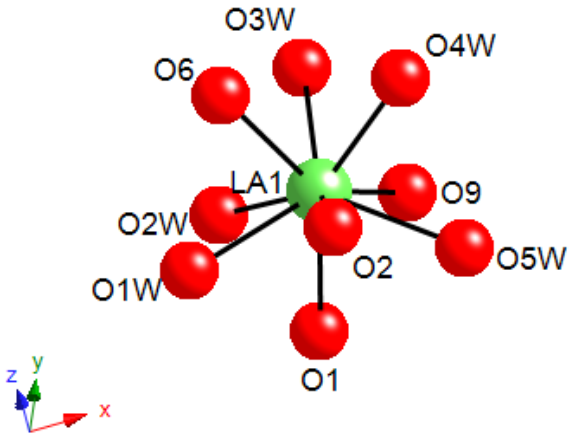

Figure 37 Coordination sphere of Lanthanum in $[La(H_2O)_5][C_8H_{17}SO_3]_3.2H_2O$ (**5**)

Table 3 Crystallographic data and refinement parameters for $[La(H_2O)_5][C_8H_{17}SO_3]_3.2H_2O$ (**5**)

Empirical formula	$C_{48}H_{130}La_2O_{32}S_6$
Formula weight	1689.70
Temperature (K)	100(2)
Wavelength (Å)	0.71073
Crystal system	Triclinic
Space group	$P\bar{1}$
a (Å)	7.0315(14)
b (Å)	13.583(3)
c (Å)	21.676(4)
α (º)	79.100(3)
β (º)	83.327(3)
γ (º)	76.782(2)
Volume ($Å^3$)	1973.3(7)
Z	1
Density (calculated) (Mg/m^3)	1.422
Absorption coefficient (mm^{-1})	2.368
Crystal	colourless; plate
Crystal size (mm^3)	0.40 x 0.20 x 0.04
θ range for data collection (º)	1.56 - 27.10
Reflections collected	11286
Independent reflections	8230[R(int)= 0.0277]
Max. and min. transmission	0.9498 and 0.6242
Goodness of fit on F2	1.085

R [F, F2 > 2σ]	0.0382
Rw (F, all data)	0.0759

No further analysis was performed on this material due to the small amount of crystals produced, therefore only single crystal structure determination was possible.

3.7 Conclusions

Phases **1** – **3**, with compositions $[Er(H_2O)_2][C_2H_2O_5P]$ (**1**), $[Yb(H_2O)_2][C_2H_2O_5P]$ (**2**) and $[Yb][C_2H_2O_5P]$ (**3**) have been successfully synthesised via a hydrothermal route with their crystal structures determined by Single Crystal X-ray Diffraction. **1** & **2** are found to have the same chemical composition with differing infinite three-dimensional structures consisting of LnO_7 polyhedra linked together via O-P-O bridges. **3** is found to be a dehydrated version of the chemical compositions of **1** & **2** and has a crystal structure which is significantly different. On dehydration the structure becomes a three-dimensional pillared layered structure consisting of infinite chains of LnO_7 polyhedra linked together by O-P-O bridges. Each phase reported is found to have a lower coordination number of the lanthanide centre to those phases seen by Li *et al.*[46] When using the earlier lanthanides (Ln = La, Pr, Nd & Sm) the lanthanide centres are found to be nine coordinate, whereas when using later lanthanides (Er & Yb) the coordination number decreases to seven. A plausible explanation for this could be due to the 'lanthanide contraction' effect, as Er and Yb are smaller in size compared to La, Pr, Nd & Sm, their coordination numbers are likely to be smaller. This may also be a valid reason for why a three-dimensional phase and not a layered phase, as seen with Ln = La, Pr, Nd & Sm, is formed with the later lanthanides. BET measurements have indicated that phases **1** - **3** are non-porous. The structure formed using La - Sm comprises of two-dimensional layers of Ln^{3+} cations which are charge balanced by phosphonoacetate anions, there is also water residing within the interlayer gallery which hydrogen bonds to the layers having a pillaring effect therefore in turn forming a three-dimensional structure.

When using lanthanides Eu – Dy less crystalline, amorphous phases were produced therefore the determination of these structures proved not possible.

A range of reaction conditions, varying temperature, concentrations and time, as well as the use of different counterions (X = Cl^-, NO_3^-), have been extensively tested with the outcome of the same phases being formed from 60 – 200 °C for phase **1** and 60 – 180 °C for **2**. Performing the reaction at a temperature of 220 °C for Yb we find a new dehydrated phase forms.

Other organophosphonates have also been used in the attempted synthesis of lanthanide organophosphonates, such as 3-phosphonopropionic acid and benzylphosphonic acid, although this proved unsuccessful with the formation of less crystalline or amorphous phases.

The successful synthesis of a coordination polymer between Nd and 2,6-AQDS has been achieved via hydrothermal route. $(Nd(H_2O)_5)_2(2,6\text{-}AQDS)_3 \cdot 2H_2O$ (**4**) was found to form a three-dimensional network in which monomeric Nd polyhedra are linked by the 2,6-AQDS anions. Each Nd cation is nine coordinate, bound to five water molecules and four 2,6-AQDS anions. The pillaring organic anions have one sulfonate group bridging between metal cations and one coordinated to a single Nd atom in the adjacent layer.

A similar structure has been synthesised using a monosulfonate, octane-1-sulfonate, via a hydrothermal route followed by slow evaporation crystallisation giving an elemental composition of $[La(H_2O)_5][C_8H_{17}SO_3]_3.2H_2O$ (**5**). This structure comprises of two-dimensional chains of lanthanum cations which are alternatively bridged together by sulfonate anions. The octane-1-sulfonate chain is found to reside in the interlayer gallery interacting with the next layer of octane-1-sulfonate anions in turn forming a two-dimensional layered structure.

3.8 References

(1) Guo, Y. Q.; Tang, S. F.; Yang, B. P.; Mao, J. G. *J. Solid State Chem.* **2008**, *181*, 2713.

(2) Poojary, D. M.; Zhang, B. L.; Bellinghausen, P.; Clearfield, A. *Inorg. Chem.* **1996**, *35*, 5254.

(3) Cao, G.; Lynch, V. M.; Swinnea, J. S.; Mallouk, T. E. *Inorg. Chem.* **1990**, *29*, 2112.

(4) Shimizu, G. K. H.; Vaidhyanathan, R.; Taylor, J. M. *Chem. Soc. Rev.* **2009**, *38*, 1430.

(5) Demadis, K. *Structural diversity in metal phosphonate frameworks: An impact on applications*; Royal Society of Chemistry, 2012.

(6) Serpaggi, F.; Ferey, G. *Journal of Materials Chemistry* **1998**, *8*, 2749.

(7) Zhang, J.; Li, J.; Sun, Z. G.; Zhao, Y.; Zhu, Y. Y.; Zhang, N.; Liu, L.; Lu, X. *Zeitschrift Fur Anorganische Und Allgemeine Chemie* **2008**, *634*, 2629.

(8) Bauer, S.; Bein, T.; Stock, N. *J. Solid State Chem.* **2006**, *179*, 145.

(9) Wang, Y.; Bao, S. S.; Xu, W.; Chen, J. S.; Gao, S.; Zheng, L. M. *J. Solid State Chem.* **2004**, *177*, 1297.

(10) Sonnauer, A.; Nather, C.; Hoppe, H. A.; Senker, J.; Stock, N. *Inorg. Chem.* **2007**, *46*, 9968.

(11) Sonnauer, A.; Stock, N. *J. Solid State Chem.* **2008**, *181*, 3065.

(12) Serpaggi, F.; Ferey, G. *Inorg. Chem.* **1999**, *38*, 4741.

(13) Sanselme, M.; Riou-Cavellec, M.; Greneche, J. M.; Ferey, G. *J. Solid State Chem.* **2002**, *164*, 354.

(14) Konar, S.; Zon, J.; Prosvirin, A. V.; Dunbar, K. R.; Clearfield, A. *Inorg. Chem.* **2007**, *46*, 5229.

(15) Clearfield, A. *Journal of Alloys and Compounds* **2006**, *418*, 128.

(16) Clearfield, A. In *Progress in Inorganic Chemistry, Vol 47*; Karlin, K. D., Ed.; John Wiley & Sons Inc: New York, 1998; Vol. 47.

(17) Mao, J. G. *Coordination Chemistry Reviews* **2007**, *251*, 1493.

(18) Merrill, C. A.; Cheetham, A. K. *Inorg. Chem.* **2005**, *44*, 5273.

(19) Alberti, G.; Marmottini, F.; Murciamascaros, S.; Vivani, R. *Angew. Chem.-Int. Edit. Engl.* **1994**, *33*, 1594.

(20) Merrill, C. A.; Cheetham, A. K. *Inorg. Chem.* **2007**, *46*, 278.

(21) Cunningham, D.; Hennelly, P. J. D. *Inorg. Chim. Acta* **1979**, *37*, 95.

(22) Fu, R. B.; Hu, S. M.; Wu, X. T. *Crystal Growth & Design* **2007**, *7*, 1134.

(23) Song, J. L.; Lei, C.; Mao, J. G. *Inorg. Chem.* **2004**, *43*, 5630.

(24) Alberti, G.; Costantino, U.; Allulli, S.; Tomassini, N. *Journal of Inorganic & Nuclear Chemistry* **1978**, *40*, 1113.

(25) Zhang, Y. P.; Clearfield, A. *Inorg. Chem.* **1992**, *31*, 2821.

(26) Stock, N.; Bein, T. *J. Solid State Chem.* **2002**, *167*, 330.

(27) Lebideau, J.; Payen, C.; Palvadeau, P.; Bujoli, B. *Inorg. Chem.* **1994**, *33*, 4885.

(28) Fu, R. B.; Hu, S. M.; Wu, X. T. *Dalton Trans.* **2009**, 9843.

(29) Tang, S. F.; Song, J. L.; Mao, J. G. *European Journal of Inorganic Chemistry* **2006**, 2011.

(30) Costantino, F.; Gentili, P. L.; Audebrand, N. *Inorganic Chemistry Communications* **2009**, *12*, 406.

(31) Serre, C.; Stock, N.; Bein, T.; Ferey, G. *Inorg. Chem.* **2004**, *43*, 3159.

(32) Serpaggi, F.; Ferey, G. *Journal of Materials Chemistry* **1998**, *8*, 2737.

(33) Serpaggi, F.; Ferey, G. *Microporous and Mesoporous Materials* **1999**, *32*, 311.

(34) Cote, A. P.; Shimizu, G. K. H. *Coordination Chemistry Reviews* **2003**, *245*, 49.

(35) Snejko, N.; Cascales, C.; Gomez-Lor, B.; Gutierrez-Puebla, E.; Iglesias, M.; Ruiz-Valero, C.; Monge, M. A. *Chem. Commun.* **2002**, 1366.

(36) Gandara, F.; Garcia-Cortes, A.; Cascales, C.; Gomez-Lor, B.; Gutierrez-Puebla, E.; Iglesias, M.; Monge, A.; Snejko, N. *Inorg. Chem.* **2007**, *46*, 3475.

(37) Li, J. T.; Zheng, L. M. *Inorg. Chim. Acta* **2009**, *362*, 1739.

(38) Milligan, W. O.; Mullica, D. F.; Beall, G. W.; Boatner, L. A. *Acta Crystallographica Section C-Crystal Structure Communications* **1983**, *39*, 23.

(39) Wenk, H. R. *Zeitschrift Fur Kristallographie* **1981**, *154*, 137.

(40) Lothian, A.; Platt, A. W. G. *Polyhedron* **1992**, *11*, 2983.

(41) Lis, S.; Piskula, Z.; Hnatejko, Z. *Journal of Alloys and Compounds* **2008**, *451*, 388.

(42) Stewart, W. E.; Siddall, T. H. *Journal of Inorganic & Nuclear Chemistry* **1968**, *30*, 1513.

(43) Lees, A. M. J.; Kresinski, R. A.; Platt, A. W. G. *New J. Chem.* **2004**, *28*, 1457.

(44) Zhang, F. X.; Lang, M.; Ewing, R. C.; Lian, J.; Wang, Z. W.; Hu, J.; Boatner, L. A. *Journal of Solid State Chemistry* **2008**, *181*, 2633.

(45) Furmanova, N. G.; Soboleva, L. V.; Khapayeva, L. I.; Belov, N. V. *Kristallografiya* **1983**, *28*, 62.

(46) Li, J. T.; Zheng, L. M. *Inorg. Chim. Acta* **2009**, *362*, 1739.

Chapter Four

In-Situ Energy Dispersive X-ray Diffraction Studies

4.0 Introduction

Energy dispersive X-ray diffraction (EDXRD) is found to be an important and powerful method for the study of solid state reactions. It allows one to gain knowledge of reaction mechanisms and kinetics of the formation of crystalline solids.

EDXRD is a non-invasive *in-situ* probe, requiring the use of a high-intensity polychromatic beam of X-rays i.e. synchrotron radiation.[1] This method employs fixed detector angles allowing the simultaneous observation of a wide range of d-spacings in a short space of time, therefore allowing observation of the product and also any intermediates which may be present within the reaction. This method differs to laboratory X-ray diffraction techniques as *ex-situ* measurements use a constant wavelength X-ray source, and a detector which sweeps across a wider range of angles over a longer period of time, allowing one to observe all Bragg reflections related to the crystalline product.

The incident X-ray flux is found to be high when using synchrotron radiation, allowing the collection of data to occur in very short acquisition times from as little as 10 s. These short collection times allow the change in intensity of a Bragg reflection to be measured as a function of time hence determination of kinetics and reaction mechanism is rendered possible. Penetration of thick-walled hydrothermal autoclaves is also found to be possible with this technique due to the high intensity of the incident X-rays. Reactions may therefore be studied under normal laboratory conditions, although now with continuous monitoring, allowing any intermediate phases formed to be observed. This is not possible with *ex-situ* techniques, therefore rendering this technique vital for further understanding of hydrothermal syntheses.[2]

A variety of reactions have been monitored using time-resolved *in-situ* EDXRD such as the hydrothermal crystallisation of zeolites,[3] gallophosphates,[4,5] mesoporous silicates,[6] crystallisation of MOFs[7], intercalation reactions of layered materials,[8] such as metal dichalogenides[9] and layered double hydroxides.[10,11] These investigations have been undertaken predominantly at the UK, SRS, Daresbury Laboratory, although some investigations have recently been conducted at the DORIS III synchrotron, HASYLAB, at DESY, Hamburg, Germany.

4.1 *In-situ* Energy Dispersive X-ray Diffraction

4.1.1 DORIS III Synchrotron

In-situ energy dispersive X-ray diffraction measurements were carried out on beamline F3 at the DORIS III synchrotron, HASYLAB, at DESY (Deutsches Elektronen-Synchrotron), Hamburg, Germany, Figure 1.

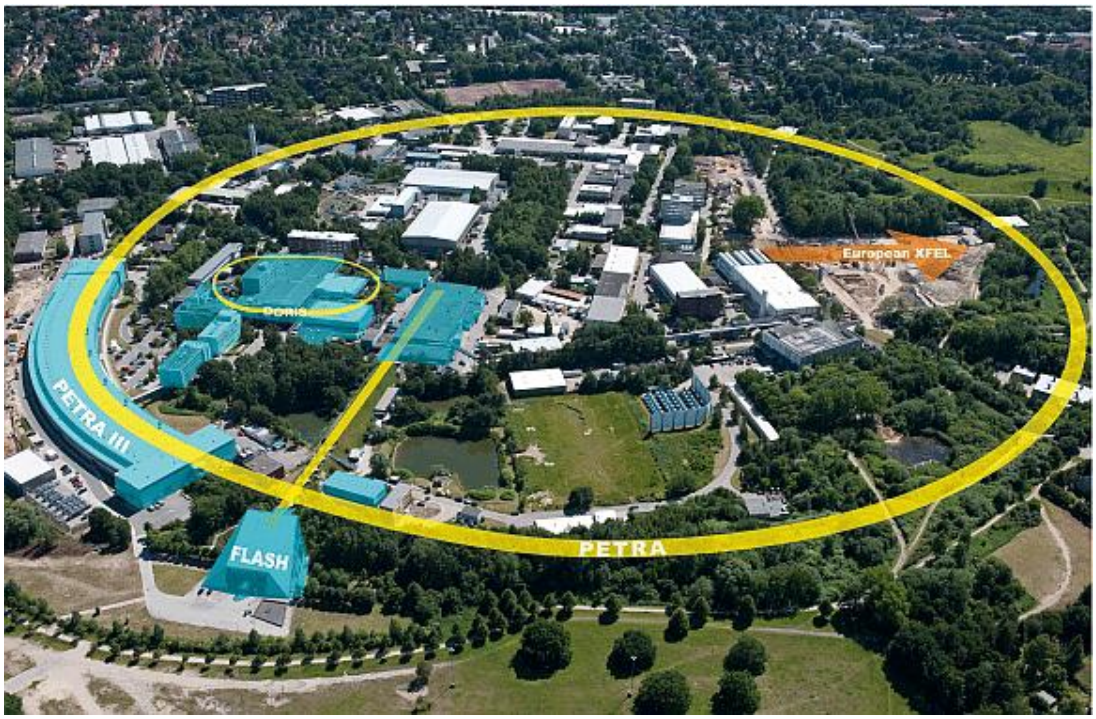

Figure 1 DESY (Deutsches Elektronen-Synchrotron), Hamburg, Germany.

DORIS III, Figure 2, is a storage ring for charged particles where synchrotron radiation is produced in the curves of the ring, where insertion devices wigglers, undulators and bending magnets, are located. The storage rings circumference is 289 m and has a bending radius of 12 m. Beamline F3 receives white beam radiation from bending magnets, with a 1.2 T magnetic field, having a critical photon energy of 16.0 keV. This gives a positron beam energy of 4.45 GeV, in bunched packages, which is optimised for energy-dispersive powder diffraction. The ring stores positrons in two or five bunches, giving an initial beam current of up to 120 mA. The time interval between bunches is typically 480 or 192 ns. Scattered X-rays are detected by a liquid Nitrogen cooled Germanium semiconducting solid state detector, with resolution of ~1%, having an angular range of $0 < 2\theta < 30°$ of scattered radiation in the horizontal plane, which measures the number of photons as a function of energy. The resolution is improved via the use of an adjustable double slit system, which reduces any Compton scattering observed from the material being studied. The radiation has usable flux falling in the range of 13.5 - 65keV, corresponding to ~10^{13} photons/s/mrad^2 in 0.1% bandwidth at 10 keV. Generation of a small and a well defined incident X-ray beam, collimated down to dimensions of 20 x 20µm, is achieved by two tungsten collimators. Further details of the beamline F3 setup, calibration, experimental apparatus and data collection and analysis can be found in Chapter 6, Section 6.1.10.

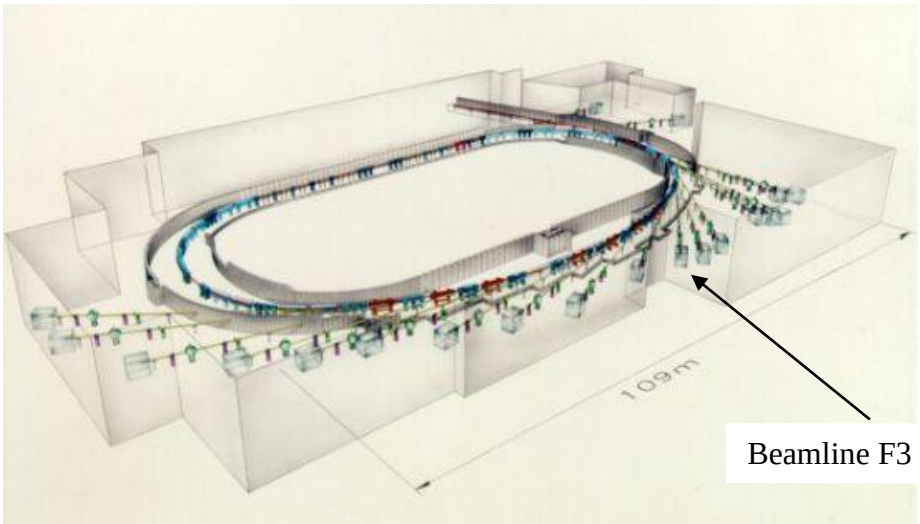

Figure 2 DORIS III storage ring, including beamlines and experimental stations.[12]

4.1.2 Energy Dispersive Bragg's Law

Bragg's law, shown in Equation 1, is applied to ex-situ PXRD studies to allow calculation of d-spacings corresponding to the lattice planes that have been observed in the data. To calculate the d-spacings of Bragg reflections observed in EDXRD measurements, a combination of Bragg's law with the Planck relationship is needed in turn forming energy dispersive Bragg's law. This combination is crucial as EDXRD is a measure of the energy of an X-ray, in keV, diffracted by each lattice plane, which Bragg's law alone does not account for.

Bragg's Law:

$$n\lambda = 2d\sin\theta$$

Equation 1

Planck's relationship:

$$E = \frac{hc}{\lambda}$$

Equation 2

Combining the above equations gives:

$$E = \frac{hc}{2d\sin\theta}$$

Equation 3

Followed by substitution of constants *h* and *c* to give the energy dispersive form of Braggs law, allowing one to calculate the d-spacing corresponding to the Bragg reflection seen:

$$E = \frac{6.19926}{d\sin\theta}$$

Equation 4

Where *E* is the energy in keV, and *d* is the d-spacing in Å associated with the lattice plane from which the photon has been diffracted.

4.1.3 Solid State Kinetics

Solid state reactions have two important processes involved within the reaction, firstly the formation and breaking of bonds and secondly the transport of matter to the reaction zone. The kinetic equation of solid state reactions generally takes the form of:

$$f(\alpha) = kt$$

Equation 5

Were α is the extent of the reaction, k is the rate constant and t is the reaction time with $f(\alpha)$ being dependent on the mechanism of the reaction in question, and geometry of the reacting particles.

Gaussian curves can be fitted to the recorded spectral data and the Bragg reflection in question can be integrated using a peak area calculation programme, this allows the growth of the peak area with time to be determined. The integrated areas can then be converted into extent of reaction at time t, $\alpha(t)$, using the relationship:

$$\alpha_{hkl}(t) = \frac{I_{hkl}(t)}{I_{hkl}(max)}$$

Equation 6

Where $I_{hkl}(t)$ denotes the integrated intensity of the (hkl) reflection at time t, and $I_{hkl}(max)$ denotes the maximum intensity of the actual peak.

Summarised in Table 1 are the rate equations which are commonly used to model solid state reactions. These rate equations have been derived for specific forms of $f(\alpha)$, from the potential nucleation mechanisms that a reaction may employ. Commonly the reactions may be, phase-boundary controlled, diffusion controlled, obey first order kinetics, or follow the Avrami-Erofe'ev rate equation.[13 14]

Table 1 Functional forms of the Common rate equations used to model solid state reactions [4]

Growth model	Equation
Acceleratory rate	
Power law	$\alpha^{1/n} = kt$
Sigmoidal rate	
Avrami Erofe'ev	
First order	$[\ln(1-\alpha)] = kt$
Second order	$[\ln(1-\alpha)]^{1/2} = kt$
Third order	$[\ln(1-\alpha)]^{1/3} = kt$
Fourth order	$[\ln(1-\alpha)]^{1/4} = kt$
Prout-Tomkins	$\ln\left[\frac{\alpha}{(1-\alpha)}\right] = kt$
Deceleratory rate	
1-D diffusion	$\alpha^2 = kt$
2-D diffusion	$(1-\alpha)\ln(1-\alpha) + \alpha = kt$
3-D diffusion	$[1-(1-\alpha)^{1/3}]^2 = kt$
Ginstling-Brounshtein	$1 - \frac{2\alpha}{3} - (1-\alpha)^{2/3} = kt$
Contracting area	$1-(1-\alpha)^{1/2} = kt$
Contracting volume	$1-(1-\alpha)^{1/3} = kt$

Once extent of reaction time has been calculated the $\alpha(t)$ data is then fitted to the most commonly used Avrami-Erofe'ev rate expression, shown in Equation 7.[15,16,17,18]

$$[-ln(1-\alpha)]^{1/n} = k(t-t_0)$$

Equation 7

Were t_0 is the induction time for the reaction, n is the exponent, k is the rate constant, α is the extent of the reaction, and t is the reaction time.

The Avrami-Erofe'ev rate expression takes into account the fact that the nucleation of a reactant may be a random process and not followed by rapid growth. As the nuclei grow larger they impose on one another, therefore any further growth is not

possible. This differs from the mechanism leading to phase boundary controlled reactions as this mechanism assumes that the nucleation step occurs almost instantaneously, with a layer of product coating the surface of each particle, therefore nucleation does not take part in the determination of the rate of reaction.[13] This process is considered by Avrami and Erofe'ev and has been applied to a number of solid state reactions such as phase transformations,[19] crystallisations,[20] [21] and intercalation reactions.[8]

The value of the Avrami exponent (*n*) is related to two entities which occur within a reaction. These entities are the dimensions of growth of the nuclei (λ) and the number of steps involved in the formation of a nucleus (β), (the region in the solid medium in which the reaction occurs), also known as the nucleation rate. Under a variety of reaction conditions Hulbert[22] analysed possible values that the exponent, *n*, may take, shown in Table 2. Reactions are found to have nucleation rates which are either instantaneous ($\beta = 0$), constant ($\beta = 1$), or deceleratory ($0 < \beta < 1$), with growth in one, two or three dimensions, $\lambda = 1\text{-}3$. Reactions are found to be either phase boundary controlled (*n*) where $n = \beta + \lambda$, or diffusion controlled processes where $m = \beta + \lambda/2$. Possible values of the exponent for these processes are found in Table 2, although it is noted that determination of the above values can be difficult, as it is hard to distinguish between β and λ, and as a result this analysis does not allow the complete and clear determination of the reaction mechanism in question.[2]

Table 2 Nucleation growth models for solid state reactions[2]

Dimension of growth (λ)	Nucleation rate (β)	Exponent value	
		Phase boundary controlled (n)	Diffusion controlled (m)
1	Zero (Instantaneous)	1	0.5
	Deceleratory	1 – 2	0.5 – 1.5
	Constant	2	1.5
2	Zero (Instantaneous)	2	1
	Deceleratory	2 – 3	1 – 2
	Constant	3	2
3	Zero (Instantaneous)	3	1.5
	Deceleratory	3 – 4	1.5 – 2.5
	Constant	4	2.5

Further kinetic analysis may be performed by creating a Sharp-Hancock plot of the data. Logarithms of the Avrami-Erofe'ev equation are taken to give the equation of Sharp-Hancock:[14]

$$\ln[-\ln(1-\alpha)] = n\ln(t-t_0) + n\ln(k)$$

Equation 8

The Sharp-Hancock plot, of ln[-ln(1-α)] versus ln(t-t_0), of a reaction should be linear between 0.15 < α < 0.85, as this would suggest that the mechanism of crystallisation

is deemed to be consistent over the course of the reaction. The gradient of this plot allows the Avrami exponent, n, to be determined, and the rate constant, *k*, to be calculated. Once the value of the exponent has been determined, the reaction mechanism may be deduced from the theoretical values shown in Table 2. Although it is noted that the full mechanism of a reaction cannot be confirmed solely from kinetic data.[13, 23]

The Sharp-Hancock plot determines if the Avrami-Erofe'ev kinetic analysis applies to the reaction mechanism in question. Avrami-Erofe'ev reaction mechanisms are either phase boundary (*n*) or diffusion controlled (*m*) processes, so to see if the correct kinetic equation is utilized a linear Sharp-Hancock plot should be produced. When the Avrami exponent is approximately equal to 0.5 this suggests that the reaction mechanism is entirely diffusion controlled, therefore an alternative kinetic equation is needed, see Table 1.

4.2 Previous Studies

Recently studied at Beamline F3 at DORIS III, HASYLAB, was the in-situ investigation of lanthanide phosphonatobutane sulfonates $Ln(O_3PC_4H_8SO_3)(H_2O)$ (Ln = La-Gd).[24] These phases have been investigated using two different heating methods, firstly a conventional method using a custom made reactor system heated by an external thermostat, and secondly under microwave heating. The latter led to shorter reaction times to form the fully crystallised product although it was found that neither of the heating methods or reaction temperatures had any significant influence on the induction time which ranged between 3 - 8 min.

The formation of $Sm(O_3PC_4H_8SO_3)(H_2O)$ was found to take place via two steps with the formation of a crystalline intermediate being observed which then transformed fully into the product phase. The intermediate was observed in all of the reactions performed, being independent of temperature and the heating method used. The rate constant, exponents and the Arrhenius activation energy for the reaction steps were determined via the Sharp-Hancock method.

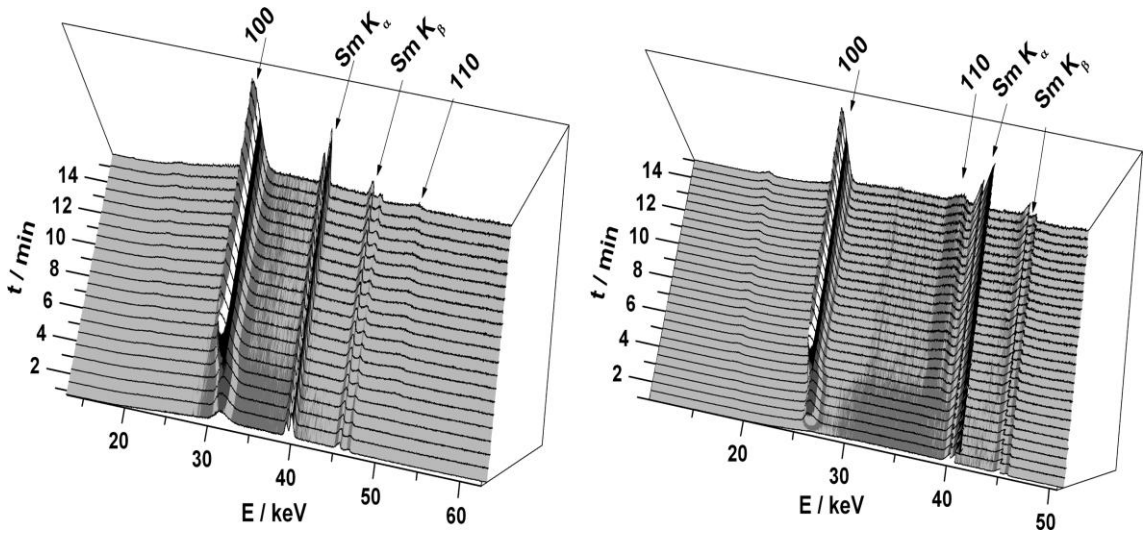

Figure 3 EDXRD patterns of the formation of $Sm(O_3PC_4H_8SO_3)(H_2O)$ by conventional heating (left) and microwave heating (right) at 150 °C.[24]

The 3D plot of the EDXRD measurements is shown in Figure 3, for both heating methods at a temperature of 150 °C. After 1 min an intermediate phase is observed lasting for approximately 5 min, then transforms into the final product, where a shift in Bragg peak is observed from 34 to 31 keV. Quenched experiments proved unsuccessful in isolating the intermediate phase with adequate crystallinity, therefore determination of the crystal structure was not achieved.

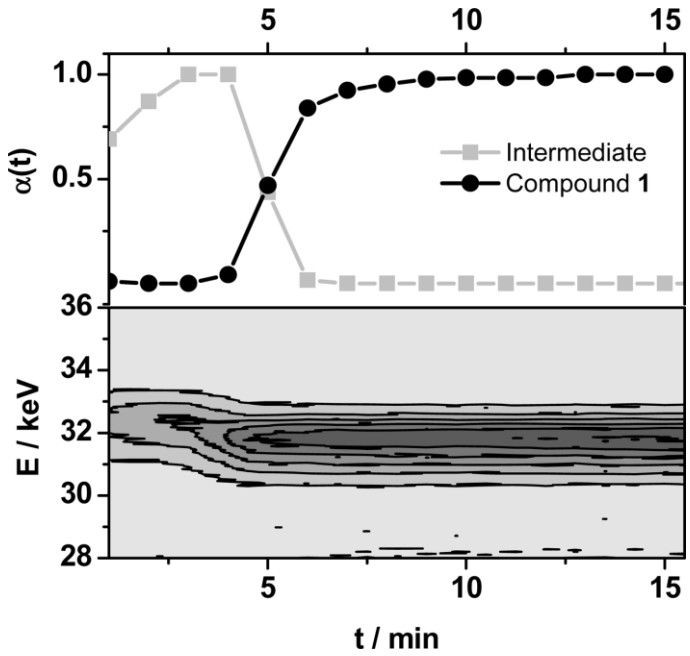

Figure 4 Extent of reaction, α(*t*), for the intermediate and final phase, and the surface plot of this transformation under conventional heating at 150 °C.[24]

Kinetic analysis was achieved by repeating the reaction at different temperatures, from 110 – 150 °C. For both heating methods, as the temperature of reaction increased shorter induction times with faster reaction rates were observed. For microwave heating the rates of reaction were found to be higher compared to that of conventional heating.

As $Sm(O_3PC_4H_8SO_3)(H_2O)$ was found to form in two steps, the Avrami Erofe'ev exponent, was determined for each process. For the transformation of the intermediate into the final phase the exponent values, n, varied from 2.1 - 3.0, this was observed for both heating methods indicating that the mechanism is nucleation controlled, whereas the later reaction step, growth of the product, n = 0.23 - 0.68, suggesting a diffusion controlled mechanism, therefore Avrami Erofe'ev kinetic analysis may not be applicable. Smaller values of Avrami exponent are known, which are due to the reaction mechanism being hindered by diffusion, therefore suggesting that the latter step of the reaction discussed here may in fact adhere to the Avrami-Erofe'ev kinetic equation.[25]

Determination of the rate constants, *k*, at different temperatures allowed calculation of the Arrhenius activation energies of the two processes for both heating methods.

The first process, of transformation of the intermediate to product, gave activation energies of +34 $kJmol^{-1}$ (microwave) and +41 $kJmol^{-1}$ (conventional heating). For the second reaction step the activation energies differ significantly, energies of +62 $kJmol^{-1}$ (microwave) and +128 $kJmol^{-1}$ (conventional heating) were calculated, this phenomenon can be explained by the fact that the molecules in the microwave heated reaction have an increased mobility under microwave irradiation compared to that of the conventionally heated molecules, therefore leading to a decrease in the activation energy.[26]

Also recently studied at Beamline F3, was the time-resolved EDXRD studies of the solvothermal formation of MOFs constructed from transition metal ions and carboxylate ligands. These frameworks include, $[Cu_3(BTC)_2(H_2O)_3]$ (HKUST-1) (BTC = 1,3,5 – benzene-tri-carboxylate) and $[Fe^{III}(OH,F)(O_2CC_6H_4CO_2)H_2O]$, iron(III) terephthalate, MIL-53.[7]

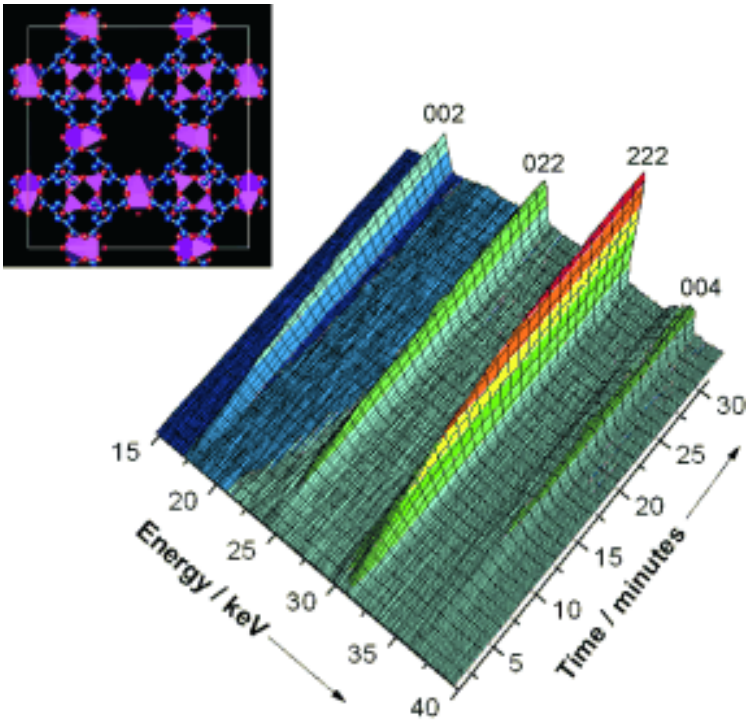

Figure 5 EDXRD patterns of the formation of $[Cu_3(BTC)_2(H_2O)_3]$ HKUST - 1 at 125 °C. Inset: view of the structure of HKUST - 1
(Colour key; Cu (five - coordinate) - pink polyhedra, C - blue and, O - red).[7]

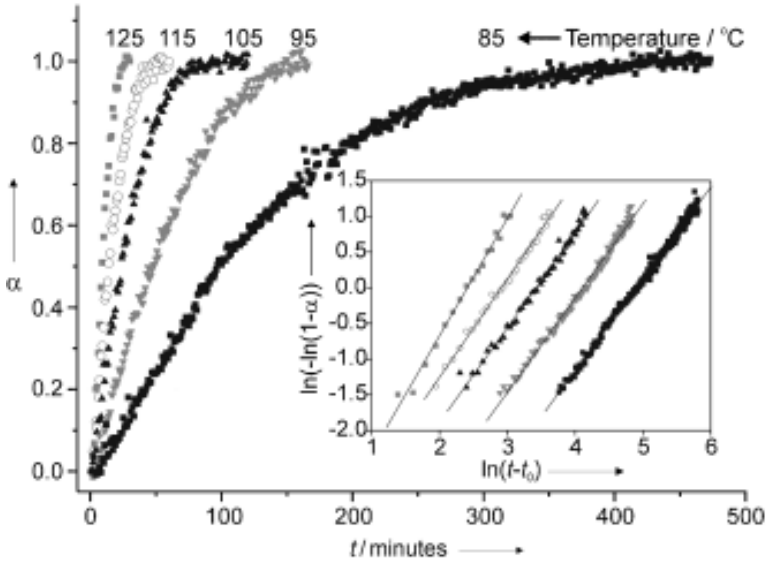

Figure 6 Plot of extent of reaction (α) against time (t) of $[Cu_3(BTC)_2(H_2O)_3]$ HKUST - 1. Inset: Sharp-Hancock plot of the crystallisation of HKUST-1 at various temperatures.[7]

For $[Cu_3(BTC)_2(H_2O)_3]$ (HKUST - 1), at 125 °C it was noted that there is no detectable induction period for the formation of this phase. The main Bragg peak, at maximum intensity, was seen after 30 min, Figure 5. This reaction was repeated over five different temperatures so that all kinetic information and the mechanism of crystallisation could be extracted. The crystallisation curves being calculated from the integration of the most intense Bragg peak, at each temperature, are shown in Figure 6. The observed Avrami exponent, n, values for this crystallisation are close to 1.5, indicating that the crystallisation is controlled by the formation of nucleation sites, rather than diffusion controlled. An Arrhenius plot of this data gave an activation energy of +73.3 $kJmol^{-1}$.

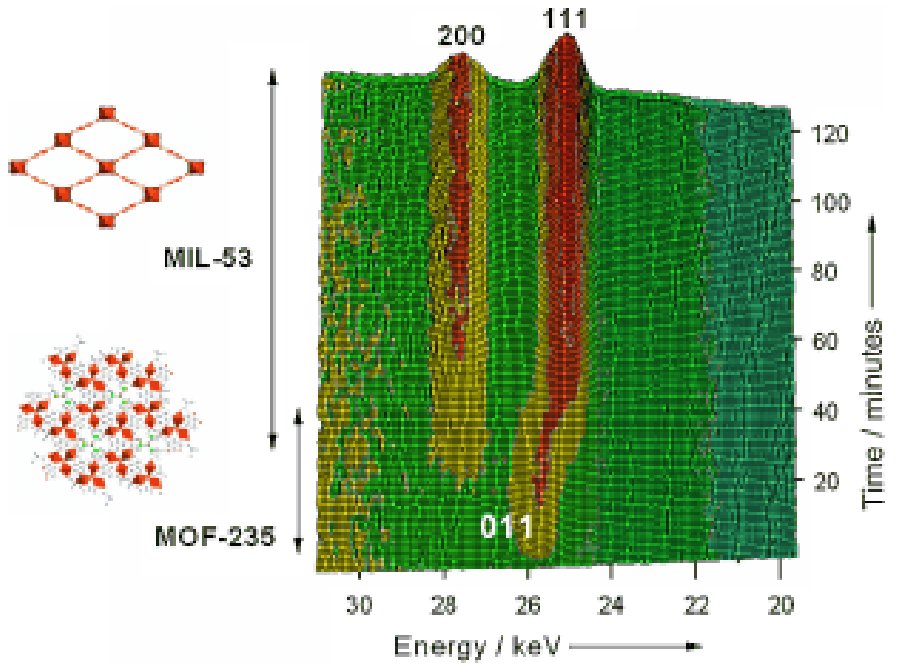

Figure 7 Time-resolved EDXRD measured during the crystallization of MIL-53 at 150 °C.[7]

The 3D plot of the EDXRD measurements of $[Fe^{III}(OH,F)(O_2CC_6H_4CO_2)H_2O]$, iron(III) terephthalate, MIL - 53 at 150 °C is shown in Figure 7. From this 3D plot a crystalline intermediate phase is seen, which disappears after 30min. This intermediate is found to have a longer lifetime when the reaction temperature is decreased to 125 °C, and at a reaction temperature of 100 °C the intermediate is found to be the sole phase for up to 6 h. The crystalline intermediate was able to be isolated, upon quenching the reaction, and its crystal structure determined using high-resolution powder diffraction. The structure is found to be related to MOF - 235, with its topology being unrelated to the final phase, therefore suggesting dissolution of this intermediate, releasing reactive species into solution, and subsequently re-crystallising into the final product.

4.3 Our Studies

The synthesis of the layered molybdate and tungstate systems, discussed in Chapter 2, were investigated using the energy dispersive *in-situ* X-ray diffraction technique. Kinetic data is to be extracted for the synthesis at various temperatures which will allow rate constants, the activation energy and also the mechanism of crystallisation to be obtained. Use of this technique will allow one to determine the pathway of formation of each compound and also to discover if any crystalline intermediates are formed during the crystallisation of each phase.

Ex-situ powder X-ray diffraction allowed the observation of a second phase within the La/WO_4/2,6-NDS system, with interlayer separations of 17.9 Å for $[La(H_2O)WO_4]_2$[2,6-NDS] and 16.4 Å for the dimerised phase of $[La_2(H_2O)_2W_2O_8]$[2,6-NDS]. Extensive reaction screening proved unsuccessful in producing a phase pure material, or in isolating each phase separately, therefore the use of *in-situ* EDXRD may allow the isolation of a phase pure material from this system, or isolation of each phase separately, and also to determine the mechanism of formation of the phase. Details of these phases can be found in Chapter 2, Section 2.2.5.

From the reactions performed in Chapter 3 it was discovered that the lanthanide coordination polymer, consisting of Ytterbium and phosphonoacetate, had a different composition and structure when increasing the synthesis temperature from 200 to 220 °C. This was observed using powder X-ray diffraction measurements, Chapter 3, Section 3.3.4. Single crystal X-ray diffraction measurements successfully determined the crystal structure of both phases, finding the higher temperature phase had dehydrated upon increasing the reaction temperature therefore producing a new phase. Upon dehydration the elemental composition changed in hydration levels from $[Yb(H_2O)_2][C_2H_5O_5P]$ to $[Yb][C_2H_5O_5P]$. The *in-situ* energy-dispersive X-ray diffraction technique was utilized to investigate this system.

4.4 Scope of Chapter

Here we report the results obtained from investigating the formation of layered lanthanide molybdate and tungstate systems using *in-situ* EDXRD. Kinetic analysis was successfully extracted for the formation of $[La(H_2O)WO_4]_2$[1,5-NDS], allowing the rate constant and the Arrhenius activation energy to be determined. This analysis was achieved by performing the synthesis at various temperatures from 120 - 200 °C.

The formation of an Ytterbium phosphonoacetate coordination polymer has also been studied using the *in-situ* EDXRD technique following the observation *ex-situ* of a hydrated phase at 200 °C and a dehydrated phase at 220 °C.

4.5 General procedure

A PC coupled to a multi-channel analyser was used for data collection and storage in the *in-situ* experiments. A standard of known d-spacings was recorded before the first set of measurement commenced in order to determine the true value of the detector angle. Resulting spectra of the syntheses were evaluated and analysed with the tools 'IDL 7.1 virtual machine application' f3_extens and f3_tool which were obtained from station F3.

Once spectra had been recorded Gaussian curves were fitted to the recorded data and the area under the peak of each Bragg reflection in question was integrated using the f3_tool programme, this allows the growth of the peak area with time to be determined. The integrated areas were then be converted into extent of reaction at time *t*, $\alpha(t)$, using Equation 6.

Once extent of reaction had been calculated the $\alpha(t)$ data was then fitted to the most commonly used Avrami-Erofe'ev rate expression, shown in Equation 7. Here the induction time, t_0, determined by the onset of diffraction intensity, for the formation of the required phase was taken into account and used to correct the data. The Avrami-Erofe'ev rate expression was utilised for our systems as other similar systems also use this expression, and literature, corresponding to syntheses studied using *in-situ* EDXRD, show that this expression is widely used.

This data was then transformed into a Sharp-Hancock plot, over the range $0.1 < \alpha < 1.0$, which is produced by taking logarithms of the Avrami-Erofe'ev equation to give the equation of Sharp-Hancock, shown in Equation 8. Data was produced, and linear regression allowed the Avrami exponent, *n*, (the gradient) to be calculated, and the rate constant, *k*, (from the intercept, $n\ln(k)$) to be calculated.

4.6 Results and discussion

In-situ EDXRD studies were performed on molybdate and tungstate phases with the general formula $[Ln(H_2O)MO_4]_2[A]$ (Ln= La- Nd, M= Mo or W, A= 1,5-Naphthalenedisulfonate or 2,6-Naphthalenedisulfonate), discussed in Chapter 2 and also on the ytterbium phosphonoacetate phase with an elemental composition of $[Yb(H_2O)_2][C_2H_5O_5P]$ and a dehydrated composition of $[Yb][C_2H_5O_5P]$. The reactions were performed under the same conditions as the *ex-situ* hydrothermal syntheses but with doubled concentrations. This is due to the data being weak when using normal concentrations, which is overcome by increasing the amount of sample within the X-ray beam. Synthesis details are found in Chapter 6.

4.6.1 *In-situ* EDXRD Study of the formation of $[Ln(H_2O)MoO_4]_2[A]$ (Ln = La or Nd, A = 1,5 or 2,6-naphthalenedisulfonate)

4.6.1.1 Formation of $[La(H_2O)MoO_4]_2$[1,5-NDS]

A study of the crystallisation of $[La(H_2O)MoO_4]_2$[1,5-NDS] was performed using the *in-situ* EDXRD technique. The three-dimensional stack plot of the EDXRD data is shown in Figure 8, with an acquisition time of each spectra of 60 s at a diffraction angle of 1.19 °2θ and a reaction temperature of 165 °C. Lanthanide $K\alpha_1$ and $K\alpha_2$ resonances where observed alongside the Bragg reflections at 33.4 and 33.0 keV and the Kβ resonance is observed at 37.8 keV, these resonances have constant intensity throughout the synthesis indicating that a constant amount of sample was maintained within the X-ray beam. The Bragg reflection associated with the required phase is

observed at 35.5 keV, 16.6 Å. The induction time of the formation of $[La(H_2O)MoO_4]_2[1,5\text{-NDS}]$ is around 3 minutes with the intensity of the product resonance increasing after 10 minutes to its maximum value after 40 minutes. No crystalline intermediates were observed in the formation of this phase.

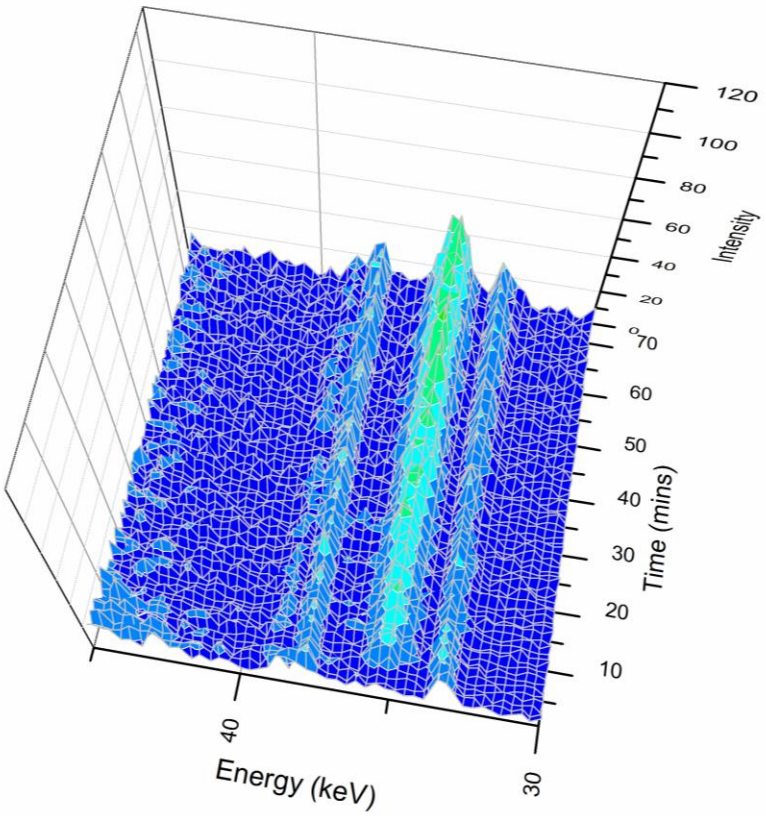

Figure 8 Three-dimensional stacked plot of the time resolved *in-situ* energy dispersive X-ray diffraction data of the formation of $[La(H_2O)MoO_4]_2[1,5\text{-NDS}]$ at 165 °C. An acquisition time of 60 s was used for each recorded spectrum and a detector angle of 1.19 ° 2θ.

The extent of reaction (α) versus time plot of the formation of $[La(H_2O)MoO_4]_2[1,5\text{-NDS}]$ at 165 °C is shown in Figure 9. It is observed that the induction time of the reaction is around 3 minutes, with the formation of the final phase proceeding for approximately 73 minutes, until the reaction was deemed complete.

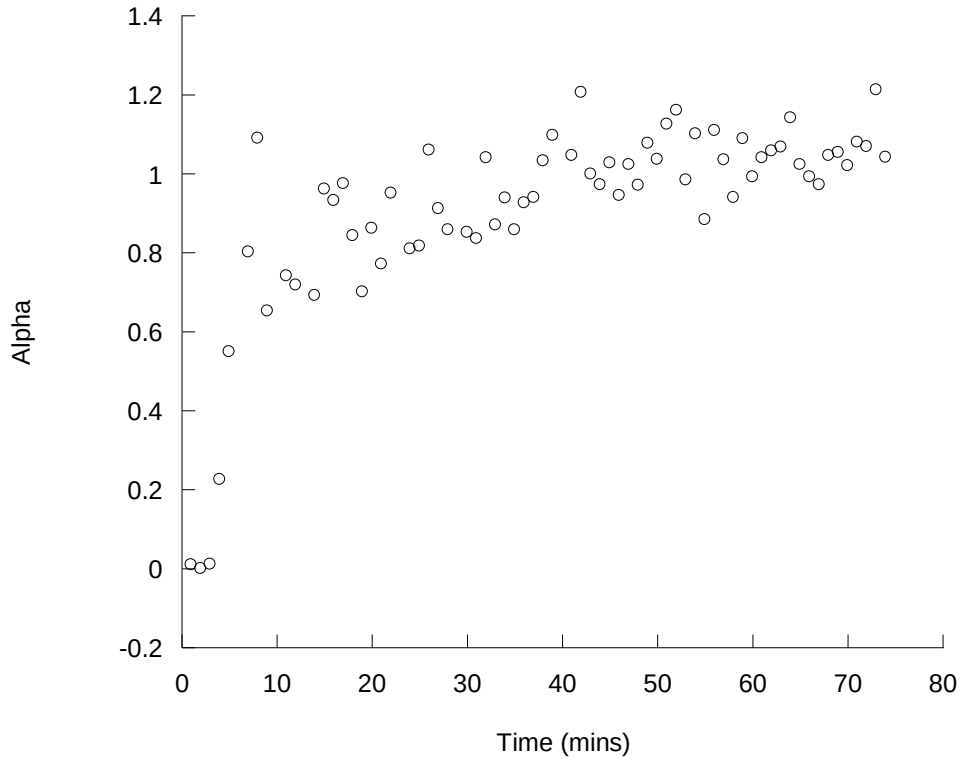

Figure 9 Plot of the extent of the reaction versus time of the formation of $[La(H_2O)MoO_4]_2$[1,5-NDS] at 165 °C

PXRD measurements, post *in-situ* synthesis, showed the formation of a crystalline phase, which is identical to the phase produced in *ex-situ* synthesis, as shown in Figure 10.

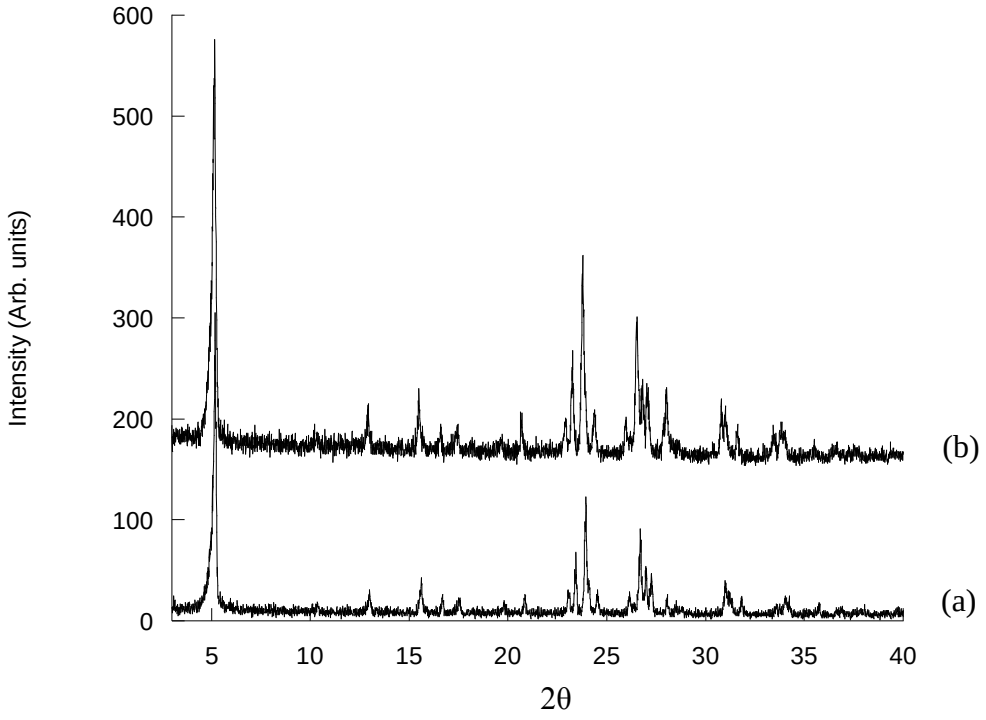

Figure 10 Powder X-ray diffraction patterns (Cu K_α radiation) of $[La(H_2O)MoO_4]_2$[1,5-NDS] (a) synthesised *in-situ* and (b) synthesised *ex-situ.*

The Sharp-Hancock plot is shown in Figure 11. The value of the exponent has been determined to have a value of 0.51, corresponding to a diffusion controlled (*m*) one-dimensional mechanism with a deceleratory nucleation rate, the Sharp-Hancock plot also concludes that the reaction mechanism obeys the Avrami-Erofe'ev solid state rate equation, due to the linearity of the Sharp-Hancock plot produced, therefore suggesting that the reaction also proceeds via a consistent mechanism. The rate constant was calculated to be 3.65 x 10^{-3} s^{-1} which is comparable to other *in-situ* syntheses such as those found in the crystallisation of a lanthanide phosphonobutanesulfonate $Ln(O_3PC_4H_8SO_3)(H_2O)$ (Ln= La- Gd), rate constants are calculated to range from 2.49 – 9.9 x10^{-3} s^{-1} with reaction temperatures ranging from 110 – 150 °C, under conventional heating.[24] The data for this synthesis is summarised in Table 3.

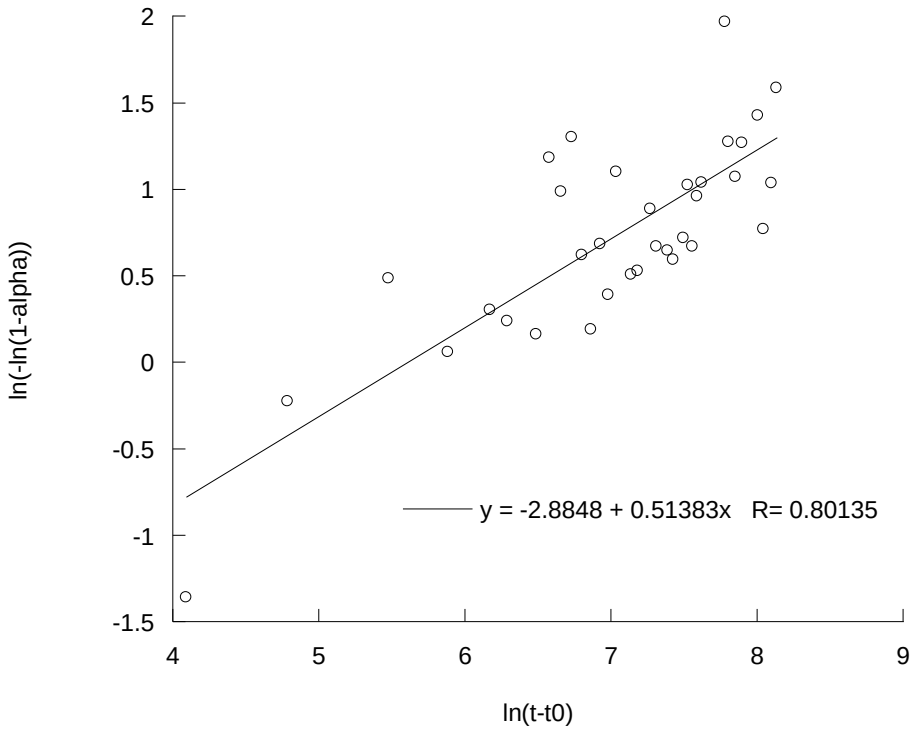

Figure 11 Sharp-Hancock plot of ln(-ln(1-α)) versus ln(t-t_0) for the formation of $[La(H_2O)MoO_4]_2$[1,5-NDS] at 165 °C.

4.6.1.2 Formation of $[Nd(H_2O)MoO_4]_2$[1,5-NDS]

A study of the crystallisation of $[Nd(H_2O)MoO_4]_2$[1,5-NDS] using *in-situ* EDXRD measurements gave interesting results. When substituting Lanthanum for Neodymium in this system it has been found that the formation of the product occurs via a different pathway. The three-dimensional stack plot of the EDXRD data is shown in Figure 12, with an acquisition time of each spectra of 60 s at a diffraction angle of 1.19 °2θ and a reaction temperature of 165 °C. The stack plot shows the presence of an intermediate phase which forms as soon as the reaction commences. This intermediate is found to be present within the reaction media for 21 min, before fully transforming into the final required phase. The intermediate is seen at 51.8 keV with a d-spacing of 11.53 Å.

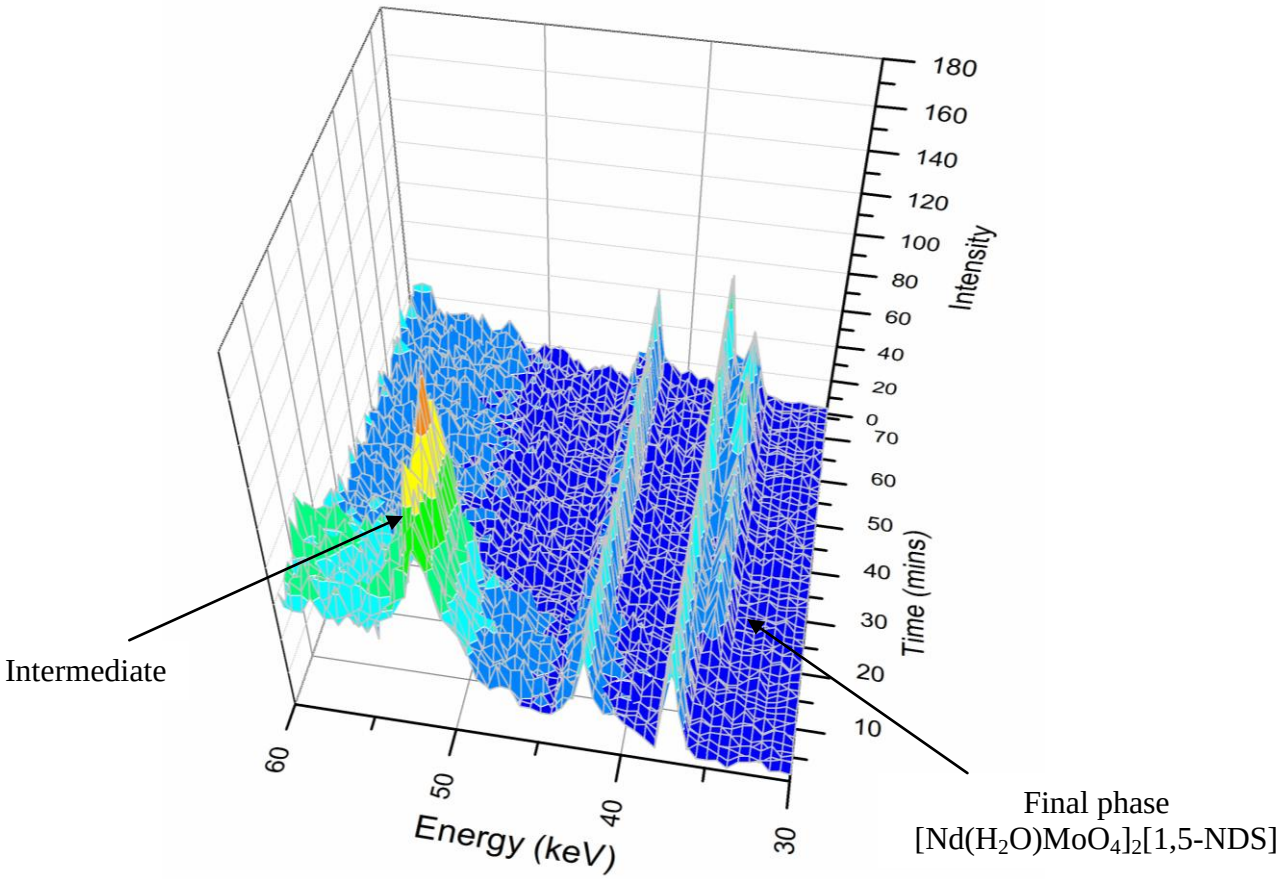

Figure 12 Three-dimensional stacked plot of the time resolved *in-situ* energy dispersive X-ray diffraction data of the formation of $[Nd(H_2O)MoO_4]_2$[1,5-NDS] at 165 °C. An acquisition time of 60 s was used for each recorded spectrum and a detector angle of 1.19 ° 2θ.

The *in-situ* product is found to form rapidly after 17 min. *Ex-situ* synthesis of this phase was performed for 14h, whereas when observing the reactions *in-situ* it was found that the formation of the required phase occurred on a much shorter time scale. Following workup of the reaction it was found that less crystalline products were produced, therefore it may be deduced that the crystallinity of a sample may increase upon increasing the reaction time. Neodymium resonances $K\alpha_1$ and $K\alpha_2$ were observed at 37.3 and 36.9 keV and the Kβ resonance at 42.3 keV. These resonances were observed alongside the product Bragg reflections, having constant intensity throughout the synthesis, indicating that a constant amount of the sample was maintained within the X-ray beam. The product $[Nd(H_2O)MoO_4]_2$[1,5-NDS] is observed at 35.6 keV with a d-spacing of 16.7 Å which is equivalent to that seen in

ex-situ PXRD measurements, Figure 13. The Nd Kα resonances are found to overlap slightly with the product resonance in this synthesis.

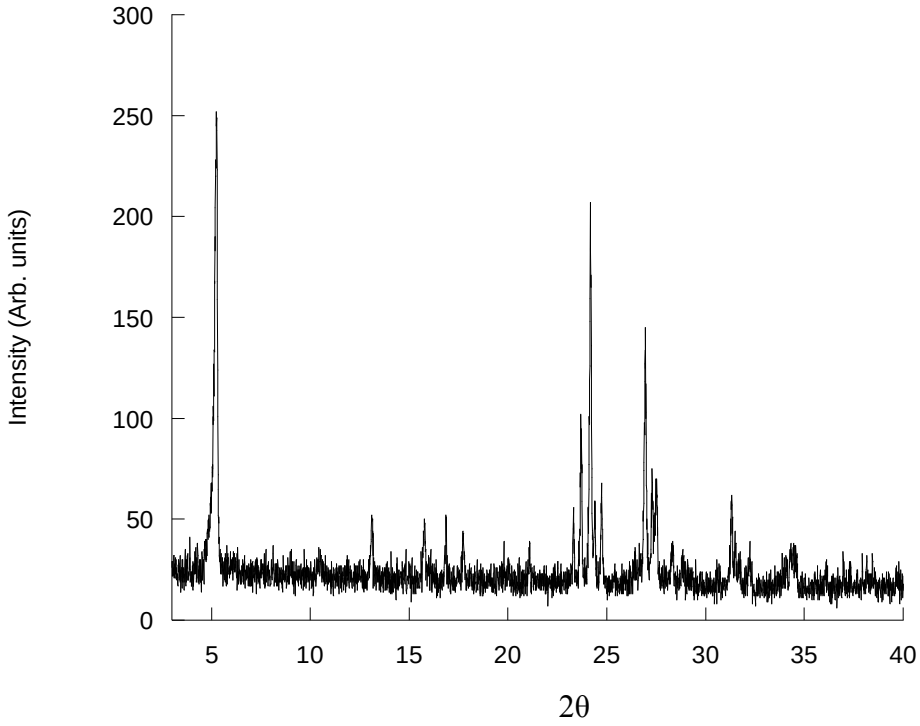

Figure 13 Powder X-ray diffraction pattern (Cu K_α radiation) of $[Nd(H_2O)MoO_4]_2$[1,5-NDS] post *in-situ* synthesis.

The extent of reaction (α) versus time plot of the formation of $[Nd(H_2O)MoO_4]_2$[1,5-NDS] at 165 °C is shown in Figure 14. It is observed that the induction time of the reaction is around 19 minutes, with the formation of the final phase proceeding for approximately 80 minutes, until the reaction was deemed complete.

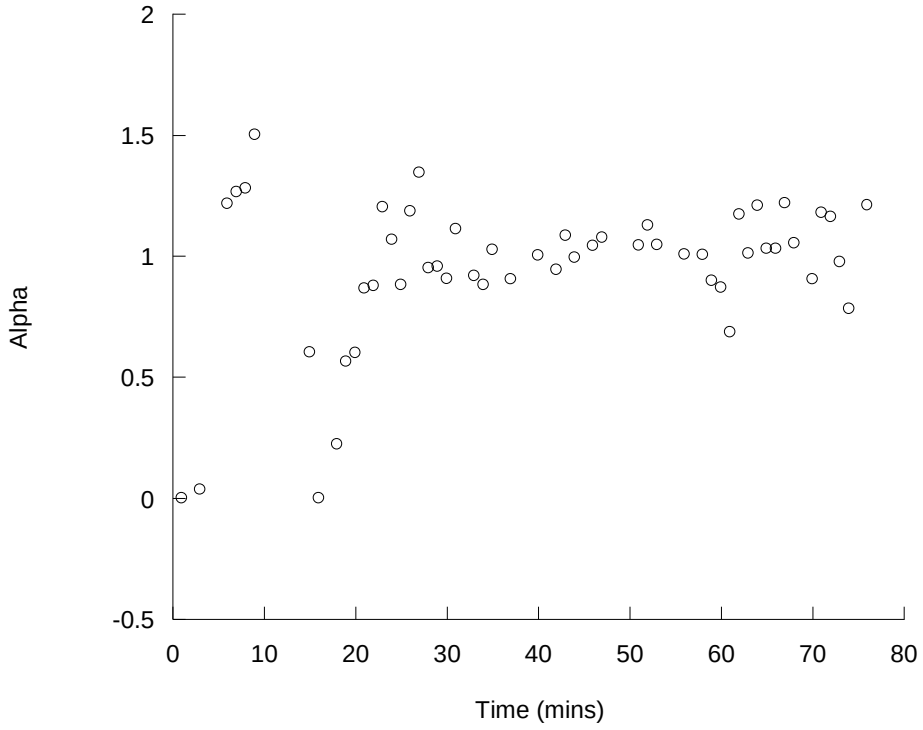

Figure 14 Plot of extent of reaction α versus time of the formation of $[Nd(H_2O)MoO_4]_2[1,5\text{-NDS}]$.

Due to the overlap of the product Bragg reflection and the Nd resonance it has proved difficult to integrate the data without the inclusion of the Neodymium Kα resonance, therefore some anomalous results occurred, such as those observed between 2 – 10 minutes, and have largely been omitted from the extent of reaction plot, and therefore in the calculation of the Avrami exponent and rate constant.

Table 3 Kinetic parameters obtained from the Sharp-Hancock analysis

Phase	Induction time (min)	Exponent (n)	k/ s^{-1}
$[Nd(H_2O)MoO_4]_2[1,5\text{-NDS}]$	19	0.38	2.55×10^{-2}
$[La(H_2O)MoO_4]_2[1,5\text{-NDS}]$	3	0.51	3.65×10^{-3}
$[Nd(H_2O)MoO_4]_2[2,6\text{-NDS}]$	15	0.28	5.16×10^{-3}

The Sharp-Hancock plot, shown in Figure 15, allows the determination of the value of the exponent. The exponent has been determined to have a value of 0.38, which most likely corresponds to a diffusion controlled (*m*) one-dimensional mechanism with a deceleratory nucleation rate, the Sharp-Hancock plot also concludes that the reaction mechanism obeys the Avrami-Erofe'ev solid state rate equation, due to the straight lined Sharp-Hancock plot produced, which also suggests that the reaction proceeds via a consistent mechanism. The rate constant was calculated to be 2.55 x 10^{-2} s^{-1} which is comparable to other *in-situ* syntheses such as those found in the crystallisation of a lanthanide phosphonobutanesulfonate, $Sm(O_3PC_4H_8SO_3)(H_2O)$, with the reaction performed under microwave heating at 150 °C, with a rate constant calculated to be 1.26 x 10^{-2} s^{-1}.[24]

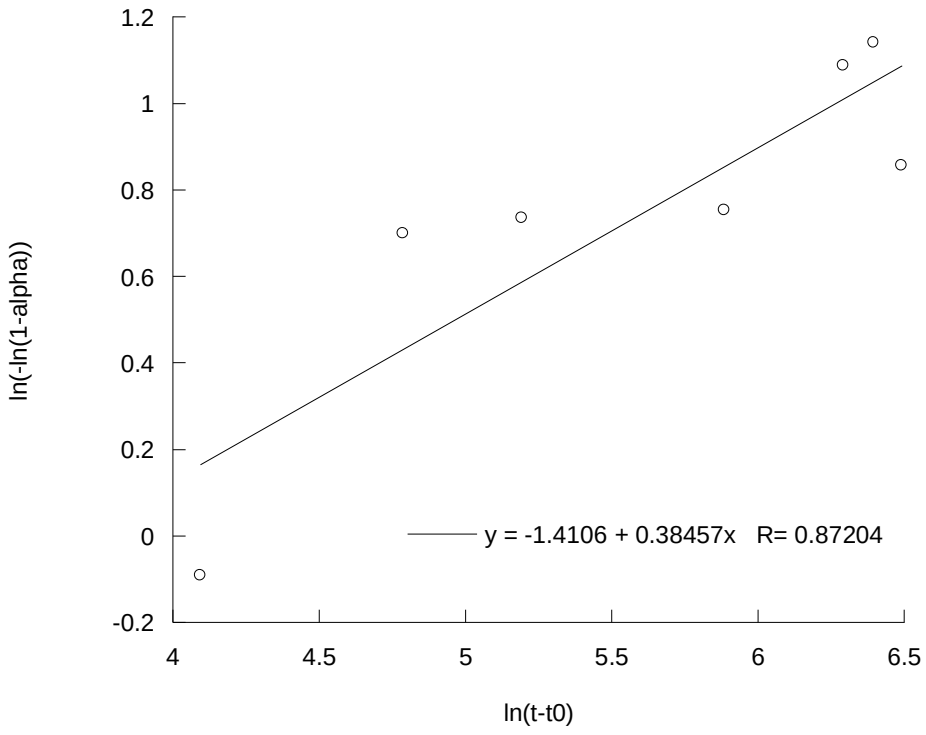

Figure 15 Sharp-Hancock plot of ln(-ln(1-α)) versus ln(t-t_0) for the formation of $[Nd(H_2O)MoO_4]_2$[1,5-NDS] at 165 °C.

4.6.1.3 Isolation and Characterisation of the Intermediate

In-situ EDXRD measurements led to the discovery of an intermediate in the formation of $[Nd(H_2O)MoO_4]_2$[1,5-NDS]. The intermediate was isolated from the reaction mixture by quenching a repeated reaction after 11 min, by submersing the autoclave into water to stop any further reaction, when the intermediate was observed. The PXRD pattern is shown in Figure 16, showing the intermediate to have a d-spacing of 11.57 Å. No further investigations were possible to determine the structure of this phase, due to the low crystallinity of the sample.

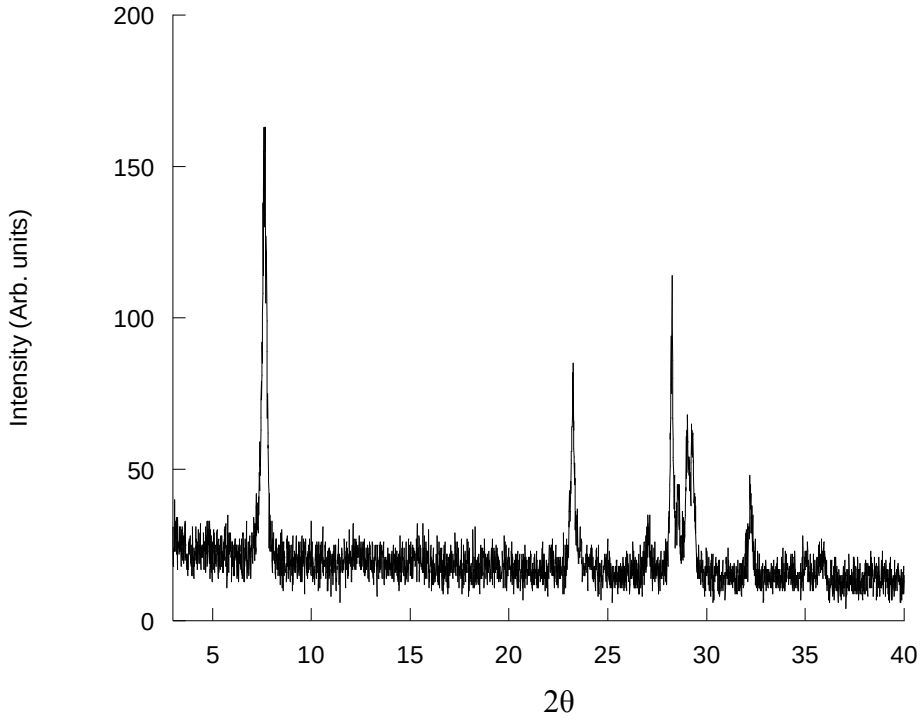

Figure 16 Powder X-ray diffraction pattern (Cu K_α radiation) of the intermediate observed in the *in-situ* synthesis of $[Nd(H_2O)MoO_4]_2$[1,5-NDS] at 165 °C.

A range of characterisation techniques were performed on this intermediate. Elemental analysis results gave 0.55 % C and 0.88 % H. This elemental analysis shows very little carbon to be present which may suggest that the intermediate phase is purely inorganic, although the low amount of carbon may be present from the adsorption of the sulfonate anions. The TGA trace is shown in Figure 17, showing two distinct mass losses. The proposed formula for the intermediate is

$(Nd_2(MoO_4)_3)(H_2O)_8$ therefore the first observed mass loss of 7.4 % below 150 °C most likely corresponds to dehydration of the material, with a loss of four water molecules to give $(Nd_2(MoO_4)_3)(H_2O)_4$ (calc – 7.9 %), and the second mass loss of 8.0 % below 250 °C corresponds to the dehydration of a further four water molecules to give an end product of $Nd_2(MoO_4)_3$ (calc – 7.9 %), giving a total mass loss of 15.4 % (calc – 15.8 %).

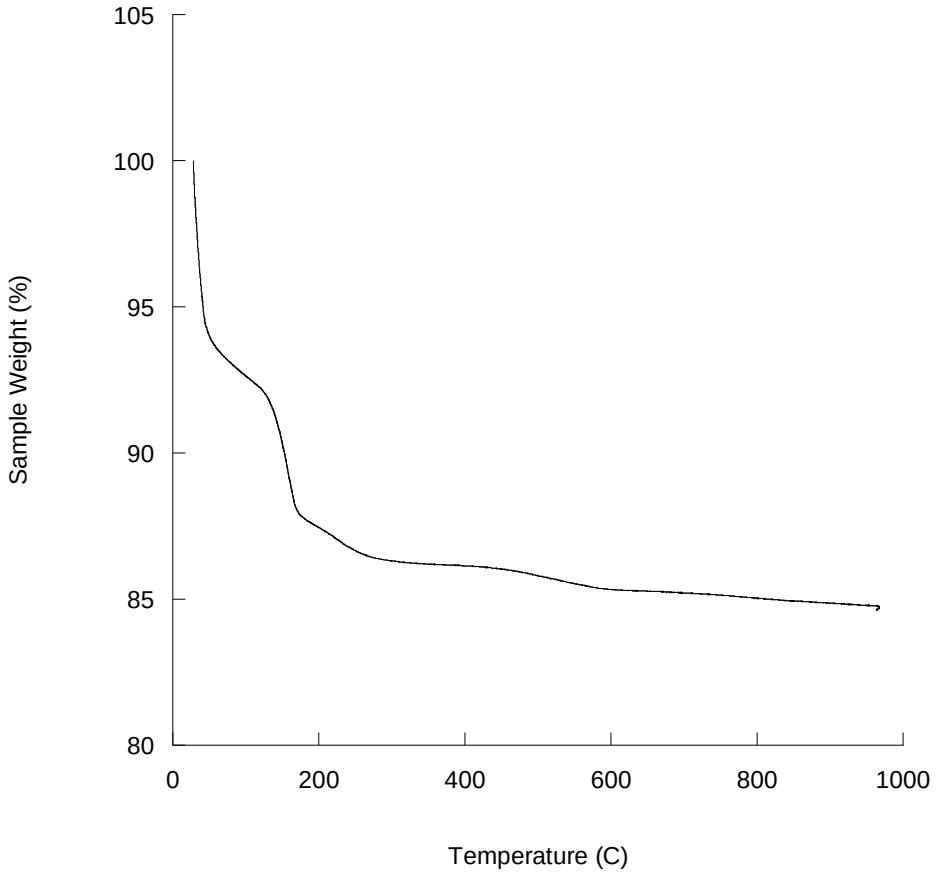

Figure 17 TGA trace of the intermediate discovered during the synthesis of $[Nd(H_2O)MoO_4]_2$[1,5-NDS] at 165 °C.

The FTIR spectrum is shown in Figure 18 and has bands due to an O-H stretch at approximately 3323 cm^{-1} and the bending mode of water at 1628 cm^{-1}. The molybdate stretching frequency is observed at 749cm^{-1}. Comparing this FTIR spectra to that of the final phase of $[Nd(H_2O)MoO_4]_2$[1,5-NDS] it is noted that the water bands are broader, suggesting a higher water content is present in the intermediate.

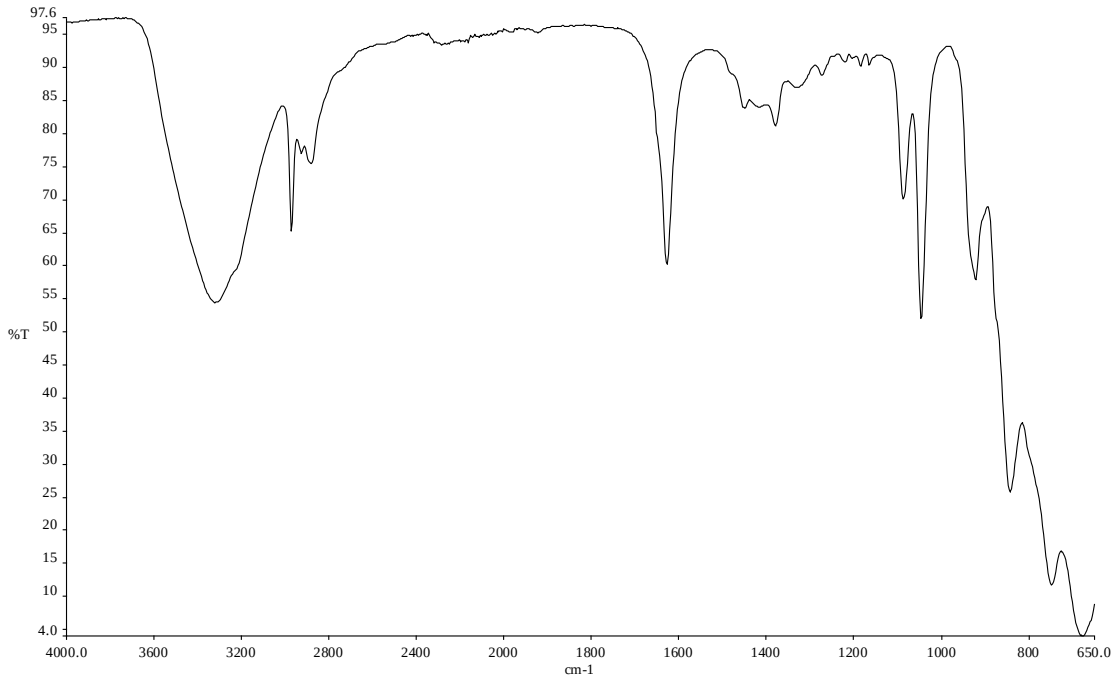

Figure 18 FTIR spectra of the intermediate discovered during the synthesis of $[Nd(H_2O)MoO_4]_2$[1,5-NDS].

After discovering the formation of the intermediate using *in-situ* measurements it was found that the isolated phase found in the synthesis of $[Nd(H_2O)MoO_4]_2$[1,5-NDS] could be obtained *ex-situ* by stirring the reaction media, containing all starting reagents, in air at room temperature for approximately 5 minutes. PXRD measurements, Figure 19, were able to determine that the same phase had indeed formed, albeit less crystalline than the *in-situ* intermediate, due to the reaction being performed at room temperature and not at 165 °C.

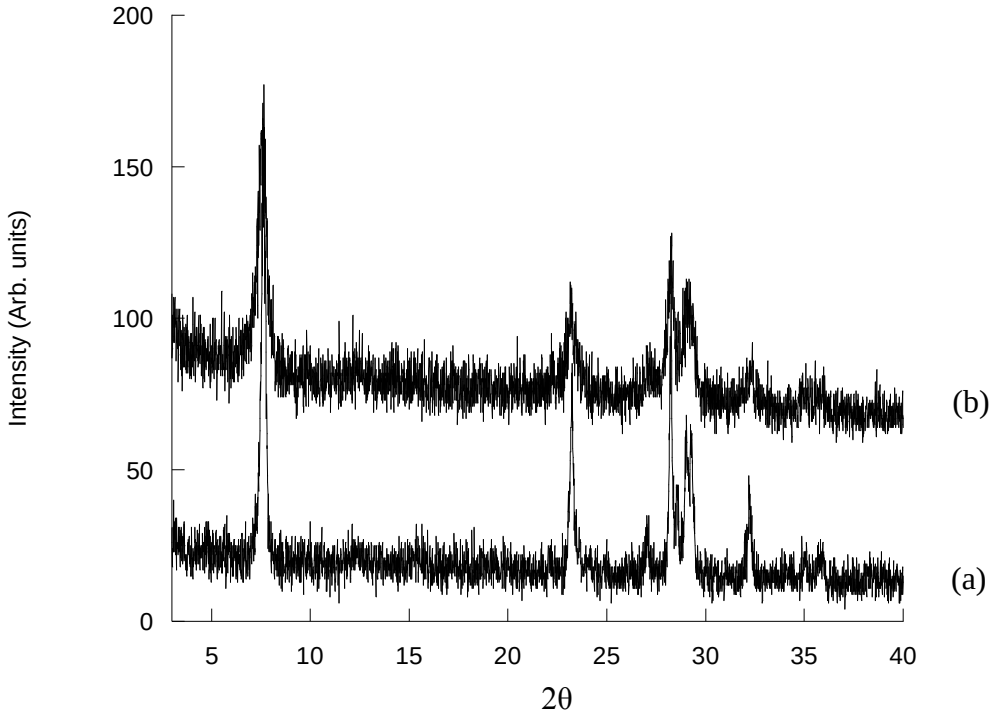

Figure 19 Powder X-ray diffraction patterns (Cu K_α radiation) of (a) the intermediate synthesised *in-situ* and (b) synthesised *ex-situ*.

It is also noted that this intermediate is observed in the synthesis of $[Nd(H_2O)MoO_4]_2$[2,6-NDS], which is further evidence to suggest that the intermediate phase is purely inorganic, but not seen when using other lanthanides such as Lanthanum, see section 4.6.1.1. This may be due to when incorporating a larger lanthanide into the synthesis the induction time for the formation of the product becomes significantly shorter, therefore the intermediate may not form or an amorphous intermediate may form at the very beginning of the synthesis and convert quickly into the required phase and therefore would not be observed using XRD techniques.

4.6.1.4 Formation of $[Nd(H_2O)MoO_4]_2$[2,6-NDS]

The formation of $[Nd(H_2O)MoO_4]_2$[2,6-NDS] is found to occur via the same pathway as the 1,5-NDS analogue, where an intermediate is initially formed which then converts into the final phase. The three-dimensional stack plot of EDXRD

measurements for the formation of $[Nd(H_2O)MoO_4]_2$[2,6-NDS] is shown in Figure 20.

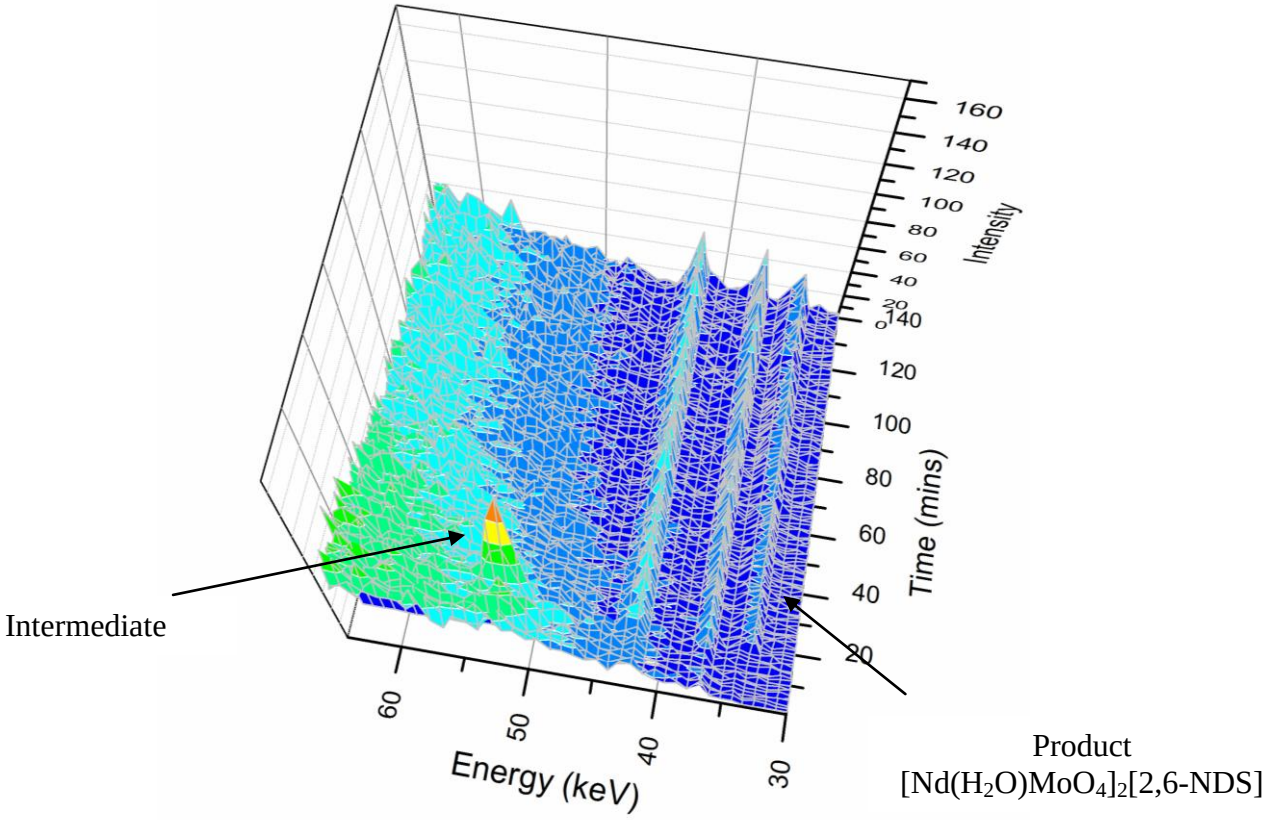

Figure 20 Three-dimensional stacked plot of the time resolved *in-situ* energy dispersive X-ray diffraction data of the formation of $[Nd(H_2O)MoO_4]_2$[2,6-NDS] at 165 °C. An acquisition time of 60 s was used for each recorded spectrum and a detector angle of 1.19 ° 2θ.

The intermediate phase is found to form after 3 minutes converting into the desired phase after 17 minutes. The required phase has an induction time of 16 minutes, and reaches maximum intensity after 46 minutes. The intermediate Bragg peak is observed at 51.8 keV corresponding to an interlayer separation of 11.5 Å, which is found to be identical to the intermediate seen in $[Nd(H_2O)MoO_4]_2$[1,5-NDS]. The final, expected phase, Bragg peak is observed at 33.8 keV corresponding to an interlayer separation of 17.6 Å, which is found to be consistent with *ex-situ* results. Neodymium $K\alpha_1$ and $K\alpha_2$ resonances are also observed at 37.3 and 36.9 keV and the $K\beta$ resonance at 42.3 keV.

Extent of reaction and the Sharp-Hancock plots for the formation of this phase are found in Appendix C, and the Avrami exponent and rate constant are shown in Table 3. The rate constant for the formation of this phase is calculated to be 5.06 $x10^{-3}$ s^{-1}, showing the reaction to proceed in a slower manner than that of the 1,5-NDS phase, calculated rate constant is 2.55 $x10^{-2}$ s^{-1}.

4.6.2 *In-situ* EDXRD Study of the formation of $[La(H_2O)WO_4]_2[A]$ (A = 1,5 or 2,6-naphthalenedisulfonate)

4.6.2.1 Kinetic Analysis of the formation of $[La(H_2O)WO_4]_2$[1,5-NDS]

Kinetic data was obtained for the formation of $[La(H_2O)WO_4]_2$[1,5-NDS] by performing the reaction over five temperatures at 120, 145, 165, 180 and 200 °C. This allowed the quantitative determination of the rate constants, exponent (to infer the mechanism of formation) at each temperature and the Arrhenius activation energy. The three-dimensional stack plot of the *in-situ* EDXRD measurements of the synthesis at 120 °C is shown in Figure 21. Data for the remainder of the reaction temperatures is found within Appendix C. As the reaction performed at 120°C is found to be the slowest, this will be the data discussed for the monitoring of the reaction kinetics, and also as it provides interesting results compared to that of the higher temperature syntheses.

The three-dimensional EDXRD plot, shows the product to start to form after 30 minutes, where a weak Bragg reflection is observed at 35.3 keV, corresponding to initial nucleation, with a d-spacing of 17.0 Å (observed for all temperatures), after 80 minutes it is noted that the intensity of this Bragg reflection increases to its maximum value remaining constant until 100 minutes where the reaction is deemed complete. No intermediate is observed in the formation of this phase which is consistent with the earlier reported $[La(H_2O)MoO_4]_2$[1,5-NDS] phase. Lanthanum $K\alpha_1$ and $K\alpha_2$ resonances are also observed at 33.4 and 33.0 keV and the $K\beta$

resonance at 37.8 keV. Tungsten $K\alpha_1$ and $K\alpha_2$ resonances are observed at 59.3 and 57.9 keV.

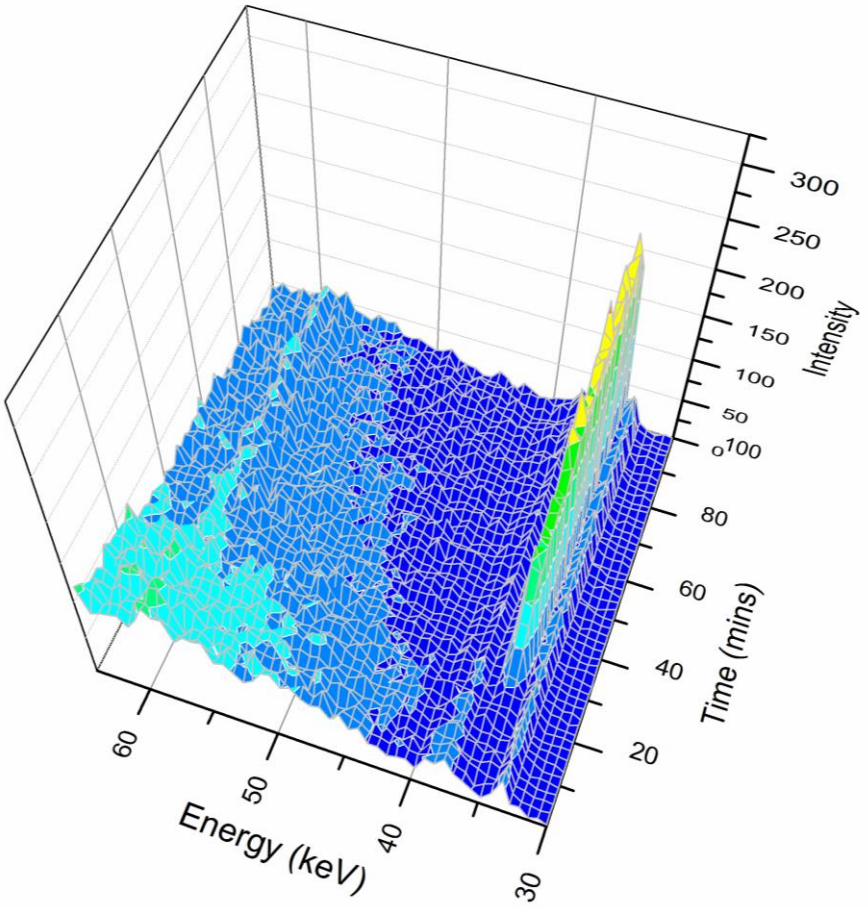

Figure 21 Three-dimensional stacked plot of the time resolved *in-situ* Energy dispersive X-ray diffraction measurements for the formation of $[La(H_2O)WO_4]_2$[1,5-NDS] at 120 °C. An acquisition time of 60s was used for each recorded spectrum and a detector angle of 1.19 ° 2θ.

The extent of reaction (α) versus time plot of the reactions at different temperatures is shown in Figure 22. It is observed that the induction time of the reaction ranged from 9 - 19 minutes, decreasing with increasing reaction temperature. The reaction time was found to increase on decreasing the reaction temperature, ranging from 40 - 100 minutes until the reaction was deemed complete. It may be noted that the *ex-situ* synthesis for the formation of $[La(H_2O)WO_4]_2$[1,5-NDS] occurs over 14h, therefore it may not be completely necessary to perform the reactions on this time scale. Crystallisation of this phase is found to occur rapidly at higher temperatures, with the

crystalline product forming fully after ca. 20 minutes at reaction temperatures of 165 – 200 °C, with total reaction times of 40 - 70 minutes (200 – 165 °C).

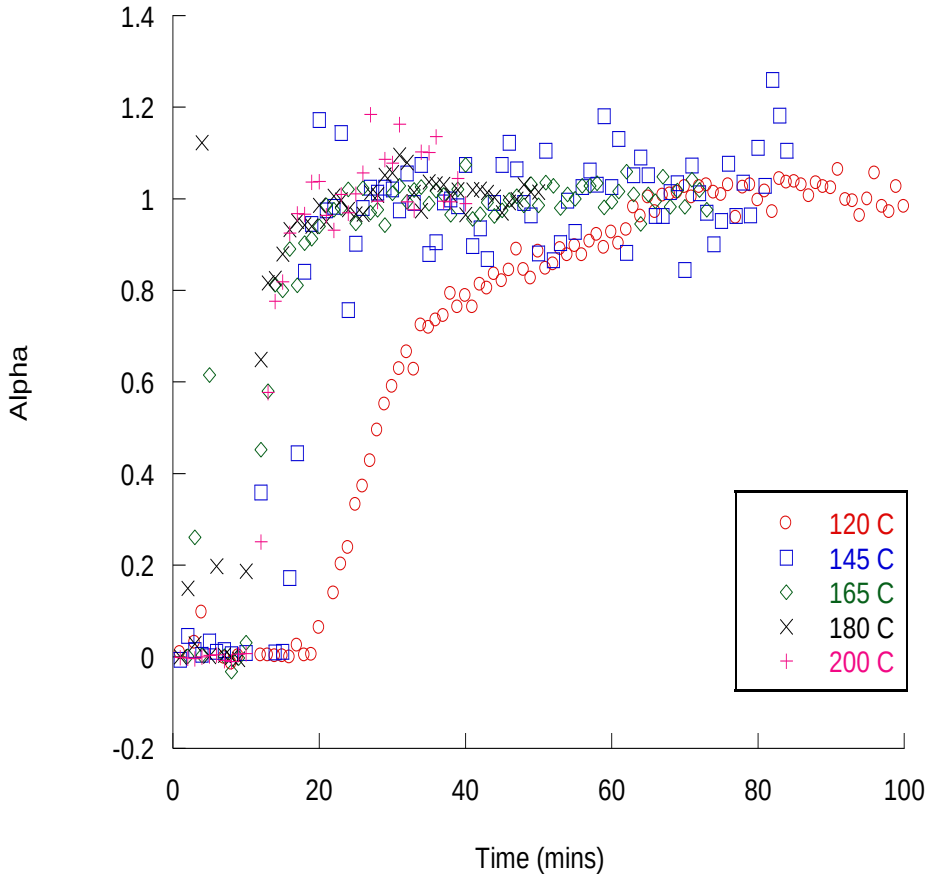

Figure 22 Plot of the extent of the reaction (α) versus time of the formation of $[La(H_2O)WO_4]_2$[1,5-NDS] over a range of temperatures from 120 - 200 °C.

PXRD measurements of the final phase, synthesised under *in-situ* conditions, showed the formation of a crystalline phase as shown in Figure 23, which is consistent with the *ex-situ* product, although it has been identified that when these reaction are performed *ex-situ,* for 14h, the crystal size of the material increases, therefore suggesting that longer reaction times may be needed for the production of larger crystals for structure determination.

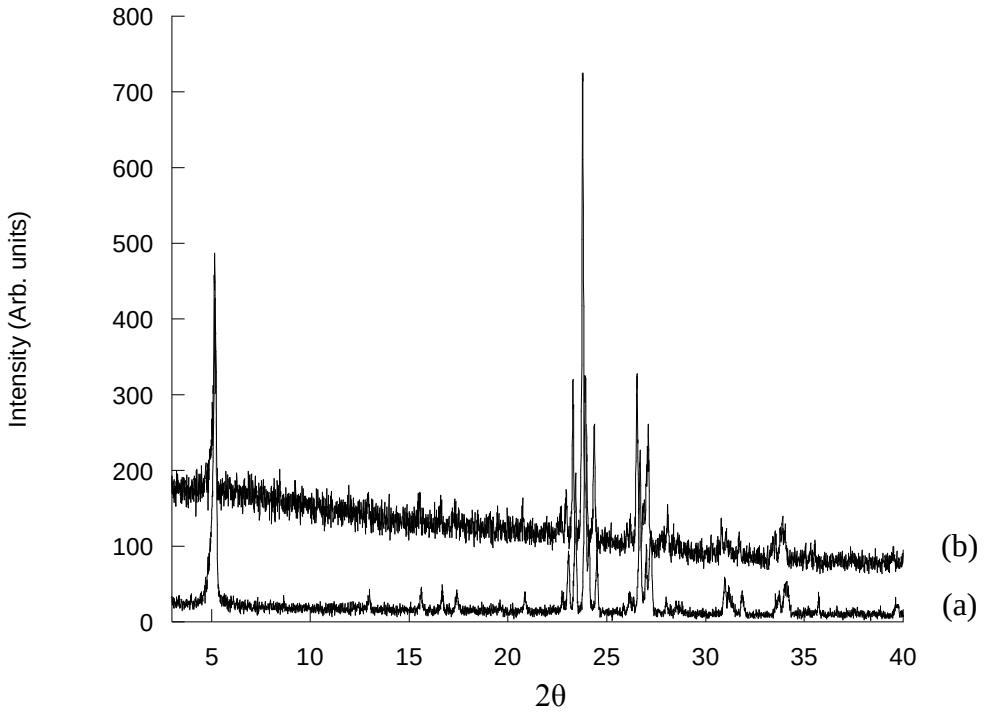

Figure 23 Powder X-ray diffraction patterns (Cu K_α radiation) of $[La(H_2O)WO_4]_2$[1,5-NDS] (a) synthesised *in-situ* at 165 °C and (b) synthesised *ex-situ* at 165 °C.

Kinetic parameters obtained from the variable temperature reactions are found in Table 4. The value of the exponent determined is in the range of 1 – 1.8, corresponding to a diffusion controlled (*m*) two-dimensional process with a deceleratory nucleation rate. The Sharp-Hancock plots, shown in Figure 24, also conclude that the reaction mechanisms obey the Avrami-Erofe'ev solid state kinetic rate equation, due to the linearity of each plot produced. Reactions of 145°C and above are found to proceed via a consistent mechanism, see Appendix C for data corresponding to each temperature.

Plots of extent of reaction, α, versus reduced time are able to prove that the reaction, at different temperatures, proceeds via a consistent mechanism. Extent of reaction is plotted against reduced time, $t/t_{1/2}$, where t is reaction time and $t_{1/2}$ is the half-life of the reaction. All reduced time plots of the formation of $[La(H_2O)WO_4]_2$[1,5-NDS] are found to be super imposable at different temperatures up to $\alpha = 0.7$, therefore it may be inferred that they proceed via the same mechanism up to this point, as shown in Figure 25, with the mechanism being independent of reaction temperature. After

the point of α = 0.7 the reaction mechanism for temperatures 145 – 200 °C are still found to be consistent, although the mechanism at 120 °C is shown to differ compared to the higher temperature syntheses, this phenomenon will be discussed further in this section.

Table 4 Kinetic parameters obtained from the Sharp-Hancock analysis

Temperature (°C)	Induction time (min)	Exponent (n)	$k/10^{-3}$ s^{-1}
120	19	Overall 0.97	Overall 1.07
		Mechanism 1- 1.15	Mechanism 1- 1.24
		Mechanism 2- 0.71	Mechanism 2- 1.33
145	15	1.51	6.13
165	10	0.97	5.30
180	9	1.09	5.22
200	10	1.76	4.66

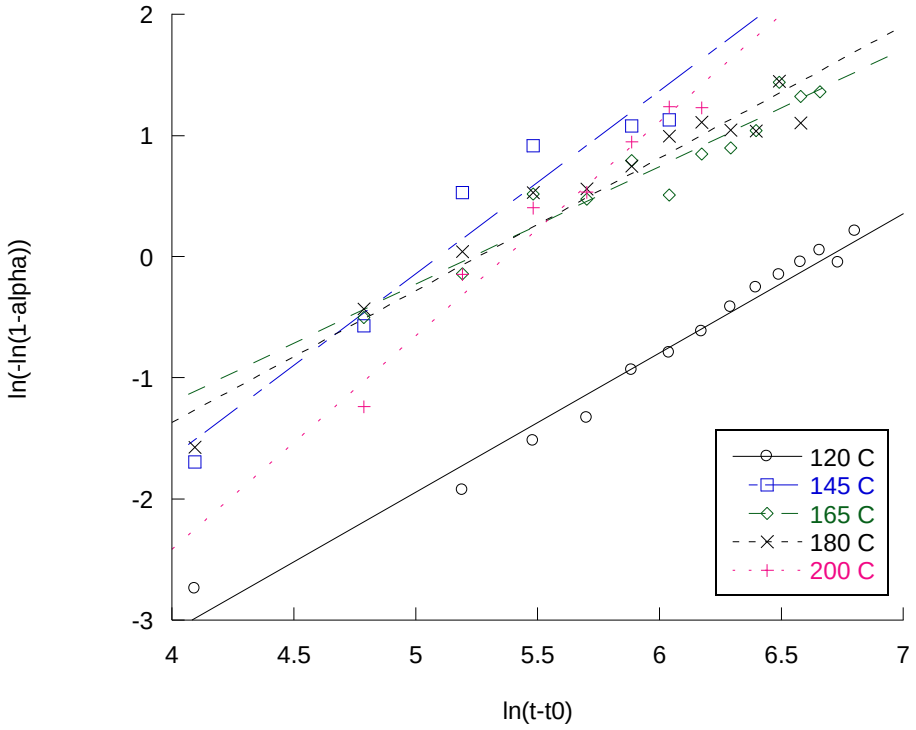

Figure 24 Sharp-Hancock plot of ln(-ln(1-α)) versus ln(t-t_0) of the formation of [La(H_2O)WO_4]$_2$[1,5-NDS] at reaction temperatures of 120 – 200 °C. (145 – 200 °C; α range 0.15 - 0.98, 120 °C partial data; α range 0.14 - 0.72)

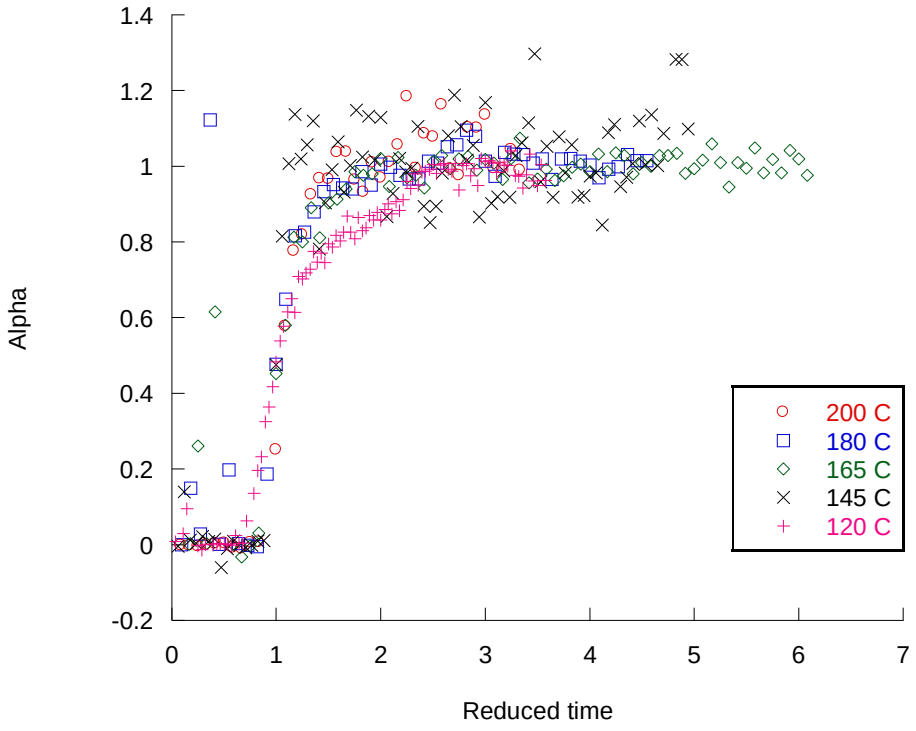

Figure 25 Reduced time plot of the formation of [La(H_2O)WO_4]$_2$[1,5-NDS] at reaction temperatures of 120 - 200°C.

The rate constants were extracted for each temperature, and were found to lie in the range of 1.1 – 4.7 x 10^{-3} s^{-1} (120 – 200 °C). Reaction temperatures above 120 °C are found to have similar rates of crystallisation, therefore reaction temperature does not make too much difference to the rate of crystallisation. Although on the other hand it is noted that the rate constants do not follow a general trend with respect to the reaction temperature, as the rate constants are found to decrease with increasing reaction temperature. This phenomenon has also been observed by Francis *et al*[4] whereby the rate constants observed were found to be non-reproducible and also decrease on increasing reaction temperature, for the formation of a gallophosphate ULM-5. Extracted rate constants for this formation lie in the range of 18.0 – 5.7 x 10^{-3} s^{-1} depending on the reaction temperature (140 – 180 °C). This group suggested that this observation may occur due to the reaction mechanism being diffusion controlled whereby the rate of crystallisation is determined by how quickly reacting species are transported to the growth centres. Therefore the rate of crystallisation may primarily depend on how vigorously the reaction media is being mechanically stirred, rather than the inherent rate of diffusion under static conditions. Overall it is proposed that the differences in the reaction rate may reflect small differences in the stirring rate used in each of the syntheses.[4] One may therefore suggest that the rate constants calculated for the formation of $[La(H_2O)WO_4]_2$[1,5-NDS] may have been effected by the stirring rate of the reaction media. The rate constants determined for the formation of $[La(H_2O)WO_4]_2$[1,5-NDS] are found to correlate well with those determined for other hydrothermal syntheses such as the formation of zeolite A, where rate constants lie in the range of 1.64 – 5.34 x 10^{-4} s^{-1} (80 – 120 °C).[3]

From the measurements undertaken at the various temperatures it has been observed that at a reaction temperature of 120 °C the Sharp-Hancock plot suggests the formation of $[La(H_2O)WO_4]_2$[1,5-NDS] to occur via a two step mechanism, as a true linear line is not observed, Figure 26. Due to these variances the Sharp-Hancock plot was divided into two separate plots Figure 27 & 28. Determination of the exponent was achieved for both plots showing that this reaction proceeded via two different mechanisms. For the first mechanism, the exponent was calculated at 1.15 which corresponds to a two-dimensional diffusion controlled mechanism (*m*) with a deceleratory nucleation rate, as seen in the higher temperature reactions, whereas the second mechanism *m* = 0.7, suggests the mechanism is one-dimensional diffusion

controlled (*m*) with a deceleratory nucleation rate. This may suggest that the mechanism of formation first starts with the formation of the layers. The 1,5-NDS anions may then approach the layers to form the phase in the third dimension, and therefore the second mechanism is one-dimensional. This conclusion is hypothetical as one does not see the two step process in the higher temperature syntheses, maybe due to the reaction occurring faster, therefore deeming it harder to extrapolate the kinetics and see the presence of the two mechanisms. Other explanations may be that the mechanisms may have merged together at higher temperatures or perhaps, more simply, the reaction mechanism changes on an increase of reaction temperature.

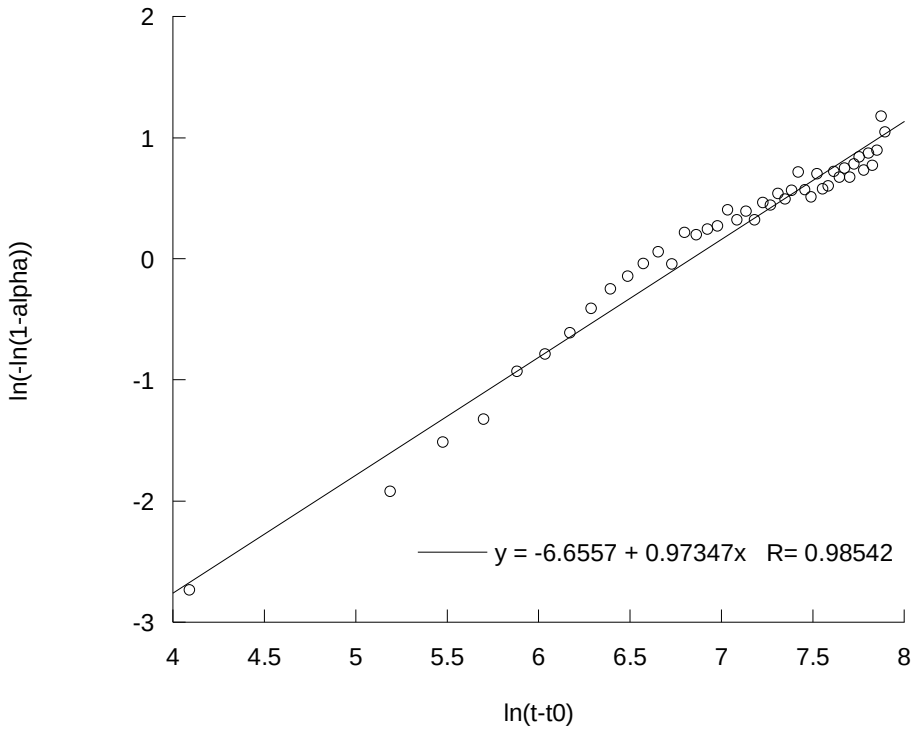

Figure 26 Sharp-Hancock plot of ln(-ln(1-α)) versus ln(t-t_0) for the formation of $[La(H_2O)WO_4]_2$[1,5-NDS] at 120 °C (Both mechanisms).

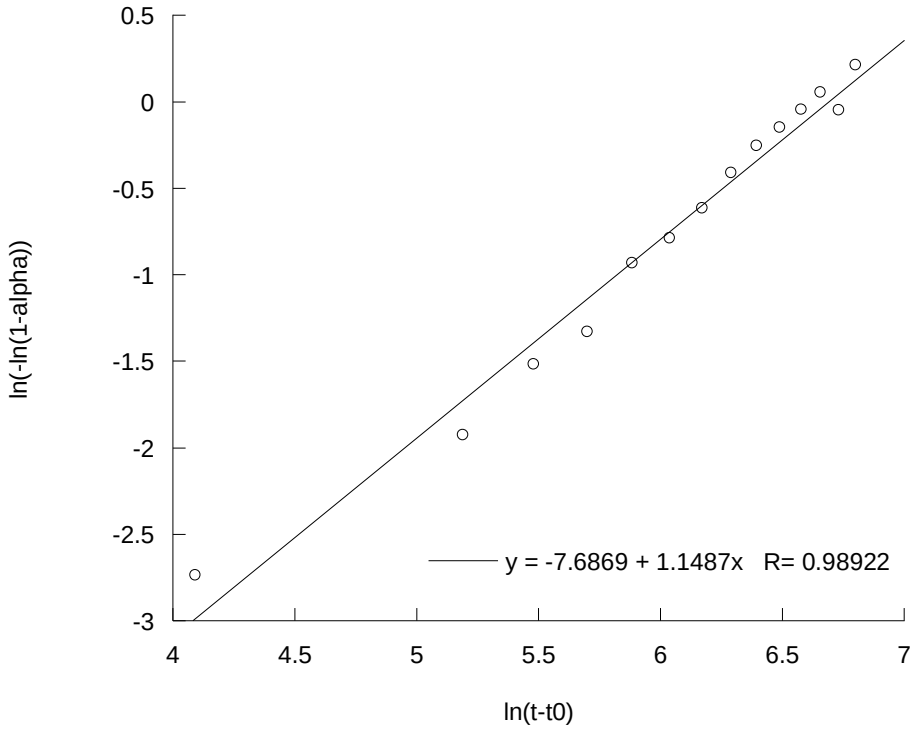

Figure 27 Sharp-Hancock plot of ln(-ln(1-α)) versus ln(t-t_0) for the formation of $[La(H_2O)WO_4]_2$[1,5-NDS] at 120 °C. (First mechanism)

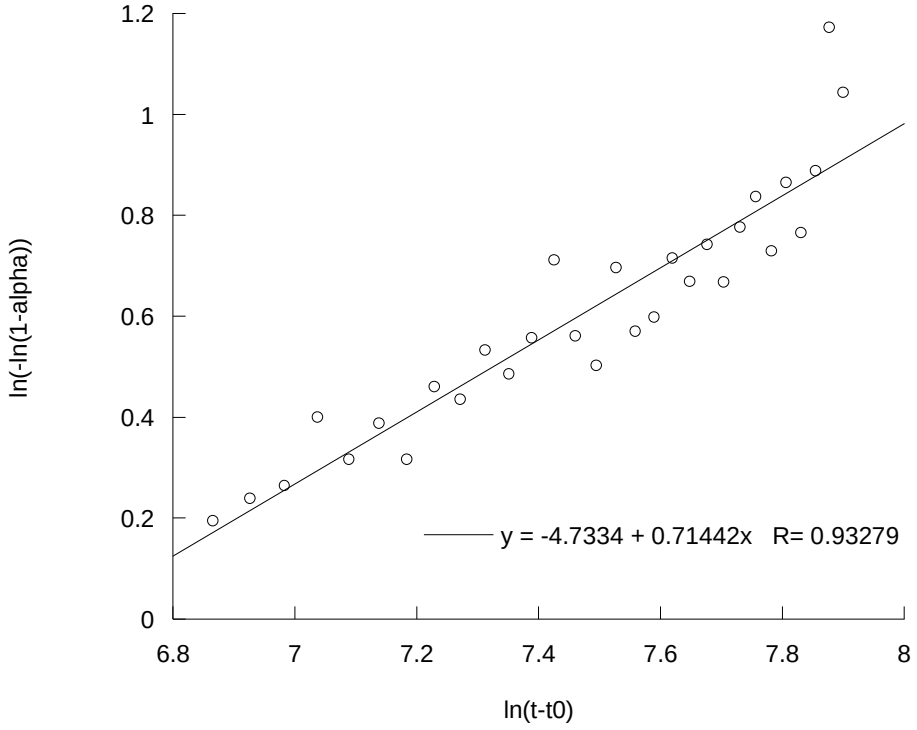

Figure 28 Sharp-Hancock plot of ln(-ln(1-α)) versus ln(t-t_0) for the formation of $[La(H_2O)WO_4]_2$[1,5-NDS] at 120 °C. (Second mechanism)

The activation energy for the formation of $[La(H_2O)WO_4]_2[1,5\text{-NDS}]$ was calculated from the rate constants obtained at different temperatures using the Arrhenius equation;

$$k = Ae^{\frac{-Ea}{RT}}$$

Equation 9

A plot of ln*k* versus 1/T, Figure 29, gave a calculated activation energy of +22 kJ mol^{-1}. This value is comparable to other kinetic studies such as the formation of a lanthanide phosphonosulfonate under microwave heating conditions, discussed in Section 3.2, having an activation energy of +34 kJ mol^{-1}, [24] and the hydrothermal reaction of the formation of a layered manganese thioantimonate with an activation energy of +53 kJ mol^{-1}.[21] (Note: the value of *k* for mechanism 1 of the 120°C reaction was used in the calculation of E_a.)

To note an anomaly is observed in the Arrhenius plot at the reaction temperature of 145 °C, this may be due the reaction proceeding in a much faster manner compared to that of the other temperatures which could be accounted for by the stirring issues mentioned above.

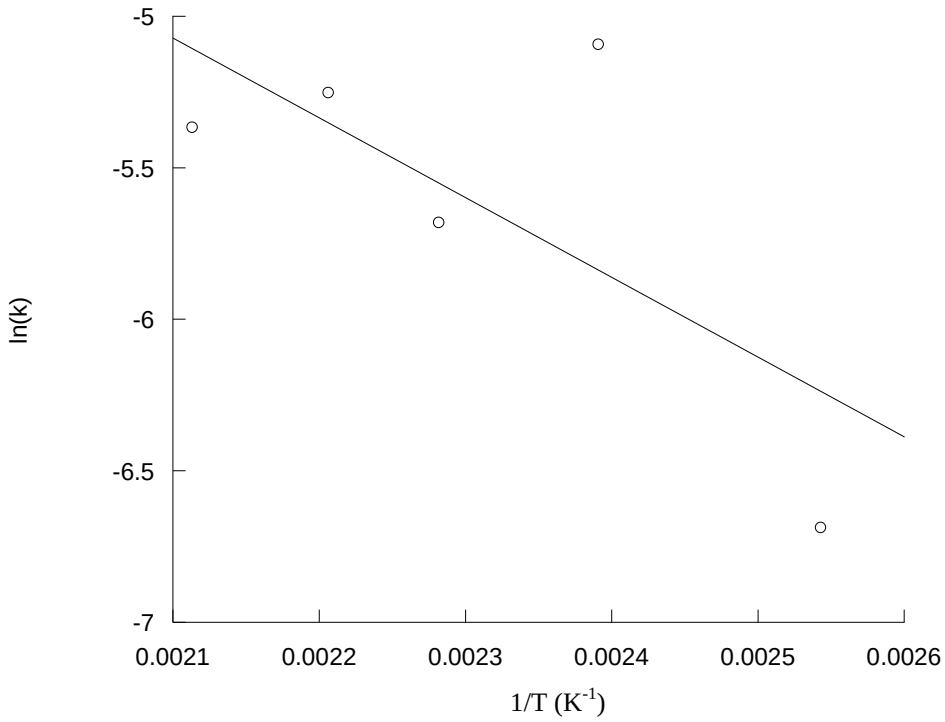

Figure 29 Arrhenius plot of ln(*k*) versus 1/T (K^{-1}) for the formation of $[La(H_2O)WO_4]_2$[1,5-NDS] at reaction temperatures of 120-200 °C.

4.6.2.2 Formation of $[La(H_2O)WO_4]_2$[2,6-NDS]

The synthesis of $[La(H_2O)WO_4]_2$[2,6-NDS] was studied using the *in-situ* EDXRD technique. It has been determined from *ex-situ* studies that this phase is biphasic, with the second phase having a dimer incorporated into the inorganic layer, with an elemental composition of $[La(H_2O)_2W_2O_8]$[2,6-NDS] (See Chapter two, Section 2.2.5, for more details of this phase). Unfortunately *in-situ* EDXRD measurements were not able to show the formation of the two phases as the dimerised phase did not form under the short reaction time used, longer reaction times were not achieved, due to time constraints, and may be necessary for the formation of $[La(H_2O)_2W_2O_8]$[2,6-NDS]. The main phase formed is that of $[La(H_2O)WO_4]_2$[2,6-NDS], as expected which is observed at 32.1 keV with an interlayer separation of 17.8 Å. The three-dimensional stack plot of the formation of this phase is shown in Figure 30, with additional data provided in Appendix C. In the formation of this phase an intermediate is seen at 48.2 keV with an interlayer separation of 11.9 Å, this

intermediate appears as the measurements commence after one minute, with the reflection disappearing after 3 minutes. Lanthanum $K\alpha_1$ and $K\alpha_2$ resonances are observed at 33.4 and 33.0 keV and the $K\beta$ resonance at 37.8 keV. Tungsten $K\alpha_1$ and $K\alpha_2$ resonances are observed at 59.3 and 57.9 keV. The intermediate observed may be iso-structural to the intermediate seen in the formation of $[Nd(H_2O)MoO_4]_2$[1,5-NDS] and $[Nd(H_2O)MoO_4]_2$[2,6-NDS] as it corresponds to a similar interlayer separation, although no quench procedure was undertaken for this synthesis.

The induction time for this phase is 8 minutes, with the reaction deemed complete after 41 minutes. PXRD measurements have confirmed that the phase synthesised *in-situ* is identical to the phase synthesised *ex-situ*, as shown in Figure 31.

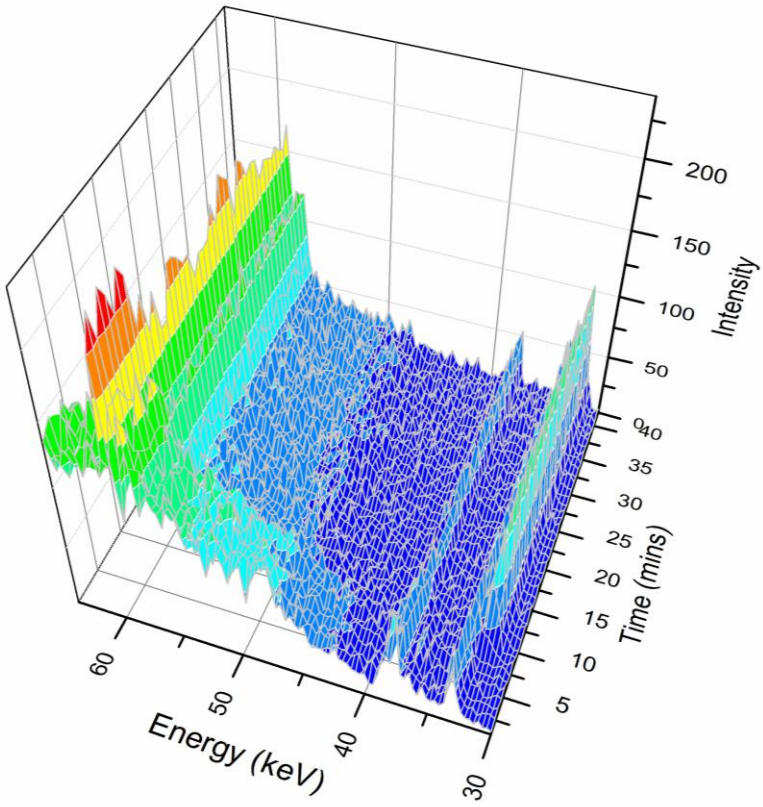

Figure 30 Three-dimensional stacked plot of the time resolved *in-situ* energy dispersive X-ray diffraction data of the formation of $[La(H_2O)WO_4]_2$[2,6-NDS] at 165 °C. An acquisition time of 60s was used for each recorded spectrum and a detector angle of 1.24 ° 2θ.

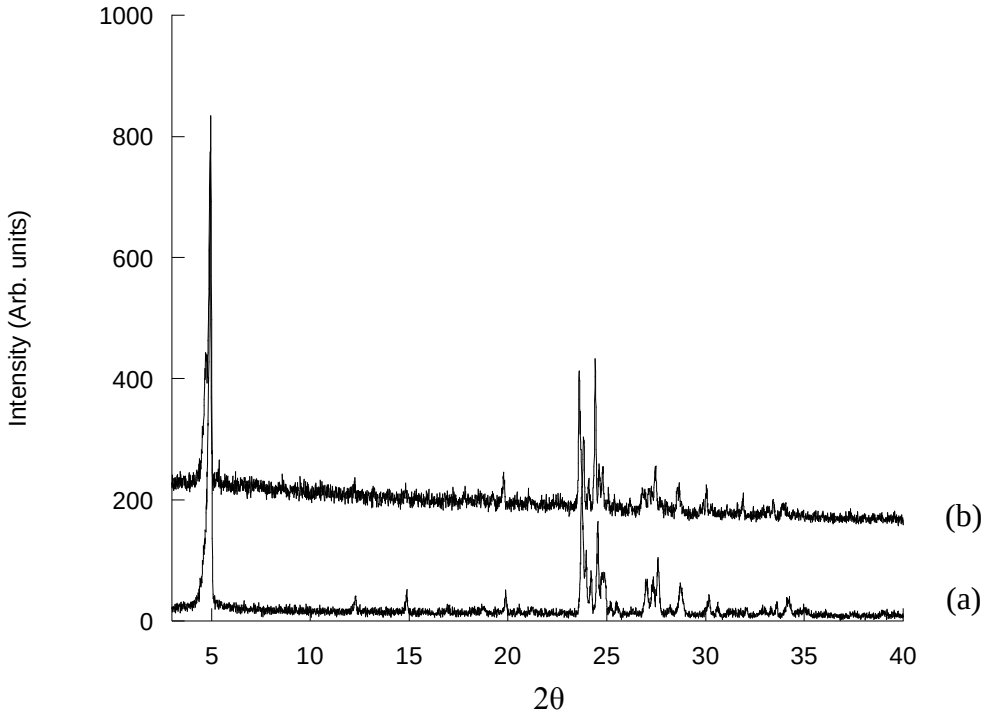

Figure 31 Powder X-ray diffraction patterns (Cu K_α radiation) of $[La(H_2O)WO_4]_2[2,6\text{-NDS}]$ (a) synthesised *in-situ* at 165 °C and (b) synthesised *ex-situ* at 165 °C.

4.6.3 *In-situ* EDXRD study of the phase transformation of $[Yb(H_2O)_2][C_2H_2O_5P]$(1) to $[Yb][C_2H_2O_5P]$(2)

The phase transformation, via dehydration, of $[Yb(H_2O)_2][C_2H_2O_5P]$ (**1**) to $[Yb][C_2H_2O_5P]$ (**2**) was studied using the *in-situ* energy dispersive X-ray diffraction technique. The three-dimensional stack plot of EDXRD measurements of this phase transformation at a reaction temperature of 220 °C is shown in Figure 32. Phases **1** at 48.3 keV and **2** at 49.3 keV are observed separately when performing the reaction at 220 °C, along with the Ytterbium $K\alpha_1$ and $K\alpha_2$ resonances at 52.4 and 51.3 keV and the $K\beta$ resonance at 59.4 keV.

The observation of two different phases has previously been discovered in *ex-situ* syntheses. When performing the reaction at 200 °C the hydrated compound $[Yb(H_2O)_2][C_2H_2O_5P]$ (**1**) is observed, whereas if the reaction temperature is

increased to 220 °C the de-hydrated [Yb][$C_2H_2O_5P$] (**2**) is observed. *Ex-situ* reactions run for 14h and details of **1** and **2** are found in Chapter 3.

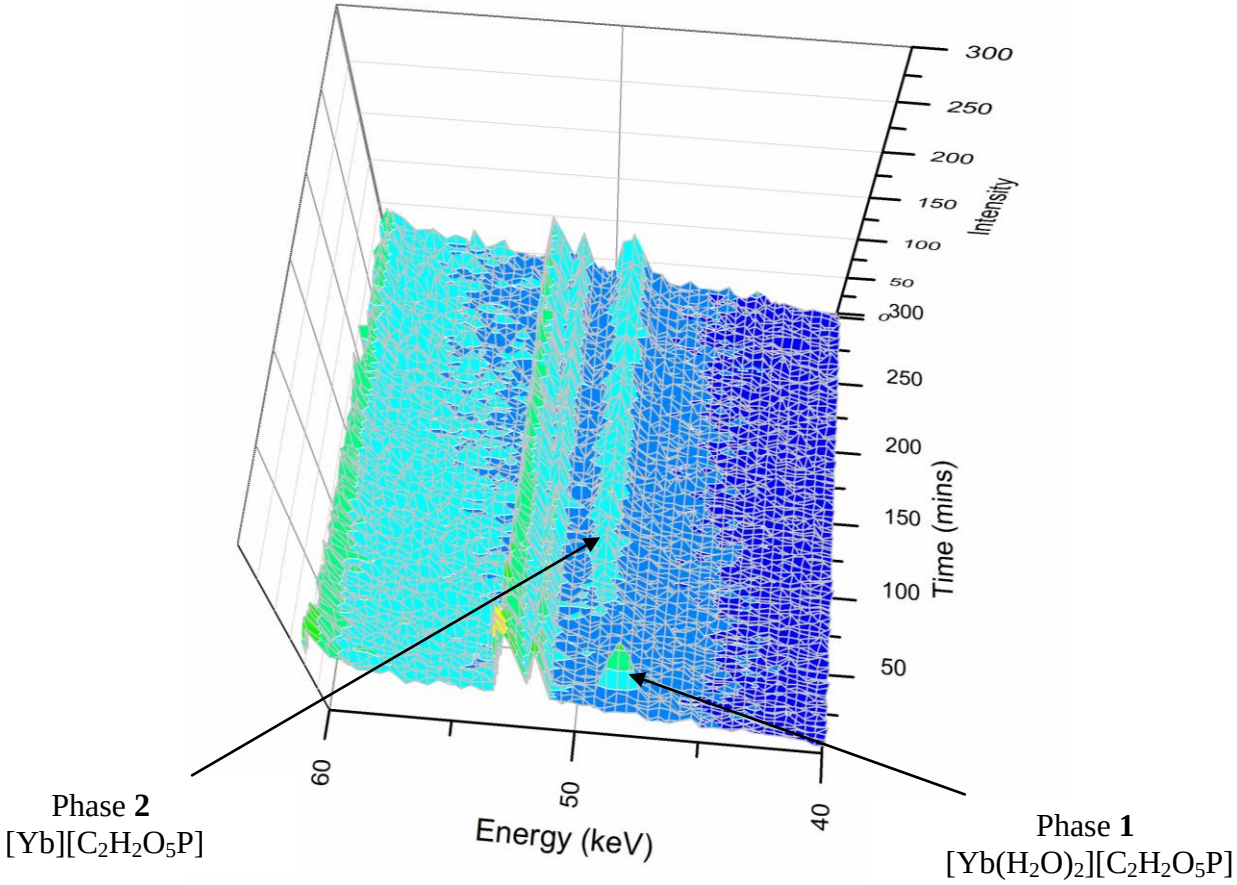

Figure 32 Three-dimensional stacked plot of the time resolved *in-situ* energy dispersive X-ray diffraction data of the transformation of [Yb(H_2O)$_2$][$C_2H_2O_5P$] to [Yb][$C_2H_2O_5P$] at 220 °C. An acquisition time of 60s was used for each recorded spectrum and a detector angle of 2.29 ° 2θ.

Phase **1** is observed at 48.3 keV with a d-spacing of 6.42 Å, and has an induction time of 9 minutes with the associated Bragg reflection reaching maximum intensity after 10 minutes and disappearing after 25 minutes, therefore suggesting that **1** is short lived within this synthesis. **2** is observed at 49.3 keV with a d-spacing of 6.29 Å, having an induction time of 53 minutes with its Bragg reflection reaching maximum intensity after 114 minutes. *In-situ* measurements show that the peak corresponding to **1** disappear and re-appear as phase **2**. The position of the Bragg reflections corresponding to phases **1** and **2** is found to change due to a decrease in

lattice parameters upon dehydration. This decrease in parameters leads to a smaller d-spacing, therefore an increase in the energy associated with the Bragg reflection of the dehydrated phase. Due to the low intensity of the Bragg reflections associated with each phase it is found to be difficult to integrate the Bragg reflections associated with **1** and **2** well. This has led to some data points becoming anomalous due to the integration not fitting the reflections perfectly, therefore these points have been omitted from the data analysis.

1 was successfully isolated by an *in-situ* quench procedure as discussed in Chapter 6, Section 6.3.2. PXRD patterns of phases **1** and **2**, produced via the *in-situ* method, are shown in Figure 33. Phase **1** was isolated from the reaction mixture by quenching the reaction after 6 min, when the Bragg reflection corresponding to **1** was observed. The PXRD pattern is shown in Figure 34, showing the intermediate to have a d-spacing of 6.42 Å, where it is compared to the phase produced *ex-situ*, showing both phases to be identical.

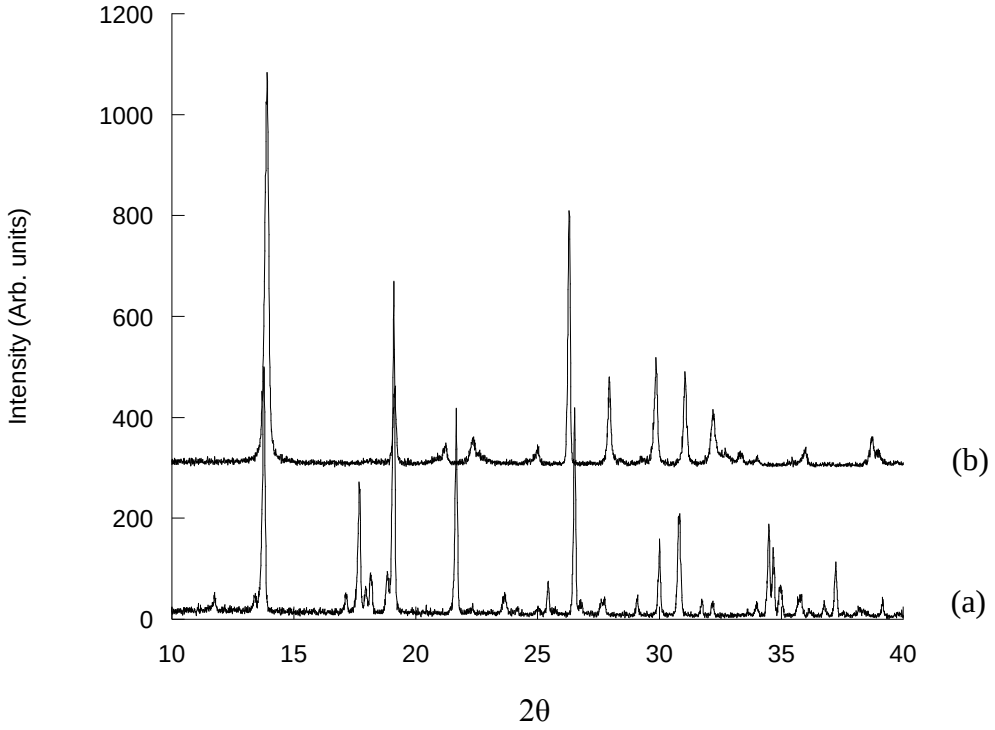

Figure 33 PXRD patterns (Cu K_α radiation) post *in-situ* synthesis of (a) $[Yb(H_2O)_2][C_2H_2O_5P]$ and (b) $[Yb][C_2H_2O_5P]$ at 220 °C.

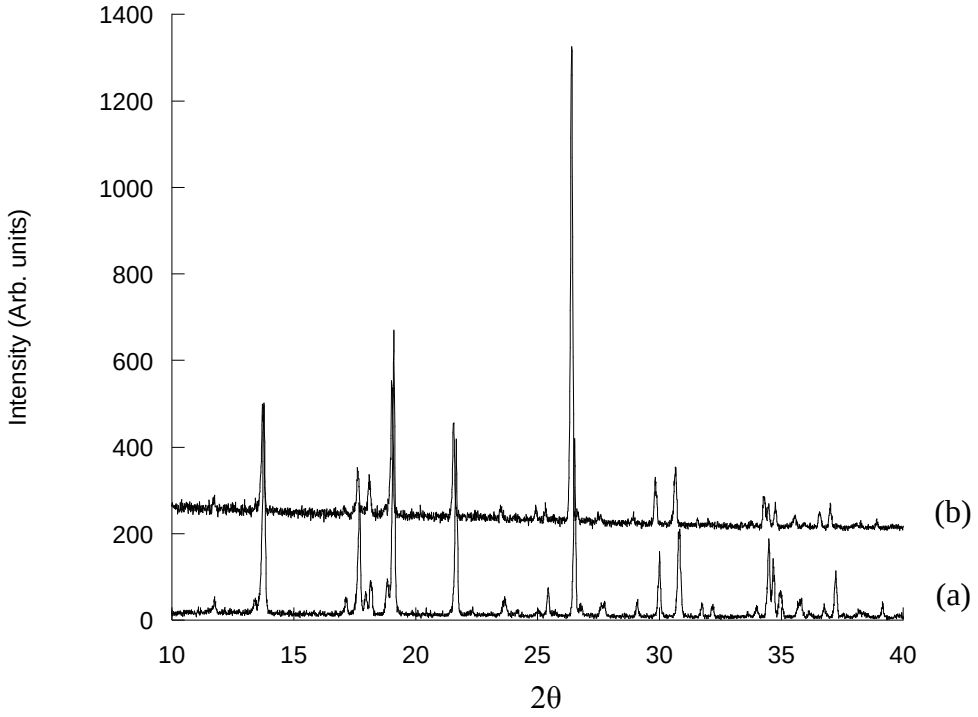

Figure 34 PXRD patterns (Cu K_α radiation) of (a) *in-situ* synthesis $[Yb(H_2O)_2][C_2H_2O_5P]$ at 220 °C and (b) *ex-situ* synthesis of $[Yb(H_2O)_2][C_2H_2O_5P]$ at 200 °C.

The plot of extent of reaction, α, versus time is shown in Figure 35, and shows the formation of phase **2** to have an induction time of 53 minutes, with the reaction deemed complete after 300 minutes.

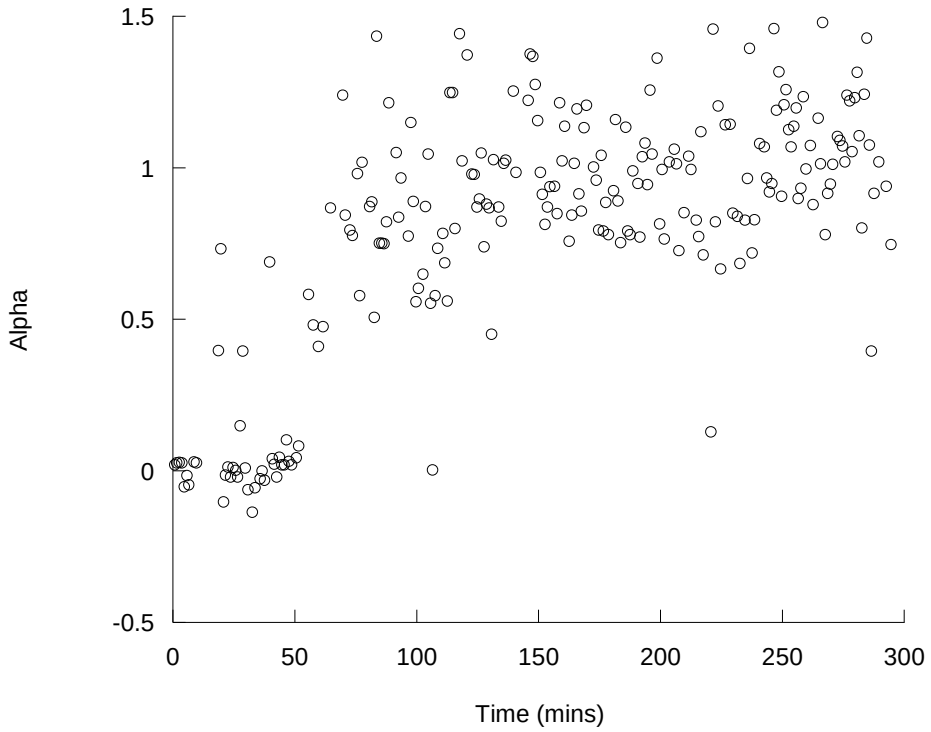

Figure 35 Plot of the extent of the reaction (α) versus time of the formation of [Yb][$C_2H_2O_5P$] at 220 °C.

The Sharp-Hancock plot of ln(-ln(1-α)) versus ln(t-t_0) for the formation of [Yb][$C_2H_2O_5P$] at 220 °C is shown in Figure 36. The value of the exponent has been extrapolated by linear regression giving a value of 1.09 corresponding to a two dimensional, diffusion controlled (m) mechanism with a deceleratory nucleation rate. The line is found to be linear, therefore satisfies the Avrami kinetics.

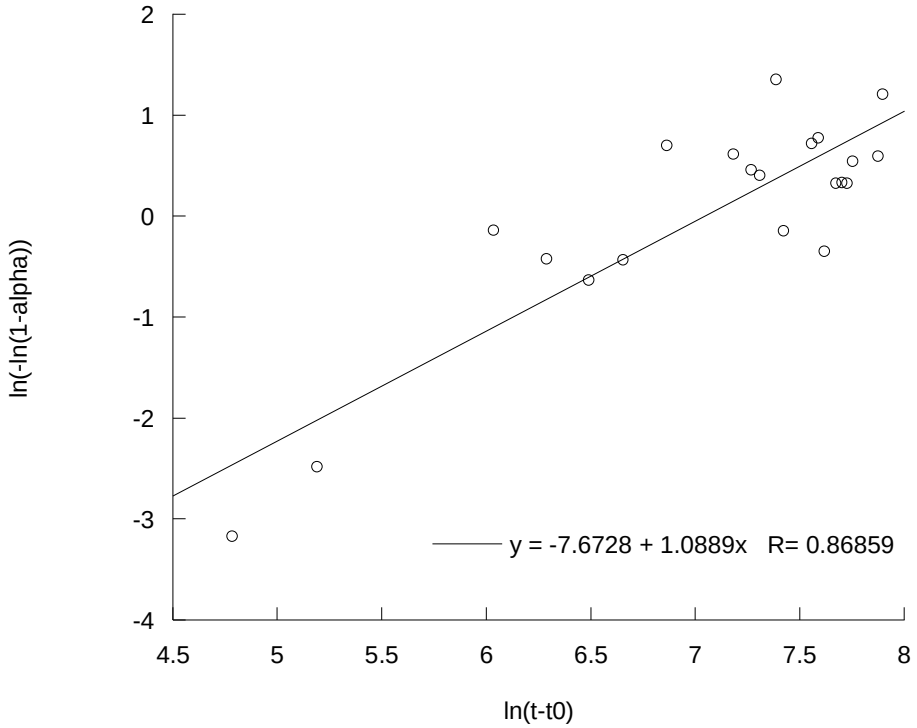

Figure 36 Sharp-Hancock plot of ln(-ln(1-α)) versus ln(t-t_0) of the formation of [Yb][$C_2H_2O_5P$] at 220 °C.

The extent of reaction, α, versus time plot of the formation of phase **1** is shown in Figure 37. This shows the phase has an induction time of 9 minutes with dissolution occurring after 25 minutes. After a further 28 minutes the Bragg reflection corresponding to **2** appears, with a total induction time of 53 minutes, the data suggests that **2** may form via a dissolution and re-precipitation mechanism of **1**. Phase **1** is found to be rather short lived before transforming into phase **2**. As the crystal structures for the two phases have previously been determined, see Chapter 3 for details, we have prior knowledge that the two differ structurally therefore suggesting that dissolution re-precipitation occurs during this transformation, **1** does not just simply dehydrate.

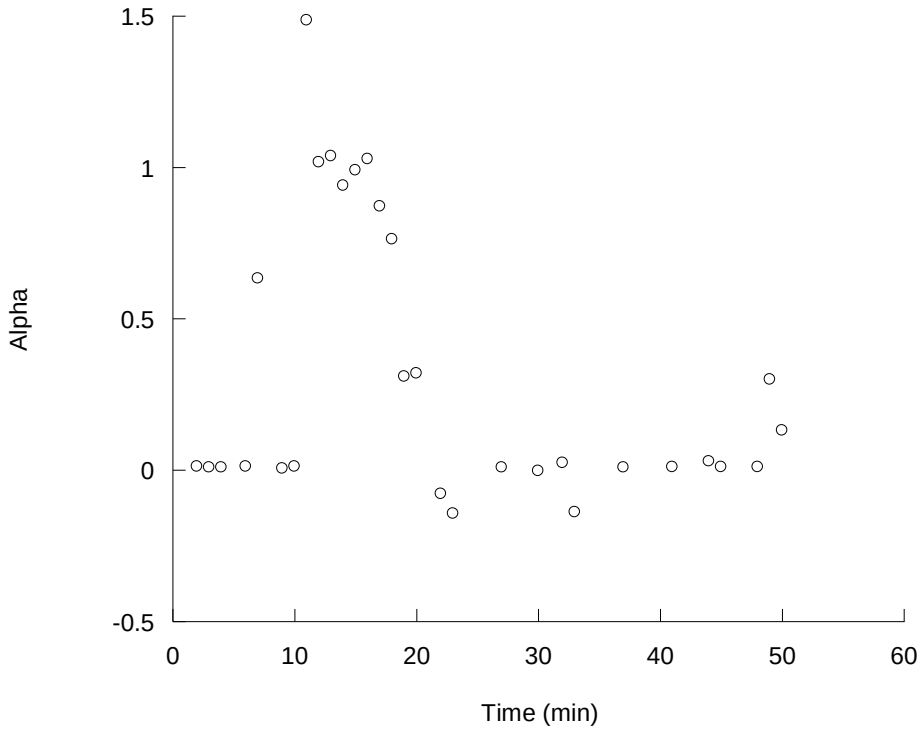

Figure 37 Plot of the extent of the reaction, α, versus time of the formation phase 1 $[Yb(H_2O)_2][C_2H_2O_5P]$ at 220 °C.

The extent of reaction, α, versus time plot is shown in Figure 38, for the phase transformation of **1** into **2**. Following dissolution of **1**, where intensity decreases to zero, formation of **2** commences, with the reaction deemed complete after ca. 180 minutes.

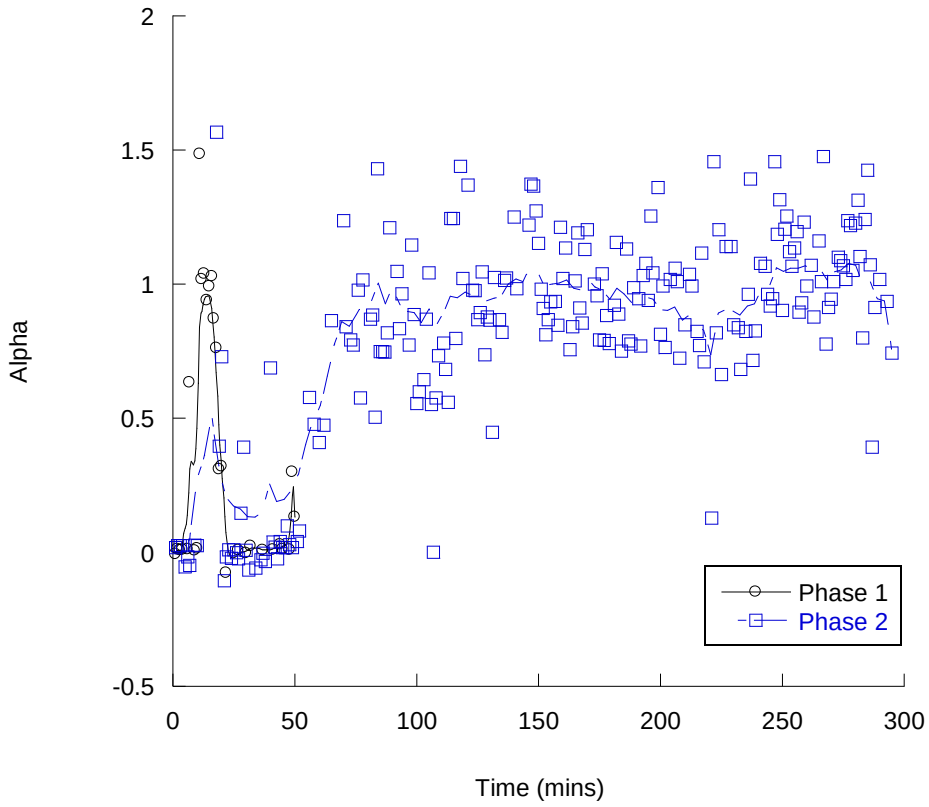

Figure 38 Plot of extent of reaction, α, versus time for the phase transformation of **1** (black) into **2** (blue) at 220 °C.

It should be noted for the formation of **1** very few usable data points were collected therefore a Sharp-Hancock plot would not be accurate or viable enough to determine the rate constant and the exponent.

4.7 Conclusions

In-situ energy dispersive X-ray diffraction measurements have allowed the successful determination of the possible mechanistic details of five phases containing either lanthanides La or Nd, molybdate or tungstate and NDS isomers. Investigations into phases containing Neodymium and molybdate allowed the determination of an intermediate phase observed during the formation of the required phase. Successful isolation of this intermediate was achieved via a quench procedure, although structure determination was not possible due to the low crystallinity of the sample.

The *in-situ* technique also allowed kinetic analysis to be extracted for the formation of $[La(H_2O)_2WO_4][1,5\text{-NDS}]$. Avrami exponents were in the range of 0.97 – 1.76 indicating the reaction mechanism to be a diffusion controlled two dimensional process with a deceleratory nucleation rate. Rate constants were calculated for each reaction temperature giving values in the range of $1.07 – 6.13 \times 10^{-3}$ s^{-1}, which are comparable to those seen for other hydrothermal reactions. The successful determination of the activation energy of +22 $kJmol^{-1}$ was extracted from an Arrhenius plot using the rate constants calculated from repeating the synthesis over a range of temperatures from 120 – 200 °C.

The investigation into the dehydration of $[Yb(H_2O)_2][C_2H_2O_5P]$ to $[Yb][C_2H_2O_5P]$ at 220 °C proved interesting. The successful isolation of $[Yb(H_2O)_2][C_2H_2O_5P]$ was achieved via a quench procedure with this phase being found to be identical to that synthesised *ex-situ* at 200 °C. It was observed from *in-situ* measurements that dehydration of this phase into $[Yb][C_2H_2O_5P]$ occurred via a dissolution/re-precipitation mechanism. The value of the exponent of 1.09 was determined corresponding to a two dimensional, diffusion controlled (*m*) mechanism with a deceleratory nucleation rate. This mechanism is found to be the same mechanism determined for the formation of the La/W/NDS systems.

4.8 References

(1) Giessen, B. C.; Gordon, G. E. *Science* **1968**, *159*, 973.

(2) G.R.Williams; Khan, A. I.; O'Hare, D.; in Layered Double Hydroxides ed.; Springer: Berlin, 2006.

(3) Walton, R. I.; Millange, F.; O'Hare, D.; Davies, A. T.; Sankar, G.; Catlow, C. R. A. *J. Phys. Chem. B* **2001**, *105*, 83.

(4) Francis, R. J.; O'Brien, S.; Fogg, A. M.; Halasyamani, P. S.; O'Hare, D.; Loiseau, T.; Ferey, G. *J. Am. Chem. Soc.* **1999**, *121*, 1002.

(5) Walton, R. I.; Loiseau, T.; Francis, R. J.; O'Hare, D.; Ferey, G. In *Solid-State Chemistry of Inorganic Materials Ii*; Kauzlarich, S. M., McCarron, E. M., Sleight, A. W., zurLoye, H. C., Eds.; Materials Research Society: Warrendale, 1999; Vol. 547.

(6) O'Brien, S.; Francis, R. J.; Fogg, A.; O'Hare, D.; Okazaki, N.; Kuroda, K. *Chem. Mat.* **1999**, *11*, 1822.

(7) Millange, F.; Medina, M. I.; Guillou, N.; Ferey, G.; Golden, K. M.; Walton, R. I. *Angew. Chem.-Int. Edit.* **2010**, *49*, 763.

(8) O'Hare, D.; Evans, J. S. O.; Fogg, A.; O'Brien, S. *Polyhedron* **2000**, *19*, 297.

(9) Evans, J. S. O.; Price, S. J.; Wong, H. V.; O'Hare, D. *J. Am. Chem. Soc.* **1998**, *120*, 10837.

(10) Fogg, A. M.; Dunn, J. S.; O'Hare, D. *Chem. Mat.* **1998**, *10*, 356.

(11) Williams, G. R.; Norquist, A. J.; O'Hare, D. *Chem. Mat.* **2004**, *16*, 975.

(12) DESY, http://hasylab.desy.de/facilities/doris_iii/machine/index_eng.html, accessed in December 2011.

(13) Sharp, J. H.; Brindley, G. W.; Achar, B. N. N. *J. Am. Ceram. Soc.* **1966**, *49*, 379.

(14) Hancock, J. D.; Sharp, J. H. *J. Am. Ceram. Soc.* **1972**, *55*, 74.

(15) Avrami, M. *J. Chem. Phys.* **1939**, *7*, 1103.

(16) Avrami, M. *J. Chem. Phys.* **1940**, *8*, 212.

(17) Avrami, M. *J. Chem. Phys.* **1941**, *9*, 177.

(18) Erofe'ev, B. V. *C. R. Doklady Akademii Nauk Sssr* **1946**, *52*, 511.

(19) Sheridan, A. K.; Anwar, J. *Chem. Mat.* **1996**, *8*, 1042.

(20) McIntyre, L. J.; Prior, T. J.; Fogg, A. M. *Chem. Mat.* **2010**, *22*, 2635.

(21) Engelke, L.; Schaefer, M.; Schur, M.; Bensch, W. *Chem. Mat.* **2001**, *13*, 1383.

(22) Hulbert, S. F. *Journal of the British Cermamic Society* **1969**, *6*, 11.

(23) Carter, R. E. *J. Chem. Phys.* **1961**, *34*, 2010.

(24) Feyand, M.; Nather, C.; Rothkirch, A.; Stock, N. *Inorg. Chem.* **2010**, *49*, 11158.

(25) Pradell, T.; Crespo, D.; Clavaguera, N.; Clavaguera-Mora, M. T. *J. Phys.-Condes. Matter* **1998**, *10*, 3833.

(26) Binner, J. G. P.; Hassine, N. A.; Cross, T. E. *J. Mater. Sci.* **1995**, *30*, 5389.

Chapter 5

Synthesis, Structure and Characterisation of Lanthanide Borates

5.0 Introduction

Materials with extended structures are most commonly based on an anionic framework with the charge being balanced by cations which reside between anionic components. A rare alternative to this concept is materials where the extended structure is cationic with the charge balanced by anions. Materials of this kind have been the subject of a recent review,[1] and include layered double hydroxides,[2] rare-earth hydroxides[3, 4] and structures based on francisite.[5, 6]

The formation of cationic inorganic framework materials is uncommon and only three frameworks of this type are known and all have been recently reported. The first cationic framework is that of an Ytterbium oxyhydroxide phase of composition $Yb_3O(OH)_6Cl.2H_2O$, shown in Figure 1(a). This phase consists of Yb_4O tetrahedra which are linked together by hydroxide anions, with an oxide anion being located within a tetrahedra of Yb cations, forming a three-dimensional framework with one-dimensional channels present in which water and chloride anions reside.[7] This phase is able to undergo successful anion exchange with carbonate, oxalate and succinate and can also be dehydrated without collapse of the structure. The second cationic phase is that of $Yb_4O(OH)_9NO_3$, shown in Figure 1(b) which has a similar framework structure to the above chloride phase. This phase consists of a three-dimensional cationic ytterbium oxyhydroxide framework with one dimensional channels running through the structure in which nitrate anions are located.[8] Anion exchange of the uncoordinated nitrate anions with small anions such as chloride or carbonate was unsuccessful for this material, suggesting that the channels are not readily accessible.

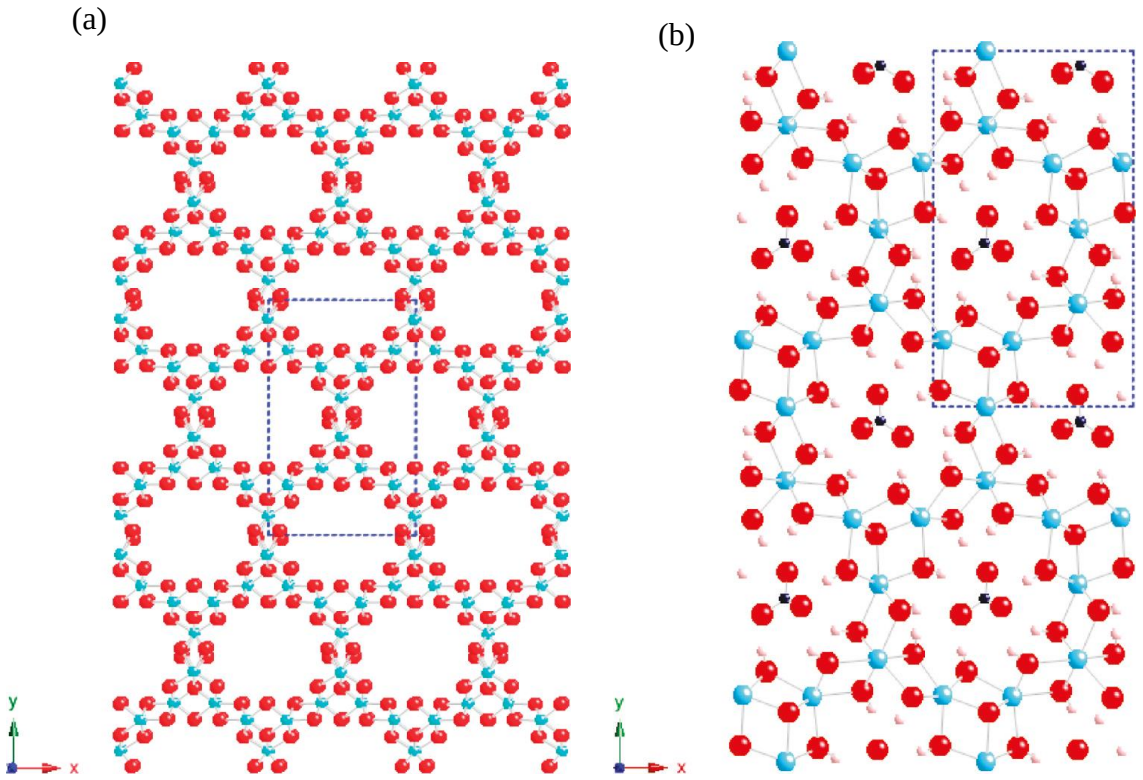

Figure 1 Crystal structures of (a) $Yb_3O(OH)_6Cl.2H_2O$. The Cl^- and water molecules are found to reside in the channels but are disordered and have been omitted for clarity[7] and (b) $Yb_4O(OH)_9NO_3$, nitrate anions are located within the channels.[8] (Colour key; Yb – blue, O – red, N – dark blue, H – pink)

The third cationic inorganic framework is that of a recently reported thorium borate compound, $[ThB_5O_6(OH_6)][BO(OH)_2].2.5H_2O$ (Notre Dame Thorium Borate-1, NDTB-1), Figure 2.[9] This three-dimensional structure comprises of twelve coordinate Th^{4+} cations surrounded by BO_3^{3-} and BO_4^{5-} anions, which polymerize to form $B_{10}O_{24}$ clusters consisting of four triangular and six tetrahedral units. Charge balancing borate anions, $BO(OH)_2^-$, are found to reside within the one-dimensional channels in this material and are able to exchange with a variety of anions such as MnO_4^-, CrO_4^{2-}, $Cr_2O_7^{2-}$ and also ReO_4^-. The successful anion exchange with CrO_4^{2-} and ReO_4^- (a model for TcO_4^-) proved very interesting as chromate, CrO_4^{2-} is toxic and pertechnetate, TcO_4^-, is radioactive. Therefore anion exchange materials, like this compound, are needed for the successful removal of these species from solution, as both materials are transported into the environment and are problematic in the clean-up of nuclear waste.[9]

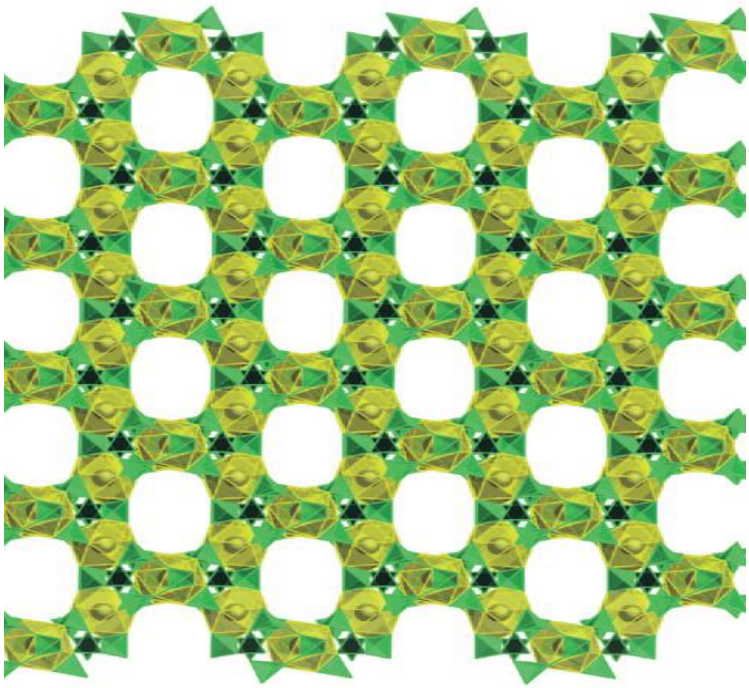

Figure 2 Crystal structure of $[ThB_5O_6(OH_6)][BO(OH)_2].2.5H_2O$ (NDTB-1), $BO(OH)_2$ anions and water reside within the channels and have been omitted for clarity.[9] (Colour key; Th – yellow, Borate - triangular and tetrahedral units – dark green and green)

Borates have interesting and diverse structural chemistry due to boron being able to adopt either tetrahedral or triangular geometry. The two geometries available leads to the formation of a variety of borate building units as the individual triangular or tetrahedral units are able to connect together through shared oxygen atoms to form either clusters, chains or sheets of borate anions. Borate units are found to consist of the borate triangles, BO_3, or borate tetrahedra BO_4, either in conjunction with one another or individually at various ratios, leading to the formation of a vast range of borate anionic units or as they are known fundamental building blocks, FBBs, which can then lead to a diverse range of structures when combined with metals. There are a vast variety of borate units that have been identified to date, with units containing from three up to sixty three boron atoms, and these are the subject of several reviews.[10,11,12]

The formation of borate units may depend on the synthetic method utilized and also many reaction variables such as reaction temperature, reagent stoichiometries,[13] cation size and also the use of counterions.[14, 15] A variety of synthetic methods have

also been employed in the formation of borate containing compounds such as the high temperature technique,[16,17] hydrothermal synthesis [18, 19, 20, 21] and the boric acid flux method.[9, 22, 23, 24, 25] Borates have been described in the literature with the incorporation of either alkali metals,[26] alkaline earth metals,[20, 27, 28, 29] transition metals[21, 30, 31] and rare-earth metals, lanthanides[13, 32, 33, 34] and actinides.[14, 15, 24]

The boric acid flux method is a relatively new method in the synthesis of borate containing compounds. In this method boric acid is utilised as a reagent as well as being the reaction medium, with little or no water added to the reaction mixture. The melting point of boric acid is 170.9 °C therefore this temperature must be exceeded to ensure that it will act as the reaction medium, with temperatures above 200 °C being common for syntheses employing this method.

Use of the high temperature technique generally leads to the formation of anhydrous borates, for example an alkaline-earth metal borate of composition CaB_6O_{10}.[17] This compound consists of two triborate units of $[B_3O_7]^{5-}$ consisting of one tetrahedral and two triangular borate anions which are linked by one oxygen atom forming a hexaborate unit $[B_6O_{13}]^{8-}$, which further condenses into three-dimensional $[B_6O_{10}]^{2-}$ network. Open channels are found to be present in this structure in which charge balancing Ca^{2+} cations reside.

On the other hand the use of the hydrothermal or the boric acid flux method commonly leads to hydrated borates; for example, a hydrothermal synthesis led to the formation of a hydrated barium borate complex of $Ba_3B_6O_9(OH)_6$.[20] This compound consists of infinite chains of $[B_6O_9(OH)_6]^{6-}$ anions, which are built up of B_3O_3 six membered rings and are charge balanced by Ba^{2+} cations which reside between the chains.

A disadvantage of employing the hydrothermal technique is that water may compete with borate for the inner-sphere coordination of, for example, lanthanides and actinides, therefore suggesting that it may become difficult to synthesise these materials using this technique or using room temperature aqueous reactions.[35]

The synthesis of hydrated rare-earth borates has been described within the literature, using either a hydrothermal or boric acid flux method, leading to the formation of a variety of structures, from two – three-dimensional, which contain different borate

units. Some examples include the formation of $Ln_2B_6O_{10}(OH)_4.H_2O$ (Ln = Pr, Nd, Sm, Eu, Gd, Ho and Y)[34] these hydrated materials have been synthesised under a hydrothermal route. The structure consists of fundamental building blocks, FBBs, of three membered rings of $[B_3O_6(OH)_2]^{5-}$ which are linked together through shared oxygen atoms to form chains of $[B_3O_5(OH)_2]^{3-}$, with these chains being further linked by Ln cations forming a layer. These layers interact together via hydrogen bonding interactions to form a two-dimensional layered structure, Figure 3.

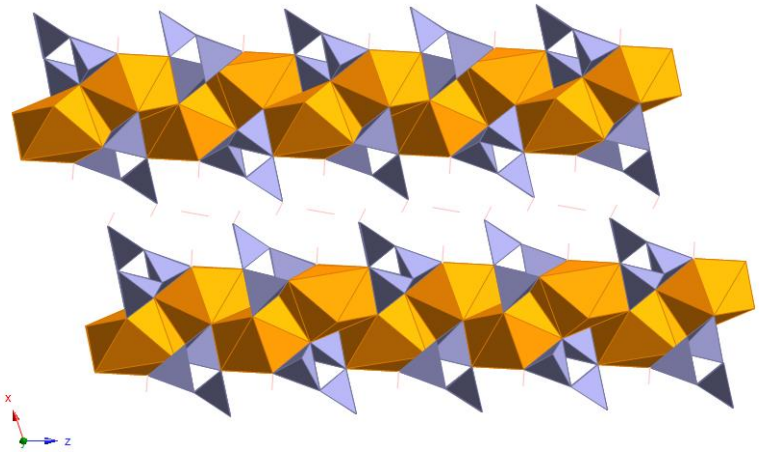

Figure 3 Crystal structure of $Nd_2B_6O_{10}(OH)_4.H_2O$ (Colour key; Nd – orange, Borate - triangular and tetrahedral units – blue).[34]

A three-dimensional structure has also been synthesised under hydrothermal conditions with the composition $Ln[B_6O_9(OH)_3]$ (Ln = Sm – Lu).[36] This structure consists of hexagonal rings of composition $[B_6O_9(OH)_3]^{3-}$ which are formed by alternating tetrahedral and triangular borate anions. Their charge is balanced by lanthanide cations which reside in the channels which are formed by these borate rings along with three pairs of tetrahedral and triangular units forming open rings, Figure 4.

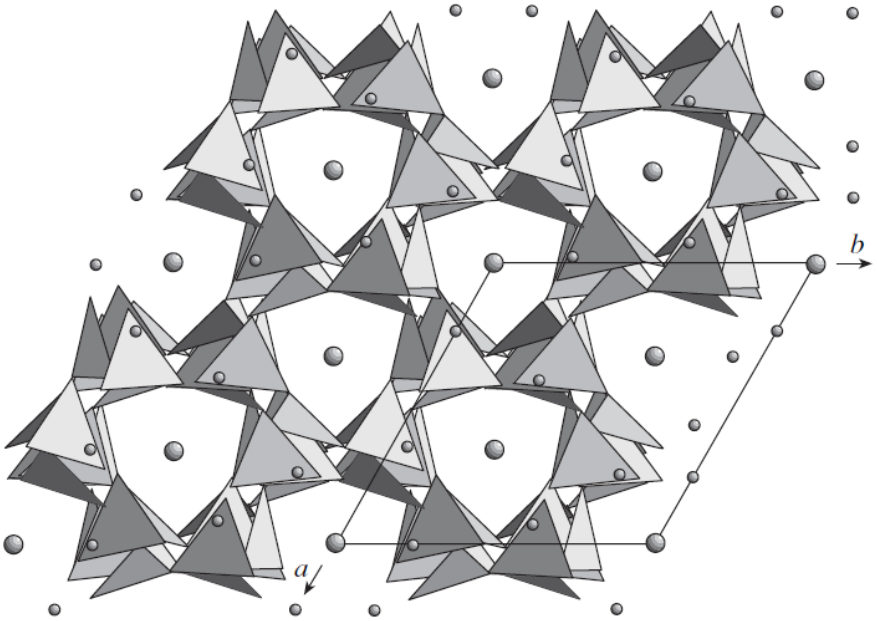

Figure 4 Crystal structure of $Ho[B_6O_9(OH)_3]$ (adapted from *Crystallogr. Rep.* **2004**, *49*, 603).[36]

An example of a three-dimensional lanthanide borate compound, synthesised via a boric acid flux method, is that of $Ln[B_9O_{13}(OH)_4].H_2O$ (Ln = Pr – Eu).[13] This compound consists of layers of $Ln[B_6O_{11}]$, with nine membered rings formed within these layers in which the lanthanide cations are located at the centre. The FBBs consist of a $[B_6O_{13}]$ unit, of three triangular and three tetrahedral borate anions, and also a three membered ring of $[B_3O_8]$, consisting of one triangular and two tetrahedral borate anions which leads to the formation of a porous three-dimensional borate framework, with water residing within the pores, Figure 5.

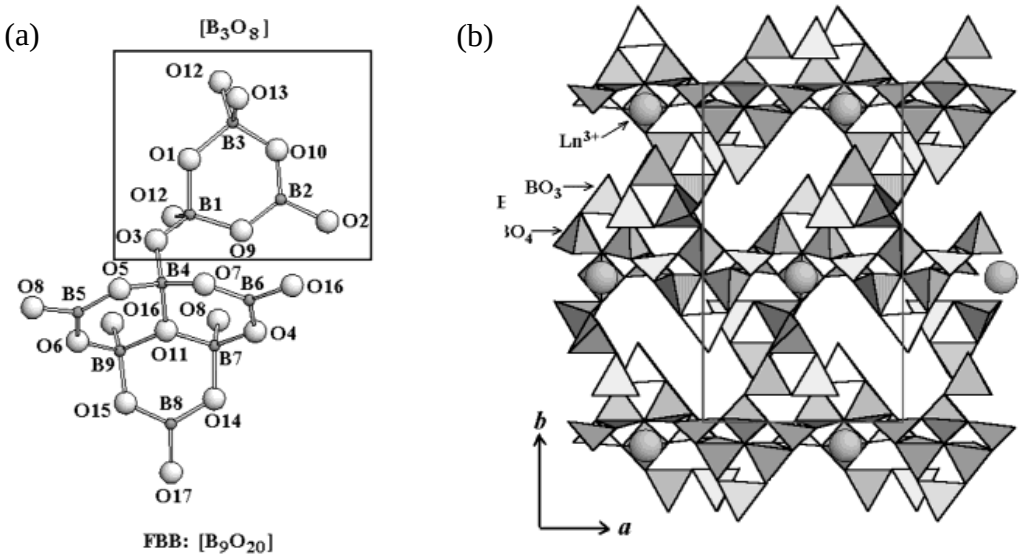

Figure 5 (a) FBBs found in $Ln[B_9O_{13}(OH)_4].H_2O$ (Ln = Pr – Eu) and (b) the crystal structure. Guest water molecules are omitted for clarity.[13]

The coordination chemistry of lanthanides is found to be rich and variable as lanthanides have high coordination numbers of 7 – 12. The incorporation of lanthanides along with borates into these materials, will allow the combination of the properties of both reagents along with their structural flexibility, to form a wide range of novel materials which may have applications in gas storage, luminescence and anion exchange.

The formation of organically templated borates, e.g. $[Ni(en)_3][B_5O_6(OH)_4]_2.2H_2O$ and $[Co(en)_3][B_4O_5(OH)_4]Cl.3H_2O$,[18] is also known,[21, 37, 38] although less well studied than the corresponding metal borates. These materials consist of three-dimensional supramolecular frameworks with the Ni^{2+} framework consisting of $[B_5O_6(OH)_4]^-$ anionic units which interact together through hydrogen bonding interactions to form channels in which the cationic $[Ni(en)_3]^{2+}$ and water molecules reside, Figure 6. In the Co^{3+} structure the units are $[Co(en)_3]^{3+}$, $[B_4O_5(OH)_4]^{2-}$, Cl^-, and water, which all connect together through extensive hydrogen bonding interactions forming a three-dimensional supramolecular framework.

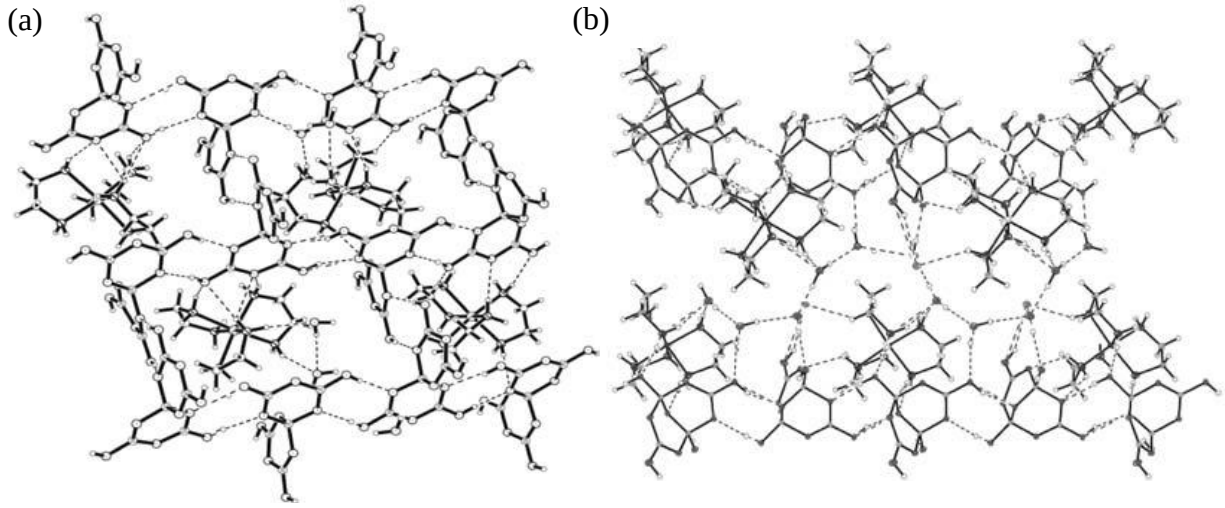

Figure 6 Crystal structures of (a) $[Ni(en)_3][B_5O_6(OH)_4]_2.2H_2O$ and (b) $[Co(en)_3][B_4O_5(OH)_4]Cl.3H_2O$.[18]

There are also examples in which borates are templated without the incorporation of a metal ion such as the formation of $[H_3N(C_6H_{10})NH_3][B_4O_5(OH)_4]$, Figure 7, and $[H_3N(C_6H_{10})NH_3][B_5O_8(OH)]$ ($H_3N(C_6H_{10})NH_3$ = trans-1,4-diaminocyclohexane).[39] These materials are known to be the first examples of organically templated borates. The structure of $[H_3N(C_6H_{10})NH_3][B_4O_5(OH)_4]$ consists of isolated $[B_4O_5(OH)_4]^{2-}$ anions of two triangular and two tetrahedral borate anions. These tetraborate groups link together via hydrogen bonding interactions to form ten membered boron ring channels leading to a three-dimensional supramolecular framework. The organic moieties reside in the channels and interact with the borate network via hydrogen bonding interactions. The second structure of $[H_3N(C_6H_{10})NH_3][B_5O_8(OH)]$ consists of $[B_5O_8(OH)]^{2-}$ units of a double ring of two different compositions. The first ring comprising of one tetrahedral and two triangular borate anions and the second of one triangular and two tetrahedral borate anions, which link together through a common tetrahedron. These double ring units link together to form sheets of nine membered rings, with the sheets linking together through hydrogen bonding interactions to form large channels consisting of fourteen membered boron rings. The organic moieties reside within the channels interacting with the inorganic framework via hydrogen bonding interactions to form a three-dimensional supramolecular framework.[39]

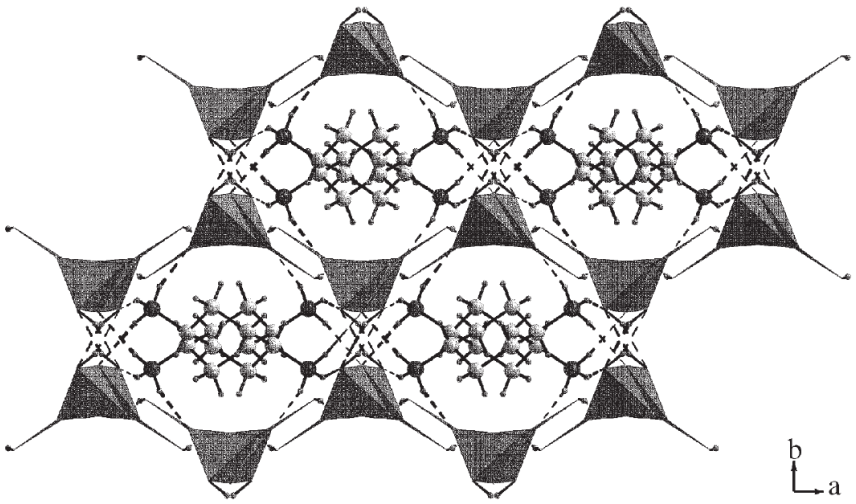

Figure 7 Crystal structure of $[H_3N(C_6H_{10})NH_3][B_4O_5(OH)_4]$.

The rules of the formation of fundamental building blocks (FBBs) of polyborate anions were first classified by Clark in 1960. In 1977 Christ and Clark re-visited these rules and adapted them to what was found previously. Firstly they discovered that boron will either link with three or four oxygen atoms, in turn forming a triangle or a tetrahedron. This rule still holds true today therefore has remained unchanged. They determined that polyborate anions are formed by corner-sharing boron-oxygen triangles or tetrahedra resulting in the formation of compact groups. A shorthand notation of the description of the FBBs, found in polyborate systems is that of n : [(n : $x\Delta + y$T)] were n = number of boron atoms characteristic of the FBB in question, x = number of triangles, Δ, and y = number of tetrahedra, T, present within the FBB. Each of these units, or FBBs, are able to combine with others to form dimers, chains, sheets, or three-dimensional networks.[10]

5.1 Objective

Chapter 2 described the successful formation of new inorganic-organic hybrid materials consisting of lanthanide cations and molybdate or tungstate tetrahedral anionic building blocks in conjunction with sulfonate or carboxylate anions, which led to the formation of positively charged layers, consisting of lanthanides and molybdate or tungstate, which were charge balanced by sulfonate or carboxylate anions in turn forming three-dimensional pillared layered structures. Recently described in the literature is the successful formation of a cationic thorium borate framework of $[ThB_5O_6(OH_6)][BO(OH)_2].2.5H_2O$ (NDTB-1), which has potential applications in anion exchange, as discussed in Section 5.0. Borate, can form either triangular BO_3 or tetrahedral BO_4 units, and can be used as alternative anionic building blocks to tetrahedral molybdate or tungstate, therefore incorporation of this building block in conjunction with lanthanide cations could result in the formation of three-dimensional cationic inorganic frameworks, which may have potential applications in gas storage and anion exchange. The use of the boric acid flux method has been described within the literature as a good method for the production of crystalline polyborate phases, therefore this synthetic method will be utilized in the formation of these materials in the hope to form lanthanide borate phases which may be analogous to the thorium borate phase recently reported.

5.2 Scope of Chapter

The boric acid flux synthesis, crystal structures and characterisation of three new lanthanide borates is described. These phases have compositions of $[Ln(NO_3)(H_2O)_2][B_6O_{10}(OH_2)]$ (**1**) (Ln = La and Ce), $[Ln(NO_3)(H_2O)_2][B_5O_9(OH_2)]$ (**2**) (Ln = Pr and Ce), and $[Ln(B_6O_{13}H_3)][BO_3H_2]$ (**3**) (Ln = Sm, Eu and Gd). **1** and **2** are found to have infinite three-dimensional structures consisting of either hexaborate clusters as found in **1** or pentaborate clusters as found in **2**, with one dimensional channels being present in both structures. **3** is found to differ to **1** and **2** as this phase has a layered structure consisting of positively charged layers of gadolinium cations coordinated to unique hexaborate clusters, which are charge balanced by non-coordinating borate

anions which reside in the interlayer gallery. The anion exchange capabilities have been tested for **3** although this proved largely unsuccessful.

5.3 Lanthanide Borates

5.3.1 General Synthesis

Three new phases, with compositions of $[Ln(NO_3)(H_2O)_2]$ $[B_6O_{10}(OH_2)]$ (**1**) (Ln = La), $[Ln(NO_3)(H_2O)_2][B_5O_9(OH_2)]$ (**2**) (Ln = Pr and Ce), and $[Ln(B_6O_{13}H_3)][BO_3H_2]$ (**3**) (Ln = Sm, Eu and Gd) have been synthesised via a boric acid flux route from $Ln(NO_3)_3.xH_2O$ and boric acid (BO_3H_3). Full crystallographic data for each phase is provided in Appendix D. The reactions were heated at 200 °C for 48 h before being cooled slowly back to room temperature. The yields of the reactions lie in the range of 28 – 54 % with respect to the Ln^{3+} cation. A variety of reaction conditions were screened, for example change in reaction temperature, time and concentration of reagents, to obtain a phase pure materials. The optimal conditions found are those stated above with others leading to less crystalline samples.

5.3.2 Characterisation of $[Ce(NO_3)(H_2O)_2][B_6O_{10}(OH_2)]$ (1)

$[Ce(NO_3)(H_2O)_2][B_6O_{10}(OH_2)]$ (**1**) has been synthesised via a boric acid flux method. Single crystal X-ray diffraction data has shown that it adopts a monoclinic structure with the space group $P2_1/n$, shown in Figure 8, with the main crystallographic and refinement data summarised in Table 1 and detailed bond lengths provided in Appendix D. This phase has also been successfully synthesised with Ln = La.

(a)

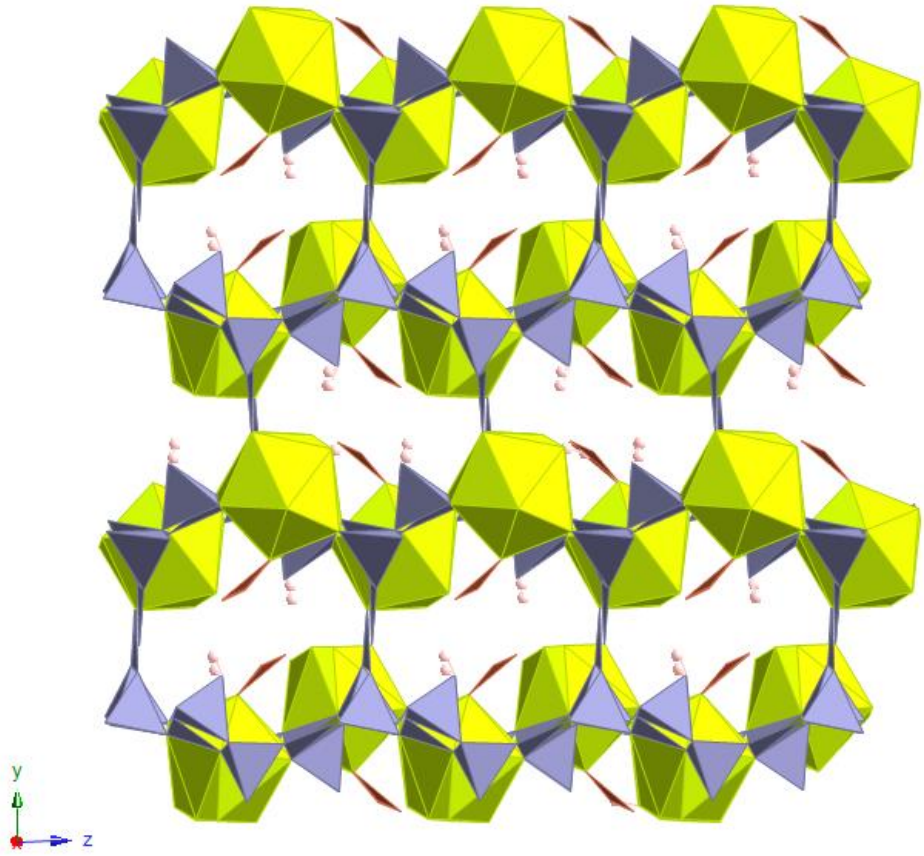

(b)

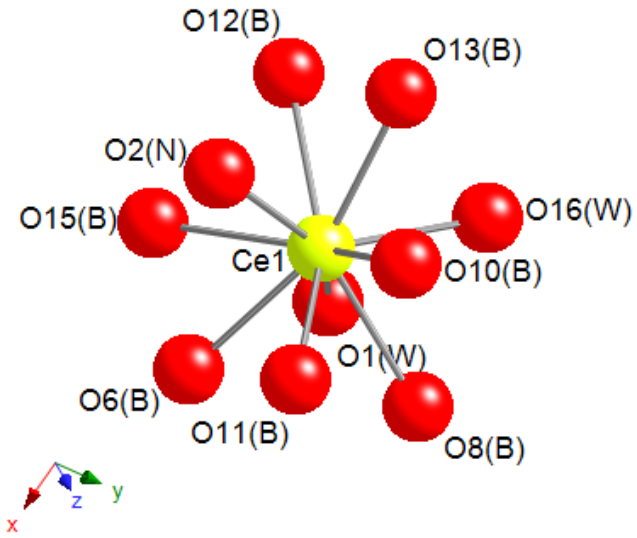

Figure 8 (a) Crystal structure of $[Ce(NO_3)(H_2O)_2]$ $[B_6O_{10}(OH_2)]$ (**1**) and (b) coordination sphere of cerium in (**1**). (Colour key; Ce – yellow, borate (triangular and tetrahedral) – blue, H - pink and nitrate – burgundy)

Table 1 Crystallographic data and refinement parameters for phases (**1 - 3**).

	(1)	**(2)**	**(3)**
Empirical formula	$H_6B_6CeNO_{16}$	$H_6B_5PrNO_{15}$	$H_5B_7GdO_{16}$
Formula weight	481.04	455.02	493.96
Temperature	120(2) K	120(2) K	100 K
Wavelength	0.71073Å	0.71073Å	0.71073Å
Crystal system	Monoclinic	Monoclinic	Triclinic
Space group	$P2_1/n$	$P2_1/n$	$P\bar{1}$
Unit cell dimensions	a = 9.8268(3) Å	a = 6.4315(2) Å	a = 6.7936(16) Å
	b = 14.7545(3) Å	b = 15.5099(7) Å	b = 7.1010(17) Å
	c = 8.0451(5) Å	c = 10.7078(3) Å	c = 12.563(3) Å
	α = 90 º	α = 90 º	α = 94.841(3) º
	β = 90.0700(10) º	β = 90.377(2) º	β = 99.127(3) º
	γ = 90 º	γ = 90 º	γ = 101.840(3) º
Volume ($Å^3$)	1166.45(8)	1068.10(7)	581.3(2)
Z	4	4	2
Density (calculated Mg/m^3)	2.769	2.830	2.822
Absorption coefficient(mm^{-1})	4.006	4.660	5.804
Crystal	sheet; colourless	fragment; colourless	plate; colourless
Crystal Size (mm^3)	0.10x0.04x0.02	0.16x0.14x0.08	0.2 x 0.073 x 0.015
θ range for data collection (deg)	3.27-27.48	3.24-27.48	2.95-27.08
Reflections collected	20534	11130	3646
Independent reflections collected	2680 [R_{int}= 0.0485]	2438 [R_{int}= 0.0629]	2205 [R_{int}= 0.0689]
Max. and min. transmission	0.9242 and 0.6901	0.7068 and 0.5226	0.9180 and 0.3898
Goodness of fit on F^2	1.405	1.139	1.050
R [F, $F^2 > 2\sigma$]	0.0384	0.0465	0.0661
R_w (F, all data)	0.0882	0.0999	0.1599
Diff. map extremes (e $Å^{-3}$)	1.142 and -0.807	1.152 and -1.097	2.841 and -3.070

The structure comprises of infinite one-dimensional chains of discrete cerium cations which are linked together via chains of hexaborate anions leading to the formation of a three-dimensional framework with one-dimensional channels running through the structure. There is one crystallographically distinct Ce cation in this structure which is ten coordinate to two water molecules (O(1) and O(16)), one nitrate anion (O(2)) and the remainder of the coordination sites being filled by oxygen atoms from clusters of corner sharing BO_3 and BO_4 anions, (O(6), O(8), O(10), O(11), O(12), O(13) and O(15)). The Ce-O bond distances lie in the range of 2.466 (12) – 2.713 (4) Å. Hydrogen bonding interactions are present in this structure between coordinated nitrate anions and water molecules, for example O(1)-H···$O(7)_{nitrate}$ - 2.9562(7) Å, which occurs between coordinated nitrate and water molecules bound to adjacent Ce centres in the *xz* plane.

There are six crystallographically distinct boron atoms within this structure which form the FBBs. The structure consists of polymerised clusters of hexaborate anions of composition $B_6O_{10}(OH_2)$, which consist of three BO_3 triangular units (Δ), two BO_4 tetrahedra (T) and one doubly protonated BO_3OH_2 tetrahedral unit (T). The terminal oxygen atom (O4) in the borate cluster is found to be doubly protonated and interacts with the bound nitrate via hydrogen bonding interactions, O(4)-H···$O(7)_{nitrate}$ 2.9344(6) Å. These FBBs are in the form of three B_3O_3 rings, which consist of alternating boron and oxygen atoms. The oxygen atoms are from two tetrahedra and one triangular borate and are linked together by a tetrahedral boron atoms (B(1), B(3) and B(4)), shown in Figure 9, forming a pyramid type cluster. The FBBs are linked together through bridging oxygen atoms O(12) and O(15) from forming a wave like chain parallel to the *z* axis, shown in Figure 10(a), and a sheet in the *xz* plane shown in Figure 10(b), the terminal oxygen atom O(8) is bound to the Cerium centre. The sheets consists of nine membered rings of borate units in which the Ce cations are located at the centre which leads to the formation of a three-dimensional structure, with one-dimensional channels running along the *x* axis. The borate clusters can also be expressed by the shorthand notation of 6 : [(6 : 3Δ + 3T)], according to the chemical classification of Christ and Clark.[10] The B-O distances of the triangular boron atoms lie in the range of 1.352(8) – 1.389(7) Å, and 1.437(8) – 1.518(7) Å for the tetrahedral boron atoms with an additional B-OH_2 bond distance of 1.415(8) Å. These bond distances are comparable to those found in previous compounds containing triangular and tetrahedral borate anions.[18, 21, 28]

Two of the known hexaborate units are shown in Figure 11, with the hexaborate unit found in this material being also observed in $Na_3[B_6O_9(VO_4)]$.[40] This structure consists of 6 : [(6 : 3Δ + 3T)] units which are joined together to form sheets which are further linked together by the VO_4 tetrahedra leading to a three-dimensional network in which channels are formed with sodium cations located within them. This unit has also been described in several hydrated borates[10, 11] where it exists as isolated units, chains or sheets for example in $SrB_6O_9(OH)_2.3H_2O$,[41] also known as 'tunellite' which consists of infinite sheets of polymerised borate anions of three triangular and three tetrahedral units, 6 : [(6 : 3Δ + 3T)], creating three six membered rings with each ring consisting of one triangular and two tetrahedral units. Sr cations and water fill the available spaces in these sheets, with the layers being held together via hydrogen bonding interactions between the borate groups with water molecules residing between the layers.[41]

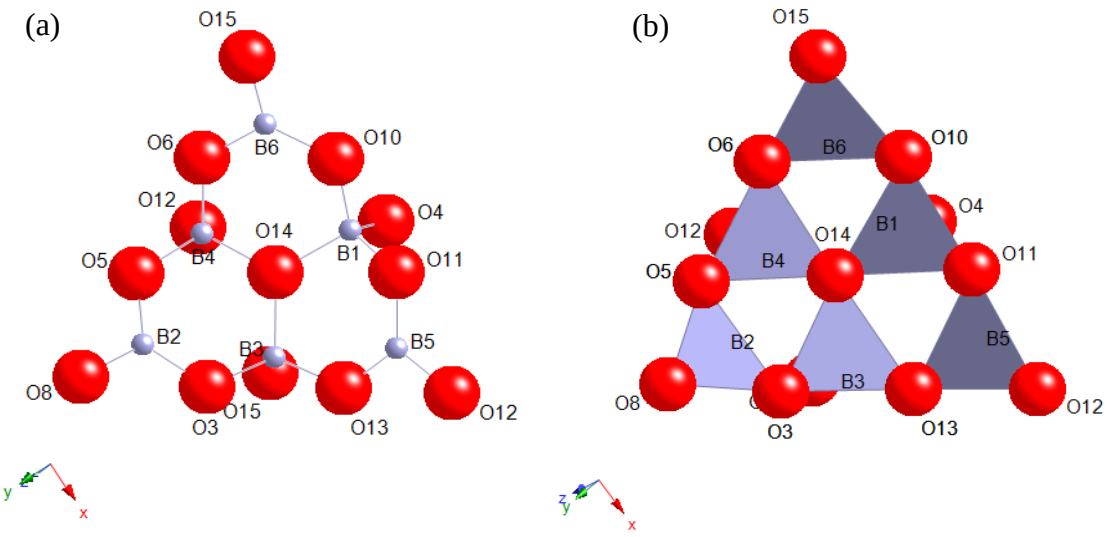

Figure 9 The hexaborate units consisting of three B_3O_3 rings, which form the FBBs in $[Ce(NO_3)(H_2O)_2][B_6O_{10}(OH_2)]$ (**1**) (a) as ball and stick borates and (b) as polyhedral borates.

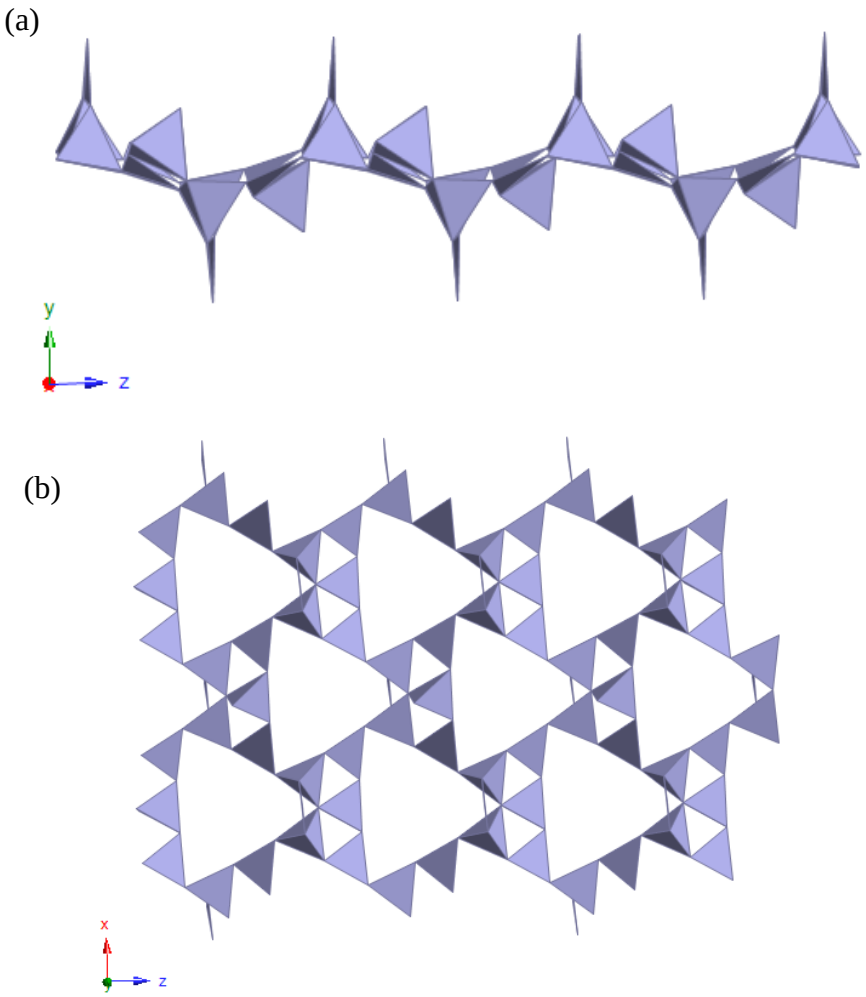

Figure 10 (a) Chains of corner sharing hexaborate anions of $B_6O_{10}(OH_2)$ and (b) linking hexaborate anions into sheets in the *xz* plane.

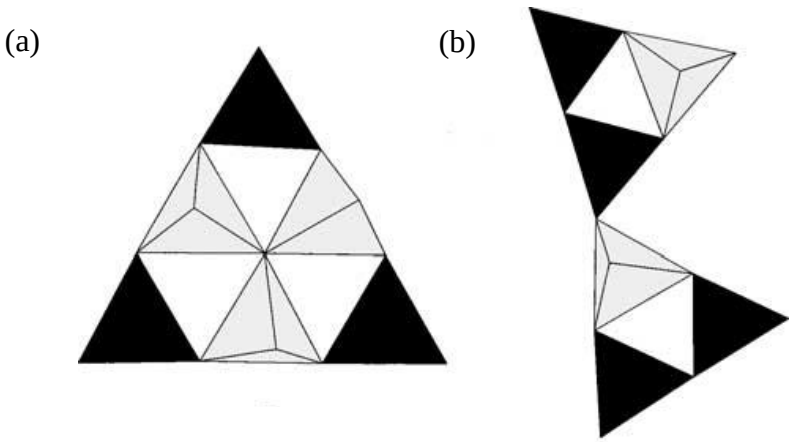

Figure 11 Two known hexaborate units of (a) 6 : [(6 : 3Δ + 3T)] and (b) 6 : 2 [(3 : 2Δ + T)].[11]

A range of analytical techniques were used to determine the composition and phase purity of this material. The powder XRD pattern of **1** is shown in Figure 12, where it is compared to one calculated from the crystal structure. A second crystalline phase is evident in the experimental data, although there is good agreement between the major crystalline phase and the experimental pattern, suggesting that the crystal structure of **1** is representative of the bulk phase. It is observed that at a reaction time of 96 h, a biphasic product is produced as determined from powder X-ray diffraction measurements. The major phase is that which is described above and the second, minor phase, is found to be iso-structural to the Pr phase as discussed in the next section, Section 5.3.3. Powder X-ray diffraction patterns of the La, Ce and Pr samples are shown in Figure 13. Also note that when this synthesis is performed with Ce with a reaction time of 48 h, this leads to a phase pure product which is iso-structural to the Pr analogue, as discussed in the next section.

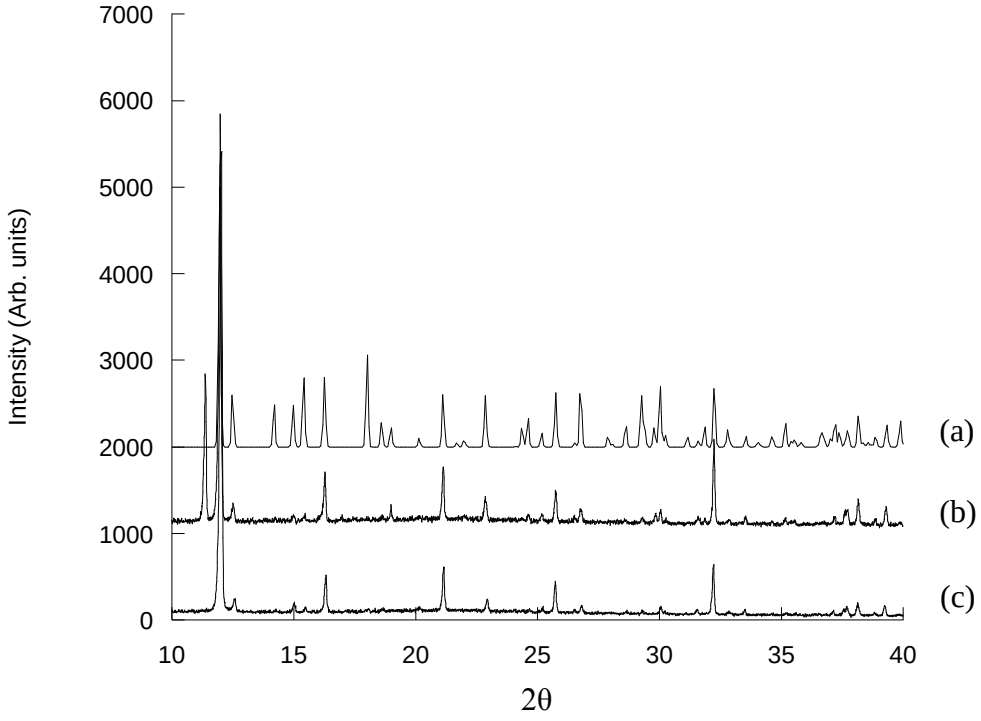

Figure 12 Powder XRD patterns (Cu K_α radiation) of
(a) $[Ce(NO_3)(H_2O)_2]$ $[B_6O_{10}(OH_2)]$ calculated from the crystal structure
(b) $[Ce(NO_3)(H_2O)_2][B_6O_{10}(OH_2)]$ and
(c) $[La(NO_3)(H_2O)_2]$ $[B_6O_{10}(OH_2)]$.

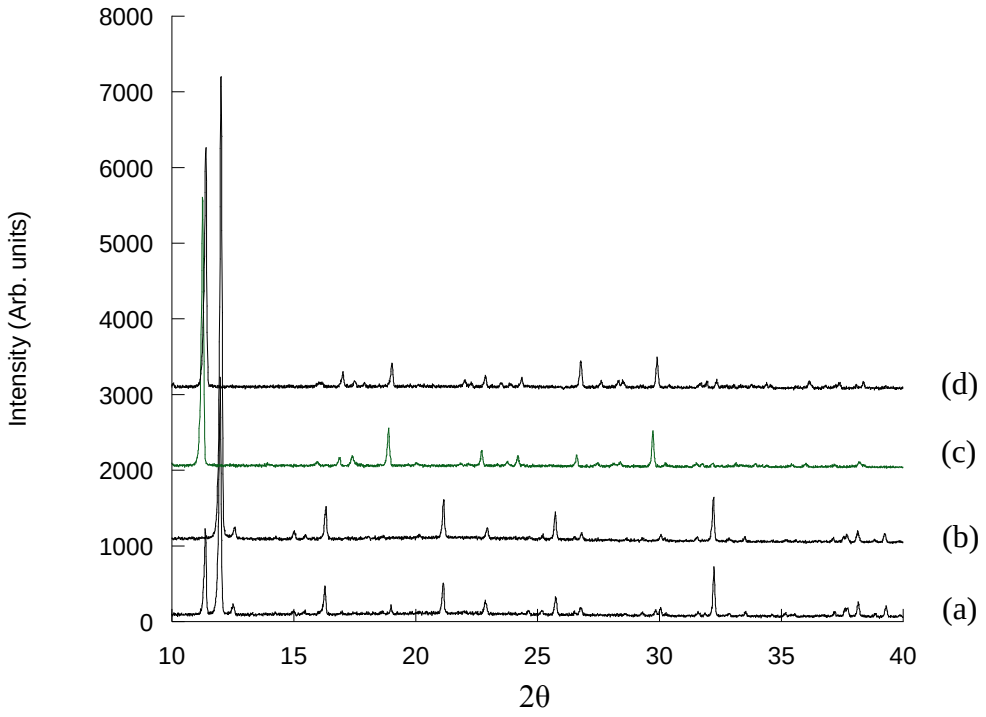

Figure 13 Powder XRD pattern (Cu K_α radiation) of iso-structural phases of (a) biphasic $[Ce(NO_3)(H_2O)_2][B_6O_{10}(OH_2)]$ synthesised after 96 h (b) $[La(NO_3)(H_2O)_2][B_6O_{10}(OH_2)]$ (c) $[Ce(NO_3)(H_2O)_2][B_5O_9(OH_2)]$ synthesised after 48 h and (d) $[Pr(NO_3)(H_2O)_2][B_5O_9(OH_2)]$.

The phase containing Ce is found to be biphasic under reaction conditions of 96 h, although when using La in the synthesis, for 48 h, it is observed that a single phase is produced which is phase pure and is found to be iso-structural to **1**, Figure 13. Due to it being phase pure the La phase will be discussed in terms of analytical characterisation.

A range of analytical techniques were used to determine the composition and phase purity of $[La(NO_3)(H_2O)_2][B_6O_{10}(OH_2)]$. Elemental analysis indicated that the sample contains 1.17 % H (calc 1.26 %) and 2.49 % N (calc 2.92 %), which is consistent with the composition obtained from the crystal structure of $[Ce(NO_3)(H_2O)_2][B_6O_{10}(OH_2)]$ and the absence of crystalline impurities in the PXRD pattern. The powder XRD pattern of the La phase (48 h) is shown in Figure 13, where it is compared to the Ce phase (96 h), showing these phases to be iso-structural.

Use of $LaCl_3.xH_2O$ instead of $La(NO_3)_3.xH_2O$ as the lanthanide source resulted in the formation of a different and less crystalline phase as determined from powder X-ray diffraction measurements, therefore confirming that nitrate is present within this phase. Structure solution for the Cl product was not possible.

The TGA trace of $[La(NO_3)(H_2O)_2][B_6O_{10}(OH_2)]$ is shown in Figure 14 and displays three mass losses below 750 °C. The first mass loss of 4.2 % below 200 °C corresponds to the removal of the water group on the borate unit leading to a composition of $[La(NO_3)(H_2O)_2][B_6O_{10}]$ and compares well to the calculated value of 3.8 %. The second mass loss of 8.1 % below 300 °C corresponds to dehydration of the material to $[La(NO_3)][B_6O_{10}]$ (calc 7.5 %). The decomposition of the phase is complete by 750 °C following an additional mass loss of 12.9 %, which corresponds to loss of the nitrate anion. A total mass loss of 24.5 % is observed which corresponds well to the calculated value of 24.2 %. Powder X-ray diffraction showed the residue to be LaB_3O_6, although an amorphous product of predicted composition of B_3O_4 must also be present in order for the calculations to agree to what is lost in the final step to leave an overall composition of LaB_6O_{10}.

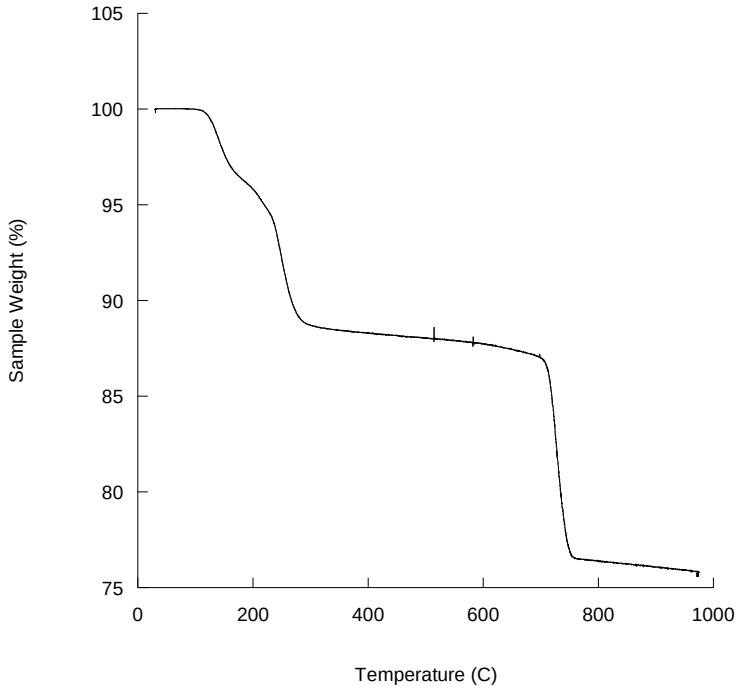

Figure 14 TGA trace of $[La(NO_3)(H_2O)_2][B_6O_{10}(OH_2)]$.

The FTIR spectrum is shown in Figure 15 and has a broad band due to an O-H stretch at approximately 3040 cm^{-1} and two bands due to the bending mode of the two different water molecules present at 1657 and 1619 cm^{-1}. The other features of the spectrum are due to the hexaborate anions and the nitrate anion present within the structure. Frequencies characteristic of the antisymmetric and symmetric stretching modes of triangular BO_3 are observed at 1416, 1334, and 904 cm^{-1} and frequencies characteristic of the antisymmetric and symmetric stretching modes of tetrahedral BO_4 are observed at 1097, 811 and 737 cm^{-1}. There are also frequencies characteristic of the in-plane bending modes B-O-H at 1156 cm^{-1} and the out-of-plane bending mode of B-O in BO_3 at 706 cm^{-1}. Due to nitrate and triangular borate having the same geometry and similar bond strengths the FTIR stretches of these groups are observed at the same wavenumber of 1334 cm^{-1}. The FTIR spectrum confirms the presence of the two different borate units of triangular and tetrahedral coordination present within the structure and therefore the spectrum is found to differ to that of pure boric acid due to BO_4 groups being present therefore more bands are observed within the recorded spectrum. The borate frequencies detected are found to be consistent with compounds containing triangular and tetrahedral borate anions reported in recent literature.[16, 18, 21, 27, 42]

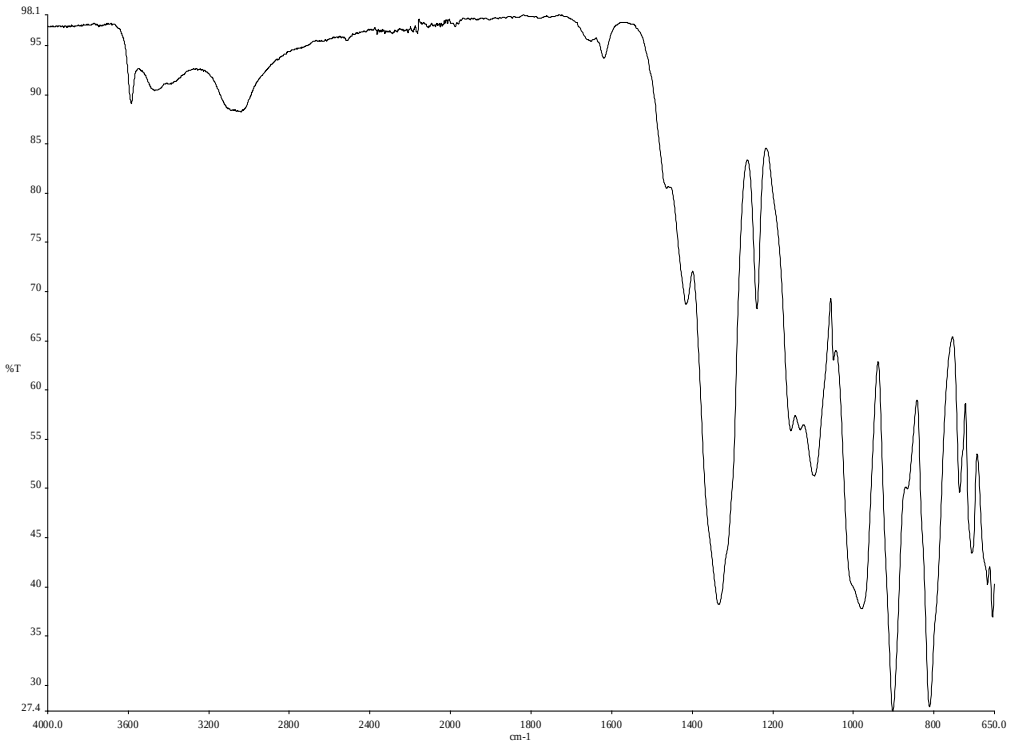

Figure 15 FTIR spectra of $[La(NO_3)(H_2O)_2][B_6O_{10}(OH_2)]$.

Channels are found in **1**, along the *x* axis, as shown in Figure 8, with a diameter of 8.1 Å, measuring the O - O distance across the channel in the *z* plane. Treatment of the phase pure La compound under vacuum at 120 °C, showed a BET surface area of 8.13 m^2/g and a type II isotherm, indicating that this material is non-porous to N_2. Analysis of this structure using PLATON indicated that there are no solvent accessible pores present within this phase. This material may not possess porosity as the coordinated nitrogen anions block the entrance to the channels therefore limiting any access to the channels. Data is provided in the appendices.

5.3.3 Characterisation of $[Pr(NO_3)(H_2O)_2][B_5O_9(OH_2)]$ (2)

$[Pr(NO_3)(H_2O)_2][B_5O_9(OH_2)]$ (**2**) has been synthesised via a boric acid flux method. Single crystal X-ray diffraction data has shown that it adopts a monoclinic structure with the space group $P2_1/n$ shown in Figure 16, with the main crystallographic and refinement data summarised in Table 1 and detailed bond lengths provided in Appendix D. This phase has also been successfully synthesised with Ln = Ce and Nd, powder X-ray diffraction patterns are shown in Figure 17, and the characterising data of each phase is provided in appendix D.

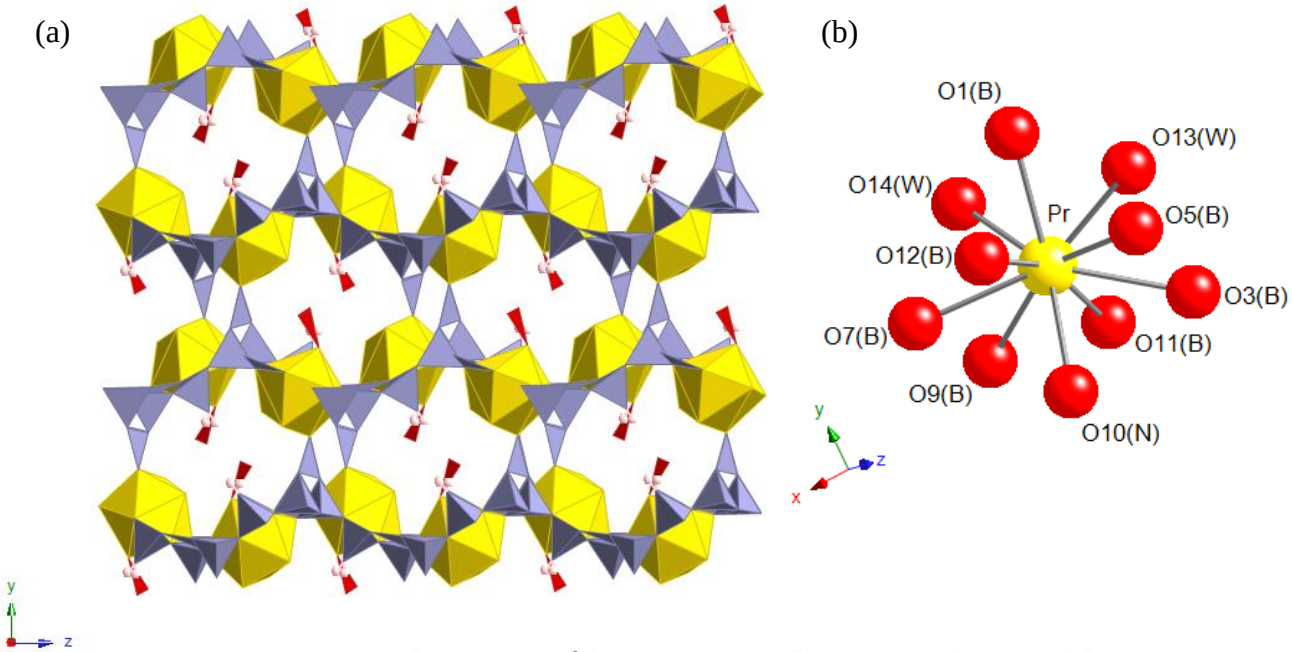

Figure 16 (a) Crystal structure of $[Pr(NO_3)(H_2O)_2][B_5O_9(OH_2)]$ (**2**) and (b) coordination sphere of praseodymium in (**2**).(Colour key; Pr – yellow, Borate (triangular and tetrahedral) – blue, H - pink and Nitrate – burgundy)

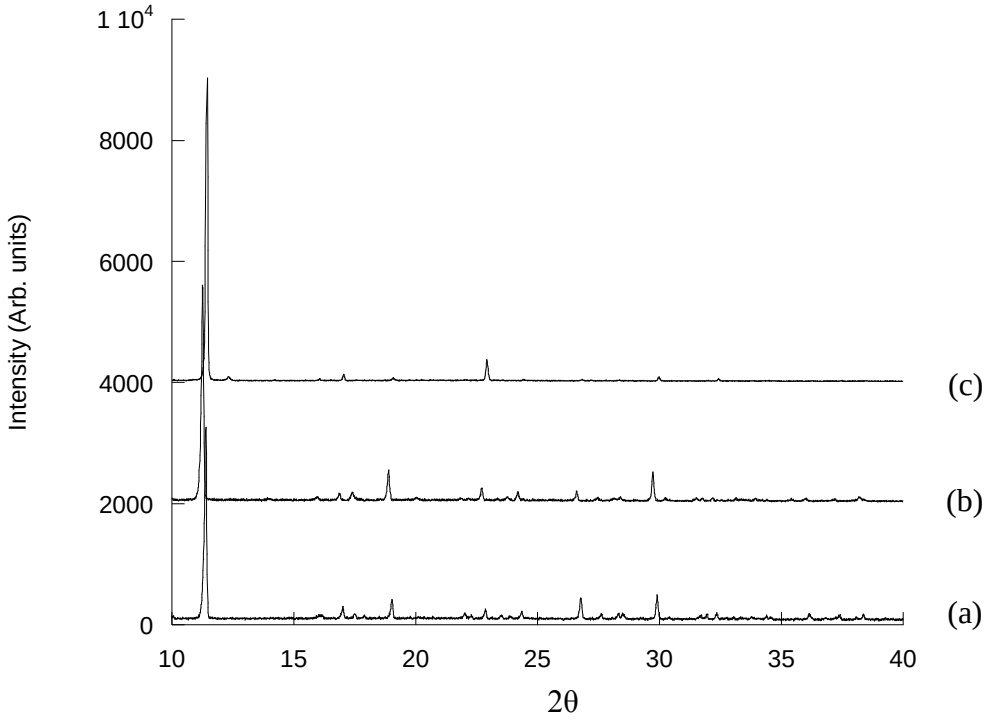

Figure 17 Powder XRD pattern (Cu K_α radiation) of
(a) $[Pr(NO_3)(H_2O)_2][B_5O_9(OH_2)]$ and iso-structural phases
(b) $[Ce(NO_3)(H_2O)_2][B_5O_9(OH_2)]$ and (c) $[Nd(NO_3)(H_2O)_2][B_5O_9(OH_2)]$.

The structure comprises of infinite one-dimensional chains of discrete praseodymium cations which are linked together via chains of pentaborate anions leading to the formation of a three-dimensional framework structure with one-dimensional channels running through the structure. There is one crystallographically distinct Pr cation in this structure which is ten coordinate to two water molecules (O(13) and O(14)), one nitrate anion (O(10)) with the remainder of the coordination sites being filled by oxygen atoms from clusters of corner sharing BO_3 and BO_4 anions, (O(1), O(3), O(5), O(7), O(9), O(11) and O(12)) . The Pr-O bond distances lie in the range of 2.499 (5) – 2.659 (5) Å.

There are five crystallographically distinct boron atoms within this structure, forming the FBBs. The structures consist of polymerised chains of pentaborate anions of $B_5O_9(OH_2)$, which consist of two BO_3 triangular units (Δ), two BO_4 tetrahedra (T) and one doubly protonated BO_3OH_2 tetrahedral unit (T), which are linked together by shared oxygen atoms. The terminal oxygen atom (O15) in the borate chain is found to be doubly protonated and interacts with the bound nitrate via hydrogen bonding

interactions, O(15)-H···O4$_{nitrate}$ 2.6961(8) Å. The FBBs are in the form of two B_3O_3 rings consisting of alternating boron and oxygen atoms linked together by a tetrahedral boron atom (B5), Figure 18. Four pentaborate FBBs are known and are shown in Figure 19, 5 : [(5 : 4Δ + T)] (a), 5 : [5 : (3Δ + 2T)] (b) and 5 : [(5 : 5T)] (d), the pentaborate unit found in **2** is identical to the previously reported 5 : [(5 : 2Δ + 3T)] FBB,[11, 23] shown in Figure 19(c). The FBBs are linked together through terminal bridging oxygen atoms O(11) and O(5) forming a wave like chain along the *z* axis, and a sheet in the *xz* plane, shown in Figure 20. These sheets and chains link together adjacent Pr centres, which reside in the nine membered rings formed in the sheets, to form a three-dimensional structure, with one-dimensional channels running along the *x* axis, Figure 16. The borate chains can also be expressed by the shorthand notation of 5 : [(5 : 2Δ + 3T)], according to the chemical classification of Christ and Clark.[10] The B-O distances of the triangular boron atoms lie in the range of 1.3504(9) – 1.3830(10) Å, and 1.3945(9) – 1.5028(9) Å for the tetrahedral boron atoms with an additional B-OH_2 bond distance of 1.6257(10) Å. These bond distances are comparable to those found in previous compounds containing triangular and tetrahedral borate anions.[18, 21, 28]

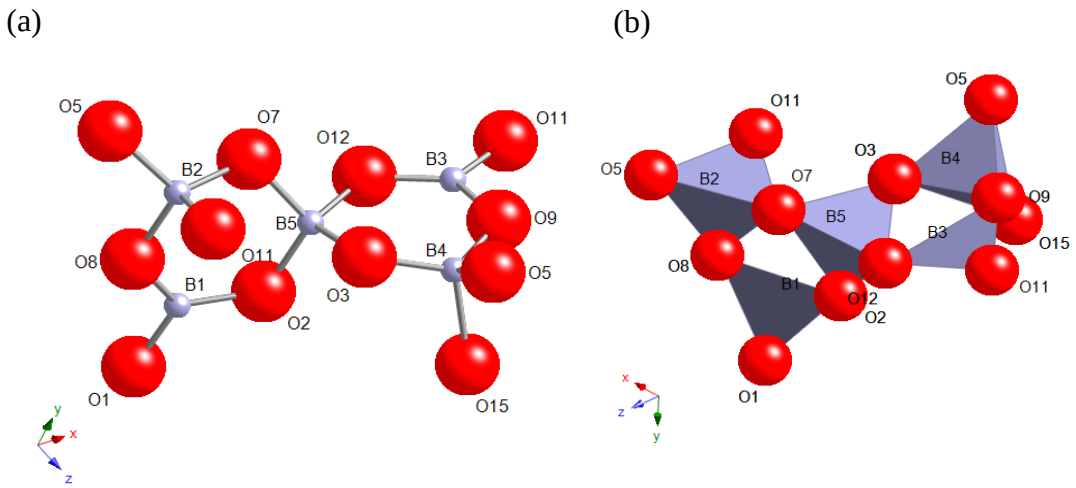

Figure 18 The pentaborate units consisting of two B_3O_3 rings, which form the FBBs in $[Pr(NO_3)(H_2O)_2][B_5O_9(OH_2)]$ (**2**) (a) as ball and stick borates and (b) as polyhedral borates.

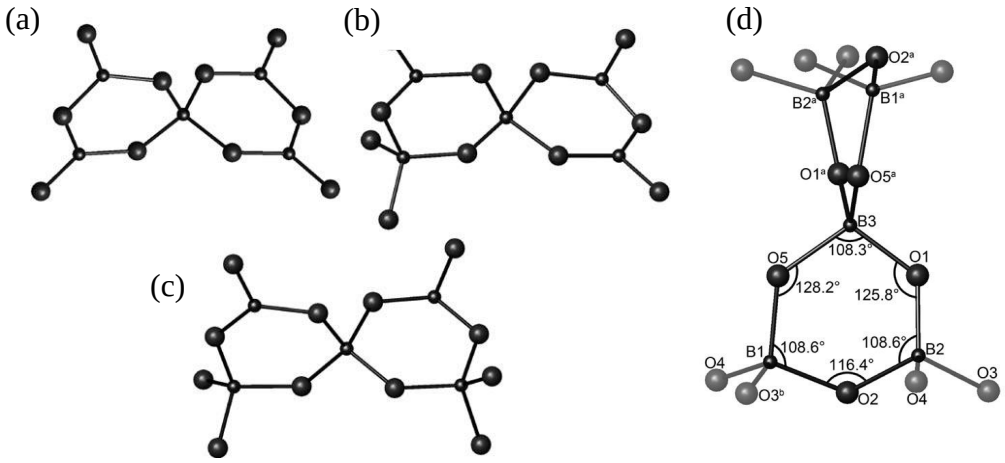

Figure 19 Showing three known pentaborate FBBs of (a) B_5O_{10} units of 5 : [(5 : 4Δ + T)], (b) B_5O_{11} units of 5 : [(5 : 3Δ + 2T)] (c) B_5O_{12} units of 5: [(5 : 2Δ + 3T)] (Small spheres – B, large spheres – O)[11] and (d) 5 : [(5 : 5T)]. (adapted from *Eur. J. Inorg. Chem.* **2010**, 1703)[23]

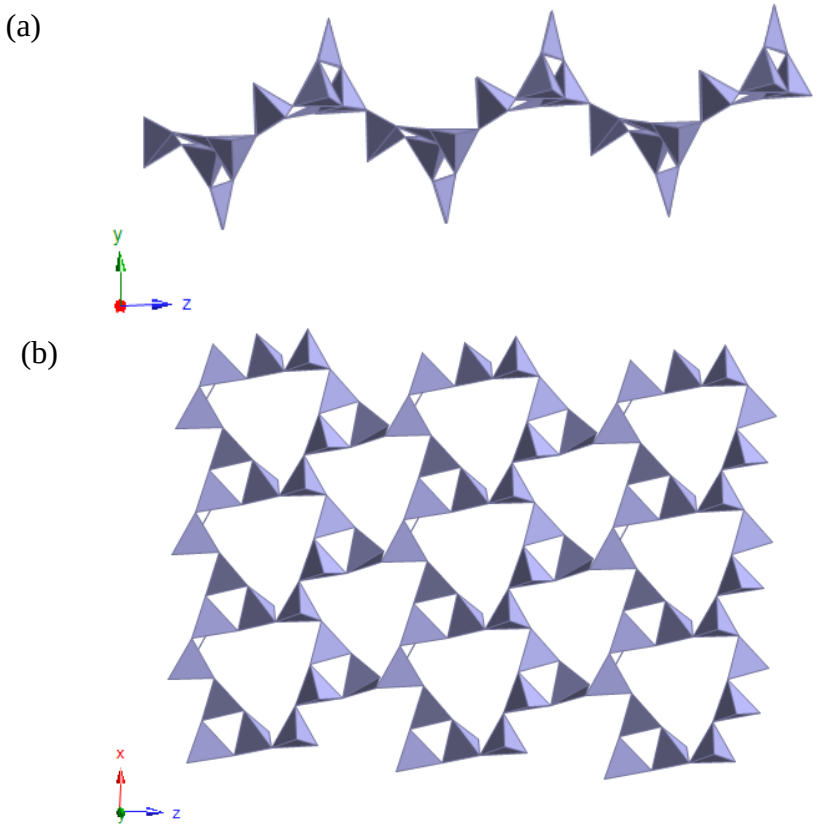

Figure 20 (a) Chains of pentaborate anions of $B_5O_9(OH_2)$ forming along the *z* axis and (b) linking pentaborate anions into sheets in the *xz* plane, forming nine-membered rings.

A range of analytical techniques were used to determine the composition and phase purity of this material. Elemental analysis indicated that the sample contains 1.34 % H (calc 1.33 %) and 2.61 % N (calc 3.08 %), which is consistent with the composition obtained from the crystal structure and the absence of crystalline impurities in the PXRD pattern. The powder XRD pattern of **2** is shown in Figure 21, where it is compared to one calculated from the crystal structure. No crystalline impurities are evident in the experimental data, and good agreement between the two patterns is apparent, suggesting that the crystal structure of **2** is representative of the bulk phase.

Use of $PrCl_3.xH_2O$ instead of $Pr(NO_3)_3.xH_2O$ as the lanthanide source resulted in the formation of a different and less crystalline phase as determined from powder X-ray diffraction measurements, therefore implying that nitrate is present within this phase.

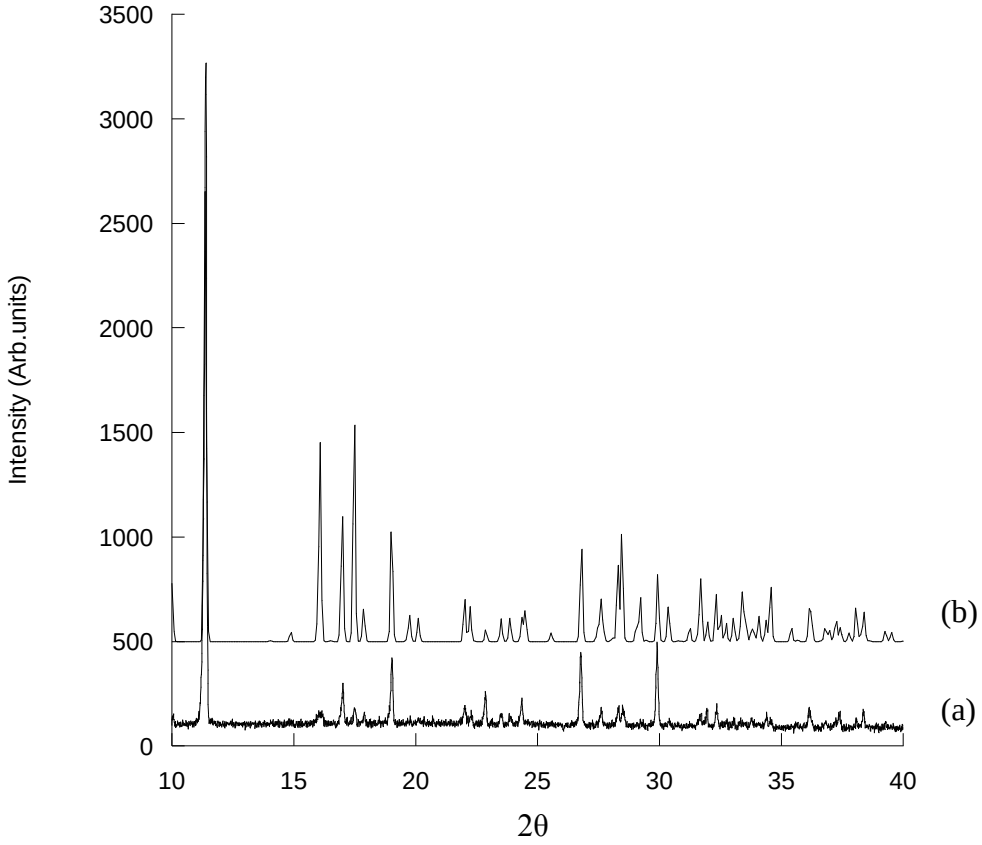

Figure 21 Powder XRD pattern (Cu K_α radiation) of (a) $[Pr(NO_3)(H_2O)_2][B_5O_9(OH_2)]$ and (b) diffraction pattern calculated from the crystal structure.

The TGA trace of $[Pr(NO_3)(H_2O)_2][B_5O_9(OH_2)]$ is shown in Figure 22 and displays two mass losses below 700 °C. The first mass loss of 14.3 % below 625 °C corresponds to the dehydration of the material and also commencement of the loss of the nitrate group (calc – 10.9 %). The decomposition of the phase is complete by 700 °C following an additional mass loss of 9.8 %, which corresponds to total loss of the nitrate anion. Total mass loss of 24.1 % which corresponds well to the calculated total mass loss of 25.5 %. Powder X-ray diffraction showed the residue to be $Pr(BO_2)_3$ and an amorphous product of B_2O_3 should also be present giving an overall composition of PrB_3O_9.

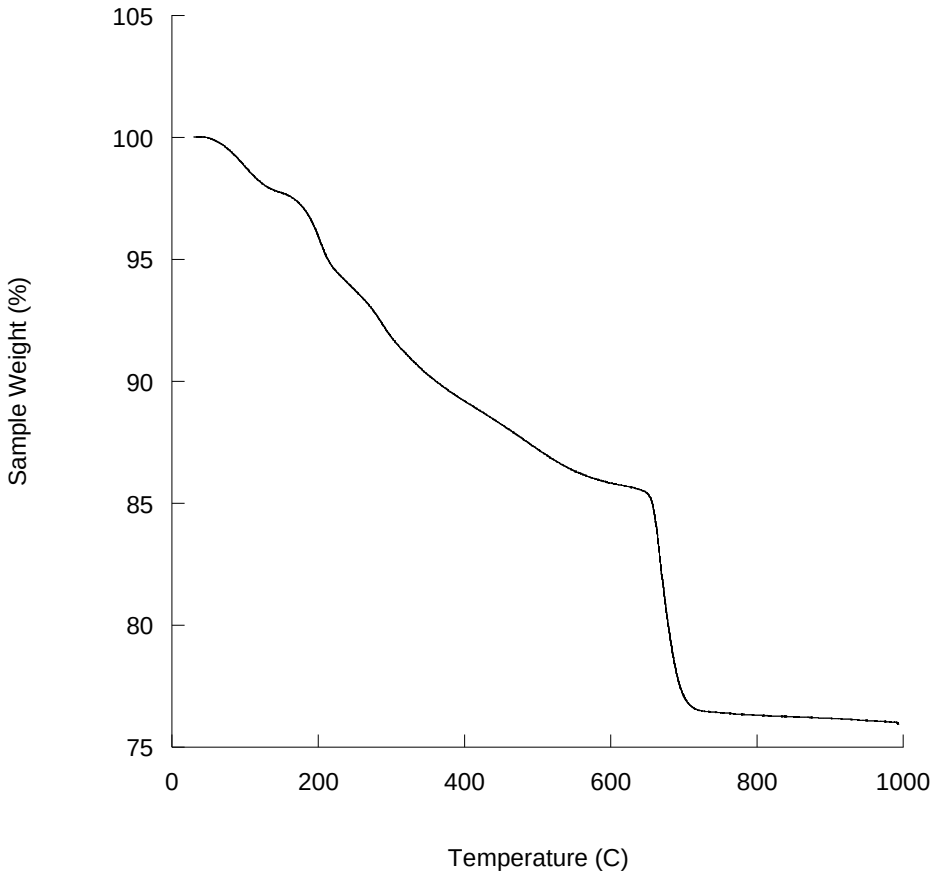

Figure 22 TGA trace of $[Pr(NO_3)(H_2O)_2][B_5O_9(OH_2)]$

The FTIR spectrum is shown in Figure 23 and has a broad band due to an O-H stretch at approximately 3187 cm^{-1} and a band due to the bending mode of water at 1619 cm^{-1}. The other features of the spectrum are due to the pentaborate anions present within the structure. Frequencies characteristic of the antisymmetric and

symmetric stretching modes of triangular BO_3 are observed at 1459, 1348, and 920 cm^{-1} and frequencies characteristic of the antisymmetric and symmetric stretching modes of tetrahedral BO_4 are observed at 1047, 818 and 744 cm^{-1}. There are also frequencies characteristic of the in-plane bending modes B-O-H at 1184 cm^{-1} and the out-of-plane bending mode of B-O in BO_3 at 650 cm^{-1}. The nitrate stretch is also expected at 1348 cm^{-1}. The FTIR spectra demonstrating the presence of the two different borate units of triangular and tetrahedral coordination present within the structure and therefore the spectrum is found to differ to that of pure boric acid due to BO_4 groups being present therefore more bands are observed within the recorded spectrum. The borate frequencies detected are found to be consistent with compounds containing triangular and tetrahedral borate anions reported in recent literature.[16, 18, 21, 27, 42]

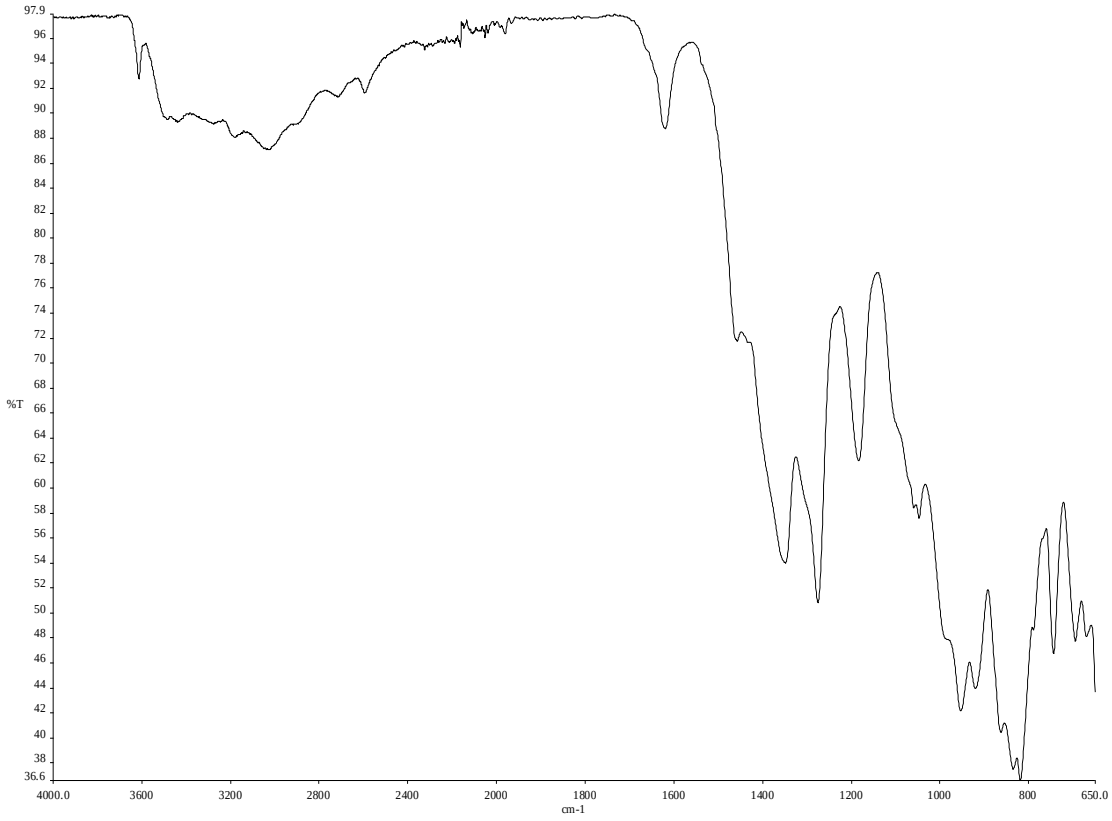

Figure 23 FTIR spectra of $[Pr(NO_3)(H_2O)_2][B_5O_9(OH_2)]$

Channels are found in this phase, along the *x* axis as shown in Figure 16, with dimensions of 9.3 Å, measuring the O - O distance across the channel in the *z* axis.

Treatment of this material under vacuum at 120 °C, showed a BET surface area of 4.52 m^2/g and a type II isotherm, indicating that this material is non-porous to N_2. Analysis of **2** using PLATON indicated that there are no solvent accessible voids in this phase. This material may not posses porosity as the coordinated nitrogen anions block the entrance to the channels therefore no access to the channels is available. Data is provided in the appendices.

This phase is found to be similar to a phase recently reported in the literature of composition $[Ce(B_5O_8(OH))NO_3].3H_2O$, Figure 24.[13] This structure consists of layers of $[Ce(B_5O_9)]$ units, consisting of nine membered ring windows, in which the cerium cations with water and nitrate coordinated reside in the centre, leading to the formation of a three-dimensional structure with large cavities. The FBBs in this structure are noted as 5 : [(5 : 3Δ + 2T)] which differ slightly to the fundamental building unit as found in **2** of 5 : [(5 : 2Δ + 3T)].

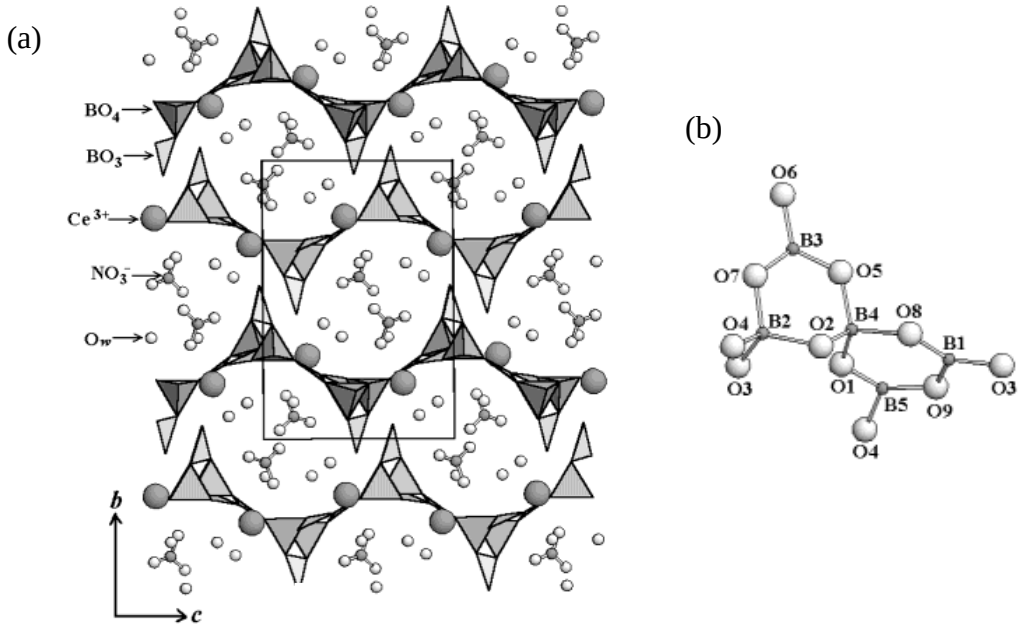

Figure 24 (a) Structure of $[Ce(B_5O_8(OH))NO_3].3H_2O$ and (b) the fundamental building blocks found within the structure.[13]

5.3.4 Characterisation of $[Gd(B_6O_{13}H_3)][BO_3H_2]$ (3)

$[Gd(B_6O_{13}H_3)][BO_3H_2]$ (**3**) has been synthesised via a boric acid flux method. Single crystal X-ray diffraction data has shown that it adopts a triclinic structure with the space group $P\bar{1}$, shown in Figure 25, with the main crystallographic and refinement data summarised in Table 1 and detailed bond lengths provided in Appendix D. This phase has also been successfully synthesised with Ln = Eu and Sm, powder XRD patterns are shown in Figure 26, characterising data of each phase is provided in the appendix, although it is noted that these lanthanides form less crystalline phases when compared to Ln = Gd.

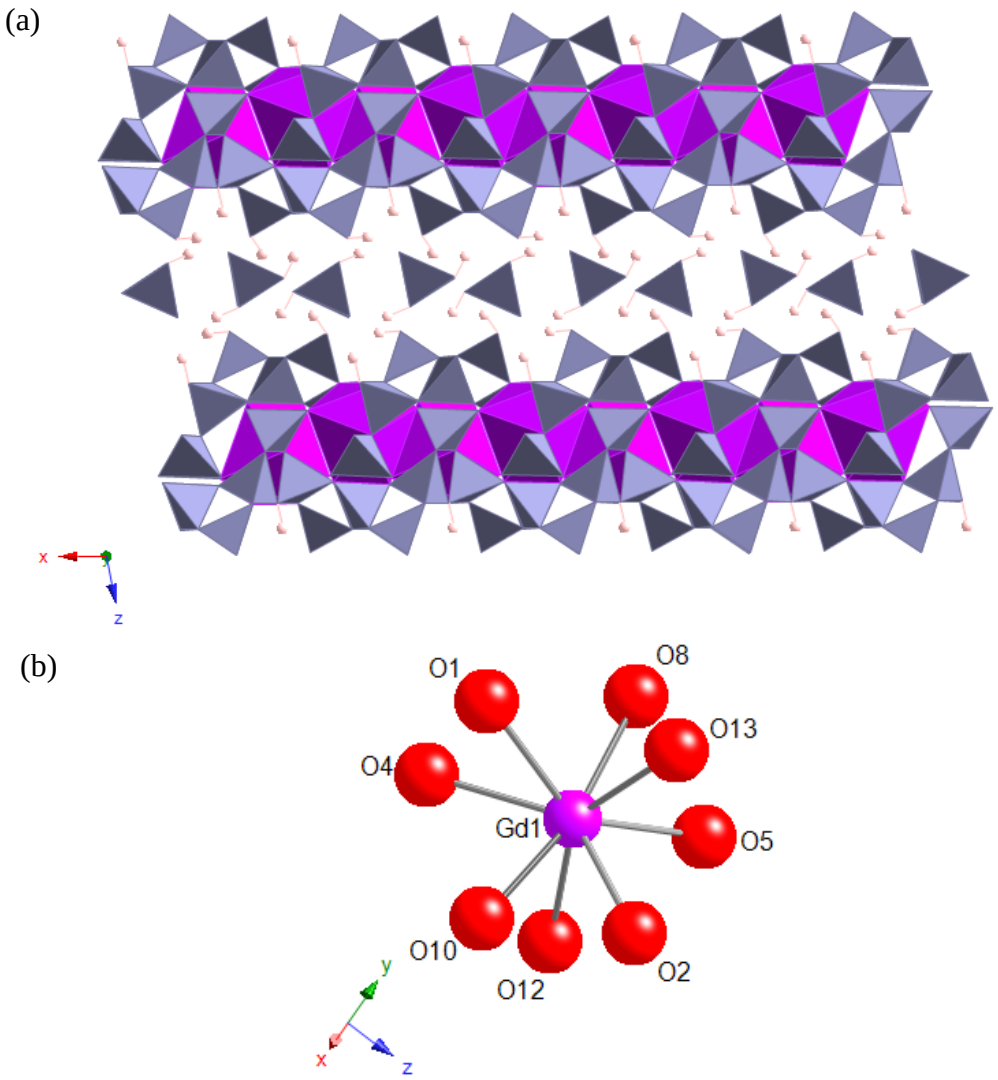

Figure 25 (a) Crystal structure of $[Gd(B_6O_{13}H_3)][BO_3H_2]$ (**3**) and (b) coordination sphere of gadolinium in (**3**). (Colour key; Gd – purple, borate (triangular and tetrahedral) – blue and H - pink, oxygen atoms omitted for clarity)

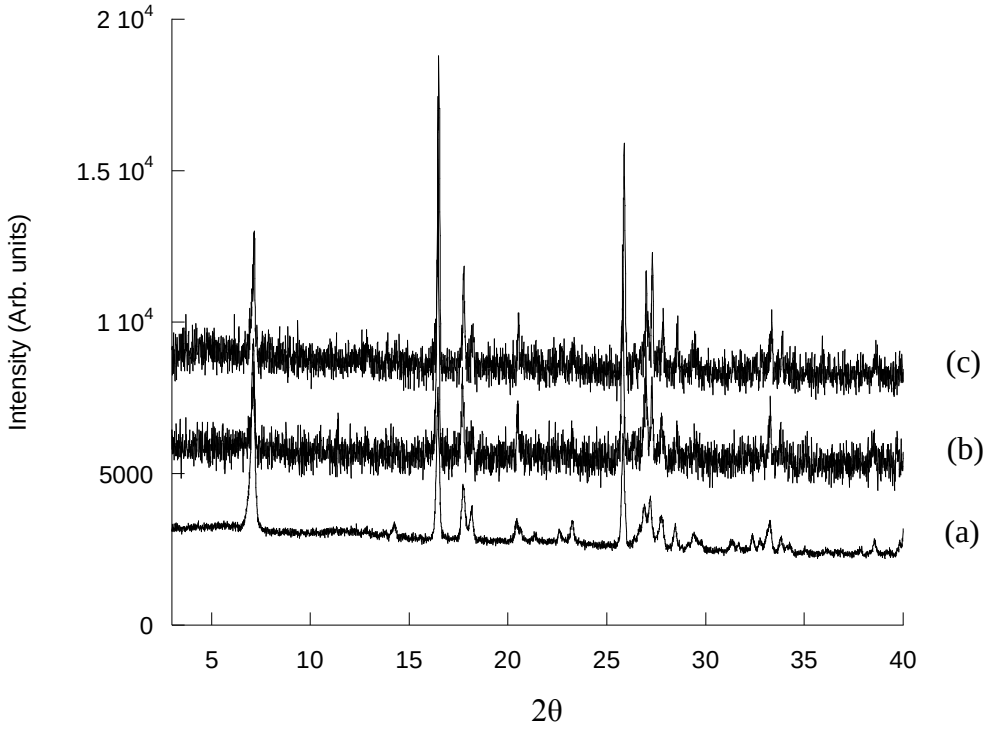

Figure 26 Powder XRD pattern (Cu K_α radiation) of (a) $[Gd(B_6O_{13}H_3)][BO_3H_2]$ and iso-structural phases (b) $[Sm(B_6O_{13}H_3)][BO_3H_2]$ and (c) $[Eu(B_6O_{13}H_3)][BO_3H_2]$.

The structure comprises infinite two-dimensional cationic inorganic lanthanide borate layers which are charge balanced by $BO_3H_2^-$ groups which reside in the interlayer gallery, in turn forming a two-dimensional layered structure. The inorganic sheets contain chains of discrete gadolinium polyhedra which are bridged together via clusters of borate anions leading to the formation of the cationic one-dimensional inorganic layer. There is one crystallographically distinct Gd atom in this structure which is eight coordinate to oxygen atoms from clusters of corner sharing BO_3 and BO_4 anions, (O(1), O(2), O(4), O(5), O(8), O(10), O(12) and O(13)). The Gd-O bond distances lie in the range of 2.3796 (10) – 2.4737 (10) Å. The triangular interlayer borate anions, $BO_3H_2^-$, interact with the inorganic layers through hydrogen bonding interactions, $O(14)\text{-}H_{interlayer}\cdots O(6)_{layer}$ 2.7381(12) Å and $O(11)_{layer}\text{-}H\cdots O(15)_{interlayer}$ 2.5628(13) Å.

There are seven crystallographically distinct boron atoms within this structure, one residing in the interlayer gallery in the form of triangular $BO_3H_2^-$ anions (B(6)), with the remaining six forming the fundamental building blocks, FBBs, of the structure. The FBBs consist of polymerised clusters of hexaborate anions $B_6O_{13}H_3$, which consist of one BO_3 Δ, one protonated BO_2OH triangle (Δ), two BO_4 tetrahedra (T) and two protonated BO_3OH tetrahedra (T), which are linked together by corner sharing oxygen atoms. The terminal oxygen atoms in the borate clusters are found to be protonated (O(7), O(9) and O(11)). The FBBs are in the form of two B_3O_3 rings consisting of alternating boron and oxygen atoms linked together by a tetrahedral boron atom (B(3)) and are orientated almost perpendicular to one another, as seen in the Pr compound discussed above, although in this phase an extra tetrahedral borate group is attached to these rings B(7), Figure 27. The FBBs are linked together through terminal bridging oxygen atoms O(10) and O(11) forming wave like chains along the *x* axis, shown in Figure 28, and in turn link together adjacent Gd centres to form a one-dimensional inorganic layer, Figure 29. The borate clusters can also be expressed by the shorthand notation of 6 : [(6 : 2Δ + 4T)], according to the chemical classification of Christ and Clark.[10] The B-O distances of the triangular boron atoms lie in the range of 1.3537(17) – 1.3917(16) Å, and 1.4234(16) – 1.4994(18) Å for the tetrahedral boron atoms. These bond distances are comparable to those found in compounds containing triangular and tetrahedral borate anions.[18]

To date no known hexaborate units of this type have been reported. As discussed above two structurally different hexaborate units have been discovered with compositions 6 : [(6 : 3Δ + 3T)] and 6 : 2 [(3 : 2Δ + T)], therefore rendering these hexaborate units found within this phase unique.

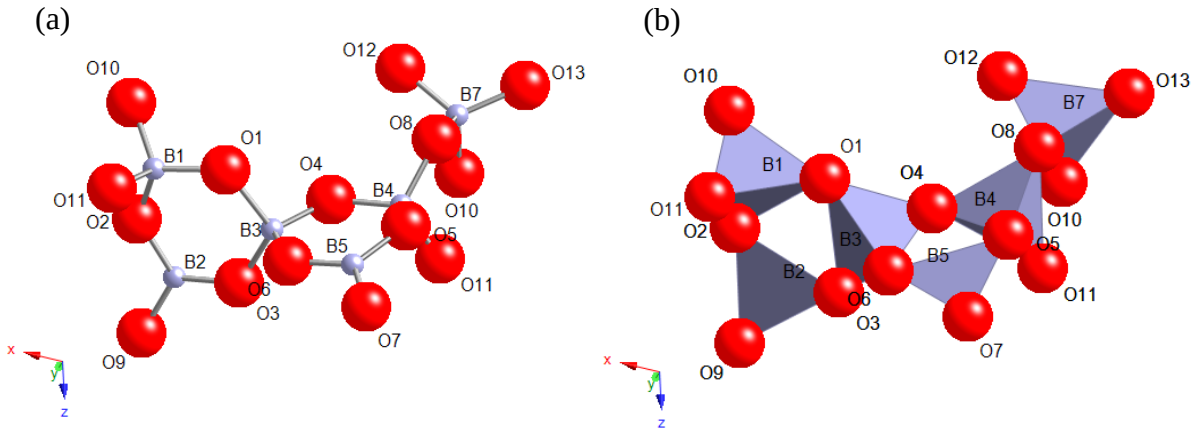

Figure 27 The hexaborate units consisting of two B_3O_3 rings with an additional tetrahedral borate group coordinated, which form the FBBs in $[Gd(B_6O_{13}H_3)][BO_3H_2]$ (**3**) (a) ball and stick borates and (b) polyhedral borates.

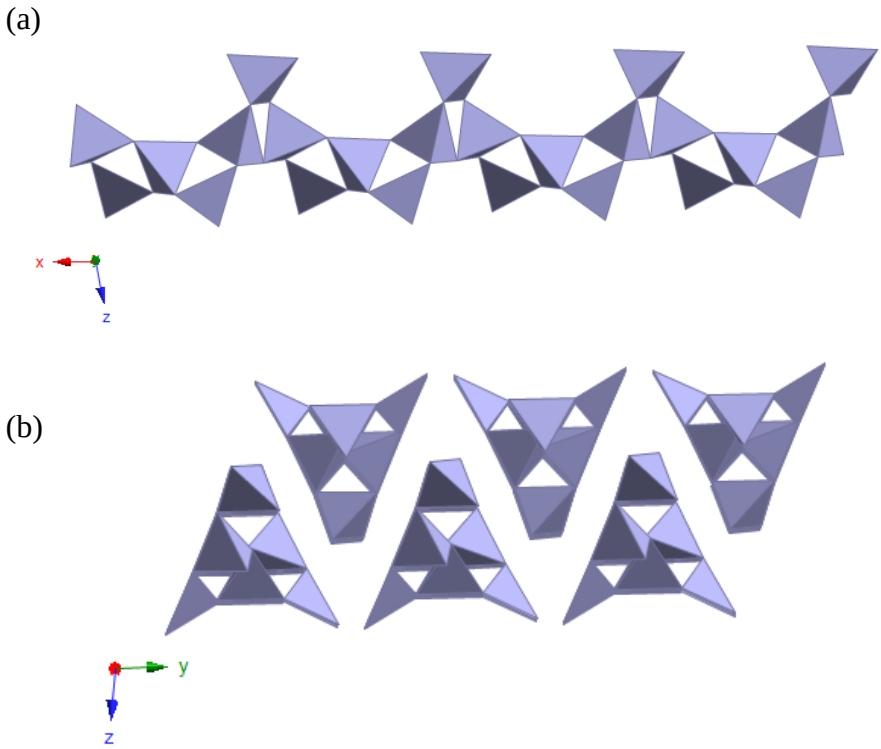

Figure 28 Repeating chains of the FBBs of $[B_6O_{13}H_3]$ found in the inorganic layers in $[Gd(B_6O_{13}H_3)][BO_3H_2]$ (**3**) (a) view along the *y* axis and (b) view along the *x* axis (Colour key; Gd – purple, B - blue with oxygen atoms omitted for clarity)

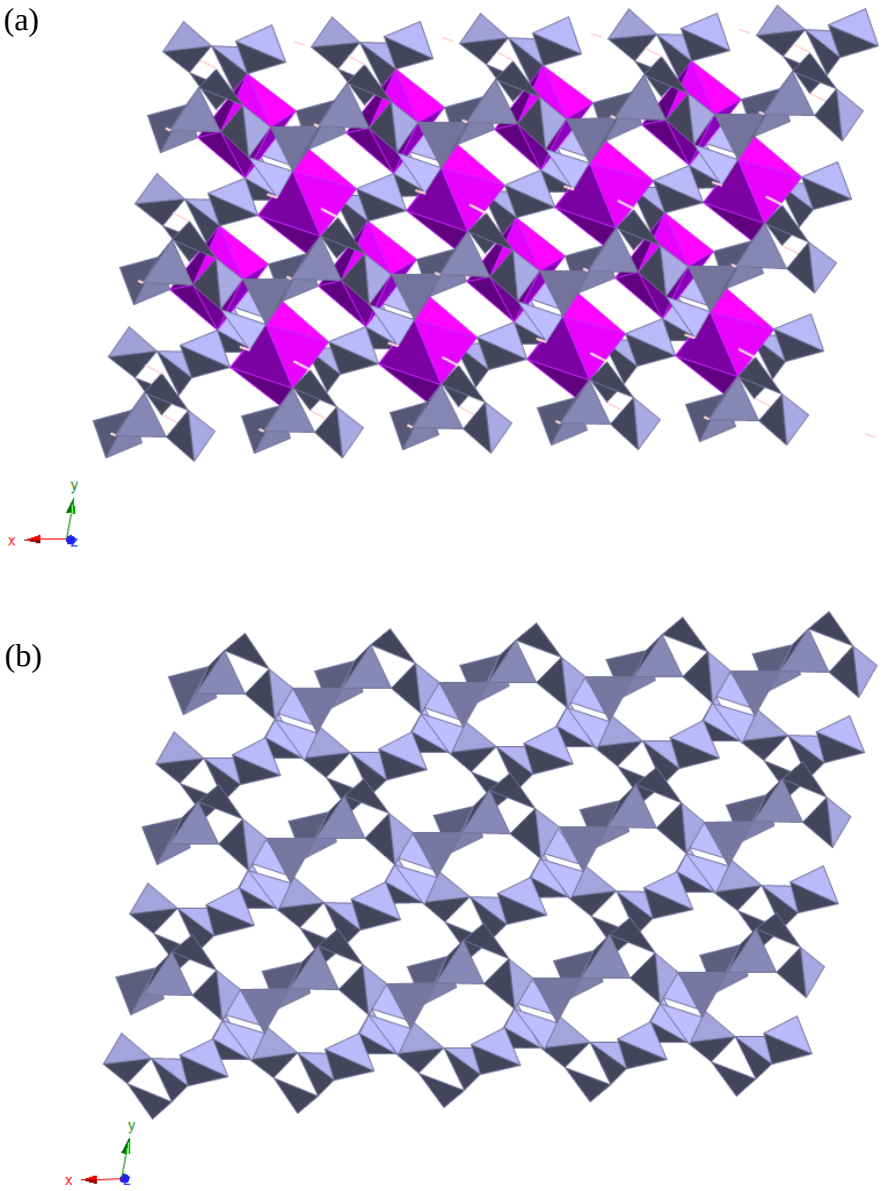

Figure 29 Layer structure of $[Gd(B_6O_{13}H_3)][BO_3H_2]$ (**3**) (a) including Gd cations and (b) layer structure excluding Gd cations. (Colour key; Gd - purple, B – blue with oxygen atoms omitted for clarity)

A range of analytical techniques were used to determine the composition and phase purity of this material. Elemental analysis indicated that the sample contains 1.36 % H (calc 1.02 %), which is consistent with the composition obtained from the crystal structure and the absence of crystalline impurities in the PXRD pattern. The powder XRD pattern of **3** is shown in Figure 30, where it is compared to one calculated from the crystal structure. No crystalline impurities are evident in the experimental data,

and good agreement between the two patterns is apparent, suggesting that the crystal structure of **3** is representative of the bulk phase.

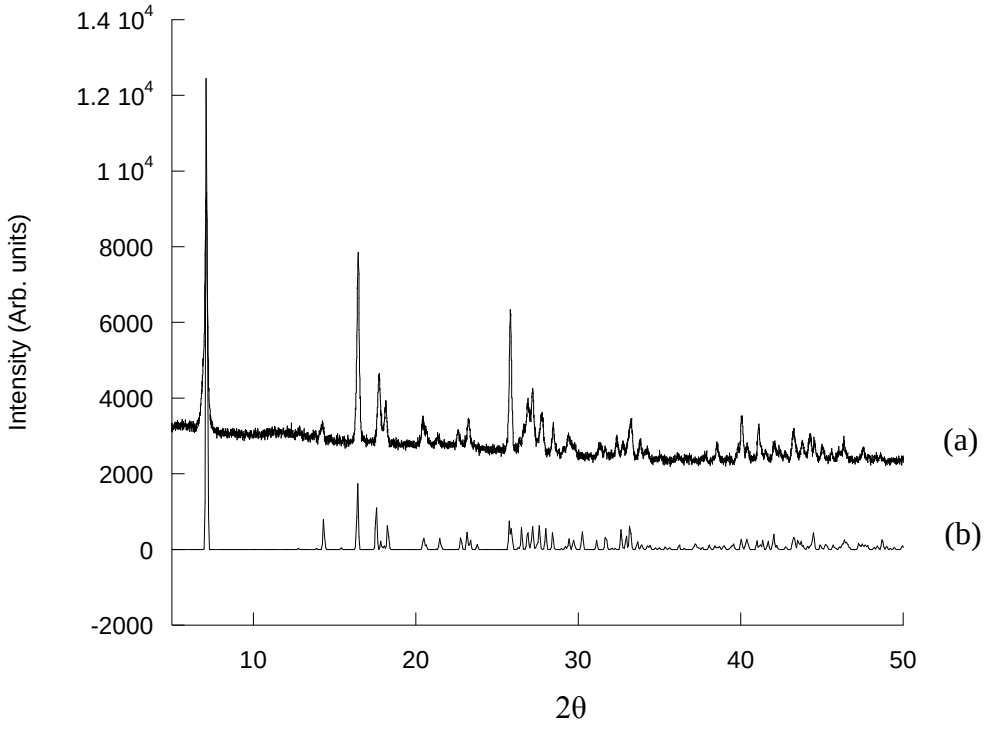

Figure 30 Powder XRD pattern (Cu K_α radiation) of (a) $[Gd(B_6O_{13}H_3)][BO_3H_2]$ and (b) diffraction pattern calculated from the crystal structure.

The TGA trace of $[Gd(B_6O_{13}H_3)][BO_3H_2]$ is shown in Figure 31 and displays two mass losses below 500 °C. The first mass loss is of 3.6 % below 400 °C corresponds to dehydration of one water molecule (calc - 3.6 %), and an additional mass loss of 10.2 % below 650 °C corresponds to further dehydration of the material (calc – 5.5 %). A total mass loss of 13.8 % is observed corresponding to the total dehydration of the material (calculated 9.1%). Powder X-ray diffraction showed the residue to be $Gd(BO_2)_3$ although an amorphous powder of nominal composition B_4O_5 should also be present leading to a final composition of GdB_7O_{11}.

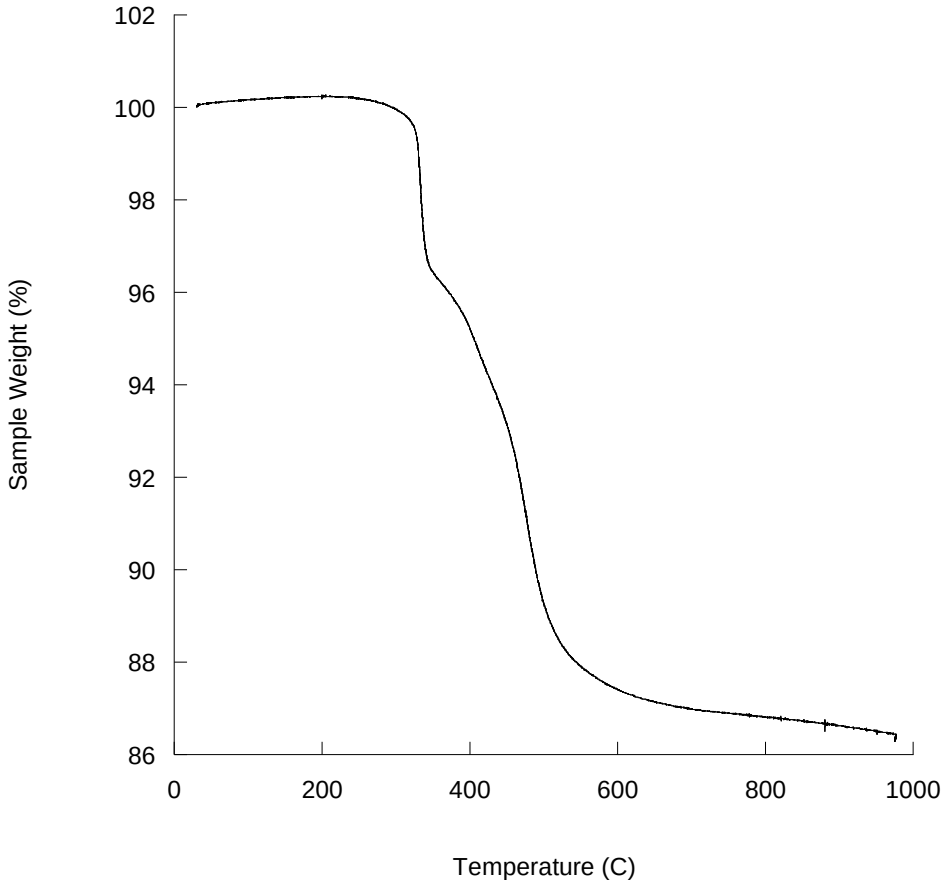

Figure 31 TGA trace of $[Gd(B_6O_{13}H_3)][BO_3H_2]$

The FTIR spectrum is shown in Figure 32 has a broad band due to an O-H stretch at approximately 3175 cm^{-1}. The other features of the spectrum are due to the hexaborate anions present within the structure. Frequencies characteristic of the antisymmetric and symmetric stretching modes of triangular BO_3 are observed at 1407, 1357, 1306 and 914 cm^{-1} and frequencies characteristic of the antisymmetric and symmetric stretching modes of tetrahedral BO_4 are observed at 1062, 808 and 732 cm^{-1}. There are also frequencies characteristic of the in-plane bending modes of B-O-H groups at 1188 cm^{-1} and the out-of-plane bending mode of B-O in BO_3 at 662 cm^{-1}. The FTIR spectra is able to show the presence of the two different borate units of triangular and tetrahedral coordination and differs to the FTIR spectrum of pure boric acid as now BO_4 groups are present therefore more bands are observed in the spectrum. The borate frequencies detected are found to be consistent with compounds containing triangular and tetrahedral borate anions reported in recent literature.[16, 18, 21, 27]

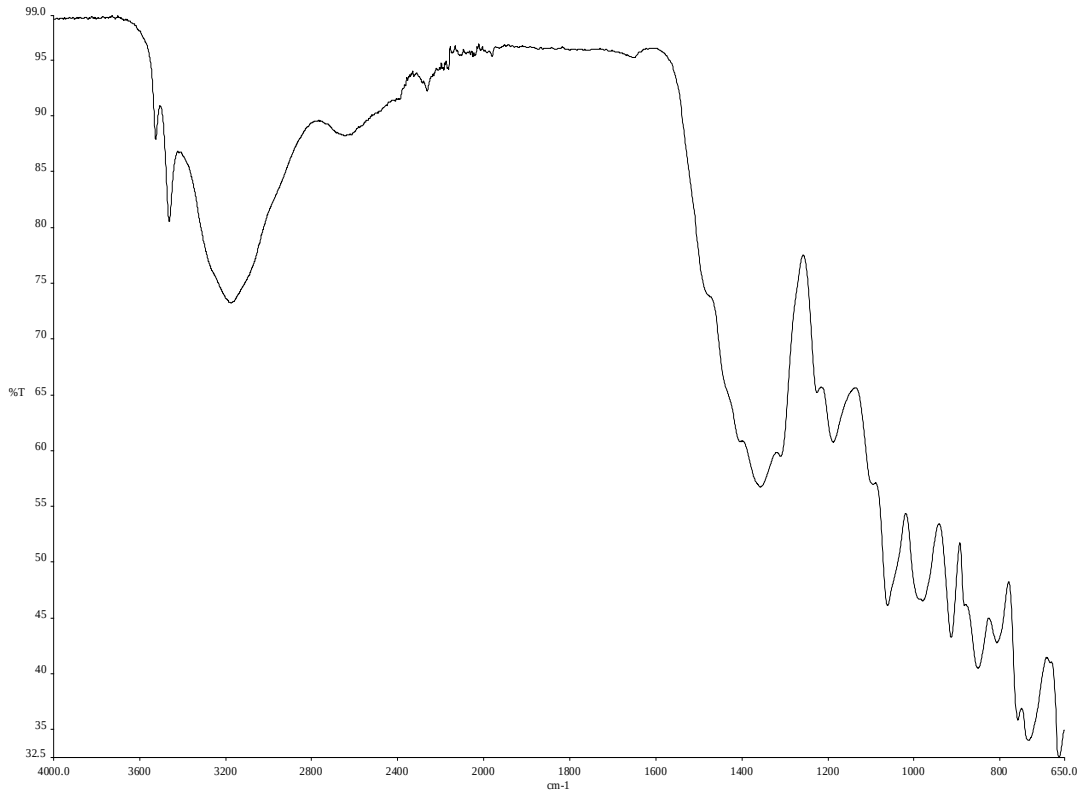

Figure 32 FTIR spectra of $[Gd(B_6O_{13}H_3)][BO_3H_2]$

The SEM image, Figure 33, shows $[Gd(B_6O_{13}H_3)][BO_3H_2]$ to exist as a microcrystalline powder, exhibiting plate-like morphology as expected for a layered phase.

Figure 33 SEM image of $[Gd(B_6O_{13}H_3)][BO_3H_2]$.

Each of the phases discussed in Sections 5.3.2 – 5.3.4, have also been attempted to be synthesised with the inclusion of extra water in the reaction medium (10 mL). Using 10 mL of water and reaction conditions of 200 °C 48 h, or on a shorter time scale of 24 h, leads to no resultant powder being produced post hydrothermal synthesis. When leaving these solutions, for slow evaporation crystallisation, crystals are produced although powder X-ray diffraction measurements have confirmed that these crystals are that of the starting material boric acid, as shown in Figure 34. Therefore it may be concluded that the addition of a small amount of water (90 µL) is a required addition for the formation of single crystals of the above phases.

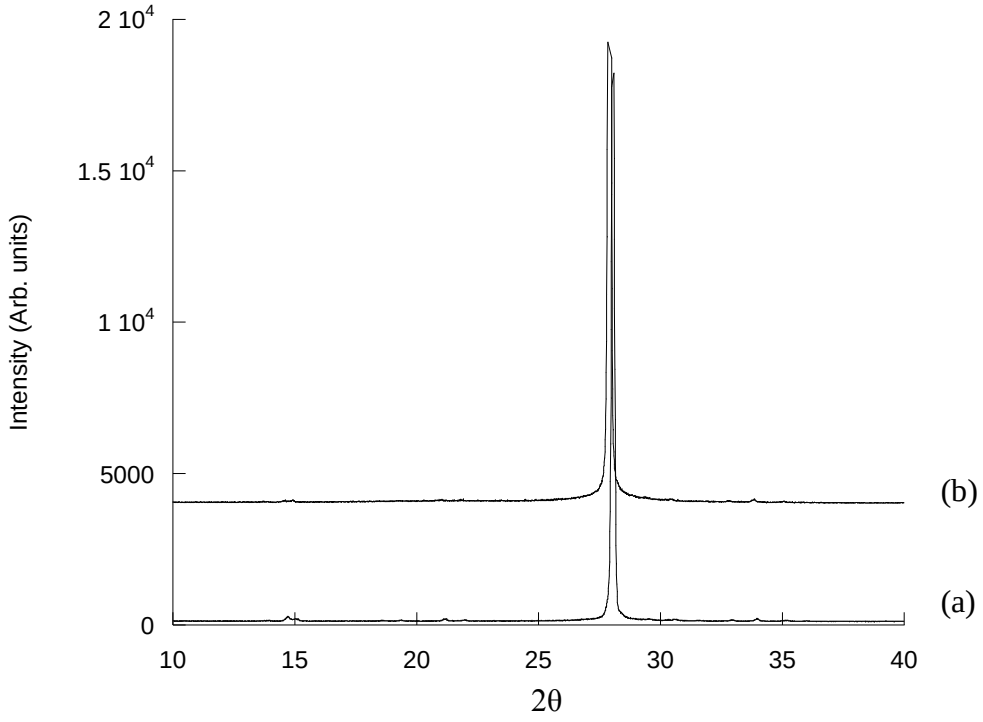

Figure 34 Powder XRD pattern (Cu K_α radiation) of (a) boric acid (BO_3H_3) and (b) post synthesis in the attempted formation of $[Gd(B_6O_{13}H_3)][BO_3H_2]$ with 10mL water in the synthesis, forming boric acid.

5.4 Anion Exchange

5.4.1 Anion Exchange Properties of $[Gd(B_6O_{13}H_3)][BO_3H_2]$

The anion exchange capability of the layered gadolinium hexaborate phase was tested, although this was found to be largely unsuccessful. Anion exchange reactions were performed using dicarboxylates or inorganic species as the exchanging anion and were typically performed at either room temperature overnight, or if anion exchange did not occur the temperature was increased to 60°C and/or the exchange reaction was performed on a longer time scale. Details of successful syntheses are given below. The synthesis of the host material and also anion exchange reactions are also discussed in Chapter 6.

Perrhenate was used as a model for pertechnetate which is a radioactive pollutant and known to intercalate into NDTB-1, although anion exchange proved unsuccessful here. Oxalate was the only anion found to display interesting exchange for this material. This reaction was performed at room temperature in 10 mL H_2O overnight. PXRD patterns of the host compared to the exchange material are shown in Figure 35.

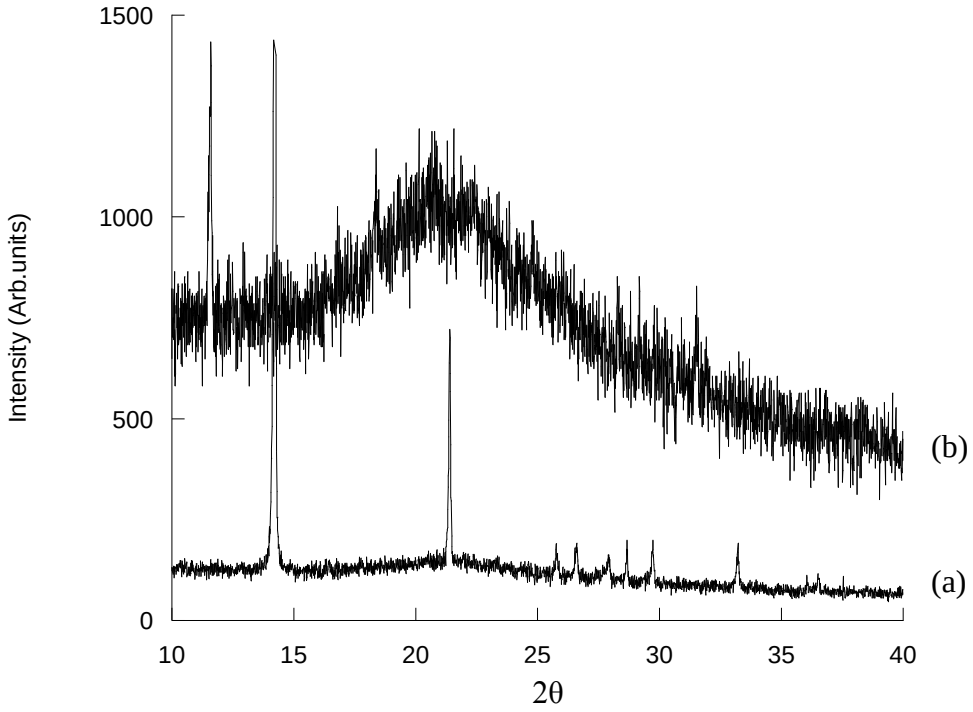

Figure 35 Powder XRD pattern (Cu K_α radiation) of (a) $[Gd(B_6O_{13}H_3)][BO_3H_2]$ (**3**) and the anion exchange product (b) $[Gd(B_6O_{13}H_3)]_2[C_2O_4].4H_2O$

Elemental analysis indicated that the sample contains 1.90 % H (calc 1.37 %) and 2.50 % C (calc 2.34 %) for a composition of $[Gd(B_6O_{13}H_3)]_2[C_2O_4].4H_2O$. The FTIR spectrum, shown in Figure 36, confirms the presence of oxalate. There is a strong and broad band present due to an O-H stretch at approximately 3360 cm^{-1} and a band corresponding to the bending mode of water at 1633 cm^{-1}. The other features of the spectrum are due to oxalate now being present in the structure. Frequencies characteristic of the C-O stretching modes are observed at 1693 cm^{-1} (anti-symmetric) and 1458 cm^{-1} (symmetric) respectively. Frequencies characteristic of the antisymmetric and symmetric stretching modes of triangular BO_3 are weakly observed in the region of 1400 – 1350 cm^{-1} with a bands clearly observed at 1365 and 920 cm^{-1} and frequencies characteristic of the antisymmetric and symmetric stretching modes of tetrahedral BO_4 are observed in the region 1100 – 1000 cm^{-1} and at 809 and 730 cm^{-1}. There are also frequencies characteristic the out-of-plane bending mode of B-O in BO_3 at 663 cm^{-1}.

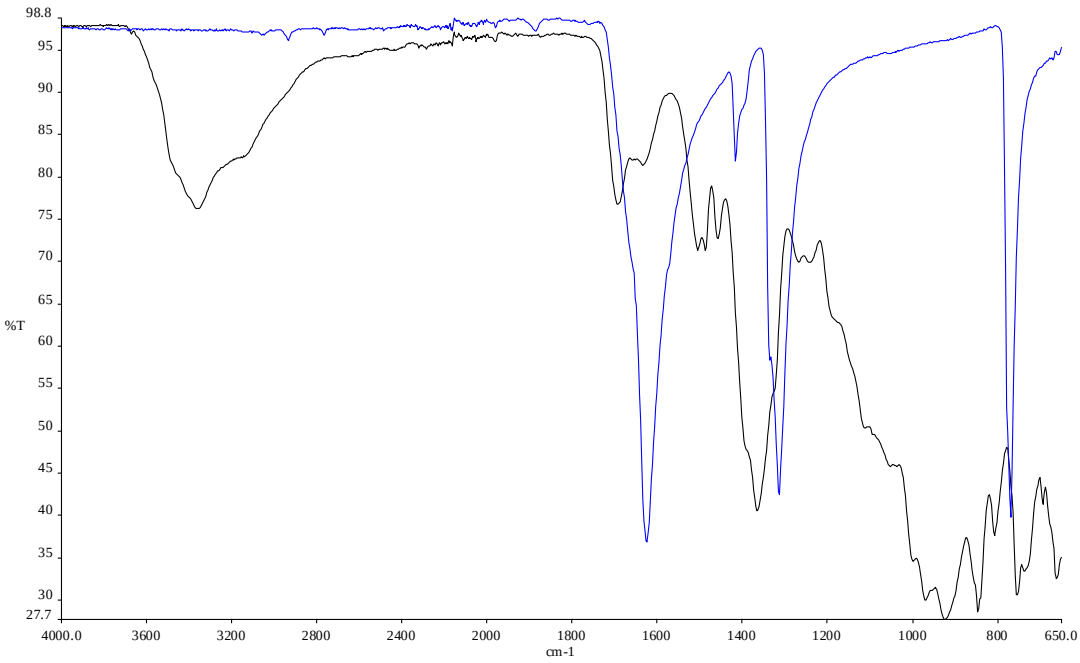

Figure 36 FTIR spectra of $[Gd(B_6O_{13}H_3)]_2[C_2O_4].4H_2O$ (black) and oxalate (blue).

No further analysis was achieved for this material due to the low amount of product formed.

Exchange reactions using other anions such as perrhenate succinate, phosphate monobasic, suberate and malonate led to no exchange being observed, although the host material was found to uptake water during the reaction in aqueous solution. The example shown is that of suberate where it is compared to a sample of the host material which had previously been stirred overnight in water, powder X-ray diffraction measurements suggest uptake of water had occurred, Figure 37.

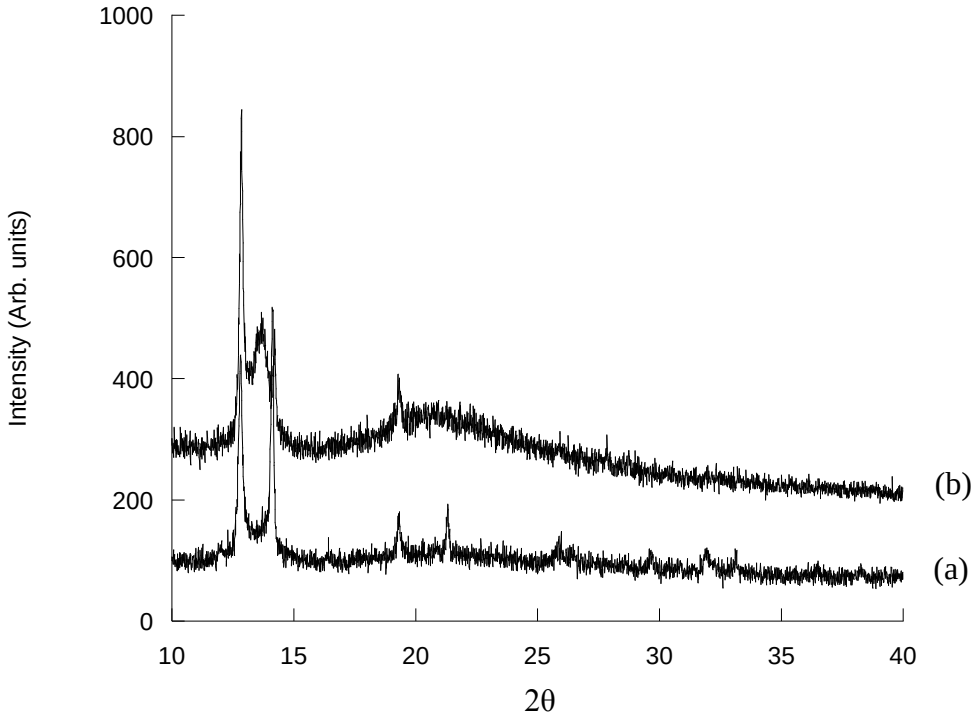

Figure 37 Powder X-ray diffraction patterns (Cu K_α radiation) of (a) post anion exchange using suberate and (b) host material stirred in water overnight.

Reactions with anions such as 2,6-NDS, phthalate, terephthalate, methane sulfonate, phosphate mono-, di-, and tribasic, tetraborate decahydrate resulted in no exchange, with or without slight loss of crystallinity in some cases when the reactions took place at room temperature or at 60 °C. The use of carbonate, molybdate or tungstate led to the decomposition of the host material post anion exchange, as shown in Figure 38.

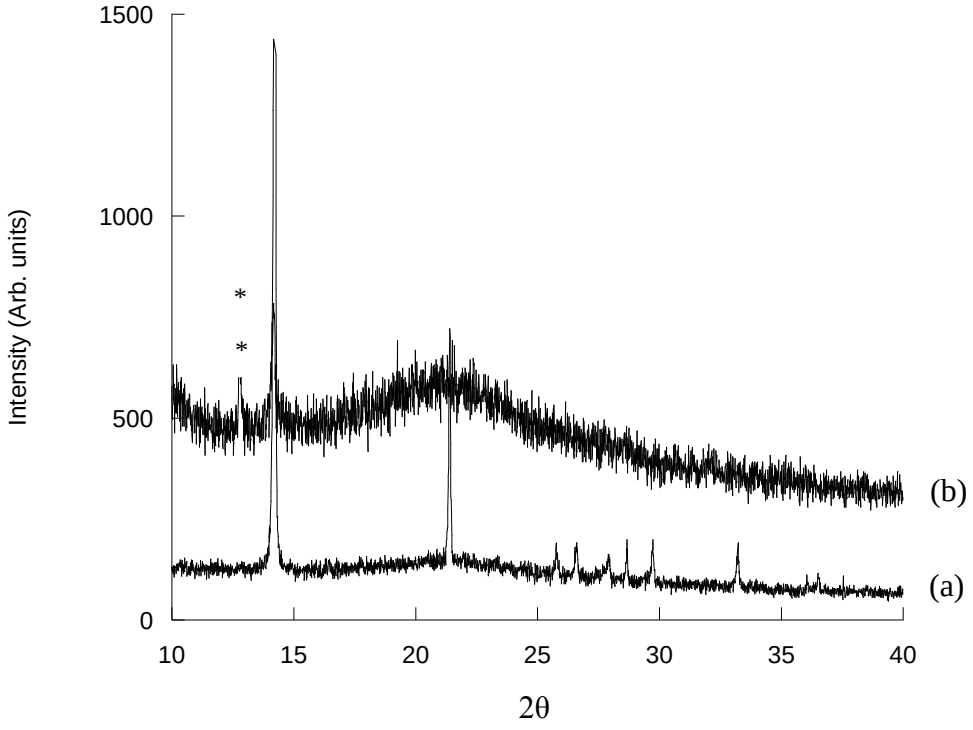

Figure 38 Powder XRD pattern (Cu K_α radiation) of (a) $[Gd(B_6O_{13}H_3)][BO_3H_2]$ (**3**) and (b) post anion exchange with carbonate at 60 °C. (* denotes up take of water in the host material)

5.4.2 Anion Exchange Properties of $[La(NO_3)(H_2O)_2][B_6O_{10}(OH_2)]$ and $[Pr(NO_3)(H_2O)_2][B_5O_9(OH_2)]$

The anion exchange capabilities of the three-dimensional pentaborate and hexaborate phases were tested. Anion exchange reactions were performed using chloride, and carbonate to exchange with coordinated nitrate. As the nitrate is found to point into the channels in both phases this might make anion exchange more accessible, although the nitrate is bound to the lanthanide centre which on the other hand may not allow exchange to take place.

Anion exchange reactions were performed at either room temperature overnight, or if anion exchange did not occur the temperature was increased to 40 °C or 60 °C, overnight. The synthesis of each host material and attempted anion exchange reaction is discussed in Chapter 6. Post anion exchange with carbonate and chloride it is noted that the phases become less crystalline therefore it is suggested that decomposition is commencing, an example of this is shown in Figure 39.

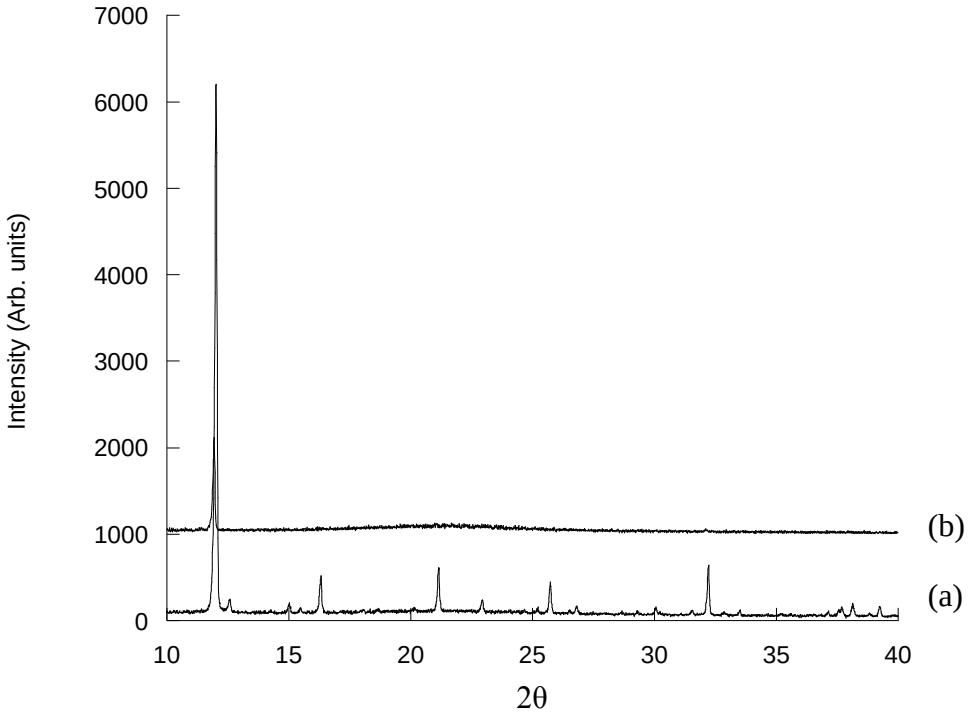

Figure 39 Powder XRD pattern (Cu K_α radiation) of (a) $[Pr(NO_3)(H_2O)_2][B_5O_9(OH_2)]$ (**2**) and (b) post exchange with chloride in methanol at room temperature in H_2O stirring overnight.

5.5 Attempted Template Reactions

As discussed in the introduction the formation of templated borate phases has been achieved using amines such as ethylenediamine and trans-1,4-diaminocyclohexane resulting in the formation of three-dimensional supramolecular frameworks with channels present. Due to these results exploratory synthesis was undertaken in an attempt to template phases $[Ln(NO_3)(H_2O)_2][B_6O_{10}(OH_2)]$ (Ln = La) and $[Ln(NO_3)(H_2O)_2][B_5O_9(OH_2)]$ (Ln = Ce, Pr and Nd) via a boric acid flux method, see Chapter 6, Section 6.5.3 for all experimental details. A variety of neutral amines and organics were incorporated in to the synthesis of these materials with the hope of forming new porous frameworks.

A range of templates were incorporated into the synthesis such as 2,2’ and 4,4’-bipyridine, aniline and tetrahydrofuran and also anions of the sodium salts of acetate, methane-, butane-, hexane- and benzenesulfonate and also phosphate mono- and

dibasic. Reaction temperature and also template concentrations were screened in order to obtain new templated phases. However screening proved unsuccessful, with the formation of either the original phase or amorphous material.

An example of a template reaction using 4,4'-bipyridine within the synthesis of the phase of $[Nd(NO_3)(H_2O)_2][B_5O_9(OH_2)]$, at 200 °C for 48 hrs, showed the formation of a less crystalline phase. The powder XRD pattern is shown in Figure 40, showing the phase produced is less crystalline than the product of $[Nd(NO_3)(H_2O)_2][B_5O_9(OH_2)]$. The main reflection is at the same position (2θ value) as the originally formed phase, therefore suggesting that there is no incorporation of the 4,4'-bipyridine template.

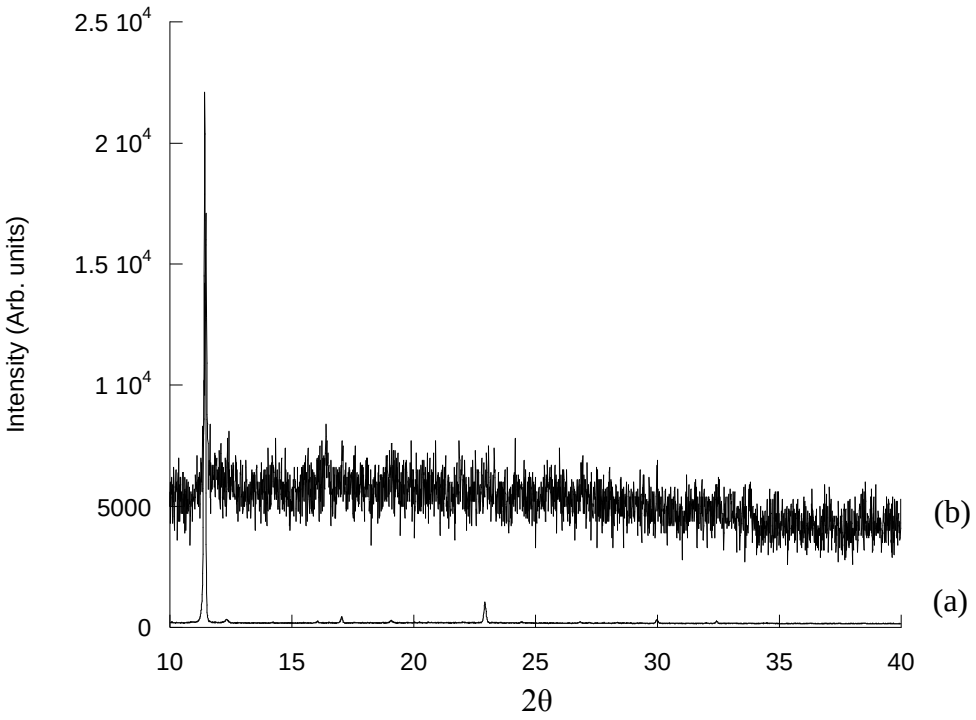

Figure 40 Powder XRD pattern (Cu K_α radiation) of (a) $[Nd(NO_3)(H_2O)_2][B_5O_9(OH_2)]$ and (b) post synthesis with incorporation of 4,4'-bipyridine.

Incorporating anions such as acetate, hexane- and benzene-sulfonate into the synthesis led to the formation of the original phases whereas phosphate mono- and dibasic in the synthesis led to the formation of lanthanide phosphates with the composition of $LnPO_4.xH_2O$.

5.6 Conclusions

Phases **1** – **3**, with compositions $[Ce(NO_3)(H_2O)_2][B_6O_{10}(OH_2)]$ (**1**) and $[Pr(NO_3)(H_2O)_2][B_5O_9(OH_2)]$ (**2**) and $[Gd(B_6O_{13}H_3)][BO_3H_2]$ (**3**) have been successfully synthesised via a boric acid flux method with their crystal structures determined by single crystal X-ray diffraction. **1** is found to form a three-dimensional network consisting of hexaborate anions which link together to form borate sheets. The Ce cations are found to reside in the centre of the rings in these borate sheets in turn forming the three-dimensional structure with one-dimensional channels present. **2** is also found to form a three-dimensional framework although this differs to **1** as it consists of pentaborate clusters. These clusters again link together to form sheets in which the Pr cations reside leading to the formation of a three-dimensional framework with one-dimensional channels present. BET measurements have indicated that phases **1** and **2** are non-porous to N_2, which may be due to the coordinated nitrate anions blocking access to the channels in both structures. Attempted synthesis of these phases with the incorporation of a template species, in order to generate larger channels in the hope of increasing porosity, proved unsuccessful.

3 is found to differ completely to that of **1** and **2** as when using smaller lanthanides a layered structure forms which consists of positively charged layers of Gd cations and hexaborate clusters, which are charge balanced by unbound borate anions residing in the interlayer gallery. Anion exchange of these unbound borate anions was performed although proved unsuccessful, maybe due to the size of the borate anions, therefore not allowing the incorporation of larger anions into the interlayer gallery.

The penta- and hexaborate units found in **1** and **2** have been previously discovered although the hexaborate unit found within the structure of **3** is found to be new.

It is observed when using the larger lanthanides, Ln = La – Nd, the coordination centres of these cations are found to be ten coordinate, whereas when using the smaller lanthanides, Sm, Eu & Gd, the coordination number decreases to eight. A plausible explanation for this could be due to the 'lanthanide contraction' effect, as Sm - Gd are smaller in size compared to La - Nd, therefore their coordination numbers are likely to be smaller. This may also be a valid reason for why a three-

dimensional phase is observed for La – Nd, whereas a layered phase is observed for the smaller lanthanides, Sm – Gd.

5.7 References

(1) Oliver, S. R. J. *Chem. Soc. Rev.* **2009**, *38*, 1868.

(2) Evans, D. G.; Slade, R. C. T. In *Layered Double Hydroxides*; Duan, X., Evans, D. G., Eds.; Springer-Verlag Berlin: Berlin, 2006; Vol. 119.

(3) Poudret, L.; Prior, T. J.; McIntyre, L. J.; Fogg, A. M. *Chem. Mat.* **2008**, *20*, 7447.

(4) McIntyre, L. J.; Jackson, L. K.; Fogg, A. M. *Chem. Mat.* **2008**, *20*, 335.

(5) Millet, P.; Bastide, B.; Pashchenko, V.; Gnatchenko, S.; Gapon, V.; Ksari, Y.; Stepanov, A. *J. Mater. Chem.* **2001**, *11*, 1152.

(6) Ok, K. M.; Halasyamani, P. S. *Inorg. Chem.* **2002**, *41*, 3805.

(7) Goulding, H. V.; Hulse, S. E.; Clegg, W.; Harrington, R. W.; Playford, H. Y.; Walton, R. I.; Fogg, A. M. *J. Am. Chem. Soc.* **2010**, *132*, 13618.

(8) McIntyre, L. J.; Prior, T. J.; Fogg, A. M. *Chem. Mat.* **2010**, *22*, 2635.

(9) Wang, S. A.; Alekseev, E. V.; Juan, D. W.; Casey, W. H.; Phillips, B. L.; Depmeier, W.; Albrecht-Schmitt, T. E. *Angew. Chem.-Int. Edit.* **2010**, *49*, 1057.

(10) Christ, C. L.; Clark, J. R. *Phys. Chem. Miner.* **1977**, *2*, 59.

(11) Touboul, M.; Penin, N.; Nowogrocki, G. *Solid State Sci.* **2003**, *5*, 1327.

(12) Burns, P. C.; Grice, J. D.; Hawthorne, F. C. *Can. Mineral.* **1995**, *33*, 1131.

(13) Li, L. Y.; Jin, X. L.; Li, G. B.; Wang, Y. X.; Liao, F. H.; Yao, G. Q.; Lin, J. H. *Chem. Mat.* **2003**, *15*, 2253.

(14) Polinski, M. J.; Wang, S. A.; Alekseev, E. V.; Depmeier, W.; Albrecht-Schmitt, T. E. *Angew. Chem.-Int. Edit.* **2011**, *50*, 8891.

(15) Wang, S. A.; Villa, E. M.; Diwu, J. A.; Alekseev, E. V.; Depmeier, W.; Albrecht-Schmitt, T. E. *Inorg. Chem.* **2011**, *50*, 2527.

(16) Lin, J. H.; You, L. P.; Lu, G. X.; Yang, L. Q.; Su, M. Z. *J. Mater. Chem.* **1998**, *8*, 1051.

(17) Chen, X., Li, M., Chang, X., Zang, H., Xiao, W. *J. Alloy. Compd.* **2008**, *464*, 332

(18) Zheng, L. J.; Zhang, J. J.; Liu, Z. H. *Chin. J. Chem.* **2009**, *27*, 494.

(19) Zhou, Y.; Hoffmann, S.; Huang, Y. X.; Prots, Y.; Schnelle, W.; Menezes, P. W.; Carrillo-Cabrera, W.; Sichelschmidt, J.; Mi, J. X.; Kniep, R. *J. Solid State Chem.* **2011**, *184*, 1517.

(20) Yu, Z. T.; Shi, Z.; Chen, W.; Jiang, Y. S.; Yuan, H. M.; Chen, J. S. *J. Chem. Soc.-Dalton Trans.* **2002**, 2031.

(21) Wang, G. M.; Li, J. H.; Li, Z. X.; Wang, P.; Li, H. *Z. Anorg. Allg. Chem.* **2008**, *634*, 1192.

(22) Li, L. Y.; Lu, P. C.; Wang, Y. Y.; Jin, X. L.; Li, G. B.; Wang, Y. X.; You, L. P.; Lin, J. H. *Chem. Mat.* **2002**, *14*, 4963.

(23) Cong, R. H.; Yang, T.; Li, H. M.; Liao, F. H.; Wang, Y. X.; Lin, J. H. *Eur. J. Inorg. Chem.* **2010**, 1703.

(24) Wang, S.; Alekseev, E. V.; Depmeier, W.; Albrecht-Schmitt, T. E. *Inorg. Chem.* **2011**, *50*, 2079.

(25) Williams, I. D.; Wu, M. M.; Sung, H. H. Y.; Zhang, X. X.; Yu, J. H. *Chem. Commun.* **1998**, 2463.

(26) Menchetti, S.; Sabelli, C.; Trostiferroni, R. *Acta Crystallogr. Sect. B-Struct. Sci.* **1982**, *38*, 2987.

(27) Sun, H. Y.; Sun, W.; Huang, Y. X.; Mi, J. X. *Z. Anorg. Allg. Chem.* **2010**, *636*, 977.

(28) Kantor, A. P.; Yamnova, N. A.; Egorov-Tismenko, Y. K.; Dimitrova, O. V. *Crystallogr. Rep.* **2004**, *49*, 936.

(29) Ferro, O.; Merlino, S.; Vinogradova, S. A.; Pushcharovsky, D. Y.; Dimitrova, O. V. *J. Alloy. Compd.* **2000**, *305*, 63.

(30) Yang, Y.; Wang, Y.; Zhu, J.; Liu, R. B.; Xu, J.; Meng, C. G. *Inorg. Chim. Acta* **2011**, *376*, 401.

(31) Chen, Y. Q.; Liang, J. K.; Gu, Y. X.; Luo, J.; Li, J. B.; Rao, G. H. *Powder Diffr.* **2010**, *25*, 9.

(32) Ivanova, A. G.; Belokoneva, E. L.; Dimitrova, O. V.; Mochenova, N. N. *Russ. J. Inorg. Chem.* **2006**, *51*, 862.

(33) Ivanova, A. G.; Belokoneva, E. L.; Dimitrova, O. V.; Mochenova, N. N. *Crystallogr. Rep.* **2006**, *51*, 584.

(34) Cong, R. H.; Yang, T.; Wang, Z. M.; Sun, J. L.; Liao, F. H.; Wang, Y. X.; Lin, J. H. *Inorg. Chem.* **2011**, *50*, 1767.

(35) Wang, S. A.; Alekseev, E. V.; Miller, H. M.; Depmeier, W.; Albrecht-Schmitt, T. E. *Inorg. Chem.* **2010**, *49*, 9755.

(36) Belokoneva, E. L.; Ivanova, A. G.; Stefanovich, S. Y.; Dimitrova, O. V.; Kurazhkovskaya, V. S. *Crystallogr. Rep.* **2004**, *49*, 603.

(37) Sung, H. H. Y.; Wu, M. M.; Williams, I. D. *Inorg. Chem. Commun.* **2000**, *3*, 401.

(38) Zhang, H. X.; Zheng, S. T.; Yang, G. Y. *Acta Crystallogr. Sect. C-Cryst. Struct. Commun.* **2004**, *60*, M241.

(39) Wang, G. M.; Sun, Y. Q.; Yang, G. Y. *J. Solid State Chem.* **2004**, *177*, 4648.

(40) Touboul, M.; Penin, N.; Nowogrocki, G. *J. Solid State Chem.* **2000**, *150*, 342.

(41) Clark, J. R. *The American Mineralogist* **1964**, *49*, 1549

(42) Medvedev, E. F.; Komarevskaya, A. S. *Glass Ceram.* **2007**, *64*, 42.

Chapter 6
Experimental Details

6.0 Introduction

This chapter gives details of the analytical techniques and experimental details of all the research undertaken during the course of study. All chemical were purchased from either Alfa Aesar or Sigma Aldrich and used without further purification.

6.1 Analytical Techniques

6.1.1 Elemental Analysis

Carbon, hydrogen, and nitrogen analyses were performed on a FlashEA 1112 instrument by Steve Apter, Jean Ellis and George Miller in the Department of Chemistry at the University of Liverpool.

6.1.2 Fourier Transform Infrared spectroscopy

Fourier transformed infrared (FTIR) spectra of solid samples were obtained using a Perkin-Elmer Spectrum 100 spectrometer fitted with the Spectrum 100 Universal Diamond/ZnSe attenuated total reflectance (ATR) accessory. Spectra were recorded over the range of 4000-650 cm^{-1} with 4 scans at a resolution of 4 cm^{-1}.

6.1.3 Gas Sorption

The surface areas of solid samples were measured by Emma Richards, by nitrogen adsorption and desorption at 77.3 K using either a Micromeritics ASAP 2420 or a

Quantrachrome NOVA 4200 volumetric adsorption analyser. Samples were degassed at 120°C for ~12h under vacuum (10^{-5} bar) before analysis. The surface areas were calculated in the relative pressure (P/P^0) range from 0.01 to 0.05.

CO_2 sorption isotherms were recorded by Dr Darren Bradshaw using a Hiden Intelligent Gravimetric Analyser (IGA) gravimetric sorption balance at 198 K. Data was recorded following activation of the sample at 120 °C and 250°C.

6.1.4 Powder X-ray Diffraction

Powder X-ray diffraction patterns of the samples were recorded with either Cu $K_{\alpha 1}$ radiation, of wavelength 1.5406 Å, on a Stoe Stadi-P diffractometer in either Bragg-Brentano (reflection) or Debye-Scherrer (transmission) geometry or with Co $K_{\alpha 1}$ radiation, of wavelength 1.7890 Å, on a Panalytical X'pert Pro diffractometer. Reflection samples were measured in the range of 10 - 40° 2θ by mounting the sample onto a zero background holder. Transmission samples were measured in the range 3 - 40° 2θ using either a sealed 0.5mm glass capillary or by using a flat plate spinner consisting of mylar discs were the sample is secured onto the discs by a minimum amount of vacuum grease.

6.1.5 Scanning Electron Microscopy

SEM images were recorded in collaboration with Liwei Fu, at the Lairdside Laser Engineering Centre, using a FEI Phenom Desktop Scanning Electron Microscope. Powder samples were prepared at room temperature and mounted onto a double sided adhesive pad attached to a sample stud. After mounting the sample compressed gas was sprayed over the surface of the stud to remove any loose particles. The sample surfaces were then scanned under vacuum using a focused electron beam, were a detector collected the reflected secondary electrons from the sample surface and converted the beam into an image of the sample surface.

6.1.6 Single Crystal X-ray Diffraction

Three single crystal X-ray diffractometers, in different locations, were used for the determination of the structures of the crystalline phases synthesised. The location of structure determination for each sample will be identified within each chapter.

Single crystal analysis was performed at the University of Liverpool by Dr John Bacsa on a Bruker D8 diffractrometer with an APEX CCD detector, and 1.5 kW graphite monochromated Mo radiation. Unit cell refinement and data reduction were performed with SAINT v6.45a.[1] A semi-empirical absorption correction using multiple-reflections was carried out using the program SADABS V2008-1,[2] the structure was solved and refined with SHELX97.[3]

Secondly structures were solved at the National Crystallography Service, University of Southampton by Dr. Samantha Callear, Dr. Graham Tizzard, Dr. Richard Stevenson or Dr. Steve Lamond. Data was collected on a Bruker APEXII CCD diffractrometer mounted at the window of a Bruker FR591 rotating anode ($\lambda_{\text{Mo K}\alpha}$ = 0.71073 Å) and equipped with an Oxford Cryosystems cryostream device (data collected at 120(2)K). Data were processed using the Collect[4] package and unit cell parameters were refined against all data. An empirical absorption correction was carried out using SADABS.[5] The structures were solved by direct methods using SHELXS97[6] and refined on F_o^2 by full-matrix least-squares refinements using SHELXL97.[7] All non-hydrogen atoms were refined with anisotropic displacement parameters. All hydrogen atoms were added at calculated positions and refined using a riding model.

Thirdly at the National Crystallography Service, were data was collected on Beamline I19 of the Diamond Light Source, using a Crystal Logics kappa-geometry diffractrometer and a Rigaku Saturn 724þ CCD detector with a Cryostream cooler (at 120 K); Rigaku CrystalClear was used to record images.

6.1.7 Thermogravimetric Analysis

Thermogravimetric analysis (TGA) measurements were performed using a Perkin-Elmer STA6000 instrument, the sample was placed in an alumina crucible and heated to 1000 °C in an atmosphere of nitrogen at a rate of 5 °C/min.

6.1.8 *In-situ* Energy Dispersive X-ray Diffraction

In-situ Energy Dispersive X-ray Diffraction measurements were carried out on beamline F3 at the DORIS III synchrotron, HASYLAB, at DESY (Deutsches Elektronen-Synchrotron), Hamburg, Germany. Particulars of HASYLAB and station F3 will be discussed in further detail in Chapter 3, Section 3.1.

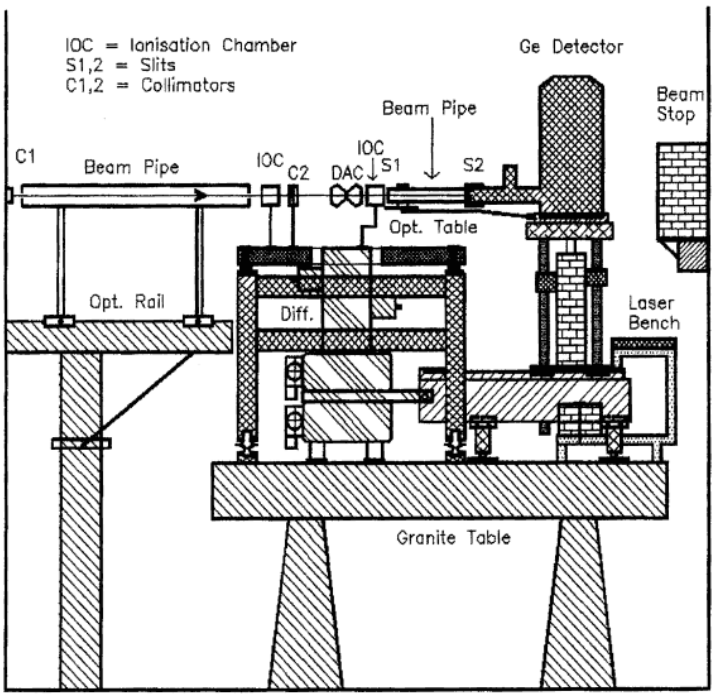

Figure 1 Schematic representation of the F3 station, HASYLAB, Germany.[8]

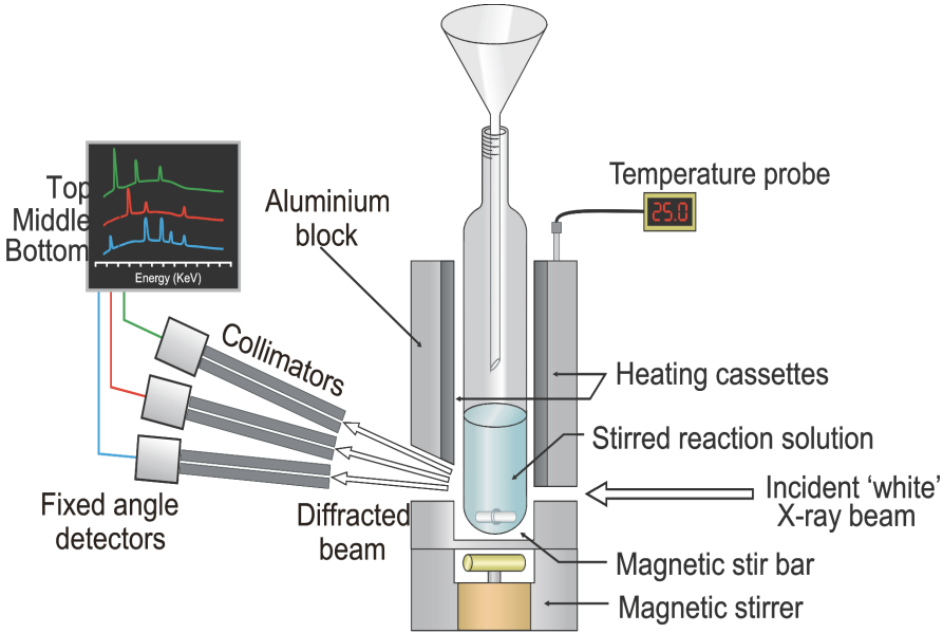

Figure 2 Schematic representation of the *in-situ* apparatus used for EDXRD measurements.

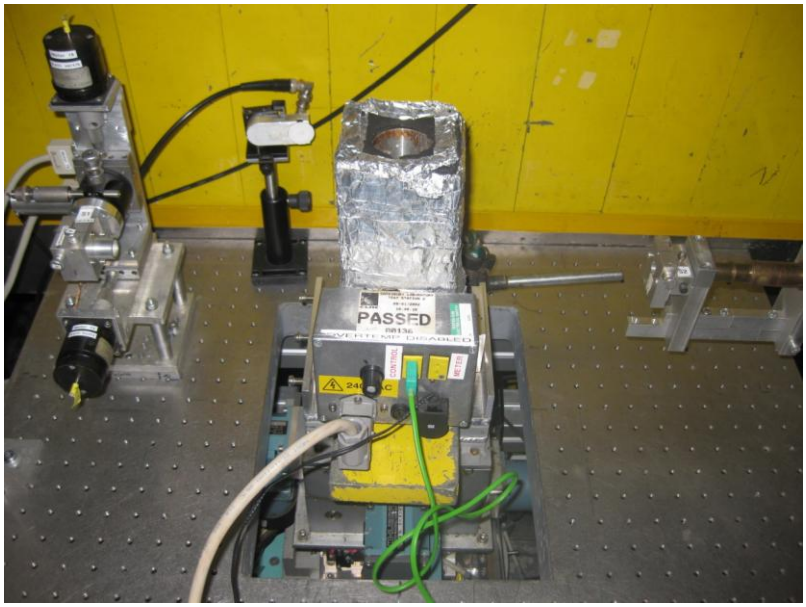

Figure 3 Apparatus used for in-situ EDXRD measurements

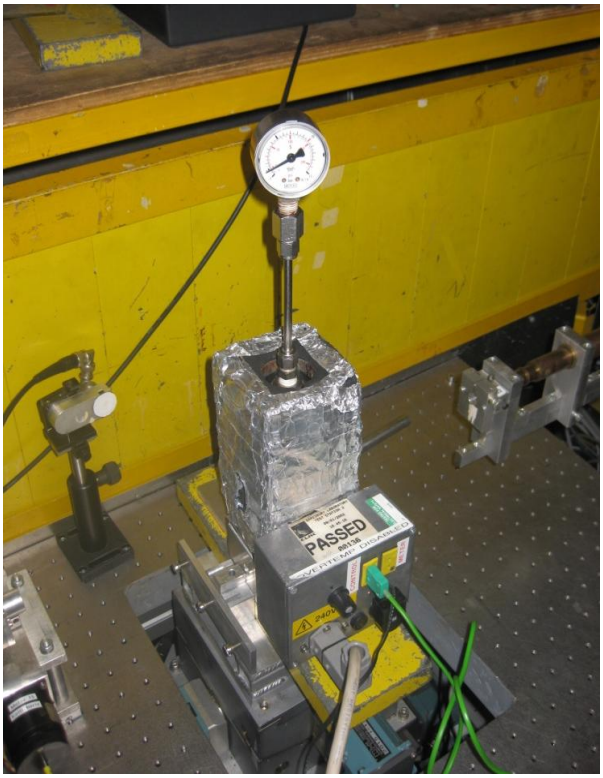

Figure 4 Apparatus set-up before measurements commenced, including the hydrothermal autoclave positioned within the thermal heating block.

Figure 5 Adapted hydrothermal autoclave used for in-situ measurements.

Figures 1-4 show the experimental set-up employed at station F3. Reactions were performed in a modified Teflon lined hydrothermal autoclave, where the walls of the autoclave have been thinned to a thickness of 0.25 and 0.3mm, to minimise absorption of X-rays. The autoclave was also fitted with an external pressure gauge to monitor the pressure gained during the reaction, Figure 5. Each reaction was homogenised by stirring the suspension with a magnetic stirrer flea to maintain a constant amount of sample was present within the X-ray beam and also to ensure that the solid material did not settle to the bottom of the autoclave. The autoclave was subsequently positioned into a temperature controlled aluminium heating block, which has been adapted over the years and converted from a circulating oil heating system to an electrical system. Both the hydrothermal autoclave and heating block were first designed by J.S.O. Evans *et al*, for prior use at the UK, SRS, Daresbury laboratory.[9, 10] To allow correct alignment the block is mounted onto a stand and has slits cut into the sides to allow the incident X-ray beam in and the diffracted beam out. The experimental rig, consisting of the reaction cell and heating block, was mounted further onto an optical bench allowing movement to achieve accurate alignment.

6.1.8.1 Calibration of Apparatus

Prior to use the apparatus requires calibration to ensure maximum diffraction intensity is achieved. Firstly the reaction vessel has to be aligned correctly both horizontally and vertically with respect to the incident X-ray beam and to the detector to achieve this maximum intensity. To ensure correct alignment X-ray sensitive paper is placed onto the centre of the reaction vessel and exposed to the X-ray beam. The beam marks the paper, allowing one to see if the reaction vessel is correctly aligned within the beam. If it is not aligned correctly the reaction vessel may be moved accordingly to the correct position.

After alignment calibration of the apparatus was achieved by using a sample which has a known set of bragg reflections and energies in keV. Caliglass, consisting of elements Mo, Sn, Ba, Gd and W, was used for our calibration as each element within the sample has known K_α and K_β resonances. This allowed the determination of the

energy range of the detector by recording the channels of highest intensity of each known Bragg reflection. As channel number is proportional to energy the calibration constants were able to be determined from a plot of energy vs channel number.

$$E = a + bC$$

Equation **1**

From the linear relationship, Equation 1, the calibration constants were determined. The constants determined are deduced from the intercept which is the offset energy (keV), corresponding to the energy of the 1st channel, and the gradient of the linear relationship of energy and corresponding channel (keV/Channel), corresponding to the energy difference per channel.

6.1.8.2 Data Collection

Data was collected in the range of 13.78 - 64.28 keV over a variety of reaction temperatures and times depending on the laboratory synthesis and the length of time the reaction proceeded for. Fixed detector angles were in place between 1.19 - 2.29°, being selected from the expected position of the product reflection, avoiding any overlap with the lanthanide and metal K_α and K_β resonances, and from taking into account any absorption due to the hydrothermal cell. The position of the detector was controlled by a series of motors allowing it to be driven remotely to the required angle. Best results were obtained by collimating the beam to 0.2 x 0.2 mm. Spectra were recorded for each synthesis with acquisition times of 60s, with the first spectrum being recorded at the start of heating of the reaction mixture. Lanthanide K_α and K_β resonances were observed alongside Bragg reflections in the collected spectra and were found to remain at a constant intensity throughout the reaction therefore indicating that a steady amount of sample suspension had been maintained in the X-ray beam.

Reactions were carried out using the standard synthesis produced in the laboratory but with doubled concentrations of all starting reagents, this in turn intensified the

Bragg reflections seen and also lowered the signal to noise ratio. Synthetic details are found below for each laboratory synthesis. For kinetic analysis of the formation of $[La(H_2O)WO_4]_2$[1,5-NDS], reactions were performed at temperatures of 120, 145, 165, 180 and 200 °C until the reaction was complete, with other reactions performed in the temperature range of 165 – 220 °C depending on their *ex-situ* synthesis.

6.1.8.3 Data Analysis

A PC coupled to a multi-channel analyser was used for data collection and storage in the *in-situ* experiments. The resulting spectra were evaluated and analysed with the tool 'IDL 7.1 virtual machine application' f3_extens and f3_tool which was obtained from station f3. Once spectra had been recorded Gaussian curves were fitted to the data and the area under the peak of each Bragg reflection in question was integrated using the f3_tool programme. The integrated areas were then converted into extent of reaction at time t, α(t). Once α(t) had been calculated the data was then fitted to the Avrami Erofe'ev rate expression and transformed in to a Sharp-Hancock plot. Details of data handling are discussed more in depth in Chapter 4, section 4.5.

6.2 Experimental Details for Chapter 2

6.2.1 Synthesis of $[Ln(H_2O)MO_4]_2$[A] (M= Mo or W, A= 1,5-NDS or 2,6-NDS) & $[Ce(H_2O)MoO_4]_2$[Fumarate]

This experimental method was adapted from the literature preparation of J.J. Luo and L. Xu.[11] Each phase was successfully synthesised via a hydrothermal route. In a typical synthesis, 0.69 mmol of $LnCl_3.xH_2O$, 0.44 mmol of Na_2MoO_4 or Na_2WO_4, and 0.44 mmol of disodium 1,5-naphthalenedisulfonate (1,5-NDS), disodium 2,6-naphthalenedisulfonate (2,6-NDS) or sodium fumarate, were dissolved in 10 mL of deionized water, and the solution was placed in a 23 mL Teflon-lined hydrothermal autoclave. The reaction mixture containing the naphthalenedisulfonates was then

heated at 165 °C for 14 h, or 145 °C for the fumarate reaction mixture, before being cooled slowly back to room temperature at a rate of 0.1 °C/min. The mixture was subsequently filtered under suction and the resulting crystalline solid washed with water and ethanol before being left to dry in air.

Powder X-ray diffraction measurements revealed the phase containing Lanthanum, WO_4^{2-} and 2,6-NDS to be biphasic. The major phase was found to have a chemical composition of $[La(H_2O)WO_4]_2$[2,6-NDS] and the minor phase $[La_2(H_2O)_2W_2O_8]$[2,6-NDS]. A variety of reaction conditions were screened, for example change in reaction temperature in the range of 100 – 200 °C, differing the concentrations of the starting reagents and also use of different solvent systems, 50:50 mixture of MeOH and H_2O, to obtain a phase pure materials. The reaction conditions screened were found to yield materials which were either less crystalline or contained significant amounts of oxide impurities, optimal conditions that were found are stated above.

Table 1. Table illustrating the lanthanide elements which successfully form $[Ln(H_2O)MO_4]_2$[A] (M= Mo or W, A= 1,5-NDS or 2,6-NDS).

	La	Ce	Pr	Nd
$[Ln(H_2O)MoO_4]_2$[1,5-NDS]	✓	✓	✓	✓
$[Ln(H_2O)MoO_4]_2$[2,6-NDS]	✓	✓	✓	✓
$[Ln(H_2O)WO_4]_2$[1,5-NDS]	✓	✓	✓	x
$[Ln(H_2O)WO_4]_2$[2,6-NDS]	✓	✓	✓	x

6.2.2 Anion Exchange

Anion exchange reactions were performed on the crystalline NDS phases. A typical anion exchange reaction was performed using a 3-fold molar excess of the exchanging organic anion and 50mg of the host material. The reactions were carried

out at room temperature with 10 mL deionized water and left stirring overnight. In the case of no exchange either the reaction time was increased, the temperature was increased to 60 °C or 90 °C, with stirring overnight, or the reactions were performed hydrothermally and were heated at 165 °C for 14 h before being cooled slowly back to room temperature at a rate of 0.1 °C/min. The resultant mixture was subsequently filtered under suction and washed with water and ethanol before being left to dry in air. The anions used in the anion exchange reactions were carboxylates- fumarate, maleate, terephthalate, malonate, succinate, oxalate, suberate, phthalate, 1,5-NDS and 2,6-NDS, 2,6-NDC, inorganics- nitrate, perrhenate, carbonate, molybdate, tungstate and phosphate dibasic. All anions used were the sodium salts except for phthalate which was the di-potassium salt.

6.2.3 Catalytic Properties

6.2.3.1 Oxidative Bromination of Phenol Red to Bromophenol Blue

This catalytic method was adapted from the literature method found by B.F Sels *et al*.[12] In a typical catalytic reaction (0.05 mmol, 0.060 g) of catalyst $[La(H_2O)WO_4]_2[A]$ (A= 1,5-Naphthalene disulfonate or 2,6-Naphthalenedisulfonate) was added to a Youngs tube containing phenol red (0.05 mmol, 0.0177 g) and ammonium bromide (2.0 mmol, 0.1959 g) in deionized water (8.8 cm^3), methanol (6.6 cm^3) and THF (4.4 cm^3) making a total solvent volume of 20 cm^3. Hydrogen peroxide (30 wt.%, 2.8 ml) was then introduced to the mixture and the solution was left stirring at room temperature until the reaction was complete, i.e. a colour change was observed, the reaction mixture changed from red to blue suggesting the conversion of phenol red to bromophenol blue was complete. After the catalytic reaction was complete the catalyst was filtered off under suction, washed with water and ethanol before being left to dry in air. A minimum amount of $KMnO_2$ was added to the bromophenol blue mixture to expel any remaining hydrogen peroxide, any excess $KMnO_2$ was then filtered off under suction. The catalytic solution was then extracted with, dichloromethane (3 x 20 ml), H_2O (10 ml) and a small amount of tetrahexyl ammonium chloride. The combined extracts were dried over $MgSO_4$.

Dichloromethane was then removed under reduced pressure yielding a blue oil like residue confirmed to be bromophenol blue. The catalytic reaction proceeded overnight, taking ~24h before completion.

6.2.4 Attempted Redox Reactions

6.2.4.1 Attempted Lithium Intercalation

$[La(H_2O)WO_4]_2$[1,5-NDS] (0.05 g) was added to a Youngs tube under an inert atmosphere, followed by n-butyl lithium (3 mL). The solution was left stirring for 24 h or until a colour change was observed. After 24 h the solution became cream/brown in colour suggesting intercalation had taken place. n-BuLi was then decanted off into iso-propanol and the product washed under an inert atmosphere with hexane (5 mL). Excess hexane was then removed from the product under reduced pressure. Powder X-ray diffraction measurement post Lithium intercalation showed that the intercalation reaction proved unsuccessful, the intercalated material remained identical to the host material.

This reaction was also tried for various reaction times from 24 – 144 h, it was found the longer the reaction time the darker the solution became in colour although no intercalation occurred.

6.2.4.2 Attempted Hydrogen Intercalation

$[La(H_2O)WO_4]_2$[1,5-NDS] (0.03 g) and HCl (5 mL, 3M) were added to a Youngs tube. Zinc metal filings (0.1 g) were slowly added to the solution and effervescence occurred. The solution changed from colourless to grey and the host material went from white to dark grey immediately. Overnight the solution became yellow in colour and the product was filtered off under suction yielding a black powder.

X-ray diffraction measurements post hydrogen intercalation, showed that the host material had collapsed in the acidic conditions, therefore hydrogen intercalation was not successful. The reaction was also tried for 3 h but also proved to be unsuccessful.

6.2.5 Attempted Hydrothermal Synthesis

The attempted synthesis of $[Ln(H_2O)MO_4]_2[A]$ (Ln= Lanthanide series, M=Mo/W, A = mono, di & tri-sulfonates) was via a hydrothermal route. In a typical synthesis, 0.69 mmol of $LnCl_3.xH_2O$, 0.44 mmol of Na_2MoO_4 or Na_2WO_4, and 0.44 mmol of A were dissolved in 10 mL of deionized water, and the solution was placed in a 23 mL Teflon-lined hydrothermal autoclave. The reaction mixtures were then heated at 165 °C for 14 h before being cooled slowly back to room temperature at a rate of 0.1 °C/min. The mixture was subsequently filtered under suction and the resulting solid washed with water and ethanol before being left to dry in air.

The sulfonates screened in these reactions were the sodium salts of methane sulfonate, propane sulfonate, butane sulfonate, pentane sulfonate, hexane sulfonate, heptane sulfonate, octane-1-sulfonate, benzene sulfonate, 1-naphthalene sulfonate, 1,3-benzene disulfonate, and 1,3,(6 or 7)-naphthalene trisulfonate.

A variety of reaction temperatures (120 - 200 °C), reaction times (12 - 72h), solvent systems (MeOH and MeOH:H_2O 50:50) and reagent concentrations were explored to find optimal conditions. Screening of these reaction conditions found the major products formed were lanthanide molybdenum/tungsten oxides, $Ln_xM_yO_z$, with no coordination of the organic anions.

6.2.6 Attempted Slow Growth Crystallisation

$LnCl_3.xH_2O$ (0.69 mmol) and benzenesulfonate (0.44 mmol) were dissolved in 5 mL of deionized water, and the solution was placed into a test tube. To this Na_2MoO_4 or Na_2WO_4 (0.44 mmol) dissolved in 5mL of MeOH was added to the test tube creating a layered effect. The solution was then left for slow growth crystallisation, at room temperature.

6.3 Experimental Details for Chapter 3

6.3.1 Synthesis of [Ln(H_2O)$_2$][Phosphonoacetate] (Ln= Ho – Lu)

$LnCl_3.xH_2O$ (0.69 mmol) and Phosphonoacetic acid (0.0616 g, 0.44 mmol) were dissolved in deionised water (10 mL) and the solution placed in a 23 mL Teflon lined hydrothermal autoclave. The reaction mixtures were then heated at 150 °C (Ho-Tm) and 165 °C for 14 h (Yb-Lu) (biphasic product produced at 150 °C), before being cooled slowly back to room temperature at a rate of 0.1 °C/min. The mixtures were subsequently filtered under suction and the resulting crystalline solids washed with water and ethanol before being left to dry in air. Single crystal X-ray diffraction measurements confirmed that the Ho-Tm and Yb-Lu phases formed at 150°C and 165°C are polymorphs.

A variety of reaction conditions were screened to find optimal reaction conditions to produce phase pure materials, such as change in reaction time (36 h and 72 h), reactant concentrations and also reaction temperature. The above phases are found to form between temperatures of 60 – 180 °C with optimal conditions stated above. At 200 °C it has been discovered that Ytterbium produces an iso-structural phase to that found with Erbium at 150 °C. At 220 °C a new phase is produced for both Erbium and Ytterbium where each phase is found to be iso-structural to one another.

Addition of NaOH to the hydrothermal reaction mixture was also attempted to determine if alternative crystalline phases could be produced. It was found from these reactions that varying the concentration of NaOH had no effect on the reaction product and yielded iso-structural phases to those stated above.

6.3.2 Synthesis of [Ln][Phosphonoacetate] (Ln=Ho-Yb)

$LnCl_3.xH_2O$ (0.69 mmol) and Phosphonoacetic acid (0.0616 g, 0.44 mmol) were dissolved in deionised water (10 mL) and the solution placed in a 23 mL Teflon lined hydrothermal autoclave. The reaction mixture was then heated at optimal conditions of 220 °C for 14 h before being cooled slowly back to room temperature at a rate of

0.1 °C/min. The mixture was subsequently filtered under suction and the resulting crystalline solid washed with water and ethanol before being left to dry in air.

6.3.3 Synthesis of $[Ln_2(H_2O)_3][Phosphonoacetate]_2.H_2O$ (Ln= La-Sm)

$LnCl_3.xH_2O$ (0.69 mmol) and Phosphonoacetic acid (0.0616 g, 0.44 mmol) were dissolved in deionised water (10 mL) and the solution placed in a 23 mL Teflon lined hydrothermal autoclave. The reaction mixture was then heated at optimal conditions of 150 °C for 14 h before being cooled slowly back to room temperature at a rate of 0.1 °C/min. The mixture was subsequently filtered under suction and the resulting crystalline solid washed with water and ethanol before being left to dry in air.

A variety of reaction conditions such as reactant concentrations, reaction time and temperature were all screened, giving the optimal conditions reported above to produce phase pure materials. It was found that these phases form between 60 °C to 180 °C with phase pure materials being formed at 150 °C.

On forming this phase it was discovered that a paper containing this phase had recently been reported by Li *et al.*,[13] therefore we will not discuss this phases any further.

6.3.4 Attempted Template Reactions

The attempted synthesis to template phases $[Ln_2(H_2O)_3][Phosphonoacetate]_2.H_2O$ (Ln = La - Sm) and $[Ln(H_2O)_2][Phosphonoacetate]$ (Ln = Ho - Tm and Yb - Lu) was via a hydrothermal route. In a typical synthesis, $LnCl_3.xH_2O$ (0.69 mmol), template (0.44 mmol or 1.76 mmol), and phosphonoacetic acid (0.44 mmol), were dissolved in 10 mL of deionized water, and the solution was placed in a 23 mL Teflon-lined hydrothermal autoclave. The reaction mixture was then heated at various temperatures (60 °C – 165 °C), for 14 h before being cooled slowly back to room temperature at a rate of 0.1 °C/min. The mixture was subsequently filtered under suction and the resulting solid washed with water and ethanol before being left to dry in air.

The templates used in the synthesis were 2,2'-bipyridine, 4'4-bipyridine, Aniline, Tetrahydrofuran, Urea and Pyridine. Reaction temperature and reagent concentrations of templates were screened in order to try and obtain a new templated phase. Screening proved unsuccessful as we found only either the original phases to be formed or amorphous phases.

6.3.5 Attempted Hydrothermal Synthesis

6.3.5.1 Attempted synthesis of $[Ln(H_2O)]_2[A]$ (Ln = Lanthanide series, A=organophosphonates)

$LnCl_3.xH_2O$ (0.69 mmol) and organophosphonate (0.44 mmol) were dissolved in deionised water (10 mL) and the solution placed in a 23 mL Teflon lined hydrothermal autoclave. The reaction mixture was then heated at 165 °C for 14 h before being cooled slowly back to room temperature at a rate of 0.1 °C/min. The mixture was subsequently filtered under suction and the resulting solid washed with water and ethanol before being left to dry in air.
Organophosphonates used within these reactions were, 3-phosphonopropionic acid and benzylphosphonic acid.

6.3.5.2 Attempted synthesis of $[Ln(H_2O)XO_4]_2[A]$ (Ln = Lanthanide series, X= mono, di & tri-phosphates sodium salts, A=1,5-NDS or 2,6-NDS)

In a typical synthesis, 0.69 mmol of $LnCl_3.xH_2O$, 0.44 mmol of NaH_2PO_4, Na_2HPO_4 or Na_3PO_4, and 0.44 mmol of disodium 1,5-naphthalenedisulfonate (1,5-NDS) or disodium 2,6-naphthalenedisulfonate (2,6-NDS), were dissolved in 10 mL of deionized water, and the solution was placed in a 23 mL Teflon-lined hydrothermal autoclave. The reaction mixtures were then heated at various temperatures and times before being cooled slowly back to room temperature at a rate of 0.1 °C/min. The

mixture was subsequently filtered under suction and the resulting solid washed with water and ethanol before being left to dry in air.

A variety of reaction conditions were screened, for example change in reaction temperature in the range of 100 - 200°C, reaction times (14 – 96 h), differing the concentrations of the starting reagents and also different solvent systems, (MeOH or 50:50 mixture of MeOH to H_2O), to obtain a phase pure materials. It was found that each synthesis produced only lanthanide phosphates, $LnPO_4$.

6.3.5.3 Attempted synthesis of $[Ln(H_2O)MO_4]_2[A]$ (Ln= Lanthanide series, M=Mo/W, A= organophosphates)

In a typical synthesis, 0.69 mmol of $LnCl_3.xH_2O$, 0.44 mmol of Na_2MoO_4 or Na_2WO_4, and 0.44 mmol of organophosphonate were dissolved in 10 mL of deionized water, and the solution was placed in a 23 mL Teflon-lined hydrothermal autoclave. The reaction mixtures were then heated at various temperatures and times before being cooled slowly back to room temperature at a rate of 0.1 °C/min. The mixture was subsequently filtered under suction and the resulting solid washed with water and ethanol before being left to dry in air.

A variety of reaction conditions were screened, for example change in reaction temperature in the range of 60 – 200 °C and different reaction times from 14 – 72 h. The organophosphonates used in these reactions were phosphonoacetic acid, benzylphosphonic acid and 3-phosphonopropionic acid.

6.3.5.4 Attempted synthesis of $[Ln(H_2O)XO_4]_2[A]$ (Ln= Lanthanide series, X= Na_2HPO_4, A= Phosphonoacetic acid)

In a typical synthesis, 0.69 mmol of $LnCl_3.xH_2O$, 0.44 mmol of NaH_2PO_4, and 0.44 mmol of phosphonoacetic acid were dissolved in 10 mL of deionized water, and the solution was placed in a 23 mL Teflon-lined hydrothermal autoclave. The reaction mixture was then heated at various temperatures, (60 °C, 165 °C and 220 °C) for 14h before being cooled slowly back to room temperature at a rate of 0.1 °C/min. The

mixture was subsequently filtered under suction and the resulting solid washed with water and ethanol before being left to dry in air. These reactions were found to only form amorphous $LnPO_4$.

6.3.5.5 Attempted synthesis of $[Ln(H_2O)]_2[A]$ (Ln = La & Nd, A=mono-sulfonate)

$LnCl_3 \cdot 6H_2O$ (0.69 mmol) and mono-sulfonate (0.44 mmol) were dissolved in 10 mL deionised water and the solution placed in a Teflon-lined hydrothermal autoclave. This was then heated at 165 °C for 14 h before being cooled slowly back to room temperature at a rate of 0.1 °C/min. No product was produced post-synthesis so the solution was left for slow evaporation crystallisation.

The mono-sulfonates used in these reactions were sodium salts of 1-naphthalenesulfonate, benzenesulfonate, methane sulfonate and octane-1-sulfonate mono-hydrate.

6.3.6 Synthesis of $[Ln(H_2O)_5]_2[2,6\text{-}AQDS]_3.2H_2O$ (Ln= La - Nd)

$[Ln(H_2O)_5]_2[2,6\text{-}AQDS]_3 \cdot 2H_2O$ was prepared via a hydrothermal route. $LnCl_3 \cdot xH_2O$ (0.69 mmol) and disodium 2,6-anthraquinonedisulfonate (2,6-AQDS) (0.1848 g, 0.44 mmol) were dissolved in 10 mL deionised water and the solution placed in a Teflon-lined hydrothermal autoclave. The solution was then heated at 165 °C for 14 h before being cooled slowly back to room temperature at a rate of 0.1 °C/min. The mixture was subsequently filtered under suction and the resulting solid washed with water and ethanol before being left to dry in air. This synthesis was also attempted with 1,5-AQDS.

6.3.7 Synthesis of $[Ln(H_2O)_5][Octanesulfonate]_3$ (Ln=La & Nd)

$[Ln(H_2O)_5][C_8H_{17}SO_3]_3$ was initially prepared via a hydrothermal route. $LnCl_3 \cdot 6H_2O$ (0.69 mmol) and sodium octane-1-sulfonate monohydrate (0.44 mmol) were dissolved in 10 mL deionised water and the solution placed in a Teflon-lined hydrothermal autoclave. This was then heated at 165 °C for 14 h before being cooled slowly back to room temperature at a rate of 0.1 °C/min. No product was produced post-synthesis so the solution was left for slow evaporation crystallisation yielding plate like crystals.

6.3.8 Attempted Slow Growth Crystallisation

6.3.8.1 Attempted formation of $[Ln(H_2O)_5][Octanesulfonate]_3$ (Ln= Ce, Er, Dy & Yb)

$LnCl_3.xH_2O$ (0.345 mmol) and octanesulfonate (0.22 mmol) were dissolved in 5 mL of deionized water, and the solution was placed into a test tube and left for slow growth crystallisation.

6.3.8.2 Attempted formation of $[Ln(H_2O)$4,4'bipyridyl] [Octanesulfonate] (Ln= La, Nd, Er, Dy & Yb)

$LnCl_3.xH_2O$ (0.69 mmol) and octanesulfonate (0.22 mmol) were dissolved in 5 mL of deionized water, and the solution was placed into a test tube. To this 4,4'-bipyridyl (0.44 mmol) dissolved in 5 mL of MeOH was added to the test tube creating a layered effect. The solution was then left for slow growth crystallisation. After one month large colourless needle crystals had grown which were found to be 4,4'-bipyridyl.

6.4 Experimental Details for Chapter 4

6.4.1 *In-situ* EDXRD Synthesis

Each phase studied using the *in-situ* Energy Dispersive X-ray Diffraction technique was synthesised via a hydrothermal route which had previously been determined under laboratory conditions. The concentrations of starting reagents were doubled for each synthesis, and each reaction took place in a specially adapted hydrothermal autoclave under continuous stirring. Reaction times for the phases studied varied, depending on the length of time taken for each product to be successfully synthesised. Reactions were stopped when the required final phase was observed and the reaction was deemed complete to determine the intermediate seen. The reactions were allowed to cool back to room temperature when the final phase appeared and the reaction was complete.

The phases studied were $[Ln(H_2O)MoO_4]_2[A]$ (Ln= La & Nd, A= 1,5-NDS or 2,6-NDS), $[La(H_2O)WO_4]_2[A]$, synthesis details are found in Section 6.2.1 and $[YbC_2H_2O_5P]$, synthesis details are found in Section 6.4.2. For $[La(H_2O)WO_4]_2$[1,5-NDS] the reaction was performed at a range of temperatures, 120, 145, 165, 180 and 200 °C so that kinetic data could be efficiently calculated. The remainder of the phases were studied under the same temperature conditions as those found in the laboratory.

6.4.2 Isolation of Intermediate Phases

The intermediate phase found in the formation of $[Nd(H_2O)MoO_4]_2$[1,5-NDS] was isolated by quenching the in-situ reaction at 165 °C after ~10 mins, with the intermediate phase forming after ~4mins. After ~20mins the intermediate converts fully into the product phase of $[Nd(H_2O)MoO_4]_2$[1,5-NDS]. The quenched reaction was allowed to cool instantly by immersing the hydrothermal autoclave into cold water.

As an intermediate was observed in the synthesis of [$YbC_2H_2O_5P$] the reaction was repeated, and the intermediate phase was isolated by quenching the in-situ reaction as soon as it was first observed. The quenched reaction was allowed to cool instantly by immersing the hydrothermal autoclave into cold water.

6.5 Experimental Details for Chapter 5

6.5.1 Synthesis of $[Ln(H_2O)_3B_6O_{10}][BO_3H_2]$ (Ln = Sm - Gd), $[Ln(NO_3)(H_2O)_2][B_5O_9(OH_2)]$ (Ln = Ce - Nd) & $[Ln(NO_3)(H_2O)_2][B_6O_{10}(OH_2)]$ (Ln = La & Ce)

This experimental method was adapted from the literature preparation of S. Wang *et* al.[14] Each phase stated above was synthesised via a hydrothermal route. $Ln(NO_3)_3 \cdot 6H_2O$ (0.416 mmol), boric acid (0.6717 g, 10.86 mmol) and 90 μL deionised water were placed in a Teflon-lined hydrothermal autoclave and heated at 200 °C for 48 h before being cooled slowly back to room temperature at a rate of 0.1 °C/min. The mixture was subsequently filtered under suction and the resulting crystalline solid washed with boiling deionized water, dissolving any remaining excess boric acid, and methanol before being left to dry in air.

A variety of reaction conditions were screened to find the optimal conditions to produce crystalline, phase pure materials. Reaction temperatures (150 – 200 °C), reaction times (14 – 240 h) and differing the amount of H_2O (0 – 10 mL) used within the reaction mixture were screened. For the reaction with no water present we found the same phases, although slightly less crystalline, formed therefore it has been determined that the reaction mainly uses the water of crystallisation found on the hydrated lanthanide salts. Using 10 mL of H_2O within the reaction media proved unsuccessful yielding no solid product. Optimal reaction conditions were found and are those stated above.

6.5.2 Attempted Anion Exchange

Anion exchange reactions were performed on the layered phase $[Gd(H_2O)_3B_6O_{10}][H_2BO_3]$. A typical anion exchange reaction was performed using a 3-fold molar excess of the exchanging organic anion and 25 mg of the host material. The reactions were carried out at room temperature with 10 mL deionized water and left stirring overnight. In the case of no exchange the temperature was increased to 60 °C with stirring overnight. The resultant mixtures were subsequently filtered under suction and washed with water and methanol before being left to dry in air. The anions used in the anion exchange reactions were carboxylates; fumarate, maleate, terephthalate, malonate, succinate, oxalate, suberate, phthalate, 1,5-NDS, and 2,6-NDS, inorganics; nitrate, perrhenate and carbonate, molybdate, tungstate, phosphate monobasic, phosphate dibasic, phosphate tribasic and tetraborate decahydrate. All anions used were the sodium salts except for phthalate which was the di-potassium salt.

6.5.3 Attempted Template Reactions

The addition of potential template molecules to the synthesis of $[Ln(NO_3)(H_2O)_2][B_5O_9(OH_2)]$ (Ln = Ce - Nd) & $[Ln(NO_3)(H_2O)_2]$ $[B_6O_{10}(OH)]$ (Ln = La & Ce) was attempted via a boric acid flux route. In a typical synthesis, $Ln(NO_3)_3.xH_2O$ (0.416 mmol), template (0.416 mmol or 2.080 mmol), boric acid (10.86 mmol) and 90 μL of deionized water were placed in a 23 mL Teflon-lined hydrothermal autoclave. The reaction mixture was then heated at 200 °C, for 48 h before being cooled slowly back to room temperature at a rate of 0.1 °C/min. The mixture was subsequently filtered under suction and the resulting solid washed with water and methanol before being left to dry in air.

The templates used in this synthesis were neutral amines; 2,2'-bipyridine, 4,4'-bipyridine, aniline and urea, tetrahydrofuran, anions include; methane sulfonate, benzene sulfonate, butane sulfonate, hexane sulfonate and sodium acetate, inorganics include; sodium phosphate monobasic and sodium phosphate dibasic.

The concentration of template, and reaction temperatures (to stop the decomposition of the template at higher temperatures) were screened in order to try and obtain a

new templated phase. Reactions were found to be unsuccessful as only phases close to amorphous were produced.

6.5.4 Attempted Hydrothermal Synthesis of $[Ln(X)(H_2O)_2][B_5O_9(OH_2)]$ (Ln = Ce - Nd) & $[Ln(X)(H_2O)_2][B_6O_{10}(OH)]$ (Ln = La & Ce, X= Halide or Anion)

Attempts were made to prevent the incorporation of NO_3^- into lanthanide borates by incorporating alternative anions via a hydrothermal route. $LnCl_3 \cdot xH_2O$ (0.416 mmol), boric acid (0.6717 g, 10.86 mmol), halide/anion (0.416 mmol) and 90 μL deionised water were placed in a Teflon-lined hydrothermal autoclave and heated at 200 °C for 48 h before being cooled slowly back to room temperature at a rate of 0.1 °C/min. The mixture was subsequently filtered under suction and the resulting solid washed with boiling deionized water, dissolving any remaining excess boric acid, and methanol before being left to dry in air.

The monohalides and monoanions used within this reaction were sodium salts of bromide, iodide and carbonate, and potassium chloride.

6.5.5 Attempted Anion Exchange

As nitrate was found to be present in the phases $[Pr(NO_3)(H_2O)_2][B_5O_9(OH_2)]$ & $[La(NO_3)(H_2O)_2][B_6O_{10}(OH)]$, we attempted to exchange each nitrate with a another anion.

A typical anion exchange reaction was performed using a 3-fold molar excess of the exchanging organic anion and 25 mg of the host material. The reactions were carried out at room temperature with 10 mL deionized water and left stirring overnight. In the case of no exchange either the reaction time was increased to four days, and the temperature was increased to either 40 °C or 60 °C, with stirring overnight. The resultant mixtures was subsequently filtered under suction and washed with water and ethanol before being left to dry in air. The reagents used in the anion exchange reactions were sodium carbonate and sodium chloride.

6.6 References

(1) Bruker. SAINT V6.45a. Madison, W., U.S.A.: Bruker AXS Inc. **2005**.

(2) Bruker. (2008). SADABS V2008-1. Madison, W., U.S.A.: Bruker AXS Inc.

(3) Sheldrick, G. M. A., 112-122. *A Short History of SHELX*. *Acta Crystallogr*.

(4) Hooft, R. N., B. V. **1998**.

(5) Sheldrick, G. M. B. A. I. M., Wisconsin, U.S.A. **2003**.

(6) Sheldrick, G. M. *Acta Crystallogr* **1990**, *Sect A*, 467.

(7) Sheldrick, G. M. *Institut fur Anorganische Chemie der Universitat:* **1998**.

(8) DESY,http://hasylab.desy.de/facilities/doris_iii/beamlines/e35190/index_eng .html , accessed in October 2011

(9) Evans, J. S. O.; Francis, R. J.; Ohare, D.; Price, S. J.; Clark, S. M.; Flaherty, J.; Gordon, J.; Nield, A.; Tang, C. C. *Rev. Sci. Instrum.* **1995**, *66*, 2442.

(10) Clark, S. M.; Nield, A.; Rathbone, T.; Flaherty, J.; Tang, C. C.; Evans, J. S. O.; Francis, R. J.; Ohare, D. *Nucl. Instrum. Methods Phys. Res. Sect. B-Beam Interact. Mater. Atoms* **1995**, *97*, 98.

(11) Luo, J. J.; Xu, L. *Inorg. Chem.* **2006**, *45*, 11030.

(12) Sels, B. F.; De Vos, D. E.; Buntinx, M.; Jacobs, P. A. *J. Catal.* **2003**, *216*, 288.

(13) Li, J. T.; Zheng, L. M. *Inorg. Chim. Acta* **2009**, *362*, 1739.

(14) Wang, S. A.; Alekseev, E. V.; Juan, D. W.; Casey, W. H.; Phillips, B. L.; Depmeier, W.; Albrecht-Schmitt, T. E. *Angew. Chem.-Int. Edit.* **2010**, *49*, 1057.

Appendix A

Chapter Two

Crystallographic data for $[Nd(H_2O)MoO_4]_2[2,6\text{-NDS}]$ (1)

Table 1 Crystal data and structure refinement details for $[Nd(H_2O)MoO_4]_2[2,6\text{-NDS}]$

Identification code	**2008src0992**	
Empirical formula	$C_5H_3MoNdO_8S$	
Formula weight	463.31	
Temperature	120(2) K	
Wavelength	0.71073 Å	
Crystal system	Monoclinic	
Space group	*C*2/*c*	
Unit cell dimensions	a = **35.6918(18) Å**	α = **90°**
	b = **7.2951(4) Å**	β = **93.730(3)°**
	c = **7.4407(4) Å**	γ = **90°**
Volume	1933.27(18) $Å^3$	
Z	8	
Density (calculated)	3.184 mg / m^3	
Absorption coefficient	6.849 mm^{-1}	
F(000)	1720	
Crystal	Needle; light purple	
Crystal size	0.14 × 0.02 × 0.01 mm^3	
θ range for data collection	3.28 – 27.48°	
Index ranges	$-46 \le h \le 46$, $-9 \le k \le 9$, $-9 \le l \le 9$	
Reflections collected	15260	
Independent reflections	2220 [R_{int} = 0.1351]	

Completeness to $\theta = 27.48°$	99.8 %
Absorption correction	Semi−empirical from equivalents
Max. and min. transmission	0.9347 and 0.4473
Refinement method	Full-matrix least-squares on F^2
Data / restraints / parameters	2220 / 4 / 115
Goodness-of-fit on F^2	1.151
Final *R* indices [$F^2 > 2\sigma(F^2)$]	*R1* = 0.0685, *wR2* = 0.1398
R indices (all data)	*R1* = 0.0839, *wR2* = 0.1468
Largest diff. peak and hole	2.085 and −1.780 e Å^{-3}

Diffractometer: *Nonius KappaCCD* area detector (ϕ scans and ω scans to fill *asymmetric unit* sphere). **Cell determination:** DirAx (Duisenberg, A.J.M.(1992). J. Appl. Cryst. 25, 92-96.) **Data collection:** Collect (Collect: Data collection software, R. Hooft, Nonius B.V., 1998). **Data reduction and cell refinement**: *Denzo* (Z. Otwinowski & W. Minor, *Methods in Enzymology* (1997) Vol. **276**: *Macromolecular Crystallography*, part A, pp. 307−326; C. W. Carter, Jr. & R. M. Sweet, Eds., Academic Press). **Absorption correction**: *SADABS* (Sheldrick, G. M. (2007). SADABS. Version 2007/2. Bruker AXS Inc., Madison, Wisconsin, USA.). S**tructure solution**: *SHELXS97* (Sheldrick, G.M. (2008). Acta Cryst. A64, 112-122.). S**tructure refinement**: *SHELXL97* (G Sheldrick, G.M. (2008). Acta Cryst. A64, 112-122.). **Graphics:** *CAMERON* (Watkin, D. M., Pearce, L. & Prout, C. K. (1993). Chemical Crystallography Lab, University of Oxford)

Table 2 Atomic coordinates [× 10^4], equivalent isotropic displacement parameters [Å^2 × 10^3] and site occupancy factors. U_{eq} is defined as one third of the trace of the orthogonalized U^{ij} tensor.

Atom	*x*	*y*	*z*	U_{eq}	*S.o.f.*
Nd1	1760(1)	3445(1)	7397(1)	13(1)	1
Mo1	2098(1)	1950(2)	2375(2)	12(1)	1
S1	1052(1)	2898(5)	3577(5)	16(1)	1
O1	993(3)	1396(13)	2287(12)	18(2)	1
O2	1256(3)	2311(15)	5246(12)	22(2)	1

O3	1220(3)	4506(13)	2810(15)	21(2)	1
O4	2019(2)	3059(13)	4405(12)	18(2)	1
O5	1887(2)	206(13)	7304(13)	18(2)	1
O6	2420(2)	3353(14)	7888(12)	18(2)	1
O7	1249(3)	1810(13)	8844(13)	19(2)	1
O8	1883(2)	3478(13)	10689(12)	16(2)	1
C1A	513(6)	5360(40)	4350(40)	7(3)	0.25
C2A	597(7)	3580(40)	3830(40)	7(3)	0.25
C3A	325(7)	2220(40)	3830(40)	7(3)	0.25
C4A	–32(7)	2640(40)	4360(40)	7(3)	0.25
C5A	–117(6)	4410(40)	4880(40)	7(3)	0.25
C6A	156(6)	5770(40)	4870(40)	7(3)	0.25
C7A	72(7)	7550(40)	5390(40)	7(3)	0.25
C8A	–285(7)	7960(40)	5920(40)	7(3)	0.25
C9A	–558(7)	6600(40)	5920(40)	7(3)	0.25
C10A	–473(6)	4830(40)	5400(40)	7(3)	0.25
C1B	479(7)	5160(40)	4100(50)	7(3)	0.25
C2B	633(7)	3430(40)	4420(50)	7(3)	0.25
C3B	425(8)	2080(40)	5220(50)	7(3)	0.25
C4B	63(8)	2460(40)	5700(50)	7(3)	0.25
C5B	–91(7)	4190(40)	5380(50)	7(3)	0.25
C6B	117(7)	5540(40)	4580(50)	7(3)	0.25
C7B	–37(8)	7270(40)	4260(50)	7(3)	0.25
C8B	–398(8)	7640(40)	4740(50)	7(3)	0.25
C9B	–606(7)	6290(50)	5540(50)	7(3)	0.25
C10B	–452(7)	4560(40)	5860(50)	7(3)	0.25

Table 3 Bond lengths [Å] and angles [°].

Nd1–O6	2.364(8)	C3A–H3A	0.9500
Nd1–O5	2.408(10)	C4A–C5A	1.3900
Nd1–O8	2.460(9)	C4A–H4A	0.9500
Nd1–O2	2.472(10)	C5A–C6A	1.3900
Nd1–O3^{i}	2.473(9)	C5A–C10A	1.3900
Nd1–O7	2.481(9)	C6A–C7A	1.3900
Nd1–O4	2.483(9)	C7A–C8A	1.3900
Nd1–O8^{ii}	2.632(9)	C7A–H7A	0.9500
Nd1–Mo1^{i}	3.5701(13)	C8A–C9A	1.3900
Mo1–O5^{iii}	1.743(10)	C8A–H8A	0.9500
Mo1–O4	1.752(9)	C9A–C10A	1.3900
Mo1–O6^{iv}	1.757(8)	C9A–S1^{vi}	1.86(2)
Mo1–O8^{v}	1.810(9)	C10A–H10A	0.9500
Mo1–Nd1^{ii}	3.5701(13)	C1B–C2B	1.3900
S1–O3	1.451(10)	C1B–C6B	1.3900
S1–O2	1.462(10)	C1B–H1B	0.9500
S1–O1	1.463(10)	C2B–C3B	1.3900
S1–C2B	1.70(2)	C3B–C4B	1.3900
S1–C2A	1.72(2)	C3B–H3B	0.9500
S1–C9B^{vi}	1.85(2)	C4B–C5B	1.3900
S1–C9A^{vi}	1.86(2)	C4B–H4B	0.9500
O3–Nd1^{ii}	2.473(9)	C5B–C6B	1.3900
O5–Mo1^{vii}	1.743(10)	C5B–C10B	1.3900
O6–Mo1^{iv}	1.757(8)	C6B–C7B	1.3900
O8–Mo1^{viii}	1.810(9)	C7B–C8B	1.3900
O8–Nd1^{i}	2.632(9)	C7B–H7B	0.9500
C1A–C2A	1.3900	C8B–C9B	1.3900
C1A–C6A	1.3900	C8B–H8B	0.9500
C1A–H1A	0.9500	C9B–C10B	1.3900
C2A–C3A	1.3900	C9B–S1^{vi}	1.85(2)
C3A–C4A	1.3900	C10B–H10B	0.9500

O6–Nd1–O5	77.8(3)	O8–Nd1–Mo1^{i}	87.5(2)
O6–Nd1–O8	74.6(3)	O2–Nd1–Mo1^{i}	123.0(2)
O5–Nd1–O8	90.9(3)	O3^{i}–Nd1–Mo1^{i}	72.4(2)
O6–Nd1–O2	140.1(3)	O7–Nd1–Mo1^{i}	135.4(2)
O5–Nd1–O2	77.5(3)	O4–Nd1–Mo1^{i}	87.5(2)
O8–Nd1–O2	136.4(3)	O8^{ii}–Nd1–Mo1^{i}	29.3(2)
O6–Nd1–O3^{i}	140.8(3)	O5^{iii}–Mo1–O4	110.5(4)
O5–Nd1–O3^{i}	138.3(3)	O5^{iii}–Mo1–O6^{iv}	107.9(4)
O8–Nd1–O3^{i}	87.8(3)	O4–Mo1–O6^{iv}	111.6(4)
O2–Nd1–O3^{i}	75.1(3)	O5^{iii}–Mo1–O8^{v}	111.8(4)
O6–Nd1–O7	132.3(3)	O4–Mo1–O8^{v}	103.2(4)
O5–Nd1–O7	71.7(3)	O6^{iv}–Mo1–O8^{v}	111.9(4)
O8–Nd1–O7	70.3(3)	O5^{iii}–Mo1–Nd1^{ii}	134.7(3)
O2–Nd1–O7	66.2(3)	O4–Mo1–Nd1^{ii}	59.2(3)
O3^{i}–Nd1–O7	68.7(3)	O6^{iv}–Mo1–Nd1^{ii}	116.9(3)
O6–Nd1–O4	73.1(3)	O8^{v}–Mo1–Nd1^{ii}	45.3(3)
O5–Nd1–O4	77.3(3)	O3–S1–O2	112.0(6)
O8–Nd1–O4	147.2(3)	O3–S1–O1	113.1(6)
O2–Nd1–O4	71.3(3)	O2–S1–O1	112.3(6)
O3^{i}–Nd1–O4	121.3(3)	O3–S1–C2B	110.9(12)
O7–Nd1–O4	131.4(3)	O2–S1–C2B	98.9(13)
O6–Nd1–O8^{ii}	84.4(3)	O1–S1–C2B	108.7(13)
O5–Nd1–O8^{ii}	141.7(3)	O3–S1–C2A	103.0(11)
O8–Nd1–O8^{ii}	116.6(2)	O2–S1–C2A	114.5(11)
O2–Nd1–O8^{ii}	96.4(3)	O1–S1–C2A	101.2(12)
O3^{i}–Nd1–O8^{ii}	72.6(3)	C2B–S1–C2A	15.6(17)
O7–Nd1–O8^{ii}	140.4(3)	O3–S1–C9B^{vi}	105.6(11)
O4–Nd1–O8^{ii}	65.1(3)	O2–S1–C9B^{vi}	100.6(12)
O6–Nd1–Mo1^{i}	72.1(2)	O1–S1–C9B^{vi}	112.4(12)
O5–Nd1–Mo1^{i}	149.2(2)	C2B–S1–C9B^{vi}	5(2)
		C2A–S1–C9B^{vi}	14.7(16)

O3–S1–C9A^{vi}	110.0(10)	C5A–C6A–C1A	120.0
O2–S1–C9A^{vi}	108.3(10)	C8A–C7A–C6A	120.0
O1–S1–C9A^{vi}	100.5(11)	C8A–C7A–H7A	120.0
C2B–S1–C9A^{vi}	10.3(16)	C6A–C7A–H7A	120.0
C2A–S1–C9A^{vi}	7.6(19)	C7A–C8A–C9A	120.0
C9B^{vi}–S1–C9A^{vi}	12.1(15)	C7A–C8A–H8A	120.0
S1–O2–Nd1	138.9(6)	C9A–C8A–H8A	120.0
S1–O3–Nd1^{ii}	152.0(6)	C10A–C9A–C8A	120.0
Mo1–O4–Nd1	156.3(5)	C10A–C9A–S1^{vi}	117.6(11)
Mo1^{vii}–O5–Nd1	165.1(5)	C8A–C9A–S1^{vi}	122.2(11)
Mo1^{iv}–O6–Nd1	163.8(5)	C9A–C10A–C5A	120.0
Mo1^{viii}–O8–Nd1	136.4(5)	C9A–C10A–H10A	120.0
Mo1^{viii}–O8–Nd1^{i}	105.5(4)	C5A–C10A–H10A	120.0
Nd1–O8–Nd1^{i}	117.7(4)	C2B–C1B–C6B	120.0
C2A–C1A–C6A	120.0	C2B–C1B–H1B	120.0
C2A–C1A–H1A	120.0	C6B–C1B–H1B	120.0
C6A–C1A–H1A	120.0	C1B–C2B–C3B	120.0
C3A–C2A–C1A	120.0	C1B–C2B–S1	119.4(13)
C3A–C2A–S1	117.2(13)	C3B–C2B–S1	120.1(13)
C1A–C2A–S1	121.6(13)	C4B–C3B–C2B	120.0
C2A–C3A–C4A	120.0	C4B–C3B–H3B	120.0
C2A–C3A–H3A	120.0	C2B–C3B–H3B	120.0
C4A–C3A–H3A	120.0	C5B–C4B–C3B	120.0
C3A–C4A–C5A	120.0	C5B–C4B–H4B	120.0
C3A–C4A–H4A	120.0	C3B–C4B–H4B	120.0
C5A–C4A–H4A	120.0	C6B–C5B–C4B	120.0
C6A–C5A–C4A	120.0	C6B–C5B–C10B	120.0
C6A–C5A–C10A	120.0	C4B–C5B–C10B	120.0
C4A–C5A–C10A	120.0	C7B–C6B–C5B	120.0
C7A–C6A–C5A	120.0	C7B–C6B–C1B	120.0
C7A–C6A–C1A	120.0	C5B–C6B–C1B	120.0

C8B–C7B–C6B	120.0
C8B–C7B–H7B	120.0
C6B–C7B–H7B	120.0
C7B–C8B–C9B	120.0
C7B–C8B–H8B	120.0
C9B–C8B–H8B	120.0
C8B–C9B–C10B	120.0
C8B–C9B–S1^{vi}	114.8(13)
C10B–C9B–S1^{vi}	124.5(13)
C9B–C10B–C5B	120.0
C9B–C10B–H10B	120.0
C5B–C10B–H10B	120.0

Symmetry transformations used to generate equivalent atoms:

(i) x,–y+1,z+1/2 (ii) x,–y+1,z–1/2 (iii) x,–y,z–1/2

(iv) –x+1/2,–y+1/2,–z+1 (v) x,y,z–1 (vi) –x,–y+1,–z+1

(vii) x,–y,z+1/2 (viii) x,y,z+1

Table 4 Anisotropic displacement parameters [$Å^2 \times 10^3$]. The anisotropic displacement factor exponent takes the form: $-2\pi^2[h^2a^{*2}U^{11} + \cdots + 2\,h\,k\,a^*\,b^*\,U^{12}]$.

Atom	U^{11}	U^{22}	U^{33}	U^{23}	U^{13}	U^{12}
Nd1	10(1)	13(1)	16(1)	1(1)	2(1)	1(1)
Mo1	10(1)	12(1)	15(1)	–1(1)	1(1)	0(1)
S1	9(2)	16(2)	23(2)	–2(1)	2(1)	–2(1)
O1	22(5)	18(5)	15(4)	–4(4)	0(4)	–4(4)
O2	23(5)	33(6)	9(4)	3(4)	1(4)	–2(4)
O3	9(5)	11(5)	43(6)	–1(4)	3(4)	2(4)
O4	7(4)	25(5)	22(5)	–1(4)	4(3)	–4(4)
O5	9(4)	19(5)	27(5)	–4(4)	4(4)	–1(4)
O6	4(4)	27(5)	24(5)	3(4)	0(3)	6(4)
O7	18(5)	12(5)	27(5)	0(4)	5(4)	–3(4)
O8	7(4)	16(5)	22(5)	–3(4)	–4(3)	–3(4)

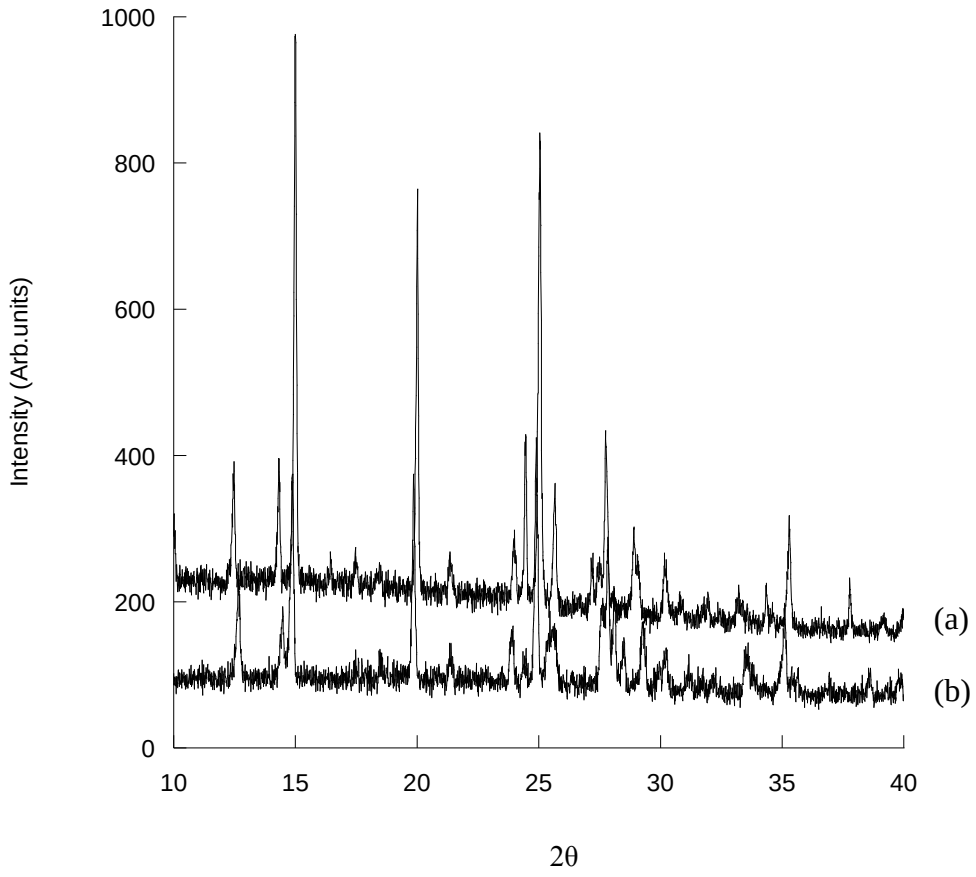

Figure 1 (a) Powder XRD pattern of $[Nd(H_2O)MoO_4]_2[2,6\text{-NDS}]$ and (b) diffraction pattern post IGA measurements.

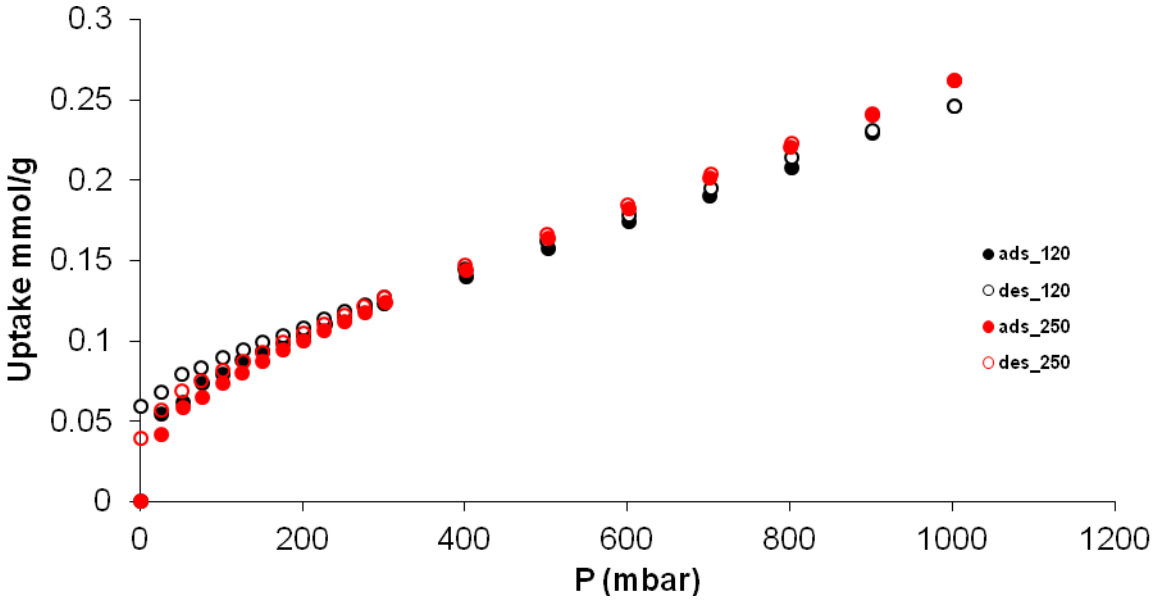

Figure 2 Adsorption and desorption isotherms for $[Nd(H_2O)MoO_4]_2[2,6\text{-NDS}]$ at 120 and 250 °C.

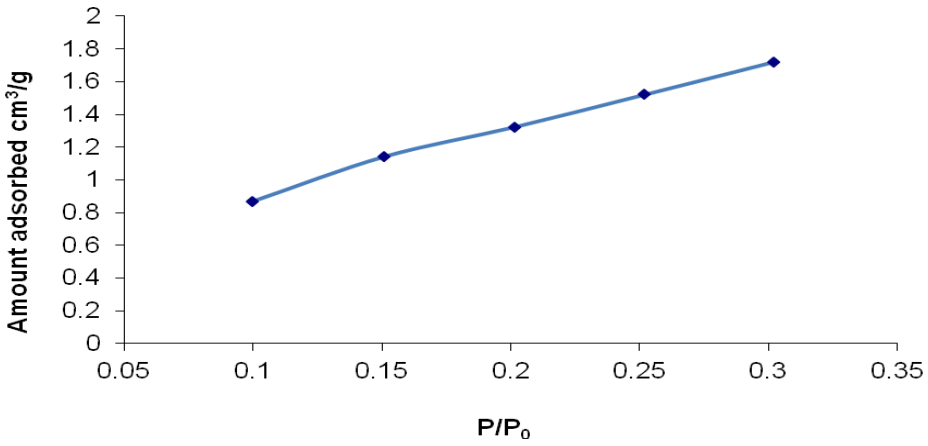

Figure 3 Adsorption isotherm for [Nd(H_2O)MoO_4]$_2$[2,6-NDS](**1**), degassed at 120 °C overnight.

Characterising data for [Ln(H_2O)MoO_4]$_2$[2,6-NDS] (La-Nd)

[La(H_2O)MoO_4]$_2$[2,6-NDS]

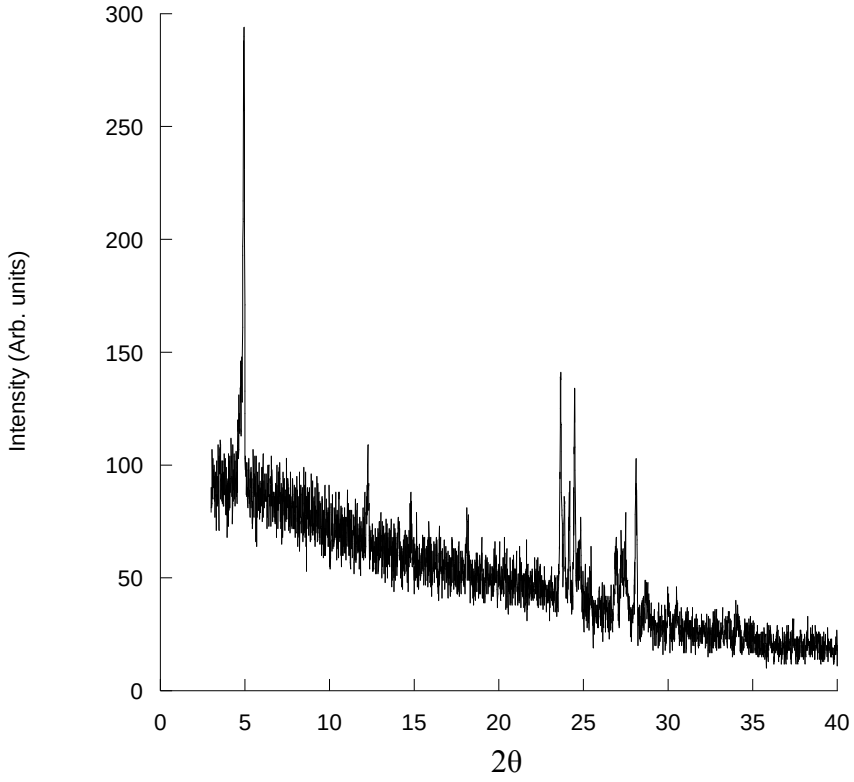

Figure 4 Powder X-ray diffraction pattern of $[La(H_2O)MoO_4]_2[2,6\text{-NDS}]$

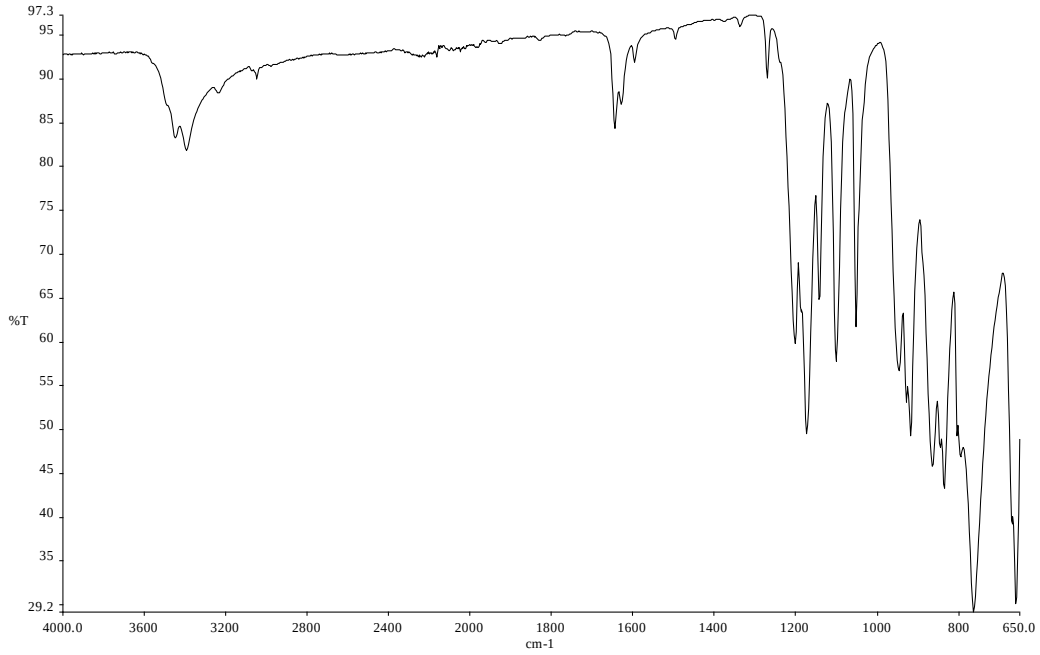

Figure 5 FTIR spectra for $[La(H_2O)MoO_4]_2[2,6\text{-NDS}]$ showing bands due to OH at 3395 cm^{-1}, S-O stretching modes at 1174 (antisymmetric) and 1053 cm^{-1} (symmetric) and the molybdate stretching frequency at 764 cm^{-1}.

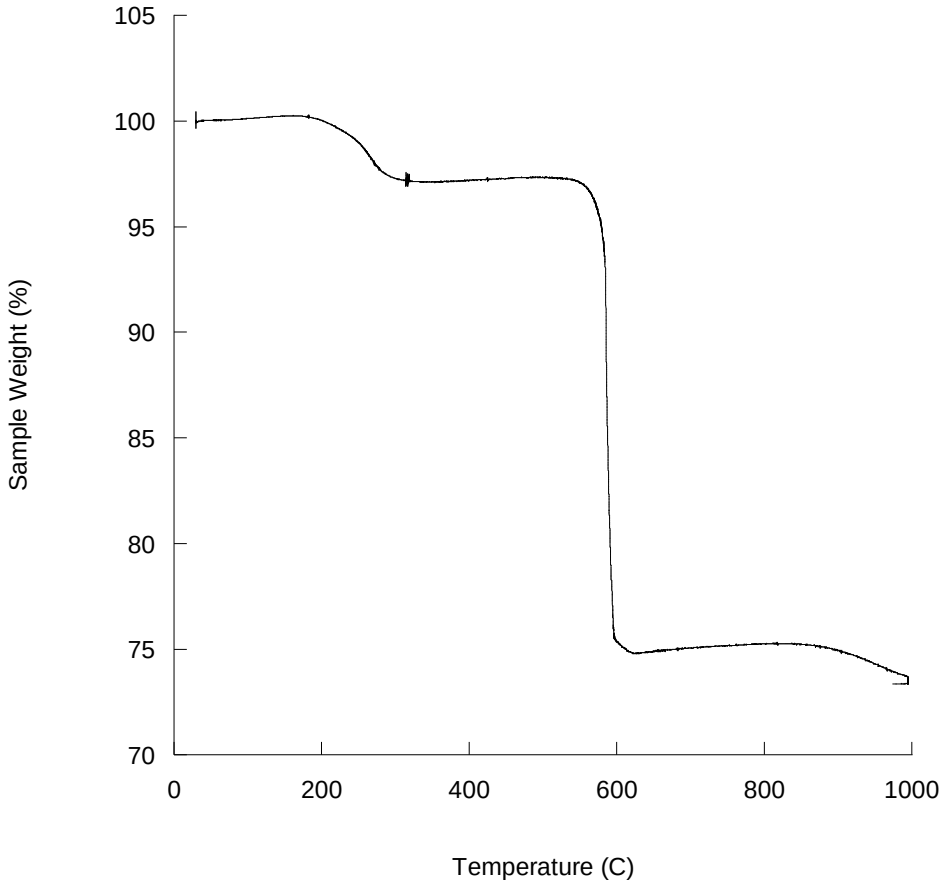

Figure 6 TGA trace of $[La(H_2O)MoO_4]_2$[2,6-NDS] showing two distinct mass losses. First mass loss of 2.7 % below 300 °C and an additional mass loss of 23.6 % by 600 °C. End product is found to be $La_2Mo_2O_9$.

$[Ce(H_2O)MoO_4]_2[2,6\text{-NDS}]$

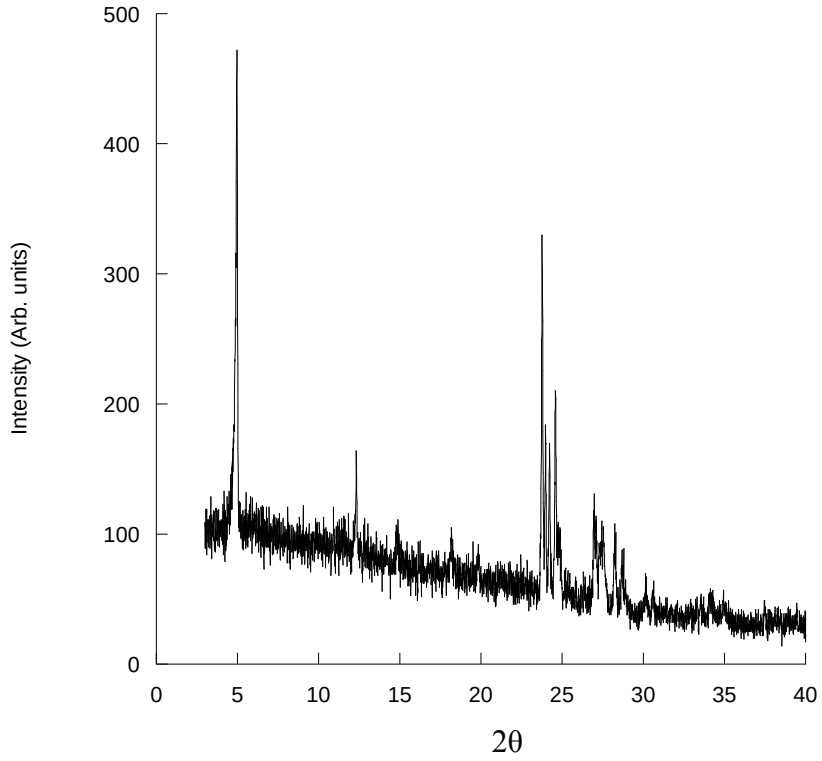

Figure 7 Powder X-ray diffraction pattern of $[Ce(H_2O)MoO_4]_2[2,6\text{-NDS}]$

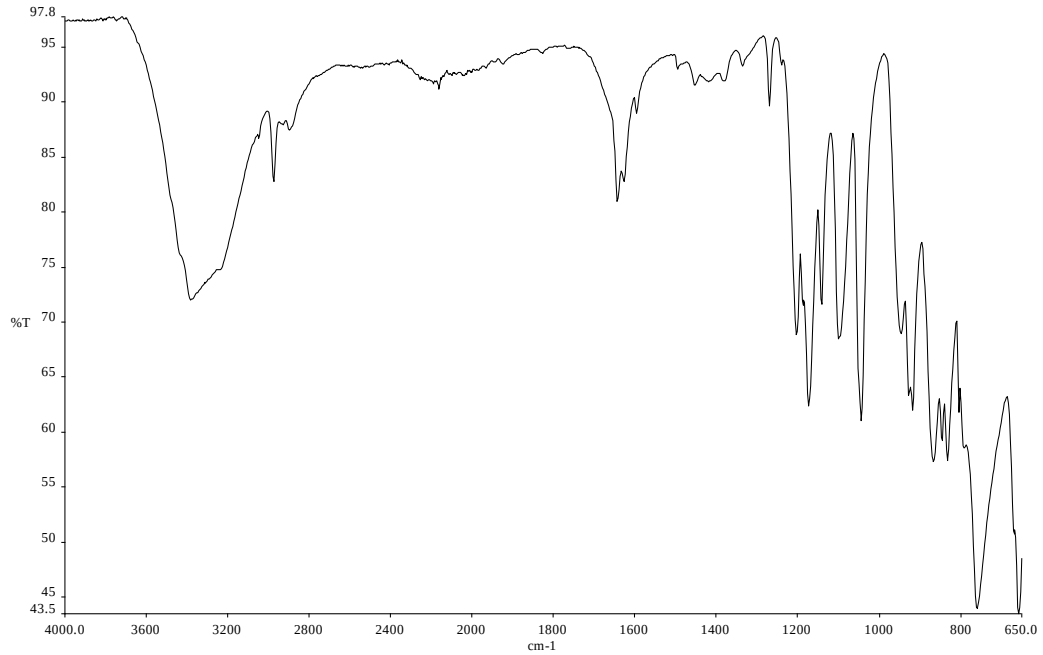

Figure 8 FTIR spectra for $[Ce(H_2O)MoO_4]_2[2,6\text{-NDS}]$ showing bands due to OH at 3383 cm^{-1}, S-O stretching modes at 1174 (antisymmetric) and 1045 cm^{-1} (symmetric) and the molybdate stretching frequency at 761 cm^{-1}.

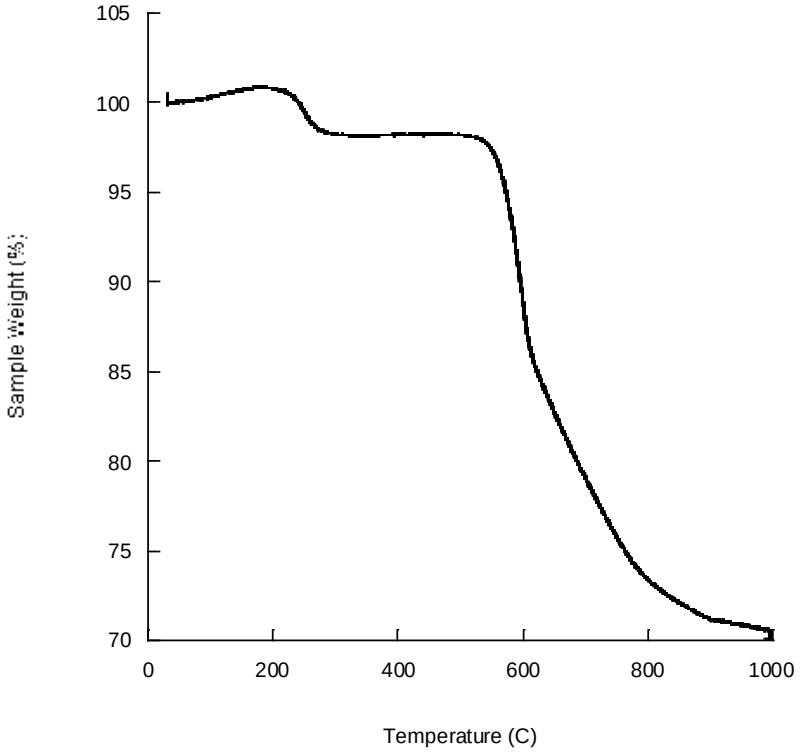

Figure 9 TGA trace of $[Ce(H_2O)MoO_4]_2$[2,6-NDS] showing two distinct mass losses. First mass loss of 1.8 % below 260 °C and an additional mass loss of 27.7 % by 995 °C. End product is found to be a mixture of $Ce_2Mo_3O_{12}$ & CeO_2.

$[Pr(H_2O)MoO_4]_2[2,6\text{-NDS}]$

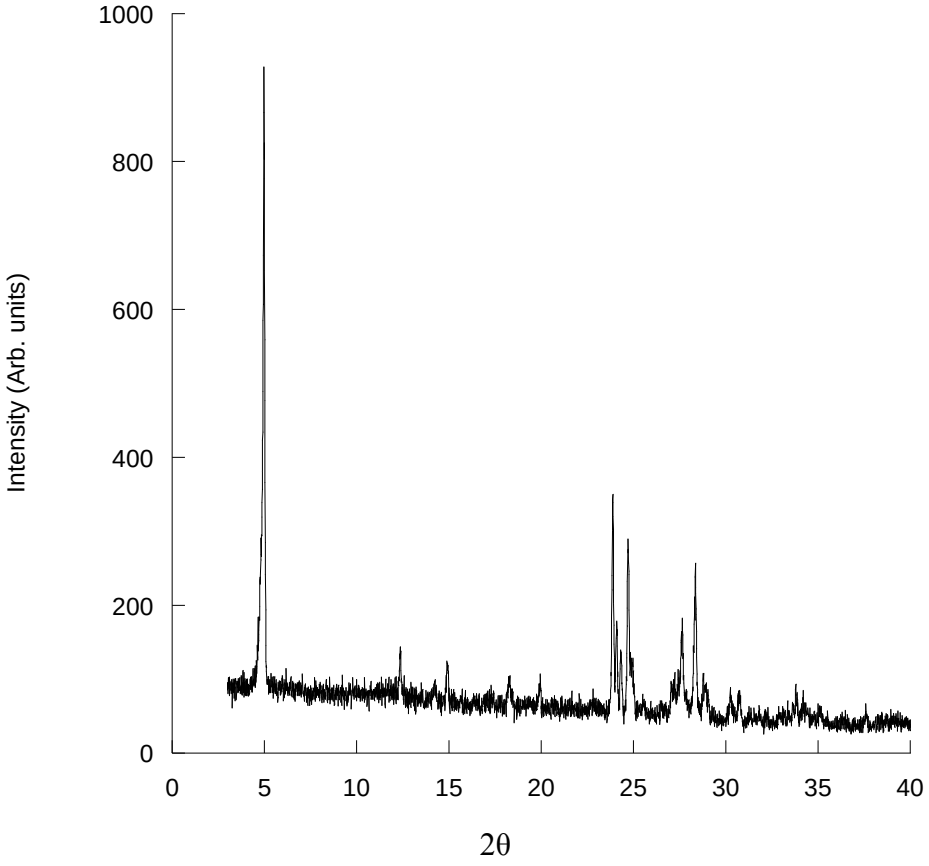

Figure 10 Powder X-ray diffraction pattern of $[Pr(H_2O)MoO_4]_2[2,6\text{-NDS}]$

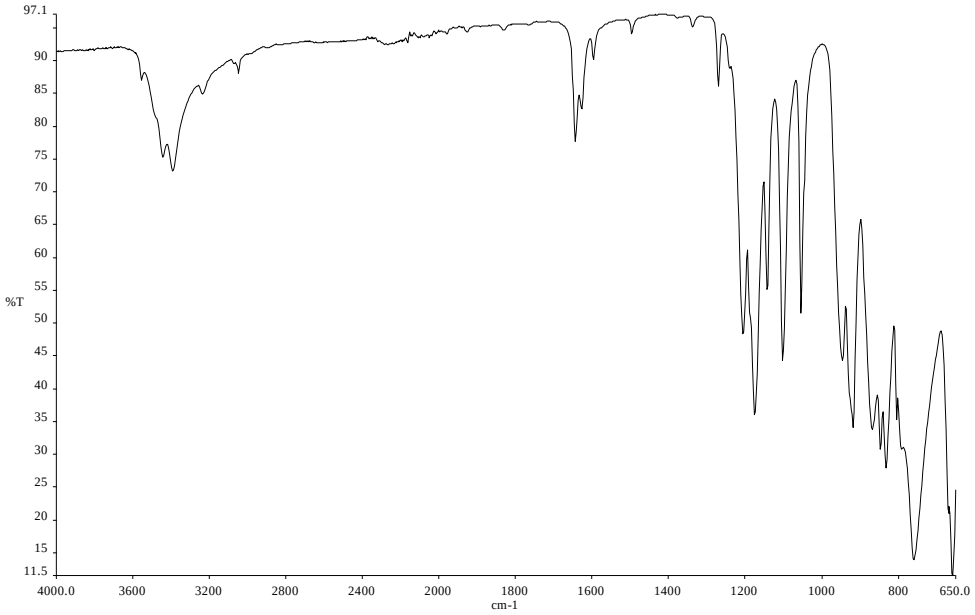

Figure 11 FTIR spectra for $[Pr(H_2O)MoO_4]_2$[2,6-NDS] showing bands due to OH at 3394 cm^{-1}, S-O stretching modes at 1176 (antisymmetric) and 1055 cm^{-1} (symmetric) and the molybdate stretching frequency at 761 cm^{-1}.

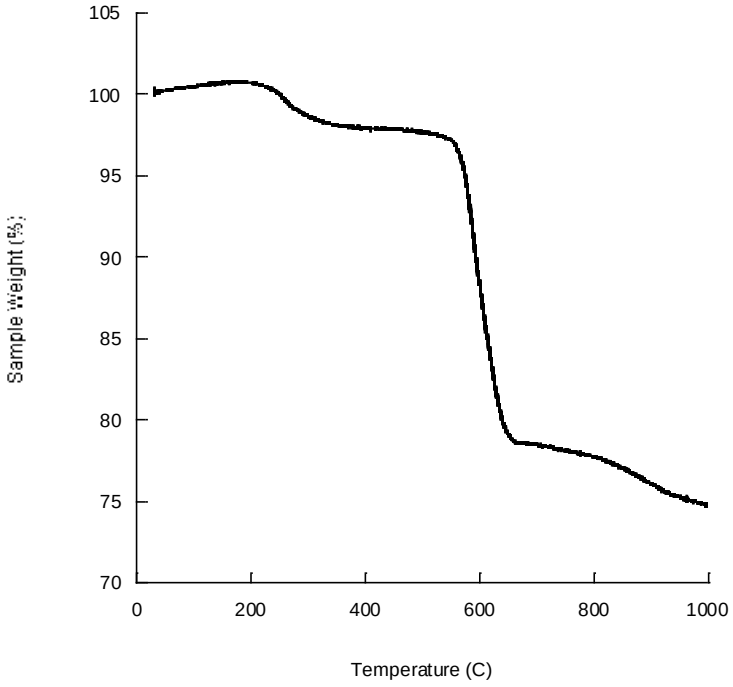

Figure 12 TGA trace of $[Pr(H_2O)MoO_4]_2$[2,6-NDS] showing two distinct mass losses. First mass loss of 3.2 % below 400 °C and an additional mass loss of 22.7 % by 990 °C. End product is found to be a mixture of $Pr_2Mo_2O_9$ & Pr_7O_{12}.

Table 5 Elemental analysis of $[Ln(H_2O)MoO_4]_2$[2,6-NDS] (La-Nd)

Lanthanide	Interlayer Separation (Å)	Elemental Analysis	
		Observed (%)	Calculated (%)
Nd	17.8	C-12.34	C-12.91
		H-0.92	H-1.08
La	17.9	C-11.49	C-13.06
		H-1.03	H-1.10
Ce	17.9	C-11.99	C-13.02
		H-0.97	H-1.09
Pr	17.8	C-7.35	C-13.00
		H-0.66	H-1.09

Anion exchange reactions of $[Nd(H_2O)MoO_4]_2$[2,6-NDS]

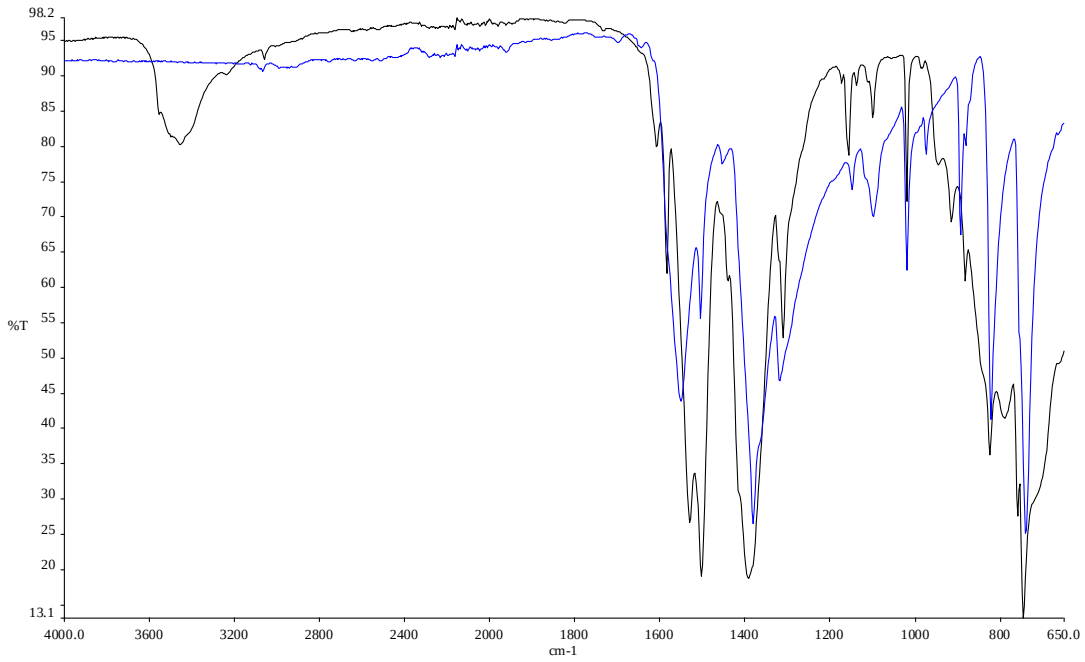

Figure 13 FTIR spectra of anion exchange product $[Nd(H_2O)MoO_4]_2$[Terephthalate] (black) showing bands due to OH at 3456 cm^{-1} and C-O stretching modes at 1531 (antisymmetric) and 1393 cm^{-1} (symmetric), and sodium terephthalate (blue).

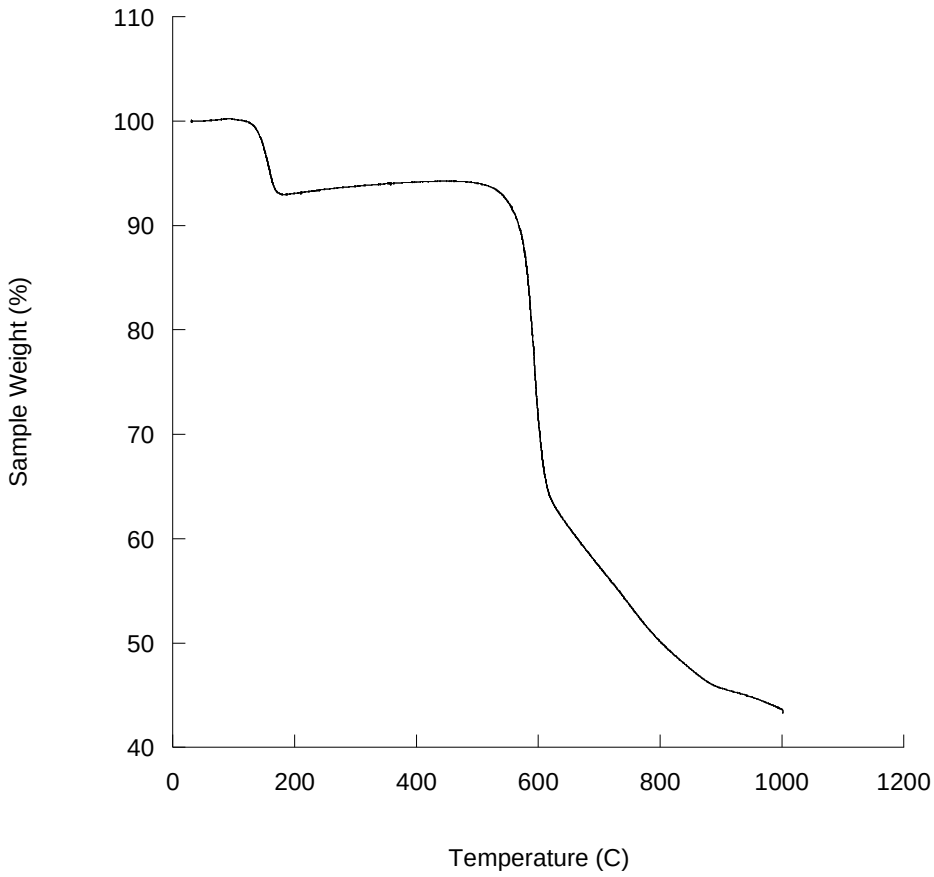

Figure 14 TGA trace of of anion exchange product $[Nd(H_2O)MoO_4]_2$[Terephthalate] showing two distinct mass losses. First mass loss of 5.8 % below 200 °C and an additional mass loss of 52.0 % by 1000 °C. End product is found to be a mixture of Nd_6MoO_{12} & Nd_2O_3.

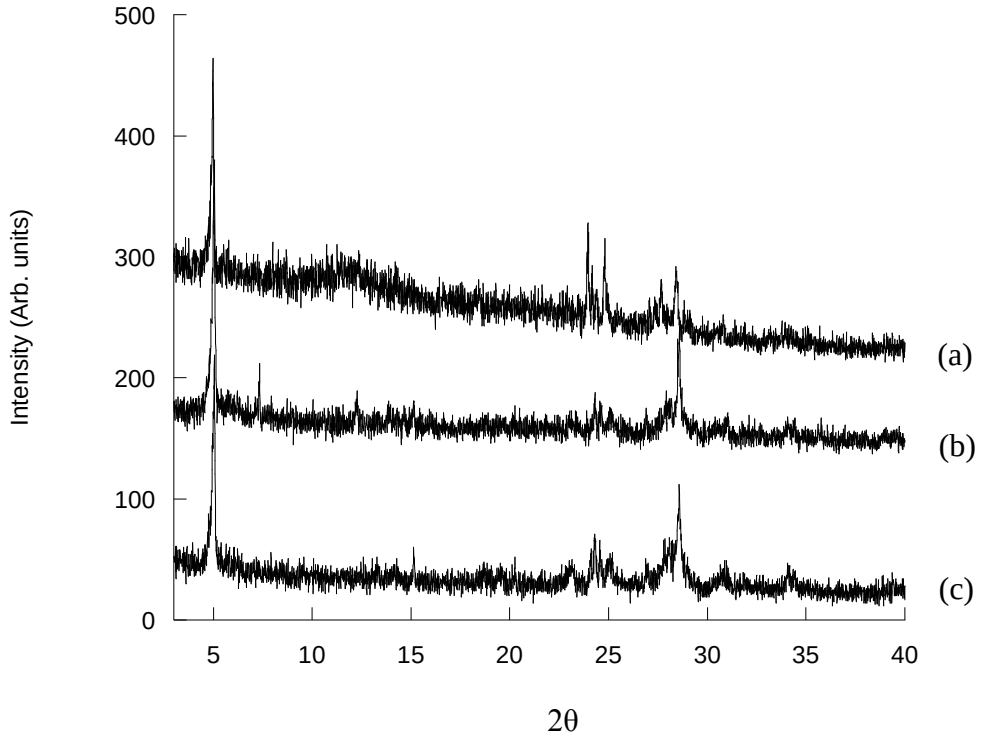

Figure 15 Powder XRD patterns of (a) $[Nd(H_2O)MoO_4]_2[2,6\text{-NDS}]$ (**1**), and anion exchange products (b) $[Nd(H_2O)MoO_4]_2[2,6\text{-NDC}]$ (90 °C) and (c) $[Nd(H_2O)MoO_4]_2[2,6\text{-NDC}]$ (hydrothermal)

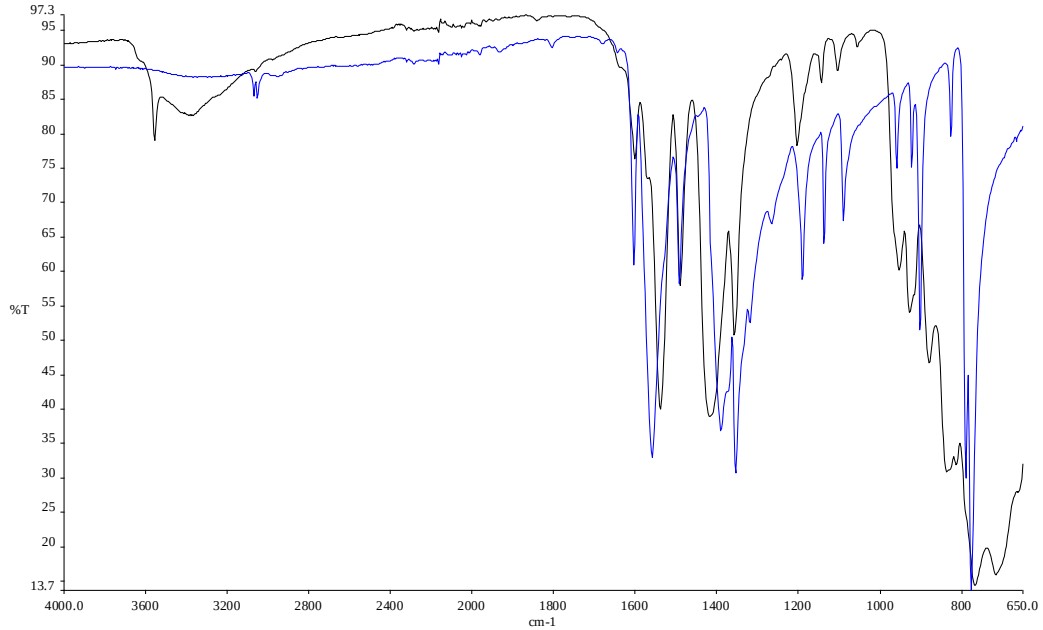

Figure 16 FTIR spectra of anion exchange product $[Nd(H_2O)MoO_4]_2[2,6\text{-NDC}]$ (90 °C, black) showing bands due to OH at 3370 cm^{-1} and C-O stretching modes at 1539 (antisymmetric) and 1418 cm^{-1} (symmetric), and 2,6-NDC (blue).

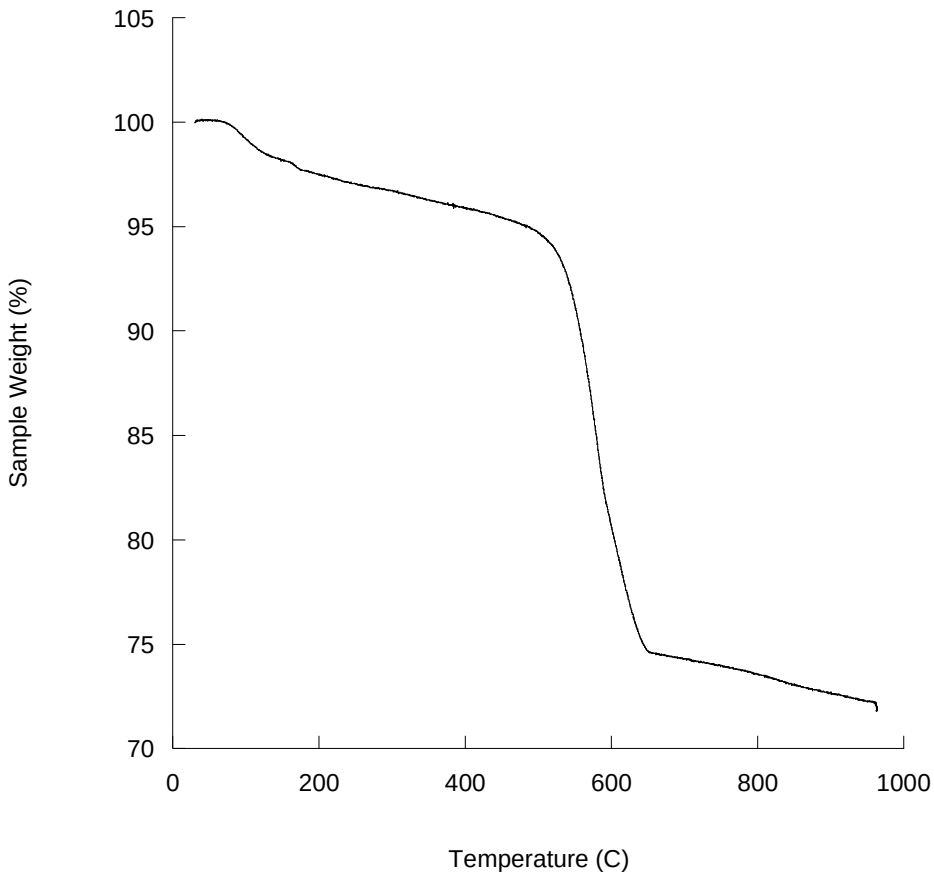

Figure 17 TGA trace of anion exchange product $[Nd(H_2O)MoO_4]_2$[2,6-NDC] (90 °C), showing two distinct mass losses. First mass loss of 4.1 % below 500 °C and an additional mass loss of 24.6 % by 700 °C. End product is found to be a mixture of $Nd_2Mo_3O_9$ & $Nd_2Mo_2O_7$.

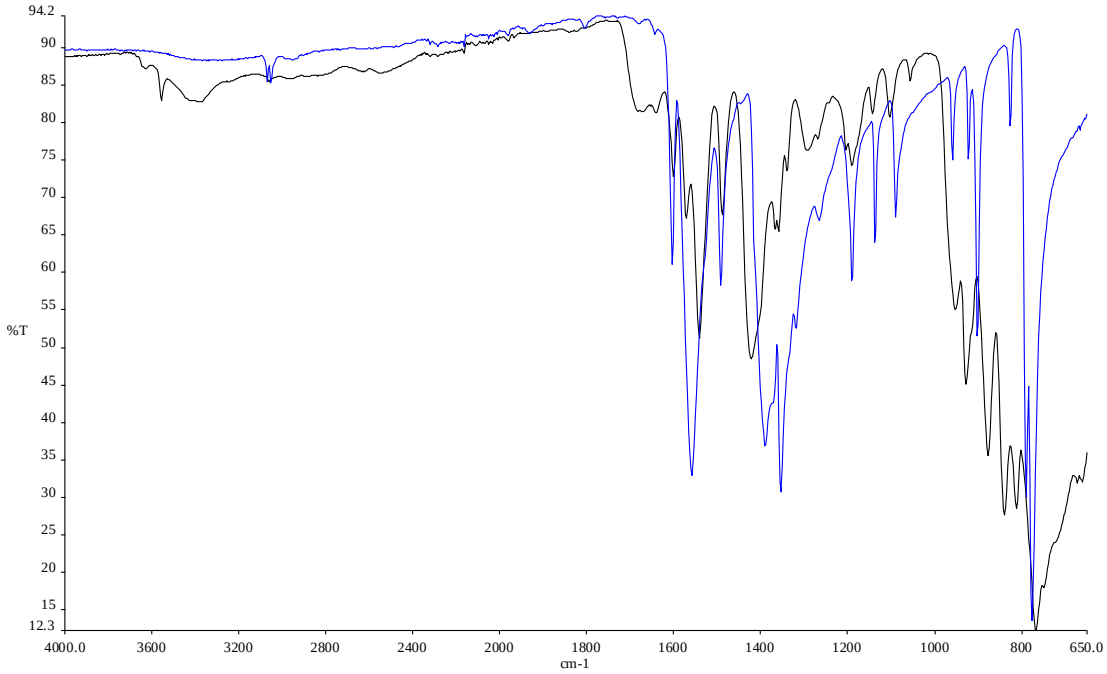

Figure 18 FTIR spectra of anion exchange product $[Nd(H_2O)MoO_4]_2$[2,6-NDC] (hydrothermally, black) showing bands due to OH at 3382 cm^{-1} and C-O stretching modes at 1542 (antisymmetric) and 1423 cm^{-1} (symmetric), and 2,6-NDC (blue).

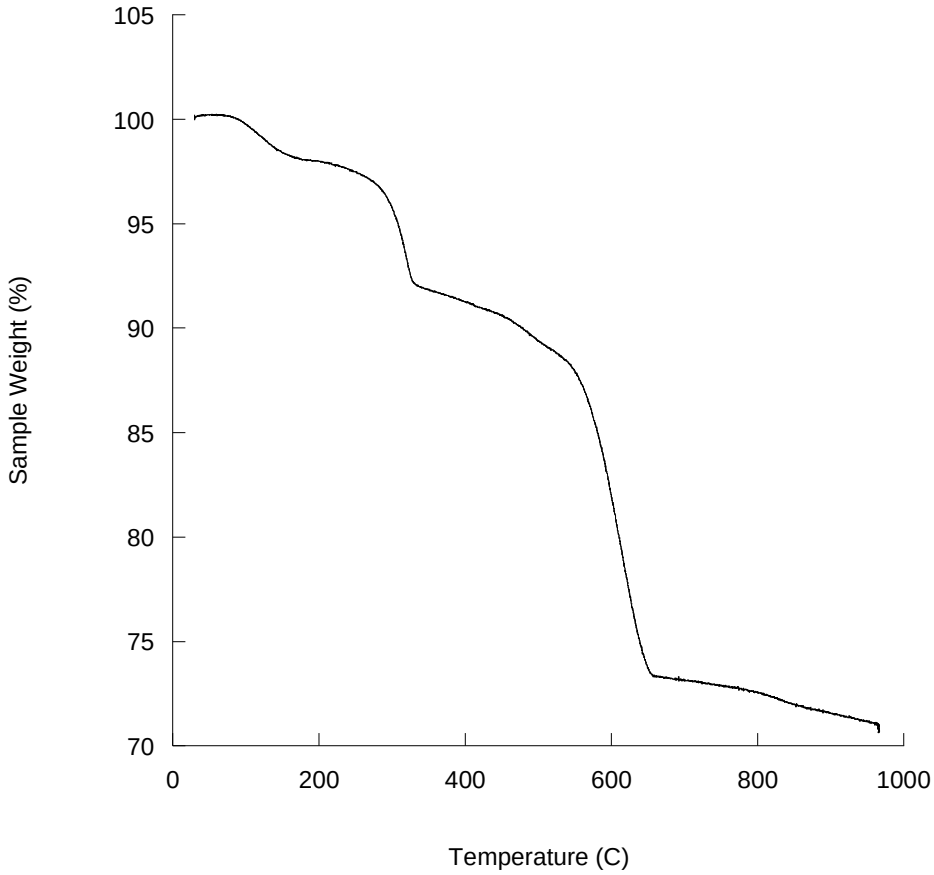

Figure 19 TGA trace of anion exchange product $[Nd(H_2O)MoO_4]_2$[2,6-NDC] (hydrothermally), showing three distinct mass losses. First two mass losses of a total of 8.7 % below 325 °C and an additional mass loss of 20.9 % by 700 °C. End product is found to be a mixture of $Nd_2Mo_3O_9$ & $Nd_2Mo_2O_7$.

Crystallographic data for $[Nd(H_2O)MoO_4]_2[1,5\text{-NDS}]$ (2)

Table 6 Crystal data and structure refinement for $[Nd(H_2O)MoO_4]_2[1,5\text{-NDS}]$

Identification code	**2008src0991 / SEH79**	
Empirical formula	$C_{10}H_5Mo_2Nd_2O_{14}S_2$	
Formula weight	893.62	
Temperature	120(2) K	
Wavelength	0.71073 Å	
Crystal system	Monoclinic	
Space group	$P2_1/c$	
Unit cell dimensions	a = 16.9552(9) Å	α = 90°
	b = 7.3924(4) Å	β = 91.079(3)°
	c = 7.5290(4) Å	γ = 90°
Volume	943.51(9) $Å^3$	
Z	2	
Density (calculated)	3.262 mg / m^3	
Absorption coefficient	7.017 mm^{-1}	
F(000)	860	
Crystal	Fragment; purple	
Crystal size	0.04 × 0.02 × 0.002 mm^3	
θ range for data collection	3.01 – 27.48°	
Index ranges	$-21 \le h \le 21$, $-9 \le k \le 9$, $-9 \le l \le 9$	
Reflections collected	16145	
Independent reflections	2157 [R_{int} = 0.0800]	
Completeness to θ = 27.48°	99.8 %	
Absorption correction	Semi–empirical from equivalents	
Max. and min. transmission	0.9861 and 0.7666	
Refinement method	Full-matrix least-squares on F^2	
Data / restraints / parameters	2157 / 0 / 145	
Goodness-of-fit on F^2	1.093	
Final R indices [$F^2 > 2\sigma(F^2)$]	*R1* = 0.0418, *wR2* = 0.0773	

R indices (all data)	*R1* = 0.0568, *wR2* = 0.0839
Largest diff. peak and hole	1.285 and −1.171 e Å^{-3}

Diffractometer: *Nonius KappaCCD* area detector (ϕ scans and ω scans to fill *asymmetric unit* sphere). **Cell determination:** DirAx (Duisenberg, A.J.M.(1992). J. Appl. Cryst. 25, 92-96.) **Data collection:** Collect (Collect: Data collection software, R. Hooft, Nonius B.V., 1998). **Data reduction and cell refinement**: *Denzo* (Z. Otwinowski & W. Minor, *Methods in Enzymology* (1997) Vol. **276**: *Macromolecular Crystallography*, part A, pp. 307−326; C. W. Carter, Jr. & R. M. Sweet, Eds., Academic Press). **Absorption correction**: *SADABS Version 2.10.* (G. M. Sheldrick (2003)) Bruker AXS Inc., Madison, Wisconsin, USA. S**tructure solution**: *SHELXS97* (G. M. Sheldrick, Acta Cryst. (1990) A**46** 467−473). S**tructure refinement**: *SHELXL97* (G. M. Sheldrick (1997), University of Göttingen, Germany). **Graphics:** *ORTEP3 for Windows* (L. J. Farrugia, J. Appl. Crystallogr. 1997, 30, 565).

Table 7 Atomic coordinates [× 10^4], equivalent isotropic displacement parameters [Å^2 × 10^3] and site occupancy factors. U_{eq} is defined as one third of the trace of the orthogonalized U^{ij} tensor.

Atom	*x*	*y*	*z*	U_{eq}	*S.o.f.*
Nd1	1542(1)	4105(1)	2634(1)	8(1)	1
O1	1297(3)	7322(8)	2354(8)	14(1)	1
O5	161(3)	4202(8)	2876(7)	13(1)	1
O4	2551(3)	5762(8)	4351(7)	15(1)	1
O3	1056(3)	4507(8)	−455(7)	15(1)	1
O2	1266(3)	3977(7)	5926(7)	11(1)	1
O6	2631(3)	2099(8)	3431(8)	15(1)	1
Mo1	858(1)	9464(1)	2482(1)	8(1)	1
S1	3018(1)	496(2)	4147(3)	9(1)	1
O8	3000(3)	−1018(7)	2904(7)	12(1)	1
O7	2718(3)	−11(8)	5867(7)	12(1)	1

C1	4030(4)	1091(11)	4413(10)	8(2)	1
C2	4261(5)	2766(11)	3879(11)	13(2)	1
C4	4592(4)	−246(11)	5009(10)	9(2)	1
C5	4378(5)	−1981(10)	5636(10)	8(2)	1
C3	5065(5)	3204(11)	3865(11)	17(2)	1

Table 8 Bond lengths [Å] and angles [°].

Nd1–O5	2.354(5)	Mo1–O2^{iv}	1.791(6)
Nd1–O1	2.423(6)	Mo1–Nd1^{viii}	3.6225(8)
Nd1–O6	2.433(6)	S1–O7	1.449(6)
Nd1–O4	2.453(6)	S1–O8	1.459(6)
Nd1–O3	2.470(6)	S1–C1	1.779(8)
Nd1–O7^{i}	2.509(5)	O7–Nd1^{vi}	2.509(5)
Nd1–O2	2.533(5)	C1–C2	1.362(11)
Nd1–O2^{i}	2.653(5)	C1–C4	1.438(11)
Nd1–Mo1^{ii}	3.6225(8)	C2–C3	1.401(12)
O1–Mo1	1.753(6)	C2–H2	0.9500
O5–Mo1^{iii}	1.753(5)	C4–C5	1.417(10)
O3–Mo1^{iv}	1.756(6)	C4–C4^{ix}	1.431(14)
O2–Mo1^{v}	1.791(6)	C5–C3^{ix}	1.356(11)
O2–Nd1^{vi}	2.653(5)	C5–H5	0.9500
O6–S1	1.454(6)	C3–C5^{ix}	1.356(11)
Mo1–O5^{vii}	1.753(5)	C3–H3	0.9500
Mo1–O3^{v}	1.756(6)		

O5–Nd1–O1	78.88(19)	O6–Nd1–O4	69.88(19)
O5–Nd1–O6	138.64(19)	O5–Nd1–O3	75.78(19)
O1–Nd1–O6	138.40(19)	O1–Nd1–O3	75.28(19)
O5–Nd1–O4	128.99(19)	O6–Nd1–O3	122.9(2)
O1–Nd1–O4	70.90(19)	O4–Nd1–O3	130.77(19)

O5–Nd1–O7^{i}	146.61(18)	Nd1–O2–Nd1^{vi}	118.2(2)
O1–Nd1–O7^{i}	80.14(19)	S1–O6–Nd1	157.4(4)
O6–Nd1–O7^{i}	71.75(19)	O5^{vii}–Mo1–O1	108.0(3)
O4–Nd1–O7^{i}	65.96(18)	O5^{vii}–Mo1–O3^{v}	110.8(3)
O3–Nd1–O7^{i}	73.94(18)	O1–Mo1–O3^{v}	111.4(3)
O5–Nd1–O2	73.89(18)	O5^{vii}–Mo1–O2^{iv}	111.2(2)
O1–Nd1–O2	94.99(18)	O1–Mo1–O2^{iv}	112.0(3)
O6–Nd1–O2	83.65(19)	O3^{v}–Mo1–O2^{iv}	103.3(3)
O4–Nd1–O2	69.07(18)	O5^{vii}–Mo1–Nd1^{viii}	115.07(19)
O3–Nd1–O2	149.42(18)	O1–Mo1–Nd1^{viii}	136.14(19)
O7^{i}–Nd1–O2	133.81(17)	O3^{v}–Mo1–Nd1^{viii}	60.42(19)
O5–Nd1–O2^{i}	84.08(18)	O2^{iv}–Mo1–Nd1^{viii}	44.28(17)
O1–Nd1–O2^{i}	140.55(18)	O7–S1–O6	112.3(4)
O6–Nd1–O2^{i}	73.89(17)	O7–S1–O8	111.8(3)
O4–Nd1–O2^{i}	143.06(18)	O6–S1–O8	112.6(3)
O3–Nd1–O2^{i}	66.09(18)	O7–S1–C1	108.5(3)
O7^{i}–Nd1–O2^{i}	96.16(17)	O6–S1–C1	105.6(3)
O2–Nd1–O2^{i}	114.08(13)	O8–S1–C1	105.7(3)
O5–Nd1–Mo1^{ii}	73.30(14)	S1–O7–Nd1^{vi}	134.4(3)
O1–Nd1–Mo1^{ii}	150.72(14)	C2–C1–C4	121.6(7)
O6–Nd1–Mo1^{ii}	70.85(13)	C2–C1–S1	118.3(6)
O4–Nd1–Mo1^{ii}	135.20(13)	C4–C1–S1	119.8(6)
O3–Nd1–Mo1^{ii}	89.04(14)	C1–C2–C3	119.8(8)
O7^{i}–Nd1–Mo1^{ii}	119.58(13)	C1–C2–H2	120.1
O2–Nd1–Mo1^{ii}	86.02(12)	C3–C2–H2	120.1
O2^{i}–Nd1–Mo1^{ii}	28.12(12)	C5–C4–C4^{ix}	119.1(9)
Mo1–O1–Nd1	162.6(3)	C5–C4–C1	123.6(7)
Mo1^{iii}–O5–Nd1	165.9(3)	C4^{ix}–C4–C1	117.2(9)
Mo1^{iv}–O3–Nd1	160.0(3)	C3^{ix}–C5–C4	120.9(7)
Mo1^{v}–O2–Nd1	134.2(3)	C3^{ix}–C5–H5	119.5
Mo1^{v}–O2–Nd1^{vi}	107.6(2)	C4–C5–H5	119.5

C5^{ix}–C3–C2	121.2(8)
C5^{ix}–C3–H3	119.4
C2–C3–H3	119.4

Symmetry transformations used to generate equivalent atoms:

(i) x,–y+1/2,z–1/2 (ii) x,y–1,z (iii) –x,y–1/2,–z+1/2

(iv) x,–y+3/2,z–1/2 (v) x,–y+3/2,z+1/2 (vi) x,–y+1/2,z+1/2

(vii) –x,y+1/2,–z+1/2 (viii) x,y+1,z (xi) –x+1,–y,–z+1

Table 9 Anisotropic displacement parameters [$Å^2 \times 10^3$]. The anisotropic displacement factor exponent takes the form: $-2\pi^2[h^2a^{*2}U^{11} + \cdots + 2\,h\,k\,a^*\,b^*\,U^{12}]$.

Atom	U^{11}	U^{22}	U^{33}	U^{23}	U^{13}	U^{12}
Nd1	7(1)	8(1)	9(1)	0(1)	0(1)	0(1)
O1	15(3)	11(3)	17(3)	1(2)	−1(2)	4(2)
O5	13(3)	11(3)	14(3)	1(2)	0(2)	2(2)
O4	17(3)	14(3)	14(3)	4(2)	−2(2)	−5(2)
O3	11(3)	23(3)	11(3)	2(2)	0(2)	3(2)
O2	8(3)	9(3)	15(3)	2(2)	−1(2)	−4(2)
O6	5(3)	15(3)	26(3)	−2(3)	−6(2)	−2(2)
Mo1	7(1)	8(1)	9(1)	0(1)	0(1)	0(1)
S1	8(1)	7(1)	12(1)	0(1)	1(1)	1(1)
O8	13(3)	7(3)	17(3)	−4(2)	−2(2)	−1(2)
O7	6(3)	18(3)	11(3)	0(2)	1(2)	−3(2)
C1	7(4)	12(4)	6(3)	−1(3)	3(3)	1(3)
C2	11(4)	9(4)	18(4)	4(3)	0(3)	3(3)
C4	2(4)	13(4)	13(4)	3(3)	1(3)	1(3)
C5	6(4)	10(4)	9(4)	2(3)	−1(3)	1(3)
C3	24(5)	8(4)	17(4)	4(3)	2(4)	2(3)

Table 10 Hydrogen coordinates [$\times 10^4$] and isotropic displacement parameters [$Å^2 \times 10^3$].

Atom	*x*	*y*	*z*	U_{eq}	*S.o.f.*
H2	3878	3636	3517	15	1

H5	3836	–2293	5709	10	1
H3	5222	4378	3499	20	1

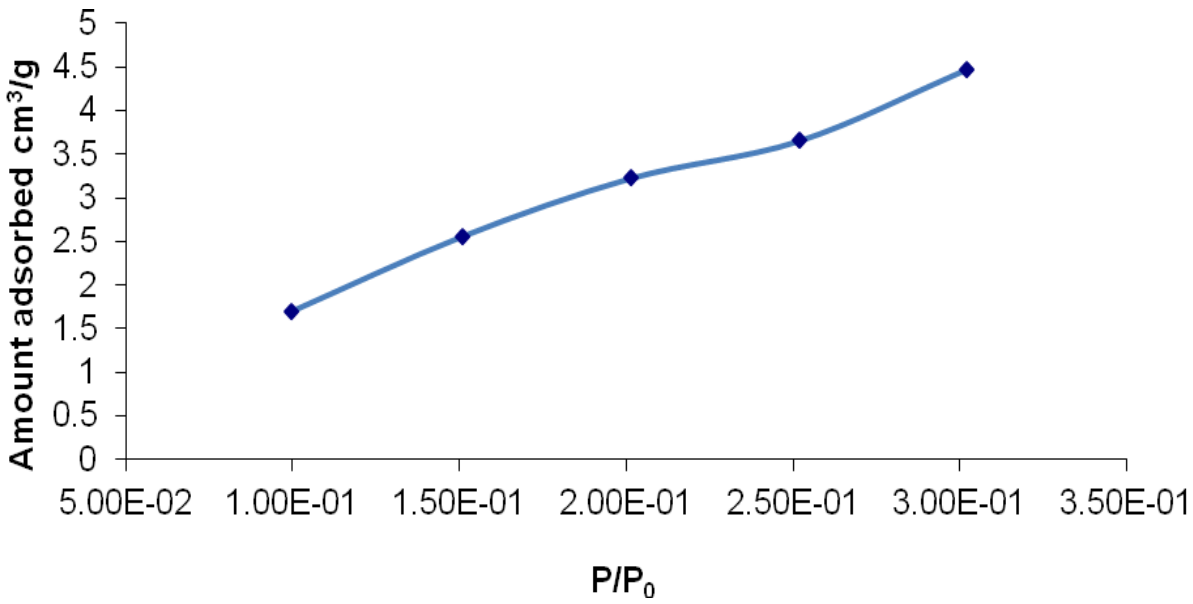

Figure 20 Adsorption isotherm for $[Nd(H_2O)MoO_4]_2$[1,5-NDS](**2**), degassed at 120 °C overnight.

Characterising data for $[Ln(H_2O)MoO_4]_2[1,5\text{-NDS}]$ (La-Nd)

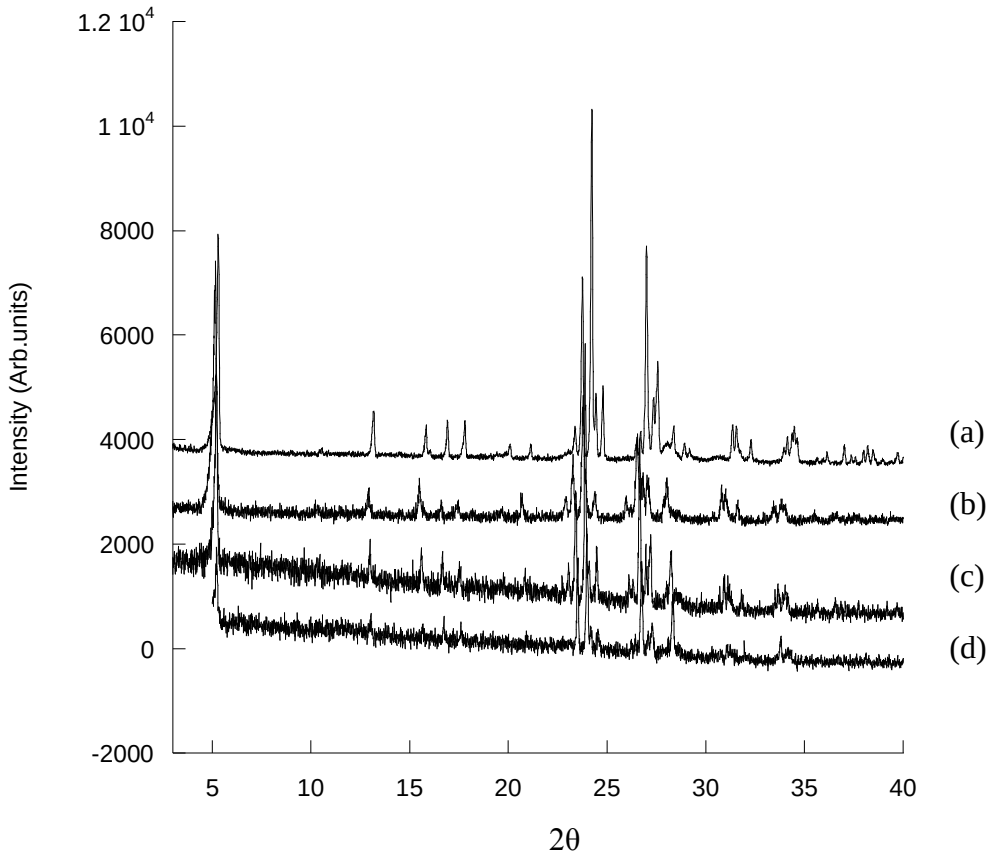

Figure 21 Powder XRD patterns of (a) $[Nd(H_2O)MoO_4]_2[1,5\text{-NDS}]$, (b) $[La(H_2O)MoO_4]_2[1,5\text{-NDS}]$, (c) $[Ce(H_2O)MoO_4]_2[1,5\text{-NDS}]$, and (d) $[Pr(H_2O)MoO_4]_2[1,5\text{-NDS}]$.

$[La(H_2O)MoO_4]_2[1,5\text{-NDS}]$

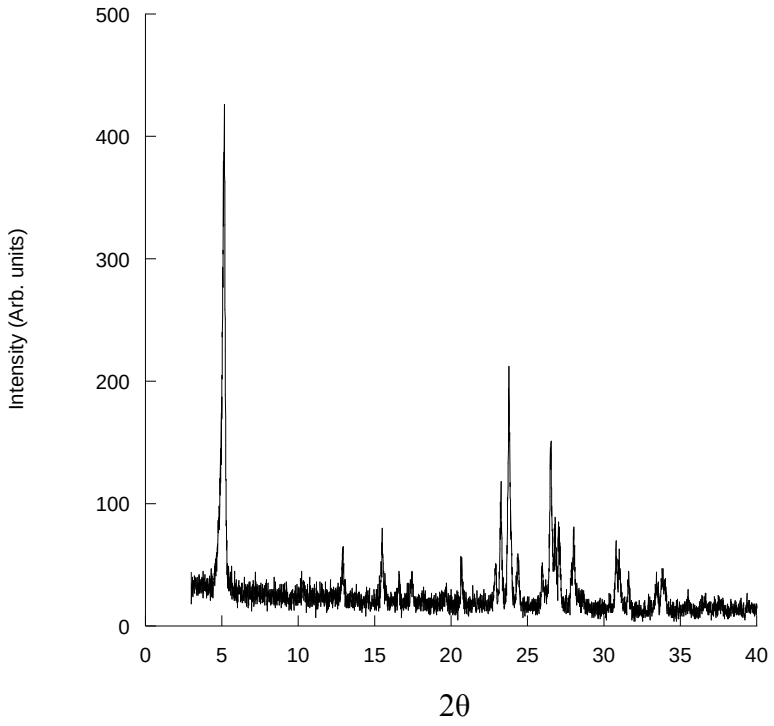

Figure 22 Powder X-ray diffraction pattern of $[La(H_2O)MoO_4]_2[1,5\text{-NDS}]$

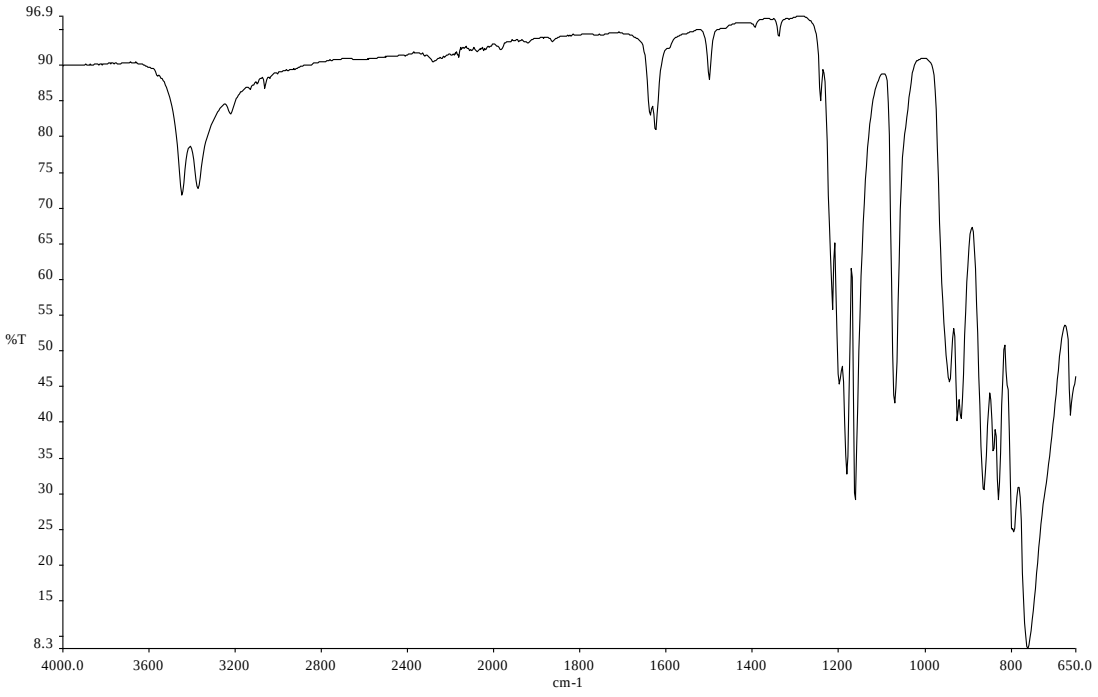

Figure 23 FTIR spectra for $[La(H_2O)MoO_4]_2[1,5\text{-NDS}]$ showing bands due to OH at 3377 cm^{-1}, S-O stretching modes at 1182 (antisymmetric) and 1071 cm^{-1} (symmetric) and the molybdate stretching frequency at 761 cm^{-1}.

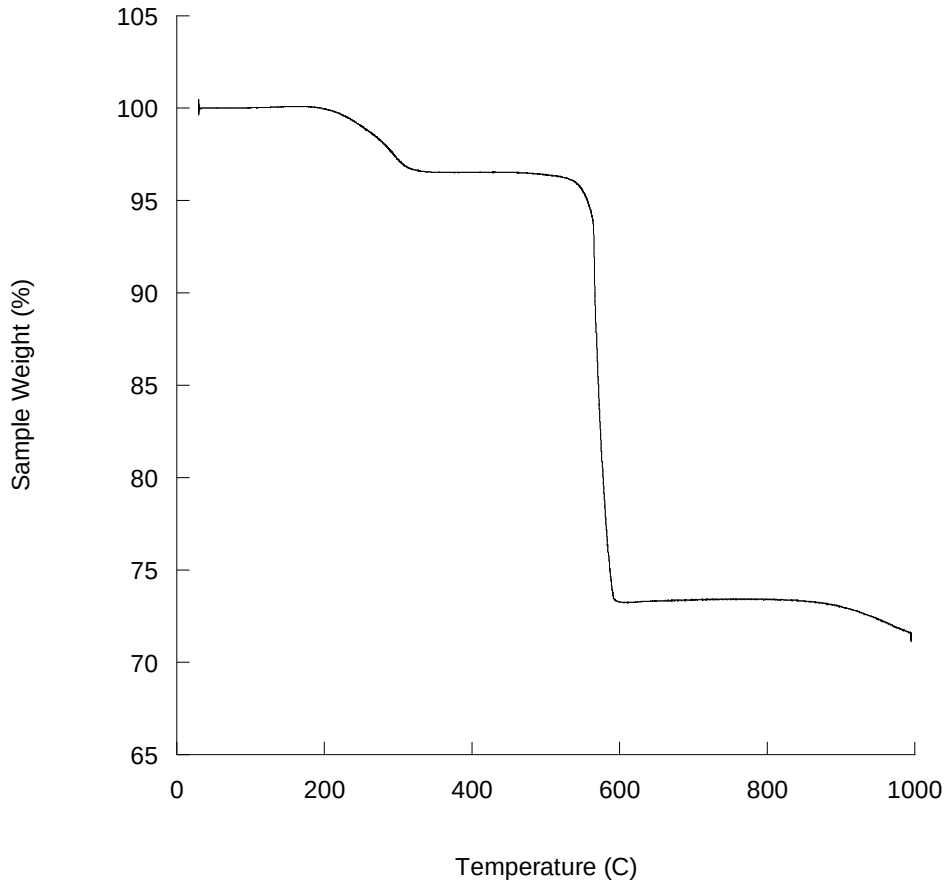

Figure 24 TGA trace of [La $(H_2O)MoO_4]_2$[1,5-NDS] showing two distinct mass losses. First mass loss of 3.6 % below 310 °C and an additional mass loss of 24.9 % by 600 °C. End product is found to be $La_2Mo_2O_9$.

$[Ce(H_2O)MoO_4]_2[1,5\text{-NDS}]$

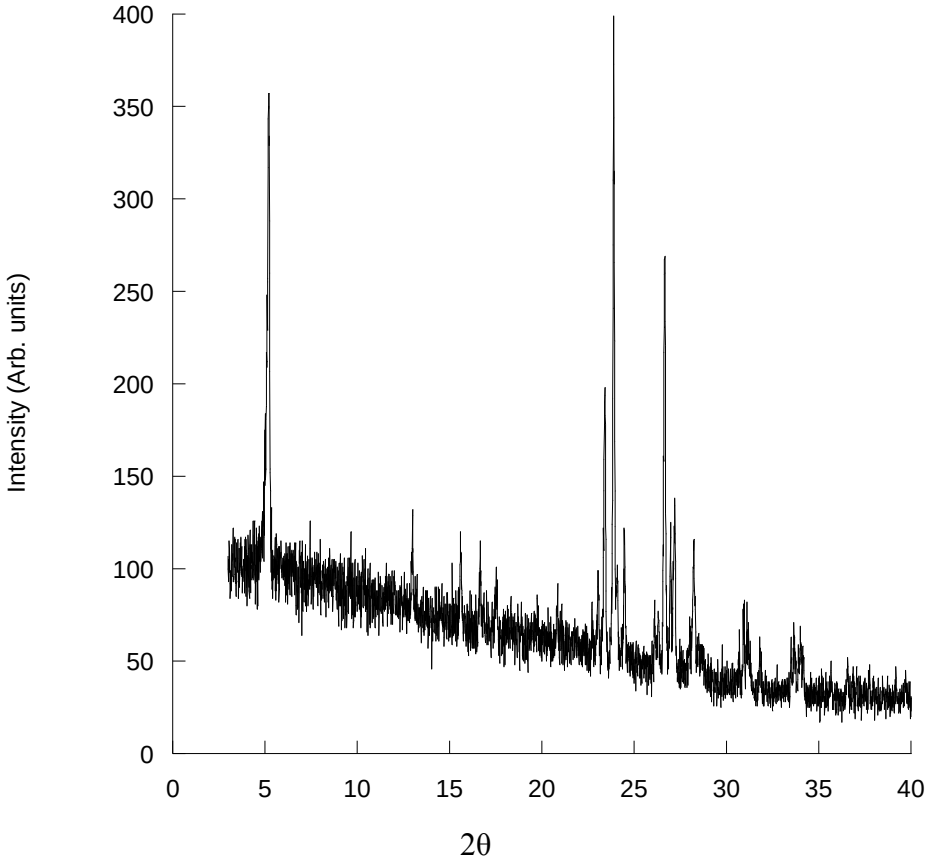

Figure 25 Powder X-ray diffraction pattern of $[Ce(H_2O)MoO_4]_2[1,5\text{-NDS}]$

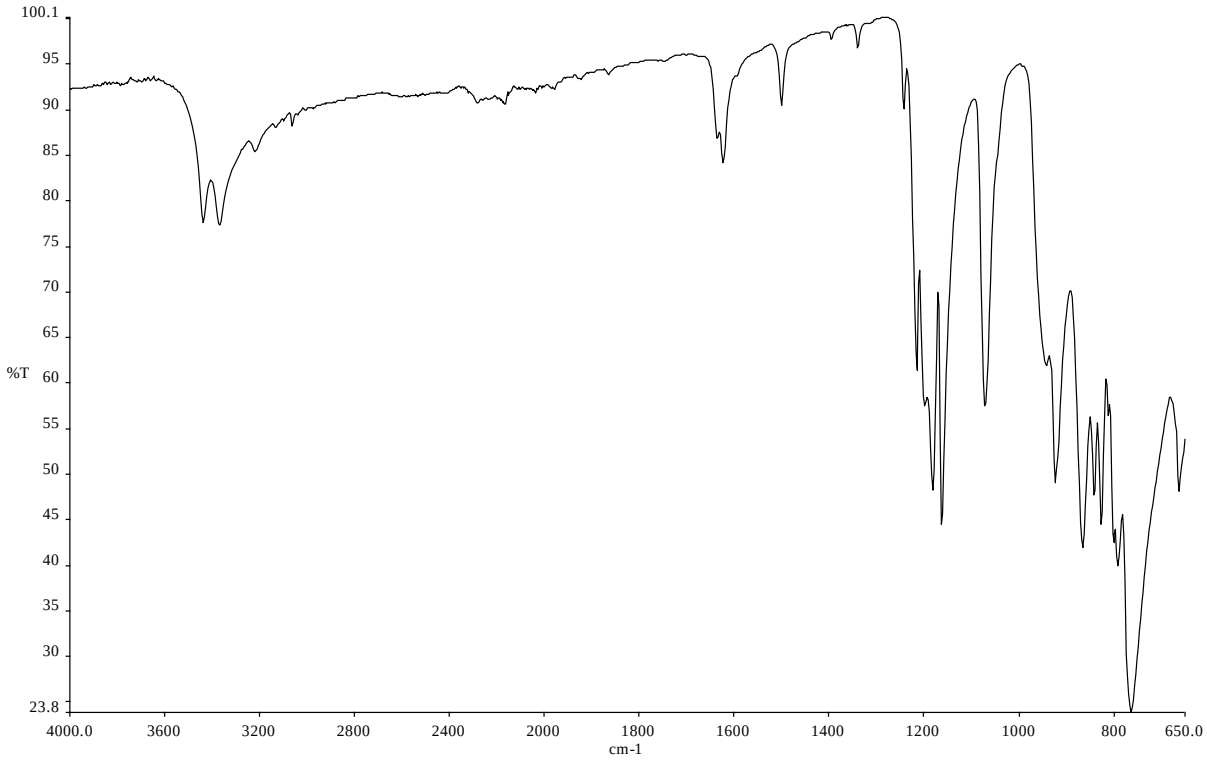

Figure 26 FTIR spectra for $[Ce(H_2O)MoO_4]_2$[1,5-NDS] showing bands due to OH at 3372 cm^{-1}, S-O stretching modes at 1183 (antisymmetric) and 1072 cm^{-1} (symmetric) and the molybdate stretching frequency at 759 cm^{-1}.

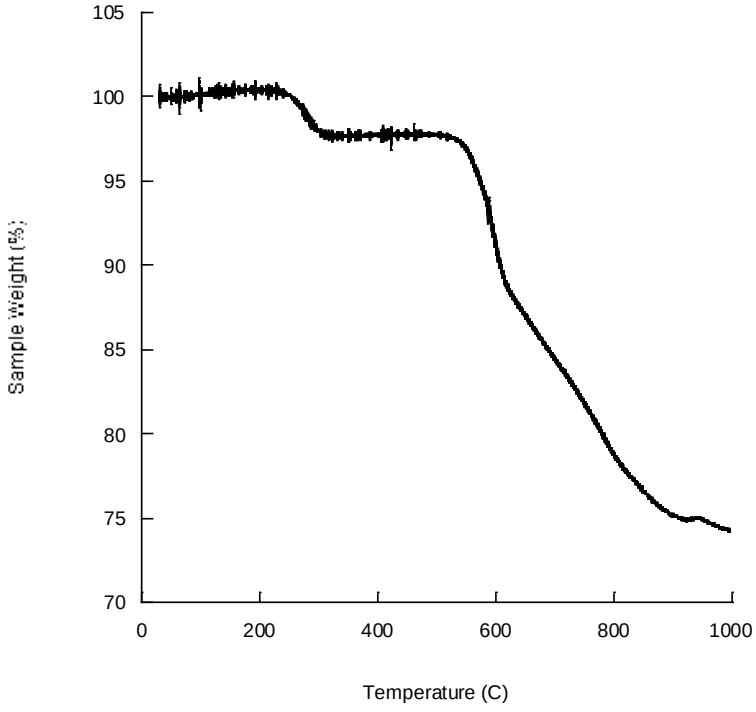

Figure 27 TGA trace of $[Ce(H_2O)MoO_4]_2$[1,5-NDS] showing two distinct mass losses. First mass loss of 2.3 % below 300 °C and an additional mass loss of 23.5 % by 995 °C. End product is found to be $Ce_2Mo_3O_{12}$.

$[Pr(H_2O)MoO_4]_2[1,5\text{-NDS}]$

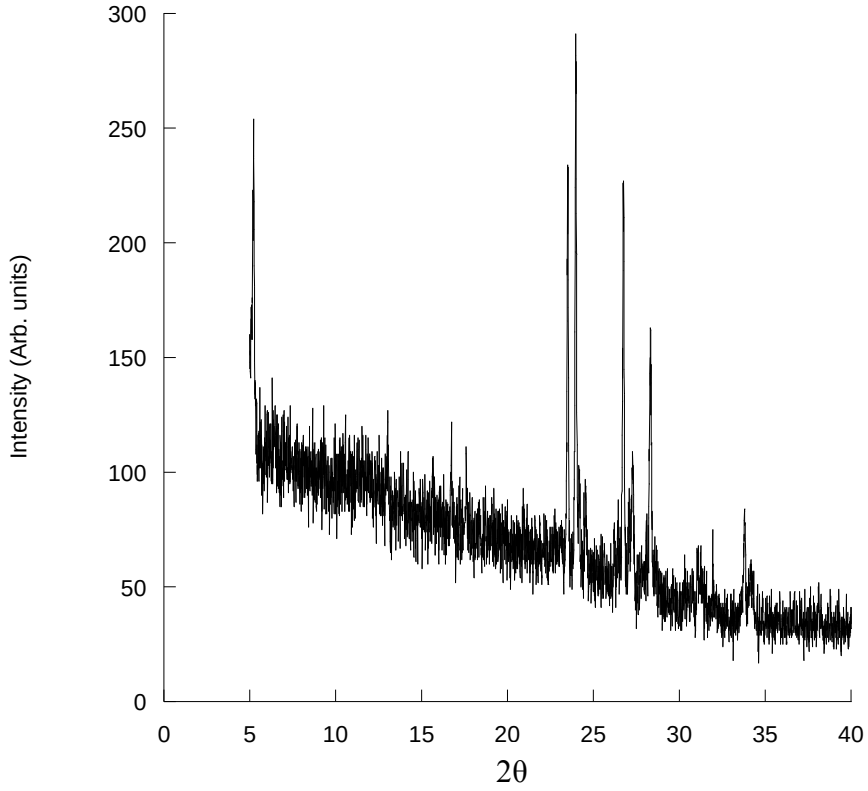

Figure 28 Powder X-ray diffraction pattern of $[Pr(H_2O)MoO_4]_2[1,5\text{-NDS}]$

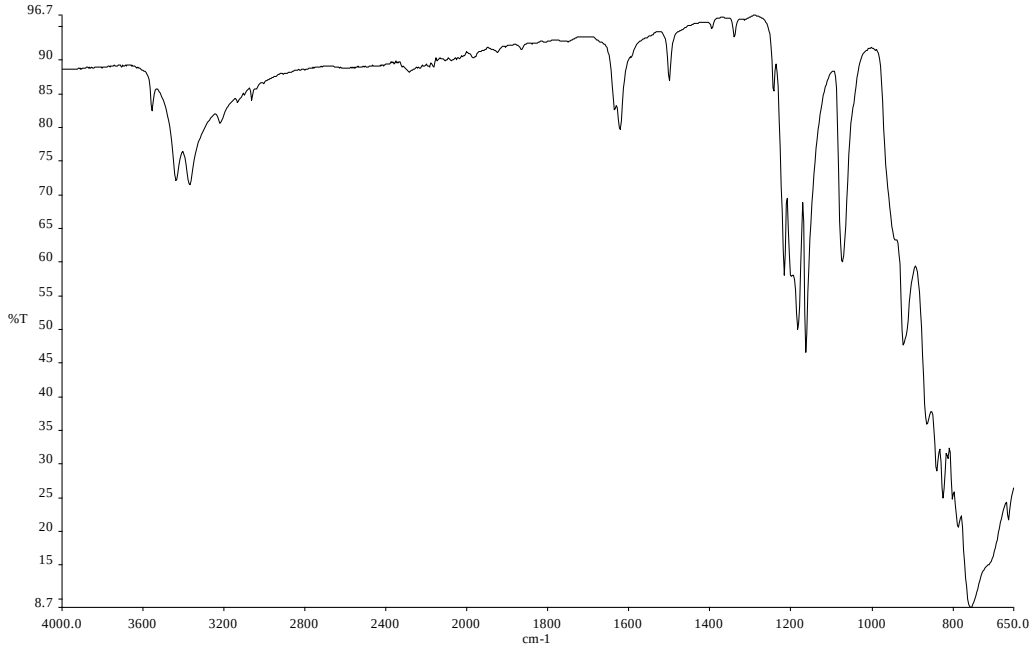

Figure 29 FTIR spectra for $[Pr(H_2O)MoO_4]_2[1,5\text{-NDS}]$ showing bands due to OH at 3371 cm^{-1}, S-O stretching modes at 1184 (antisymmetric) and 1074 cm^{-1} (symmetric) and the molybdate stretching frequency at 756 cm^{-1}.

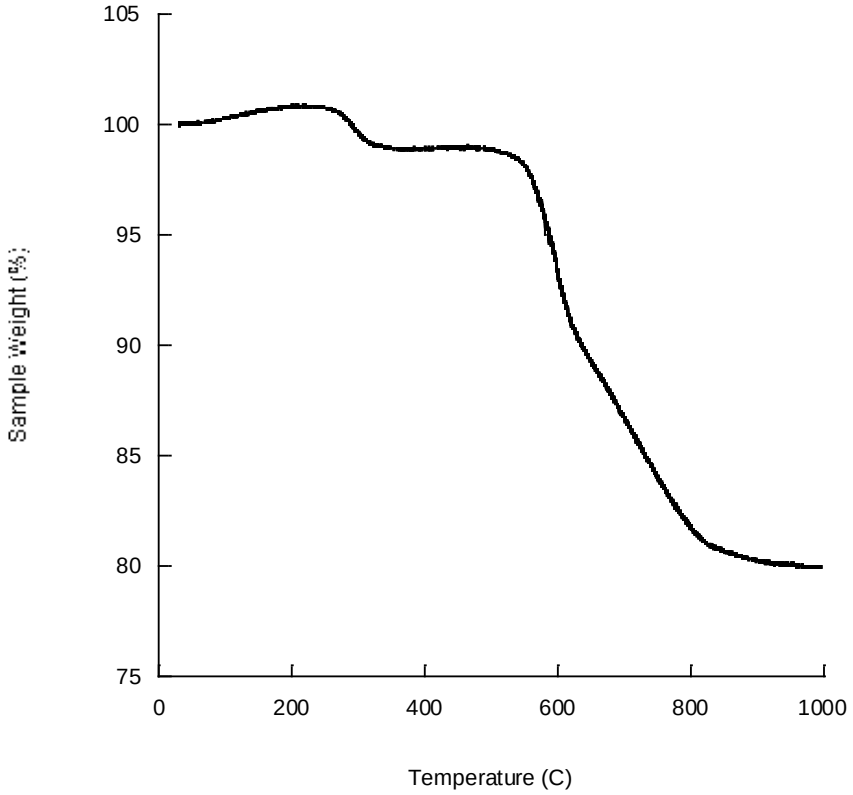

Figure 30 TGA trace of $[Pr(H_2O)MoO_4]_2$[1,5-NDS] showing two distinct mass losses. First mass loss of 1.0 % below 310 °C and an additional mass loss of 19.0 % by 900 °C. End product is found to be a mixture of Pr_2MoO_6 & Pr_6O_{11}.

Table 11 Elemental analysis of $[Ln(H_2O)MoO_4]_2$[1,5-NDS] (La-Nd)

Lanthanide	Interlayer Separation (Å)	Elemental Analysis	
		Observed (%)	Calculated (%)
Nd	16.7	C-9.57	C-12.91
		H-0.81	H-1.08
La	17.2	C-11.57	C-12.99
		H-1.07	H-1.08
Ce	17.0	C-10.23	C-13.02
		H-0.83	H-1.09
Pr	16.9	C-10.09	C-13.00
		H-0.82	H-1.09

Anion Exchange reactions of $[Nd(H_2O)MoO_4]_2$[1,5-NDS]

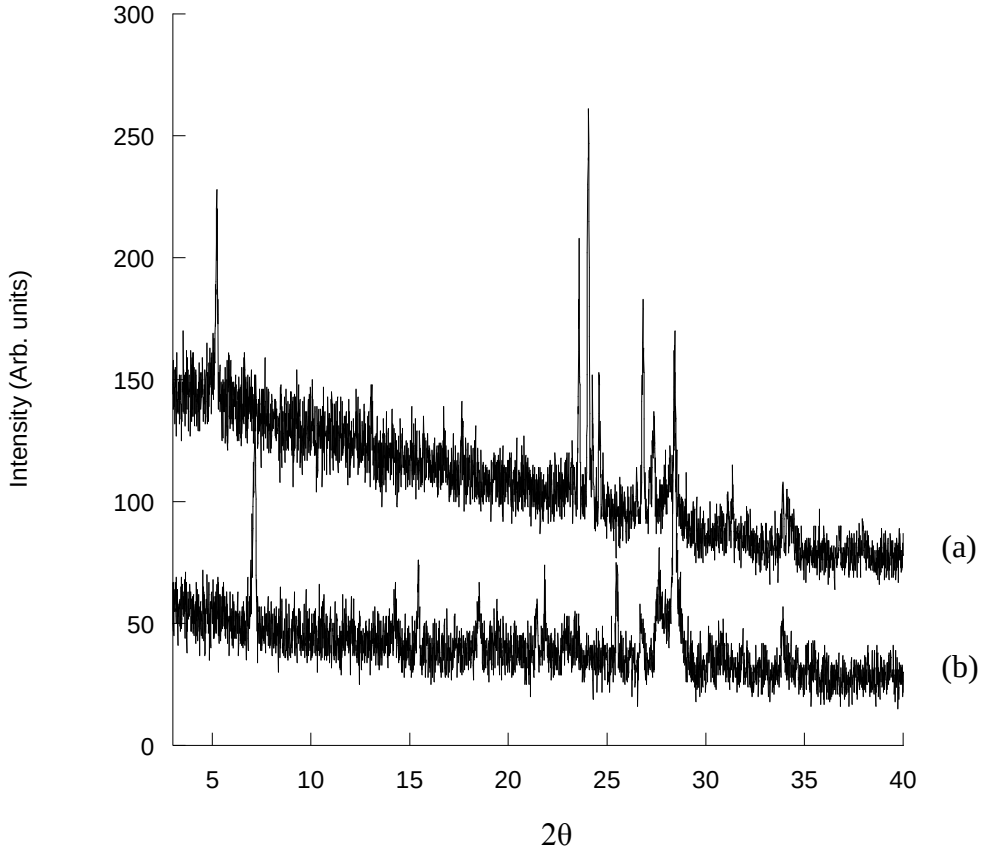

Figure 31 (a) Powder XRD pattern of $[Nd(H_2O)MoO_4]_2$[1,5-NDS] (**3**) and anion exchange product (b) $[Nd(H_2O)MoO_4]_2$[Fumarate]

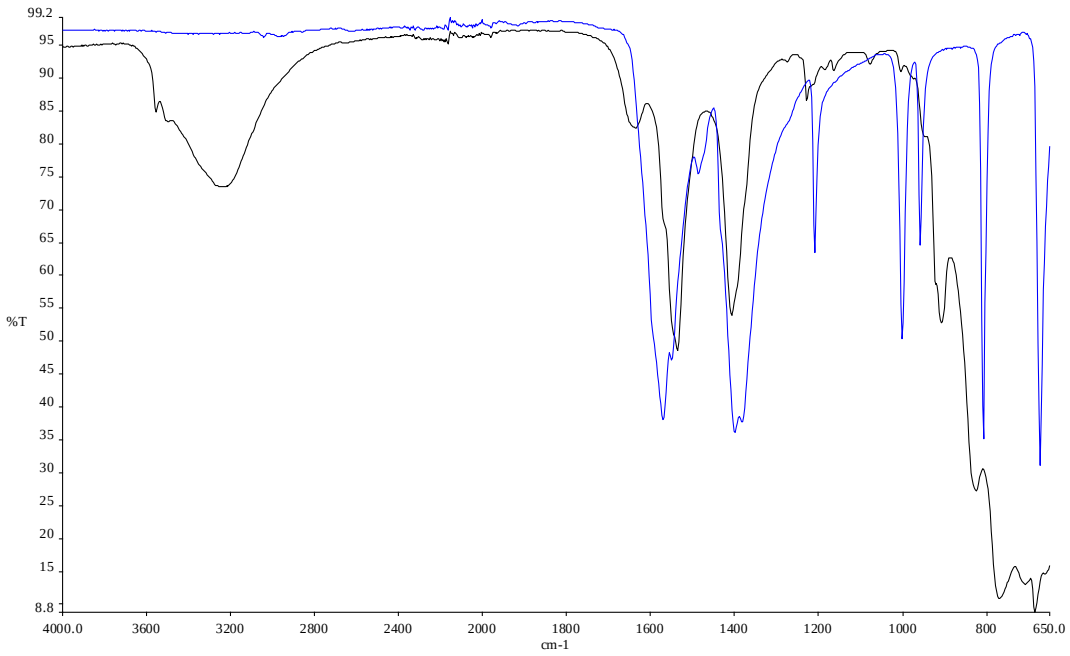

Figure 32 FTIR spectra of $[Nd(H_2O)MoO_4]_2$[Fumarate] (black) showing bands due to OH at 3225 cm^{-1} and C-O stretching modes at 1537 (antisymmetric) and 1408 cm^{-1} (symmetric), and sodium fumarate (blue).

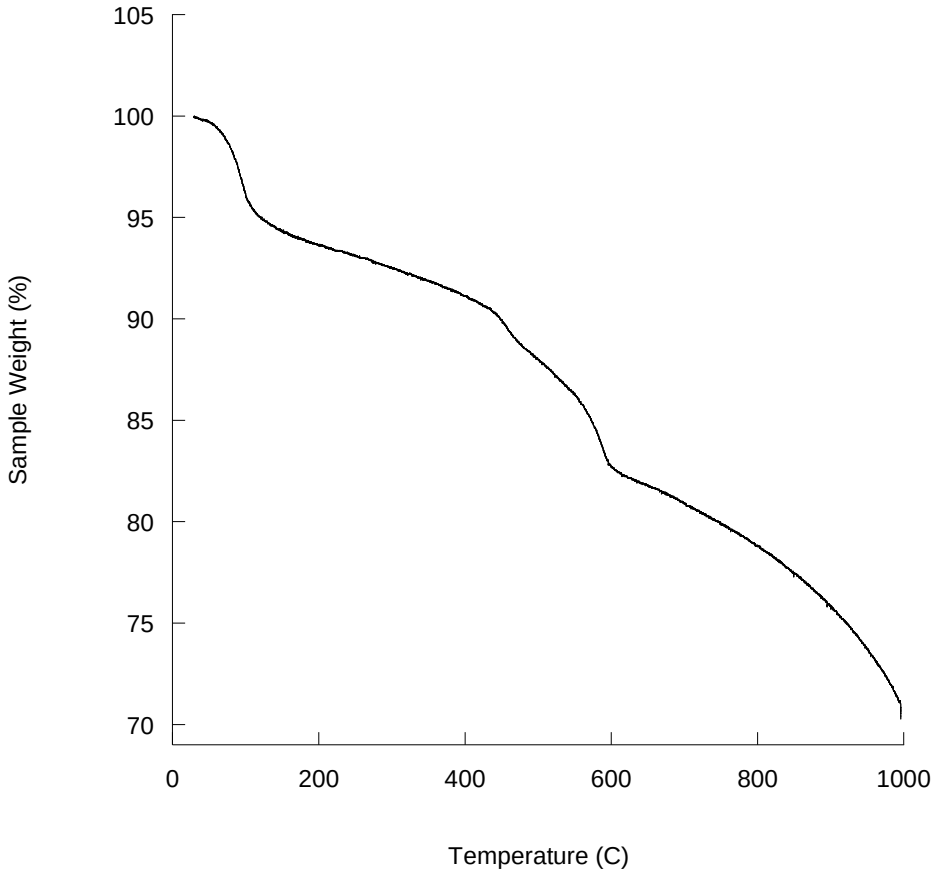

Figure 33 TGA trace anion exchange product of $[Nd(H_2O)MoO_4]_2$[Fumarate] showing first mass loss of 6.4 % below 100 °C and an additional mass loss of 26.7 % by 996 °C. End products are found to be $(Nd_2(MoO_4)_3)_{1.33}$ & Nd_6MoO_{12}.

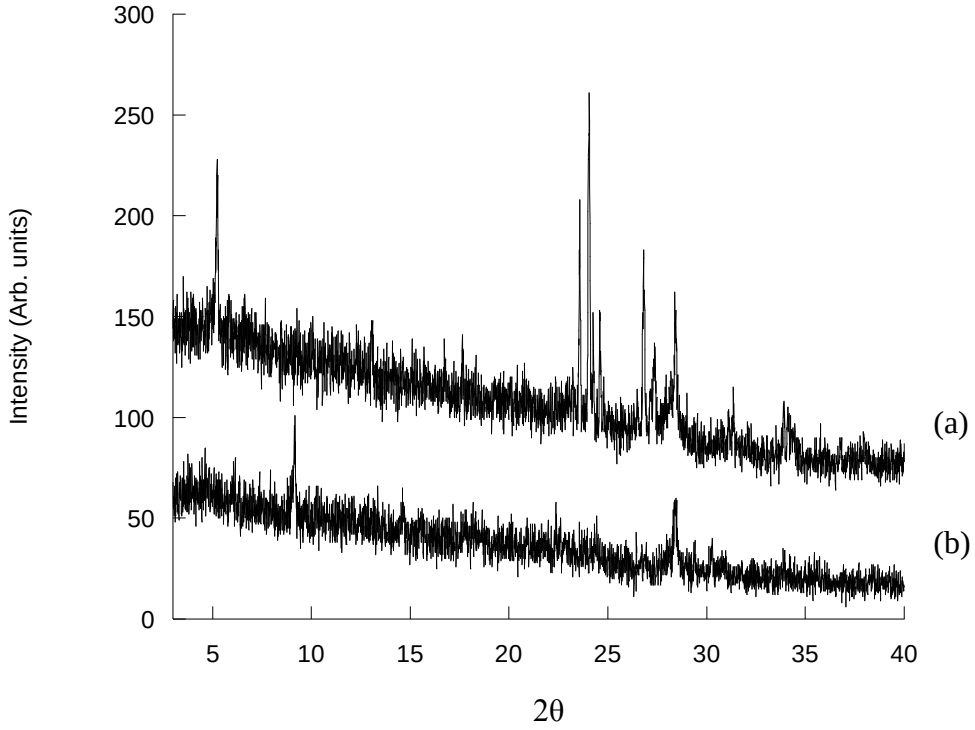

Figure 34 (a) Powder XRD pattern of $[Nd(H_2O)MoO_4]_2$[1,5-NDS] (**3**) and anion exchange product (b) $[Nd(H_2O)MoO_4]_2$[Terephthalate]

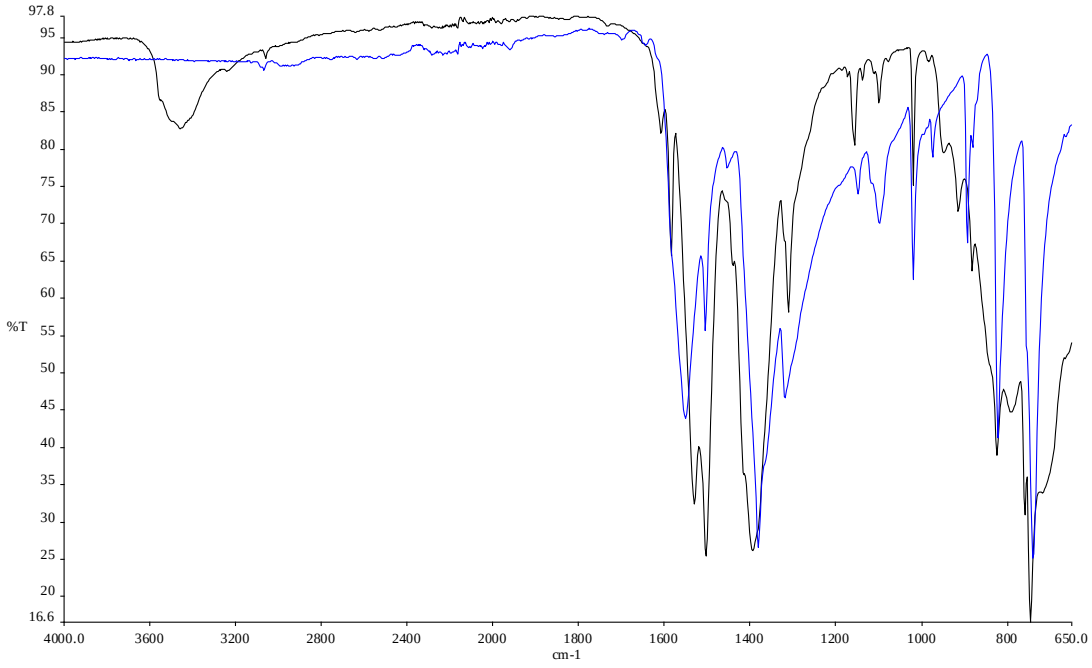

Figure 35 FTIR spectra of $[Nd(H_2O)MoO_4]_2$[Terephthalate] (black) showing bands due to OH at 3461 cm^{-1} and C-O stretching modes at 1531 (antisymmetric) and 1395 cm^{-1} (symmetric), and sodium terephthalate (blue).

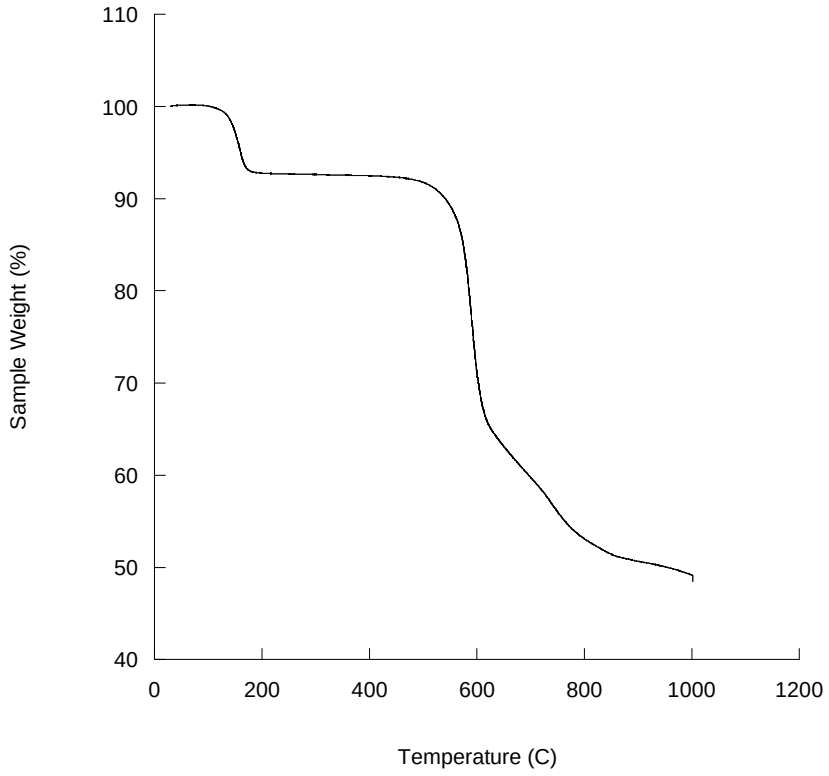

Figure 36 TGA trace of anion exchanged material $[Nd(H_2O)MoO_4]_2$[Terephthalate], showing two distinct mass losses. First mass loss of 7.4 % below 200 °C and an additional mass loss of 43.5 % by 1000 °C. End product is found to be Nd_6MoO_{12}.

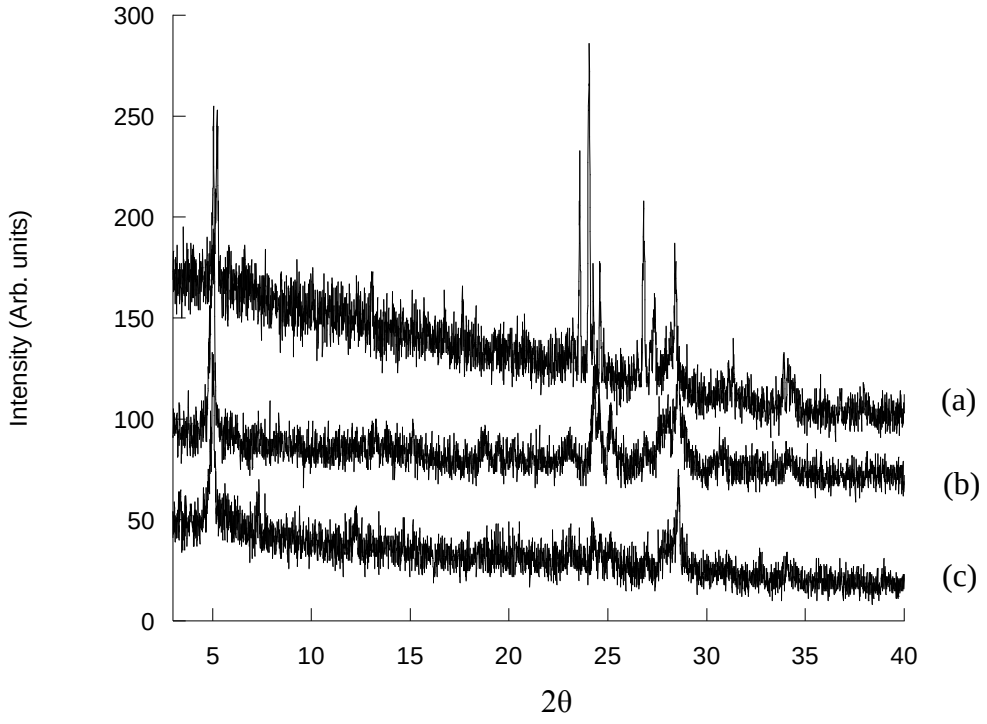

Figure 37 (a) Powder XRD pattern of $[Nd(H_2O)MoO_4]_2$[1,5-NDS] (**3**) and anion exchange products (b) $[Nd(H_2O)MoO_4]_2$[2,6-NDC] (hydrothermal) (c) $[Nd(H_2O)MoO_4]_2$[2,6-NDC] (90 °C, 4 days).

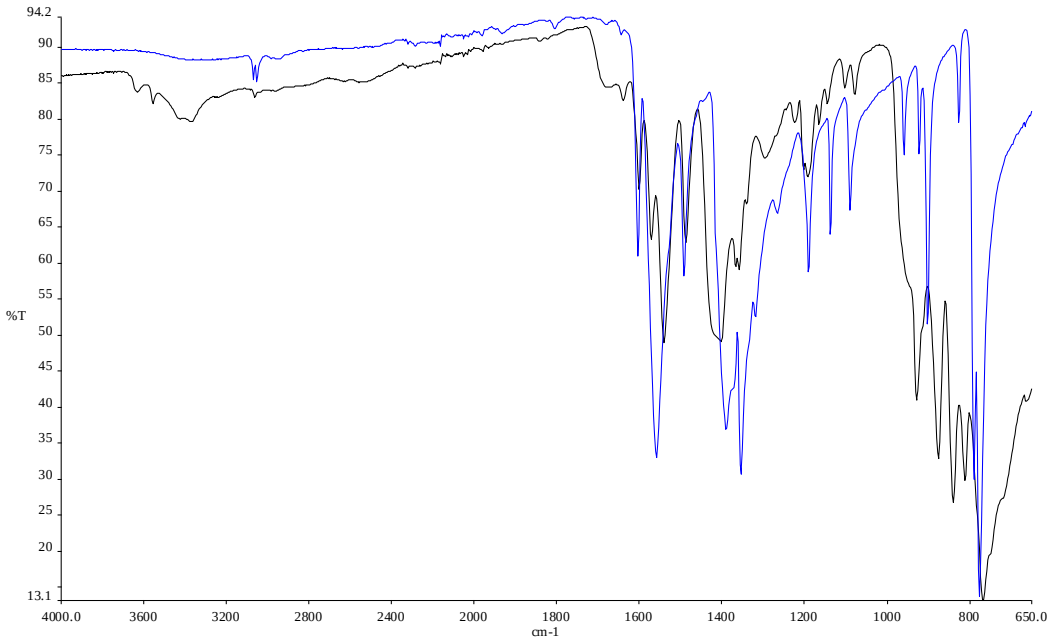

Figure 38 FTIR spectra of $[Nd(H_2O)MoO_4]_2[2,6\text{-NDC}]$ (hydrothermal, black) showing bands due to OH at 3372 cm^{-1} and C-O stretching modes at 1541 (antisymmetric) and 1403 cm^{-1} (symmetric), and 2,6-NDC (blue).

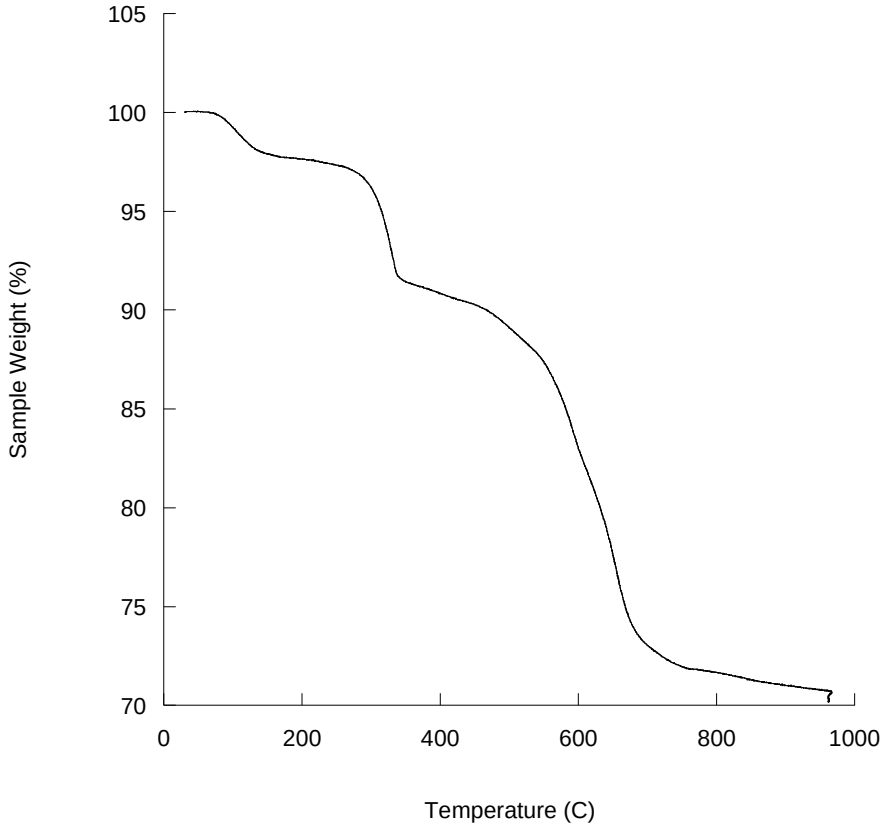

Figure 39 TGA trace of anion exchanged material $[Nd(H_2O)MoO_4]_2[2,6\text{-NDC}]$ (hydrothermal), showing three distinct mass losses. First two mass losses of a total of 9.2 % below 350 °C and an additional mass loss of 20.6 % by 700 °C. End product is found to be $Nd_2Mo_3O_9$ & $Nd_2Mo_2O_7$.

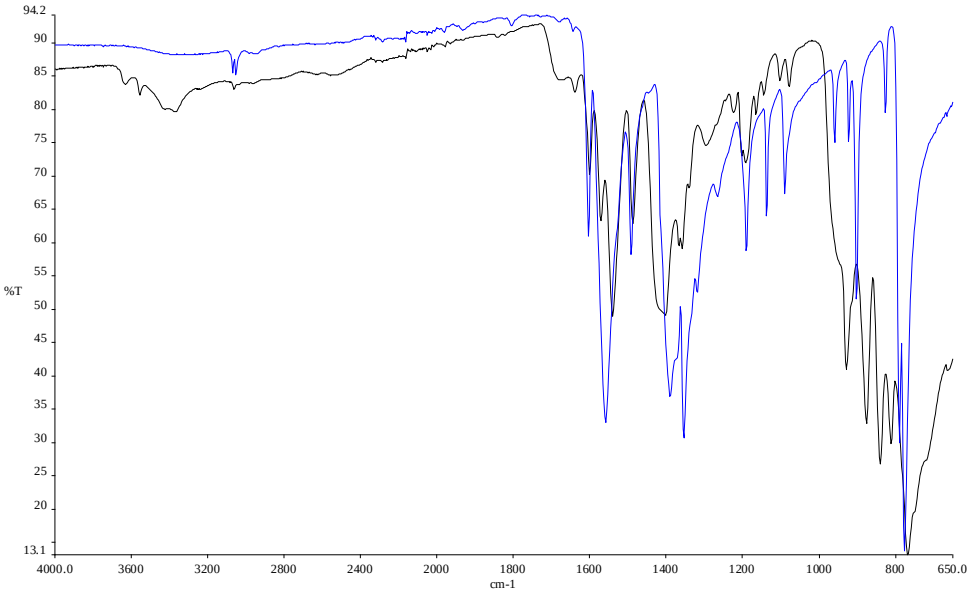

Figure 40 FTIR spectra of $[Nd(H_2O)MoO_4]_2[2,6\text{-NDC}]$ (90°C, black) showing bands due to OH at 3369 cm^{-1} and C-O stretching modes at 1539 (antisymmetric) and 1418 cm^{-1} (symmetric), and 2,6-NDC (blue).

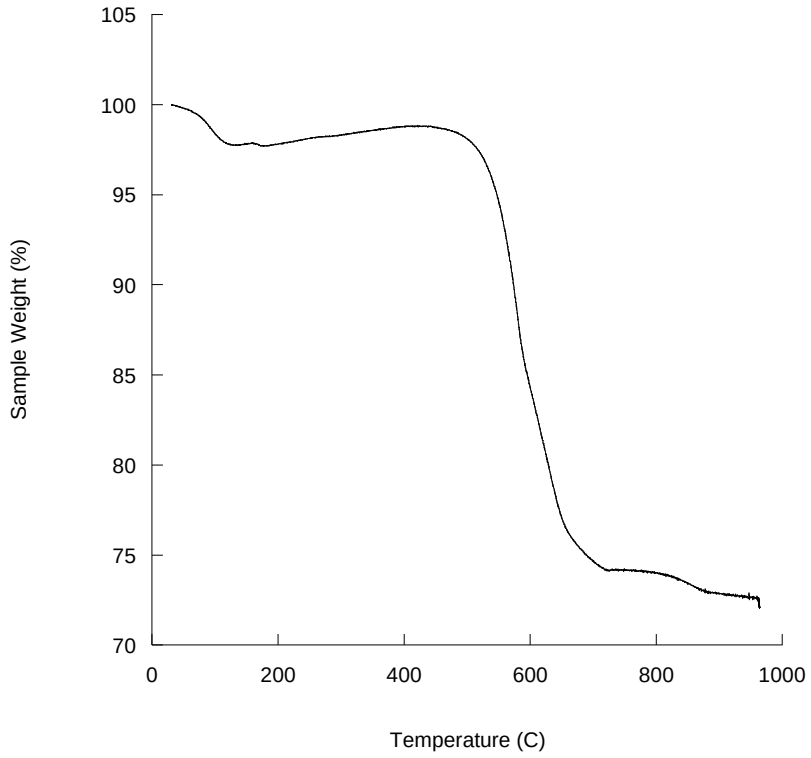

Figure 41 TGA trace of the anion exchanged material $[Nd(H_2O)MoO_4]_2[2,6\text{-NDC}]$ (90°C). First mass loss of 2.2 % below 200 °C and an additional mass loss of 25.7 % by 964 °C. End product is found to be $Nd_2Mo_3O_9$ & $Nd_2Mo_2O_7$.

Table 12 Characterisation data for anion exchange reactions using the host material $[Nd(H_2O)MoO_4]_2$[1,5-NDS]

Anion	Interlayer Separation (Å)	Elemental Analysis	
		Observed (%)	Calculated (%)
Fumarate	12.4	C-3.56	C-6.33
		H-1.17	H-0.80
Terephthalate	9.7	C-20.95	C-11.88
		H-1.82	H-1.00
2,6-NDC	17.6	C-13.68	C-16.79
(90 °C, 4days)		H-0.96	H-1.17
2,6-NDC	17.6	C-17.59	C-16.79
(hydrothermal)		H-1.16	H-1.17

Table 13 Orientation of guest anions using host material $[Nd(H_2O)MoO_4]_2$[1,5-NDS] with a layer thickness of 9.1 Å

Anion	Orientation of anion (°)
Fumarate	34
Terephthalate	4
2,6-NDC	67
1,5-NDS (host)	68

Crystallographic data for $[La(H_2O)WO_4]_2[1,5\text{-NDS}]$ (3)

Table 14 Crystal data and structure refinement details for $[La(H_2O)WO_4]_2[1,5\text{-NDS}]$ (**3**)

Identification code	**2009src0059p21c (JN50)**	
Empirical formula	$C_{10}H_{10}La_2O_{16}S_2W_2$	
Formula weight	1095.82	
Temperature	120(2) K	
Wavelength	0.71073 Å	
Crystal system	Monoclinic	
Space group	$P2_1/c$	
Unit cell dimensions	a = 17.1242(11) Å	α = 90°
	b = 7.4638(5) Å	β = 91.048(4)°
	c = 7.6228(5) Å	γ = 90°
Volume	974.12(11) Å^3	
Z	2	
Density (calculated)	3.736 mg / m^3	
Absorption coefficient	16.365 mm^{-1}	
F(000)	984	
Crystal	Lath; colourless	
Crystal size	0.10 × 0.04 × 0.01 mm^3	
θ range for data collection	2.98 – 27.47°	
Index ranges	$-22 \le h \le 22$, $-9 \le k \le 9$, $-9 \le l \le 9$	
Reflections collected	10570	
Independent reflections	2214 [R_{int} = 0.0782]	
Completeness to θ = 27.47°	99.8 %	
Absorption correction	Semi–empirical from equivalents	
Max. and min. transmission	0.8535 and 0.2914	
Refinement method	Full-matrix least-squares on F^2	
Data / restraints / parameters	2214 / 33 / 153	
Goodness-of-fit on F^2	1.121	
Final R indices [$F^2 > 2\sigma(F^2)$]	*R1* = 0.0595, *wR2* = 0.1166	
R indices (all data)	*R1* = 0.0770, *wR2* = 0.1255	
Largest diff. peak and hole	2.082 and –2.510 e Å^{-3}	

Diffractometer: *Nonius KappaCCD* area detector (ϕ scans and ω scans to fill *asymmetric unit*). **Cell determination:** DirAx (Duisenberg, A.J.M.(1992). J. Appl. Cryst. 25, 92-96.) **Data collection:** Collect (Collect: Data collection software, R. Hooft, Nonius B.V., 1998). **Data reduction and cell refinement**: *Denzo* (Z. Otwinowski & W. Minor, *Methods in Enzymology* (1997) Vol. **276**: *Macromolecular Crystallography*, part A, pp. 307–326; C. W. Carter, Jr. & R. M. Sweet, Eds., Academic Press). **Absorption correction**: Sheldrick, G. M. SADABS - Bruker Nonius area detector scaling and absorption correction - V2.10 **Structure solution**: *SHELXS97* (G. M. Sheldrick, Acta Cryst. (1990) A**46** 467–473). **Structure refinement**: *SHELXL97* (G. M. Sheldrick (1997), University of Göttingen, Germany). **Graphics:** ORTEP-3 (L.G. Farrugia, J. Appl. Cryst. (1997) **30**, 565).

Special details:

All hydrogen atoms except water hydrogens were fixed using a standard riding model. The water hydrogen atoms were restrained used DFIX, DANG and the thermal parameters were refined.

The ISOR command was used for atoms C1, C2, C3, C4, C5 and C6 as these were non-positive definites. This is not surprising for these types of structures were a number of heavy atoms are present with light atoms.

The second WGHT parameter is larger than usual - this is due to the difference in the weights of the atoms present. To address this problem a number of absorption corrections were tried, of which this was found to give the best results.

Table 15 Atomic coordinates [$\times 10^4$], equivalent isotropic displacement parameters [$Å^2 \times 10^3$] and site occupancy factors. U_{eq} is defined as one third of the trace of the orthogonalized U^{ij} tensor.

Atom	*x*	*y*	*z*	U_{eq}	*S.o.f.*
C1	963(9)	3930(20)	620(20)	18(3)	1
C2	741(9)	2270(20)	1140(20)	15(3)	1
C3	–58(9)	1810(20)	1167(18)	16(3)	1
C4	401(9)	5240(20)	–30(20)	18(3)	1

C5	618(9)	6970(20)	–627(19)	13(3)	1
O3	3919(7)	4440(16)	492(15)	26(3)	1
O4	3734(7)	4058(14)	4103(15)	23(3)	1
O21	1973(7)	6050(15)	2107(14)	23(3)	1
O22	2246(7)	5021(17)	–850(15)	25(3)	1
O23	2348(7)	2951(16)	1598(15)	24(3)	1
O1W	2403(7)	−725(16)	649(15)	23(3)	1
O1	5145(7)	5808(15)	2828(13)	19(2)	1
O2	3685(6)	7686(15)	2565(14)	20(2)	1
La1	3445(1)	917(1)	2377(1)	14(1)	1
W1	4134(1)	5552(1)	2508(1)	14(1)	1
S1	1956(2)	4537(5)	875(5)	17(1)	1

Table 16 Bond lengths [Å] and angles [°].

C1–C2	1.36(2)	O22–S1	1.459(12)
C1–C4	1.45(2)	O22–La1^{ii}	2.575(12)
C1–S1	1.768(16)	O23–S1	1.464(12)
C2–C3	1.41(2)	O23–La1	2.480(11)
C2–H2	0.9500	O1W–La1	2.518(11)
C3–C5^{i}	1.38(2)	O1W–H2W	0.85(2)
C3–H3	0.9500	O1W–H1W	0.85(2)
C4–C5	1.42(2)	O1–W1	1.755(12)
C4–C4^{i}	1.42(3)	O1–La1^{iv}	2.423(12)
C5–C3^{i}	1.38(2)	O2–W1	1.770(11)
C5–H5	0.9500	O2–La1^{v}	2.450(11)
O3–W1	1.779(12)	La1–O1^{vi}	2.423(12)
O3–La1^{ii}	2.510(12)	La1–O2^{vii}	2.450(11)
O4–W1	1.795(11)	La1–O3^{iii}	2.510(12)
O4–La1^{iii}	2.553(12)	La1–O4^{ii}	2.553(12)
O4–La1	2.729(11)	La1–O22^{iii}	2.575(12)
O21–S1	1.469(12)	La1–W1	3.6555(10)

C2–C1–C4	121.9(14)	O2^{vii}–La1–O1W	70.6(4)
C2–C1–S1	118.5(12)	O23–La1–O1W	69.3(4)
C4–C1–S1	119.5(12)	O3^{iii}–La1–O1W	131.1(4)
C1–C2–C3	120.1(14)	O1^{vi}–La1–O4^{ii}	74.1(4)
C1–C2–H2	119.9	O2^{vii}–La1–O4^{ii}	91.7(4)
C3–C2–H2	119.9	O23–La1–O4^{ii}	85.5(4)
C5^{i}–C3–C2	120.3(14)	O3^{iii}–La1–O4^{ii}	149.4(4)
C5^{i}–C3–H3	119.9	O1W–La1–O4^{ii}	68.9(4)
C2–C3–H3	119.9	O1^{vi}–La1–O22^{iii}	146.0(4)
C5–C4–C4^{i}	120.0(18)	O2^{vii}–La1–O22^{iii}	80.6(4)
C5–C4–C1	123.2(14)	O23–La1–O22^{iii}	71.6(4)
C4^{i}–C4–C1	116.8(18)	O3^{iii}–La1–O22^{iii}	73.8(4)
C3^{i}–C5–C4	120.7(14)	O1W–La1–O22^{iii}	65.0(4)
C3^{i}–C5–H5	119.6	O4^{ii}–La1–O22^{iii}	133.3(4)
C4–C5–H5	119.6	O1^{vi}–La1–O4	83.6(4)
W1–O3–La1^{ii}	157.7(7)	O2^{vii}–La1–O4	142.0(3)
W1–O4–La1^{iii}	137.8(6)	O23–La1–O4	73.7(4)
W1–O4–La1	106.0(5)	O3^{iii}–La1–O4	65.3(4)
La1^{iii}–O4–La1	116.2(4)	O1W–La1–O4	142.3(4)
S1–O22–La1^{ii}	133.9(7)	O4^{ii}–La1–O4	115.4(3)
S1–O23–La1	157.8(7)	O22^{iii}–La1–O4	96.9(4)
La1–O1W–H2W	136(10)	O1^{vi}–La1–W1	73.3(3)
La1–O1W–H1W	114(10)	O2^{vii}–La1–W1	151.2(3)
H2W–O1W–H1W	108(5)	O23–La1–W1	70.7(3)
W1–O1–La1^{iv}	167.5(6)	O3^{iii}–La1–W1	88.6(3)
W1–O2–La1^{v}	163.2(6)	O1W–La1–W1	134.5(3)
O1^{vi}–La1–O2^{vii}	78.7(4)	O4^{ii}–La1–W1	87.2(2)
O1^{vi}–La1–O23	139.2(4)	O22^{iii}–La1–W1	120.2(3)
O2^{vii}–La1–O23	137.9(4)	O4–La1–W1	28.2(2)
O1^{vi}–La1–O3^{iii}	75.7(4)	O1–W1–O2	109.0(5)
O2^{vii}–La1–O3^{iii}	77.8(4)	O1–W1–O3	111.1(5)
O23–La1–O3^{iii}	121.5(4)	O2–W1–O3	111.0(5)
O1^{vi}–La1–O1W	130.4(4)	O1–W1–O4	111.2(5)

O2–W1–O4	111.8(5)
O3–W1–O4	102.7(5)
O1–W1–La1	115.1(4)
O2–W1–La1	135.4(4)
O3–W1–La1	58.2(4)
O4–W1–La1	45.9(4)
O22–S1–O23	112.2(7)
O22–S1–O21	112.5(7)
O23–S1–O21	112.2(7)
O22–S1–C1	107.9(7)
O23–S1–C1	105.4(7)
O21–S1–C1	106.1(7)

Symmetry transformations used to generate equivalent atoms:

(i) –x,–y+1,–z (ii) x,–y+1/2,z–1/2 (iii) x,–y+1/2,z+1/2

(iv) –x+1,y+1/2,–z+1/2 (v) x,y+1,z (vi) –x+1,y–1/2,–z+1/2

(vii) x,y–1,z

Table 17 Anisotropic displacement parameters [$Å^2 \times 10^3$]. The anisotropic displacement factor exponent takes the form: $-2\pi^2[h^2a^{*2}U^{11} + \cdots + 2\,h\,k\,a^*\,b^*\,U^{12}]$.

Atom	U^{11}	U^{22}	U^{33}	U^{23}	U^{13}	U^{12}
C1	18(6)	18(6)	18(6)	–6(5)	–1(5)	–3(5)
C2	12(6)	14(6)	21(6)	–5(5)	0(5)	7(5)
C3	25(7)	17(6)	5(5)	–7(5)	1(5)	0(5)
C4	19(6)	19(6)	16(6)	–1(5)	–3(5)	6(5)
C5	15(6)	11(6)	15(6)	0(5)	1(5)	–3(5)
O3	30(7)	27(7)	21(6)	1(5)	10(5)	4(5)
O4	28(7)	7(5)	33(7)	3(5)	–4(5)	4(5)
O21	38(7)	15(6)	15(5)	3(4)	–1(5)	–6(5)
O22	21(6)	31(7)	24(6)	4(5)	0(5)	4(5)
O23	16(6)	24(6)	31(6)	8(5)	–7(5)	6(5)
O1W	32(7)	20(6)	17(6)	6(4)	–6(5)	–17(5)
O1	30(6)	18(6)	11(5)	4(4)	7(4)	–3(5)
O2	18(6)	15(6)	27(6)	1(5)	–5(5)	–1(4)
La1	17(1)	11(1)	14(1)	0(1)	0(1)	1(1)
W1	17(1)	10(1)	14(1)	0(1)	0(1)	0(1)
S1	19(2)	14(2)	18(2)	2(1)	1(1)	–1(2)

Table 18 Hydrogen bonds [Å and °].

D–H···*A*	*d*(*D*–H)	*d*(H···*A*)	*d*(*D*···*A*)	∠(*D*H*A*)
O1W–H2W···O21^{ii}	0.85(2)	1.95(3)	2.796(15)	176(22)

O1W–H2W···S1[ii]	0.85(2)	3.01(6)	3.810(12)	158(13)
O1W–H1W···S1[vii]	0.85(2)	2.89(9)	3.622(12)	145(13)
O1W–H1W···O21[vii]	0.85(2)	1.92(4)	2.756(15)	169(16)

Symmetry transformations used to generate equivalent atoms:

(i) –x,–y+1,–z (ii) x,–y+1/2,z–1/2 (iii) x,–y+1/2,z+1/2

(iv) –x+1,y+1/2,–z+1/2 (v) x,y+1,z (vi) –x+1,y–1/2,–z+1/2

(vii) x,y–1,z

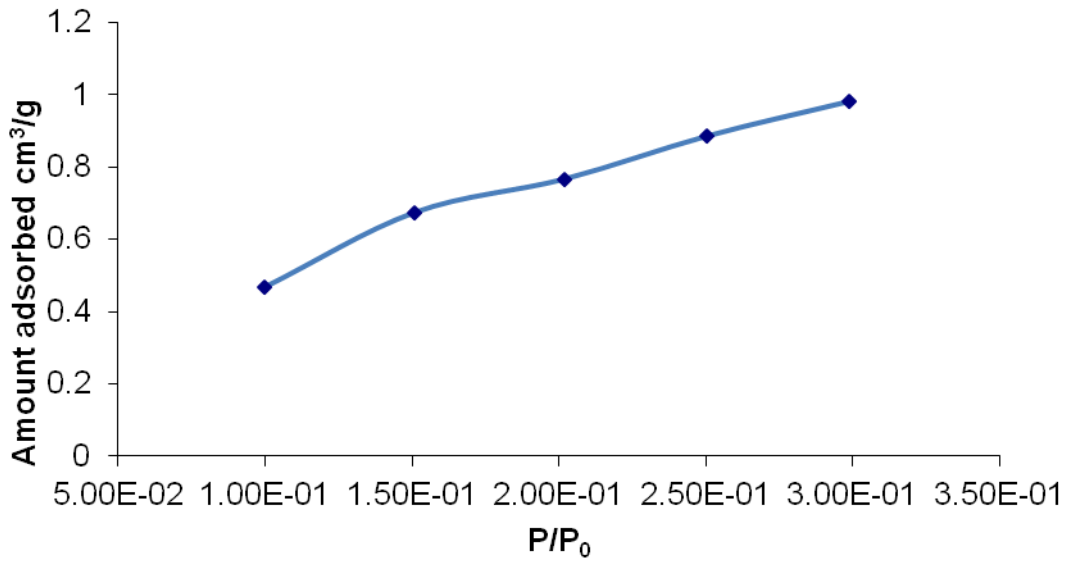

Figure 42 Adsorption isotherm for $[La(H_2O)WO_4]_2[1,5\text{-NDS}]$ (**3**), degassed at 120°C overnight.

Characterising data for $[Ln(H_2O)WO_4]_2[1,5\text{-NDS}]$ (La-Ce)

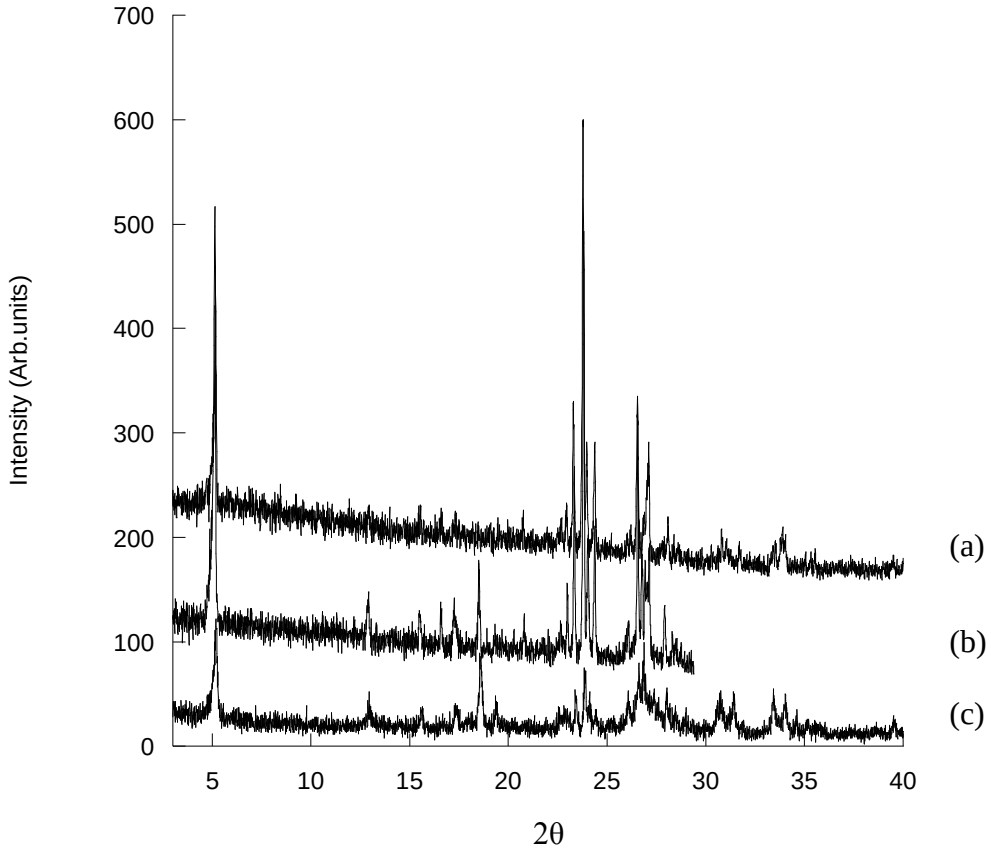

Figure 43 Powder XRD patterns of iso-structural phases (a) $[La(H_2O)WO_4]_2[1,5\text{-NDS}]$, (b) $[Ce(H_2O)WO_4]_2[1,5\text{-NDS}]$ and (c) $[Pr(H_2O)WO_4]_2[1,5\text{-NDS}]$

[Ce(H_2O)WO_4]$_2$[1,5-NDS]

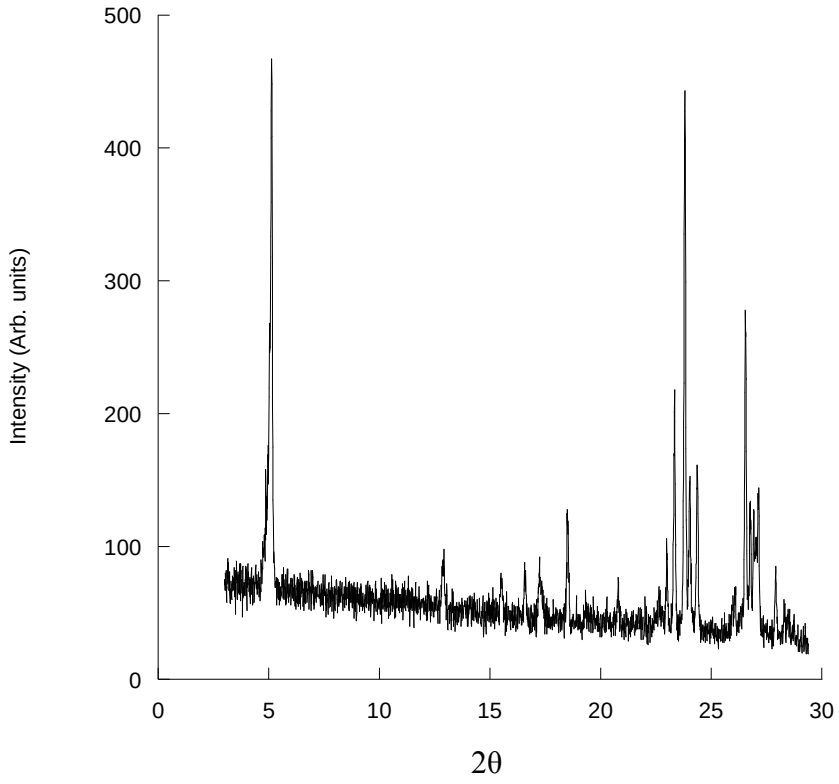

Figure 44 Powder X-ray diffraction pattern of [Ce(H_2O)WO_4]$_2$[1,5-NDS]

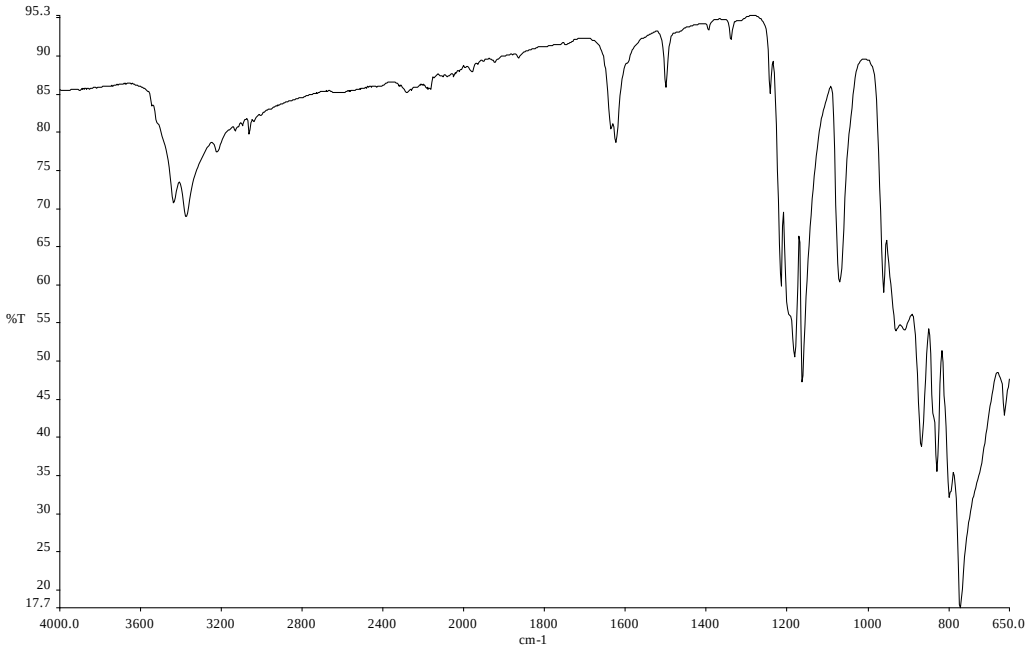

Figure 45 FTIR spectra of [Ce(H_2O)WO_4]$_2$[1,5-NDS], showing bands due to OH at 3376 cm^{-1}, S-O stretching modes at 1183 (antisymmetric) and 1071 cm^{-1} (symmetric) and the tungstate stretching frequency at 776 cm^{-1}.

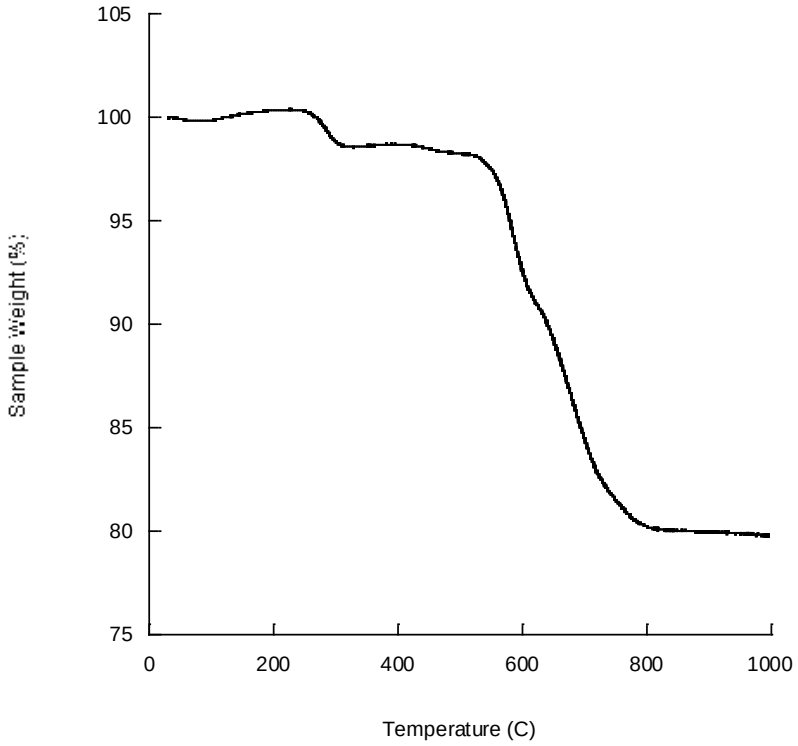

Figure 46 TGA trace of $[Ce(H_2O)WO_4]_2$[1,5-NDS] showing two distinct mass losses. First mass loss of 1.8 % below 300 °C and an additional mass loss of 18.4 % by 800 °C. End product is found to be $Ce_2(WO_4)_3$.

$[Pr(H_2O)WO_4]_2$[1,5-NDS]

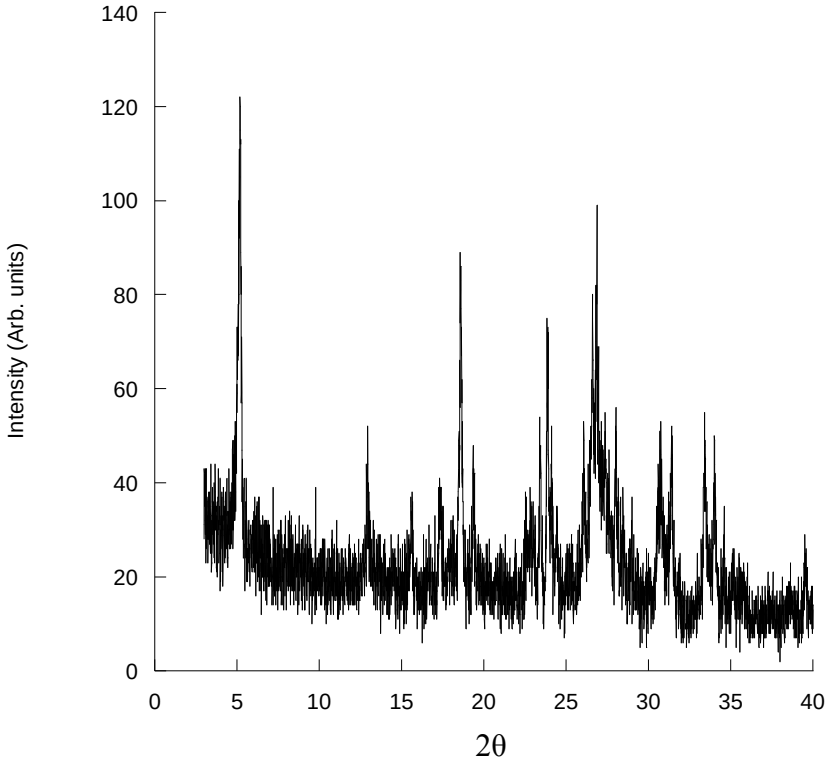

Figure 47 Powder X-ray diffraction pattern of $[Pr(H_2O)WO_4]_2$[1,5-NDS]

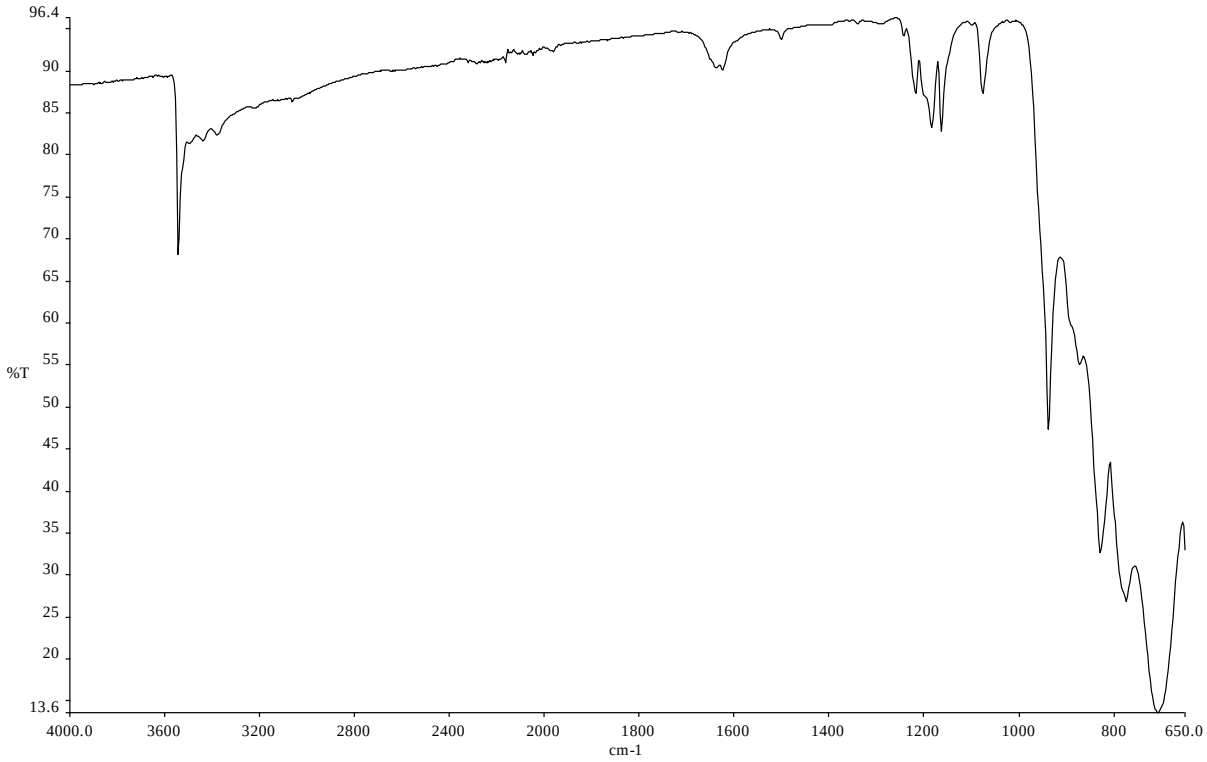

Figure 48 FTIR spectra of $[Pr(H_2O)WO_4]_2$[1,5-NDS], showing bands due to OH at 3379 cm^{-1}, S-O stretching modes at 1184 (antisymmetric) and 1076 cm^{-1} (symmetric) and the tungstate stretching frequency at 771 cm^{-1}.

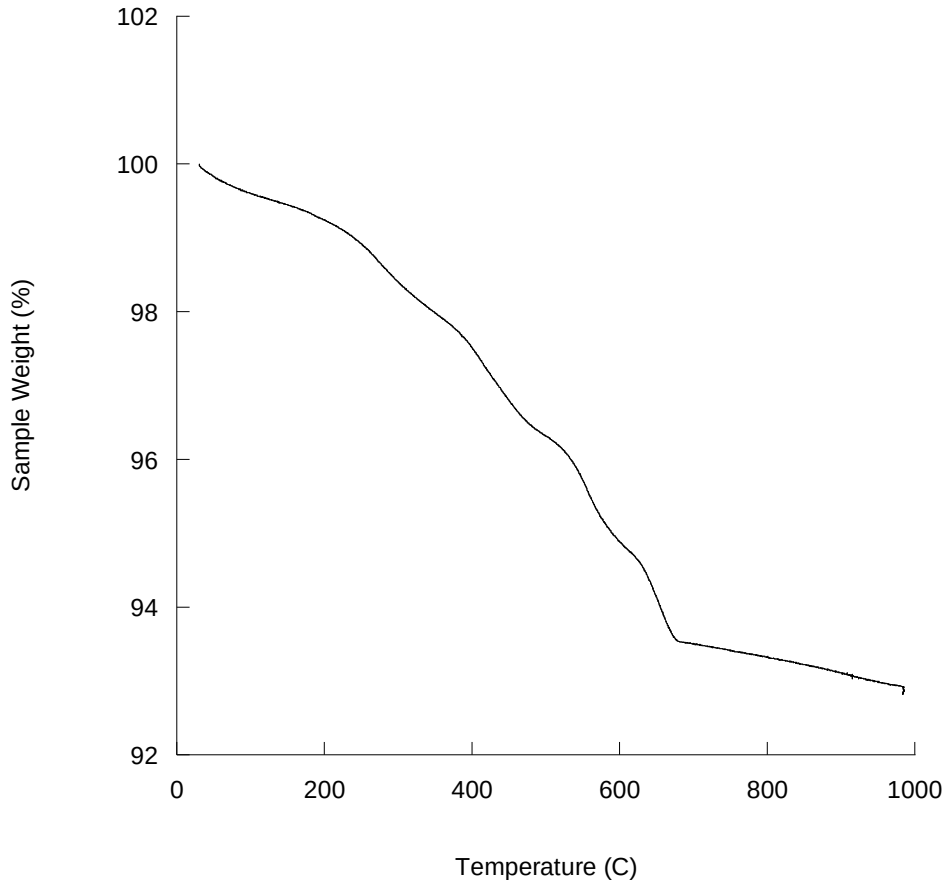

Figure 49 TGA trace of $[Pr(H_2O)WO_4]_2[1,5\text{-NDS}]$ a total mass loss of 7.2 % by 700°C. End product is found to be $Pr_2O_3(WO_3)_3$

Table 19 Elemental Analysis of $[Ln(H_2O)WO_4]_2[1,5\text{-NDS}]$ (Ln= La, Ce & Pr)

Lanthanide	Interlayer Separation (Å)	Elemental Analysis	
		Observed (%)	Calculated (%)
La	17.0	C-8.46	C-10.95
		H-0.77	H-0.91
Ce	17.3	C-7.98	C-10.94
		H-0.85	H-0.92
Pr	16.9	C-2.40	C-10.92
		H-0.43	H-0.92

Anion Exchange Reactions of $[La(H_2O)WO_4]_2[1,5\text{-NDS}]$

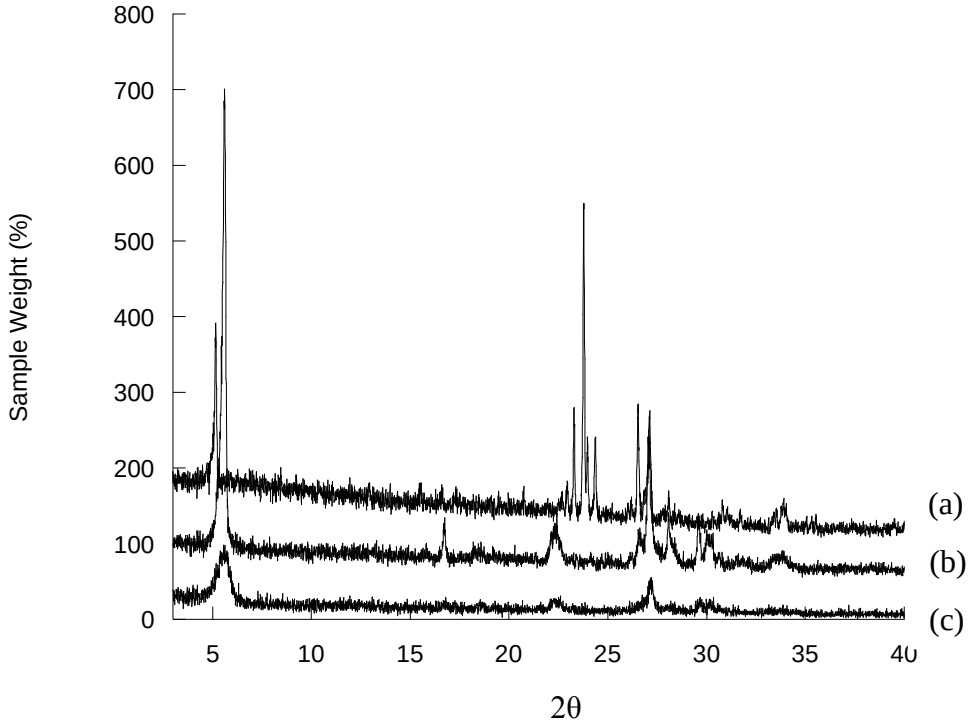

Figure 50 (a) Powder XRD patterns of $[La(H_2O)WO_4]_2[1,5\text{-NDS}]$ (**3**), and anion exchange products (b) $[La(H_2O)WO_4]_2[\text{Terephthalate}]$ (hydrothermal) (c) $[La(H_2O)WO_4]_2[\text{Terephthalate}]$ (90 °C).

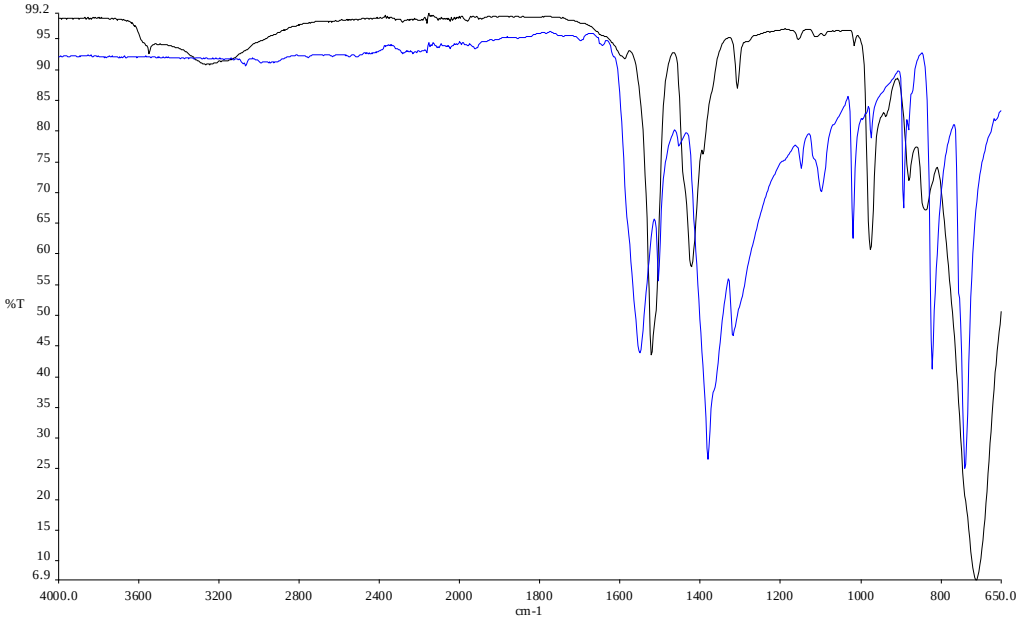

Figure 51 FTIR spectra of $[La(H_2O)WO_4]_2[\text{Terephthalate}]$ (90 °C- black) showing bands due to OH at 3251 cm^{-1} and C-O stretching modes at 1522 (antisymmetric) and 1424 cm^{-1} (symmetric), and sodium terephthalate (blue).

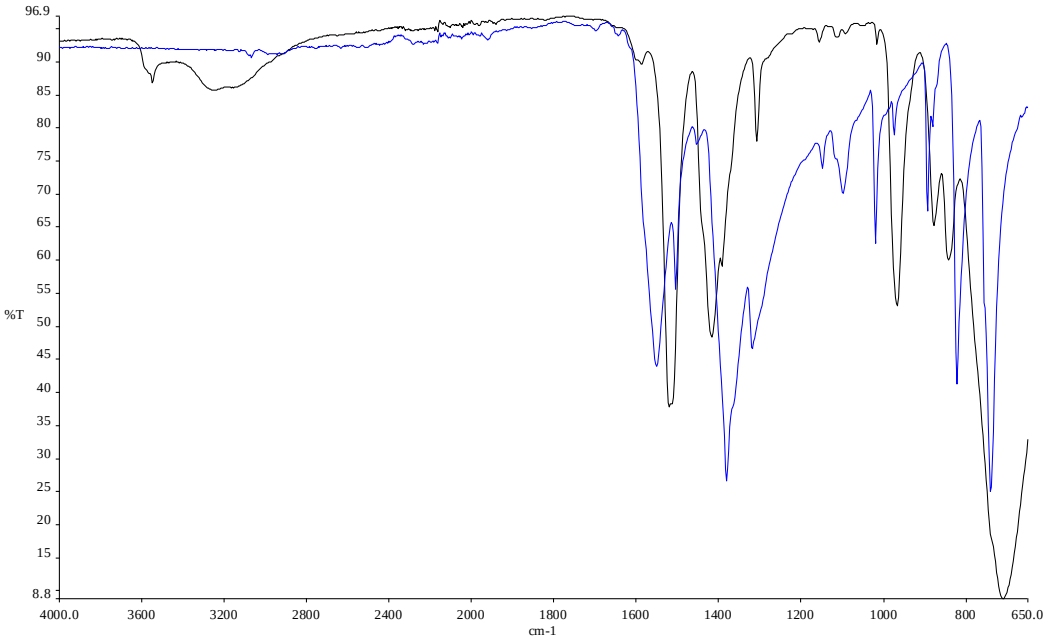

Figure 52 FTIR spectra of $[La(H_2O)WO_4]_2$[Terephthalate] (hydrothermally- black) showing bands due to OH at 3250cm^{-1} and C-O stretching modes at 1521 (antisymmetric) and 1418cm^{-1} (symmetric), and sodium terephthalate (blue).

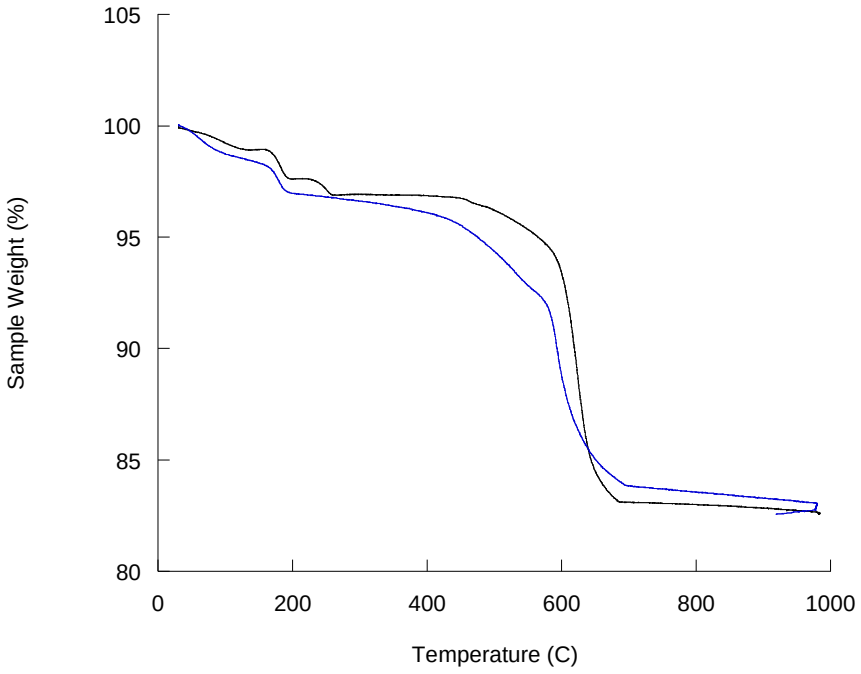

Figure 53 TGA trace of $[La(H_2O)WO_4]_2$[Terephthalate] hydrothermally (black) showing a mass loss of 3.1 % below 300 °C, corresponding to dehydration of the phase followed by an additional mass loss of 14.4 % by 700 °C. End product is found to be $La_2W_2O_9$. and $[La(H_2O)WO_4]_2$[Terephthalate] at 90 °C (blue), showing mass losses of 2.4 % below 200 °C and an additional mass loss of 14.2 % by 700 °C. End product is found to be $La_2W_2O_9$.

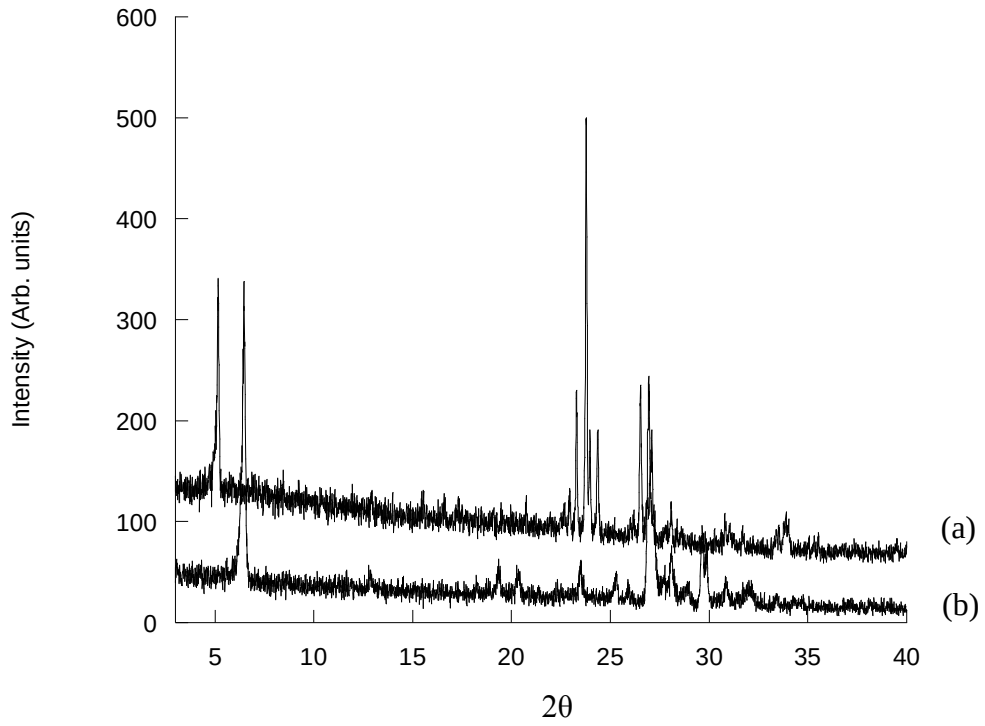

Figure 54 (a) Powder XRD pattern of $[La(H_2O)WO_4]_2[1,5\text{-NDS}]$ (**3**) and anion exchange product (b) $[La(H_2O)WO_4]_2[Fumarate]$

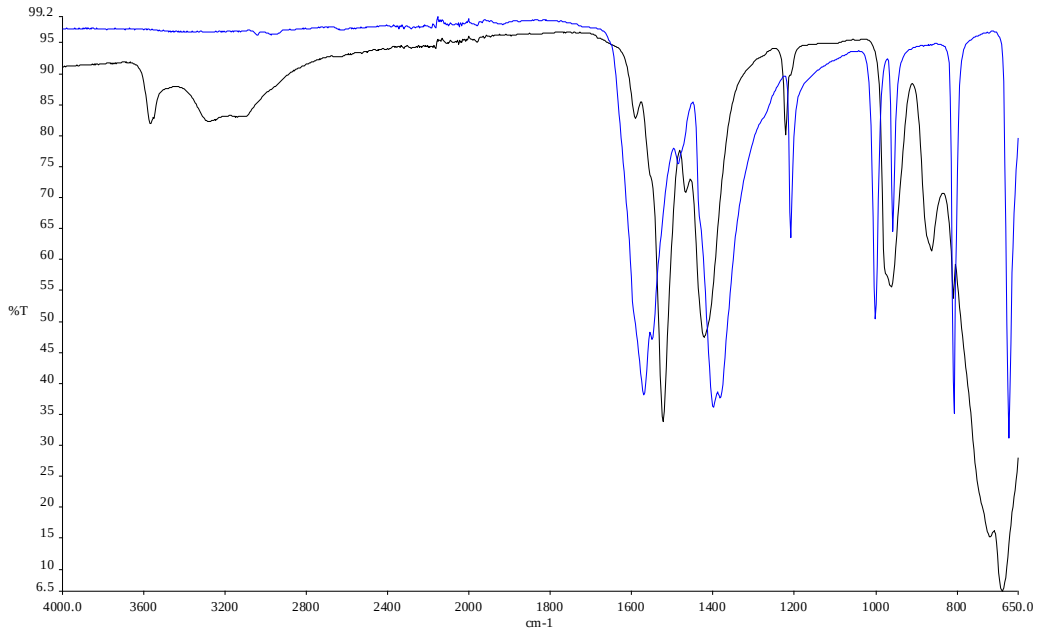

Figure 55 FTIR spectra of anion exchange product $[La(H_2O)WO_4]_2[Fumarate]$ (black) showing bands due to OH at 3286 cm^{-1} and C-O stretching modes at 1524 (antisymmetric) and 1423 cm^{-1} (symmetric), and sodium fumarate (blue).

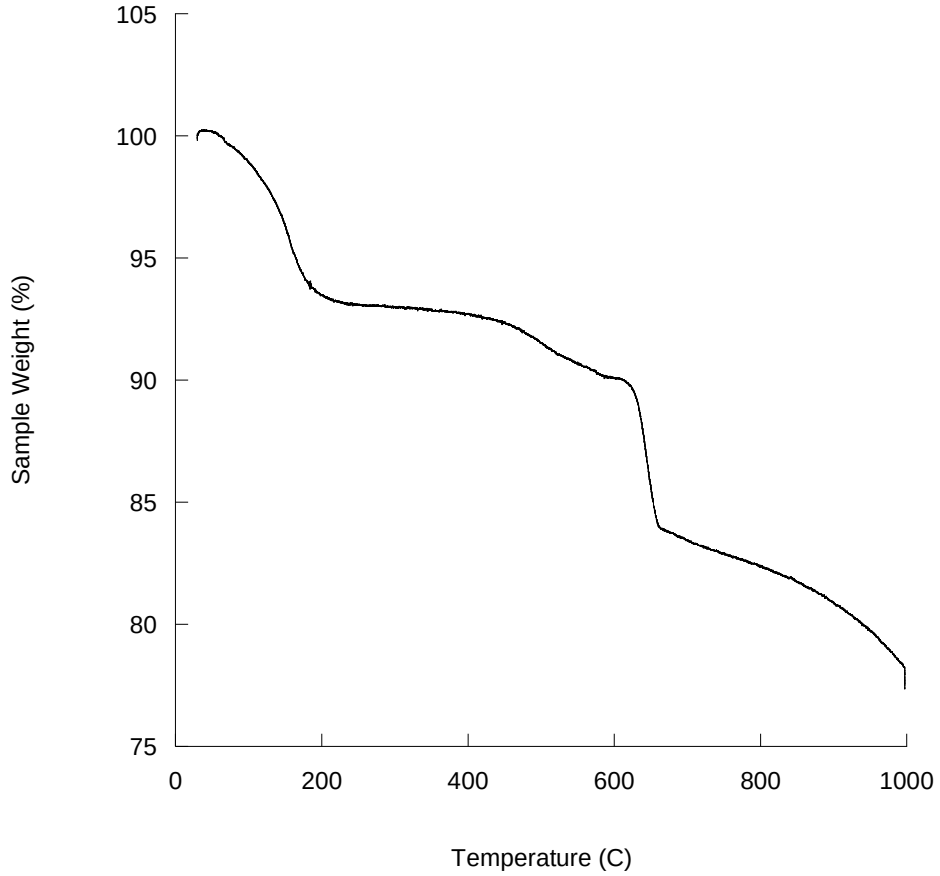

Figure 56 TGA trace of anion exchange product $[La(H_2O)WO_4]_2$[Fumarate] showing two distinct mass losses. First mass loss of 7.0 % below 200 °C and an additional mass loss of 14.7 % by 995 °C. End product is found to be $La_2W_2O_9$.

Crystallographic data for $[La_2(H_2O)_2W_2O_8]$[2,6-NDS] (5)

Table 20 Crystal data and structure refinement details.

Identification code	**2009src0060p–1 (JN51)**	
Empirical formula	$C_{20}H_{20}La_4O_{32}S_4W_4$	
Formula weight	2191.64	
Temperature	120(2) K	
Wavelength	0.71073 Å	
Crystal system	Triclinic	
Space group	*P*–1	
Unit cell dimensions	a = 7.2550(2) Å	α = 80.4080(10)°
	b = 8.1110(2) Å	β = 78.6810(10)°

	c = 16.9310(4) Å γ = 89.6740(10)°
Volume	962.90(4) Å^3
Z	1
Density (calculated)	3.780 mg / m^3
Absorption coefficient	16.555 mm^{-1}
F(000)	984
Crystal	Blade; colourless
Crystal size	0.14 × 0.03 × 0.01 mm^3
θ range for data collection	3.02 – 27.48°
Index ranges	$-9 \le h \le 9$, $-10 \le k \le 10$, $-21 \le l \le 21$
Reflections collected	19673
Independent reflections	4394 [R_{int} = 0.0598]
Completeness to θ = 27.48°	99.6 %
Absorption correction	Semi–empirical from equivalents
Max. and min. transmission	0.8519 and 0.2052
Refinement method	Full-matrix least-squares on F^2
Data / restraints / parameters	4394 / 18 / 289
Goodness-of-fit on F^2	1.119
Final R indices [$F^2 > 2\sigma(F^2)$]	*R1* = 0.0387, *wR2* = 0.0779
R indices (all data)	*R1* = 0.0483, *wR2* = 0.0827
Largest diff. peak and hole	2.116 and –1.758 e Å^{-3}

Diffractometer: *Nonius KappaCCD* area detector (ϕ scans and ω scans to fill *asymmetric unit*). **Cell determination:** DirAx (Duisenberg, A.J.M.(1992). J. Appl. Cryst. 25, 92-96.) **Data collection:** Collect (Collect: Data collection software, R. Hooft, Nonius B.V., 1998). **Data reduction and cell refinement**: *Denzo* (Z. Otwinowski & W. Minor, *Methods in Enzymology* (1997) Vol. **276**: *Macromolecular Crystallography*, part A, pp. 307–326; C. W. Carter, Jr. & R. M. Sweet, Eds., Academic Press). **Absorption correction**: Sheldrick, G. M. SADABS - Bruker Nonius area detector scaling and absorption correction - V2.10 **Structure solution**: *SHELXS97* (G. M. Sheldrick, Acta Cryst. (1990) A**46** 467–473). **Structure refinement**: *SHELXL97* (G. M. Sheldrick (1997), University of Göttingen, Germany). **Graphics:** ORTEP-3 (L.G. Farrugia, J. Appl. Cryst. (1997) **30**, 565).

Special details:

All hydrogens were fixed using a standard riding model. Hydrogen atoms on the water molecules O1w and O2w could not be located from the difference map. This is not surprising when heavy atoms are involved in the structure. The location of one of the hydrogens on each of the water molecules can be deduced from the short contact with the sulphate oxygen (O1w-H...O3 and O2w-H...O23) however the location of the second hydrogen is not certain.

The second WGHT parameter is higher than usual due to the large difference in atom weights present in the structure.

As there are 2 independent W_2O_8 units present in the structure (though half of each is related by symmetry) the formula is that shown above in spite of the alerts Checkcif brings up (due to the manner it calculates Z).

O32 and O36 were modelled using the ISOR restraint due to the former being a non-positive definite, and the latter having a very small ADP in one direction. This appears to be a trend for oxygen atoms that are positioned within a lattice surrounded by 3 co-ordinating cations.

Table 21 Atomic coordinates [× 10^4], equivalent isotropic displacement parameters [$Å^2$ × 10^3] and site occupancy factors. U_{eq} is defined as one third of the trace of the orthogonalized U^{ij} tensor.

Atom	*x*	*y*	*z*	U_{eq}	*S.o.f.*
C1	–3243(15)	–386(13)	882(6)	19(2)	1
C2	–2083(14)	–1515(12)	1261(6)	14(2)	1
C3	–207(14)	–1586(12)	959(6)	13(2)	1
C4	588(13)	–555(12)	204(6)	13(2)	1
C5	–2508(14)	599(14)	168(7)	20(2)	1
O1	–1619(9)	–3825(8)	2471(4)	12(1)	1
O2	–3965(9)	–1760(9)	2756(4)	14(1)	1
O3	–4525(9)	–3892(9)	1980(4)	14(1)	1
S1	–3125(3)	–2843(3)	2179(1)	11(1)	1
C21	2485(14)	–6484(12)	688(6)	13(2)	1
C22	728(12)	–6842(11)	1238(6)	10(2)	1
C23	–907(13)	–6246(12)	1042(6)	12(2)	1
C24	–882(13)	–5184(12)	277(6)	14(2)	1
C25	–2553(14)	–4530(14)	52(6)	19(2)	1
O21	1016(9)	–6859(9)	2739(4)	15(1)	1
O22	–1147(9)	–8844(8)	2464(4)	14(1)	1
O23	2210(9)	–9213(8)	2099(4)	11(1)	1
S21	692(3)	–8035(3)	2203(1)	9(1)	1
O1W	2032(9)	–3005(9)	2620(4)	18(2)	1
O2W	–4925(10)	–7997(10)	2646(5)	21(2)	1
O31	–3126(9)	–6755(8)	3739(4)	11(1)	1
O32	–855(9)	–6520(8)	5124(4)	12(1)	1
O33	–819(8)	–9309(8)	4498(4)	11(1)	1
O34	–5770(9)	–8448(8)	4859(4)	14(1)	1
O35	–6948(9)	–5674(8)	3848(4)	11(1)	1
O36	–6283(8)	–5702(8)	5504(4)	9(1)	1
O37	–3030(9)	–9271(9)	6121(4)	14(1)	1
O38	711(9)	–8237(8)	6259(4)	12(1)	1

La1	−332(1)	−4856(1)	3702(1)	8(1)	1
La2	−3494(1)	−9859(1)	3728(1)	8(1)	1
W1	−781(1)	−8691(1)	5563(1)	8(1)	1
W2	−5262(1)	−6282(1)	4427(1)	8(1)	1

Table 22 Bond lengths [Å] and angles [°].

C1–C5	1.346(15)	O1W–La1	2.536(7)
C1–C2	1.402(15)	O2W–La2	2.554(7)
C2–C3	1.362(14)	O31–W2	1.828(7)
C2–S1	1.772(10)	O31–La2	2.537(6)
C3–C4	1.423(13)	O31–La1	2.537(6)
C4–C5^{i}	1.415(14)	O32–W1	1.798(6)
C4–C4^{i}	1.426(19)	O32–La1	2.514(7)
C5–C4^{i}	1.415(14)	O32–La1^{iv}	2.713(7)
O1–S1	1.464(7)	O33–W1	1.955(6)
O1–La1	2.468(7)	O33–W1^{v}	1.995(6)
O2–S1	1.464(7)	O33–La2	2.619(6)
O2–La2^{ii}	2.506(7)	O34–W2	1.797(7)
O3–S1	1.452(7)	O34–La2^{vi}	2.511(7)
C21–C25^{iii}	1.372(14)	O34–La2	2.678(7)
C21–C22	1.422(13)	O35–W2	1.733(6)
C22–C23	1.358(13)	O35–La1^{vii}	2.587(6)
C22–S21	1.751(10)	O36–W2	1.961(6)
C23–C24	1.428(14)	O36–W2^{viii}	1.998(6)
C24–C25	1.415(14)	O36–La1^{viii}	2.634(6)
C24–C24^{iii}	1.431(19)	O37–W1	1.742(6)
C25–C21^{iii}	1.372(14)	O37–La2^{vi}	2.575(7)
O21–S21	1.471(7)	O38–W1	1.830(7)
O21–La1	2.549(7)	O38–La1^{iv}	2.532(7)
O22–S21	1.444(7)	O38–La2^{v}	2.536(7)
O22–La2	2.481(7)	La1–O38^{iv}	2.532(7)
O23–S21	1.458(6)	La1–O35^{ix}	2.587(6)

La1–O36^{viii}	2.634(6)	La2–W2	3.4601(6)
La1–O32^{iv}	2.713(7)	La2–W1^{v}	3.6596(6)
La1–W1^{iv}	3.4769(6)	W1–O33^{v}	1.995(6)
La1–W2	3.6725(6)	W1–W1^{v}	3.1465(7)
La2–O2(x)	2.506(7)	W1–La1^{iv}	3.4769(6)
La2–O34^{vi}	2.511(7)	W1–La2^{v}	3.6596(6)
La2–O38^{v}	2.536(7)	W2–O36^{viii}	1.998(6)
La2–O37^{vi}	2.575(7)	W2–W2^{viii}	3.1421(7)

C5–C1–C2	119.2(10)	C23–C24–C24^{iii}	118.4(11)
C3–C2–C1	122.4(9)	C21^{iii}–C25–C24	120.3(9)
C3–C2–S1	119.8(8)	S21–O21–La1	148.7(4)
C1–C2–S1	117.7(8)	S21–O22–La2	140.5(4)
C2–C3–C4	118.9(9)	O22–S21–O23	113.1(4)
C5^{i}–C4–C3	122.6(9)	O22–S21–O21	111.9(4)
C5^{i}–C4–C4^{i}	118.1(11)	O23–S21–O21	111.6(4)
C3–C4–C4^{i}	119.3(11)	O22–S21–C22	106.5(4)
C1–C5–C4^{i}	122.0(10)	O23–S21–C22	106.5(4)
S1–O1–La1	143.3(4)	O21–S21–C22	106.6(4)
S1–O2–La2^{ii}	148.0(4)	W2–O31–La2	103.7(3)
O3–S1–O1	112.0(4)	W2–O31–La1	113.6(3)
O3–S1–O2	112.2(4)	La2–O31–La1	133.5(3)
O1–S1–O2	111.4(4)	W1–O32–La1	135.9(3)
O3–S1–C2	106.9(4)	W1–O32–La1^{iv}	98.8(3)
O1–S1–C2	107.1(4)	La1–O32–La1^{iv}	118.0(2)
O2–S1–C2	106.9(4)	W1–O33–W1^{v}	105.6(3)
C25^{iii}–C21–C22	119.6(9)	W1–O33–La2	134.2(3)
C23–C22–C21	121.8(9)	W1^{v}–O33–La2	104.2(3)
C23–C22–S21	119.4(7)	W2–O34–La2^{vi}	136.1(3)
C21–C22–S21	118.8(7)	W2–O34–La2	99.4(3)
C22–C23–C24	120.0(9)	La2^{vi}–O34–La2	115.9(2)
C25–C24–C23	121.7(9)	W2–O35–La1^{vii}	152.1(3)
C25–C24–C24^{iii}	119.9(11)	W2–O36–W2^{viii}	105.1(3)

W2–O36–La1^{viii}	134.8(3)	O35^{ix}–La1–O36^{viii}	145.0(2)
W2^{viii}–O36–La1^{viii}	104.1(3)	O1–La1–O32^{iv}	136.4(2)
W1–O37–La2^{vi}	153.7(4)	O32–La1–O32^{iv}	62.0(2)
W1–O38–La1^{iv}	104.6(3)	O38^{iv}–La1–O32^{iv}	59.9(2)
W1–O38–La2^{v}	112.9(3)	O1W–La1–O32^{iv}	89.6(2)
La1^{iv}–O38–La2^{v}	133.0(3)	O31–La1–O32^{iv}	132.4(2)
O1–La1–O32	148.1(2)	O21–La1–O32^{iv}	135.7(2)
O1–La1–O38^{iv}	76.7(2)	O35^{ix}–La1–O32^{iv}	67.4(2)
O32–La1–O38^{iv}	110.9(2)	O36^{viii}–La1–O32^{iv}	84.25(19)
O1–La1–O1W	68.1(2)	O1–La1–W1^{iv}	105.83(16)
O32–La1–O1W	143.7(2)	O32–La1–W1^{iv}	90.30(15)
O38^{iv}–La1–O1W	66.4(2)	O38^{iv}–La1–W1^{iv}	30.62(15)
O1–La1–O31	73.0(2)	O1W–La1–W1^{iv}	69.97(17)
O32–La1–O31	77.1(2)	O31–La1–W1^{iv}	140.49(15)
O38^{iv}–La1–O31	121.4(2)	O21–La1–W1^{iv}	142.63(15)
O1W–La1–O31	136.9(2)	O35^{ix}–La1–W1^{iv}	83.38(15)
O1–La1–O21	77.3(2)	O36^{viii}–La1–W1^{iv}	81.82(13)
O32–La1–O21	106.4(2)	O32^{iv}–La1–W1^{iv}	30.74(13)
O38^{iv}–La1–O21	141.3(2)	O1–La1–W2	79.73(15)
O1W–La1–O21	77.4(2)	O32–La1–W2	68.53(15)
O31–La1–O21	76.7(2)	O38^{iv}–La1–W2	99.28(15)
O1–La1–O35^{ix}	130.3(2)	O1W–La1–W2	146.89(16)
O32–La1–O35^{ix}	77.9(2)	O31–La1–W2	27.14(15)
O38^{iv}–La1–O35^{ix}	109.4(2)	O21–La1–W2	103.80(15)
O1W–La1–O35^{ix}	70.0(2)	O35^{ix}–La1–W2	141.92(15)
O31–La1–O35^{ix}	128.5(2)	O36^{viii}–La1–W2	31.86(13)
O21–La1–O35^{ix}	68.4(2)	O32^{iv}–La1–W2	109.36(14)
O1–La1–O36^{viii}	84.3(2)	W1^{iv}–La1–W2	113.465(16)
O32–La1–O36^{viii}	70.7(2)	O22–La2–O2(x)	75.3(2)
O38^{iv}–La1–O36^{viii}	69.6(2)	O22–La2–O34^{vi}	148.9(2)
O1W–La1–O36^{viii}	132.1(2)	O2(x) –La2–O34^{vi}	107.2(2)
O31–La1–O36^{viii}	58.7(2)	O22–La2–O38^{v}	73.1(2)
O21–La1–O36^{viii}	135.0(2)	O2(x) –La2–O38^{v}	77.2(2)

O34^{vi}–La2–O38^{v}	77.2(2)	O34^{vi}–La2–W2	92.04(15)
O22–La2–O31	76.1(2)	O38^{v}–La2–W2	141.14(15)
O2(x) –La2–O31	139.0(2)	O31–La2–W2	30.88(15)
O34^{vi}–La2–O31	112.6(2)	O2W–La2–W2	69.11(17)
O38^{v}–La2–O31	121.0(2)	O37^{vi}–La2–W2	84.93(15)
O22–La2–O2W	67.4(2)	O33–La2–W2	82.28(14)
O2(x) –La2–O2W	75.9(2)	O34–La2–W2	30.83(14)
O34^{vi}–La2–O2W	143.8(2)	O22–La2–W1^{v}	80.94(16)
O38^{v}–La2–O2W	136.4(2)	O2(x) –La2–W1^{v}	104.63(15)
O31–La2–O2W	66.2(2)	O34^{vi}–La2–W1^{v}	68.31(15)
O22–La2–O37^{vi}	128.8(2)	O38^{v}–La2–W1^{v}	27.43(15)
O2(x) –La2–O37^{vi}	67.4(2)	O31–La2–W1^{v}	99.26(14)
O34^{vi}–La2–O37^{vi}	77.5(2)	O2W–La2–W1^{v}	147.25(17)
O38^{v}–La2–O37^{vi}	127.3(2)	O37^{vi}–La2–W1^{v}	140.89(16)
O31–La2–O37^{vi}	111.3(2)	O33–La2–W1^{v}	31.90(14)
O2W–La2–O37^{vi}	70.4(2)	O34–La2–W1^{v}	110.99(15)
O22–La2–O33	85.3(2)	W2–La2–W1^{v}	113.978(16)
O2(x) –La2–O33	135.6(2)	O37–W1–O32	106.6(3)
O34^{vi}–La2–O33	71.3(2)	O37–W1–O38	109.1(3)
O38^{v}–La2–O33	58.9(2)	O32–W1–O38	92.5(3)
O31–La2–O33	69.6(2)	O37–W1–O33	103.3(3)
O2W–La2–O33	132.1(2)	O32–W1–O33	89.8(3)
O37^{vi}–La2–O33	145.7(2)	O38–W1–O33	145.3(3)
O22–La2–O34	136.0(2)	O37–W1–O33^{v}	110.5(3)
O2(x) –La2–O34	135.0(2)	O32–W1–O33^{v}	142.0(3)
O34^{vi}–La2–O34	64.1(2)	O38–W1–O33^{v}	82.9(3)
O38^{v}–La2–O34	134.6(2)	O33–W1–O33^{v}	74.4(3)
O31–La2–O34	60.4(2)	O37–W1–W1^{v}	111.4(2)
O2W–La2–O34	87.9(2)	O32–W1–W1^{v}	119.8(2)
O37^{vi}–La2–O34	67.6(2)	O38–W1–W1^{v}	115.6(2)
O33–La2–O34	85.9(2)	O33–W1–W1^{v}	37.63(19)
O22–La2–W2	105.15(16)	O33^{v}–W1–W1^{v}	36.76(18)
O2(x) –La2–W2	141.05(16)	O37–W1–La1^{iv}	103.5(2)

O32–W1–La1^{iv}	50.4(2)	O35–W2–La1	121.0(2)
O38–W1–La1^{iv}	44.8(2)	O34–W2–La1	118.8(2)
O33–W1–La1^{iv}	137.0(2)	O31–W2–La1	39.29(19)
O33^{v}–W1–La1^{iv}	124.86(18)	O36–W2–La1	111.36(17)
W1^{v}–W1–La1^{iv}	144.749(19)	O36^{viii}–W2–La1	44.08(18)
O37–W1–La2^{v}	122.9(2)	W2^{viii}–W2–La1	76.730(15)
O32–W1–La2^{v}	117.7(2)	La2–W2–La1	81.585(14)
O38–W1–La2^{v}	39.7(2)		
O33–W1–La2^{v}	110.61(18)		
O33^{v}–W1–La2^{v}	43.94(18)		
W1^{v}–W1–La2^{v}	76.245(15)		
La1^{iv}–W1–La2^{v}	81.226(14)		
O35–W2–O34	106.4(3)		
O35–W2–O31	108.2(3)		
O34–W2–O31	92.8(3)		
O35–W2–O36	105.0(3)		
O34–W2–O36	88.8(3)		
O31–W2–O36	144.8(3)		
O35–W2–O36^{viii}	110.2(3)		
O34–W2–O36^{viii}	142.6(3)		
O31–W2–O36^{viii}	82.8(3)		
O36–W2–O36^{viii}	74.9(3)		
O35–W2–W2^{viii}	112.4(2)		
O34–W2–W2^{viii}	119.5(2)		
O31–W2–W2^{viii}	115.5(2)		
O36–W2–W2^{viii}	37.89(17)		
O36^{viii}–W2–W2^{viii}	37.06(18)		
O35–W2–La2	103.5(2)		
O34–W2–La2	49.8(2)		
O31–W2–La2	45.43(19)		
O36–W2–La2	135.01(19)		
O36^{viii}–W2–La2	125.15(18)		
W2^{viii}–W2–La2	143.85(2)		

Symmetry transformations used to generate equivalent atoms:

(i) –x,–y,–z (ii) x,y+1,z (iii) –x,–y–1,–z (iv) –x,–y–1,–z+1

(v) –x,–y–2,–z+1 (vi) –x–1,–y–2,–z+1 (vii) x–1,y,z

(viii) –x–1,–y–1,–z+1 (xi) x+1,y,z (x) x,y–1,z

Table 23 Anisotropic displacement parameters [$Å^2 \times 10^3$]. The anisotropic displacement factor exponent takes the form: $-2\pi^2[h^2a^{*2}U^{11} + \cdots + 2\,h\,k\,a^*\,b^*\,U^{12}]$.

Atom	U^{11}	U^{22}	U^{33}	U^{23}	U^{13}	U^{12}
C1	21(5)	20(5)	15(5)	–5(4)	0(4)	0(4)
C2	22(5)	8(4)	13(5)	–5(4)	–3(4)	–4(4)
C3	21(5)	13(5)	6(4)	–2(4)	–3(4)	1(4)
C4	16(5)	11(5)	12(5)	–2(4)	–8(4)	–3(4)
C5	18(5)	24(6)	22(6)	–10(5)	–4(4)	10(4)
O1	12(3)	16(3)	9(3)	–4(3)	–1(2)	0(3)
O2	16(3)	16(4)	10(3)	–4(3)	0(3)	0(3)
O3	10(3)	20(4)	11(3)	–7(3)	3(3)	–3(3)
S1	10(1)	12(1)	11(1)	–3(1)	–2(1)	–1(1)
C21	19(5)	11(5)	11(5)	0(4)	–9(4)	2(4)
C22	6(4)	8(4)	11(5)	0(4)	5(3)	0(3)
C23	13(4)	13(5)	12(5)	–2(4)	–5(4)	–7(4)
C24	19(5)	12(5)	11(5)	–1(4)	–5(4)	0(4)
C25	13(5)	30(6)	14(5)	–7(4)	2(4)	–9(4)
O21	15(3)	15(4)	15(4)	–2(3)	–6(3)	–2(3)
O22	12(3)	15(3)	14(4)	–1(3)	–1(3)	–3(3)
O23	14(3)	9(3)	11(3)	–1(2)	–6(2)	7(2)
S21	6(1)	12(1)	9(1)	–2(1)	–1(1)	–1(1)
O1W	14(3)	18(4)	18(4)	4(3)	–3(3)	–4(3)
O2W	18(4)	24(4)	22(4)	–4(3)	–8(3)	3(3)

O31	15(3)	8(3)	9(3)	2(3)	−4(3)	−5(3)
O32	16(3)	4(3)	16(3)	1(2)	−6(2)	0(2)
O33	7(3)	17(3)	10(3)	−3(3)	−3(2)	1(3)
O34	17(3)	8(3)	18(4)	−4(3)	1(3)	0(3)
O35	9(3)	17(3)	8(3)	−5(3)	0(2)	3(3)
O36	8(3)	9(3)	9(3)	−1(2)	−1(2)	−7(2)
O37	15(3)	17(4)	10(3)	−6(3)	1(3)	−3(3)
O38	14(3)	12(3)	11(3)	−4(3)	−2(3)	1(3)
La1	7(1)	7(1)	9(1)	−1(1)	−1(1)	−2(1)
La2	7(1)	7(1)	9(1)	−2(1)	−1(1)	−1(1)
W1	8(1)	7(1)	9(1)	−1(1)	−1(1)	−1(1)
W2	8(1)	7(1)	9(1)	−2(1)	−2(1)	−1(1)

Crystallographic data for $[La(H_2O)WO_4]_2[2,6\text{-NDS}]$ (4)

Table 24 Crystal data and structure refinement details for $[La(H_2O)WO_4]_2[2,6\text{-NDS}]$.

Identification code	**2009src1129rd**	
Empirical formula	$C_5H_3LaO_8SW$	
Formula weight	545.89	
Temperature	120(2) K	
Wavelength	0.71073 Å	
Crystal system	Monoclinic	
Space group	*C*2/*c*	
Unit cell dimensions	a = **36.204(6) Å**	α = **90°**
	b = **7.4451(10) Å**	β = **93.731(10)°**
	c = **7.5711(9) Å**	γ = **90°**
Volume	2036.4(5) $Å^3$	
Z	8	

Density (calculated)	3.561 mg / m^3
Absorption coefficient	15.656 mm^{-1}
F(000)	1952
Crystal	Plate; colourless
Crystal size	0.10 × 0.07 × 0.02 mm^3
θ range for data collection	3.22 – 27.48°
Index ranges	$-46 \le h \le 46$, $-9 \le k \le 9$, $-9 \le l \le 9$
Reflections collected	14611
Independent reflections	2326 [R_{int} = 0.0895]
Completeness to θ = 27.48°	99.9 %
Absorption correction	Semi–empirical from equivalents
Max. and min. transmission	0.7448 and 0.3035
Refinement method	Full-matrix least-squares on F^2
Data / restraints / parameters	2326 / 104 / 173
Goodness-of-fit on F^2	1.142
Final *R* indices [$F^2 > 2\sigma(F^2)$]	*R1* = 0.0509, *wR2* = 0.1220
R indices (all data)	*R1* = 0.0577, *wR2* = 0.1261
Largest diff. peak and hole	1.914 and –2.672 e $Å^{-3}$

Diffractometer: *Nonius KappaCCD* area detector (ϕ scans and ω scans to fill *asymmetric unit* sphere). **Cell determination:** DirAx (Duisenberg, A.J.M.(1992). J. Appl. Cryst. 25, 92-96.) **Data collection:** Collect (Collect: Data collection software, R. Hooft, Nonius B.V., 1998). **Data reduction and cell refinement**: *Denzo* (Z. Otwinowski & W. Minor, *Methods in Enzymology* (1997) Vol. **276**: *Macromolecular Crystallography*, part A, pp. 307–326; C. W. Carter, Jr. & R. M. Sweet, Eds., Academic Press). **Absorption correction**: *SADABS* (Sheldrick, G. M. (2007). SADABS. Version 2007/2. Bruker AXS Inc., Madison, Wisconsin, USA.). S**tructure solution**: *SHELXS97* (Sheldrick, G.M. (2008). Acta Cryst. A64, 112-122.). S**tructure refinement**: *SHELXL97* (G Sheldrick, G.M. (2008). Acta Cryst. A64, 112-122.). **Graphics:** *CAMERON* (Watkin, D. M., Pearce, L. & Prout, C. K. (1993). Chemical Crystallography Lab, University of Oxford)

Special details:

Table 25 Atomic coordinates [$\times 10^4$], equivalent isotropic displacement parameters [$Å^2 \times 10^3$] and site occupancy factors. U_{eq} is defined as one third of the trace of the orthogonalized U^{ij} tensor.

Atom	*x*	*y*	*z*	U_{eq}	*S.o.f.*
W3	2092(1)	1941(1)	–2615(1)	16(1)	1
La1	1752(1)	3455(1)	2394(1)	17(1)	1
S8	1038(1)	7105(5)	3580(4)	21(1)	1
O1	1208(3)	5518(14)	2796(13)	29(2)	1
O2	1242(3)	7702(14)	5209(11)	26(2)	1
O3	980(2)	8586(13)	2318(11)	23(2)	1
O4	2012(3)	3115(13)	–652(11)	23(2)	1
O5	2431(3)	3378(13)	2875(11)	25(2)	1
O6	1876(3)	210(12)	2338(12)	24(2)	1
O7	1882(3)	6592(12)	713(11)	22(2)	1
O8	1229(3)	1824(13)	3856(12)	26(2)	1
C2	484(4)	4786(18)	4288(18)	27(3)	1
C3	115(4)	4353(18)	4731(14)	29(3)	1
C1A	614(13)	6370(60)	4490(40)	22(6)	0.48(2)
C4A	47(7)	7410(40)	5690(30)	26(6)	0.48(2)
C5A	386(6)	7830(30)	5250(30)	17(5)	0.48(2)
C1B	579(13)	6560(60)	3990(40)	19(5)	0.52(2)
C4B	–47(7)	7450(30)	4430(30)	21(5)	0.52(2)
C5B	302(7)	7800(30)	3980(30)	23(5)	0.52(2)

Table 26 Bond lengths [Å] and angles [°].

W3–O4	1.765(9)	C3–C4A^{vi}	1.46(4)
W3–O5^{i}	1.767(9)	C3–C4B^{vi}	1.51(3)
W3–O6^{ii}	1.781(9)	C1A–C5A	1.50(5)
W3–O7^{iii}	1.803(8)	C4A–C5A	1.33(4)
W3–La1^{iii}	3.6424(10)	C4A–C3^{vi}	1.46(4)
La1–O6	2.458(9)	C4A–H4A	0.9500
La1–O5	2.462(9)	C5A–H5A	0.9500
La1–O7^{iv}	2.527(8)	C1B–C5B	1.36(5)
La1–O1	2.533(10)	C4B–C5B	1.36(4)
La1–O2^{iii}	2.548(9)	C4B–C3^{vi}	1.51(3)
La1–O8	2.560(9)	C4B–H4B	0.9500
La1–O4	2.559(9)	C5B–H5B	0.9500
La1–O7	2.715(9)		
La1–W3^{iv}	3.6424(10)	O4–W3–O5^{i}	112.1(4)
S8–O2	1.464(9)	O4–W3–O6^{ii}	111.5(4)
S8–O3	1.465(10)	O5^{i}–W3–O6^{ii}	107.9(4)
S8–O1	1.473(10)	O4–W3–O7^{iii}	101.9(4)
S8–C1A	1.81(5)	O5^{i}–W3–O7^{iii}	112.0(4)
S8–C1B	1.76(5)	O6^{ii}–W3–O7^{iii}	111.5(4)
O2–La1^{iv}	2.548(9)	O4–W3–La1^{iii}	57.2(3)
O5–W3^{i}	1.767(9)	O5^{i}–W3–La1^{iii}	117.4(3)
O6–W3^{v}	1.781(9)	O6^{ii}–W3–La1^{iii}	134.3(3)
O7–W3^{iv}	1.803(8)	O7^{iii}–W3–La1^{iii}	45.9(3)
O7–La1^{iii}	2.527(8)	O6–La1–O5	78.3(3)
C2–C1B	1.39(5)	O6–La1–O7^{iv}	88.9(3)
C2–C1A	1.28(5)	O5–La1–O7^{iv}	74.5(3)
C2–C3	1.433(19)	O6–La1–O1	137.9(3)
C2–H2	0.9500	O5–La1–O1	140.7(3)
C3–C3^{vi}	1.35(3)	O7^{iv}–La1–O1	89.1(3)

O6–La1–O2^{iii}	77.4(3)	O2–S8–O1	112.5(6)
O5–La1–O2^{iii}	139.7(3)	O3–S8–O1	112.7(6)
O7^{iv}–La1–O2^{iii}	136.1(3)	O2–S8–C1A	99.4(11)
O1–La1–O2^{iii}	75.3(3)	O3–S8–C1A	112.7(10)
O6–La1–O8	71.5(3)	O1–S8–C1A	107.3(15)
O5–La1–O8	133.2(3)	O2–S8–C1B	110.5(13)
O7^{iv}–La1–O8	70.0(3)	O3–S8–C1B	101.1(12)
O1–La1–O8	68.4(3)	O1–S8–C1B	108.0(16)
O2^{iii}–La1–O8	66.1(3)	C1A–S8–C1B	13.2(13)
O6–La1–O4	79.0(3)	S8–O1–La1	151.9(6)
O5–La1–O4	73.1(3)	S8–O2–La1^{iv}	138.4(6)
O7^{iv}–La1–O4	147.1(3)	W3–O4–La1	153.9(5)
O1–La1–O4	120.2(3)	W3^{i}–O5–La1	163.8(5)
O2^{iii}–La1–O4	71.0(3)	W3^{v}–O6–La1	164.5(5)
O8–La1–O4	131.9(3)	W3^{iv}–O7–La1^{iii}	138.5(5)
O6–La1–O7	143.1(3)	W3^{iv}–O7–La1	105.7(4)
O5–La1–O7	83.6(3)	La1^{iii}–O7–La1	115.3(3)
O7^{iv}–La1–O7	116.8(2)	C1B–C2–C1A	17.2(18)
O1–La1–O7	72.2(3)	C1B–C2–C3	120(2)
O2^{iii}–La1–O7	97.3(3)	C1A–C2–C3	121(2)
O8–La1–O7	140.0(3)	C1B–C2–H2	117.9
O4–La1–O7	65.0(3)	C1A–C2–H2	119.3
O6–La1–W3^{iv}	149.6(2)	C3–C2–H2	119.3
O5–La1–W3^{iv}	71.8(2)	C3^{vi}–C3–C2	120.8(17)
O7^{iv}–La1–W3^{iv}	88.5(2)	C3^{vi}–C3–C4A^{vi}	117.1(18)
O1–La1–W3^{iv}	72.3(2)	C2–C3–C4A^{vi}	121.1(15)
O2^{iii}–La1–W3^{iv}	123.2(2)	C3^{vi}–C3–C4B^{vi}	112.7(16)
O8–La1–W3^{iv}	135.0(2)	C2–C3–C4B^{vi}	118.5(14)
O4–La1–W3^{iv}	87.0(2)	C4A^{vi}–C3–C4B^{vi}	38.9(13)
O7–La1–W3^{iv}	28.46(17)	C2–C1A–C5A	120(4)
O2–S8–O3	111.3(6)	C2–C1A–S8	123(3)

C5A–C1A–S8	116(3)
C5A–C4A–C3^{vi}	121(2)
C5A–C4A–H4A	119.3
C3^{vi}–C4A–H4A	119.3
C4A–C5A–C1A	118(3)
C4A–C5A–H5A	121.1
C1A–C5A–H5A	121.1
C2–C1B–C5B	117(4)
C2–C1B–S8	120(3)
C5B–C1B–S8	123(3)
C5B–C4B–C3^{vi}	117(2)
C5B–C4B–H4B	121.4
C3^{vi}–C4B–H4B	121.4
C4B–C5B–C1B	124(3)
C4B–C5B–H5B	117.8
C1B–C5B–H5B	117.8

Symmetry transformations used to generate equivalent atoms:

(i) –x+1/2,–y+1/2,–z (ii) x,–y,z–1/2 (iii) x,–y+1,z–1/2

(iv) x,–y+1,z+1/2 (v) x,–y,z+1/2 (vi) –x,–y+1,–z+1

Table 27 Anisotropic displacement parameters [$Å^2 \times 10^3$]. The anisotropic displacement

factor exponent takes the form: $-2\pi^2[h^2a^{*2}U^{11} + \cdots + 2\ h\ k\ a^*\ b^*\ U^{12}\ ]$.

Atom	U^{11}	U^{22}	U^{33}	U^{23}	U^{13}	U^{12}
W3	16(1)	20(1)	13(1)	0(1)	1(1)	0(1)
La1	17(1)	20(1)	12(1)	0(1)	1(1)	1(1)
S8	18(1)	26(2)	20(1)	5(1)	4(1)	2(1)
O1	20(5)	29(6)	40(6)	1(4)	11(4)	2(4)
O2	26(5)	35(6)	16(4)	2(4)	0(4)	5(4)
O3	20(4)	31(5)	17(4)	–2(4)	–4(3)	2(4)
O4	27(5)	27(5)	16(4)	1(4)	5(4)	–5(4)
O5	25(5)	31(6)	17(4)	9(4)	–6(4)	5(4)
O6	28(5)	15(5)	31(5)	0(4)	2(4)	9(4)
O7	30(5)	24(5)	11(4)	–9(3)	2(3)	–1(4)
O8	32(5)	26(5)	20(4)	–3(4)	3(4)	–8(4)
C2	23(6)	15(5)	42(7)	–4(5)	3(5)	1(5)
C3	28(6)	19(7)	41(8)	–6(6)	13(6)	–1(5)
C1A	21(11)	12(11)	34(17)	5(14)	4(13)	9(8)
C4A	19(9)	38(14)	22(12)	8(11)	7(9)	11(10)
C5A	13(9)	14(9)	24(11)	–3(8)	–5(8)	5(7)
C1B	23(10)	19(9)	15(12)	15(11)	3(11)	4(7)
C4B	26(9)	18(11)	20(11)	–13(9)	–2(8)	–3(8)
C5B	27(9)	15(8)	27(11)	–6(9)	1(9)	–3(7)

Characterising data for $[Ln(H_2O)WO_4]_2[2,6\text{-NDS}]$ (La-Ce)

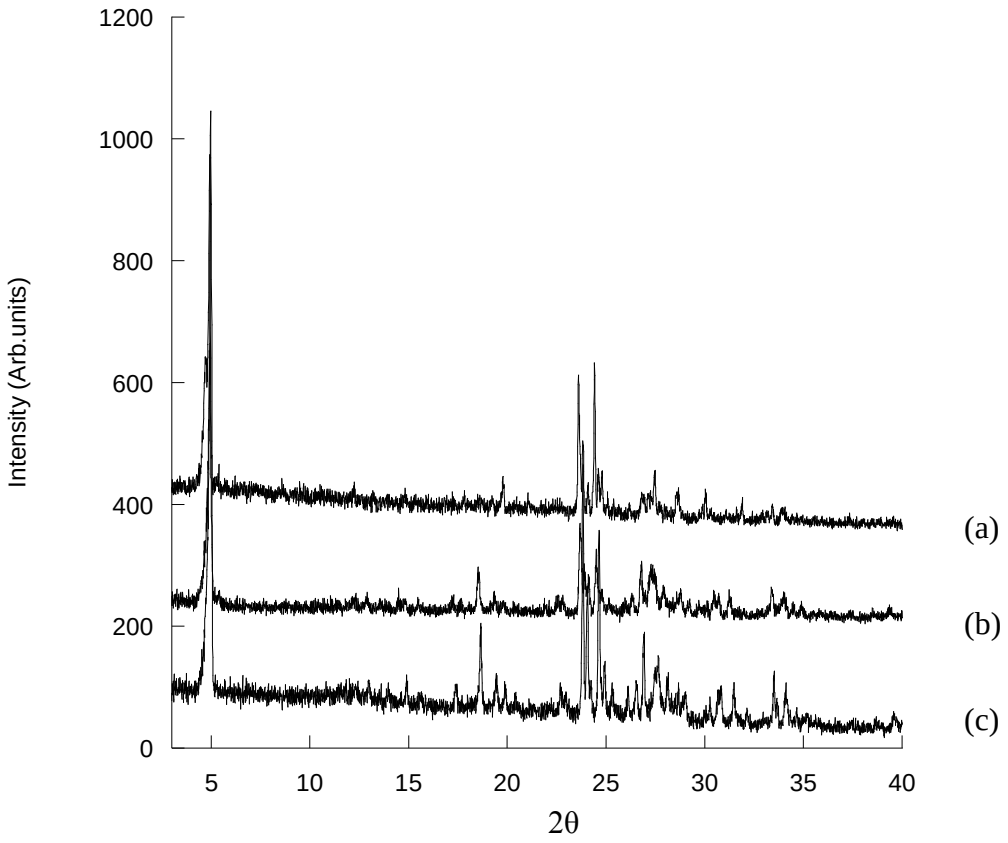

Figure 57 Powder XRD patterns of (a) La/W/2,6-NDS system, (b) $[Ce(H_2O)WO_4]_2[2,6\text{-NDS}]$, and (c) $[Pr(H_2O)WO_4]_2[2,6\text{-NDS}]$.

[Ce(H$_2$O)WO$_4$]$_2$[2,6-NDS]

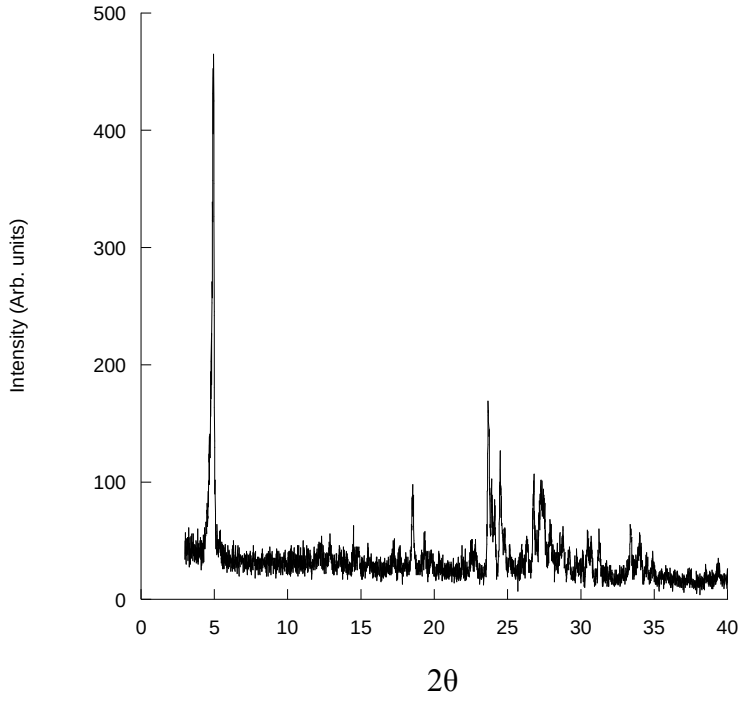

Figure 58 Powder X-ray diffraction pattern of [Ce(H$_2$O)WO$_4$]$_2$[2,6-NDS]

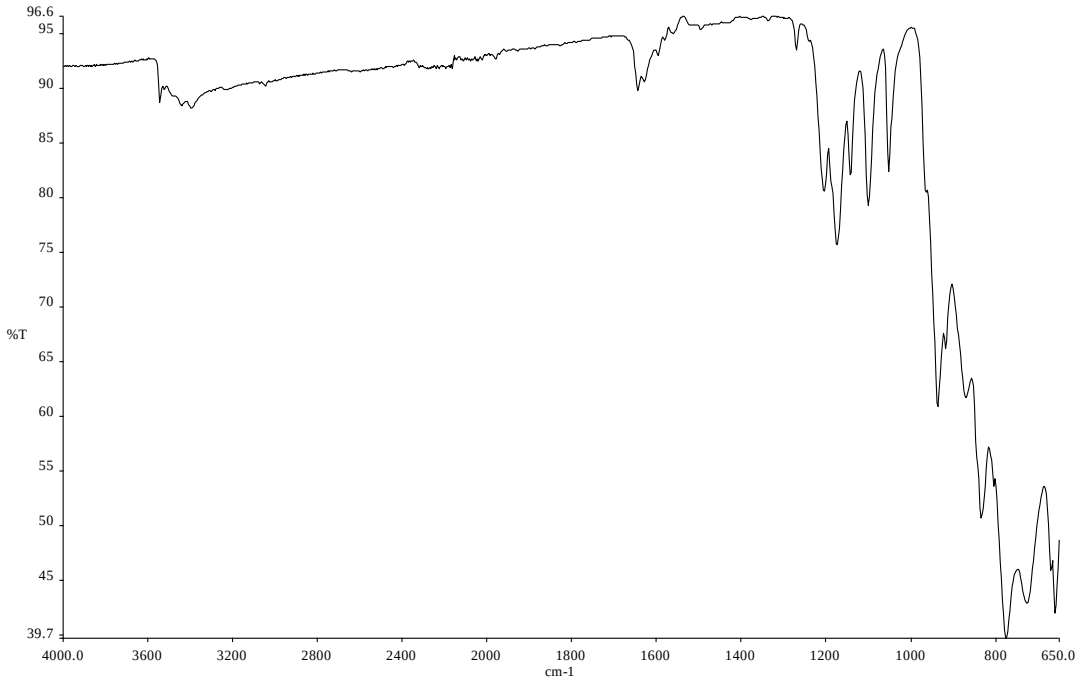

Figure 59 FTIR spectra for [Ce(H$_2$O)WO$_4$]$_2$[2,6-NDS] showing bands due to OH at 3396 cm^{-1}, S-O stretching modes at 1176 (antisymmetric) and 1054 cm^{-1} (symmetric) and the tungstate stretching frequency at 776 cm^{-1}.

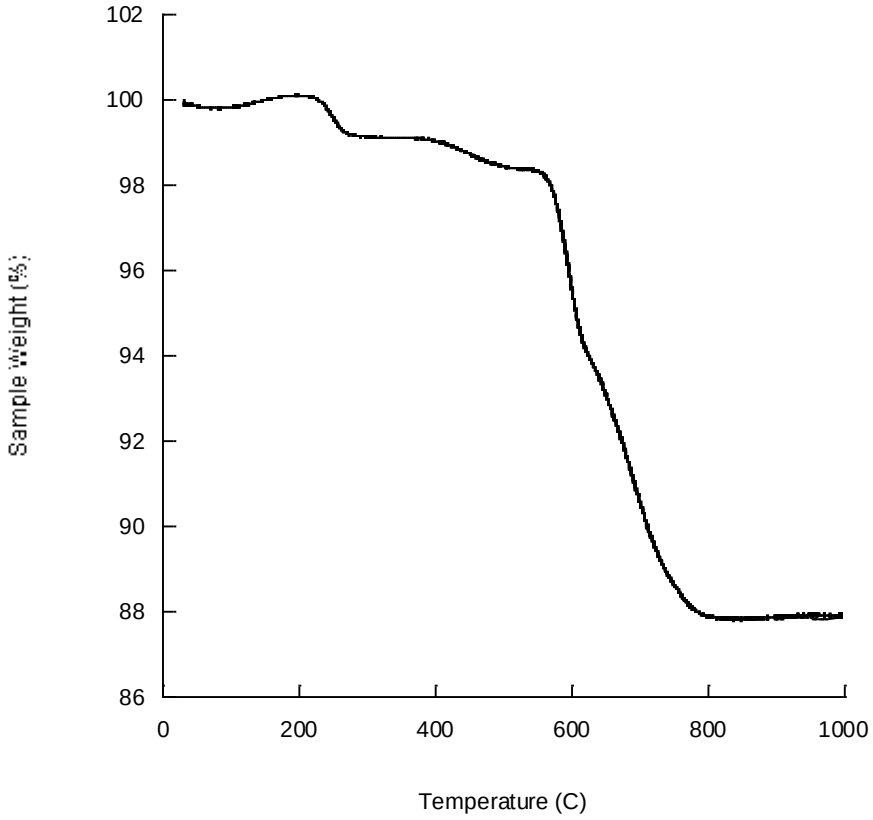

Figure 60 TGA trace of $[Ce(H_2O)WO_4]_2$[2,6-NDS] showing two distinct mass losses 1.7 % at 550 °C and 10.4 % at 80 0°C decomposition complete by 800°C total mass loss of 12.1 %. End product is found to be a mixture of $Ce_2(WO_4)_3$ & CeO_2.

$[Pr(H_2O)WO_4]_2[2,6\text{-NDS}]$

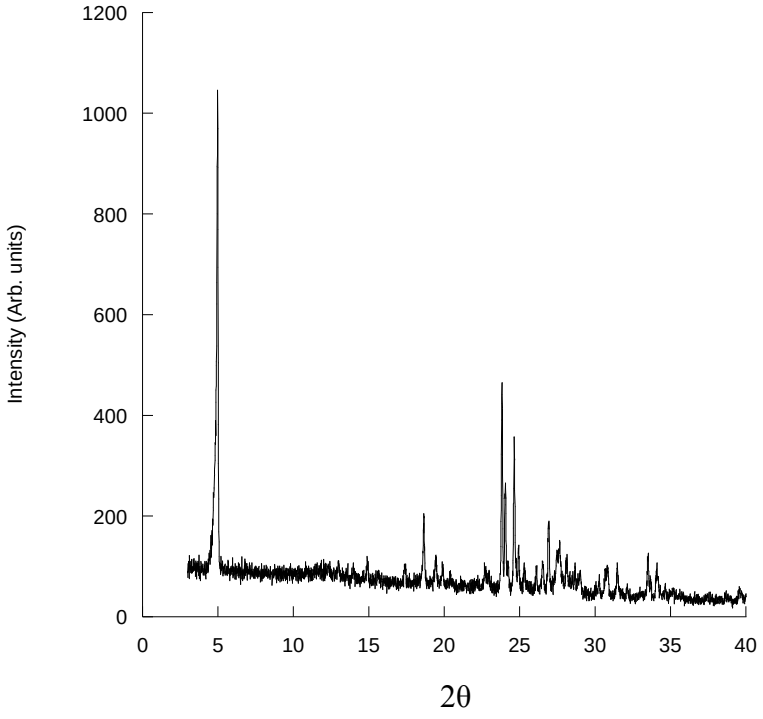

Figure 61 Powder X-ray diffraction pattern of $[Pr(H_2O)WO_4]_2[2,6\text{-NDS}]$

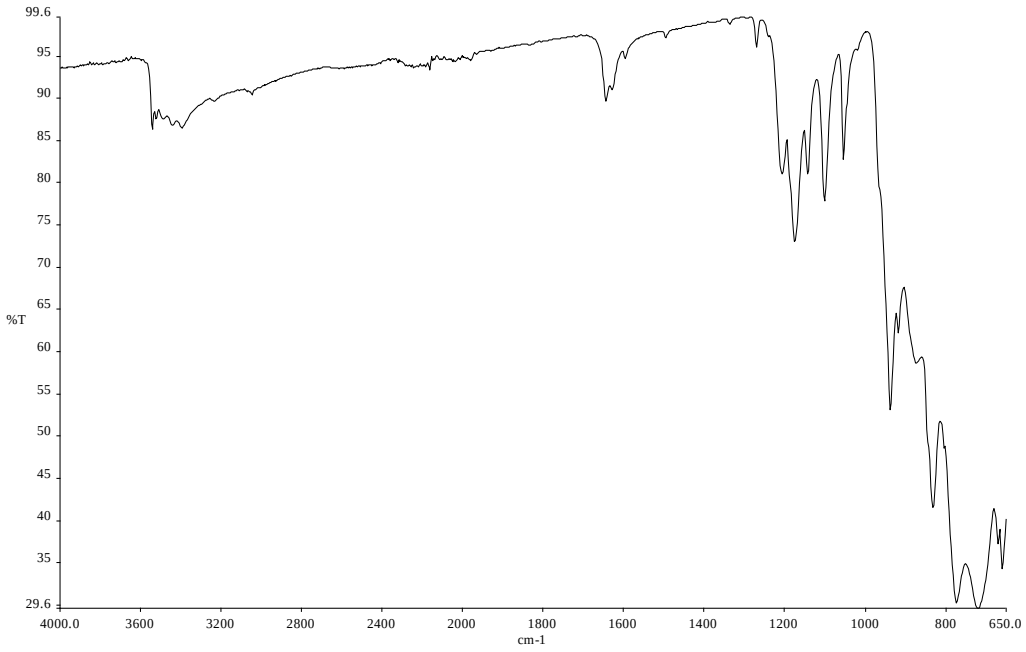

Figure 62 FTIR spectra for $[Pr(H_2O)WO_4]_2[2,6\text{-NDS}]$ showing bands due to OH at 3396 cm^{-1}, S-O stretching modes at 1177 (antisymmetric) and 1055 cm^{-1} (symmetric) and the tungstate stretching frequency at 775 cm^{-1}.

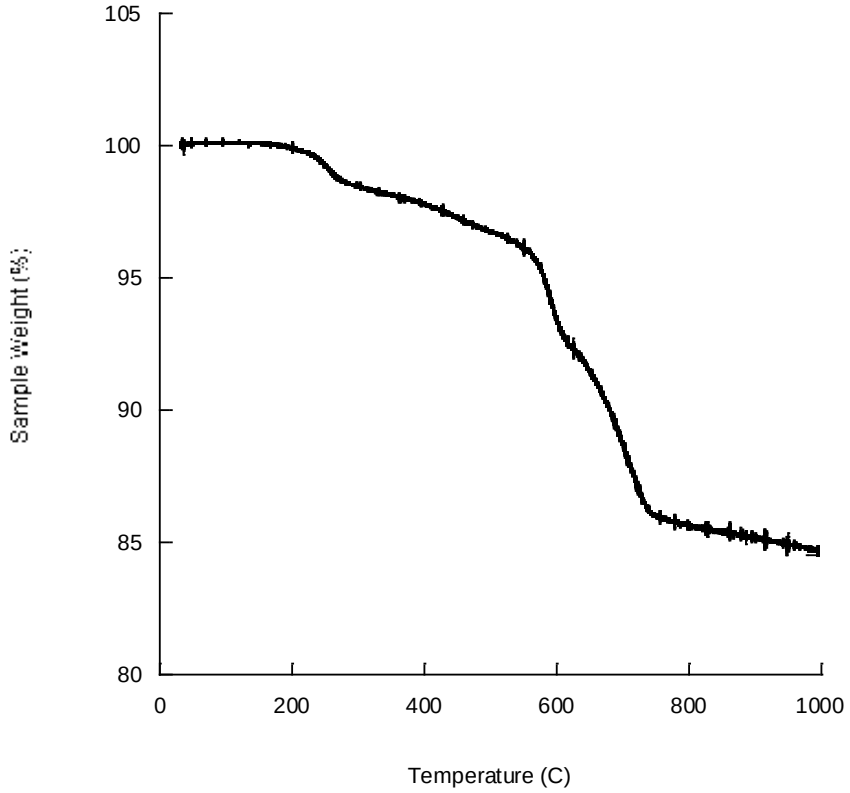

Figure 63 TGA trace of $[Pr(H_2O)WO_4]_2$[2,6-NDS] showing two distinct mass loss. First mass loss of 3.2 % below 550 °C and an additional mass loss of 12.0 % by 750 °C. End product is found to be a mixture of Pr_2O_3 $3(WO_3)$ & $Pr_2W_2O_9$.

Table 28 Elemental analysis of $[Ln(H_2O)WO_4]_2$[2,6-NDS] (Ln= La, Ce & Pr)

Lanthanide	Interlayer Separation (Å)	Elemental Analysis	
		Observed (%)	Calculated (%)
La	17.9, 16.4	C-10.73	C-10.95
		H-1.04	H-0.91
Ce	18.0	C-8.12	C-10.94
		H-0.73	H-0.92
Pr	17.8	C-4.54	C-10.92
		H-0.55	H-0.92

Anion Exchange Reactions of La/W/2,6-NDS system

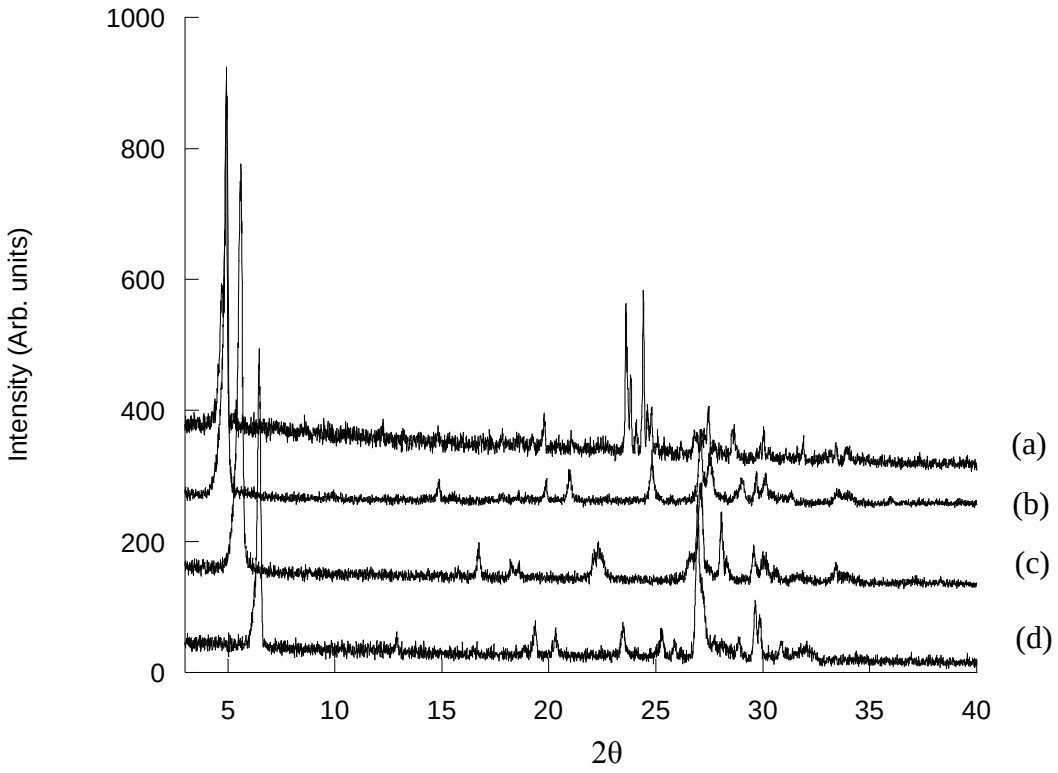

Figure 64 (a) Powder XRD patterns of La/WO_4/2,6-NDS system (**4** & **5**), and anion exchange products (b) [La(H_2O)WO_4]$_2$[2,6-NDC] (hydrothermal) (c) [La(H_2O)WO_4]$_2$[Terephthalate] (hydrothermal) and (d) [La(H_2O)WO_4]$_2$[Fumarate] (hydrothermal)

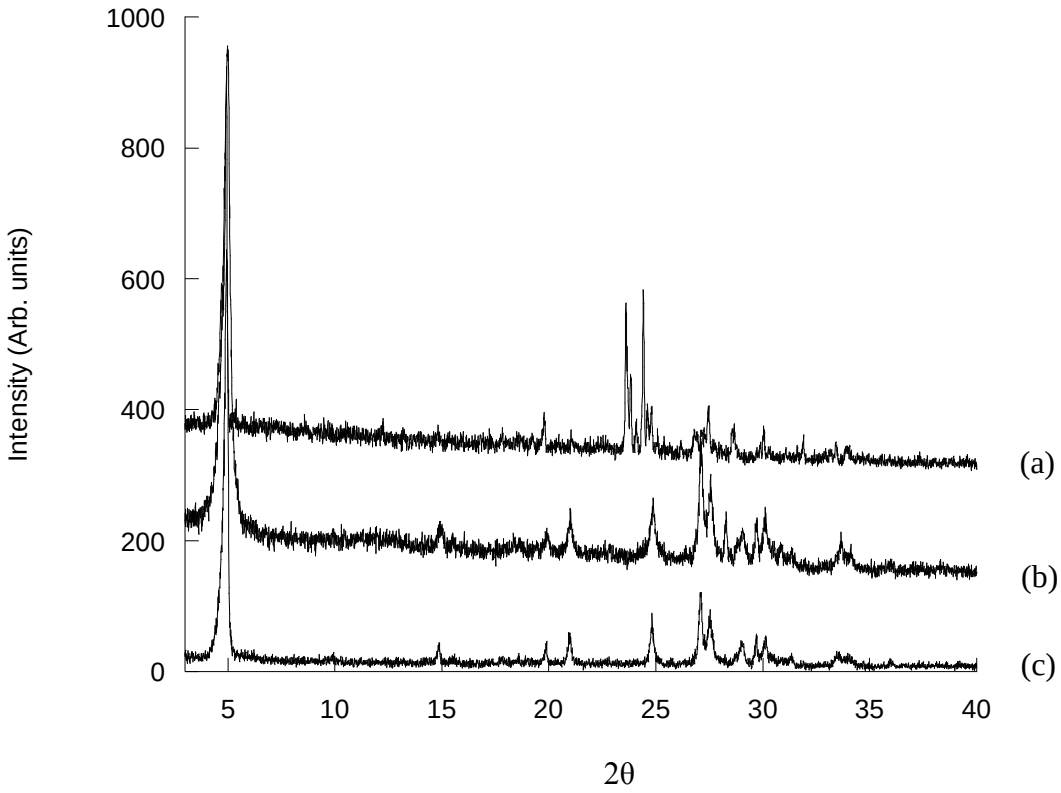

Figure 65 (a) Powder XRD patterns of La/WO_4/2,6-NDS system (**4** & **5**), and anion exchange products (b) [La(H_2O)WO_4]$_2$[2,6-NDC] (90°C) and (c) [La(H_2O)WO_4]$_2$[2,6-NDC] (hydrothermal)

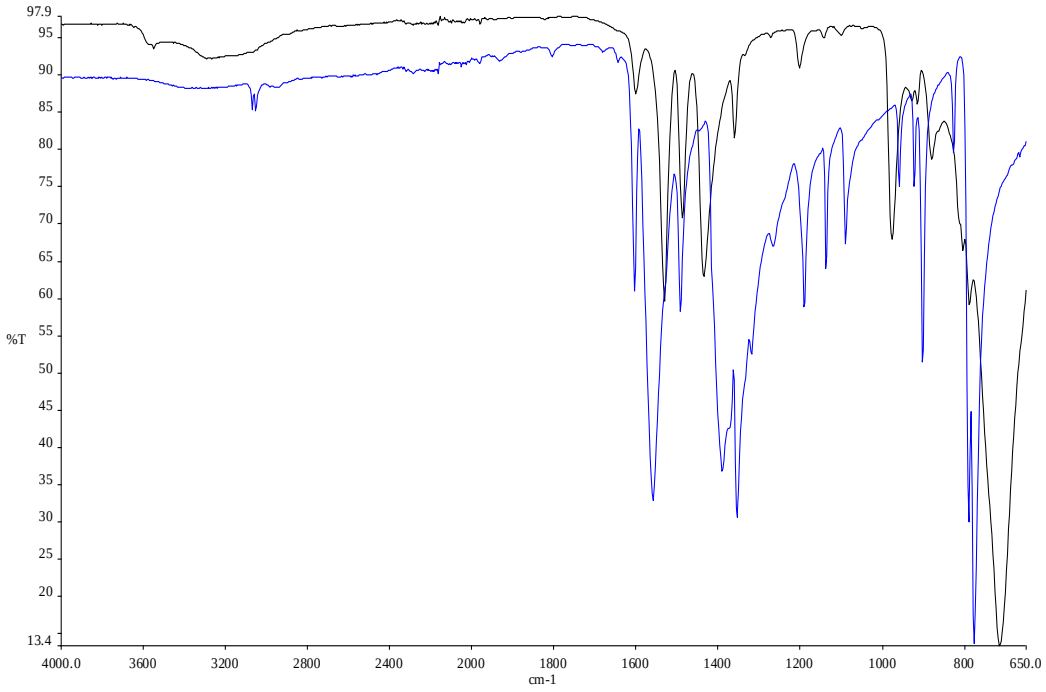

Figure 66 FTIR spectra of anion exchange product [La(H_2O)WO_4]$_2$[2,6-NDC] (90 °C, black) showing bands due to OH at 3267 cm^{-1} and C-O stretching modes at 1532 (antisymmetric) and 1436 cm^{-1} (symmetric), and 2,6-NDC (blue).

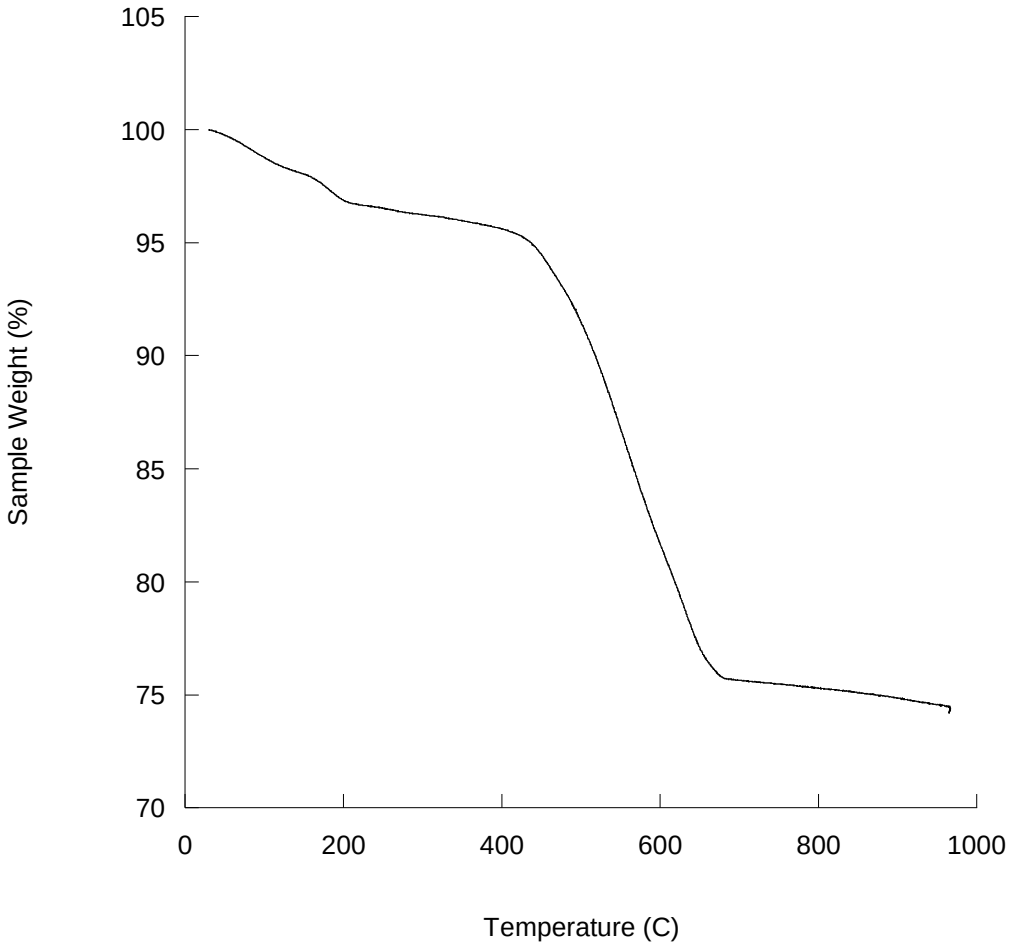

Figure 67 TGA trace of anion exchange product $[La(H_2O)WO_4]_2$[2,6-NDC] (90°C) showing two distinct mass losses. First mass loss of 4.4 % below 200 °C and an additional mass loss of 21.3 % by 700 °C. End product is found to be $La_2W_2O_9$.

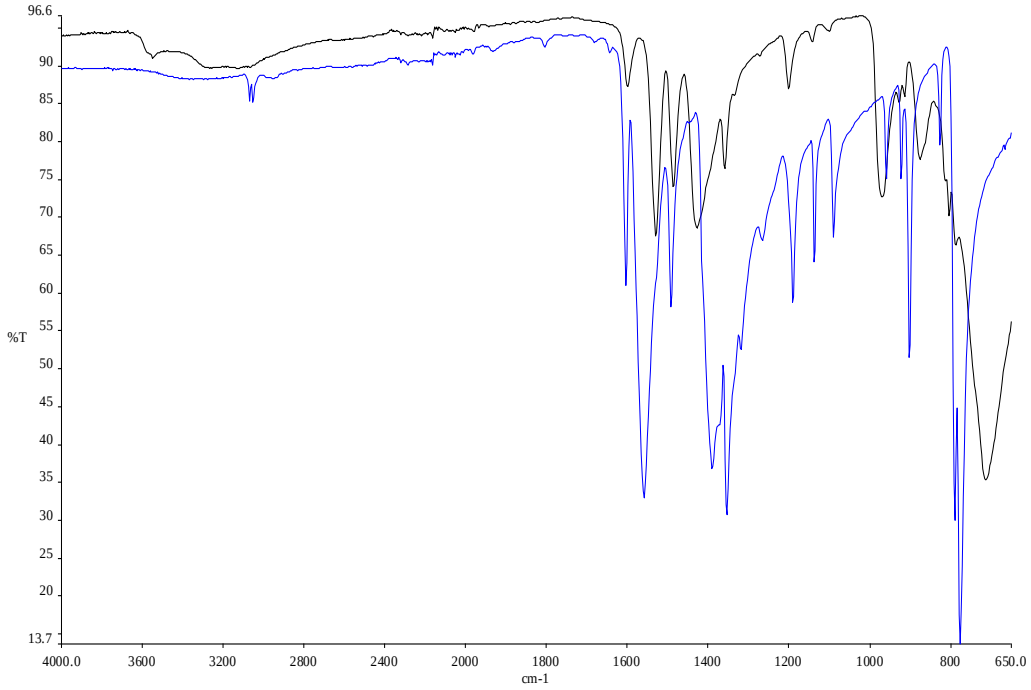

Figure 68 FTIR spectra of anion exchange product $[La(H_2O)WO_4]_2[2,6\text{-NDC}]$ (hydrothermal, black), showing bands due to OH at 3250 cm^{-1} and C-O stretching modes at 1531 (antisymmetric) and 1428 cm^{-1} (symmetric), and 2,6-NDC (blue).

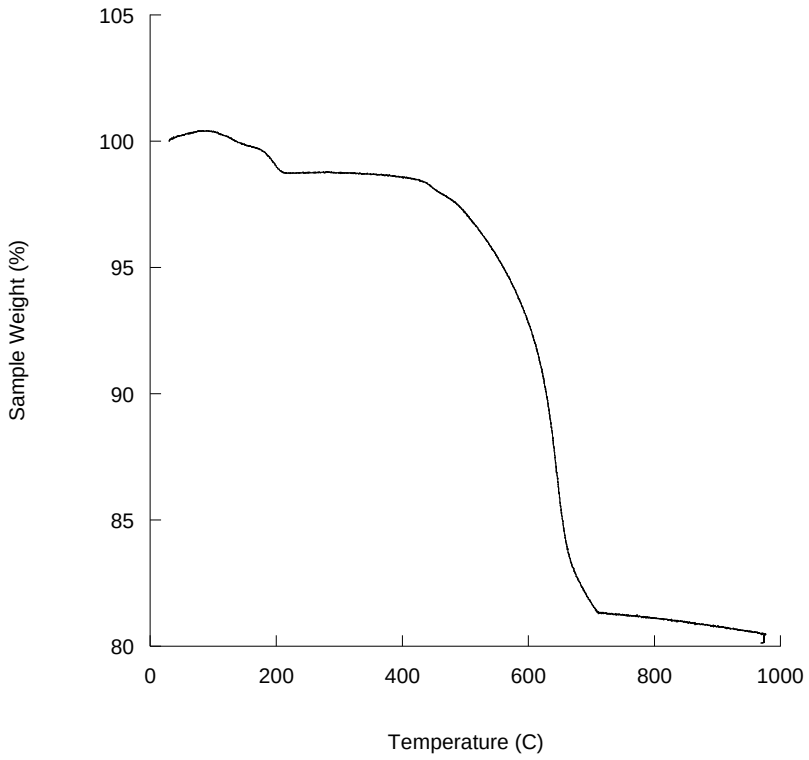

Figure 69 TGA trace of anion exchange product $[La(H_2O)WO_4]_2[2,6\text{-NDC}]$ (hydrothermally). First two mass loss of 1.4 % below 200 °C and an additional mass loss of 18.2 % by 700 °C. End product is found to be $La_2W_2O_9$.

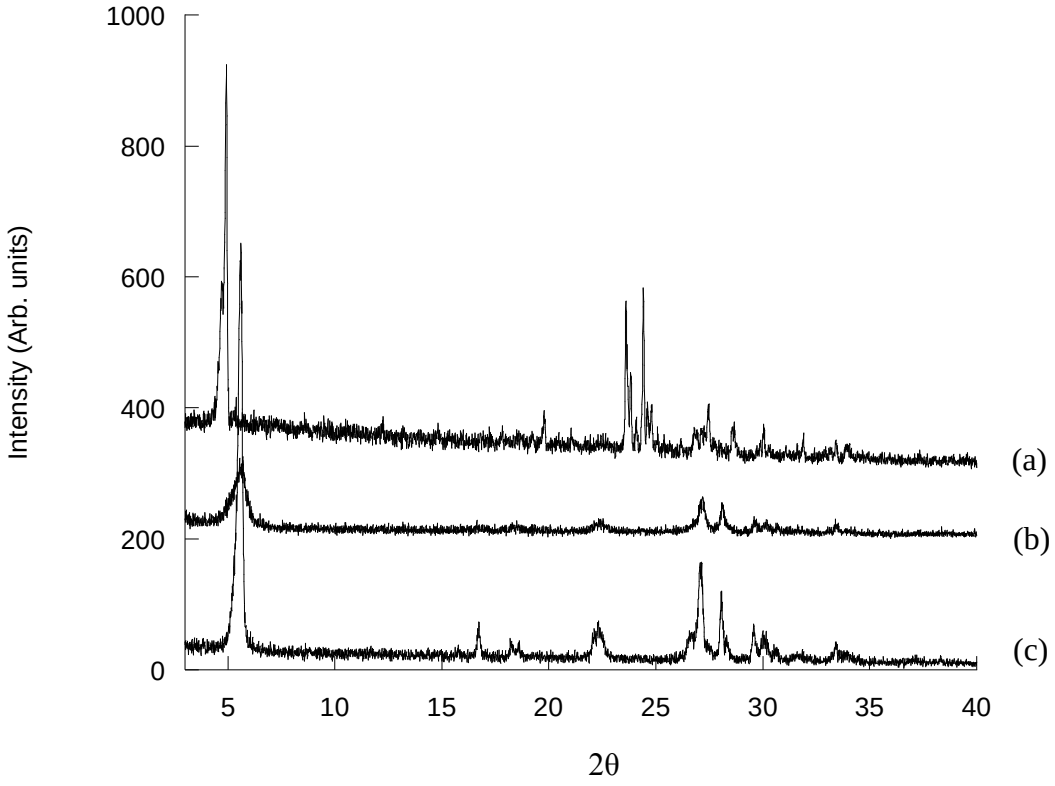

Figure 70 (a) Powder XRD patterns of La/WO_4/2,6-NDS system (**4** & **5**), and anion exchange products (b) [La(H_2O)WO_4]$_2$[Terephthalate] (90 °C) and (c) [La(H_2O)WO_4]$_2$[Terephthalate] (hydrothermal)

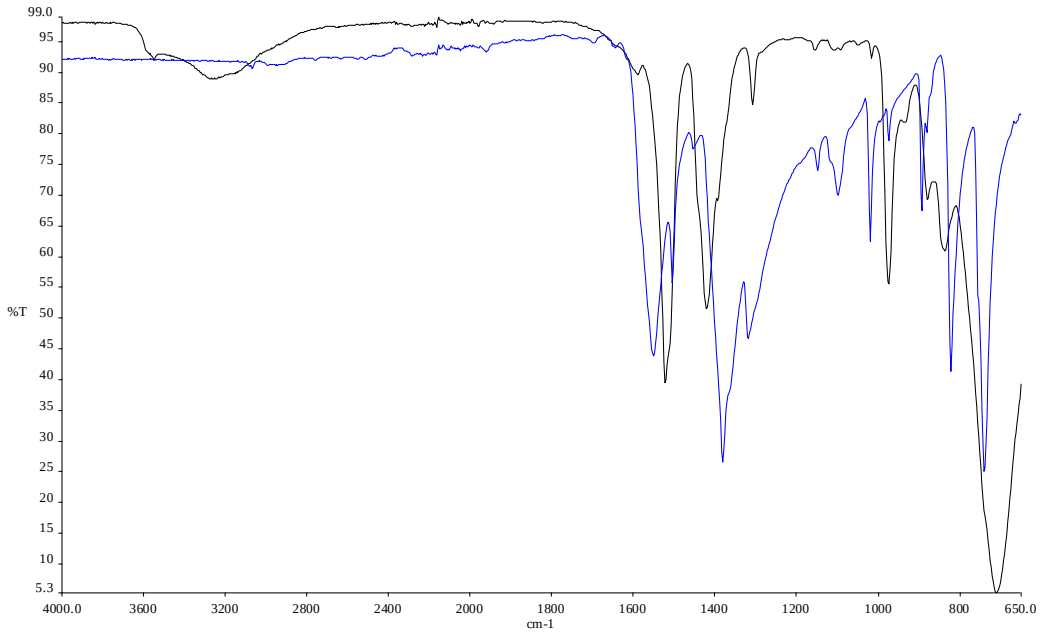

Figure 71 FTIR spectra of anion exchange product $[La(H_2O)WO_4]_2$[Terephthalate] (90 °C, black) showing bands due to OH at 3275 cm^{-1} and C-O stretching modes at 1522 (antisymmetric) and 1422 cm^{-1} (symmetric), and sodium terephthalate (blue).

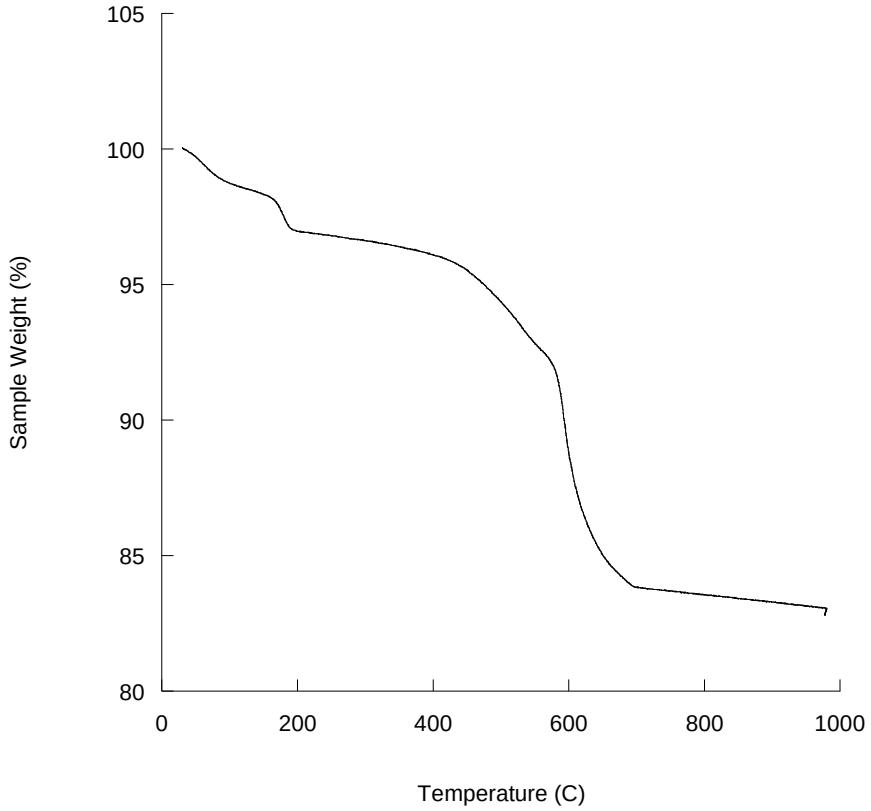

Figure 72 TGA trace of anion exchange product $[La(H_2O)WO_4]_2$[Terephthalate] (90 °C). First two mass losses of a total of 3.9 % below 200 °C and an additional mass loss of 13.3 % by 700 °C. End product is found to be $La_2W_2O_9$ & La_2O_3.

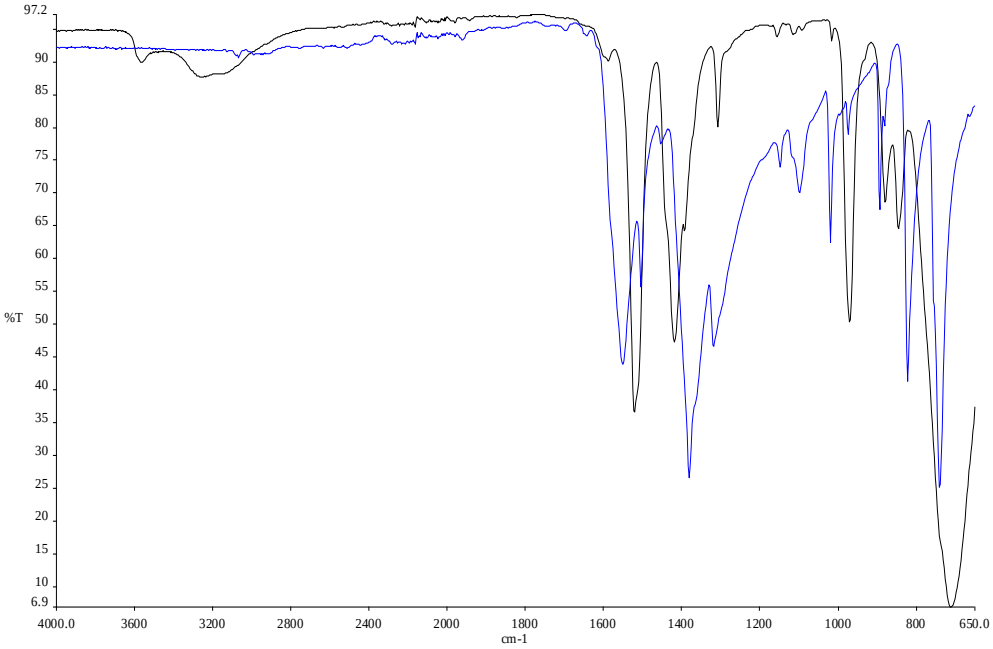

Figure 73 FTIR spectra of anion exchange product $[La(H_2O)WO_4]_2$[Terephthalate] (hydrothermal, black) showing bands due to OH at 3256 cm^{-1} and C-O stretching modes at 1522 (antisymmetric) and 1419 cm^{-1} (symmetric), and sodium terephthalate (blue).

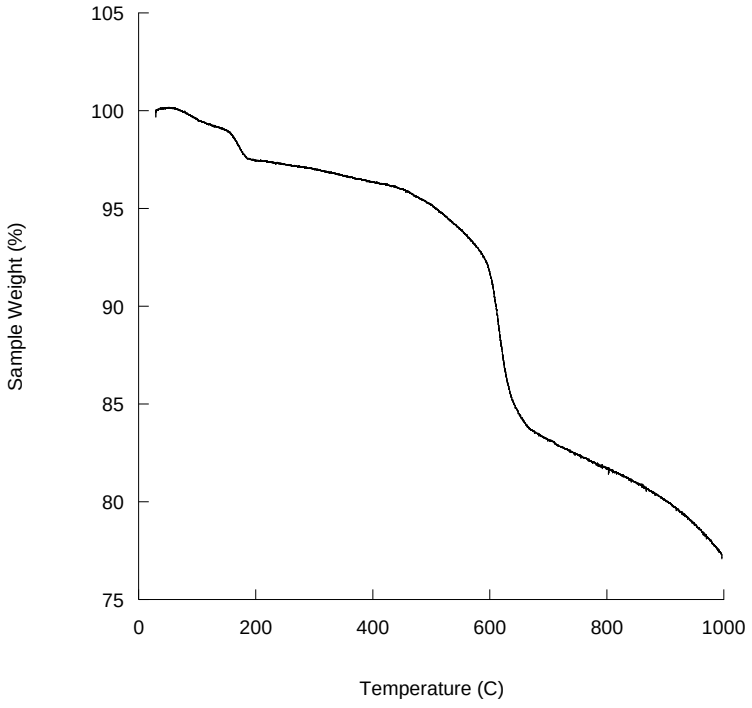

Figure 74 TGA trace of anion exchange product $[La(H_2O)WO_4]_2$[Terephthalate] (hydrothermally) showing three distinct mass losses. First two mass losses of a total of 3.0 % below 200 °C and an additional mass loss of 21.7 % by 700 °C. End product is found to be $La_2W_2O_9$.

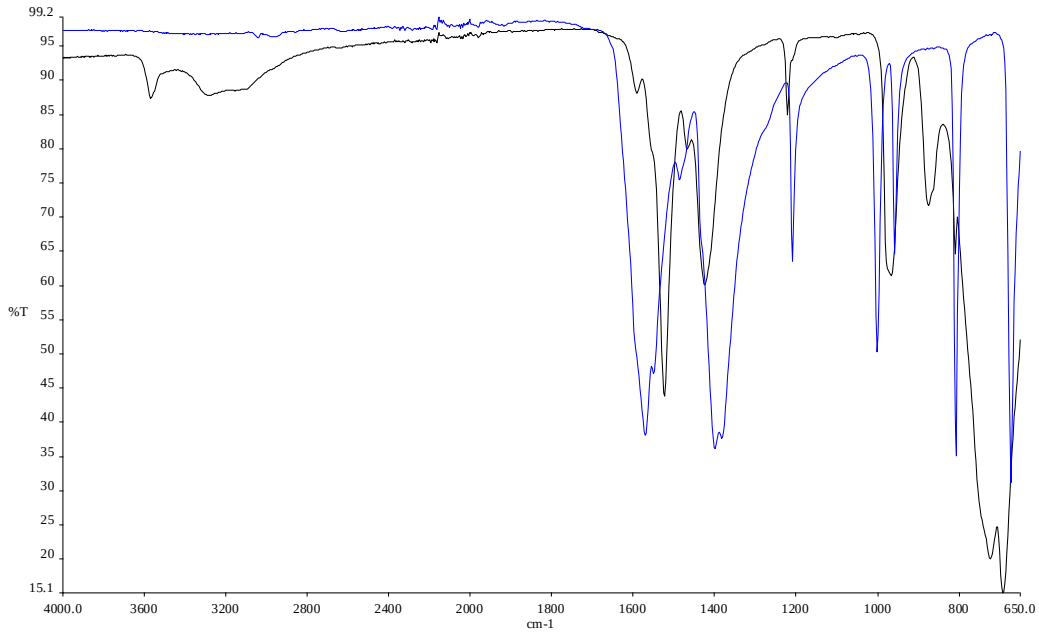

Figure 75 FTIR spectra of anion exchange product $[La(H_2O)WO_4]_2$[Fumarate] (hydrothermally, black) showing bands due to OH at 3279 cm^{-1} and C-O stretching modes at 1524 (antisymmetric) and 1425 cm^{-1} (symmetric), and sodium fumarate (blue).

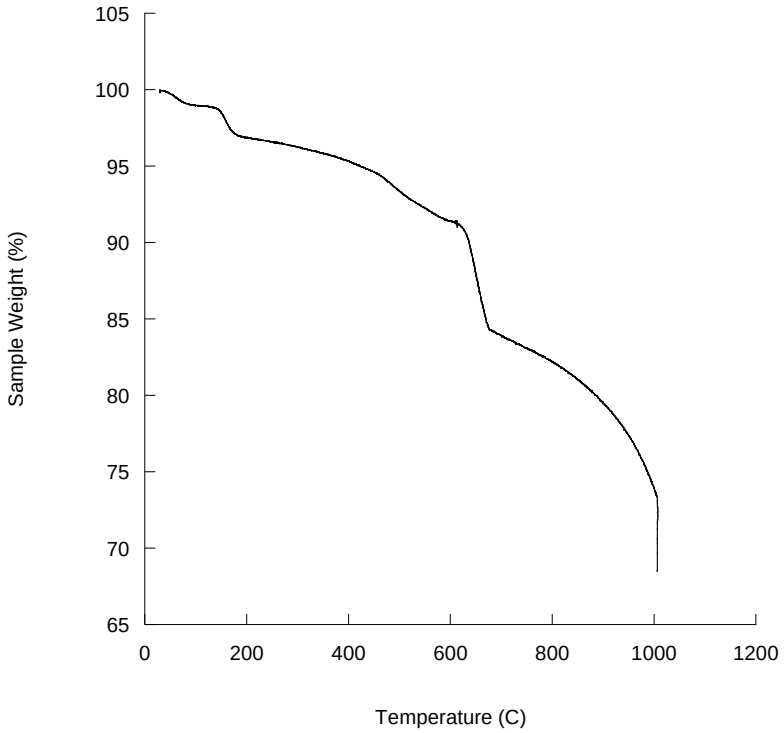

Figure 76 TGA trace of anion exchange product $[La(H_2O)WO_4]_2$[Fumarate] (hydrothermally), showing three distinct mass losses. First two mass losses of a total of 4.7 % below 600 °C and an additional mass loss of 21.9 % by 1006 °C. End product is found to be $La_2W_2O_9$.

Table 29 Characterisation data for anion exchange reactions using the host material $[La(H_2O)WO_4]_2$[2,6-NDS]

Anion	Interlayer Separation (Å)	Elemental Analysis Observed (%)	Calculated(%)
Fumarate	13.7	C – 4.35	C - 5.20
		H - 0.86	H - 0.65
Terephthalate (90°C)	15.9	C - 8.24	C - 9.87
		H - 0.66	H - 0.83
Terephthalate (Hydrothermal)	15.9	C - 8.29	C - 9.87
		H - 0.98	H - 0.83
2,6-NDC (90°C)	17.9	C - 12.88	C - 14.08
		H - 0.85	H - 0.98
2,6-NDC (hydrothermal)	18.0	C – 12.63	C - 14.08
		H - 0.81	H - 0.98

Table 30 Orientation of guest anions using host material $[La(H_2O)WO_4]_2$[2,6-NDS] with a layer thickness of 9.4 Å

Anion	Orientation of anion (°)
Fumarate	47
Terephthalate	54
2,6-NDC	67, 68
2,6-NDS (host)	55

Crystallographic data for $[Ce(H_2O)MoO_4]_2$[Fumarate] (6)

Table 31 Crystal data and structure refinement for ssi0053, $[Ce(H_2O)MoO_4]_2$[Fumarate]

Identification code	ssi0053	
Chemical formula (moiety)	$Ce_2(MoO_4)_2(H_2O)_2(C_4H_2O_4)$	
Chemical formula (total)	$C_4H_6Ce_2Mo_2O_{14}$	
Formula weight	750.21	
Temperature	120(2) K	
Radiation, wavelength	synchrotron, 0.6889 Å	
Crystal system, space group	triclinic, $P\bar{1}$	
Unit cell parameters	a = 7.2307(9) Å	α = 78.671(6)°
	b = 7.4798(9) Å	β = 85.649(7)°
	c = 13.5668(7) Å	γ = 87.288(11)°
Cell volume	716.98(13) $Å^3$	
Z	2	
Calculated density	3.475 g/cm^3	
Absorption coefficient □	8.007 mm^{-1}	
F(000)	684	
Crystal colour and size	black, 0.05 × 0.04 × 0.02 mm^3	
Reflections for cell refinement	10001 (θ range 1.5 to 29.9°)	
Data collection method	Rigaku Saturn 724 on Crystal Logic goniometer	
	thin-slice □ scans	
θ range for data collection	4.1 to 30.0°	
Index ranges	h –10 to 6, k –8 to 9, l –19 to 19	
Completeness to θ = 30.0°	79.4 %	
Intensity decay	0%	
Reflections collected	4475	
Independent reflections	4475 (R_{int} = 0.0000)	
Reflections with $F^2>2\theta$	4125	
Absorption correction	semi-empirical from equivalents	

Min. and max. transmission	0.690 and 0.897
Structure solution	direct methods
Refinement method	Full-matrix least-squares on F^2
Weighting parameters a, b	0.1073, 38.4881
Data / restraints / parameters	4475 / 72 / 201
Final R indices [$F^2>2\theta$]	R1 = 0.0714, wR2 = 0.2033
R indices (all data)	R1 = 0.0772, wR2 = 0.2096
Goodness-of-fit on F^2	1.098
Extinction coefficient	0.0032(13)
Largest and mean shift/su	0.002 and 0.000
Largest diff. peak and hole	3.02 and –2.70 e $Å^{-3}$

Table 32 Atomic coordinates and equivalent isotropic displacement parameters ($Å^2$) for ssi0053. U_{eq} is defined as one third of the trace of the orthogonalized U^{ij} tensor.

	x	y	z	U_{eq}
Ce(1)	0.09514(10)	0.67063(11)	0.20010(5)	0.0091(2)
Ce(2)	0.37279(10)	0.16882(11)	0.20574(5)	0.0086(2)
O(1)	0.3076(15)	0.6222(15)	0.3477(7)	0.0142(19)
O(2)	0.3467(16)	0.3217(15)	0.3512(6)	0.0151(19)
C(1)	0.3735(19)	0.465(2)	0.3817(9)	0.0112(19)
C(2)	0.4940(18)	0.4386(19)	0.4709(9)	0.011(2)
O(3)	–0.0914(14)	0.8055(16)	0.3400(7)	0.0138(18)
O(4)	0.1434(14)	0.9948(16)	0.3235(7)	0.0147(19)
C(3)	0.0047(18)	0.919(2)	0.3715(9)	0.0113(19)
C(4)	–0.054(2)	0.957(2)	0.4760(10)	0.015(2)
Mo(1)	–0.07818(15)	0.21461(17)	0.11014(8)	0.0092(3)
O(5)	0.0683(14)	0.3479(15)	0.1682(7)	0.014(2)
O(6)	–0.1125(15)	0.3119(15)	–0.0180(7)	0.015(2)
O(7)	–0.2933(15)	0.1931(16)	0.1804(8)	0.017(2)
O(8)	0.0350(15)	–0.0018(15)	0.1191(7)	0.014(2)
Mo(2)	0.55742(15)	0.70199(16)	0.10918(7)	0.0087(3)
O(9)	0.4185(14)	0.5084(15)	0.1434(8)	0.014(2)
O(10)	0.3998(15)	0.8677(15)	0.1528(7)	0.015(2)

O(11)	0.7635(15)	0.6712(15)	0.1729(8)	0.015(2)
O(12)	0.6108(15)	0.7625(17)	–0.0220(7)	0.019(2)
O(13)	–0.0625(18)	0.4346(18)	0.3544(9)	0.024(3)
O(14)	0.5285(14)	–0.0694(15)	0.3410(7)	0.016(2)

Table 33 Bond lengths [Å] and angles [°] for ssi0053.

Ce(1)–O(1)	2.575(10)	Ce(1)–O(3)	2.583(10)
Ce(1)–O(5)	2.553(12)	Ce(1)–O(6A)	2.442(9)
Ce(1)–O(8B)	2.513(10)	Ce(1)–O(9)	2.712(10)
Ce(1)–O(10)	2.675(11)	Ce(1)–O(11C)	2.454(11)
Ce(1)–O(13)	2.679(12)	Ce(2)–O(2)	2.459(10)
Ce(2)–O(4D)	2.446(10)	Ce(2)–O(5)	2.554(10)
Ce(2)–O(7E)	2.423(11)	Ce(2)–O(9)	2.543(11)
Ce(2)–O(10D)	2.490(12)	Ce(2)–O(12F)	2.439(10)
Ce(2)–O(14)	2.579(8)	O(1)–C(1)	1.259(17)
O(2)–C(1)	1.25(2)	C(1)–C(2)	1.520(18)
C(2)–C(2G)	1.33(3)	O(3)–C(3)	1.275(18)
O(4)–Ce(2B)	2.446(10)	O(4)–C(3)	1.250(16)
C(3)–C(4)	1.526(18)	C(4)–C(4H)	1.31(3)
Mo(1)–O(5)	1.809(12)	Mo(1)–O(6)	1.779(9)
Mo(1)–O(7)	1.759(10)	Mo(1)–O(8)	1.766(11)
O(6)–Ce(1A)	2.442(9)	O(7)–Ce(2C)	2.423(11)
O(8)–Ce(1D)	2.513(10)	Mo(2)–O(9)	1.767(11)
Mo(2)–O(10)	1.799(11)	Mo(2)–O(11)	1.762(11)
Mo(2)–O(12)	1.766(9)	O(10)–Ce(2B)	2.490(12)
O(11)–Ce(1E)	2.454(11)	O(12)–Ce(2F)	2.439(10)

O(1)–Ce(1)–O(3)	74.9(3)	O(1)–Ce(1)–O(5)	102.9(3)
O(1)–Ce(1)–O(6A)	140.3(4)	O(1)–Ce(1)–O(8B)	114.9(3)
O(1)–Ce(1)–O(9)	71.6(3)	O(1)–Ce(1)–O(10)	68.5(3)
O(1)–Ce(1)–O(11C)	138.9(3)	O(1)–Ce(1)–O(13)	71.4(4)
O(3)–Ce(1)–O(5)	125.4(3)	O(3)–Ce(1)–O(6A)	140.9(3)
O(3)–Ce(1)–O(8B)	76.3(3)	O(3)–Ce(1)–O(9)	146.4(3)
O(3)–Ce(1)–O(10)	105.8(3)	O(3)–Ce(1)–O(11C)	71.2(3)
O(3)–Ce(1)–O(13)	62.8(4)	O(5)–Ce(1)–O(6A)	72.2(3)
O(5)–Ce(1)–O(8B)	141.0(3)	O(5)–Ce(1)–O(9)	64.7(3)
O(5)–Ce(1)–O(10)	124.4(3)	O(5)–Ce(1)–O(11C)	79.4(4)
O(5)–Ce(1)–O(13)	65.0(4)	O(6A)–Ce(1)–O(8B)	72.5(4)
O(6A)–Ce(1)–O(9)	70.9(3)	O(6A)–Ce(1)–O(10)	81.9(4)

O(6A)–Ce(1)–O(11C)	80.1(4)	O(6A)–Ce(1)–O(13)	132.5(4)
O(8B)–Ce(1)–O(9)	117.3(3)	O(8B)–Ce(1)–O(10)	65.4(3)
O(8B)–Ce(1)–O(11C)	78.6(4)	O(8B)–Ce(1)–O(13)	135.6(4)
O(9)–Ce(1)–O(10)	60.4(3)	O(9)–Ce(1)–O(11C)	139.1(3)
O(9)–Ce(1)–O(13)	106.4(4)	O(10)–Ce(1)–O(11C)	143.2(3)
O(10)–Ce(1)–O(13)	139.9(4)	O(11C)–Ce(1)–O(13)	72.9(4)
O(2)–Ce(2)–O(4D)	75.7(4)	O(2)–Ce(2)–O(5)	81.8(4)
O(2)–Ce(2)–O(7E)	94.2(4)	O(2)–Ce(2)–O(9)	71.1(3)
O(2)–Ce(2)–O(10D)	144.7(3)	O(2)–Ce(2)–O(12F)	141.0(4)
O(2)–Ce(2)–O(14)	78.1(4)	O(4D)–Ce(2)–O(5)	76.4(3)
O(4D)–Ce(2)–O(7E)	139.0(3)	O(4D)–Ce(2)–O(9)	133.3(4)
O(4D)–Ce(2)–O(10D)	78.5(4)	O(4D)–Ce(2)–O(12F)	129.2(4)
O(4D)–Ce(2)–O(14)	68.3(3)	O(5)–Ce(2)–O(7E)	142.4(3)
O(5)–Ce(2)–O(9)	67.2(3)	O(5)–Ce(2)–O(10D)	115.0(4)
O(5)–Ce(2)–O(12F)	77.4(3)	O(5)–Ce(2)–O(14)	142.6(3)
O(7E)–Ce(2)–O(9)	76.1(3)	O(7E)–Ce(2)–O(10D)	89.6(4)
O(7E)–Ce(2)–O(12F)	83.1(4)	O(7E)–Ce(2)–O(14)	70.7(3)
O(9)–Ce(2)–O(10D)	143.3(3)	O(9)–Ce(2)–O(12F)	70.5(4)
O(9)–Ce(2)–O(14)	132.3(3)	O(10D)–Ce(2)–O(12F)	74.4(4)
O(10D)–Ce(2)–O(14)	70.1(4)	O(12F)–Ce(2)–O(14)	135.4(4)
Ce(1)–O(1)–C(1)	120.0(9)	Ce(2)–O(2)–C(1)	145.6(8)
O(1)–C(1)–O(2)	126.6(12)	O(1)–C(1)–C(2)	119.1(13)
O(2)–C(1)–C(2)	114.3(11)	C(1)–C(2)–C(2G)	124.0(15)
Ce(1)–O(3)–C(3)	110.7(8)	Ce(2B)–O(4)–C(3)	169.0(9)
O(3)–C(3)–O(4)	124.3(12)	O(3)–C(3)–C(4)	116.6(12)
O(4)–C(3)–C(4)	119.1(13)	C(3)–C(4)–C(4H)	121.8(16)
O(5)–Mo(1)–O(6)	113.1(5)	O(5)–Mo(1)–O(7)	108.2(5)
O(5)–Mo(1)–O(8)	105.7(5)	O(6)–Mo(1)–O(7)	109.8(5)
O(6)–Mo(1)–O(8)	110.2(5)	O(7)–Mo(1)–O(8)	109.7(5)
Ce(1)–O(5)–Ce(2)	109.1(4)	Ce(1)–O(5)–Mo(1)	141.0(5)
Ce(2)–O(5)–Mo(1)	108.9(5)	Ce(1A)–O(6)–Mo(1)	156.8(6)
Ce(2C)–O(7)–Mo(1)	155.7(6)	Ce(1D)–O(8)–Mo(1)	154.1(5)
O(9)–Mo(2)–O(10)	99.0(5)	O(9)–Mo(2)–O(11)	111.3(5)
O(9)–Mo(2)–O(12)	113.0(5)	O(10)–Mo(2)–O(11)	112.2(5)

O(10)–Mo(2)–O(12)	111.1(5)	O(11)–Mo(2)–O(12)	109.9(5)
Ce(1)–O(9)–Ce(2)	104.7(4)	Ce(1)–O(9)–Mo(2)	99.6(5)
Ce(2)–O(9)–Mo(2)	152.8(5)	Ce(1)–O(10)–Ce(2B)	114.0(4)
Ce(1)–O(10)–Mo(2)	100.1(5)	Ce(2B)–O(10)–Mo(2)	145.0(6)
Ce(1E)–O(11)–Mo(2)	159.5(5)	Ce(2F)–O(12)–Mo(2)	169.7(6)

Symmetry operations for equivalent atoms

A –x,–y+1,–z B x,y+1,z C x–1,y,z D x,y–1,z

E x+1,y,z F –x+1,–y+1,–z G –x+1,–y+1,–z+1

H –x,–y+2,–z+1

Table 34 Anisotropic displacement parameters ($Å^2$) for ssi0053. The anisotropic displacement factor exponent takes the form: $–2\pi^2[h^2a^{*2}U^{11} + ...+ 2hka^*b^*U^{12}]$

	U^{11}	U^{22}	U^{33}	U^{23}	U^{13}	U^{12}
Ce(1)	0.0063(3)	0.0095(5)	0.0113(3)	–0.0016(2)	–0.0013(2)	–0.0001(2)
Ce(2)	0.0071(3)	0.0079(5)	0.0108(3)	–0.0012(2)	–0.0008(2)	–0.0006(2)
O(1)	0.014(4)	0.011(5)	0.017(4)	–0.001(3)	–0.006(3)	–0.002(3)
O(2)	0.024(5)	0.014(5)	0.007(3)	–0.002(3)	0.003(3)	–0.002(4)
C(1)	0.012(4)	0.011(4)	0.011(3)	–0.002(3)	–0.001(3)	0.000(3)
C(2)	0.009(4)	0.012(6)	0.010(4)	–0.003(3)	0.005(3)	0.003(4)
O(3)	0.008(4)	0.019(5)	0.017(4)	–0.011(3)	0.004(3)	–0.003(3)
O(4)	0.008(4)	0.019(5)	0.017(4)	–0.004(3)	0.004(3)	–0.005(3)
C(3)	0.006(4)	0.018(5)	0.012(3)	–0.006(3)	0.000(3)	–0.005(3)

C(4)	0.015(5)	0.014(6)	0.015(4)	–0.007(4)	0.004(4)
	0.005(4)				
Mo(1)	0.0063(4)	0.0093(7)	0.0119(4)	–0.0014(4)	–0.0012(3)
–0.0010(4)					
O(5)	0.012(4)	0.011(6)	0.018(4)	–0.001(3)	0.002(3)
	0.000(4)				
O(6)	0.021(5)	0.016(6)	0.009(3)	–0.003(3)	–0.002(3)
	0.004(4)				
O(7)	0.010(4)	0.013(6)	0.025(5)	0.000(4)	0.001(4)
	0.001(4)				
O(8)	0.016(5)	0.012(6)	0.012(4)	0.006(3)	–0.004(3)
–0.004(4)					
Mo(2)	0.0070(5)	0.0082(7)	0.0113(4)	–0.0024(4)	–0.0008(3)
–0.0012(4)					
O(9)	0.008(4)	0.014(6)	0.022(4)	–0.010(4)	–0.003(3)
–0.001(4)					
O(10)	0.014(5)	0.012(6)	0.017(4)	–0.002(4)	0.000(3)
–0.001(4)					
O(11)	0.013(5)	0.011(6)	0.022(4)	–0.005(4)	–0.001(4)
–0.007(4)					
O(12)	0.014(5)	0.025(7)	0.014(4)	0.005(4)	0.000(3)
–0.005(4)					
O(13)	0.021(6)	0.021(7)	0.030(5)	–0.005(5)	0.004(5)
	0.000(5)				
O(14)	0.013(4)	0.015(6)	0.017(4)	0.008(4)	–0.010(3)
–0.001(4)					

Table 35 Hydrogen coordinates and isotropic displacement parameters ($Å^2$) for ssi0053.

	x	y	z	U
H(2)	0.5650	0.3277	0.4861	0.013
H(4)	–0.1706	0.9177	0.5073	0.017

Appendix B

Chapter Three

$[Er(H_2O)_2][C_2H_2O_5P]$

Table 1 Crystal data and structure refinement for jn452mfin- $[Er(H_2O)_2][C_2H_2O_5P]$

Identification code	jn452m	
Empirical formula	C2 H5 Er O7 P	
Formula weight	339.29	
Temperature	100(2) K	
Wavelength	0.71073 Å	
Crystal system	Orthorhombic	
Space group	Pnma	
Unit cell dimensions	a = 12.933(6) Å	α= 90°.
	b = 6.790(3) Å	β= 90°.
	c = 7.734(4) Å	γ = 90°.
Volume	679.2(6) $Å^3$	
Z	4	
Density (calculated)	3.318 mg/m^3	
Absorption coefficient	12.582 mm^{-1}	
F(000)	624	
Crystal size	0.55 x 0.10 x 0.08 mm^3	
Theta range for data collection	3.07 to 27.46°.	
Index ranges	-16<=h<=11, -8<=k<=8, -9<=l<=9	
Reflections collected	3126	
Independent reflections	811 [R(int) = 0.0483]	
Completeness to theta = 27.46°	96.0 %	
Absorption correction	Numerical	
Max. and min. transmission	0.4364 and 0.0549	
Refinement method	Full-matrix least-squares on F^2	
Data / restraints / parameters	800 / 12 / 73	

Goodness-of-fit on F^2	1.131
Final R indices [I>2sigma(I)]	R1 = 0.0348, wR2 = 0.0844
R indices (all data)	R1 = 0.0355, wR2 = 0.0848
Largest diff. peak and hole	2.219 and -2.117 e.$Å^{-3}$

Table 2 Atomic coordinates (x 10^4) and equivalent isotropic displacement parameters ($Å^2$x 10^3) for jn452mfin. U(eq) is defined as one third of the trace of the orthogonalized U^{ij} tensor.

	x	y	z	U(eq)
Er(1)	3351(1)	2500	-1289(1)	11(1)
P(1)	1389(2)	2500	1958(3)	10(1)
O(1)	-946(5)	4110(8)	3759(7)	16(2)
O(1W)	2634(7)	2500	-4047(12)	32(3)
O(2)	1625(4)	671(9)	2981(9)	21(2)
O(2W)	5049(7)	2500	-2109(12)	13(3)
O(3)	1926(7)	2500	217(12)	35(3)
C(1)	-667(7)	2500	3075(18)	12(3)
C(2)	2(9)	2500	1505(14)	13(3)

Table 3 Bond lengths [Å] and angles [°] for jn452mfin.

Er(1)-O(1W)	2.326(9)
Er(1)-O(2W)	2.284(8)
Er(1)-O(3)	2.182(8)
Er(1)-O(2)#1	2.226(6)
Er(1)-O(1)#2	2.421(6)
Er(1)-O(1)#3	2.421(6)
Er(1)-O(2)#4	2.226(6)
P(1)-O(2)	1.504(7)

P(1)-O(3)	1.512(9)
P(1)-C(2)	1.829(11)
P(1)-O(2)#5	1.504(7)
O(1)-C(1)	1.267(8)
O(1W)-H(1W)	0.95(3)
O(1W)-H(1W)#5	0.95(3)
O(2W)-H(2W)	0.95(6)
O(2W)-H(2W)#5	0.95(6)
C(1)-C(2)	1.491(15)
C(2)-H(2)	0.99(5)
C(2)-H(2)#5	0.99(5)

O(1W)-Er(1)-O(2W)	97.4(3)
O(1W)-Er(1)-O(3)	98.8(3)
O(1W)-Er(1)-O(2)#1	76.88(17)
O(1)#2-Er(1)-O(1W)	153.11(13)
O(1W)-Er(1)-C(1)#2	176.4(3)
O(1)#3-Er(1)-O(1W)	153.11(13)
O(1W)-Er(1)-O(2)#4	76.88(17)
O(2W)-Er(1)-O(3)	163.8(3)
O(2)#1-Er(1)-O(2W)	85.20(15)
O(1)#2-Er(1)-O(2W)	82.2(2)
O(2W)-Er(1)-C(1)#2	79.0(3)
O(1)#3-Er(1)-O(2W)	82.2(2)
O(2)#4-Er(1)-O(2W)	85.20(15)
O(2)#1-Er(1)-O(3)	98.47(15)
O(1)#2-Er(1)-O(3)	83.4(2)
O(3)-Er(1)-C(1)#2	84.8(3)
O(1)#3-Er(1)-O(3)	83.4(2)
O(2)#4-Er(1)-O(3)	98.47(15)
O(1)#2-Er(1)-O(2)#1	76.3(2)
O(2)#1-Er(1)-C(1)#2	102.68(17)
O(1)#3-Er(1)-O(2)#1	129.6(2)
O(2)#1-Er(1)-O(2)#4	150.6(3)

O(1)#2-Er(1)-C(1)#2	26.95(13)
O(1)#2-Er(1)-O(1)#3	53.72(18)
O(1)#2-Er(1)-O(2)#4	129.6(2)
O(1)#3-Er(1)-C(1)#2	26.95(13)
O(2)#4-Er(1)-C(1)#2	102.68(17)
O(1)#3-Er(1)-O(2)#4	76.3(2)
O(2)-P(1)-O(3)	112.0(3)
O(2)-P(1)-C(2)	107.5(3)
O(2)-P(1)-O(2)#5	111.3(4)
O(3)-P(1)-C(2)	106.2(5)
O(2)#5-P(1)-O(3)	112.0(3)
O(2)#5-P(1)-C(2)	107.5(3)
Er(1)#6-O(1)-C(1)	93.1(5)
Er(1)#7-O(2)-P(1)	159.2(4)
Er(1)-O(3)-P(1)	149.6(5)
Er(1)-O(1W)-H(1W)	123(6)
Er(1)-O(1W)-H(1W)#5	123(6)
H(1W)-O(1W)-H(1W)#5	112(5)
Er(1)-O(2W)-H(2W)	116(4)
Er(1)-O(2W)-H(2W)#5	116(4)
H(2W)-O(2W)-H(2W)#5	116(6)
O(1)-C(1)-O(1)#5	119.5(9)
O(1)-C(1)-C(2)	120.3(5)
Er(1)#6-C(1)-O(1)	60.0(5)
Er(1)#6-C(1)-O(1)#5	60.0(5)
Er(1)#6-C(1)-C(2)	171.8(7)
O(1)#5-C(1)-C(2)	120.3(5)
P(1)-C(2)-C(1)	114.3(8)
P(1)-C(2)-H(2)	113(4)
P(1)-C(2)-H(2)#5	113(4)
C(1)-C(2)-H(2)	110(4)
C(1)-C(2)-H(2)#5	110(4)
H(2)-C(2)-H(2)#5	95(4)

Symmetry transformations used to generate equivalent atoms:
#1 1/2-x,-y,1/2+z-1 #2 1/2+x,1/2-y,1/2-z #3 x-1/2,y,1/2-z
#4 1/2-x,1/2+y,1/2+z-1 #5 x,1/2-y,z #6 1/2+x-1,1/2-y,1/2-z
#7 1/2-x,-y,1/2+z

Table 4 Anisotropic displacement parameters ($Å^2 x\ 10^3$)for jn452mfin. The anisotropic
displacement factor exponent takes the form: $-2p^2[\ h^2 a^{*2} U^{11} + ... + 2\ h\ k\ a^*\ b^*\ U^{12}\ ]$

	U^{11}	U^{22}	U^{33}	U^{23}	U^{13}	U^{12}
Er(1)	7(1)	9(1)	16(1)	0	0(1)	0
P(1)	8(1)	5(1)	14(2)	0	2(1)	0
O(3)	4(4)	77(9)	22(5)	0	-2(4)	0
O(2)	10(3)	12(3)	39(4)	10(3)	10(3)	2(3)
O(1)	13(3)	13(3)	21(3)	1(3)	-1(2)	-1(3)
O(1W)	20(4)	49(8)	25(6)	0	-14(5)	0
O(2W)	8(4)	8(4)	23(5)	0	-2(4)	0
C(1)	8(5)	8(6)	20(6)	0	-3(5)	0
C(2)	13(6)	11(6)	16(6)	0	-3(5)	0

Table 5 Hydrogen coordinates ($x\ 10^4$) and isotropic displacement parameters ($Å^2 x\ 10^3$)
for jn452mfin.

	x	y	z	U(eq)
H(1W)	2550(150)	1340(30)	-4720(70)	20(50)

H(2)	-210(50)	1430(70)	710(70)	50(17)
H(2W)	5420(60)	1310(70)	-1920(110)	10(20)

Table 6 Torsion angles [°] for jn452mfin.

O(1W)-Er(1)-O(3)-P(1)	180.00
O(2)-P(1)-O(3)-Er(1)	-63.0(3)
C(2)-P(1)-O(3)-Er(1)	180.00
O(2)-P(1)-C(2)-C(1)	59.9(3)
O(3)-P(1)-C(2)-C(1)	180.00
O(1)-C(1)-C(2)-P(1)	89.5(9)

Symmetry transformations used to generate equivalent atoms:
#1 1/2-x,-y,1/2+z-1 #2 1/2+x,1/2-y,1/2-z #3 x-1/2,y,1/2-z
#4 1/2-x,1/2+y,1/2+z-1 #5 x,1/2-y,z #6 1/2+x-1,1/2-y,1/2-z
#7 1/2-x,-y,1/2+z

Table 7 Hydrogen bonds for jn452mfin [Å and °].

D-H...A	d(D-H)	d(H...A)	d(D...A)	<(DHA)
O(1W)-H(1W)...O(2)#8	0.95(3)	2.19(12)	2.920(11)	133(11)
O(2W)-H(2W)...O(1)#9	0.95(6)	1.72(6)	2.663(7)	169(7)

Symmetry transformations used to generate equivalent atoms:
#1 1/2-x,-y,1/2+z-1 #2 1/2+x,1/2-y,1/2-z #3 x-1/2,y,1/2-z
#4 1/2-x,1/2+y,1/2+z-1 #5 x,1/2-y,z #6 1/2+x-1,1/2-y,1/2-z
#7 1/2-x,-y,1/2+z #8 x,y,z-1 #9 1/2-x,1/2+y-1,1/2+z-1

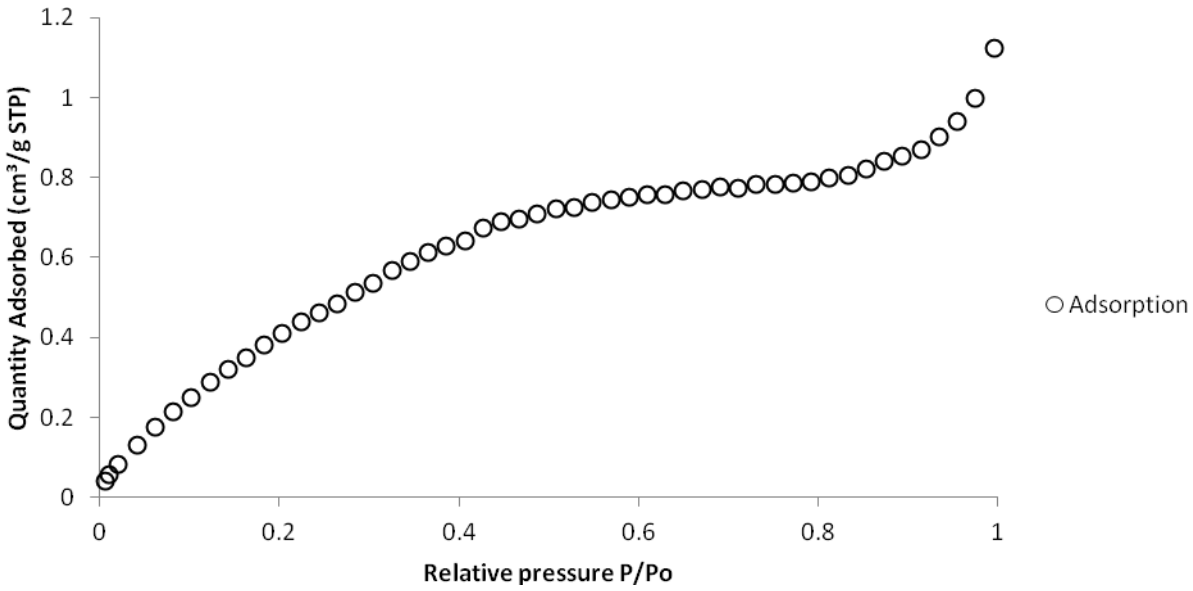

Figure 1 Adsorption isotherm for $[Er(H_2O)_2][C_2H_2O_5P]$(**1**) degassed at 120 °C overnight

Characterising data for $[Ln(H_2O)_2][C_2H_2O_5P]$ (Ln=Ho-Tm)

$[Ho(H_2O)_2][C_2H_2O_5P]$

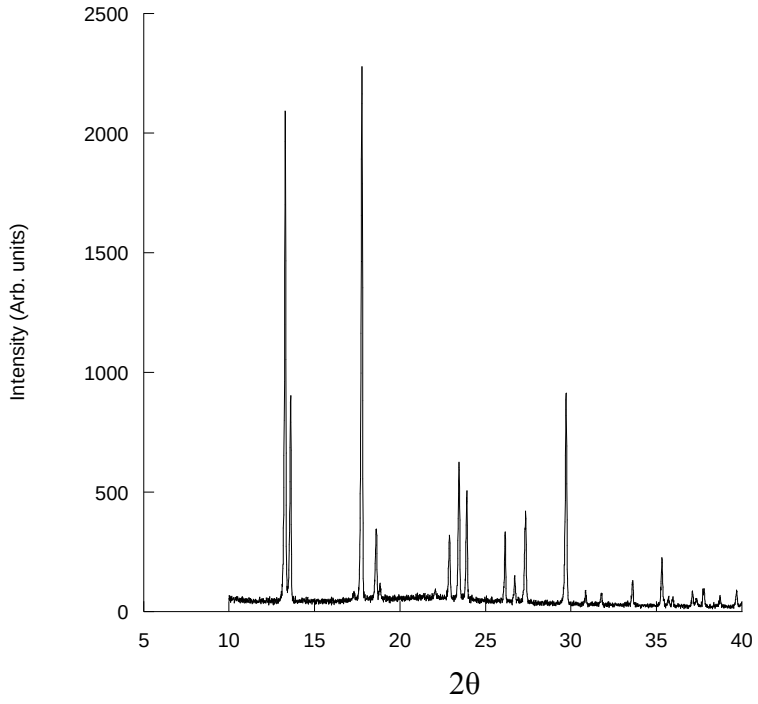

Figure 2 Powder X-ray diffraction pattern of $[Ho(H_2O)_2][C_2H_2O_5P]$

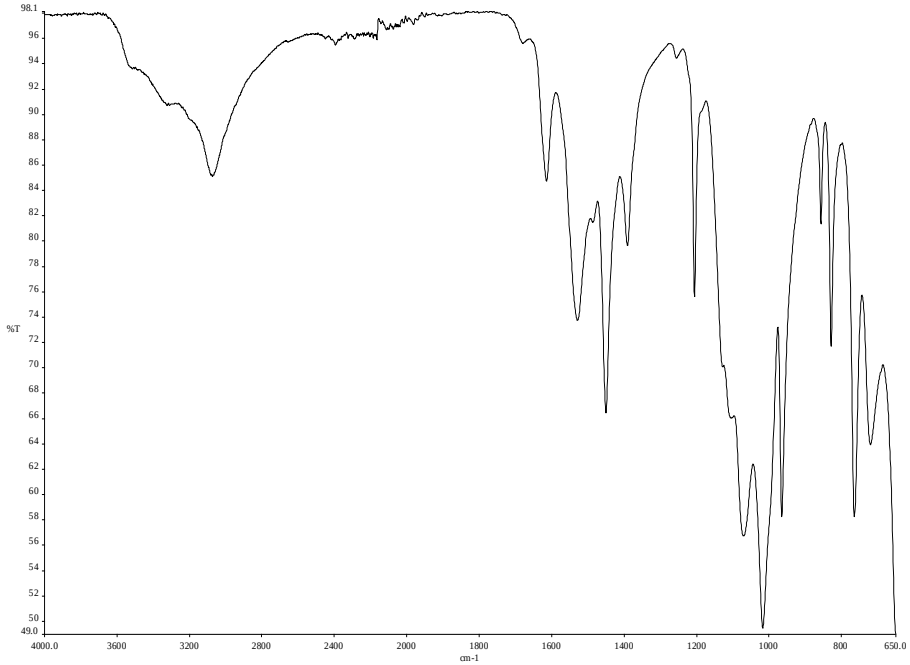

Figure 3 FTIR spectra of $[Ho(H_2O)_2][C_2H_2O_5P]$ showing bands corresponding to OH stretch and bending mode of water at 3073 and 1679 cm^{-1}, P=O and P-O modes at 1206 and 1017 cm^{-1} and C-O symmetric and asymmetric stretches at 1614 and 1128 cm^{-1}.

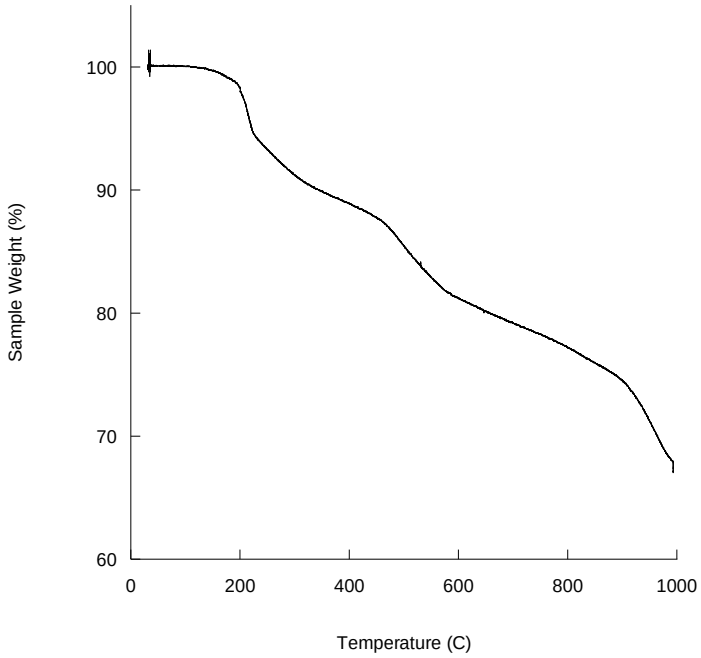

Figure 4 TGA trace of $[Ho(H_2O)_2][C_2H_2O_5P]$ showing three mass losses. First mass loss of 11.1% below 400° C , second mass loss of 11.7% below 800°C and an additional mass loss of 9.2% by 992°C. End product $HoPO_4$.

$[Tm(H_2O)_2][C_2H_2O_5P]$

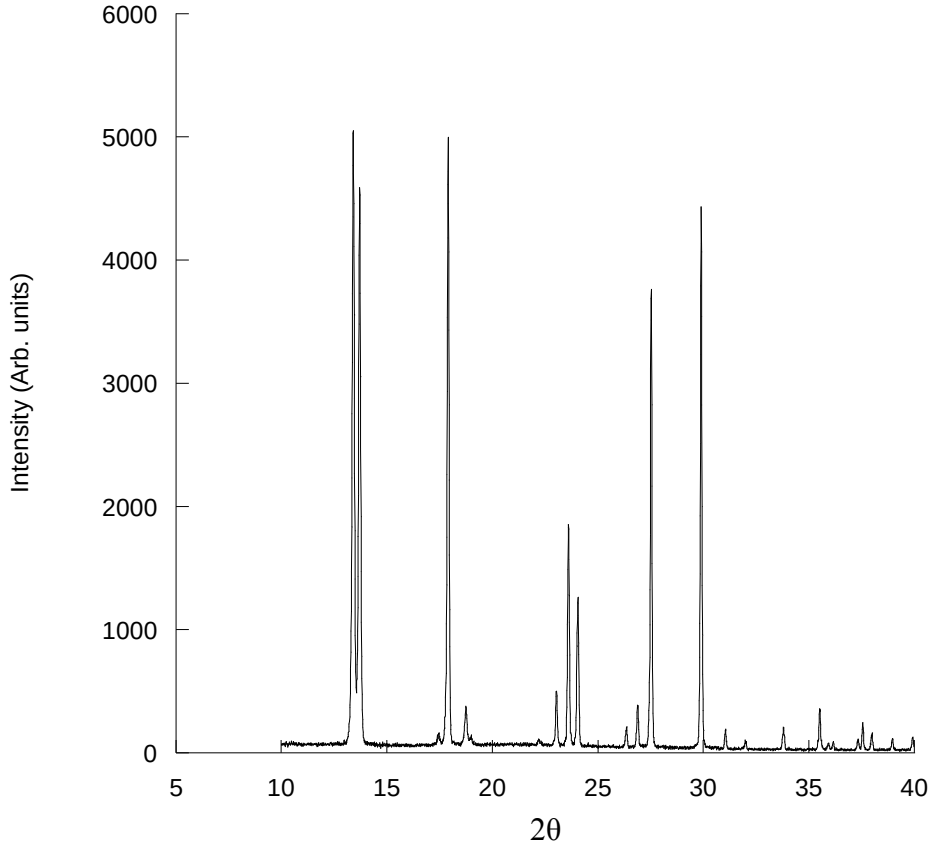

Figure 5 Powder X-ray diffraction pattern of $[Tm(H_2O)_2][C_2H_2O_5P]$

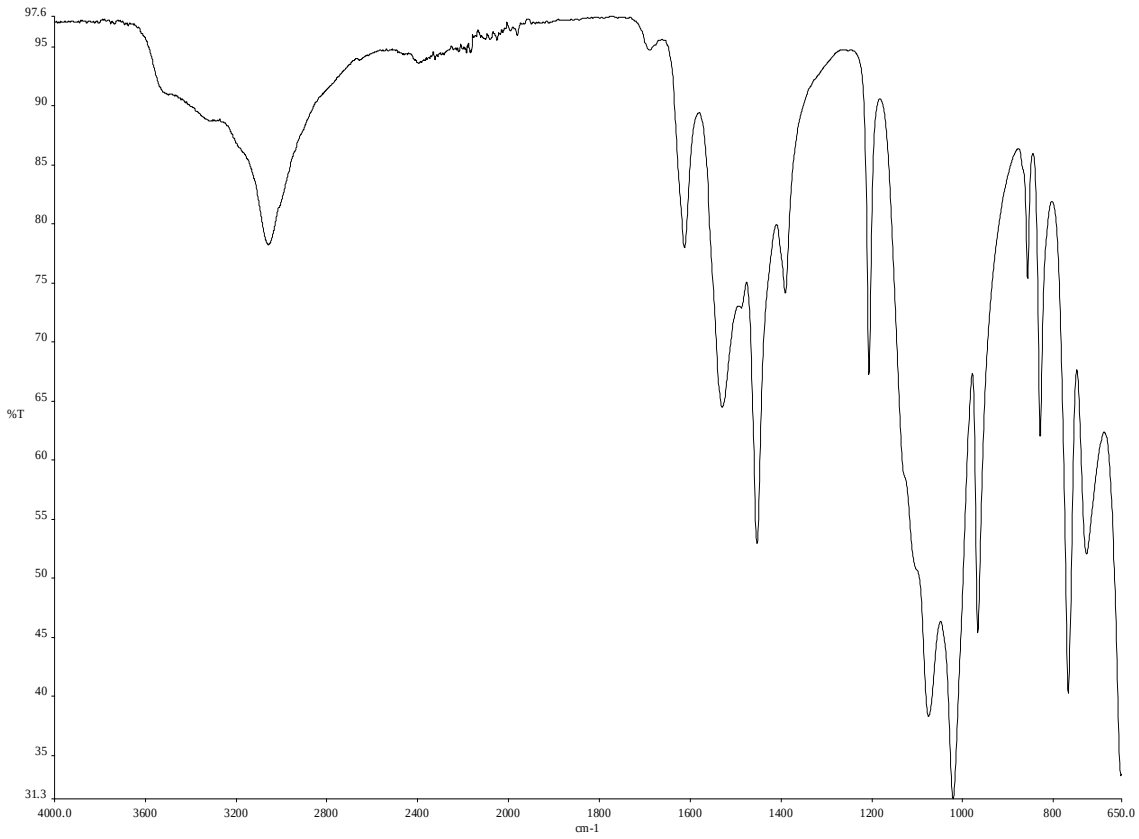

Figure 6 FTIR spectra of $[Tm(H_2O)_2][C_2H_2O_5P]$ showing bands corresponding to OH stretch and bending mode of water at 3057 and 1689 cm^{-1}, P=O and P-O modes at 1207 and 1021 cm^{-1} and C-O symmetric and asymmetric stretches at 1612 and 1106 cm^{-1}.

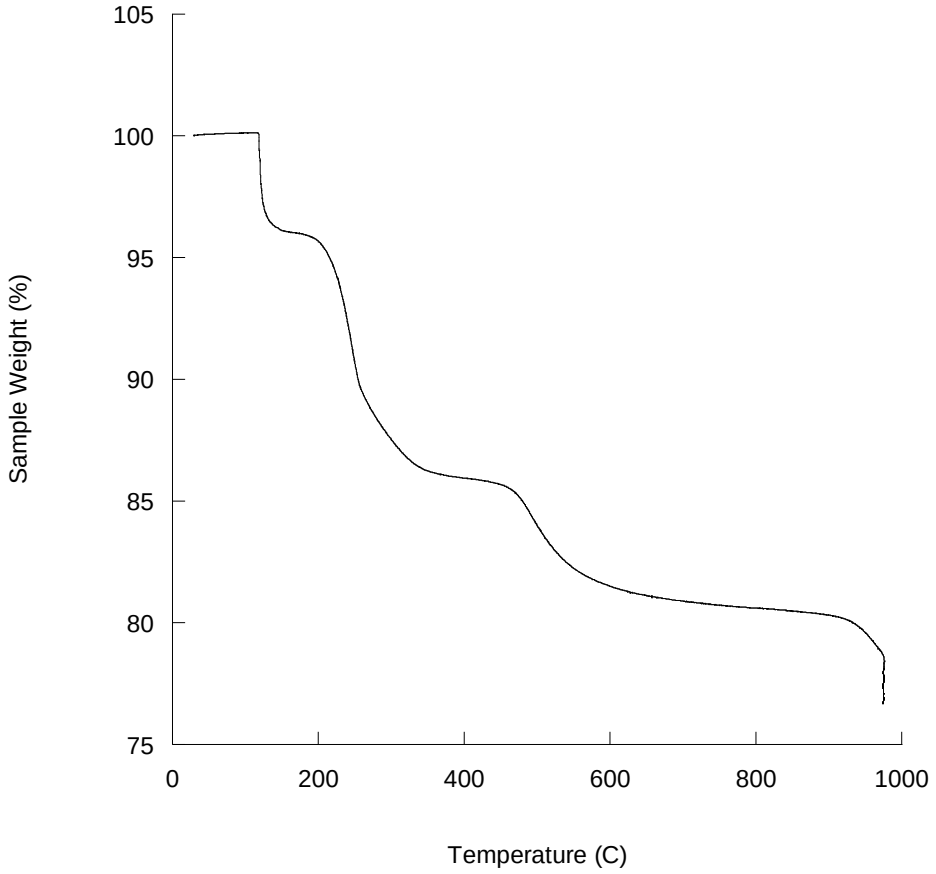

Figure 7 TGA trace of $[Tm(H_2O)_2][C_2H_2O_5P]$ showing three distinct mass losses. First mass loss of 3.9% below 150°C, second mass loss of 10.2% below 350°C and a final mass loss of 7.8% by 975°C. End product $TmPO_4$.

Table 8 Elemental analysis of $[Ln(H_2O)_2][C_2H_5O_5P]$ (Ln= Ho – Tm)

Lanthanide	Elemental Analysis	
	Observed (%)	Calculated (%)
Er	C-6.44	C-7.06
	H-1.66	H-1.78
Ho (165°C)	C-5.83	C-7.11
	H-1.21	H-1.79
Tm	C-6.42	C-7.02
	H-1.69	H-1.77

Characterising data for $[Ln(H_2O)_2][C_2H_2O_5P]$ (Ln=Yb & Lu)

$[Yb(H_2O)_2][C_2H_2O_5P]$

Table 9 Crystal data and structure refinement details for $[Yb(H_2O)_2][C_2H_2O_5P]$

Identification code	2009src1290	
Empirical formula	$C_8H_{24}O_{28}P_4Yb_4$	
Formula weight	1384.31	
Temperature	120(2) K	
Wavelength	0.71073 Å	
Crystal system	Monoclinic	
Space group	*P*21/*n*	
Unit cell dimensions	a = 6.7557(5) Å	α = 90°
	b = 15.1624(13) Å	β = 90.44°
	c = 7.0945(6) Å	γ = 90°
Volume	726.69(10) Å^3	
Z	1	
Density (calculated)	3.163 mg / m^3	
Absorption coefficient	13.081 mm^{-1}	
F(000)	636	
Crystal	plate; colourless	
Crystal size	0.10 × 0.05 × 0.01 mm^3	
θ range for data collection	3.02 – 27.48°	
Index ranges	$-8 \le h \le 8$, $-19 \le k \le 18$, $-9 \le l \le 9$	
Reflections collected	8376	
Independent reflections	1664 [R_{int} = 0.0442]	
Completeness to θ = 27.48°	99.7 %	
Absorption correction	Semi–empirical from equivalents	
Max. and min. transmission	0.8803 and 0.3546	
Refinement method	Full-matrix least-squares on F^2	
Data / restraints / parameters	1664 / 6 / 101	
Goodness-of-fit on F^2	1.071	

Final *R* indices [$F^2 > 2\sigma(F^2)$] *R1* = 0.0383, *wR2* = 0.0816

R indices (all data) *R1* = 0.0427, *wR2* = 0.0848

Largest diff. peak and hole 1.727 and –2.474 e $Å^{-3}$

Diffractometer: *Nonius KappaCCD* area detector (ϕ scans and ω scans to fill *asymmetric unit* sphere). Cell determination: DirAx (Duisenberg, A.J.M.(1992). J. Appl. Cryst. 25, 92-96.) Data collection: Collect (Collect: Data collection software, R. Hooft, Nonius B.V., 1998). Data reduction and cell refinement: *Denzo* (Z. Otwinowski & W. Minor, *Methods in Enzymology* (1997) Vol. 276: *Macromolecular Crystallography*, part A, pp. 307–326; C. W. Carter, Jr. & R. M. Sweet, Eds., Academic Press). Absorption correction: *SADABS* (Sheldrick, G. M. (2007). SADABS. Version 2007/2. Bruker AXS Inc., Madison, Wisconsin, USA.). Structure solution: *SHELXS97* (Sheldrick, G.M. (2008). Acta Cryst. A64, 112-122.). Structure refinement: *SHELXL97* (G Sheldrick, G.M. (2008). Acta Cryst. A64, 112-122.). Graphics: *CAMERON* (Watkin, D. M., Pearce, L. & Prout, C. K. (1993). Chemical Crystallography Lab, University of Oxford)

Special details:
Merohedral twin (1 0 0 0 -1 0 0 0 -1), BASF = 42.9%

H Atoms attached to coordinated waters cannot be located from difference map and are thus omitted from the model, although included in the structural formula.

Table 10 Atomic coordinates [$\times 10^4$], equivalent isotropic displacement parameters [$Å^2 \times 10^3$] and site occupancy factors. U_{eq} is defined as one third of the trace of the orthogonalized U^{ij} tensor.

Atom	*x*	*y*	*z*	U_{eq}	*S.o.f.*
C1	2510(30)	9864(6)	7659(13)	12(2)	1
C3	2560(20)	10754(6)	8573(12)	15(2)	1
O1	2180(15)	7487(5)	7005(11)	18(2)	1
O2	2950(13)	7431(5)	2695(12)	20(2)	1
O3	2560(18)	9664(5)	2947(10)	14(2)	1

O4	–460(12)	8371(5)	4098(12)	14(2)	1
O5	5859(11)	8473(5)	4528(11)	12(2)	1
O6	4145(12)	9461(6)	7291(12)	14(2)	1
O7	905(12)	9513(6)	7118(13)	16(2)	1
P3	2529(4)	6651(2)	8134(3)	8(1)	1
Yb	2614(1)	8522(1)	4982(1)	9(1)	1

Table 11 Bond lengths [Å] and angles [°].

C1–O7	1.264(19)
C1–O6	1.292(19)
C1–C3	1.497(13)
C1–Yb	2.785(10)
C3–P3^{i}	1.822(10)
C3–H3A	0.9900
C3–H3B	0.9900
O1–P3	1.517(7)
O1–Yb	2.148(7)
O2–Yb	2.329(8)
O3–Yb	2.255(7)
O4–P3^{ii}	1.517(8)
O4–Yb	2.176(8)
O5–P3^{iii}	1.518(7)
O5–Yb	2.220(7)
O6–Yb	2.399(8)
O7–Yb	2.432(9)
P3–O4^{iv}	1.517(8)
P3–O5^{v}	1.518(7)
P3–C3^{vi}	1.822(10)

O7–C1–O6	118.2(9)
O7–C1–C3	121.8(14)
O6–C1–C3	119.8(13)
O7–C1–Yb	60.8(6)
O6–C1–Yb	59.3(5)
C3–C1–Yb	162.4(6)
C1–C3–P3^{i}	112.6(6)
C1–C3–H3A	109.1
P3^{i}–C3–H3A	109.1
C1–C3–H3B	109.1
P3^{i}–C3–H3B	109.1
H3A–C3–H3B	107.8
P3–O1–Yb	160.3(6)
P3^{ii}–O4–Yb	169.0(6)
P3^{iii}–O5–Yb	147.0(5)
C1–O6–Yb	93.1(7)
C1–O7–Yb	92.3(8)
O4^{iv}–P3–O1	113.1(5)
O4^{iv}–P3–O5^{v}	111.8(5)
O1–P3–O5^{v}	109.5(5)
O4^{iv}–P3–C3^{vi}	107.9(5)
O1–P3–C3^{vi}	105.6(4)
O5^{v}–P3–C3^{vi}	108.7(5)
O1–Yb–O4	88.9(4)
O1–Yb–O5	102.3(3)
O4–Yb–O5	153.6(3)
O1–Yb–O3	170.8(4)
O4–Yb–O3	83.4(4)
O5–Yb–O3	86.8(4)
O1–Yb–O2	87.8(3)
O4–Yb–O2	79.8(3)
O5–Yb–O2	76.9(3)
O3–Yb–O2	95.8(3)
O1–Yb–O6	92.2(3)
O4–Yb–O6	131.6(3)
O5–Yb–O6	72.4(3)
O3–Yb–O6	89.2(3)
O2–Yb–O6	148.6(3)
O1–Yb–O7	88.1(3)
O4–Yb–O7	77.8(3)
O5–Yb–O7	125.8(3)

O3–Yb–O7	85.3(3)
O2–Yb–O7	157.3(3)
O6–Yb–O7	54.0(2)
O1–Yb–C1	94.2(3)
O4–Yb–C1	104.1(4)
O5–Yb–C1	98.8(4)
O3–Yb–C1	82.8(3)
O2–Yb–C1	175.6(4)
O6–Yb–C1	27.6(4)
O7–Yb–C1	27.0(4)

Symmetry transformations used to generate equivalent atoms:

(i) –x+1/2,y+1/2,–z+3/2 (ii) x–1/2,–y+3/2,z–1/2

(iii) x+1/2,–y+3/2,z–1/2 (iv) x+1/2,–y+3/2,z+1/2

(v) x–1/2,–y+3/2,z+1/2 (vi) –x+1/2,y–1/2,–z+3/2

Table 12 Anisotropic displacement parameters [$Å^2 \times 10^3$]. The anisotropic displacement factor exponent takes the form: $-2\pi^2[h^2a^{*2}U^{11} + ... + 2\,h\,k\,a^*\,b^*\,U^{12}]$.

Atom	U^{11}	U^{22}	U^{33}	U^{23}	U^{13}	U^{12}
C1	17(6)	13(5)	6(4)	6(3)	0(6)	–5(6)
C3	24(6)	18(5)	3(4)	2(3)	–7(5)	–3(5)
O1	29(6)	11(3)	15(3)	8(3)	7(4)	2(4)
O2	16(6)	21(4)	22(4)	–6(3)	0(4)	–3(4)
O3	9(4)	15(3)	19(3)	8(3)	–2(5)	0(4)
O4	7(4)	17(4)	17(4)	0(3)	–9(3)	5(3)
O5	2(3)	13(3)	22(5)	–2(3)	5(3)	–3(3)
O6	9(4)	18(4)	16(4)	–7(3)	–1(3)	0(3)
O7	16(4)	12(4)	21(4)	0(3)	–2(4)	–1(3)
P3	6(1)	10(1)	7(1)	1(1)	–3(1)	1(1)
Yb	11(1)	8(1)	9(1)	1(1)	1(1)	0(1)

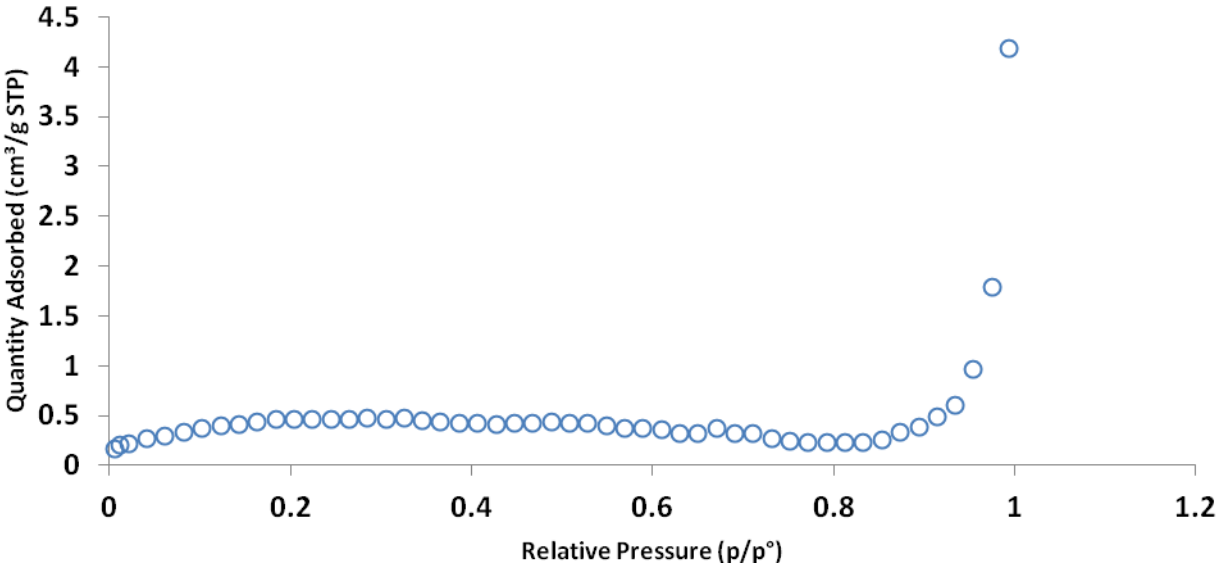

Figure 8 Adsorption isotherm for $[Yb(H_2O)_2][C_2H_2O_5P]$(**1**) degassed at 120 °C overnight

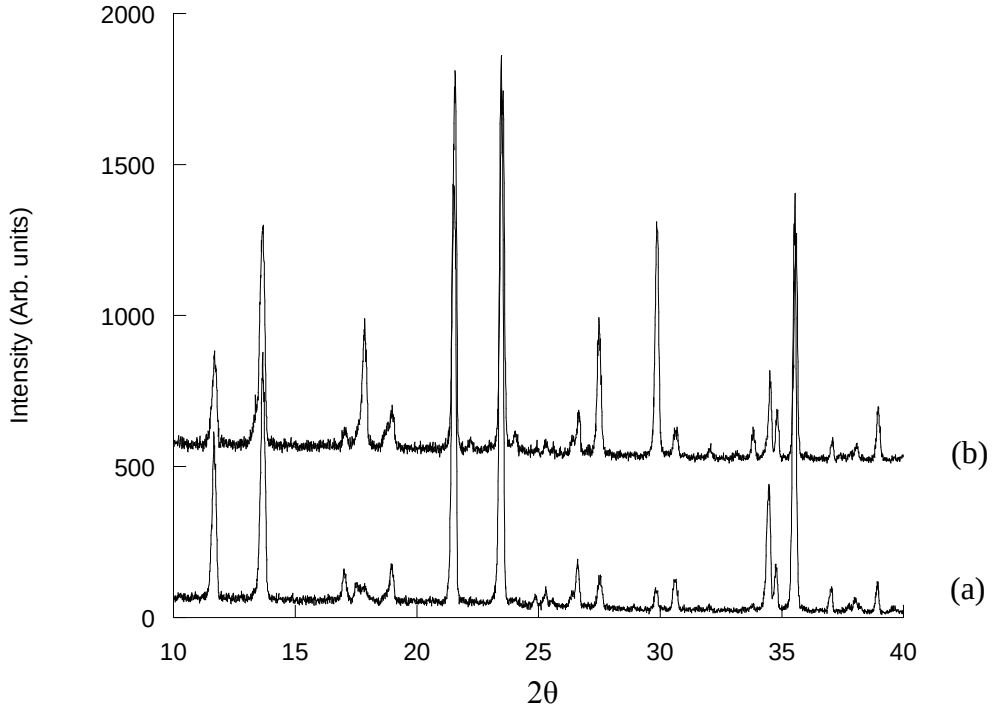

Figure 9 Powder XRD patterns of iso-structural phases (a) $[Yb(H_2O)_2][C_2H_2O_5P]$(**2**) and (b) $[Lu(H_2O)_2][C_2H_2O_5P]$.

$[Lu(H_2O)_2][C_2H_2O_5P]$

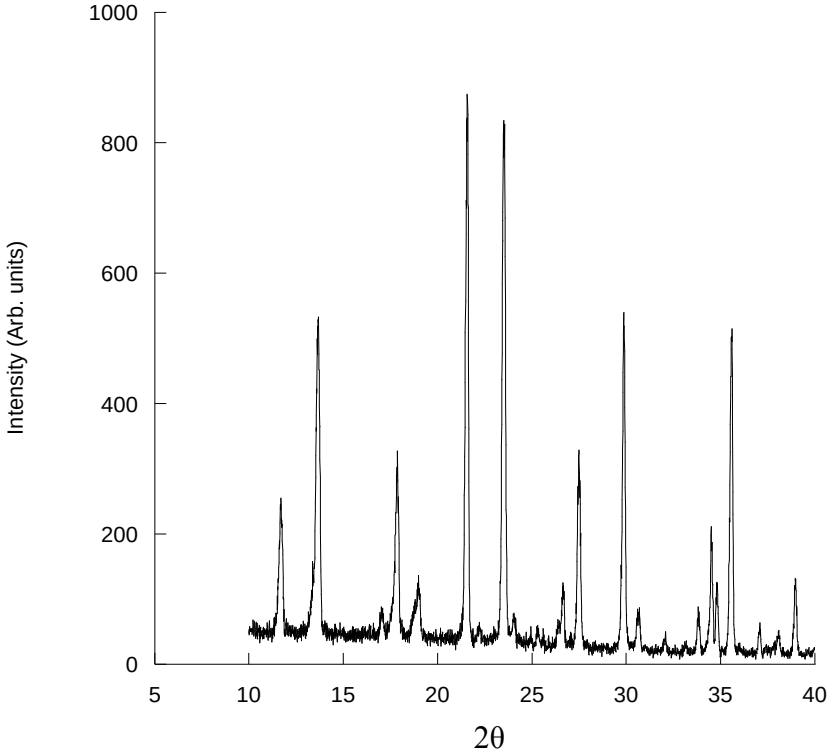

Figure 10 Powder X-ray diffraction pattern of $[Lu(H_2O)_2][C_2H_2O_5P]$

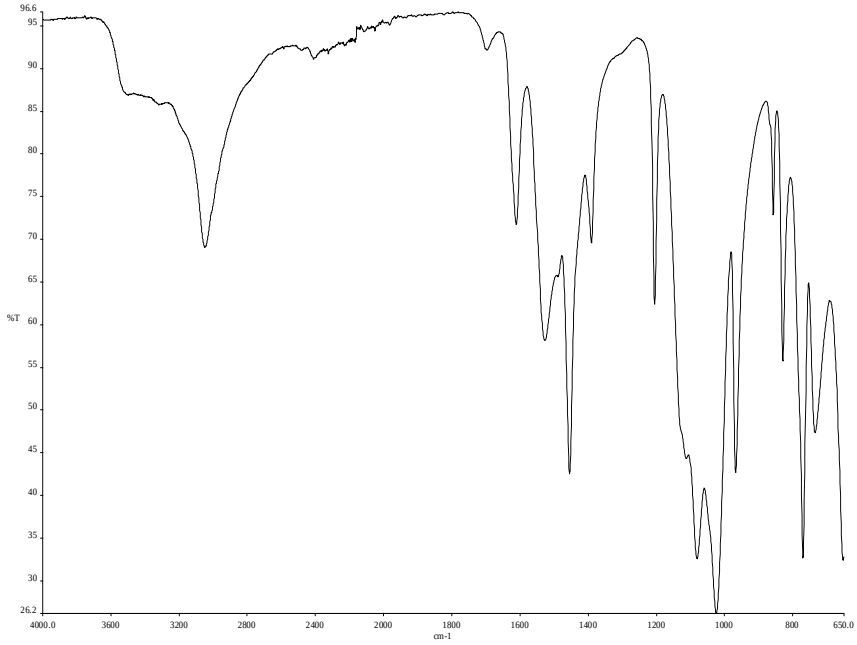

Figure 11 FTIR spectra of $[Lu(H_2O)_2][C_2H_2O_5P]$ showing bands corresponding to OH stretch and bending mode of water at 3050 and 1697cm^{-1}, P=O and P-O modes at 1205 and 1021 cm^{-1} and C-O symmetric and asymmetric stretches at 1611 and 1110 cm^{-1}.

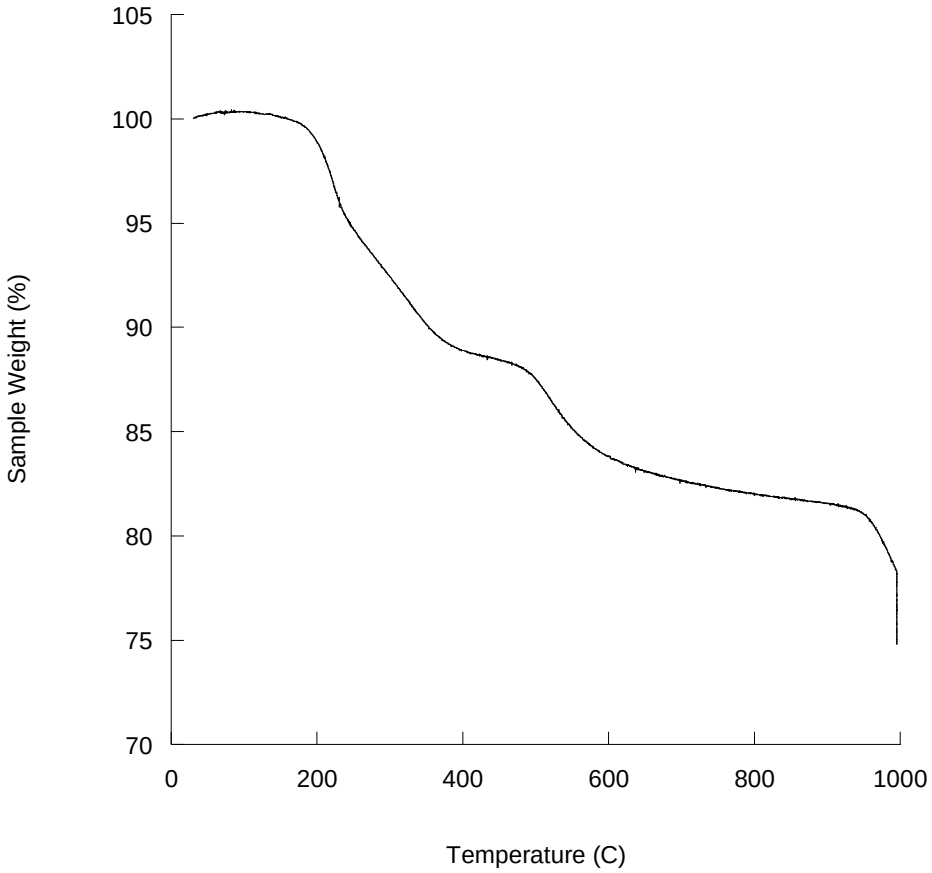

Figure 12 TGA trace of $[Lu(H_2O)_2][C_2H_2O_5P]$ showing two distinct mass losses. First mass loss of 11.6% below 400°C and an additional mass loss of 10.1% by 995°C. End product $LuPO_4$

Table 13 Elemental analysis of $[Ln(H_2O)_2][C_2H_5O_5P]$ (Ln= Yb & Lu)

Lanthanide	Elemental Analysis	
	Observed (%)	Calculated (%)
Yb	C-7.39	C-6.94
	H-1.88	H-1.75
Lu* 165 °C	C-6.04	C-6.90
	H-1.63	H-1.74

*At 150°C powder X-ray diffraction measurements confirms that this phase becomes iso-structural to that of (**1**).

Characterising data for [$LnC_2H_2O_5P$] (Ln=Er & Yb)

[$YbC_2H_2O_5P$]

Table 14 Crystal data and structure refinement details for [$YbC_2H_2O_5P$]

Identification code	**2011src0114r2b**	
Empirical formula	$C_2H_2O_5PYb$	
Formula weight	310.05	
Temperature	120(2) K	
Wavelength	0.71073 Å	
Crystal system	Monoclinic	
Space group	*P*21/*m*	
Unit cell dimensions	a = **6.4798(5) Å**	α = **90°**
	b = **6.7979(6) Å**	β = **99.227(4)°**
	c = **6.5084(5) Å**	γ = **90°**
Volume	282.98(4) $Å^3$	
Z	2	
Density (calculated)	3.639 mg / m^3	
Absorption coefficient	16.748 mm^{-1}	
F(000)	278	
Crystal	Needle; colourless	
Crystal size	0.04 × 0.01 × 0.01 mm^3	
θ range for data collection	3.17 – 27.48°	
Index ranges	$-8 \le h \le 8$, $0 \le k \le 8$, $0 \le l \le 8$	
Reflections collected	699	
Independent reflections	699 [R_{int} = 0.0000]	
Completeness to θ = 27.48°	99.4 %	
Absorption correction	Semi–empirical from equivalents	
Max. and min. transmission	0.8504 and 0.5539	
Refinement method	Full-matrix least-squares on F^2	

Data / restraints / parameters	699 / 17 / 53
Goodness-of-fit on F^2	1.254
Final R indices [$F^2 > 2\sigma(F^2)$]	$R1$ = 0.0429, $wR2$ = 0.1078
R indices (all data)	$R1$ = 0.0447, $wR2$ = 0.1095
Largest diff. peak and hole	2.511 and –3.272 e Å^{-3}

Diffractometer: *Nonius KappaCCD* area detector (ϕ scans and ω scans to fill *asymmetric unit* sphere). **Cell determination:** DirAx (Duisenberg, A.J.M.(1992). J. Appl. Cryst. 25, 92-96.) **Data collection:** Collect (Collect: Data collection software, R. Hooft, Nonius B.V., 1998). **Data reduction and cell refinement**: *Denzo* (Z. Otwinowski & W. Minor, *Methods in Enzymology* (1997) Vol. **276**: *Macromolecular Crystallography*, part A, pp. 307–326; C. W. Carter, Jr. & R. M. Sweet, Eds., Academic Press). **Absorption correction**: *SADABS* (Sheldrick, G. M. (2007). SADABS. Version 2007/2. Bruker AXS Inc., Madison, Wisconsin, USA.). S**tructure solution**: *SHELXS97* (Sheldrick, G.M. (2008). Acta Cryst. A64, 112-122.) S**tructure refinement**: *SHELXL97* (G Sheldrick, G.M. (2008). Acta Cryst. A64, 112-122.). **Graphics:** *OLEX2* (Dolomanov, O. V., Bourhis, L. J., Gildea, R. J., Howard, J. A. K. & Puschmann, H. (2009). J. Appl. Cryst. 42, 339-341.)

Table 15 Atomic coordinates [$\times 10^4$], equivalent isotropic displacement parameters [Å$^2 \times 10^3$] and site occupancy factors. U_{eq} is defined as one third of the trace of the orthogonalized U^{ij} tensor.

Atom	*x*	*y*	*z*	U_{eq}	*S.o.f.*
C1	12320(30)	2500	–3880(30)	13(4)	1
C2	9930(30)	2500	–4630(30)	8(3)	1
O1	5230(30)	2500	–400(30)	24(4)	1
O2	11799(14)	710(14)	–226(15)	14(2)	1
O3	9370(30)	2500	3390(20)	26(4)	1
O4	8640(20)	2500	–3440(20)	9(3)	1
P1	12945(8)	2500	–1059(8)	12(1)	1
Yb1	8650(1)	2500	43(2)	10(1)	1

Table 16 Bond lengths [Å] and angles [°].

C1–C2	1.55(3)	O4–C2–O3^{i}	121.7(19)
C1–P1	1.82(2)	O4–C2–C1	123.5(16)
C1–H1A	0.9900	O3^{i}–C2–C1	114.8(18)
C1–H1B	0.9900	P1^{ii}–O1–Yb1	170.6(12)
C2–O4	1.23(2)	P1–O2–Yb1^{iii}	149.4(6)
C2–O3^{i}	1.28(2)	P1–O2–Yb1	95.0(5)
O1–P1^{ii}	1.477(17)	Yb1^{iii}–O2–Yb1	112.0(4)
O1–Yb1	2.186(16)	C2^{iv}–O3–Yb1	176.4(17)
O2–P1	1.567(10)	C2–O4–Yb1	137.4(13)
O2–Yb1^{iii}	2.207(10)	O1^{v}–P1–O2	114.1(6)
O2–Yb1	2.406(9)	O1^{v}–P1–O2^{vi}	114.1(6)
O3–C2^{iv}	1.28(2)	O2–P1–O2^{vi}	101.9(8)
O3–Yb1	2.151(15)	O1^{v}–P1–C1	110.3(10)
O4–Yb1	2.267(14)	O2–P1–C1	107.9(6)
P1–O1^{v}	1.477(17)	O2^{vi}–P1–C1	107.9(6)
P1–O2^{vi}	1.567(10)	O1^{v}–P1–Yb1	149.5(8)
P1–Yb1	2.983(5)	O2–P1–Yb1	53.5(4)
Yb1–O2^{iii}	2.207(10)	O2^{vi}–P1–Yb1	53.5(4)
Yb1–O2^{vii}	2.207(10)	C1–P1–Yb1	100.2(7)
Yb1–O2^{vi}	2.406(9)	O3–Yb1–O1	100.6(7)
Yb1–Yb1^{viii}	3.8273(8)	O3–Yb1–O2^{iii}	87.4(3)
Yb1–Yb1^{iii}	3.8273(8)	O1–Yb1–O2^{iii}	82.4(2)
		O3–Yb1–O2^{vii}	87.4(3)
C2–C1–P1	111.6(13)	O1–Yb1–O2^{vii}	82.4(2)
C2–C1–H1A	109.3	O2^{iii}–Yb1–O2^{vii}	162.7(5)
P1–C1–H1A	109.3	O3–Yb1–O4	167.8(6)
C2–C1–H1B	109.3	O1–Yb1–O4	91.6(6)
P1–C1–H1B	109.3	O2^{iii}–Yb1–O4	94.3(3)
H1A–C1–H1B	108.0	O2^{vii}–Yb1–O4	94.3(3)

O3–Yb1–O2^{vi}	91.4(5)
O1–Yb1–O2^{vi}	147.5(3)
O2^{iii}–Yb1–O2^{vi}	128.7(3)
O2^{vii}–Yb1–O2^{vi}	68.0(4)
O4–Yb1–O2^{vi}	78.2(4)
O3–Yb1–O2	91.4(5)
O1–Yb1–O2	147.5(3)
O2^{iii}–Yb1–O2	68.0(4)
O2^{vii}–Yb1–O2	128.7(3)
O4–Yb1–O2	78.2(4)
O2^{vi}–Yb1–O2	60.8(5)
O3–Yb1–P1	100.5(5)
O1–Yb1–P1	158.9(5)
O2^{iii}–Yb1–P1	98.6(2)
O2^{vii}–Yb1–P1	98.6(2)
O4–Yb1–P1	67.3(4)
O2^{vi}–Yb1–P1	31.6(2)
O2–Yb1–P1	31.6(2)
O3–Yb1–Yb1^{viii}	89.4(2)
O1–Yb1–Yb1^{viii}	116.99(5)
O2^{iii}–Yb1–Yb1^{viii}	160.6(2)
O2^{vii}–Yb1–Yb1^{viii}	35.6(2)
O4–Yb1–Yb1^{viii}	85.06(17)
O2^{vi}–Yb1–Yb1^{viii}	32.3(2)
O2–Yb1–Yb1^{viii}	93.0(2)
P1–Yb1–Yb1^{viii}	63.27(2)
O3–Yb1–Yb1^{iii}	89.4(2)
O1–Yb1–Yb1^{iii}	116.99(5)
O2^{iii}–Yb1–Yb1^{iii}	35.6(2)
O2^{vii}–Yb1–Yb1^{iii}	160.6(2)
O4–Yb1–Yb1^{iii}	85.06(17)
O2^{vi}–Yb1–Yb1^{iii}	93.0(2)
O2–Yb1–Yb1^{iii}	32.3(2)
P1–Yb1–Yb1^{iii}	63.27(2)
Yb1^{viii}–Yb1–Yb1^{iii}	125.27(4)

Symmetry transformations used to generate equivalent atoms:

(i) x,y,z–1 (ii) x–1,y,z (iii) –x+2,–y,–z (iv) x,y,z+1

(v) x+1,y,z (vi) x,–y+1/2,z (vii) –x+2,y+1/2,–z

(viii) –x+2,–y+1,–z

Table 17 Anisotropic displacement parameters [Å^2× 10^3]. The anisotropic displacement factor exponent takes the form: $-2\pi^2[h^2a^{*2}U^{11} + \cdots + 2\,h\,k\,a^*\,b^*\,U^{12}]$.

Atom	U^{11}	U^{22}	U^{33}	U^{23}	U^{13}	U^{12}
C1	11(7)	17(10)	10(6)	0	3(7)	0
C2	16(7)	1(7)	6(7)	0	–4(5)	0
O1	15(8)	36(11)	22(9)	0	4(7)	0
O2	12(4)	15(4)	16(5)	8(4)	3(4)	–1(4)
O3	32(10)	40(11)	4(6)	0	–5(7)	0
O4	13(6)	7(6)	8(6)	0	2(5)	0
P1	7(2)	14(2)	14(2)	0	0(2)	0
Yb1	6(1)	14(1)	10(1)	0	1(1)	0

Table 18 Hydrogen coordinates [× 10^4] and isotropic displacement parameters [Å^2 × 10^3].

Atom	*x*	*y*	*z*	U_{eq}	*S.o.f.*
H1A	12939	3678	–4436	15	0.50
H1B	12939	1322	–4436	15	0.50

Characterising data for $[Ln(H_2O)_5]_2[2,6\text{-}AQDS]_3.2H_2O$ (Ln= La-Nd)

$[Nd(H_2O)_5]_2[2,6\text{-}AQDS]_3.2H_2O$

Table 20 Crystal data and structure refinement for jn69m_pub. $[Nd(H_2O)_5]_2[2,6\text{-}AQDS]_3.2H_2O$

Identification code	jn69m	
Empirical formula	C42 H32 Nd2 O36 S6	
Formula weight	1597.55	
Temperature	100(2) K	
Wavelength	0.71073 Å	
Crystal system	Monoclinic	
Space group	P21/m	
Unit cell dimensions	a = 7.4571(12) Å	α= 90°.
	b = 29.029(5) Å	
	β=101.404(4)°.	
	c = 12.046(2) Å	γ = 90°.
Volume	2556.1(7) $Å^3$	
Z	2	
Density (calculated)	2.073 mg/m^3	
Absorption coefficient	2.368 mm^{-1}	
F(000)	1580	
Crystal size	0.50 x 0.30 x 0.10 mm^3	
Theta range for data collection	2.72 to 25.35°.	
Index ranges	-6<=h<=8, -34<=k<=31, -14<=l<=14	
Reflections collected	13055	
Independent reflections	4747 [R(int) = 0.0259]	
Completeness to theta = 25.35°	99.6 %	
Absorption correction	Semi-empirical from equivalents	
Max. and min. transmission	0.7976 and 0.3839	
Refinement method	Full-matrix least-squares on F^2	
Data / restraints / parameters	4747 / 60 / 484	

Goodness-of-fit on F^2	1.181
Final R indices [I>2sigma(I)]	R1 = 0.0341, wR2 = 0.0771
R indices (all data)	R1 = 0.0374, wR2 = 0.0784
Largest diff. peak and hole	0.936 and -1.003 e.$Å^{-3}$

Table 21 Atomic coordinates (x 10^4) and equivalent isotropic displacement parameters ($Å^2$x 10^3) for jn69m_pub. U(eq) is defined as one third of the trace of the orthogonalized U^{ij} tensor.

	x	y	z	U(eq)
Nd(1)	8456(1)	2500	2960(1)	8(1)
Nd(2)	4224(1)	7500	2010(1)	7(1)
S(1)	7053(1)	3344(1)	496(1)	10(1)
S(2)	1169(1)	6549(1)	2849(1)	9(1)
S(3)	12512(1)	3362(1)	3777(1)	9(1)
O(1)	6962(4)	3070(1)	1501(2)	19(1)
O(1W)	5126(6)	2500	2894(4)	17(1)
O(2)	6246(4)	3102(1)	-546(2)	16(1)
O(3)	8855(4)	3523(1)	496(2)	16(1)
O(3W)	10265(6)	2500	1494(3)	18(1)
O(4)	-354(4)	6611(1)	1891(2)	12(1)
O(4W)	7460(4)	3233(1)	3848(3)	24(1)
O(5)	604(4)	6579(1)	3944(2)	15(1)
O(5W)	9435(9)	2500	5087(4)	41(2)
O(6)	2691(4)	6859(1)	2802(3)	16(1)
O(6W)	6584(4)	6909(1)	2767(2)	18(1)
O(7)	5691(4)	4532(1)	3594(2)	15(1)
O(7W)	6763(5)	7500	914(3)	13(1)
O(8)	1653(4)	5234(1)	-241(2)	15(1)
O(8W)	4663(6)	7500	4140(3)	16(1)
O(9)	10996(4)	3047(1)	3484(3)	22(1)
O(9W)	894(5)	7500	1145(3)	13(1)

O(10)	13606(4)	3376(1)	2898(2)	16(1)
O(11)	13623(4)	3281(1)	4893(2)	17(1)
O(12)	8244(4)	5415(1)	3091(2)	15(1)
C(1)	5638(5)	3835(1)	542(3)	9(1)
C(2)	5734(5)	4062(2)	1569(3)	11(1)
C(3)	4718(5)	4460(2)	1612(3)	11(1)
C(4)	3600(5)	4633(1)	614(3)	10(1)
C(5)	3482(6)	4392(2)	-404(3)	12(1)
C(6)	4492(6)	3995(2)	-443(3)	11(1)
C(7)	2571(5)	5073(2)	624(3)	10(1)
C(8)	2747(5)	5327(2)	1729(3)	10(1)
C(9)	3871(5)	5149(2)	2715(3)	11(1)
C(10)	4836(5)	4699(2)	2716(3)	10(1)
C(11)	1849(6)	5749(2)	1758(3)	11(1)
C(12)	2086(5)	5990(1)	2773(3)	9(1)
C(13)	3203(6)	5816(2)	3760(4)	14(1)
C(14)	4068(6)	5400(2)	3720(3)	13(1)
C(15)	11561(5)	3918(1)	3824(3)	10(1)
C(16)	10668(6)	4127(2)	2820(3)	12(1)
C(17)	9867(6)	4553(2)	2869(3)	11(1)
C(18)	9940(5)	4769(1)	3914(3)	10(1)
C(19)	10844(5)	4556(1)	4915(3)	9(1)
C(20)	11660(6)	4128(2)	4866(3)	11(1)
C(21)	9048(6)	5222(2)	3949(3)	12(1)
O(2W)	2287(4)	1844(1)	538(3)	19(1)

Table 22 Bond lengths [Å] and angles [°] for jn69m_pub.

Nd(1)-O(1)	2.509(3)
Nd(1)-O(1W)	2.469(5)
Nd(1)-O(3W)	2.425(4)
Nd(1)-O(4W)	2.557(4)
Nd(1)-O(5W)	2.521(5)

Nd(1)-O(9)	2.457(3)
Nd(1)-O(1)#1	2.509(3)
Nd(1)-O(4W)#1	2.557(4)
Nd(1)-O(9)#1	2.457(3)
Nd(2)-O(6)	2.472(3)
Nd(2)-O(6W)	2.498(3)
Nd(2)-O(7W)	2.514(4)
Nd(2)-O(8W)	2.521(4)
Nd(2)-O(9W)	2.496(4)
Nd(2)-O(2)#2	2.458(3)
Nd(2)-O(2)#3	2.458(3)
Nd(2)-O(6)#4	2.472(3)
Nd(2)-O(6W)#4	2.498(3)
S(1)-O(1)	1.460(3)
S(1)-O(2)	1.460(3)
S(1)-O(3)	1.441(3)
S(1)-C(1)	1.781(4)
S(2)-O(4)	1.461(3)
S(2)-O(5)	1.464(3)
S(2)-O(6)	1.458(3)
S(2)-C(12)	1.771(4)
S(3)-O(9)	1.442(3)
S(3)-O(10)	1.459(3)
S(3)-O(11)	1.452(3)
S(3)-C(15)	1.768(4)
O(7)-C(10)	1.222(5)
O(8)-C(7)	1.221(5)
O(12)-C(21)	1.222(5)
O(1W)-H(1W)#1	0.979(18)
O(1W)-H(1W)	0.979(18)
O(3W)-H(3W)	0.98(4)
O(3W)-H(3W)#1	0.98(4)
O(4W)-H(4WB)	0.99(6)
O(4W)-H(4W)	0.99(4)

O(5W)-H(5W)	0.99(3)
O(5W)-H(5W)#1	0.99(3)
O(6W)-H(6WB)	0.97(4)
O(6W)-H(6WA)	0.99(4)
O(7W)-H(7W)	0.981(19)
O(7W)-H(7W)#4	0.981(19)
O(8W)-H(8W)	0.98(3)
O(8W)-H(8W)#4	0.98(3)
O(9W)-H(9W)	0.97(3)
O(9W)-H(9W)#4	0.97(3)
O(2W)-H(2WB)	0.98(5)
O(2W)-H(2WA)	0.98(5)
C(1)-C(6)	1.398(5)
C(1)-C(2)	1.392(5)
C(2)-C(3)	1.388(6)
C(3)-C(4)	1.412(5)
C(3)-C(10)	1.487(5)
C(4)-C(7)	1.492(6)
C(4)-C(5)	1.399(5)
C(5)-C(6)	1.381(6)
C(7)-C(8)	1.504(5)
C(8)-C(11)	1.402(6)
C(8)-C(9)	1.410(5)
C(9)-C(14)	1.396(5)
C(9)-C(10)	1.490(6)
C(11)-C(12)	1.389(5)
C(12)-C(13)	1.404(6)
C(13)-C(14)	1.375(6)
C(15)-C(16)	1.399(5)
C(15)-C(20)	1.385(5)
C(16)-C(17)	1.380(6)
C(17)-C(18)	1.398(5)
C(18)-C(19)	1.404(5)
C(18)-C(21)	1.478(6)

C(19)-C(21)#5	1.500(5)
C(19)-C(20)	1.389(6)
C(2)-H(2)	0.98(3)
C(5)-H(5)	0.98(4)
C(6)-H(6)	0.97(3)
C(11)-H(11)	0.97(4)
C(13)-H(13)	0.98(3)
C(14)-H(14)	0.97(4)
C(16)-H(16)	0.98(3)
C(17)-H(17)	0.97(3)
C(20)-H(20)	0.98(3)

O(1)-Nd(1)-O(1W)	70.91(10)
O(1)-Nd(1)-O(3W)	73.96(10)
O(1)-Nd(1)-O(4W)	67.58(10)
O(1)-Nd(1)-O(5W)	135.32(8)
O(1)-Nd(1)-O(9)	88.08(10)
O(1)-Nd(1)-O(1)#1	82.54(9)
O(1)-Nd(1)-O(4W)#1	135.77(10)
O(1)-Nd(1)-O(9)#1	145.02(10)
O(1W)-Nd(1)-O(3W)	132.63(15)
O(1W)-Nd(1)-O(4W)	68.90(9)
O(1W)-Nd(1)-O(5W)	96.90(19)
O(1W)-Nd(1)-O(9)	136.71(8)
O(1)#1-Nd(1)-O(1W)	70.91(10)
O(1W)-Nd(1)-O(4W)#1	68.90(9)
O(1W)-Nd(1)-O(9)#1	136.71(8)
O(3W)-Nd(1)-O(4W)	123.65(8)
O(3W)-Nd(1)-O(5W)	130.47(18)
O(3W)-Nd(1)-O(9)	71.06(11)
O(1)#1-Nd(1)-O(3W)	73.96(10)
O(3W)-Nd(1)-O(4W)#1	123.65(8)
O(3W)-Nd(1)-O(9)#1	71.06(11)
O(4W)-Nd(1)-O(5W)	67.96(10)

O(4W)-Nd(1)-O(9)	68.14(10)
O(1)#1-Nd(1)-O(4W)	135.77(10)
O(4W)-Nd(1)-O(4W)#1	112.65(11)
O(4W)-Nd(1)-O(9)#1	134.72(11)
O(5W)-Nd(1)-O(9)	71.67(14)
O(1)#1-Nd(1)-O(5W)	135.32(8)
O(4W)#1-Nd(1)-O(5W)	67.96(10)
O(5W)-Nd(1)-O(9)#1	71.67(14)
O(1)#1-Nd(1)-O(9)	145.02(10)
O(4W)#1-Nd(1)-O(9)	134.72(11)
O(9)-Nd(1)-O(9)#1	80.55(10)
O(1)#1-Nd(1)-O(4W)#1	67.58(10)
O(1)#1-Nd(1)-O(9)#1	88.08(10)
O(4W)#1-Nd(1)-O(9)#1	68.14(10)
O(6)-Nd(2)-O(6W)	71.83(10)
O(6)-Nd(2)-O(7W)	131.05(7)
O(6)-Nd(2)-O(8W)	65.44(10)
O(6)-Nd(2)-O(9W)	70.32(9)
O(2)#2-Nd(2)-O(6)	143.20(10)
O(2)#3-Nd(2)-O(6)	74.38(10)
O(6)-Nd(2)-O(6)#4	97.66(11)
O(6)-Nd(2)-O(6W)#4	136.28(10)
O(6W)-Nd(2)-O(7W)	69.03(8)
O(6W)-Nd(2)-O(8W)	71.84(9)
O(6W)-Nd(2)-O(9W)	136.33(7)
O(2)#2-Nd(2)-O(6W)	137.77(10)
O(2)#3-Nd(2)-O(6W)	76.33(9)
O(6)#4-Nd(2)-O(6W)	136.28(10)
O(6W)-Nd(2)-O(6W)#4	86.82(10)
O(7W)-Nd(2)-O(8W)	125.09(13)
O(7W)-Nd(2)-O(9W)	124.83(12)
O(2)#2-Nd(2)-O(7W)	68.79(9)
O(2)#3-Nd(2)-O(7W)	68.79(9)
O(6)#4-Nd(2)-O(7W)	131.05(7)

O(6W)#4-Nd(2)-O(7W)	69.03(8)
O(8W)-Nd(2)-O(9W)	110.08(13)
O(2)#2-Nd(2)-O(8W)	134.56(7)
O(2)#3-Nd(2)-O(8W)	134.56(7)
O(6)#4-Nd(2)-O(8W)	65.44(10)
O(6W)#4-Nd(2)-O(8W)	71.84(9)
O(2)#2-Nd(2)-O(9W)	73.22(9)
O(2)#3-Nd(2)-O(9W)	73.22(9)
O(6)#4-Nd(2)-O(9W)	70.32(9)
O(6W)#4-Nd(2)-O(9W)	136.33(7)
O(2)#2-Nd(2)-O(2)#3	90.58(9)
O(2)#2-Nd(2)-O(6)#4	74.38(10)
O(2)#2-Nd(2)-O(6W)#4	76.33(9)
O(2)#3-Nd(2)-O(6)#4	143.20(10)
O(2)#3-Nd(2)-O(6W)#4	137.77(10)
O(6)#4-Nd(2)-O(6W)#4	71.83(10)
O(1)-S(1)-O(2)	111.89(18)
O(1)-S(1)-O(3)	113.10(17)
O(1)-S(1)-C(1)	106.52(18)
O(2)-S(1)-O(3)	113.54(17)
O(2)-S(1)-C(1)	105.41(18)
O(3)-S(1)-C(1)	105.61(19)
O(4)-S(2)-O(5)	112.79(17)
O(4)-S(2)-O(6)	112.55(19)
O(4)-S(2)-C(12)	108.61(17)
O(5)-S(2)-O(6)	111.28(19)
O(5)-S(2)-C(12)	106.48(18)
O(6)-S(2)-C(12)	104.59(18)
O(9)-S(3)-O(10)	111.36(19)
O(9)-S(3)-O(11)	113.54(19)
O(9)-S(3)-C(15)	106.63(18)
O(10)-S(3)-O(11)	112.21(17)
O(10)-S(3)-C(15)	106.44(18)
O(11)-S(3)-C(15)	106.10(18)

Nd(1)-O(1)-S(1)	148.46(19)
Nd(2)#6-O(2)-S(1)	159.19(19)
Nd(2)-O(6)-S(2)	154.5(2)
Nd(1)-O(9)-S(3)	178.7(2)
Nd(1)-O(1W)-H(1W)#1	126.2(13)
H(1W)-O(1W)-H(1W)#1	106(2)
Nd(1)-O(1W)-H(1W)	126.2(13)
Nd(1)-O(3W)-H(3W)	126(3)
Nd(1)-O(3W)-H(3W)#1	126(3)
H(3W)-O(3W)-H(3W)#1	106(4)
Nd(1)-O(4W)-H(4W)	116(5)
Nd(1)-O(4W)-H(4WB)	128(5)
H(4W)-O(4W)-H(4WB)	108(7)
Nd(1)-O(5W)-H(5W)#1	125(2)
H(5W)-O(5W)-H(5W)#1	104(3)
Nd(1)-O(5W)-H(5W)	125(2)
Nd(2)-O(6W)-H(6WA)	133(3)
H(6WB)-O(6W)-H(6WA)	106(4)
Nd(2)-O(6W)-H(6WB)	122(3)
H(7W)-O(7W)-H(7W)#4	105.1(19)
Nd(2)-O(7W)-H(7W)#4	114(4)
Nd(2)-O(7W)-H(7W)	114(4)
H(8W)-O(8W)-H(8W)#4	106(3)
Nd(2)-O(8W)-H(8W)	120(2)
Nd(2)-O(8W)-H(8W)#4	120(2)
Nd(2)-O(9W)-H(9W)	115(3)
Nd(2)-O(9W)-H(9W)#4	115(3)
H(9W)-O(9W)-H(9W)#4	107(3)
H(2WA)-O(2W)-H(2WB)	106(4)
C(2)-C(1)-C(6)	120.7(4)
S(1)-C(1)-C(6)	120.5(3)
S(1)-C(1)-C(2)	118.8(3)
C(1)-C(2)-C(3)	119.7(3)
C(4)-C(3)-C(10)	121.1(4)

C(2)-C(3)-C(4)	119.9(3)
C(2)-C(3)-C(10)	119.0(3)
C(5)-C(4)-C(7)	119.5(3)
C(3)-C(4)-C(7)	121.0(3)
C(3)-C(4)-C(5)	119.6(4)
C(4)-C(5)-C(6)	120.4(4)
C(1)-C(6)-C(5)	119.7(3)
O(8)-C(7)-C(8)	120.3(4)
C(4)-C(7)-C(8)	118.1(3)
O(8)-C(7)-C(4)	121.6(3)
C(7)-C(8)-C(9)	120.0(4)
C(9)-C(8)-C(11)	120.5(3)
C(7)-C(8)-C(11)	119.5(3)
C(8)-C(9)-C(10)	121.9(3)
C(8)-C(9)-C(14)	118.8(4)
C(10)-C(9)-C(14)	119.3(3)
O(7)-C(10)-C(9)	121.1(3)
C(3)-C(10)-C(9)	117.7(3)
O(7)-C(10)-C(3)	121.2(4)
C(8)-C(11)-C(12)	118.9(3)
C(11)-C(12)-C(13)	121.1(4)
S(2)-C(12)-C(11)	121.5(3)
S(2)-C(12)-C(13)	117.2(3)
C(12)-C(13)-C(14)	119.4(4)
C(9)-C(14)-C(13)	121.3(4)
S(3)-C(15)-C(20)	118.8(3)
C(16)-C(15)-C(20)	121.6(4)
S(3)-C(15)-C(16)	119.6(3)
C(15)-C(16)-C(17)	119.2(3)
C(16)-C(17)-C(18)	120.1(3)
C(17)-C(18)-C(19)	120.1(4)
C(19)-C(18)-C(21)	120.7(3)
C(17)-C(18)-C(21)	119.2(3)
C(20)-C(19)-C(21)#5	118.5(3)

C(18)-C(19)-C(20)	119.9(3)
C(18)-C(19)-C(21)#5	121.6(4)
C(15)-C(20)-C(19)	119.2(3)
C(18)-C(21)-C(19)#5	117.7(3)
O(12)-C(21)-C(19)#5	120.3(4)
O(12)-C(21)-C(18)	122.0(3)
C(3)-C(2)-H(2)	115(3)
C(1)-C(2)-H(2)	125(3)
C(4)-C(5)-H(5)	117(3)
C(6)-C(5)-H(5)	123(3)
C(5)-C(6)-H(6)	122(2)
C(1)-C(6)-H(6)	118(2)
C(8)-C(11)-H(11)	124(3)
C(12)-C(11)-H(11)	117(3)
C(14)-C(13)-H(13)	120(2)
C(12)-C(13)-H(13)	121(2)
C(9)-C(14)-H(14)	117(3)
C(13)-C(14)-H(14)	121(3)
C(17)-C(16)-H(16)	123(2)
C(15)-C(16)-H(16)	118(2)
C(16)-C(17)-H(17)	123(2)
C(18)-C(17)-H(17)	117(2)
C(15)-C(20)-H(20)	118(2)
C(19)-C(20)-H(20)	123(2)

Symmetry transformations used to generate equivalent atoms:

#1 x,1/2-y,z #2 -x+1,y+1/2,-z #3 -x+1,-y+1,-z

#4 x,1/2-y+1,z #5 -x+2,-y+1,-z+1 #6 -x+1,y-1/2,-z

Table 23 Anisotropic displacement parameters ($Å^2 x\ 10^3$)for jn69m_pub. The anisotropic displacement factor exponent takes the form: $-2p^2[\ h^2 a^{*2} U^{11} + ... + 2\ h\ k\ a^*\ b^*\ U^{12}\ ]$

	U^{11}	U^{22}	U^{33}	U^{23}	U^{13}	U^{12}
Nd(1)	7(1)	10(1)	9(1)	0	2(1)	0
Nd(2)	6(1)	8(1)	7(1)	0	1(1)	0
S(1)	10(1)	10(1)	9(1)	-1(1)	2(1)	2(1)
S(2)	9(1)	8(1)	10(1)	0(1)	3(1)	0(1)
S(3)	9(1)	9(1)	10(1)	0(1)	2(1)	1(1)
O(1)	24(2)	21(2)	13(2)	6(1)	8(1)	9(1)
O(1W)	8(2)	17(2)	27(2)	0	5(2)	0
O(2)	13(2)	15(2)	18(2)	-8(1)	1(1)	2(1)
O(3)	10(2)	18(2)	18(2)	-3(1)	1(1)	2(1)
O(3W)	19(2)	25(3)	10(2)	0	6(2)	0
O(4)	9(2)	15(2)	13(1)	-1(1)	1(1)	1(1)
O(4W)	14(2)	31(2)	25(2)	-8(2)	1(1)	3(1)
O(5)	20(2)	16(2)	11(1)	0(1)	6(1)	3(1)
O(5W)	77(4)	27(3)	18(3)	0	7(3)	0
O(6)	13(2)	14(2)	20(2)	5(1)	0(1)	-2(1)
O(6W)	16(2)	23(2)	15(2)	6(1)	5(1)	7(1)
O(7)	19(2)	15(2)	9(1)	1(1)	1(1)	5(1)
O(7W)	11(2)	14(2)	14(2)	0	4(2)	0
O(8)	16(2)	17(2)	11(2)	1(1)	-2(1)	5(1)
O(8W)	20(2)	13(2)	14(2)	0	2(2)	0
O(9)	15(2)	12(2)	38(2)	-7(1)	4(1)	-2(1)
O(9W)	11(2)	14(2)	13(2)	0	1(2)	0
O(10)	19(2)	16(2)	17(2)	2(1)	10(1)	6(1)
O(11)	26(2)	15(2)	10(1)	-1(1)	0(1)	9(1)
O(12)	19(2)	15(2)	11(1)	0(1)	-1(1)	6(1)
C(1)	9(2)	7(2)	13(2)	1(2)	4(2)	-1(2)
C(2)	8(2)	13(2)	11(2)	2(2)	2(2)	-2(2)
C(3)	9(2)	14(2)	10(2)	0(2)	5(2)	-2(2)
C(4)	9(2)	11(2)	9(2)	0(2)	2(2)	-3(2)
C(5)	9(2)	17(2)	9(2)	1(2)	0(2)	0(2)
C(6)	12(2)	11(2)	11(2)	-1(2)	3(2)	-2(2)

C(7)	9(2)	12(2)	10(2)	-1(2)	2(2)	-1(2)
C(8)	10(2)	13(2)	8(2)	0(2)	2(2)	-2(2)
C(9)	10(2)	12(2)	10(2)	1(2)	2(2)	0(2)
C(10)	9(2)	12(2)	10(2)	1(2)	2(2)	-2(2)
C(11)	10(2)	13(2)	9(2)	2(2)	0(2)	1(2)
C(12)	7(2)	8(2)	14(2)	-1(2)	5(2)	-1(2)
C(13)	15(2)	15(2)	11(2)	-3(2)	1(2)	1(2)
C(14)	12(2)	16(2)	10(2)	0(2)	0(2)	2(2)
C(15)	7(2)	11(2)	13(2)	1(2)	2(2)	1(2)
C(16)	11(2)	16(2)	9(2)	-3(2)	1(2)	-3(2)
C(17)	11(2)	14(2)	8(2)	-2(2)	0(2)	-2(2)
C(18)	9(2)	11(2)	10(2)	-1(2)	3(2)	-1(2)
C(19)	7(2)	10(2)	11(2)	-2(2)	1(2)	-1(2)
C(20)	8(2)	12(2)	12(2)	1(2)	3(2)	-2(2)
C(21)	10(2)	14(2)	12(2)	1(2)	2(2)	-2(2)
O(2W)	11(2)	21(2)	23(2)	5(1)	-1(1)	-3(1)

Table 24 Hydrogen coordinates (x 10^4) and isotropic displacement parameters (Å^{2}x 10^3) for jn69m_pub.

	x	y	z	U(eq)
H(1W)	4320(30)	2769(2)	2780(60)	30(20)
H(2)	6540(60)	3976(17)	2280(20)	23(13)
H(6WB)	6650(70)	6770(20)	3510(30)	30(20)
H(3W)	10550(100)	2768(2)	1070(40)	30(19)
H(6WA)	7660(50)	6790(20)	2490(40)	30(20)
H(4W)	8100(80)	3300(30)	4630(20)	40(20)
H(5)	2670(50)	4517(17)	-1070(30)	40(13)
H(4WB)	6230(60)	3370(30)	3740(90)	40(40)
H(5W)	9340(130)	2770(2)	5580(30)	30(30)
H(6)	4440(60)	3823(14)	-1140(20)	40(120)
H(7W)	6770(100)	7232(2)	420(20)	50(20)

H(8W)	5190(80)	7231(2)	4570(30)	50(19)
H(9W)	220(60)	7231(2)	1320(60)	50(19)
H(11)	1030(50)	5883(16)	1110(30)	19(13)
H(13)	3400(50)	5990(13)	4470(20)	20(10)
H(14)	4900(50)	5277(16)	4380(30)	17(1)
H(16)	10590(60)	3956(14)	2110(20)	10(1)
H(17)	9260(50)	4721(13)	2200(20)	20(10)
H(20)	12390(50)	3977(14)	5530(20)	20(10)
H(2WA)	2980(70)	1682(18)	1200(40)	40(20)
H(2WB)	1280(60)	1637(17)	210(50)	40(20)

Table 25 Torsion angles [°] for jn69m_pub.

O(1W)-Nd(1)-O(1)-S(1)	-159.6(4)
O(3W)-Nd(1)-O(1)-S(1)	-11.9(3)
O(4W)-Nd(1)-O(1)-S(1)	126.1(4)
O(5W)-Nd(1)-O(1)-S(1)	120.2(4)
O(9)-Nd(1)-O(1)-S(1)	59.0(3)
O(1)#1-Nd(1)-O(1)-S(1)	-87.2(3)
O(4W)#1-Nd(1)-O(1)-S(1)	-133.9(3)
O(9)#1-Nd(1)-O(1)-S(1)	-11.5(5)
O(6W)-Nd(2)-O(6)-S(2)	-146.4(5)
O(7W)-Nd(2)-O(6)-S(2)	-108.1(5)
O(8W)-Nd(2)-O(6)-S(2)	135.8(5)
O(9W)-Nd(2)-O(6)-S(2)	11.5(4)
O(2)#2-Nd(2)-O(6)-S(2)	3.2(6)
O(2)#3-Nd(2)-O(6)-S(2)	-65.9(5)
O(6)#4-Nd(2)-O(6)-S(2)	77.3(5)
O(6W)#4-Nd(2)-O(6)-S(2)	149.0(4)
O(2)-S(1)-O(1)-Nd(1)	92.1(4)
O(3)-S(1)-O(1)-Nd(1)	-37.7(4)
C(1)-S(1)-O(1)-Nd(1)	-153.2(3)

O(1)-S(1)-O(2)-Nd(2)#6	-60.4(6)
O(3)-S(1)-O(2)-Nd(2)#6	69.2(6)
C(1)-S(1)-O(2)-Nd(2)#6	-175.7(5)
O(1)-S(1)-C(1)-C(2)	43.1(4)
O(1)-S(1)-C(1)-C(6)	-138.6(3)
O(2)-S(1)-C(1)-C(2)	162.2(3)
O(2)-S(1)-C(1)-C(6)	-19.6(4)
O(3)-S(1)-C(1)-C(2)	-77.4(3)
O(3)-S(1)-C(1)-C(6)	100.9(3)
O(4)-S(2)-O(6)-Nd(2)	5.7(5)
O(5)-S(2)-O(6)-Nd(2)	-122.0(5)
C(12)-S(2)-O(6)-Nd(2)	123.5(4)
O(4)-S(2)-C(12)-C(11)	22.8(4)
O(4)-S(2)-C(12)-C(13)	-162.8(3)
O(5)-S(2)-C(12)-C(11)	144.5(3)
O(5)-S(2)-C(12)-C(13)	-41.1(4)
O(6)-S(2)-C(12)-C(11)	-97.6(4)
O(6)-S(2)-C(12)-C(13)	76.9(4)
O(9)-S(3)-C(15)-C(16)	-69.4(4)
O(9)-S(3)-C(15)-C(20)	108.2(4)
O(10)-S(3)-C(15)-C(16)	49.6(4)
O(10)-S(3)-C(15)-C(20)	-132.9(3)
O(11)-S(3)-C(15)-C(16)	169.3(3)
O(11)-S(3)-C(15)-C(20)	-13.2(4)
S(1)-C(1)-C(2)-C(3)	176.5(3)
C(6)-C(1)-C(2)-C(3)	-1.7(6)
S(1)-C(1)-C(6)-C(5)	-176.4(3)
C(2)-C(1)-C(6)-C(5)	1.8(6)
C(1)-C(2)-C(3)-C(4)	-0.2(6)
C(1)-C(2)-C(3)-C(10)	180.0(4)
C(2)-C(3)-C(4)-C(5)	2.0(6)
C(2)-C(3)-C(4)-C(7)	-176.7(4)
C(10)-C(3)-C(4)-C(5)	-178.2(4)
C(10)-C(3)-C(4)-C(7)	3.0(6)

C(2)-C(3)-C(10)-O(7)	-5.8(6)
C(2)-C(3)-C(10)-C(9)	174.3(4)
C(4)-C(3)-C(10)-O(7)	174.4(4)
C(4)-C(3)-C(10)-C(9)	-5.5(6)
C(3)-C(4)-C(5)-C(6)	-1.9(6)
C(7)-C(4)-C(5)-C(6)	176.9(4)
C(3)-C(4)-C(7)-O(8)	177.3(4)
C(3)-C(4)-C(7)-C(8)	-0.4(6)
C(5)-C(4)-C(7)-O(8)	-1.5(6)
C(5)-C(4)-C(7)-C(8)	-179.2(4)
C(4)-C(5)-C(6)-C(1)	0.0(7)
O(8)-C(7)-C(8)-C(9)	-177.3(4)
O(8)-C(7)-C(8)-C(11)	0.0(6)
C(4)-C(7)-C(8)-C(9)	0.4(5)
C(4)-C(7)-C(8)-C(11)	177.8(4)
C(7)-C(8)-C(9)-C(10)	-3.1(6)
C(7)-C(8)-C(9)-C(14)	177.5(4)
C(11)-C(8)-C(9)-C(10)	179.6(4)
C(11)-C(8)-C(9)-C(14)	0.2(6)
C(7)-C(8)-C(11)-C(12)	-177.2(4)
C(9)-C(8)-C(11)-C(12)	0.1(6)
C(8)-C(9)-C(10)-O(7)	-174.3(4)
C(8)-C(9)-C(10)-C(3)	5.6(6)
C(14)-C(9)-C(10)-O(7)	5.1(6)
C(14)-C(9)-C(10)-C(3)	-175.1(4)
C(8)-C(9)-C(14)-C(13)	-0.5(6)
C(10)-C(9)-C(14)-C(13)	-179.9(4)
C(8)-C(11)-C(12)-S(2)	174.2(3)
C(8)-C(11)-C(12)-C(13)	-0.1(6)
S(2)-C(12)-C(13)-C(14)	-174.7(3)
C(11)-C(12)-C(13)-C(14)	-0.2(6)
C(12)-C(13)-C(14)-C(9)	0.5(7)
S(3)-C(15)-C(16)-C(17)	177.5(3)
C(20)-C(15)-C(16)-C(17)	0.0(6)

S(3)-C(15)-C(20)-C(19)	-177.1(3)
C(16)-C(15)-C(20)-C(19)	0.4(6)
C(15)-C(16)-C(17)-C(18)	-0.5(7)
C(16)-C(17)-C(18)-C(19)	0.6(6)
C(16)-C(17)-C(18)-C(21)	-179.1(4)
C(17)-C(18)-C(19)-C(20)	-0.3(6)
C(17)-C(18)-C(19)-C(21)#5	180.0(4)
C(21)-C(18)-C(19)-C(20)	179.4(4)
C(21)-C(18)-C(19)-C(21)#5	-0.4(6)
C(17)-C(18)-C(21)-O(12)	0.1(6)
C(17)-C(18)-C(21)-C(19)#5	-180.0(4)
C(19)-C(18)-C(21)-O(12)	-179.6(4)
C(19)-C(18)-C(21)-C(19)#5	0.4(6)
C(18)-C(19)-C(20)-C(15)	-0.2(6)
C(21)#5-C(19)-C(20)-C(15)	179.6(4)
C(18)-C(19)-C(21)#5-O(12)#5	-179.6(4)
C(18)-C(19)-C(21)#5-C(18)#5	0.4(6)
C(20)-C(19)-C(21)#5-O(12)#5	0.6(6)
C(20)-C(19)-C(21)#5-C(18)#5	-179.4(4)

Symmetry transformations used to generate equivalent atoms:

#1 x,1/2-y,z #2 -x+1,y+1/2,-z #3 -x+1,-y+1,-z

#4 x,1/2-y+1,z #5 -x+2,-y+1,-z+1 #6 -x+1,y-1/2,-z

Table 26 Hydrogen bonds for jn69m_pub [Å and °].

D-H...A	d(D-H)	d(H...A)	d(D...A)	<(DHA)
O(2W)-H(2WA)...O(10)#7	0.98(5)	2.01(5)	2.890(4)	148(4)
O(1W)-H(1W)...O(10)#8	0.979(18)	1.854(11)	2.785(4)	158(3)
O(2W)-H(2WB)...O(4)#9	0.98(5)	2.49(6)	3.070(4)	118(4)
O(2W)-H(2WB)...O(3)#7	0.98(5)	1.97(5)	2.762(4)	137(4)
O(6W)-H(6WB)...O(11)#5	0.97(4)	1.98(4)	2.906(3)	158(5)
O(3W)-H(3W)...O(3)	0.98(4)	2.56(4)	3.296(4)	133(5)

O(3W)-H(3W)...O(2W)#1	0.98(4)	1.92(6)	2.814(5)	151(6)
O(6W)-H(6WA)...O(4)#1	10.99(4)	1.85(4)	2.833(4)	175(4)
O(6W)-H(6WA)...O(5)#1	10.99(4)	2.60(4)	3.199(4)	119(3)
O(4W)-H(4W)...O(5)#12	0.99(4)	1.83(3)	2.817(4)	177(7)
O(4W)-H(4WB)...O(10)#8	0.99(6)	2.02(7)	2.906(4)	149(9)
O(5W)-H(5W)...O(5)#12	0.99(3)	1.973(13)	2.920(4)	158(3)
O(7W)-H(7W)...O(2W)#2	0.98(2)	1.85(4)	2.772(4)	156(6)
O(8W)-H(8W)...O(11)#5	0.98(3)	1.79(3)	2.746(4)	168(4)
O(9W)-H(9W)...O(4)	0.97(3)	2.00(3)	2.945(3)	162(4)
C(2)-H(2)...O(7)	0.98(3)	2.43(4)	2.801(5)	102(3)
C(5)-H(5)...O(8)	0.98(4)	2.49(5)	2.825(5)	100(3)
C(5)-H(5)...O(12)#3	0.98(4)	2.40(4)	3.287(4)	150(3)
C(6)-H(6)...O(2)	0.97(3)	2.52(4)	2.919(5)	105(2)
C(14)-H(14)...O(7)	0.97(4)	2.48(4)	2.811(5)	100(3)
C(16)-H(16)...O(3)	0.98(3)	2.46(3)	3.353(5)	152(4)
C(17)-H(17)...O(12)	0.97(3)	2.47(4)	2.815(5)	100(2)
C(17)-H(17)...O(8)#3	0.97(3)	2.33(2)	3.205(4)	150(3)
C(20)-H(20)...O(11)	0.98(3)	2.41(4)	2.859(5)	108(2)

Symmetry transformations used to generate equivalent atoms:

#1 x,1/2-y,z #2 -x+1,y+1/2,-z #3 -x+1,-y+1,-z

#4 x,1/2-y+1,z #5 -x+2,-y+1,-z+1 #6 -x+1,y-1/2,-z

#7 x-1,1/2-y,z #8 x-1,y,z #9 -x,y-1/2,-z

#10 x+1,1/2-y,z #11 x+1,y,z #12 -x+1,-y+1,-z+1

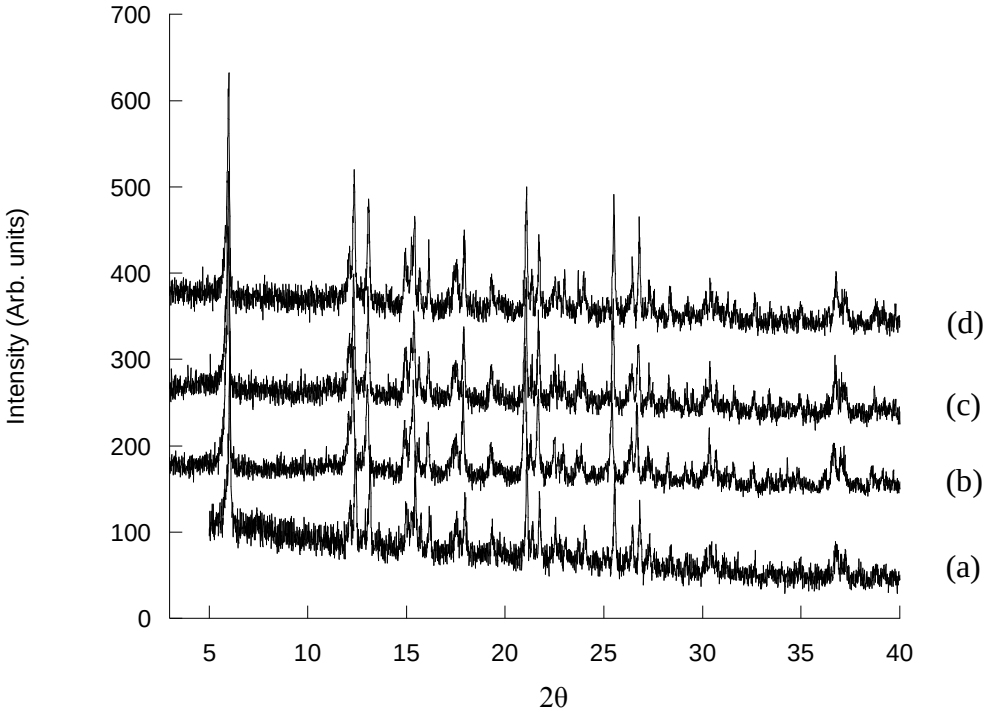

Figure 31 PXRD patterns of iso-structural phases

(a) $[Nd(H_2O)_5]_2[2,6\text{-AQDS}]_3.2H_2O$, (b) $[La(H_2O)_5]_2[2,6\text{-AQDS}]_3.2H_2O$,

(c) $[Ce(H_2O)_5]_2[2,6\text{-AQDS}]_3.2H_2O$ and (d) $[Pr(H_2O)_5]_2[2,6\text{-AQDS}]_3.2H_2O$

$[La(H_2O)_5]_2[2,6\text{-}AQDS]_3.2H_2O$

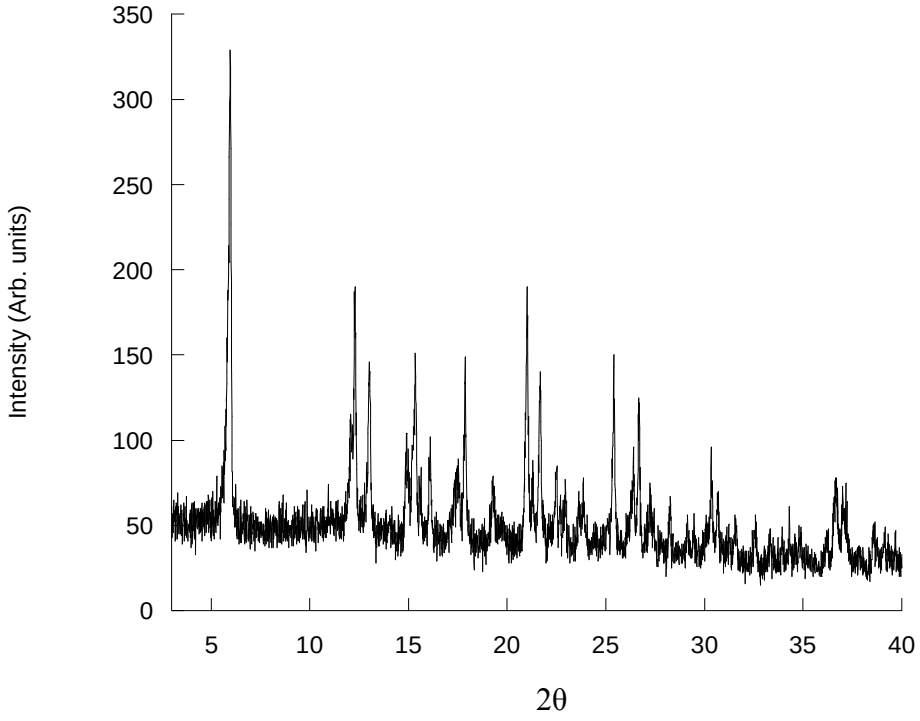

Figure 32 PXRD pattern of $[La(H_2O)_5]_2[2,6\text{-}AQDS]_3.2H_2O$.

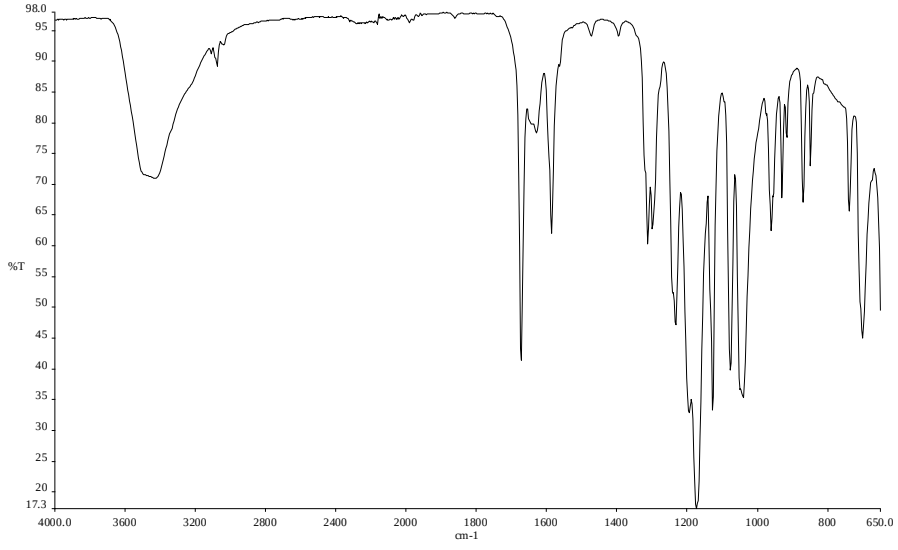

Figure 33 FTIR spectra of $[La(H_2O)_5]_2[2,6\text{-}AQDS]_3.2H_2O$ showing bands corresponding to an OH stretch and the bending mode water at 3430 and 1630 cm^{-1}, C=O stretch at 1674 cm^{-1} and the symmetric and asymmetric stretches of the sulfonate groups at 1041 and 1171 cm^{-1}

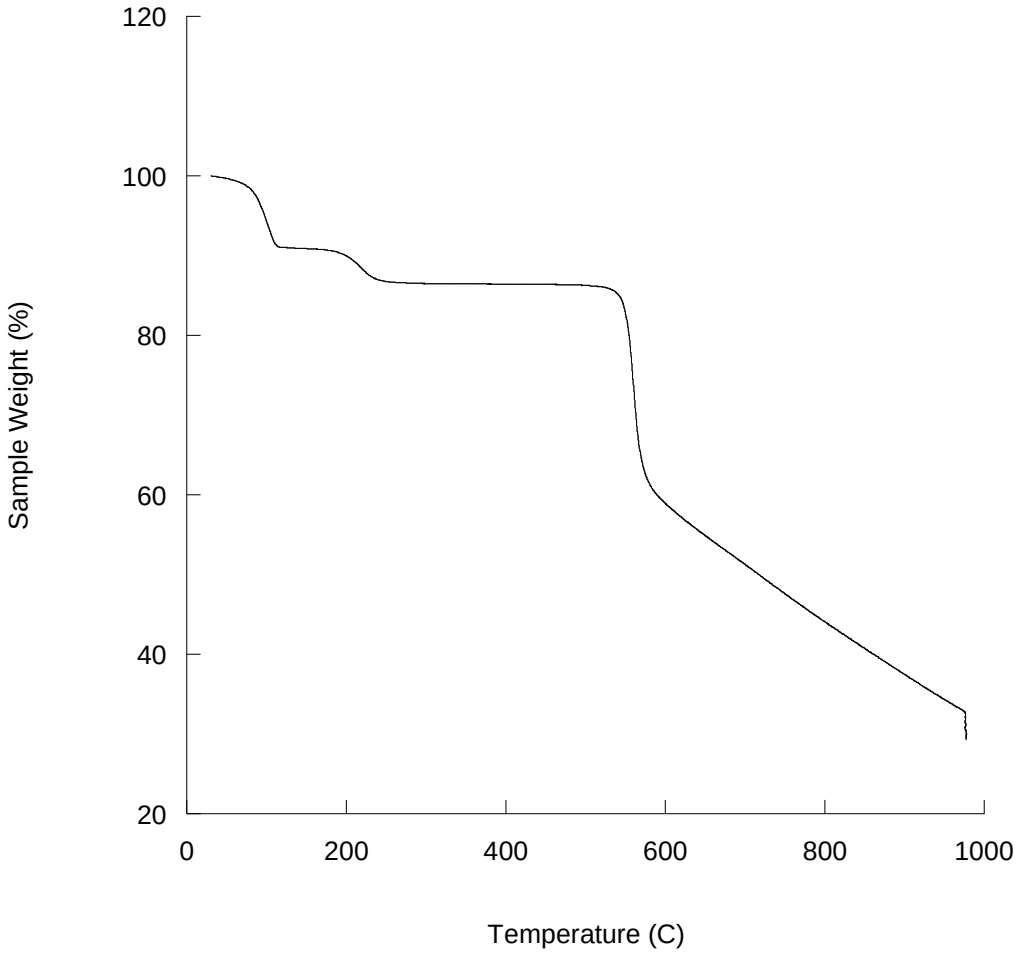

Figure 34 TGA trace of $[La(H_2O)_5]_2[2,6\text{-AQDS}]_3.2H_2O$ showing three distinct mass losses. First mass loss of 9.1% below 100°C, second mass loss of 4.5% below 225 °C and an additional mass loss of 54.3% by 978°C. End product is found to be La_2O_2S.

$[Ce(H_2O)_5]_2[2,6\text{-}AQDS]_3.2H_2O$

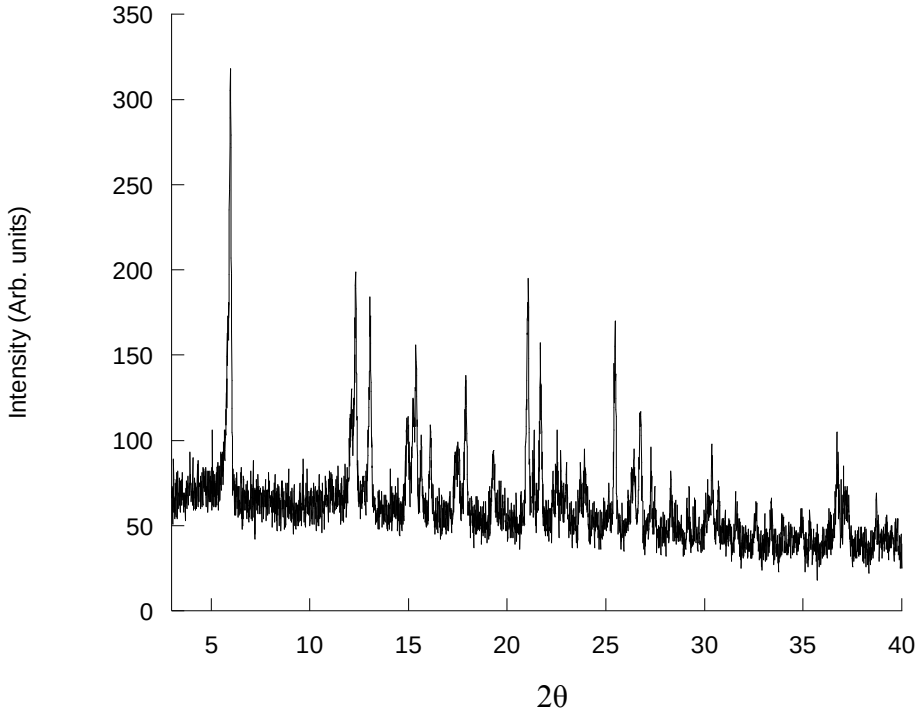

Figure 35 PXRD pattern of $[Ce(H_2O)_5]_2[2,6\text{-}AQDS]_3.2H_2O$.

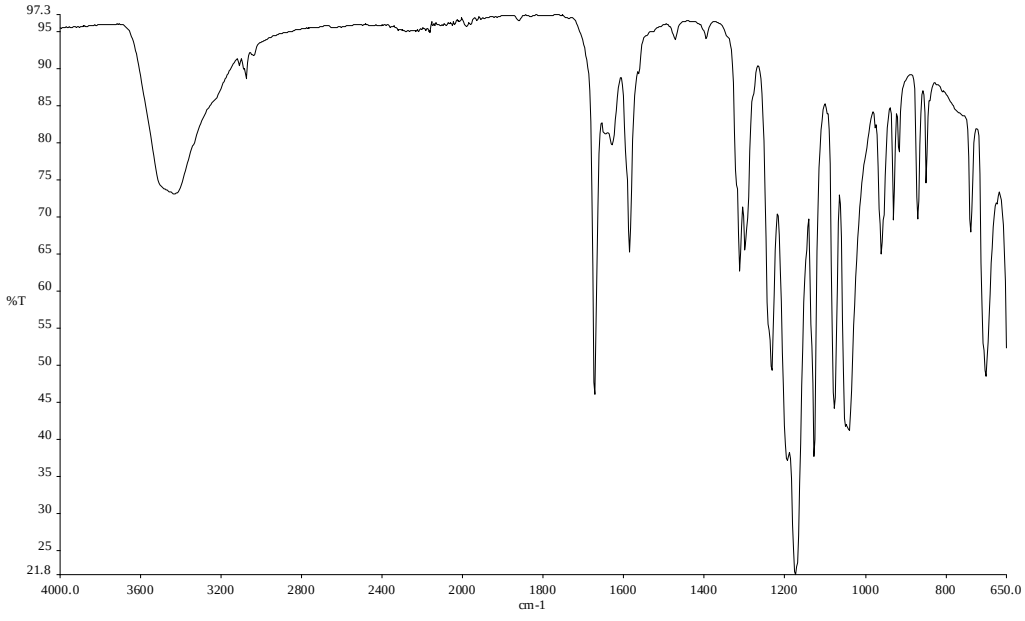

Figure 36 FTIR spectra of $[Ce(H_2O)_5]_2[2,6\text{-}AQDS]_3.2H_2O$ showing bands corresponding to an OH stretch and the bending mode water at 3430 and 1630 cm^{-1}, C=O stretch at 1674 cm^{-1} and the symmetric and asymmetric stretches of the sulfonate groups at 1042 and 1171 cm^{-1}

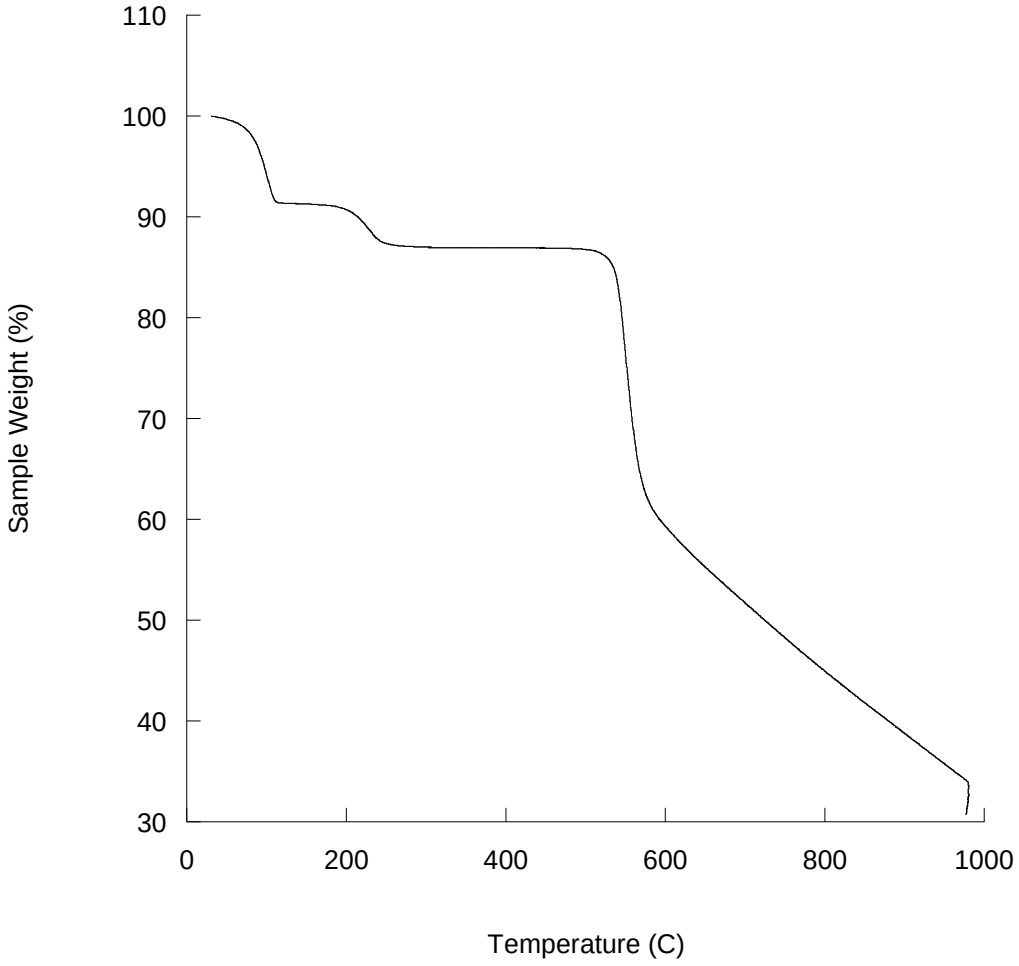

Figure 37 TGA trace of $[Ce(H_2O)_5]_2[2,6\text{-AQDS}]_3.2H_2O$ showing three distinct mass losses. First mass loss of 9.3% below 100°C, second mass loss of 3.8% below 225 °C and an additional mass loss of 56.4% by 980°C. End product is found to be Ce_2O_2.

$[Pr(H_2O)_5]_2[2,6\text{-}AQDS]_3.2H_2O$

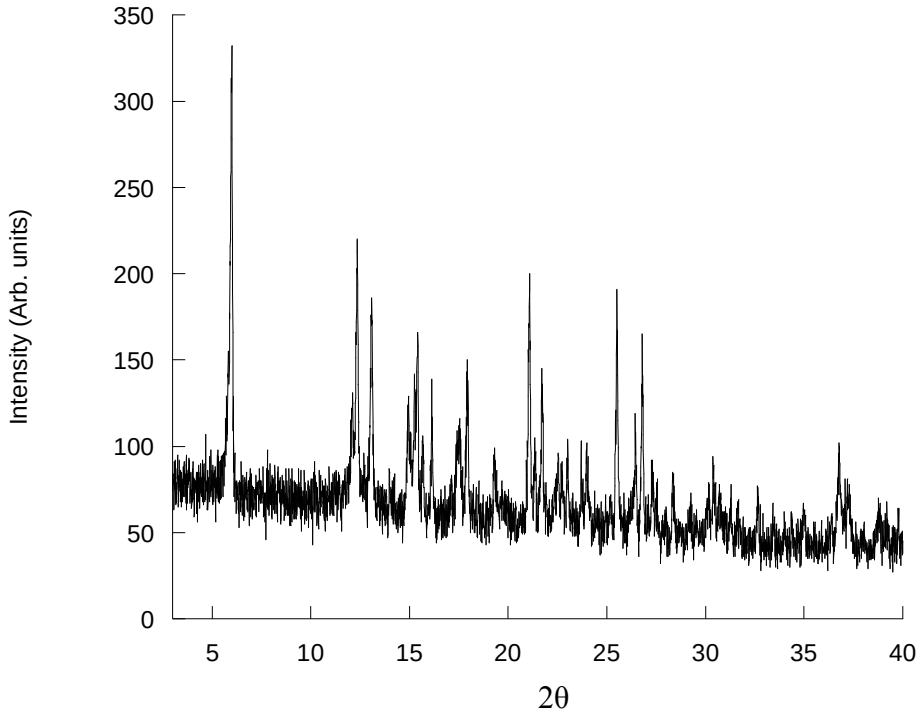

Figure 38 PXRD pattern of $[Pr(H_2O)_5]_2[2,6\text{-}AQDS]_3.2H_2O$.

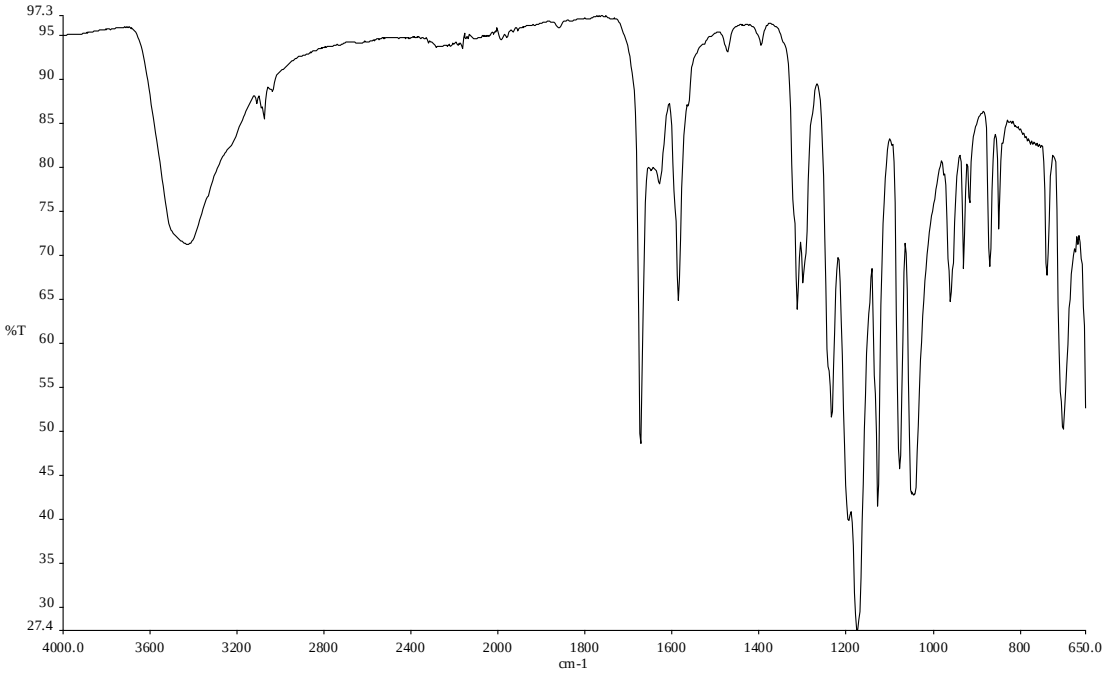

Figure 39 FTIR spectra of $[Pr(H_2O)_5]_2[2,6\text{-}AQDS]_3.2H_2O$ showing bands corresponding to an OH stretch and the bending mode water at 3431 and 1630 cm^{-1}, C=O stretch at 1674 cm^{-1} and the symmetric and asymmetric stretches of the sulfonate groups at 1047 and 1176 cm^{-1}.

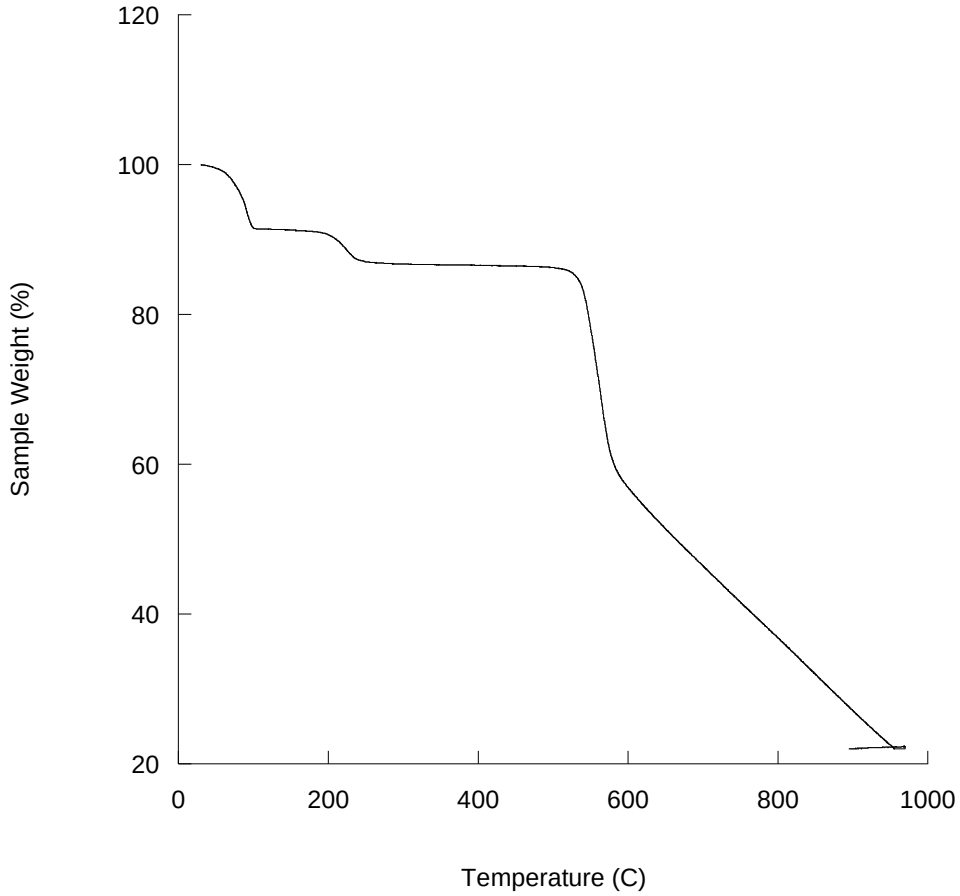

Figure 40 TGA trace of $[Pr(H_2O)_5]_2[2,6\text{-AQDS}]_3.2H_2O$ showing three distinct mass losses. First mass loss of 9.4% below 100°C, second mass loss of 4.1% below 225 °C and an additional mass loss of 64.2% by 968°C. End product is found to be $Pr_2O_2SO_4$.

Table 27 Elemental analysis of iso-structural phases of $[Ln(H_2O)_5]_2$[2,6-AQDS $]_3$ $.2H_2O$ (Ln= La - Nd)

Lanthanide	Elemental Analysis	
	Observed (%)	Calculated (%)
La	C-31.75	C-31.67
	H-2.41	H-2.66
Ce	C-31.42	C-31.62
	H-2.37	H-2.65
Pr	C-31.77	C-31.59
	H-2.37	H-2.65
Nd	C-31.79	C-31.46
	H-2.45	H-2.64

$[Nd(H_2O)_5][Octanesulfonate]_3.2H_2O$

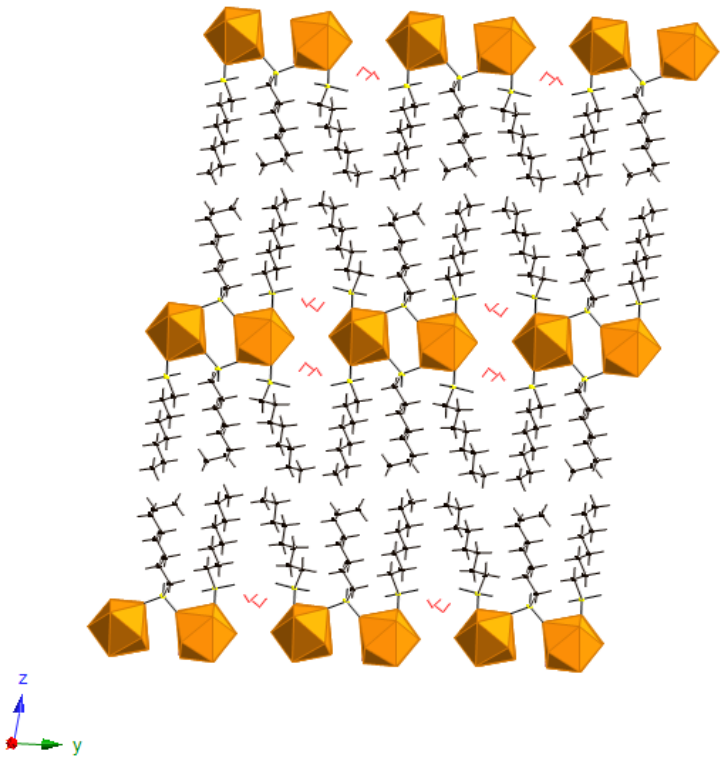

Figure 41 Crystal structure of $[Nd(H_2O)_5][C_8H_{17}SO_3]_3.2H_2O$

Table 28 Crystal data and structure refinement for JN198m.

$[Nd(H_2O)_5][C_8H_{17}SO_3]_3.2H_2O$

Identification code	jn198m	
Empirical formula	C48 H130 Nd2 O32 S6	
Formula weight	1700.36	
Temperature	100.0 K	
Wavelength	0.71073 Å	
Crystal system	Triclinic	
Space group	P-1	
Unit cell dimensions	a = 6.9996(16) Å	α= 79.318(3)°.
	b = 13.489(3) Å	β= 83.405(3)°.
	c = 21.650(5) Å	γ =76.760(2)°.
Volume	1949.7(8) $Å^3$	
Z	1	
Density (calculated)	1.448 mg/m^3	
Absorption coefficient	1.552 mm^{-1}	
F(000)	890	
Crystal size	0.25 x 0.20 x 0.02 mm^3	
Theta range for data collection	1.57 to 27.61°.	
Index ranges	-8<=h<=9, -15<=k<=17, -21<=l<=27	
Reflections collected	12503	
Independent reflections	7989 [R(int) = 0.0411]	
Completeness to theta = 25.00°	94.2 %	
Absorption correction	Numerical	
Max. and min. transmission	0.7455 and 0.5549	
Refinement method	Full-matrix least-squares on F^2	
Data / restraints / parameters	7989 / 26 / 442	
Goodness-of-fit on F^2	1.030	
Final R indices [I>2sigma(I)]	R1 = 0.0550, wR2 = 0.1315	
R indices (all data)	R1 = 0.0777, wR2 = 0.1401	
Largest diff. peak and hole	4.770 and -2.232 e.$Å^{-3}$	

Table 29 Atomic coordinates (x 10^4) and equivalent isotropic displacement parameters ($Å^2$x 10^3) for JN198m. U(eq) is defined as one third of the trace of the orthogonalized U^{ij} tensor.

	x	y	z	U(eq)
Nd(1)	6031(1)	7843(1)	60(1)	12(1)
S(1)	3234(2)	6745(1)	1542(1)	16(1)
S(2)	5440(2)	9699(1)	1152(1)	14(1)
S(3)	9374(2)	7574(1)	-1455(1)	16(1)
O(10)	2396(5)	8821(3)	378(2)	17(1)
O(8)	10621(5)	8252(3)	-1354(2)	20(1)
O(11)	8815(5)	8991(3)	-262(2)	15(1)
O(2)	1370(5)	7500(3)	1470(2)	20(1)
O(9)	10510(5)	6586(3)	-1604(2)	19(1)
O(1)	4629(5)	6891(3)	998(2)	19(1)
O(14)	6821(6)	5967(3)	43(2)	20(1)
O(3)	2996(5)	5680(3)	1688(2)	20(1)
O(7)	7908(5)	7436(3)	-926(2)	16(1)
O(12)	9036(5)	7027(3)	588(2)	20(1)
O(4)	6336(5)	8751(3)	903(2)	17(1)
O(5)	3711(5)	9602(3)	1566(2)	22(1)
O(6)	5094(5)	10575(3)	640(2)	21(1)
O(13)	3705(5)	7366(3)	-533(2)	21(1)
C(24)	-1077(11)	7793(8)	-4556(4)	49(2)
C(21)	2868(9)	8223(6)	-3554(3)	32(2)
C(17)	8048(8)	8198(5)	-2116(3)	19(1)
C(4)	9072(9)	5613(6)	3019(3)	33(2)
C(5)	9805(9)	5574(6)	3655(3)	33(2)
C(11)	9396(8)	9432(5)	2464(3)	23(1)
C(9)	7232(8)	9946(5)	1576(3)	17(1)
C(6)	11878(10)	4933(6)	3739(4)	40(2)
C(10)	7734(8)	9177(5)	2169(3)	19(1)

C(3)	7055(9)	6300(5)	2916(3)	25(2)
C(1)	4293(8)	6964(5)	2188(3)	22(1)
C(14)	12624(11)	8202(6)	3876(4)	39(2)
C(16)	14477(12)	9382(6)	4253(4)	46(2)
C(8)	14602(11)	4179(6)	4466(4)	48(2)
C(7)	12547(10)	4831(6)	4392(4)	39(2)
C(2)	6297(9)	6258(5)	2298(3)	27(2)
C(18)	6591(8)	7601(5)	-2259(3)	23(1)
C(19)	5469(8)	8173(5)	-2825(3)	24(1)
C(23)	412(12)	8306(7)	-4338(4)	46(2)
C(20)	3947(9)	7636(6)	-2985(3)	30(2)
C(22)	1338(9)	7722(6)	-3746(3)	32(2)
C(13)	11864(9)	8930(5)	3294(3)	27(2)
C(12)	10065(9)	8703(5)	3065(3)	27(2)
C(15)	14564(11)	8333(6)	4074(4)	40(2)
O(15)	6043(5)	4407(3)	1041(2)	20(1)
O(16)	944(6)	5039(3)	883(2)	20(1)

Table 30 Bond lengths [Å] and angles [°] for JN198m.

Nd(1)-O(10)	2.662(4)
Nd(1)-O(11)	2.711(4)
Nd(1)-O(1)	2.428(4)
Nd(1)-O(14)	2.469(4)
Nd(1)-O(7)	2.459(4)
Nd(1)-O(12)	2.443(4)
Nd(1)-O(4)	2.432(4)
Nd(1)-O(6)#1	2.403(4)
Nd(1)-O(13)	2.445(4)
S(1)-O(2)	1.464(4)
S(1)-O(1)	1.455(4)
S(1)-O(3)	1.457(4)
S(1)-C(1)	1.755(6)

S(2)-O(4)	1.460(4)
S(2)-O(5)	1.437(4)
S(2)-O(6)	1.460(4)
S(2)-C(9)	1.759(6)
S(3)-O(8)	1.460(4)
S(3)-O(9)	1.458(4)
S(3)-O(7)	1.462(4)
S(3)-C(17)	1.765(6)
O(10)-H(10A)	0.863(10)
O(10)-H(10B)	0.866(10)
O(11)-H(11A)	0.867(10)
O(11)-H(11B)	0.867(10)
O(14)-H(14A)	0.865(10)
O(14)-H(14B)	0.867(10)
O(12)-H(12A)	0.873(10)
O(12)-H(12B)	0.871(10)
O(6)-Nd(1)#1	2.403(4)
O(13)-H(13A)	0.874(10)
O(13)-H(13B)	0.868(10)
C(24)-H(24A)	0.9800
C(24)-H(24B)	0.9800
C(24)-H(24C)	0.9800
C(24)-C(23)	1.533(10)
C(21)-H(21A)	0.9900
C(21)-H(21B)	0.9900
C(21)-C(20)	1.514(9)
C(21)-C(22)	1.521(9)
C(17)-H(17A)	0.9900
C(17)-H(17B)	0.9900
C(17)-C(18)	1.525(8)
C(4)-H(4A)	0.9900
C(4)-H(4B)	0.9900
C(4)-C(5)	1.512(9)
C(4)-C(3)	1.516(8)

C(5)-H(5A)	0.9900
C(5)-H(5B)	0.9900
C(5)-C(6)	1.521(9)
C(11)-H(11C)	0.9900
C(11)-H(11D)	0.9900
C(11)-C(10)	1.521(8)
C(11)-C(12)	1.527(9)
C(9)-H(9A)	0.9900
C(9)-H(9B)	0.9900
C(9)-C(10)	1.515(8)
C(6)-H(6A)	0.9900
C(6)-H(6B)	0.9900
C(6)-C(7)	1.512(10)
C(10)-H(10C)	0.9900
C(10)-H(10D)	0.9900
C(3)-H(3A)	0.9900
C(3)-H(3B)	0.9900
C(3)-C(2)	1.509(9)
C(1)-H(1A)	0.9900
C(1)-H(1B)	0.9900
C(1)-C(2)	1.520(8)
C(14)-H(14C)	0.9900
C(14)-H(14D)	0.9900
C(14)-C(13)	1.514(9)
C(14)-C(15)	1.526(9)
C(16)-H(16A)	0.9800
C(16)-H(16B)	0.9800
C(16)-H(16C)	0.9800
C(16)-C(15)	1.521(11)
C(8)-H(8A)	0.9800
C(8)-H(8B)	0.9800
C(8)-H(8C)	0.9800
C(8)-C(7)	1.513(10)
C(7)-H(7A)	0.9900

C(7)-H(7B)	0.9900
C(2)-H(2A)	0.9900
C(2)-H(2B)	0.9900
C(18)-H(18A)	0.9900
C(18)-H(18B)	0.9900
C(18)-C(19)	1.519(8)
C(19)-H(19A)	0.9900
C(19)-H(19B)	0.9900
C(19)-C(20)	1.521(9)
C(23)-H(23A)	0.9900
C(23)-H(23B)	0.9900
C(23)-C(22)	1.505(10)
C(20)-H(20A)	0.9900
C(20)-H(20B)	0.9900
C(22)-H(22A)	0.9900
C(22)-H(22B)	0.9900
C(13)-H(13C)	0.9900
C(13)-H(13D)	0.9900
C(13)-C(12)	1.517(9)
C(12)-H(12C)	0.9900
C(12)-H(12D)	0.9900
C(15)-H(15A)	0.9900
C(15)-H(15B)	0.9900
O(15)-H(15C)	0.872(10)
O(15)-H(15D)	0.873(10)
O(16)-H(16D)	0.869(10)
O(16)-H(16E)	0.871(10)

O(10)-Nd(1)-O(11)	117.42(12)
O(1)-Nd(1)-O(10)	68.99(13)
O(1)-Nd(1)-O(11)	138.84(12)
O(1)-Nd(1)-O(14)	68.19(13)
O(1)-Nd(1)-O(7)	136.63(13)
O(1)-Nd(1)-O(12)	80.50(13)

O(1)-Nd(1)-O(4)	75.67(14)
O(1)-Nd(1)-O(13)	87.42(14)
O(14)-Nd(1)-O(10)	121.21(13)
O(14)-Nd(1)-O(11)	121.36(12)
O(7)-Nd(1)-O(10)	135.72(12)
O(7)-Nd(1)-O(11)	69.85(12)
O(7)-Nd(1)-O(14)	68.51(13)
O(12)-Nd(1)-O(10)	137.11(13)
O(12)-Nd(1)-O(11)	68.67(13)
O(12)-Nd(1)-O(14)	69.81(13)
O(12)-Nd(1)-O(7)	87.10(13)
O(12)-Nd(1)-O(13)	138.64(13)
O(4)-Nd(1)-O(10)	74.15(12)
O(4)-Nd(1)-O(11)	68.48(13)
O(4)-Nd(1)-O(14)	128.81(14)
O(4)-Nd(1)-O(7)	137.29(12)
O(4)-Nd(1)-O(12)	69.48(13)
O(4)-Nd(1)-O(13)	144.61(13)
O(6)#1-Nd(1)-O(10)	66.26(13)
O(6)#1-Nd(1)-O(11)	67.32(12)
O(6)#1-Nd(1)-O(1)	135.25(13)
O(6)#1-Nd(1)-O(14)	138.58(14)
O(6)#1-Nd(1)-O(7)	79.81(14)
O(6)#1-Nd(1)-O(12)	135.94(14)
O(6)#1-Nd(1)-O(4)	92.57(14)
O(6)#1-Nd(1)-O(13)	77.75(14)
O(13)-Nd(1)-O(10)	70.78(12)
O(13)-Nd(1)-O(11)	133.71(14)
O(13)-Nd(1)-O(14)	68.97(14)
O(13)-Nd(1)-O(7)	75.01(13)
O(2)-S(1)-C(1)	107.4(3)
O(1)-S(1)-O(2)	111.7(2)
O(1)-S(1)-O(3)	111.1(2)
O(1)-S(1)-C(1)	106.4(3)

O(3)-S(1)-O(2)	113.4(2)
O(3)-S(1)-C(1)	106.3(3)
O(4)-S(2)-C(9)	106.2(2)
O(5)-S(2)-O(4)	112.4(2)
O(5)-S(2)-O(6)	113.1(2)
O(5)-S(2)-C(9)	109.3(3)
O(6)-S(2)-O(4)	110.4(2)
O(6)-S(2)-C(9)	104.8(3)
O(8)-S(3)-O(7)	111.7(2)
O(8)-S(3)-C(17)	107.0(3)
O(9)-S(3)-O(8)	112.6(2)
O(9)-S(3)-O(7)	111.7(2)
O(9)-S(3)-C(17)	107.1(3)
O(7)-S(3)-C(17)	106.3(3)
Nd(1)-O(10)-H(10A)	116(3)
Nd(1)-O(10)-H(10B)	116(3)
H(10A)-O(10)-H(10B)	112(3)
Nd(1)-O(11)-H(11A)	108(3)
Nd(1)-O(11)-H(11B)	108(3)
H(11A)-O(11)-H(11B)	111(3)
S(1)-O(1)-Nd(1)	155.7(3)
Nd(1)-O(14)-H(14A)	124.5(18)
Nd(1)-O(14)-H(14B)	124.3(17)
H(14A)-O(14)-H(14B)	110(3)
S(3)-O(7)-Nd(1)	154.2(2)
Nd(1)-O(12)-H(12A)	120(2)
Nd(1)-O(12)-H(12B)	121(2)
H(12A)-O(12)-H(12B)	108(2)
S(2)-O(4)-Nd(1)	140.6(2)
S(2)-O(6)-Nd(1)#1	168.2(3)
Nd(1)-O(13)-H(13A)	125.2(17)
Nd(1)-O(13)-H(13B)	126.5(17)
H(13A)-O(13)-H(13B)	107(2)
H(24A)-C(24)-H(24B)	109.5

H(24A)-C(24)-H(24C)	109.5
H(24B)-C(24)-H(24C)	109.5
C(23)-C(24)-H(24A)	109.5
C(23)-C(24)-H(24B)	109.5
C(23)-C(24)-H(24C)	109.5
H(21A)-C(21)-H(21B)	107.5
C(20)-C(21)-H(21A)	108.4
C(20)-C(21)-H(21B)	108.4
C(20)-C(21)-C(22)	115.4(6)
C(22)-C(21)-H(21A)	108.4
C(22)-C(21)-H(21B)	108.4
S(3)-C(17)-H(17A)	109.0
S(3)-C(17)-H(17B)	109.0
H(17A)-C(17)-H(17B)	107.8
C(18)-C(17)-S(3)	113.0(4)
C(18)-C(17)-H(17A)	109.0
C(18)-C(17)-H(17B)	109.0
H(4A)-C(4)-H(4B)	107.6
C(5)-C(4)-H(4A)	108.6
C(5)-C(4)-H(4B)	108.6
C(5)-C(4)-C(3)	114.6(6)
C(3)-C(4)-H(4A)	108.6
C(3)-C(4)-H(4B)	108.6
C(4)-C(5)-H(5A)	108.7
C(4)-C(5)-H(5B)	108.7
C(4)-C(5)-C(6)	114.1(6)
H(5A)-C(5)-H(5B)	107.6
C(6)-C(5)-H(5A)	108.7
C(6)-C(5)-H(5B)	108.7
H(11C)-C(11)-H(11D)	107.5
C(10)-C(11)-H(11C)	108.5
C(10)-C(11)-H(11D)	108.5
C(10)-C(11)-C(12)	115.1(5)
C(12)-C(11)-H(11C)	108.5

C(12)-C(11)-H(11D)	108.5
S(2)-C(9)-H(9A)	108.5
S(2)-C(9)-H(9B)	108.5
H(9A)-C(9)-H(9B)	107.5
C(10)-C(9)-S(2)	115.0(4)
C(10)-C(9)-H(9A)	108.5
C(10)-C(9)-H(9B)	108.5
C(5)-C(6)-H(6A)	108.8
C(5)-C(6)-H(6B)	108.8
H(6A)-C(6)-H(6B)	107.7
C(7)-C(6)-C(5)	113.9(6)
C(7)-C(6)-H(6A)	108.8
C(7)-C(6)-H(6B)	108.8
C(11)-C(10)-H(10C)	109.7
C(11)-C(10)-H(10D)	109.7
C(9)-C(10)-C(11)	109.8(5)
C(9)-C(10)-H(10C)	109.7
C(9)-C(10)-H(10D)	109.7
H(10C)-C(10)-H(10D)	108.2
C(4)-C(3)-H(3A)	108.9
C(4)-C(3)-H(3B)	108.9
H(3A)-C(3)-H(3B)	107.7
C(2)-C(3)-C(4)	113.3(5)
C(2)-C(3)-H(3A)	108.9
C(2)-C(3)-H(3B)	108.9
S(1)-C(1)-H(1A)	109.0
S(1)-C(1)-H(1B)	109.0
H(1A)-C(1)-H(1B)	107.8
C(2)-C(1)-S(1)	112.9(4)
C(2)-C(1)-H(1A)	109.0
C(2)-C(1)-H(1B)	109.0
H(14C)-C(14)-H(14D)	107.5
C(13)-C(14)-H(14C)	108.4
C(13)-C(14)-H(14D)	108.4

C(13)-C(14)-C(15)	115.4(6)
C(15)-C(14)-H(14C)	108.4
C(15)-C(14)-H(14D)	108.4
H(16A)-C(16)-H(16B)	109.5
H(16A)-C(16)-H(16C)	109.5
H(16B)-C(16)-H(16C)	109.5
C(15)-C(16)-H(16A)	109.5
C(15)-C(16)-H(16B)	109.5
C(15)-C(16)-H(16C)	109.5
H(8A)-C(8)-H(8B)	109.5
H(8A)-C(8)-H(8C)	109.5
H(8B)-C(8)-H(8C)	109.5
C(7)-C(8)-H(8A)	109.5
C(7)-C(8)-H(8B)	109.5
C(7)-C(8)-H(8C)	109.5
C(6)-C(7)-C(8)	112.9(6)
C(6)-C(7)-H(7A)	109.0
C(6)-C(7)-H(7B)	109.0
C(8)-C(7)-H(7A)	109.0
C(8)-C(7)-H(7B)	109.0
H(7A)-C(7)-H(7B)	107.8
C(3)-C(2)-C(1)	113.4(5)
C(3)-C(2)-H(2A)	108.9
C(3)-C(2)-H(2B)	108.9
C(1)-C(2)-H(2A)	108.9
C(1)-C(2)-H(2B)	108.9
H(2A)-C(2)-H(2B)	107.7
C(17)-C(18)-H(18A)	109.4
C(17)-C(18)-H(18B)	109.4
H(18A)-C(18)-H(18B)	108.0
C(19)-C(18)-C(17)	111.1(5)
C(19)-C(18)-H(18A)	109.4
C(19)-C(18)-H(18B)	109.4
C(18)-C(19)-H(19A)	108.7

C(18)-C(19)-H(19B)	108.7
C(18)-C(19)-C(20)	114.1(5)
H(19A)-C(19)-H(19B)	107.6
C(20)-C(19)-H(19A)	108.7
C(20)-C(19)-H(19B)	108.7
C(24)-C(23)-H(23A)	108.8
C(24)-C(23)-H(23B)	108.8
H(23A)-C(23)-H(23B)	107.7
C(22)-C(23)-C(24)	113.9(7)
C(22)-C(23)-H(23A)	108.8
C(22)-C(23)-H(23B)	108.8
C(21)-C(20)-C(19)	112.6(6)
C(21)-C(20)-H(20A)	109.1
C(21)-C(20)-H(20B)	109.1
C(19)-C(20)-H(20A)	109.1
C(19)-C(20)-H(20B)	109.1
H(20A)-C(20)-H(20B)	107.8
C(21)-C(22)-H(22A)	109.0
C(21)-C(22)-H(22B)	109.0
C(23)-C(22)-C(21)	112.8(6)
C(23)-C(22)-H(22A)	109.0
C(23)-C(22)-H(22B)	109.0
H(22A)-C(22)-H(22B)	107.8
C(14)-C(13)-H(13C)	108.7
C(14)-C(13)-H(13D)	108.7
C(14)-C(13)-C(12)	114.3(6)
H(13C)-C(13)-H(13D)	107.6
C(12)-C(13)-H(13C)	108.7
C(12)-C(13)-H(13D)	108.7
C(11)-C(12)-H(12C)	109.1
C(11)-C(12)-H(12D)	109.1
C(13)-C(12)-C(11)	112.3(6)
C(13)-C(12)-H(12C)	109.1
C(13)-C(12)-H(12D)	109.1

H(12C)-C(12)-H(12D)	107.9
C(14)-C(15)-H(15A)	108.7
C(14)-C(15)-H(15B)	108.7
C(16)-C(15)-C(14)	114.3(7)
C(16)-C(15)-H(15A)	108.7
C(16)-C(15)-H(15B)	108.7
H(15A)-C(15)-H(15B)	107.6
H(15C)-O(15)-H(15D)	106(2)
H(16D)-O(16)-H(16E)	109(2)

Symmetry transformations used to generate equivalent atoms:
#1 -x+1,-y+2,-z

Table 31 Anisotropic displacement parameters ($Å^2 x\ 10^3$)for JN198m. The anisotropic displacement factor exponent takes the form: $-2\pi^2[h^2 a^{*2} U^{11} + ... + 2\ h\ k\ a^*\ b^*\ U^{12}]$

	U^{11}	U^{22}	U^{33}	U^{23}	U^{13}	U^{12}
Nd(1)	5(1)	4(1)	28(1)	-3(1)	-2(1)	0(1)
S(1)	12(1)	10(1)	27(1)	-2(1)	-1(1)	-3(1)
S(2)	10(1)	6(1)	26(1)	-3(1)	0(1)	-1(1)
S(3)	12(1)	10(1)	25(1)	-3(1)	-1(1)	-1(1)
O(10)	10(2)	12(2)	29(2)	-5(2)	-4(2)	0(2)
O(8)	18(2)	16(2)	26(2)	-3(2)	-3(2)	-4(2)
O(11)	14(2)	3(2)	28(2)	-4(2)	1(2)	-1(2)
O(2)	15(2)	11(2)	32(3)	-2(2)	-3(2)	-2(2)
O(9)	12(2)	10(2)	33(3)	-9(2)	1(2)	2(2)
O(1)	9(2)	14(2)	32(2)	-1(2)	-1(2)	-3(2)
O(14)	16(2)	8(2)	33(3)	-3(2)	2(2)	-2(2)
O(3)	17(2)	10(2)	34(3)	-1(2)	-2(2)	-6(2)
O(7)	13(2)	8(2)	28(2)	-5(2)	2(2)	-6(2)
O(12)	13(2)	8(2)	38(3)	-6(2)	-7(2)	-1(2)

O(4)	14(2)	11(2)	29(2)	-11(2)	-1(2)	-2(2)
O(5)	15(2)	17(3)	35(3)	-8(2)	6(2)	-6(2)
O(6)	16(2)	10(2)	36(3)	1(2)	-6(2)	0(2)
O(13)	12(2)	12(2)	39(3)	-10(2)	-6(2)	4(2)
C(24)	40(4)	76(7)	40(5)	-15(4)	-15(4)	-20(4)
C(21)	25(3)	42(5)	29(4)	-11(3)	-5(3)	-1(3)
C(17)	20(3)	13(3)	24(3)	-2(3)	-2(2)	-1(2)
C(4)	23(3)	44(5)	29(4)	2(3)	-7(3)	-7(3)
C(5)	28(3)	41(5)	32(4)	-4(3)	-7(3)	-10(3)
C(11)	19(3)	20(4)	28(4)	-6(3)	-2(3)	-1(2)
C(9)	14(3)	13(3)	24(3)	-5(3)	1(2)	-7(2)
C(6)	31(4)	38(5)	48(5)	5(4)	-9(3)	-7(3)
C(10)	12(3)	17(3)	30(4)	-7(3)	-1(2)	-5(2)
C(3)	24(3)	21(4)	32(4)	-6(3)	-6(3)	-4(3)
C(1)	23(3)	14(4)	29(4)	-3(3)	0(3)	-3(2)
C(14)	42(4)	37(5)	40(5)	1(4)	-14(3)	-13(3)
C(16)	53(5)	45(6)	45(5)	-1(4)	-16(4)	-19(4)
C(8)	47(5)	37(5)	58(6)	-4(4)	-23(4)	-1(4)
C(7)	38(4)	31(5)	48(5)	-3(4)	-23(4)	-1(3)
C(2)	23(3)	27(4)	26(4)	0(3)	-4(3)	0(3)
C(18)	19(3)	22(4)	30(4)	-4(3)	-2(3)	-7(3)
C(19)	18(3)	24(4)	26(4)	-2(3)	-4(3)	0(3)
C(23)	51(5)	48(6)	43(5)	-3(4)	-20(4)	-12(4)
C(20)	24(3)	37(5)	28(4)	-6(3)	-3(3)	-8(3)
C(22)	25(3)	45(5)	29(4)	-16(3)	-2(3)	-2(3)
C(13)	27(3)	26(4)	28(4)	-5(3)	-1(3)	-9(3)
C(12)	26(3)	26(4)	30(4)	-8(3)	-1(3)	-7(3)
C(15)	37(4)	43(5)	41(5)	-2(4)	-19(3)	-8(3)
O(15)	11(2)	11(2)	37(3)	-6(2)	-4(2)	4(2)
O(16)	14(2)	5(2)	41(3)	-4(2)	-1(2)	-1(2)

Table 32 Hydrogen coordinates (x 10^4) and isotropic displacement parameters ($Å^2$x 10^3) for JN198m.

	x	y	z	U(eq)
H(24A)	-1592	8202	-4948	74
H(24B)	-2163	7753	-4230	74
H(24C)	-426	7095	-4629	74
H(21A)	3850	8313	-3916	39
H(21B)	2208	8920	-3466	39
H(17A)	7322	8891	-2039	23
H(17B)	8989	8293	-2489	23
H(4A)	9031	4904	2970	39
H(4B)	10028	5861	2687	39
H(5A)	8894	5286	3987	40
H(5B)	9773	6288	3716	40
H(11C)	8966	10142	2561	27
H(11D)	10540	9426	2149	27
H(9A)	8450	9957	1295	20
H(9B)	6763	10643	1692	20
H(6A)	11937	4235	3646	48
H(6B)	12804	5253	3428	48
H(10C)	8140	8471	2066	23
H(10D)	6560	9202	2473	23
H(3A)	6112	6088	3265	31
H(3B)	7117	7021	2929	31
H(1A)	4433	7691	2116	27
H(1B)	3398	6858	2571	27
H(14C)	12795	7484	3801	47
H(14D)	11611	8299	4231	47
H(16A)	14226	9920	3882	69
H(16B)	15734	9386	4410	69
H(16C)	13415	9516	4584	69
H(8A)	15542	4503	4173	72
H(8B)	14651	3489	4375	72
H(8C)	14946	4123	4899	72

H(7A)	11617	4517	4704	47
H(7B)	12512	5528	4483	47
H(2A)	6207	5540	2289	32
H(2B)	7253	6455	1949	32
H(18A)	7310	6912	-2344	28
H(18B)	5649	7500	-1887	28
H(19A)	6422	8260	-3195	28
H(19B)	4797	8871	-2741	28
H(23A)	1465	8376	-4679	56
H(23B)	-260	9009	-4265	56
H(20A)	4611	6937	-3068	35
H(20B)	2980	7556	-2618	35
H(22A)	1969	7010	-3811	39
H(22B)	294	7678	-3398	39
H(13C)	12928	8894	2950	32
H(13D)	11535	9644	3386	32
H(12C)	8976	8767	3400	32
H(12D)	10370	7983	2984	32
H(15A)	14971	7791	4438	48
H(15B)	15586	8226	3723	48
H(14A)	6640(90)	5502(16)	365(12)	30
H(14B)	7490(80)	5682(19)	-265(14)	30
H(16D)	400(90)	4540(40)	1090(20)	30
H(16E)	1460(90)	5290(40)	1150(20)	30
H(15C)	7010(60)	4080(50)	1270(20)	30
H(15D)	5170(60)	4740(50)	1290(20)	30
H(11A)	9360(80)	8880(30)	-632(13)	30
H(11B)	8250(60)	9635(12)	-270(20)	30
H(13A)	3870(60)	6780(20)	-670(30)	30
H(13B)	2700(60)	7780(20)	-710(30)	30
H(12A)	9320(70)	7270(30)	907(19)	30
H(12B)	9430(70)	6358(9)	650(20)	30
H(10A)	1520(40)	8830(50)	126(15)	30

H(10B)	1980(50)	8670(50)	769(7)	30

Table 33 Torsion angles [°] for JN198m.

S(1)-C(1)-C(2)-C(3)	-169.4(5)
S(2)-C(9)-C(10)-C(11)	176.0(4)
S(3)-C(17)-C(18)-C(19)	179.3(4)
O(10)-Nd(1)-O(1)-S(1)	-15.4(6)
O(10)-Nd(1)-O(7)-S(3)	104.0(5)
O(10)-Nd(1)-O(4)-S(2)	-33.2(4)
O(8)-S(3)-O(7)-Nd(1)	11.5(6)
O(8)-S(3)-C(17)-C(18)	-177.0(4)
O(11)-Nd(1)-O(1)-S(1)	92.7(6)
O(11)-Nd(1)-O(7)-S(3)	-5.1(5)
O(11)-Nd(1)-O(4)-S(2)	95.6(4)
O(2)-S(1)-O(1)-Nd(1)	21.9(7)
O(2)-S(1)-C(1)-C(2)	-177.3(4)
O(9)-S(3)-O(7)-Nd(1)	138.6(5)
O(9)-S(3)-C(17)-C(18)	62.1(5)
O(1)-Nd(1)-O(7)-S(3)	-146.3(5)
O(1)-Nd(1)-O(4)-S(2)	-105.0(4)
O(1)-S(1)-C(1)-C(2)	-57.6(5)
O(14)-Nd(1)-O(1)-S(1)	-154.1(6)
O(14)-Nd(1)-O(7)-S(3)	-142.8(6)
O(14)-Nd(1)-O(4)-S(2)	-150.7(3)
O(3)-S(1)-O(1)-Nd(1)	149.7(6)
O(3)-S(1)-C(1)-C(2)	60.9(5)
O(7)-Nd(1)-O(1)-S(1)	-150.6(5)
O(7)-Nd(1)-O(4)-S(2)	109.0(4)
O(7)-S(3)-C(17)-C(18)	-57.4(5)
O(12)-Nd(1)-O(1)-S(1)	134.0(6)
O(12)-Nd(1)-O(7)-S(3)	-73.4(6)
O(12)-Nd(1)-O(4)-S(2)	170.0(4)

O(4)-Nd(1)-O(1)-S(1)	62.9(6)
O(4)-Nd(1)-O(7)-S(3)	-18.3(7)
O(4)-S(2)-O(6)-Nd(1)#1	150.1(12)
O(4)-S(2)-C(9)-C(10)	-67.6(5)
O(5)-S(2)-O(4)-Nd(1)	83.6(4)
O(5)-S(2)-O(6)-Nd(1)#1	23.0(14)
O(5)-S(2)-C(9)-C(10)	53.9(5)
O(6)#1-Nd(1)-O(1)-S(1)	-16.1(7)
O(6)#1-Nd(1)-O(7)-S(3)	64.3(6)
O(6)#1-Nd(1)-O(4)-S(2)	31.3(4)
O(6)-S(2)-O(4)-Nd(1)	-43.8(4)
O(6)-S(2)-C(9)-C(10)	175.4(4)
O(13)-Nd(1)-O(1)-S(1)	-85.8(6)
O(13)-Nd(1)-O(7)-S(3)	144.3(6)
O(13)-Nd(1)-O(4)-S(2)	-41.1(5)
C(24)-C(23)-C(22)-C(21)	177.7(6)
C(17)-S(3)-O(7)-Nd(1)	-104.9(6)
C(17)-C(18)-C(19)-C(20)	-178.5(5)
C(4)-C(5)-C(6)-C(7)	-175.7(7)
C(4)-C(3)-C(2)-C(1)	-178.8(6)
C(5)-C(4)-C(3)-C(2)	-175.5(6)
C(5)-C(6)-C(7)-C(8)	179.3(7)
C(9)-S(2)-O(4)-Nd(1)	-156.9(4)
C(9)-S(2)-O(6)-Nd(1)#1	-95.9(13)
C(10)-C(11)-C(12)-C(13)	173.8(5)
C(3)-C(4)-C(5)-C(6)	-176.6(6)
C(1)-S(1)-O(1)-Nd(1)	-95.0(6)
C(14)-C(13)-C(12)-C(11)	-178.0(6)
C(18)-C(19)-C(20)-C(21)	-179.6(5)
C(20)-C(21)-C(22)-C(23)	-176.3(6)
C(22)-C(21)-C(20)-C(19)	179.3(6)
C(13)-C(14)-C(15)-C(16)	62.5(9)
C(12)-C(11)-C(10)-C(9)	-179.3(5)
C(15)-C(14)-C(13)-C(12)	173.3(6)

Symmetry transformations used to generate equivalent atoms:

#1 -x+1,-y+2,-z

Appendix C

Chapter Four

In-situ formation of $[La(H_2O)MoO_4]_2[1,5\text{-NDS}]$

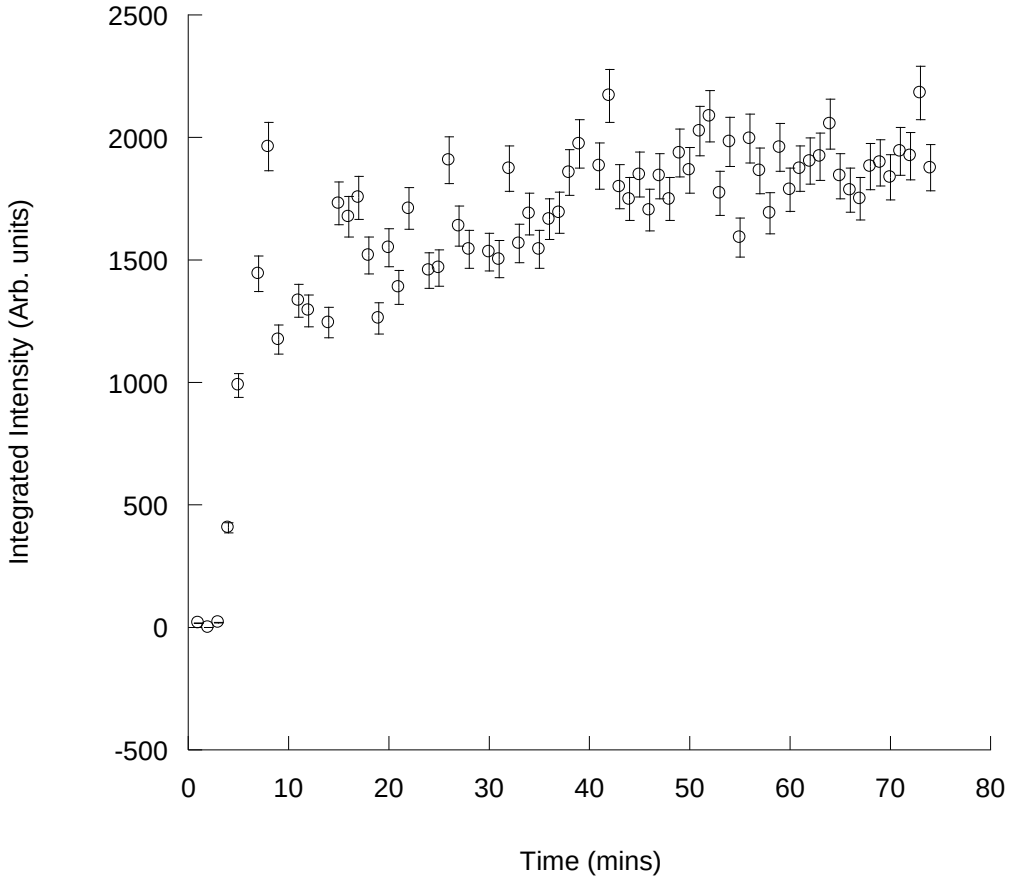

Figure 1 Integrated intensity versus time plot of the formation of $[La(H_2O)MoO_4]_2[1,5\text{-NDS}]$ at 165 °C. (Including errors)

In-situ formation of $[Nd(H_2O)MoO_4]_2$[1,5-NDS]

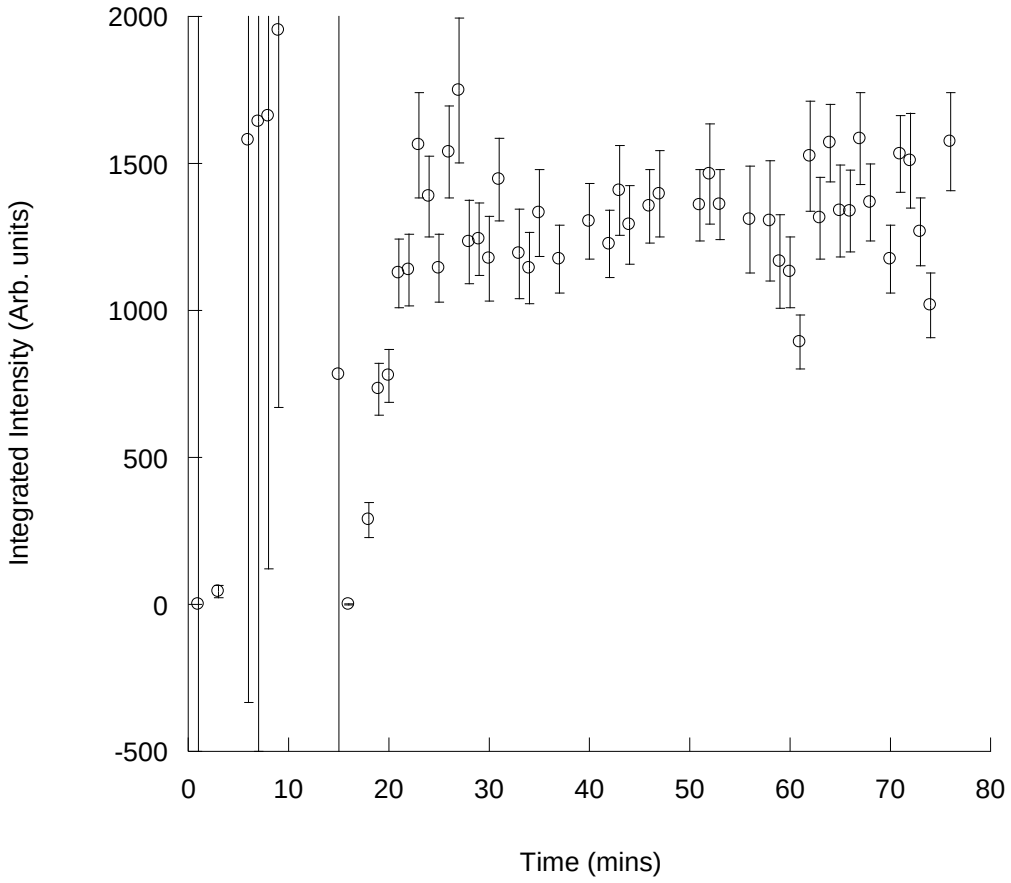

Figure 2 Integrated intensity versus time plot of the formation of $[Nd(H_2O)MoO_4]_2$[1,5-NDS] at 165 °C. (Including errors)

In-situ formation of $[Nd(H_2O)MoO_4]_2$[2,6-NDS]

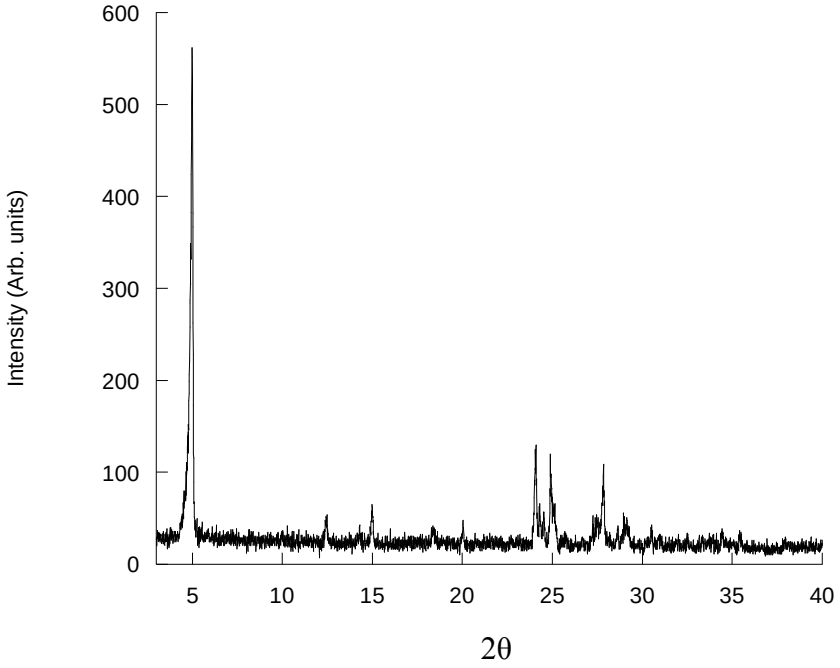

Figure 3 PXRD pattern of the *in-situ* formation of $[Nd(H_2O)MoO_4]_2$[2,6-NDS] at 165 °C.

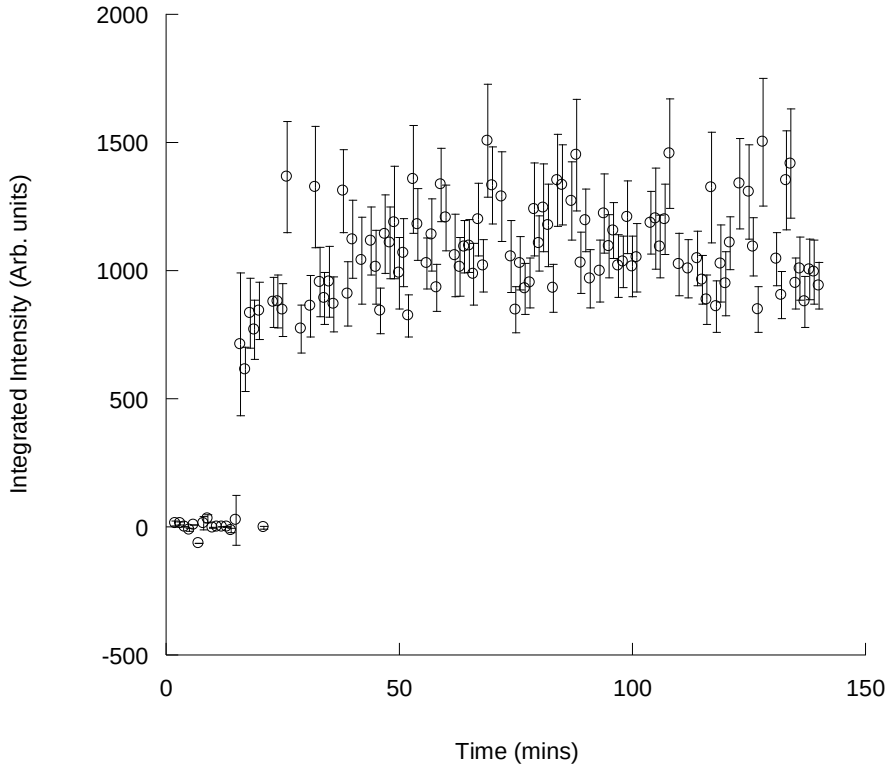

Figure 4 Integrated intensity versus time plot of the formation of $[Nd(H_2O)MoO_4]_2$[2,6-NDS] at 165 °C. (Including errors)

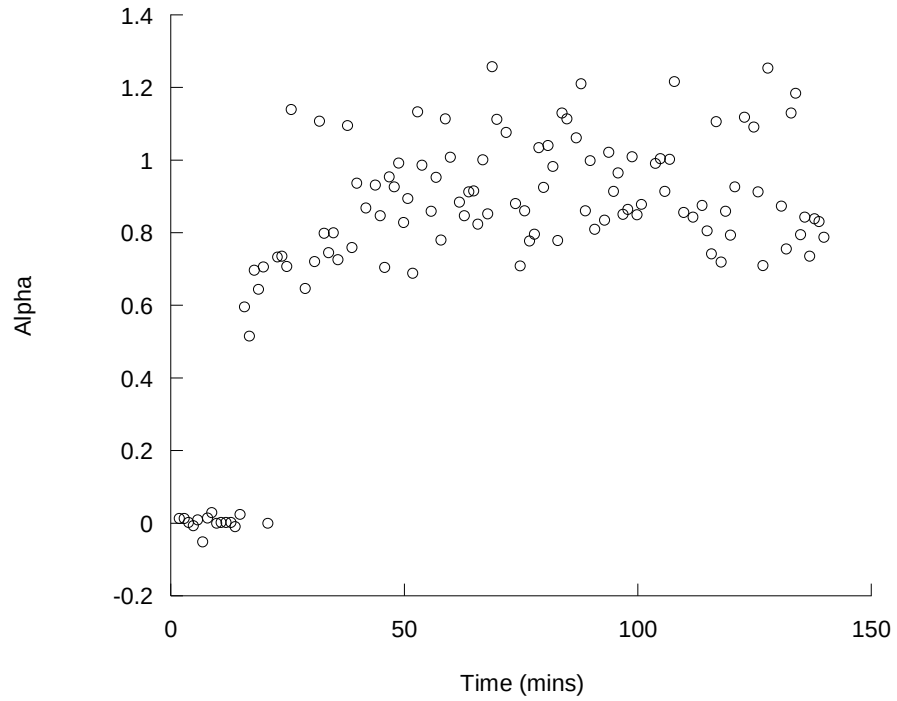

Figure 5 Extent of reaction (α) versus time plot of the formation of $[Nd(H_2O)MoO_4]_2$[2,6-NDS] at 165 °C.

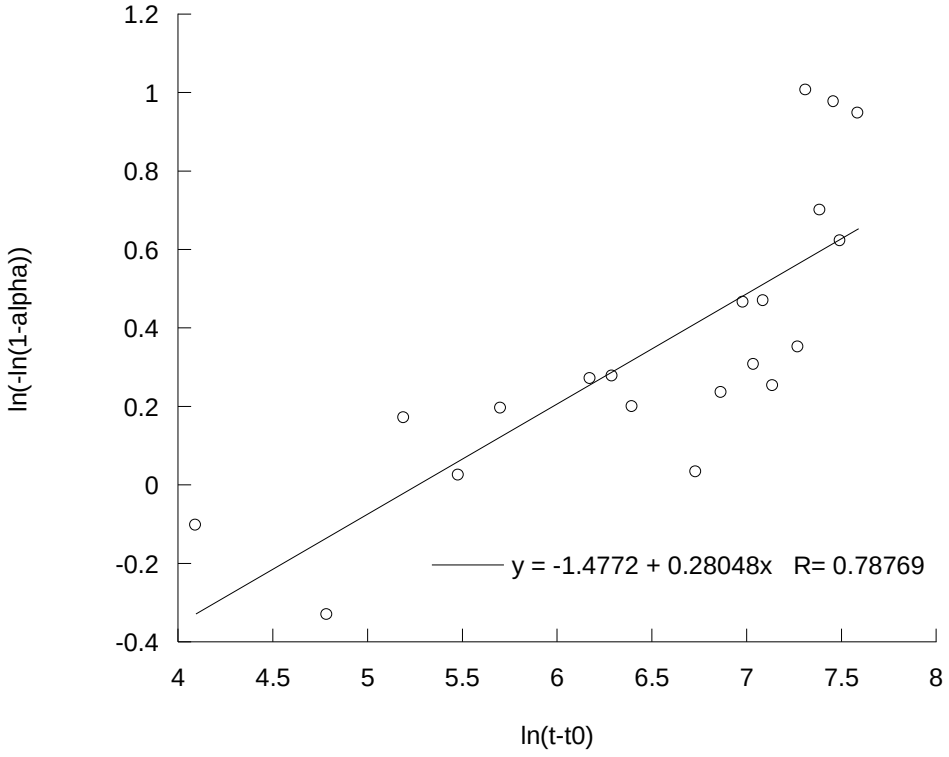

Figure 6 Sharp-Hancock plot of ln(-ln(1-α) versus ln(t-t_0) of the formation of [Nd(H_2O)MoO_4]$_2$[2,6-NDS] at 165 °C.

In-situ formation of [La(H_2O)WO_4]$_2$[1,5-NDS] at various temperatures

Synthesis at 120 °C

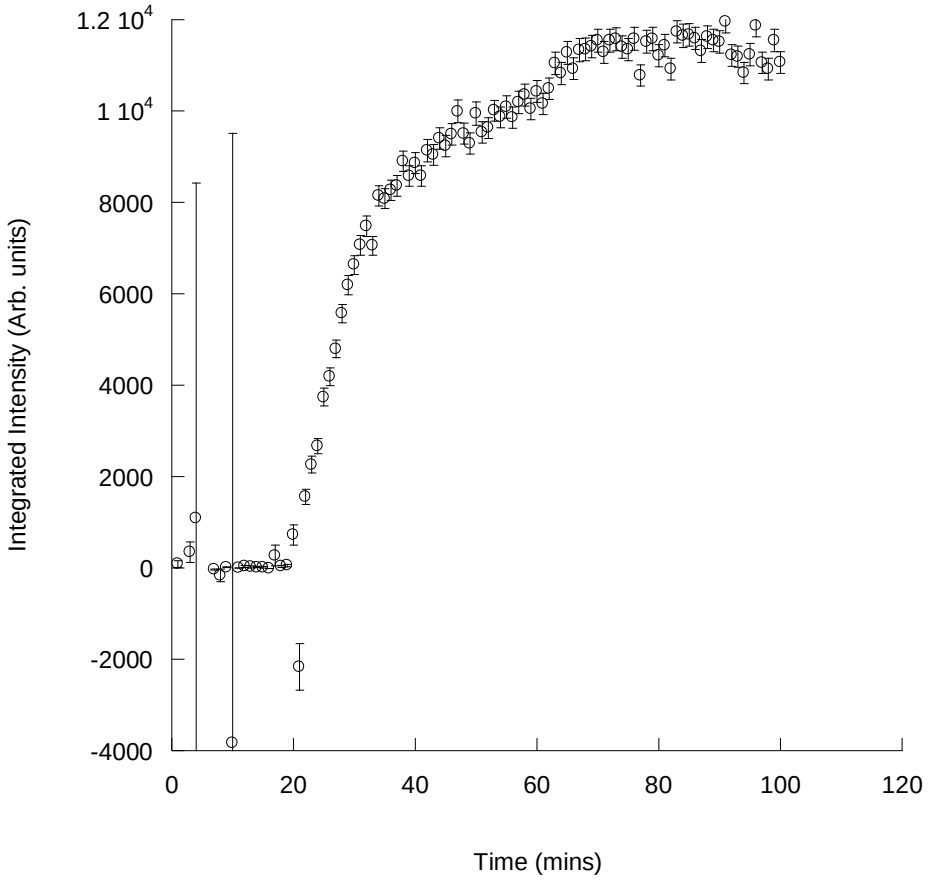

Figure 7 Integrated intensity versus time plot of the formation of [La(H_2O)WO_4]$_2$[1,5-NDS] at 120 °C. (Including errors)

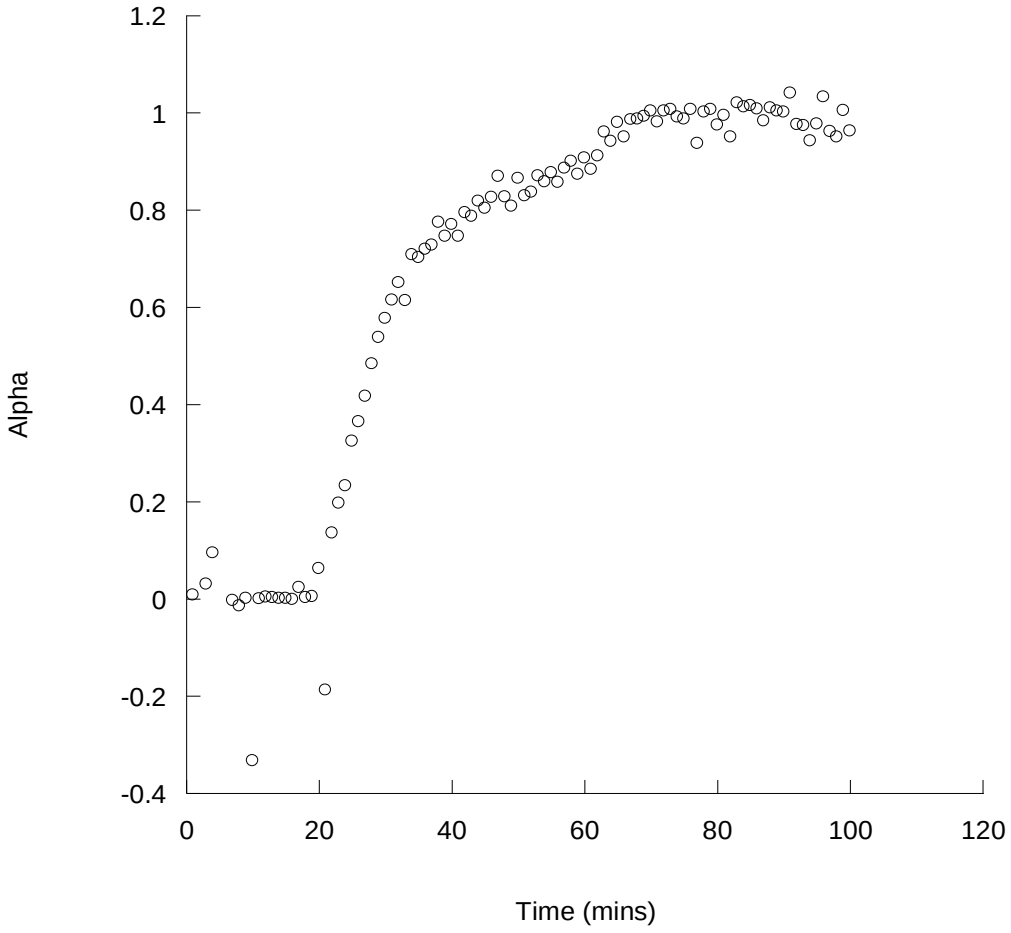

Figure 8 Extent of reaction, α, versus time plot of the formation of $[La(H_2O)WO_4]_2[1,5\text{-NDS}]$ at 120 °C.

Synthesis at 145 °C

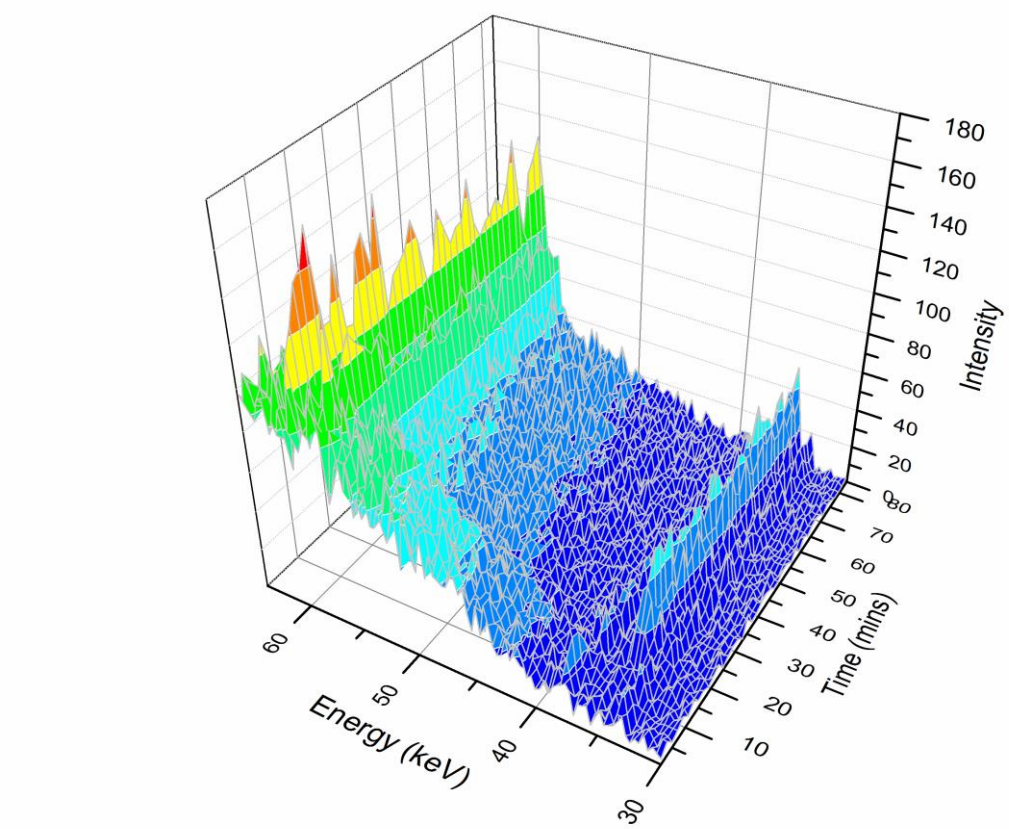

Figure 9 Three-dimensional stacked plot of the time resolved *in-situ* Energy dispersive X-ray diffraction measurements for the formation of $[La(H_2O)WO_4]_2[1,5\text{-}NDS]$ at 145 °C. An acquisition time of 60s was used for each recorded spectrum and a detector angle of 1.19 ° 2θ.

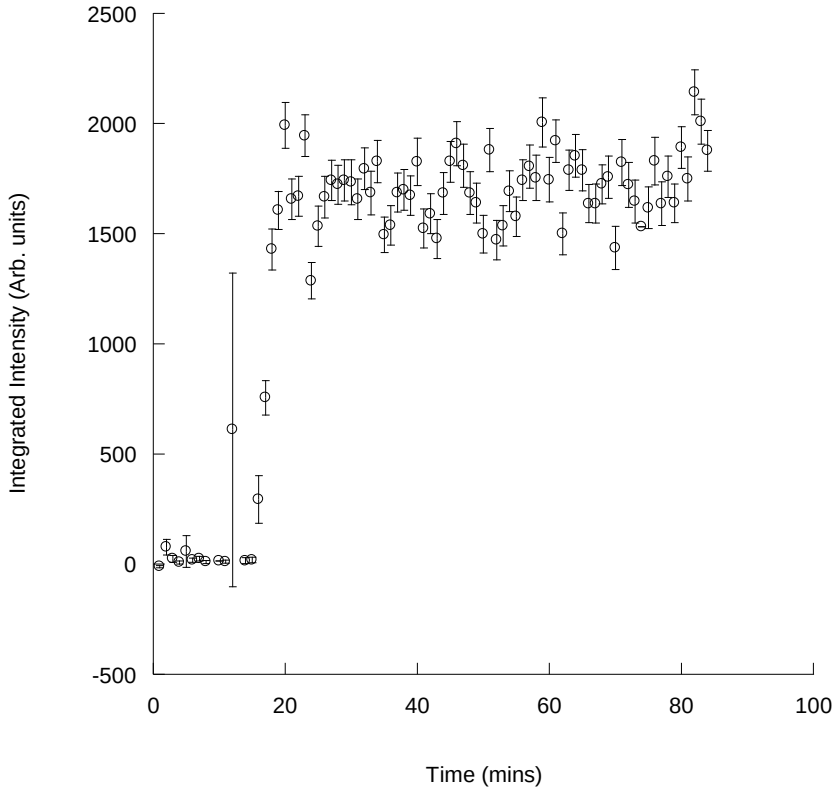

Figure 10 Integrated intensity versus time plot of the formation of $[La(H_2O)WO_4]_2[1,5\text{-NDS}]$ at 145 °C. (Including errors)

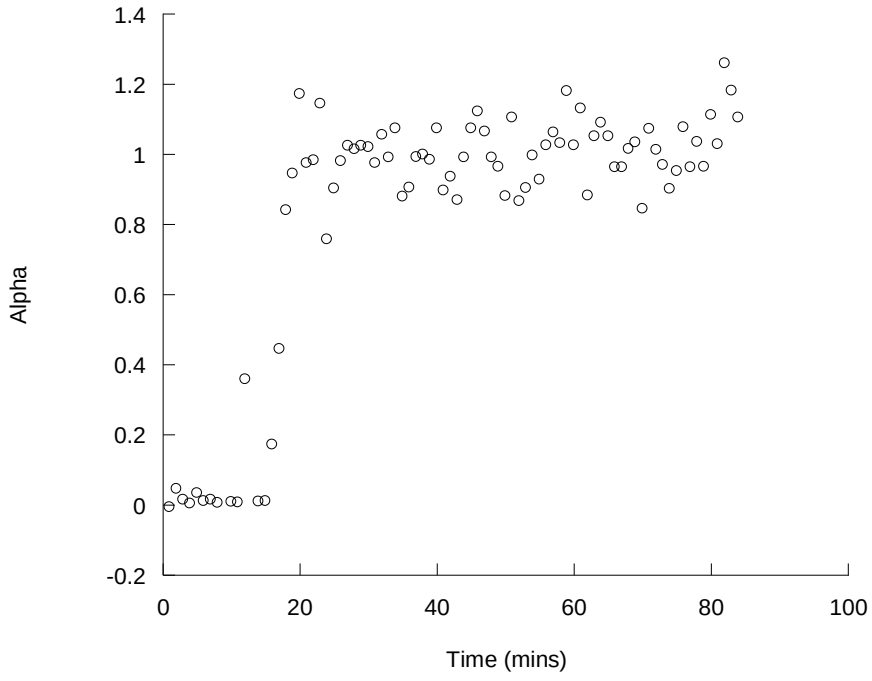

Figure 11 Extent of reaction, α, versus time plot of the formation of $[La(H_2O)WO_4]_2[1,5\text{-NDS}]$ at 145 °C.

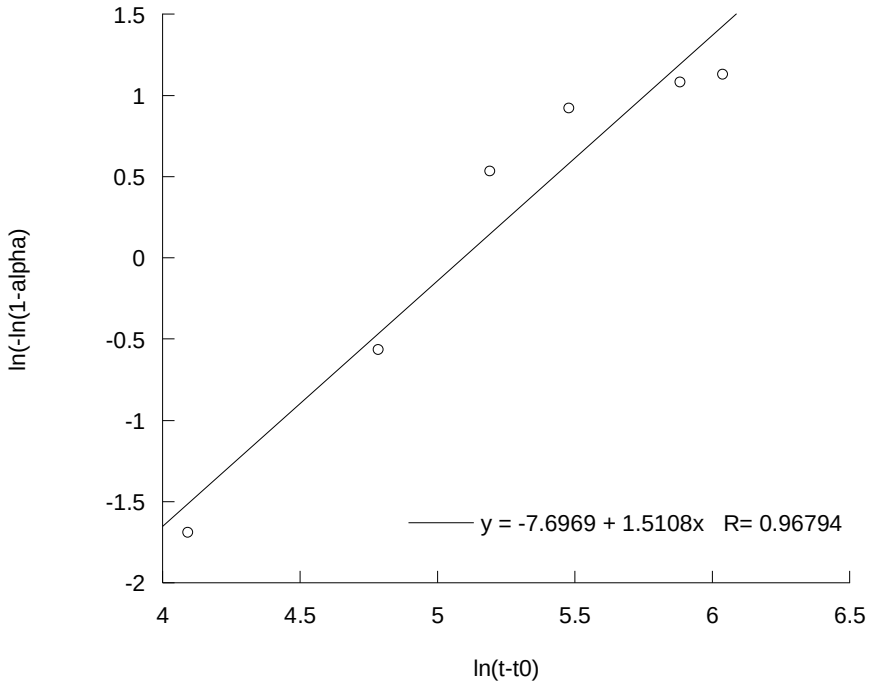

Figure 12 Sharp-Hancock plot of ln(-ln(1-α) versus ln(t-t_0) of the formation of $[La(H_2O)WO_4]_2$[1,5-NDS] at 145 °C.

Synthesis at 165°C

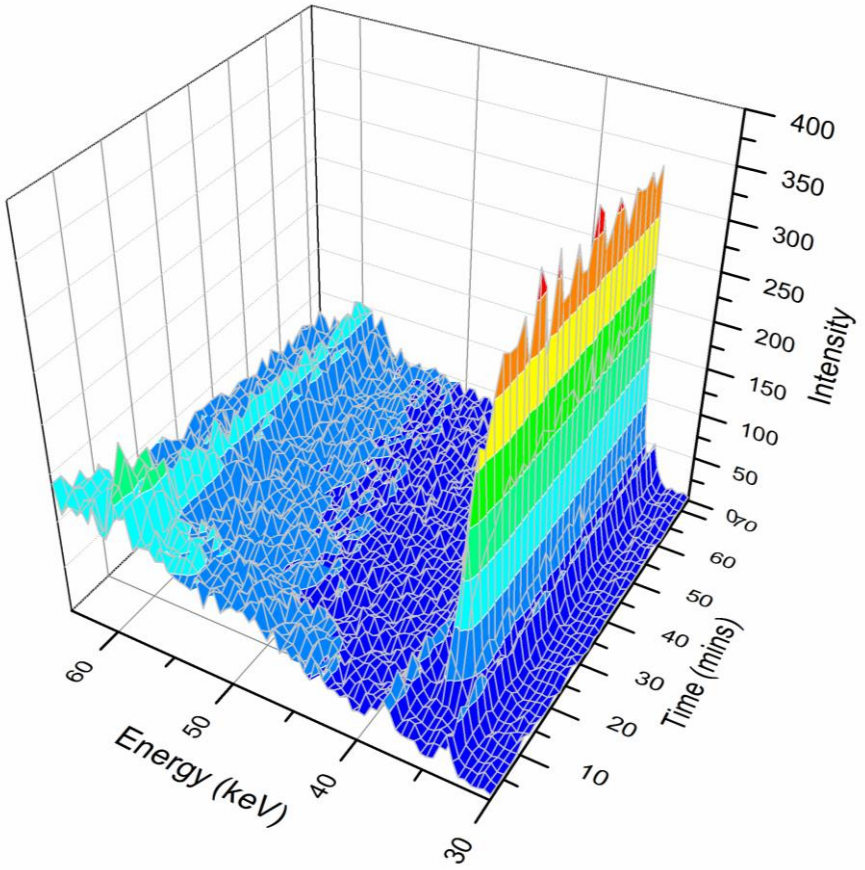

Figure 13 Three-dimensional stacked plot of the time resolved *in-situ* Energy dispersive X-ray diffraction measurements for the formation of $[La(H_2O)WO_4]_2[1,5\text{-}NDS]$ at 165 °C. An acquisition time of 60s was used for each recorded spectrum and a detector angle of 1.19 °2θ.

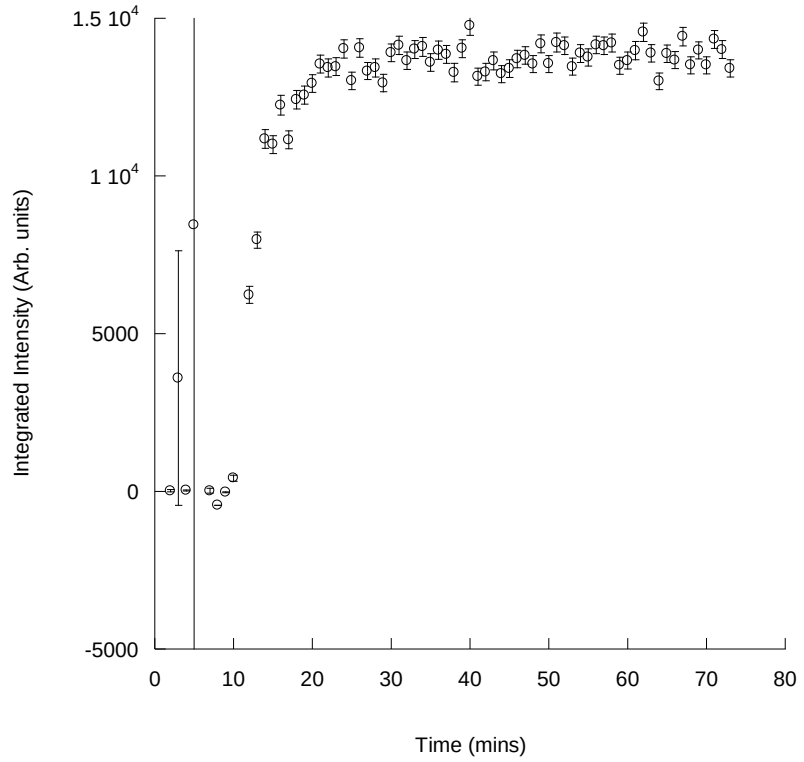

Figure 14 Integrated intensity versus time plot of the formation of $[La(H_2O)WO_4]_2[1,5\text{-NDS}]$ at 165 °C. (Including errors)

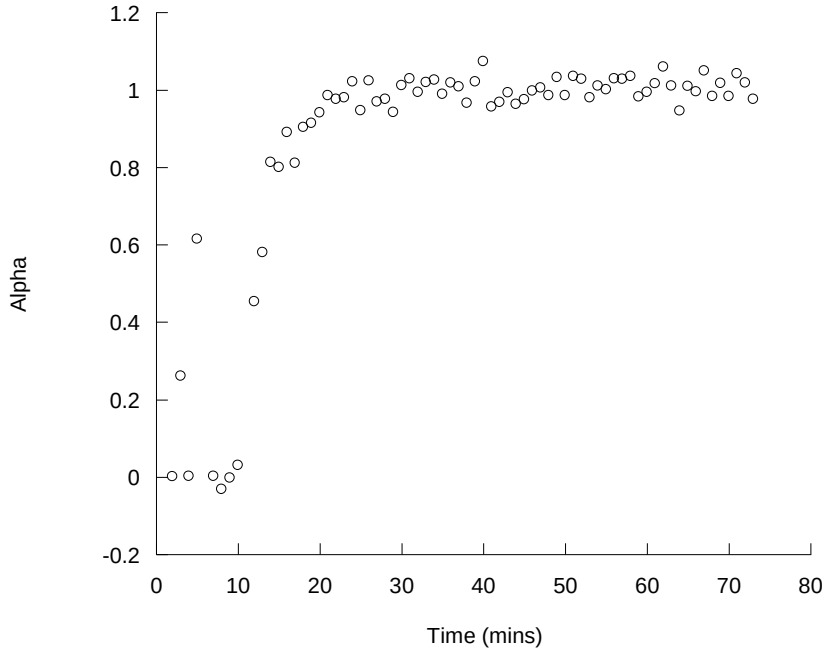

Figure 15 Extent of reaction (α) vs time plot of the formation of $[La(H_2O)WO_4]_2[1,5\text{-NDS}]$ at 165 °C.

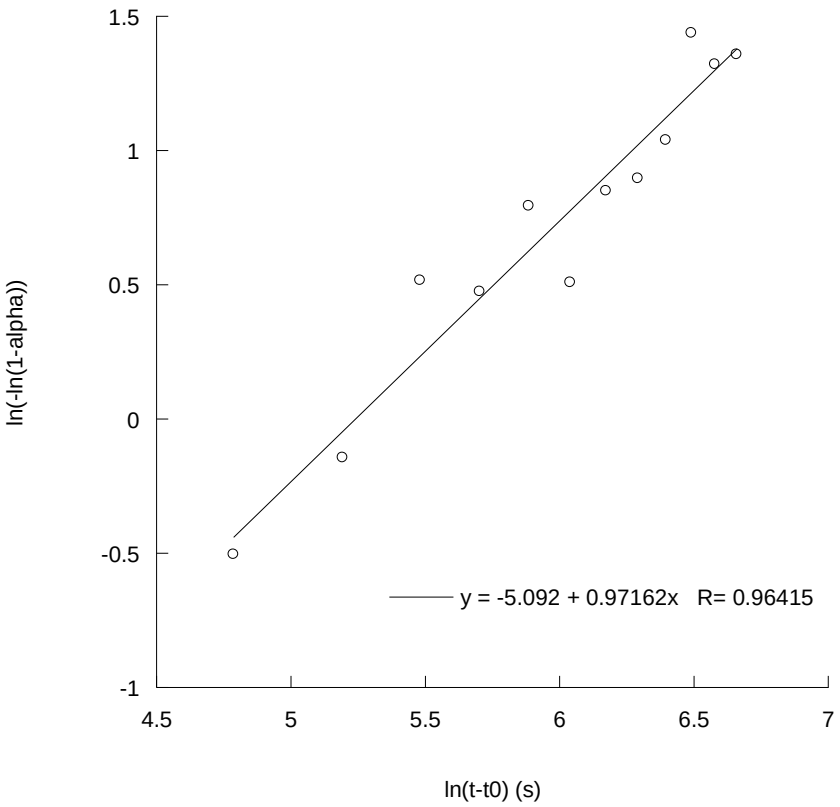

Figure 16 Sharp-Hancock plot of ln(-ln(1-α) versus ln(t-t_0) of the formation of $[La(H_2O)WO_4]_2$[1,5-NDS] at 165 °C.

Synthesis at 180 °C

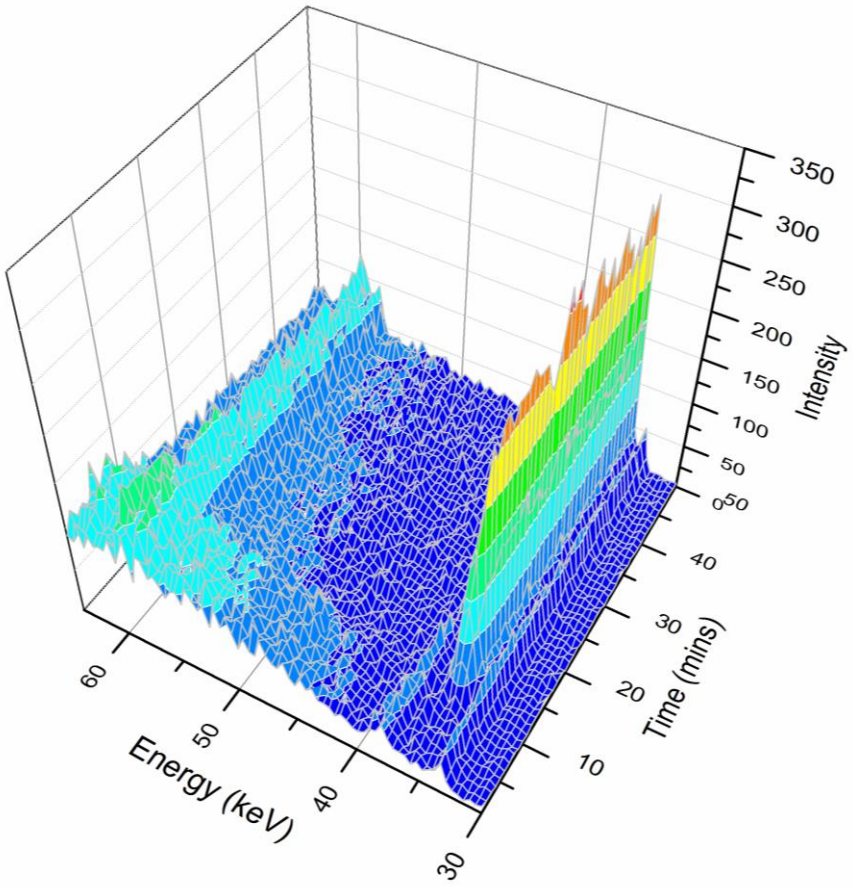

Figure 17 Three-dimensional stacked plot of the time resolved *in-situ* Energy dispersive X-ray diffraction measurements for the formation of $[La(H_2O)WO_4]_2$[1,5-NDS] at 180 °C. An acquisition time of 60s was used for each recorded spectrum and a detector angle of 1.19 ° 2θ.

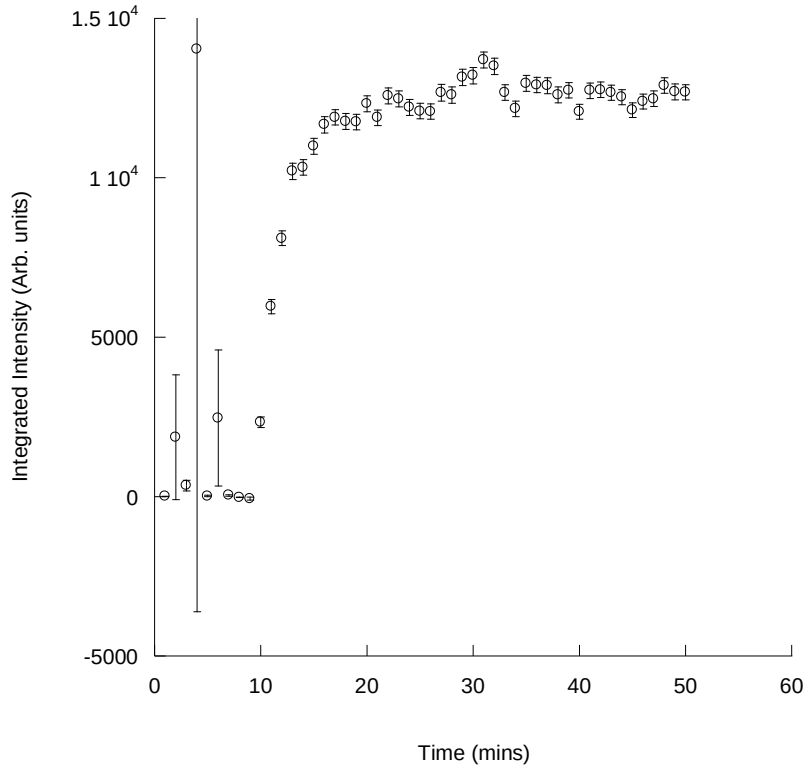

Figure 18 Integrated intensity versus time plot of the formation of $[La(H_2O)WO_4]_2[1,5\text{-NDS}]$ at 180 °C. (Including errors)

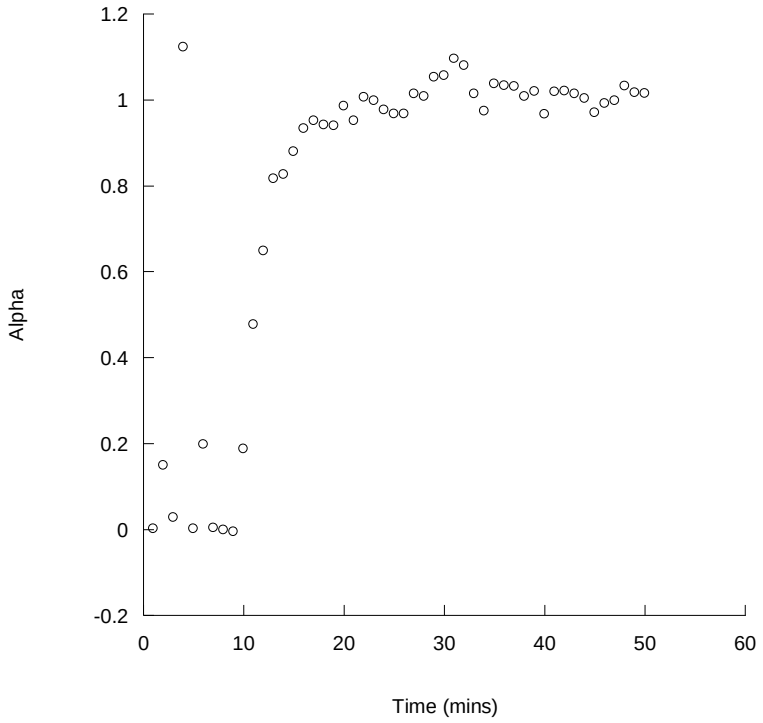

Figure 19 Extent of reaction (α) versus time plot of the formation of $[La(H_2O)WO_4]_2[1,5\text{-NDS}]$ at 180 °C.

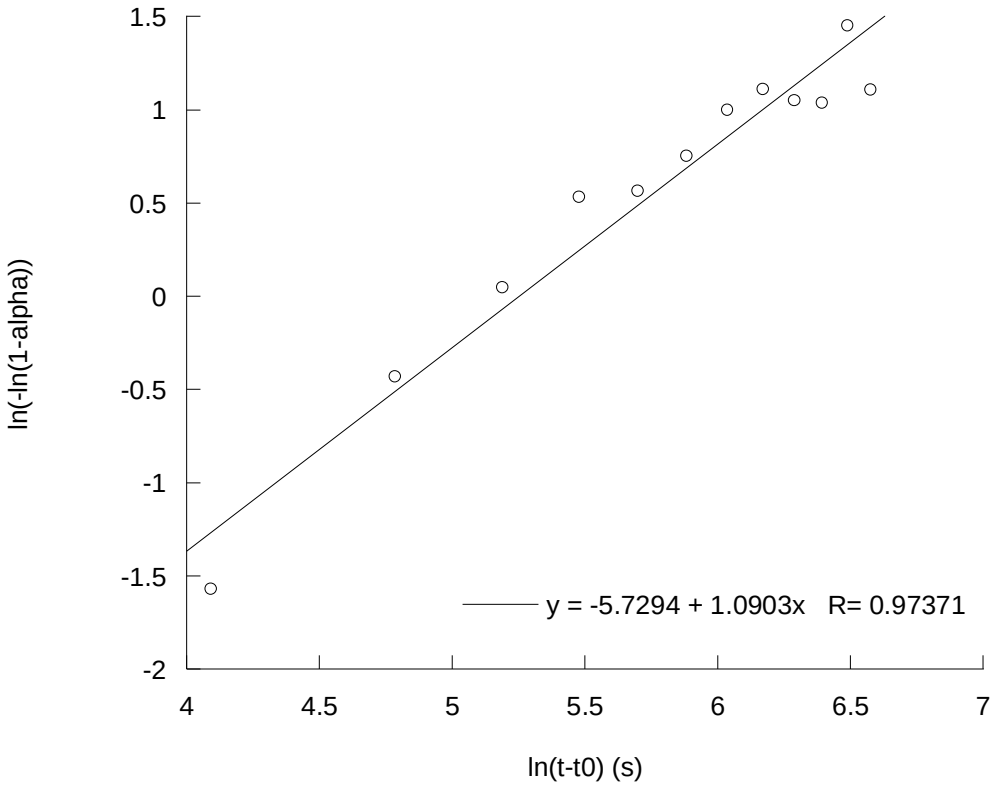

Figure 20 Sharp-Hancock plot of ln(-ln(1-α) versus ln(t-t_0) of the formation of $[La(H_2O)WO_4]_2$[1,5-NDS] at 180 °C.

Synthesis at 200 °C

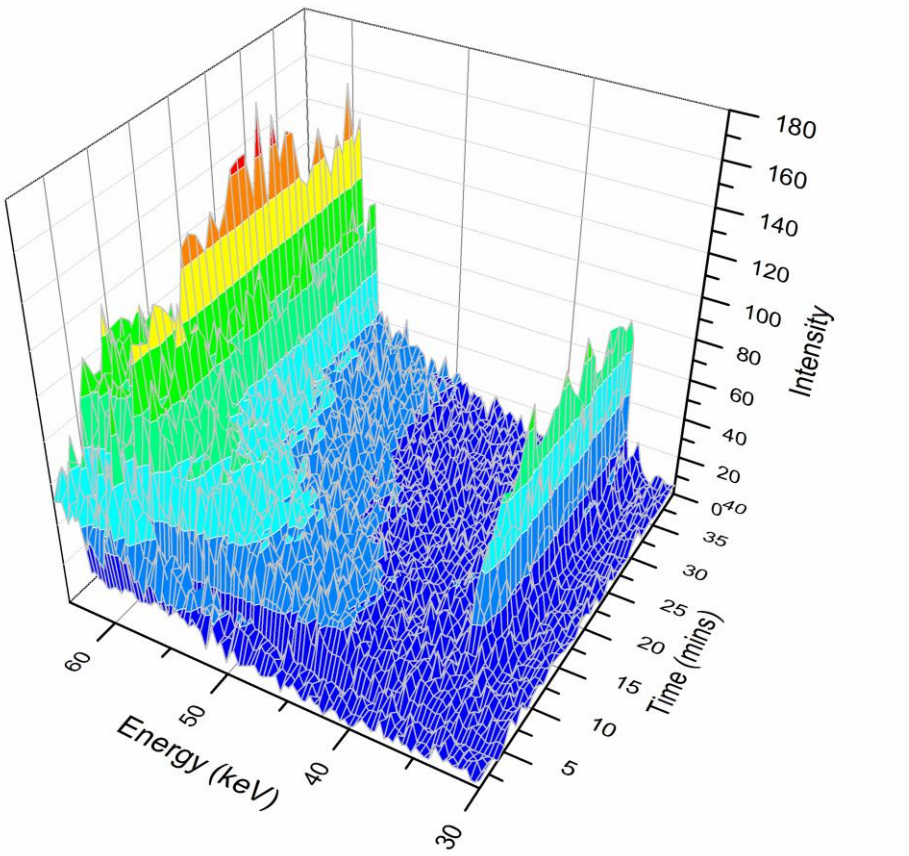

Figure 21 Three-dimensional stacked plot of the time resolved *in-situ* Energy dispersive X-ray diffraction measurements for the formation of $[La(H_2O)WO_4]_2$[1,5-NDS] at 200 °C. An acquisition time of 60s was used for each recorded spectrum and a detector angle of 1.19 ° 2θ.

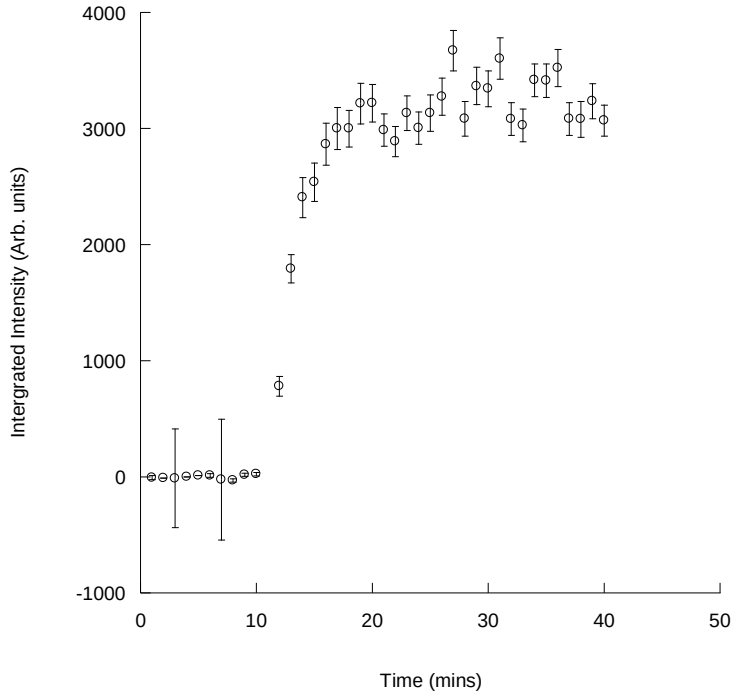

Figure 22 Integrated intensity versus time plot of the formation of $[La(H_2O)WO_4]_2[1,5\text{-NDS}]$ at 200 °C. (Including errors)

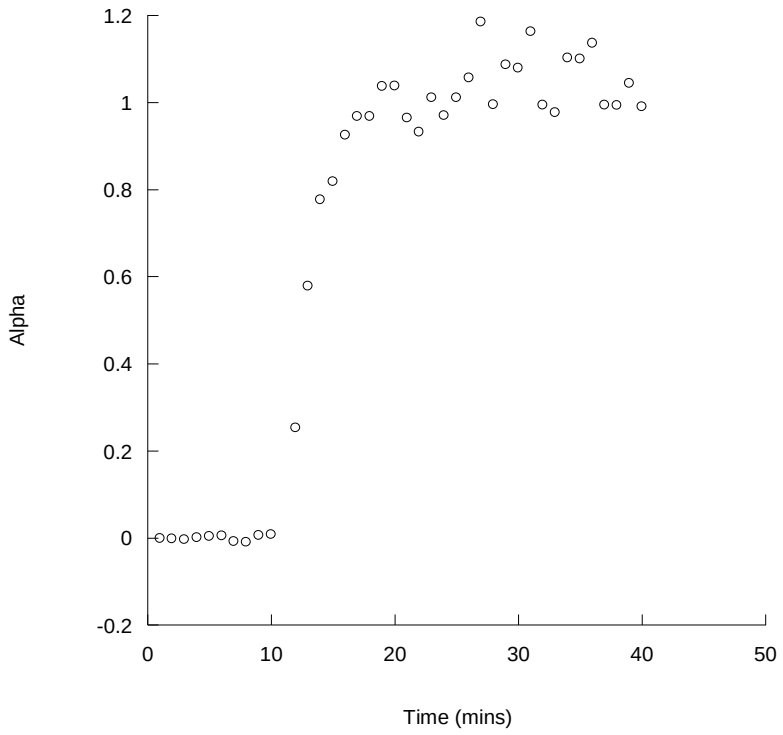

Figure 23 Extent of reaction (α) vs time plot of the formation of $[La(H_2O)WO_4]_2[1,5\text{-NDS}]$ at 200 °C.

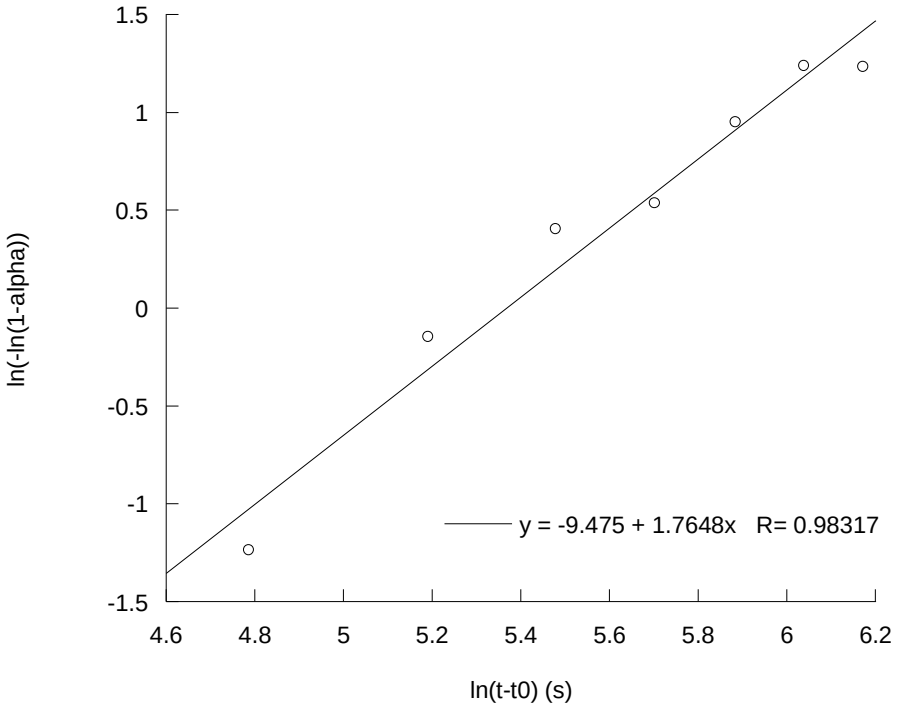

Figure 24 Sharp-Hancock plot of ln(-ln(1-α) versus ln(t-t_0) of the formation of $[La(H_2O)WO_4]_2$[1,5-NDS] at 200 °C.

In-situ formation of $[La(H_2O)WO_4]_2[2,6\text{-NDS}]$

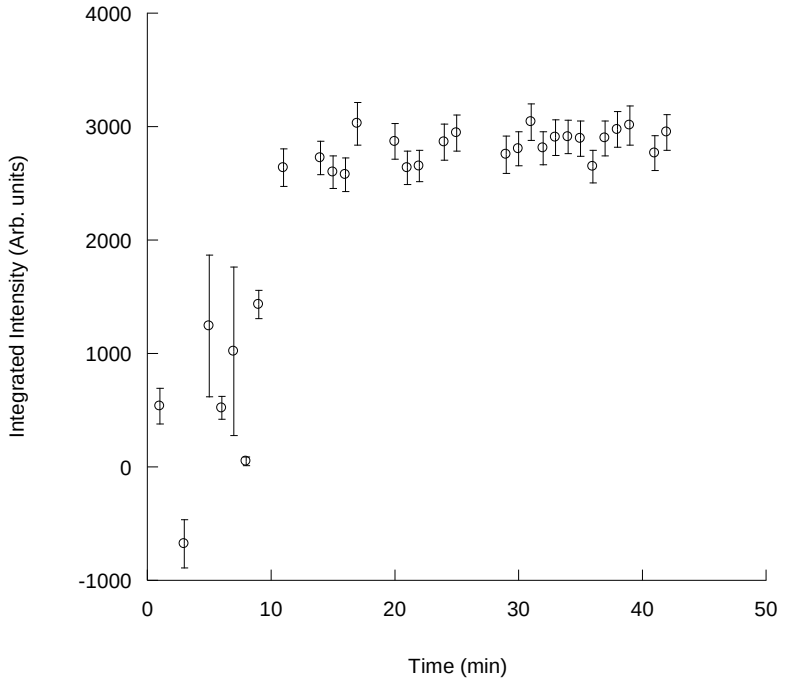

Figure 25 Integrated intensity versus time plot of the formation of $[La(H_2O)WO_4]_2[2,6\text{-NDS}]$ at 165 °C. (Including errors)

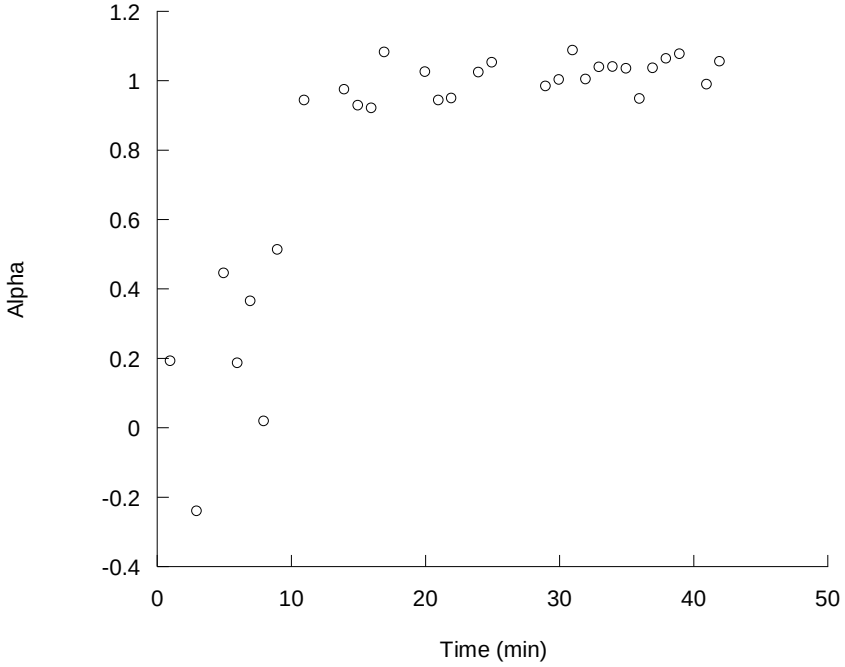

Figure 26 Extent of reaction (α) versus time plot of the formation of $[La(H_2O)WO_4]_2[2,6\text{-NDS}]$ at 165 °C.

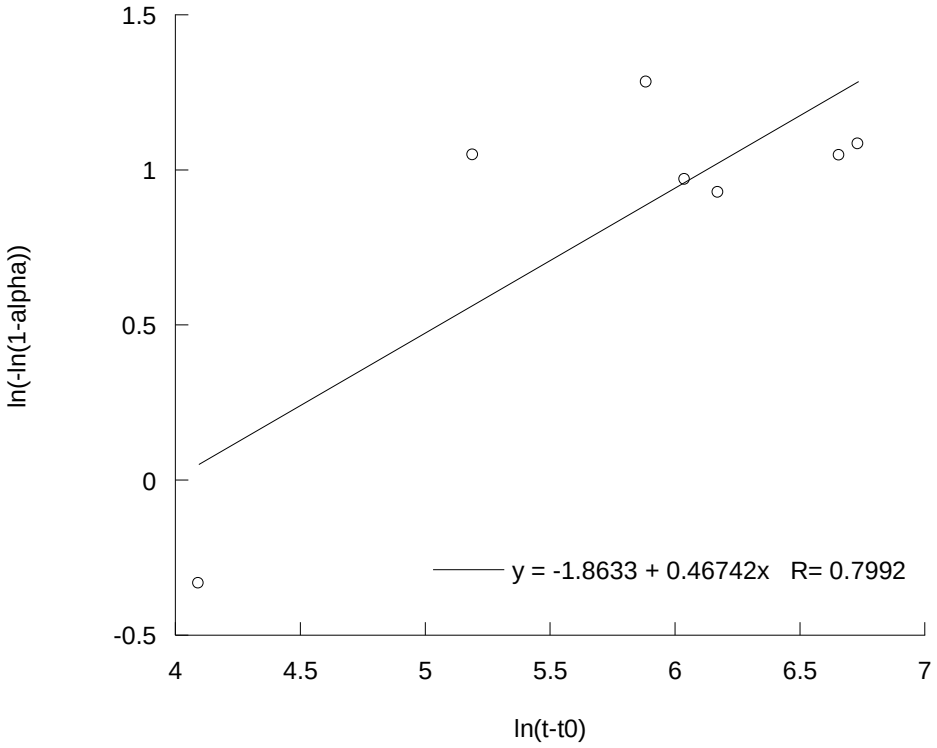

Figure 27 Sharp and Hancock plot of ln(-ln(1-α)) versus ln(t-t_0) of the formation of $[La(H_2O)WO_4]_2$[2,6-NDS] at 165 °C.

In-situ formation of $[YbC_2H_2O_5P]$

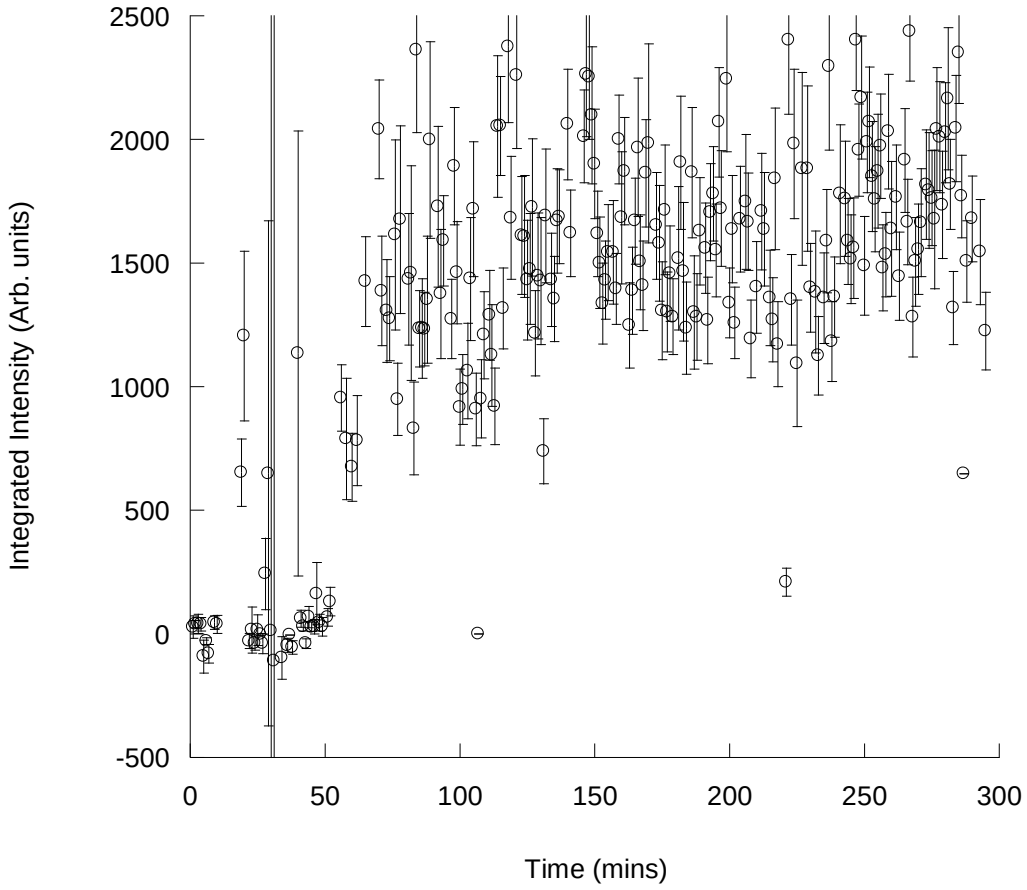

Figure 28 Integrated intensity versus time plot of the formation of $[YbC_2H_2O_5P]$ at 220 °C. (Including errors)

Appendix D

Chapter Five

$[Ce(NO_3)(H_2O)_2][B_6O_{10}(OH_2)]$

Table 1 Crystal data and structure refinement details.

Identification code	2010src0771b	
Empirical formula	$B_6CeH_6NO_{16}$	
Formula weight	481.04	
Temperature	120(2) K	
Wavelength	0.71073 Å	
Crystal system	Monoclinic	
Space group	*P*21/*n*	
Unit cell dimensions	a = 9.8268(3) Å	α = 90°
	b = 14.7545(3) Å	β = 90.0700(10)°
	c = 8.0451(5) Å	γ = 90°
Volume	1166.45(8) $Å^3$	
Z	4	
Density (calculated)	2.739 mg / m^3	
Absorption coefficient	4.006 mm^{-1}	
F(000)	916	
Crystal	sheet; colourless	
Crystal size	0.10 × 0.04 × 0.02 mm^3	
θ range for data collection	3.27 – 27.48°	
Index ranges	$-12 \le h \le 12$, $-19 \le k \le 19$, $-10 \le l \le 10$	
Reflections collected	20534	
Independent reflections	2680 [R_{int} = 0.0485]	
Completeness to θ = 27.48°	99.9 %	
Absorption correction	Semi–empirical from equivalents	
Max. and min. transmission	0.9242 and 0.6901	

Refinement method	Full-matrix least-squares on F^2
Data / restraints / parameters	2680 / 12 / 251
Goodness-of-fit on F^2	1.405
Final R indices [$F^2 > 2\sigma(F^2)$]	$R1$ = 0.0384, $wR2$ = 0.0870
R indices (all data)	$R1$ = 0.0419, $wR2$ = 0.0882
Largest diff. peak and hole	1.142 and –0.807 e Å^{-3}

Diffractometer: *Nonius KappaCCD* area detector (ϕ scans and ω scans to fill *asymmetric unit* sphere). **Cell determination:** DirAx (Duisenberg, A.J.M.(1992). J. Appl. Cryst. 25, 92-96.) **Data collection:** Collect (Collect: Data collection software, R. Hooft, Nonius B.V., 1998). **Data reduction and cell refinement**: *Denzo* (Z. Otwinowski & W. Minor, *Methods in Enzymology* (1997) Vol. **276**: *Macromolecular Crystallography*, part A, pp. 307–326; C. W. Carter, Jr. & R. M. Sweet, Eds., Academic Press). **Absorption correction**: *SADABS* (Sheldrick, G. M. (2007). SADABS. Version 2007/2. Bruker AXS Inc., Madison, Wisconsin, USA.). S**tructure solution**: SUPERFLIP (Palatinus, L. & Chapuis, G. (2007). J. Appl. Cryst. 40, 786-790.) S**tructure refinement**: *SHELXL97* (G Sheldrick, G.M. (2008). Acta Cryst. A64, 112-122.). **Graphics:** *OLEX2* (Dolomanov, O. V., Bourhis, L. J., Gildea, R. J., Howard, J. A. K. & Puschmann, H. (2009). J. Appl. Cryst. 42, 339-341.)

Special details:

Coordinated H2O molecule (O16) disordered about two positions, ~50:50 occupancy.

Table 2 Atomic coordinates [$\times 10^4$], equivalent isotropic displacement parameters [Å$^2 \times 10^3$] and site occupancy factors. U_{eq} is defined as one third of the trace of the orthogonalized U^{ij} tensor.

Atom	*x*	*y*	*z*	U_{eq}	*S.o.f.*
Ce1	2887(1)	3188(1)	1386(1)	8(1)	1
O1	1657(5)	4207(3)	3402(5)	16(1)	1

O2	3414(5)	1584(3)	703(6)	19(1)	1
O3	3145(4)	5890(3)	–279(5)	10(1)	1
O4	2662(4)	3864(3)	–3646(5)	10(1)	1
O5	746(4)	6038(3)	–3(5)	8(1)	1
O6	371(4)	2769(3)	1416(5)	9(1)	1
O7	3664(5)	646(3)	–1348(5)	17(1)	1
O8	1784(4)	4585(3)	–89(5)	11(1)	1
O9	1657(5)	897(4)	–343(7)	32(1)	1
O10	4078(4)	3101(3)	–1631(5)	8(1)	1
O11	1755(4)	2868(3)	–1504(5)	8(1)	1
O12	4384(4)	2521(3)	3757(5)	8(1)	1
O13	5515(4)	2929(3)	1399(5)	10(1)	1
O14	2936(4)	2277(3)	–3903(4)	5(1)	1
O15	1478(4)	2234(3)	3697(5)	10(1)	1
O16A	4332(12)	4550(8)	1600(40)	20(5)	0.50(5)
O16B	4212(12)	4524(8)	2490(40)	16(5)	0.50(5)
N1	2900(6)	1032(3)	–350(6)	14(1)	1
B1	2853(6)	3066(5)	–2698(8)	9(1)	1
B2	1889(6)	5524(4)	–135(8)	8(1)	1
B3	3333(6)	6855(5)	–358(8)	8(1)	1
B4	757(6)	7012(4)	–311(8)	8(1)	1
B5	5603(6)	2527(4)	2911(8)	7(1)	1
B6	277(7)	2272(5)	2858(8)	10(1)	1

Table 3 Bond lengths [Å] and angles [°].

Ce1–O16A	2.466(12)	O11–B5^{iii}	1.357(7)
Ce1–O2	2.484(4)	O11–B1	1.474(7)
Ce1–O1	2.521(4)	O12–B5	1.379(7)
Ce1–O16B	2.524(12)	O12–B4^{iv}	1.465(7)
Ce1–O6	2.549(4)	O13–B5	1.356(7)
Ce1–O12	2.601(4)	O13–B3^{v}	1.445(7)
Ce1–O13	2.610(4)	O14–B4^{vi}	1.484(7)
Ce1–O8	2.614(4)	O14–B3^{vi}	1.514(7)
Ce1–O11	2.619(4)	O14–B1	1.518(7)
Ce1–O10	2.699(4)	O15–B6	1.360(8)
Ce1–O15	2.713(4)	O15–B3^{iv}	1.460(7)
Ce1–B5	3.094(6)	O16A–H6AA	0.85(2)
O1–H1B	0.85(2)	O16A–H6AB	0.85(2)
O1–H1A	0.85(2)	O16A–H6BB	1.18(8)
O2–N1	1.278(7)	O16B–H6AA	0.56(16)
O3–B2	1.352(8)	O16B–H6AB	1.21(8)
O3–B3	1.437(8)	O16B–H6BA	0.86(2)
O4–B1	1.415(8)	O16B–H6BB	0.85(2)
O4–H4A	0.85(2)	B3–O13^{v}	1.445(7)
O4–H4B	0.86(2)	B3–O15^{vii}	1.460(7)
O5–B2	1.360(7)	B3–O14^{viii}	1.514(7)
O5–B4	1.458(7)	B4–O6^{i}	1.457(7)
O6–B6	1.375(8)	B4–O12^{vii}	1.465(7)
O6–B4^{i}	1.457(7)	B4–O14^{viii}	1.484(7)
O7–N1	1.239(7)	B5–O11^{ix}	1.357(7)
O8–B2	1.389(7)	B6–O10(x)	1.365(8)
O9–N1	1.238(7)		
O10–B6^{ii}	1.365(8)	O16A–Ce1–O2	132.2(4)
O10–B1	1.479(7)	O16A–Ce1–O1	75.3(6)

O2–Ce1–O1 144.13(15)

O16A–Ce1–O16B 16.8(3)

O2–Ce1–O16B 135.6(3)

O1–Ce1–O16B 63.6(6)

O16A–Ce1–O6 139.1(3)

O2–Ce1–O6 88.47(15)

O1–Ce1–O6 70.88(14)

O16B–Ce1–O6 133.3(4)

O16A–Ce1–O12 86.1(6)

O2–Ce1–O12 71.56(13)

O1–Ce1–O12 91.43(13)

O16B–Ce1–O12 75.3(5)

O6–Ce1–O12 116.66(12)

O16A–Ce1–O13 63.2(3)

O2–Ce1–O13 69.83(14)

O1–Ce1–O13 124.05(14)

O16B–Ce1–O13 66.6(3)

O6–Ce1–O13 157.53(13)

O12–Ce1–O13 51.93(12)

O16A–Ce1–O8 68.2(4)

O2–Ce1–O8 137.51(14)

O1–Ce1–O8 67.85(13)

O16B–Ce1–O8 76.0(5)

O6–Ce1–O8 78.10(13)

O12–Ce1–O8 149.96(13)

O13–Ce1–O8 121.80(13)

O16A–Ce1–O11 116.9(8)

O2–Ce1–O11 73.77(13)

O1–Ce1–O11 118.35(13)

O16B–Ce1–O11 132.3(7)

O6–Ce1–O11 63.49(12)

O12–Ce1–O11 145.30(12)

O13–Ce1–O11 113.35(12)

O8–Ce1–O11 64.11(13)

O16A–Ce1–O10 81.5(8)

O2–Ce1–O10 70.45(14)

O1–Ce1–O10 144.65(13)

O16B–Ce1–O10 97.5(8)

O6–Ce1–O10 114.76(12)

O12–Ce1–O10 113.36(12)

O13–Ce1–O10 64.32(12)

O8–Ce1–O10 78.98(12)

O11–Ce1–O10 51.49(12)

O16A–Ce1–O15 132.0(8)

O2–Ce1–O15 76.35(14)

O1–Ce1–O15 67.84(14)

O16B–Ce1–O15 115.2(8)

O6–Ce1–O15 51.07(12)

O12–Ce1–O15 65.77(12)

O13–Ce1–O15 115.29(12)

O8–Ce1–O15 120.57(12)

O11–Ce1–O15 107.35(12)

O10–Ce1–O15 144.48(12)

O16A–Ce1–B5 74.5(4)

O2–Ce1–B5 66.88(15)

O1–Ce1–B5 110.31(15)

O16B–Ce1–B5 70.2(3)

O6–Ce1–B5 139.11(15)

O12–Ce1–B5 26.24(14)

O13–Ce1–B5 25.77(14)

O8–Ce1–B5 141.82(15)

O11–Ce1–B5 131.35(14)

O10–Ce1–B5 88.11(14)

O15–Ce1–B5 90.31(14)

Ce1–O1–H1B 104(5)

Ce1–O1–H1A 123(5)

H1B–O1–H1A 106(3)

N1–O2–Ce1 132.1(4)

B2–O3–B3 121.1(5)

B1–O4–H4A 99(5)

B1–O4–H4B 113(5)

H4A–O4–H4B 105(3)

B2–O5–B4 122.0(5)

B6–O6–B4^{i} 125.5(5)

B6–O6–Ce1 101.7(3)

B4^{i}–O6–Ce1 132.7(3)

B2–O8–Ce1 140.1(4)

B6^{ii}–O10–B1 120.9(5)

B6^{ii}–O10–Ce1 131.7(4)

B1–O10–Ce1 99.8(3)

B5^{iii}–O11–B1 118.0(4)

B5^{iii}–O11–Ce1 137.6(3)

B1–O11–Ce1 103.4(3)

B5–O12–B4^{iv} 120.5(4)

B5–O12–Ce1 97.3(3)

B4^{iv}–O12–Ce1 140.0(3)

B5–O13–B3^{v} 124.6(5)

B5–O13–Ce1 97.4(3)

B3^{v}–O13–Ce1 137.9(3)

B4^{vi}–O14–B3^{vi} 115.9(4)

B4^{vi}–O14–B1 121.4(4)

B3^{vi}–O14–B1 121.4(4)

B6–O15–B3^{iv} 125.4(5)

B6–O15–Ce1 94.7(3)

B3^{iv}–O15–Ce1 139.6(3)

Ce1–O16A–H6AA 108(10)

Ce1–O16A–H6AB 130(10)

H6AA–O16A–H6AB 108(4)

Ce1–O16A–H6BB 104(7)

H6AA–O16A–H6BB 74(10)

H6AB–O16A–H6BB 56(10)

Ce1–O16B–H6AA 119(10)

Ce1–O16B–H6AB 106(5)

H6AA–O16B–H6AB 95(10)

Ce1–O16B–H6BA 115(9)

H6AA–O16B–H6BA 64(10)

H6AB–O16B–H6BA 139(10)

Ce1–O16B–H6BB 114(9)

H6AA–O16B–H6BB 124(10)

H6AB–O16B–H6BB 54(9)

H6BA–O16B–H6BB 107(3)

O9–N1–O7 121.8(5)

O9–N1–O2 119.3(5)

O7–N1–O2 118.9(5)

O4–B1–O11 114.8(5)

O4–B1–O10 113.0(5)

O11–B1–O10 103.0(4)

O4–B1–O14 107.6(4)

O11–B1–O14 107.7(5)

O10–B1–O14 110.7(5)

O3–B2–O5 122.5(5)

O3–B2–O8 118.0(5)

O5–B2–O8 119.5(5)

O3–B3–O13^{v} 110.1(5)

O3–B3–O15^{vii} 110.8(5)

O13^{v}–B3–O15^{vii} 110.3(5)

O3–B3–O14^{viii} 108.6(4)

O13^{v}–B3–O14^{viii} 109.1(5)

O15^{vii}–B3–O14^{viii} 107.8(4)

O6^{i}–B4–O5 108.4(5)

O6^{i}–B4–O12^{vii} 109.6(5)

O5–B4–O12^{vii} 111.1(5)

O6^{i}–B4–O14^{viii} 109.9(5)

O5–B4–O14^{viii} 109.8(5)

O12^{vii}–B4–O14^{viii} 108.2(4)

O13–B5–O11^{ix} 123.4(5)

O13–B5–O12 113.0(5)

O11^{ix}–B5–O12 123.4(5)

O13–B5–Ce1 56.8(3)

O11^{ix}–B5–Ce1 172.7(4)

O12–B5–Ce1 56.5(3)

O15–B6–O10(x) 125.6(6)

O15–B6–O6 112.4(5)

O10(x) –B6–O6 121.9(5)

O15–B6–Ce1 59.7(3)

O10(x) –B6–Ce1 174.7(4)

O6–B6–Ce1 52.8(3)

Symmetry transformations used to generate equivalent atoms:

(i) –x,–y+1,–z (ii) x+1/2,–y+1/2,z–1/2 (iii) x–1/2,–y+1/2,z–1/2

(iv) –x+1/2,y–1/2,–z+1/2 (v) –x+1,–y+1,–z (vi) –x+1/2,y–1/2,–z–1/2

(vii) –x+1/2,y+1/2,–z+1/2 (viii) –x+1/2,y+1/2,–z–1/2

(xi) x+1/2,–y+1/2,z+1/2 (x) x–1/2,–y+1/2,z+1/2

Table 4 Anisotropic displacement parameters [$Å^2 \times 10^3$]. The anisotropic displacement factor exponent takes the form: $-2\pi^2[h^2a^{*2}U^{11} + ... + 2\ h\ k\ a^*\ b^*\ U^{12}]$.

Atom	U^{11}	U^{22}	U^{33}	U^{23}	U^{13}	U^{12}
Ce1	6(1)	9(1)	9(1)	0(1)	0(1)	0(1)
O1	20(2)	17(2)	9(2)	–1(2)	0(2)	4(2)
O2	29(3)	11(2)	17(2)	–5(2)	–8(2)	3(2)
O3	8(2)	9(2)	13(2)	–1(2)	–2(2)	0(2)
O4	9(2)	9(2)	11(2)	1(2)	0(2)	–1(2)
O5	9(2)	7(2)	9(2)	2(2)	4(2)	0(2)
O6	6(2)	15(2)	7(2)	2(2)	1(2)	0(2)
O7	24(2)	20(2)	8(2)	–4(2)	7(2)	5(2)
O8	13(2)	9(2)	11(2)	0(2)	0(2)	3(2)
O9	18(3)	33(3)	45(3)	–12(3)	10(2)	–9(2)
O10	6(2)	11(2)	9(2)	–1(2)	0(1)	1(2)
O11	7(2)	11(2)	6(2)	0(2)	2(2)	0(2)
O12	7(2)	11(2)	5(2)	–1(2)	2(1)	1(2)
O13	7(2)	12(2)	10(2)	4(2)	0(2)	0(2)
O14	6(2)	7(2)	2(2)	–1(1)	2(1)	1(1)
O15	6(2)	15(2)	9(2)	1(2)	–2(2)	0(2)
O16A	12(5)	21(6)	26(14)	–1(6)	5(5)	–1(4)
O16B	6(5)	9(5)	33(14)	–4(5)	–4(5)	3(4)

N1	23(3)	9(2)	11(2)	1(2)	3(2)	0(2)
B1	4(3)	15(3)	8(3)	−1(2)	0(2)	1(2)
B2	9(3)	7(3)	9(3)	0(2)	1(2)	1(2)
B3	4(3)	15(3)	7(3)	−2(2)	0(2)	1(2)
B4	5(3)	11(3)	8(3)	0(2)	0(2)	−1(2)
B5	10(3)	8(3)	5(3)	−2(2)	1(2)	−3(2)
B6	11(3)	13(3)	7(3)	−3(2)	1(2)	0(2)

Table 5 Hydrogen coordinates [× 10^4] and isotropic displacement parameters [$Å^2$ × 10^3].

Atom	*x*	*y*	*z*	U_{eq}	*S.o.f.*	
H1B	2030(50)	4090(50)	4340(50)	15	1	
H1A	800(20)	4180(50)	3560(70)	15	1	
H4A	1850(30)	3990(40)	−3360(90)	15	1	
H4B	3140(50)	4310(30)	−3300(80)	15	1	
H6AA	4020(110)	4870(100)	2380(170)	15	0.50(5)	
H6AB	5190(30)	4600(100)	1600(170)	15	0.50(5)	
H6BA	3850(110)	4790(90)	3330(120)	15	0.50(5)	
H6BB	5030(50)	4400(100)	2760(150)	15	0.50(5)	

Characterising data for $[La(NO_3)(H_2O)_2][B_6O_{10}(OH_2)]$

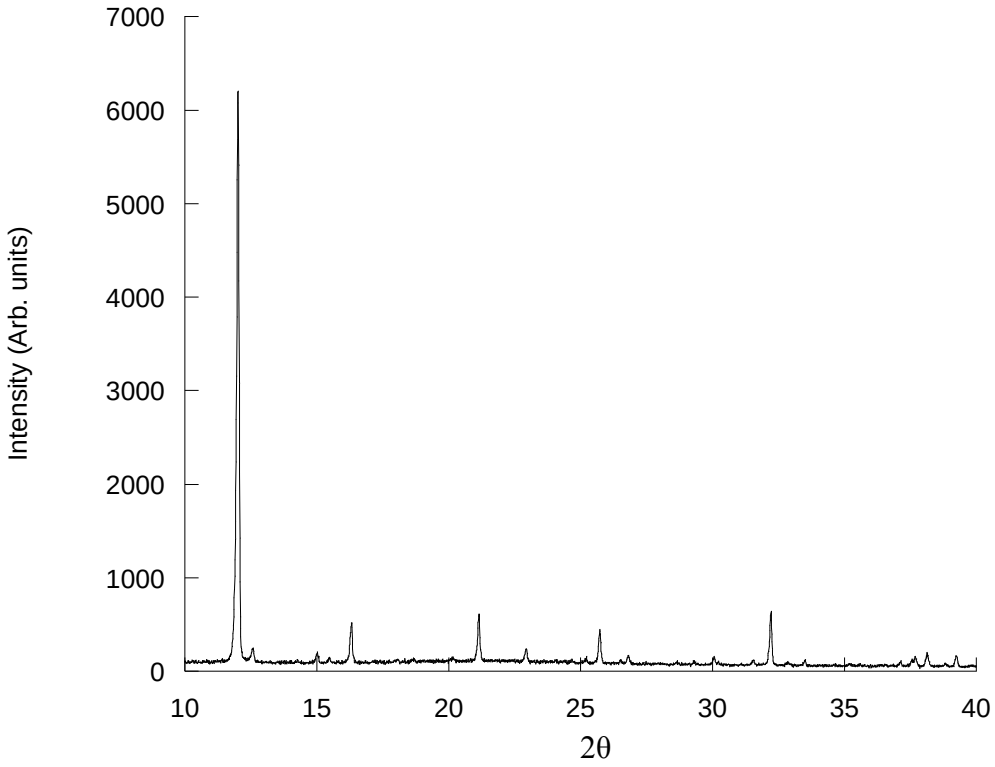

Figure 1 Powder XRD pattern of $[La(NO_3)(H_2O)_2][B_6O_{10}(OH_2)]$.

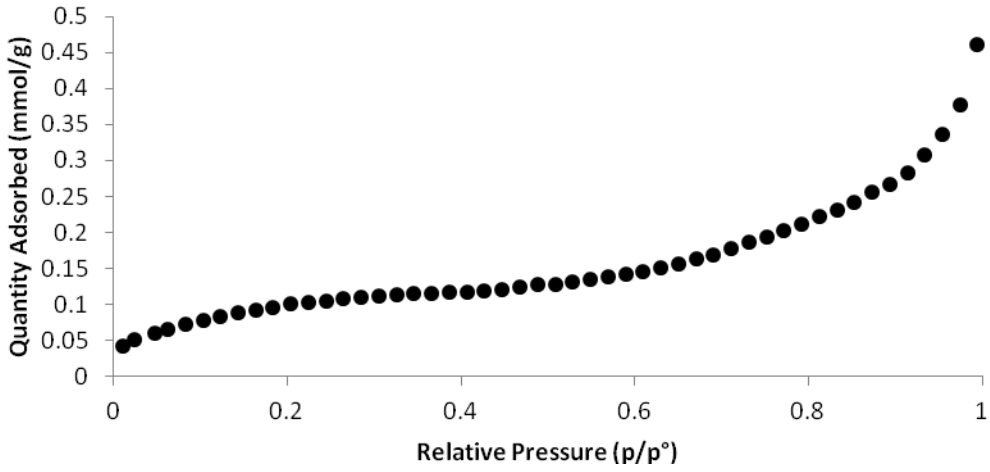

Figure 2 Adsorption isotherm for $[La(NO_3)(H_2O)_2][B_6O_{10}(OH_2)]$ degassed at 120 °C overnight.

$[Pr(NO_3)(H_2O)_2][B_5O_9(OH_2)]$

Table 6 Crystal data and structure refinement details.

Identification code	2010src0770b	
Empirical formula	$B_5H_6NO_{15}Pr$	
Formula weight	455.02	
Temperature	120(2) K	
Wavelength	0.71073 Å	
Crystal system	Monoclinic	
Space group	*P*21/*n*	
Unit cell dimensions	a = 6.4315(2) Å	α = 90°
	b = 15.5099(7) Å	β = 90.377(2)°
	c = 10.7078(3) Å	γ = 90°
Volume	1068.10(7) Å^3	
Z	4	
Density (calculated)	2.830 mg / m^3	
Absorption coefficient	4.660 mm^{-1}	
F(000)	868	
Crystal	Fragment; colourless	
Crystal size	0.16 × 0.14 × 0.08 mm^3	
θ range for data collection	3.24 – 27.48°	
Index ranges	$-8 \le h \le 8$, $-18 \le k \le 20$, $-13 \le l \le 13$	
Reflections collected	11130	
Independent reflections	2438 [R_{int} = 0.0629]	
Completeness to θ = 27.48°	99.5 %	
Absorption correction	Semi−empirical from equivalents	
Max. and min. transmission	0.7068 and 0.5226	
Refinement method	Full-matrix least-squares on F^2	
Data / restraints / parameters	2438 / 40 / 212	

Goodness-of-fit on F^2	1.139
Final R indices [$F^2 > 2\sigma(F^2)$]	$R1$ = 0.0465, $wR2$ = 0.0917
R indices (all data)	$R1$ = 0.0618, $wR2$ = 0.0999
Largest diff. peak and hole	1.152 and –1.097 e Å^{-3}

Diffractometer: *Nonius KappaCCD* area detector (ϕ scans and ω scans to fill *asymmetric unit* sphere). **Cell determination:** DirAx (Duisenberg, A.J.M.(1992). J. Appl. Cryst. 25, 92-96.) **Data collection:** Collect (Collect: Data collection software, R. Hooft, Nonius B.V., 1998). **Data reduction and cell refinement**: *Denzo* (Z. Otwinowski & W. Minor, *Methods in Enzymology* (1997) Vol. **276**: *Macromolecular Crystallography*, part A, pp. 307–326; C. W. Carter, Jr. & R. M. Sweet, Eds., Academic Press). **Absorption correction**: *SADABS* (Sheldrick, G. M. (2007). SADABS. Version 2007/2. Bruker AXS Inc., Madison, Wisconsin, USA.). S**tructure solution**: SUPERFLIP (Palatinus, L. & Chapuis, G. (2007). J. Appl. Cryst. 40, 786-790.) S**tructure refinement**: *SHELXL97* (G Sheldrick, G.M. (2008). Acta Cryst. A64, 112-122.). **Graphics:** *OLEX2* (Dolomanov, O. V., Bourhis, L. J., Gildea, R. J., Howard, J. A. K. & Puschmann, H. (2009). J. Appl. Cryst. 42, 339-341.)

Special details:

O5 refined isotropically. Anisotropic refinement results in NPD atom, likely due to proximity of Pr.

Table 7 Atomic coordinates [$\times 10^4$], equivalent isotropic displacement parameters [Å$^2 \times 10^3$] and site occupancy factors. U_{eq} is defined as one third of the trace of the orthogonalized U^{ij} tensor.

Atom	*x*	*y*	*z*	U_{eq}	*S.o.f.*
Pr1	8505(1)	2022(1)	1399(1)	7(1)	1
B1	7603(12)	–362(5)	892(8)	9(2)	1
B2	3576(11)	1828(5)	–375(7)	6(2)	1
B3	11560(11)	2921(5)	3207(7)	7(1)	1

B4	4092(12)	2795(6)	1528(7)	10(2)	1
B5	5227(12)	3371(6)	3625(8)	11(2)	1
O1	7256(8)	518(3)	884(5)	9(1)	1
O2	9393(7)	–681(3)	1406(5)	8(1)	1
O3	5636(7)	3000(3)	2402(4)	6(1)	1
O4	7032(9)	4720(4)	790(6)	20(1)	1
O5	4778(7)	2163(3)	701(4)	7(1)	1
O6	10250(9)	4529(4)	1347(6)	26(1)	1
O7	11390(7)	2036(3)	–369(4)	6(1)	1
O8	6108(7)	–888(3)	382(4)	8(1)	1
O9	12021(7)	2663(3)	2013(4)	10(1)	1
O10	8540(8)	3490(3)	386(5)	13(1)	1
O11	9513(7)	2804(3)	3471(4)	8(1)	1
O12	8004(7)	1761(3)	–996(4)	6(1)	1
O13	6562(9)	1353(4)	3165(5)	15(1)	1
O14	11000(8)	880(4)	2188(5)	16(1)	1
O15	3693(9)	3671(4)	681(6)	21(1)	1
N1	8605(10)	4249(5)	858(7)	19(2)	1

Table 8 Bond lengths [Å] and angles [°].

Pr1–O13	2.499(5)	Pr1–O3	2.624(5)
Pr1–O5	2.516(5)	Pr1–O7	2.659(5)
Pr1–O10	2.522(5)	Pr1–B3	3.082(7)
Pr1–O1	2.527(5)	Pr1–B4	3.085(8)
Pr1–O14	2.532(5)	B1–O2	1.366(9)
Pr1–O9	2.552(5)	B1–O8	1.372(9)
Pr1–O11	2.606(5)	B1–O1	1.383(10)
Pr1–O12	2.615(5)	B2–O7^{i}	1.443(8)

B2–O8^{ii}	1.472(9)	O15–H15A	0.86(2)
B2–O5	1.477(9)	O15–H15B	0.85(2)
B2–O11^{iii}	1.492(9)		
B3–O12^{iv}	1.350(9)	O13–Pr1–O5	77.35(17)
B3–O11	1.360(9)	O13–Pr1–O10	134.95(18)
B3–O9	1.373(9)	O5–Pr1–O10	78.74(16)
B4–O5	1.394(9)	O13–Pr1–O1	67.78(17)
B4–O3	1.397(9)	O5–Pr1–O1	73.42(15)
B4–O9^{i}	1.447(9)	O10–Pr1–O1	138.00(16)
B4–O15	1.653(10)	O13–Pr1–O14	77.04(19)
B5–O7^{v}	1.452(9)	O5–Pr1–O14	139.52(17)
B5–O3	1.456(9)	O10–Pr1–O14	140.16(17)
B5–O2^{vi}	1.490(10)	O1–Pr1–O14	68.07(16)
B5–O12^{v}	1.503(9)	O13–Pr1–O9	114.42(17)
O2–B5^{vii}	1.490(10)	O5–Pr1–O9	152.07(16)
O4–N1	1.250(8)	O10–Pr1–O9	75.45(17)
O6–N1	1.255(9)	O1–Pr1–O9	134.07(16)
O7–B2^{viii}	1.443(8)	O14–Pr1–O9	68.17(17)
O7–B5^{ix}	1.452(9)	O13–Pr1–O11	70.86(17)
O8–B2^{ii}	1.472(9)	O5–Pr1–O11	116.35(15)
O9–B4^{viii}	1.447(9)	O10–Pr1–O11	86.76(16)
O10–N1	1.281(9)	O1–Pr1–O11	133.79(15)
O11–B2^{iv}	1.492(9)	O14–Pr1–O11	83.56(16)
O12–B3^{iii}	1.350(9)	O9–Pr1–O11	52.01(15)
O12–B5^{ix}	1.503(9)	O13–Pr1–O12	128.24(16)
O13–H13A	0.85(2)	O5–Pr1–O12	67.10(14)
O13–H13B	0.85(2)	O10–Pr1–O12	73.69(16)
O14–H14A	0.84(2)	O1–Pr1–O12	66.80(15)
O14–H14B	0.84(2)	O14–Pr1–O12	107.02(16)

O9–Pr1–O12	114.60(15)	O13–Pr1–B4	70.3(2)
O11–Pr1–O12	159.30(15)	O5–Pr1–B4	26.41(18)
O13–Pr1–O3	64.79(17)	O10–Pr1–B4	71.3(2)
O5–Pr1–O3	53.14(15)	O1–Pr1–B4	94.43(19)
O10–Pr1–O3	70.28(15)	O14–Pr1–B4	147.0(2)
O1–Pr1–O3	113.56(15)	O9–Pr1–B4	130.63(19)
O14–Pr1–O3	135.55(17)	O11–Pr1–B4	90.30(18)
O9–Pr1–O3	107.08(15)	O12–Pr1–B4	89.80(17)
O11–Pr1–O3	63.55(14)	O3–Pr1–B4	26.80(17)
O12–Pr1–O3	114.12(14)	O7–Pr1–B4	132.47(18)
O13–Pr1–O7	153.69(17)	B3–Pr1–B4	112.3(2)
O5–Pr1–O7	117.10(14)	O2–B1–O8	122.1(7)
O10–Pr1–O7	71.24(16)	O2–B1–O1	119.7(7)
O1–Pr1–O7	94.25(15)	O8–B1–O1	118.2(6)
O14–Pr1–O7	78.42(17)	$O7^{i}$–B2–$O8^{ii}$	110.8(6)
O9–Pr1–O7	63.84(14)	$O7^{i}$–B2–O5	115.0(6)
O11–Pr1–O7	115.55(14)	$O8^{ii}$–B2–O5	106.3(5)
O12–Pr1–O7	52.05(14)	$O7^{i}$–B2–$O11^{iii}$	108.5(5)
O3–Pr1–O7	141.50(15)	$O8^{ii}$–B2–$O11^{iii}$	108.6(6)
O13–Pr1–B3	91.86(19)	O5–B2–$O11^{iii}$	107.4(5)
O5–Pr1–B3	138.55(18)	$O12^{iv}$–B3–O11	125.4(6)
O10–Pr1–B3	81.6(2)	$O12^{iv}$–B3–O9	122.8(6)
O1–Pr1–B3	139.01(19)	O11–B3–O9	111.7(6)
O14–Pr1–B3	73.0(2)	$O12^{iv}$–B3–Pr1	174.2(5)
O9–Pr1–B3	26.11(17)	O11–B3–Pr1	57.1(3)
O11–Pr1–B3	25.98(17)	O9–B3–Pr1	54.9(3)
O12–Pr1–B3	139.47(17)	O5–B4–O3	111.0(6)
O3–Pr1–B3	85.91(17)	O5–B4–$O9^{i}$	115.2(6)
O7–Pr1–B3	89.92(17)	O3–B4–$O9^{i}$	116.3(6)

O5–B4–O15	106.1(6)	B3–O11–B2^{iv}	121.2(5)
O3–B4–O15	106.7(6)	B3–O11–Pr1	96.9(4)
O9^{i}–B4–O15	100.0(6)	B2^{iv}–O11–Pr1	141.6(4)
O5–B4–Pr1	53.4(3)	B3^{iii}–O12–B5^{ix}	122.1(6)
O3–B4–Pr1	57.9(3)	B3^{iii}–O12–Pr1	130.0(4)
O9^{i}–B4–Pr1	144.1(5)	B5^{ix}–O12–Pr1	100.0(4)
O15–B4–Pr1	115.7(4)	Pr1–O13–H13A	121(6)
O7^{v}–B5–O3	113.6(6)	Pr1–O13–H13B	115(6)
O7^{v}–B5–O2^{vi}	111.2(6)	H13A–O13–H13B	107(3)
O3–B5–O2^{vi}	109.8(6)	Pr1–O14–H14A	102(6)
O7^{v}–B5–O12^{v}	103.1(6)	Pr1–O14–H14B	145(6)
O3–B5–O12^{v}	111.5(6)	H14A–O14–H14B	110(3)
O2^{vi}–B5–O12^{v}	107.3(6)	B4–O15–H15A	124(6)
B1–O1–Pr1	149.2(5)	B4–O15–H15B	123(6)
B1–O2–B5^{vii}	119.1(6)	H15A–O15–H15B	106(3)
B4–O3–B5	124.1(5)	O4–N1–O6	120.0(7)
B4–O3–Pr1	95.3(4)	O4–N1–O10	119.4(7)
B5–O3–Pr1	136.7(4)	O6–N1–O10	120.6(6)
B4–O5–B2	125.2(6)		
B4–O5–Pr1	100.2(4)		
B2–O5–Pr1	133.9(4)		
B2^{viii}–O7–B5^{ix}	113.4(5)		
B2^{viii}–O7–Pr1	133.3(4)		
B5^{ix}–O7–Pr1	99.6(4)		
B1–O8–B2^{ii}	119.7(5)		
B3–O9–B4^{viii}	119.9(6)		
B3–O9–Pr1	99.0(4)		
B4^{viii}–O9–Pr1	141.1(4)		
N1–O10–Pr1	131.3(4)		

Symmetry transformations used to generate equivalent atoms:

(i) x−1,y,z (ii) −x+1,−y,−z (iii) x−1/2,−y+1/2,z−1/2

(iv) x+1/2,−y+1/2,z+1/2 (v) x−1/2,−y+1/2,z+1/2

(vi) −x+3/2,y+1/2,−z+1/2 (vii) −x+3/2,y−1/2,−z+1/2

(viii) x+1,y,z (xi) x+1/2,−y+1/2,z−1/2

Table 9 Anisotropic displacement parameters [$Å^2 \times 10^3$]. The anisotropic displacement factor exponent takes the form: $-2\pi^2[h^2a^{*2}U^{11} + \cdots + 2\,h\,k\,a^*\,b^*\,U^{12}]$.

Atom	U^{11}	U^{22}	U^{33}	U^{23}	U^{13}	U^{12}
Pr1	7(1)	6(1)	8(1)	0(1)	−1(1)	0(1)
B1	7(4)	5(4)	16(4)	4(3)	3(3)	3(3)
B2	4(3)	5(4)	9(4)	1(3)	−4(3)	2(3)
B3	7(3)	11(4)	2(3)	−3(3)	0(3)	−2(3)
B4	8(4)	17(5)	5(4)	−7(3)	1(3)	0(3)
B5	4(3)	14(4)	15(4)	−1(3)	−1(3)	−1(3)
O1	10(2)	5(3)	12(3)	1(2)	−1(2)	3(2)
O2	7(2)	6(3)	12(3)	3(2)	−2(2)	3(2)
O3	6(2)	7(2)	5(2)	−1(2)	3(2)	−3(2)
O4	15(3)	10(3)	34(3)	3(2)	2(2)	2(2)
O6	20(3)	18(3)	38(4)	−7(3)	0(3)	1(2)
O7	3(2)	9(2)	6(2)	−3(2)	−2(2)	1(2)
O8	6(2)	8(3)	10(2)	−1(2)	−5(2)	−1(2)
O9	8(2)	12(3)	9(3)	−2(2)	3(2)	1(2)
O10	17(3)	9(3)	13(3)	1(2)	4(2)	0(2)
O11	4(2)	8(3)	12(3)	−1(2)	−1(2)	−1(2)
O12	5(2)	4(2)	10(2)	1(2)	3(2)	4(2)
O13	21(3)	9(3)	15(3)	−1(2)	6(2)	−3(2)
O14	9(3)	14(3)	24(3)	−1(2)	−6(2)	−1(2)
O15	22(3)	13(3)	29(3)	2(2)	2(3)	2(2)
N1	11(3)	20(4)	26(4)	7(3)	9(3)	5(3)

Table 10 Hydrogen coordinates [× 10^4] and isotropic displacement parameters [$Å^2$ × 10^3].

Atom	*x*	*y*	*z*	U_{eq}	*S.o.f.*
H13A	6960(150)	880(30)	3500(70)	28	1
H13B	6280(150)	1700(40)	3760(50)	28	1
H14A	10300(100)	420(30)	2100(90)	28	1
H14B	12260(40)	750(50)	2290(90)	28	1
H15A	4670(90)	3990(40)	390(90)	28	1
H15B	2640(80)	4000(40)	770(90)	28	1

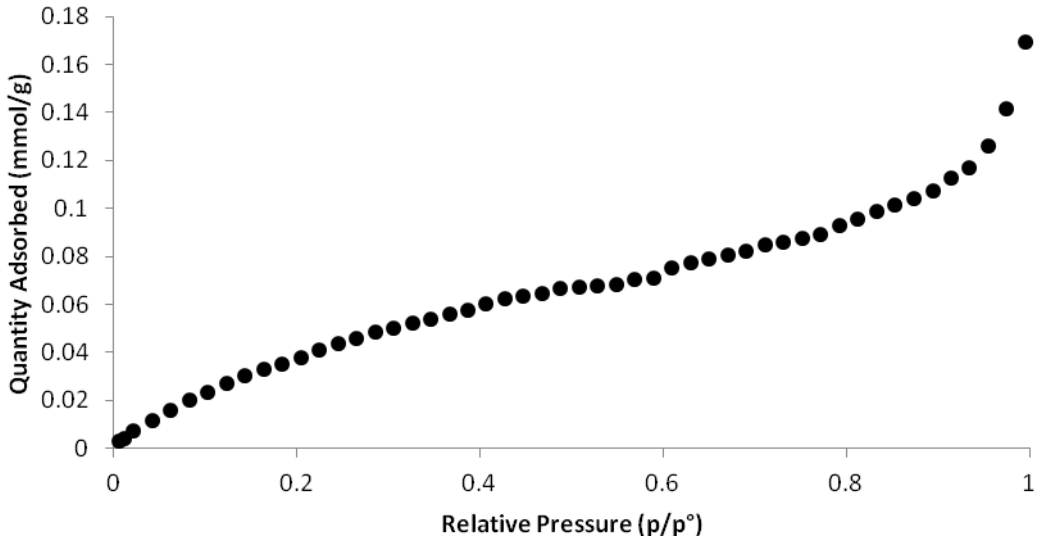

Figure 3 Adsorption isotherm for [$Pr(NO_3)(H_2O)_2$][$B_5O_9(OH_2)$] degassed at 120 °C overnight.

Characterising data for $[Ce(NO_3)(H_2O)_2][B_5O_9(OH_2)]$

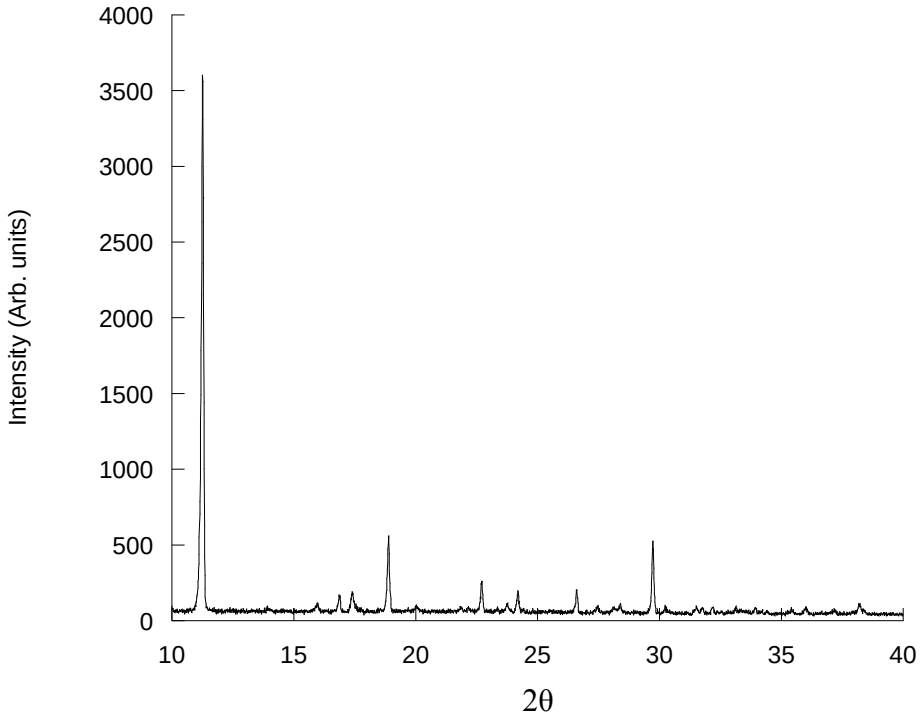

Figure 4 Powder X-ray diffraction pattern of $[Ce(NO_3)(H_2O)_2][B_5O_9(OH_2)]$.

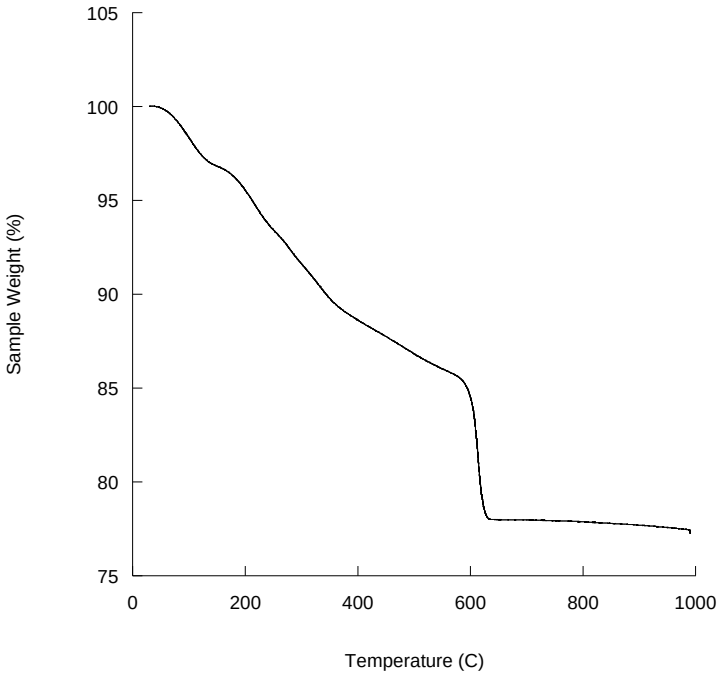

Figure 5 TGA trace of $[Ce(NO_3)(H_2O)_2][B_5O_9(OH_2)]$ showing three mass losses. First mass loss of 3.2 % below 150° C , second mass loss of 10.9 % below 600°C and an additional mass loss of 8.7 % by 995°C. End products CeO_2 and H_3BO_3.

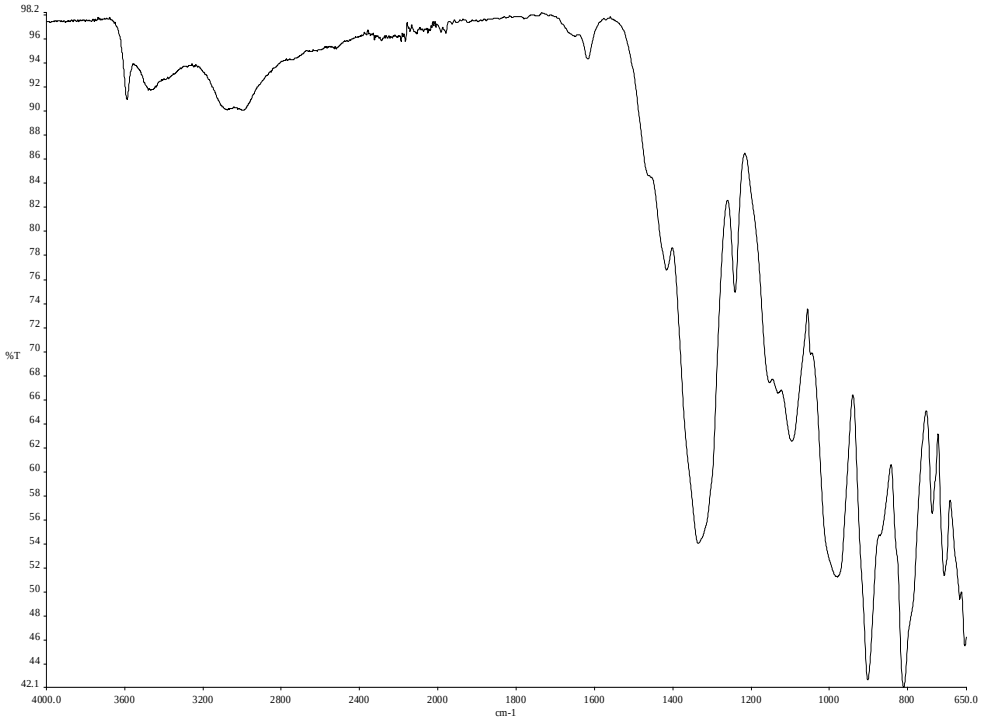

Figure 6 FTIR spectra of $[Ce(NO_3)(H_2O)_2][B_5O_9(OH_2)]$ showing bands corresponding to OH stretch and bending modes of water at 3040, 1657 and 1616 cm^{-1}, BO_3 asymmetric and symmetric stretches at 1415, 1335 (also nitrate) and 902 cm^{-1}, BO_4 asymmetric and symmetric stretches at 1096, 811 and 738 cm^{-1}. The in-plane bending modes, B-O-H, are observed at 1154 cm^{-1} and the out-of-plane bending mode of B-O in BO_3 at 707 cm^{-1}.

Characterising data for $[Nd(NO_3)(H_2O)_2][B_5O_9(OH_2)]$

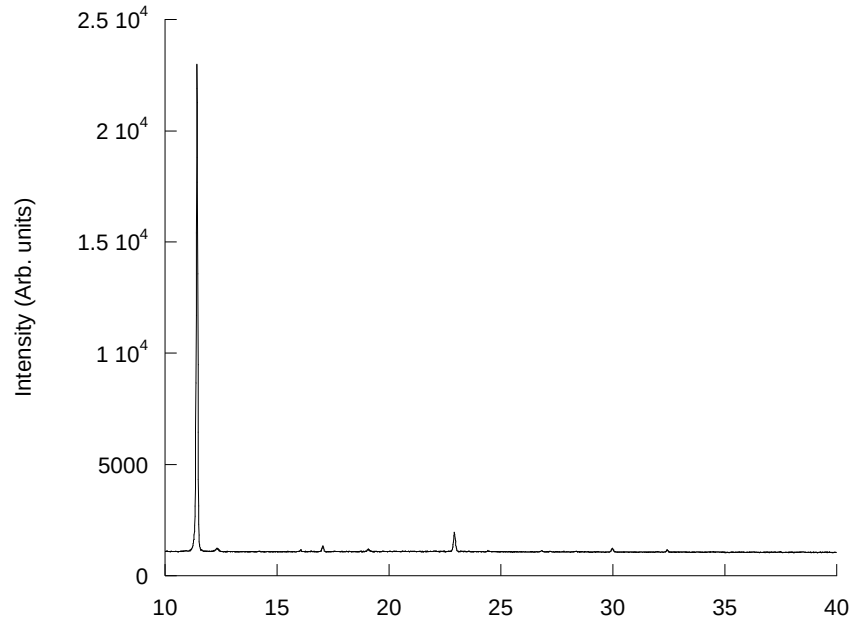

Figure 7 Powder X-ray diffraction pattern of $[Nd(NO_3)(H_2O)_2][B_5O_9(OH_2)]$.

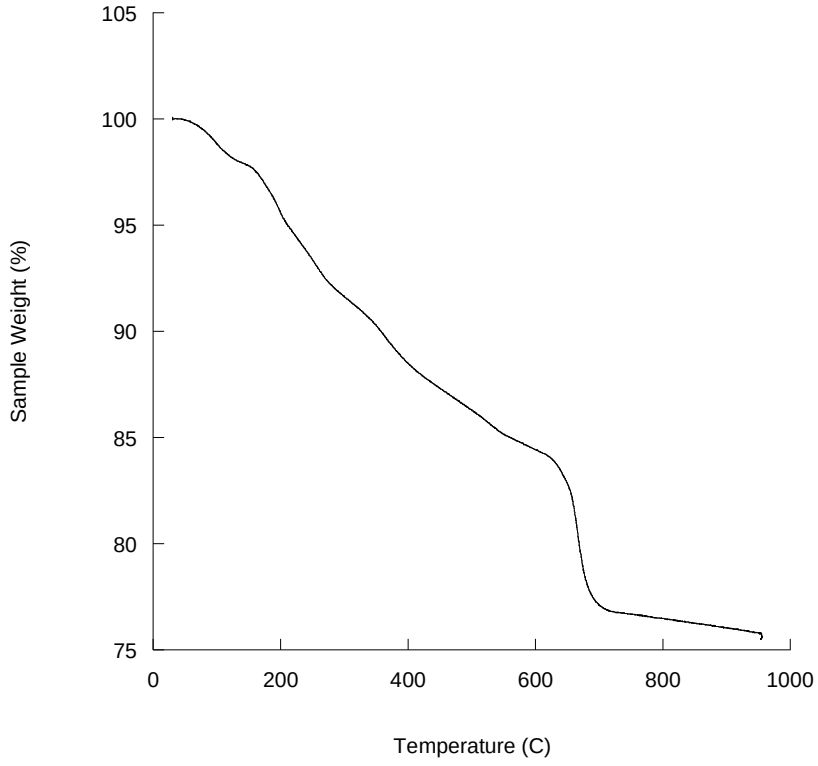

Figure 8 TGA trace of $[Nd(NO_3)(H_2O)_2][B_5O_9(OH_2)]$ showing three mass losses. First mass loss of 3.0 % below 175 °C , second mass loss of 12.5 % below 600°C and an additional mass loss of 8.8 % by 995°C. End product $Nd(BO_2)_3$.

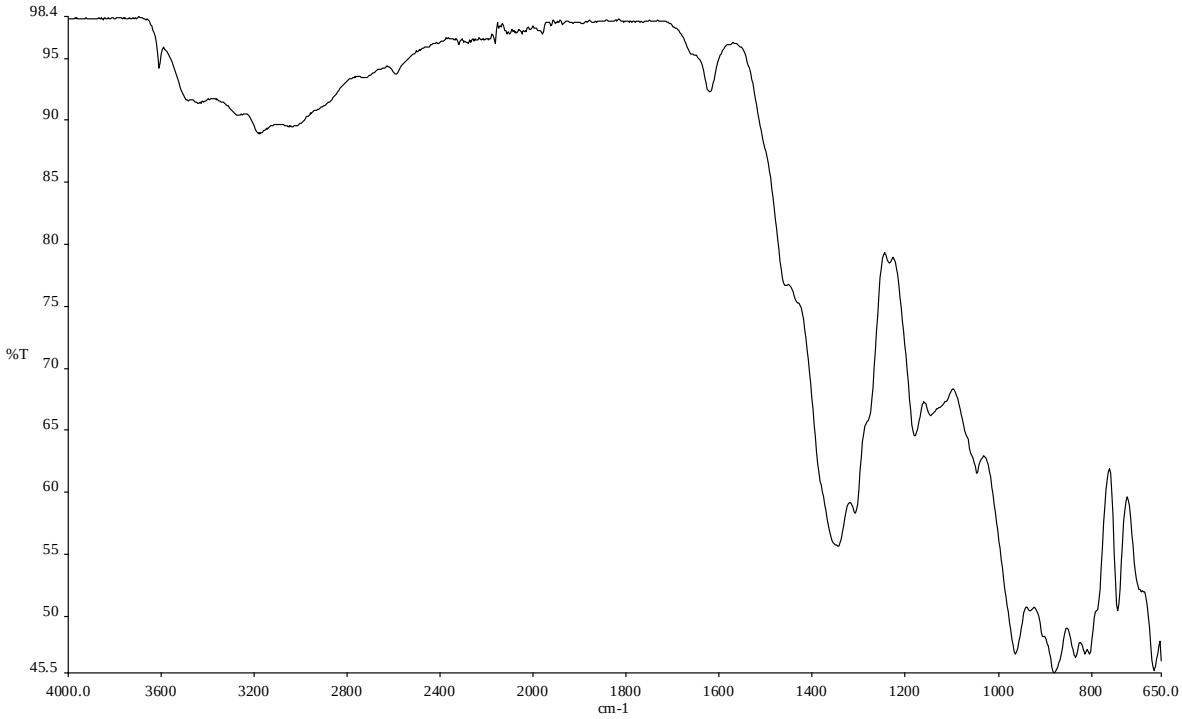

Figure 9 FTIR spectra of $[Nd(NO_3)(H_2O)_2][B_5O_9(OH_2)]$.

Table 11 Elemental analysis of $[Ln(NO_3)(H_2O)_2][B_5O_9(OH_2)]$ (Ln= Pr, Ce & Nd)

Lanthanide	Elemental Analysis	
	Observed (%)	Calculated (%)
Pr	H – 1.34	H - 1.33
	N - 2.61	N – 3.08
Ce	H - 1.25	H - 1.33
	N – 2.58	N – 3.08
Nd	C - 0.09	C – 0.00
	H - 1.13	H - 1.32
	N – 2.51	N – 3.06

Characterising data for $[Ln(B_6O_{13}H_3)][BO_3H_2]$

$[Sm(B_6O_{13}H_3)][BO_3H_2]$

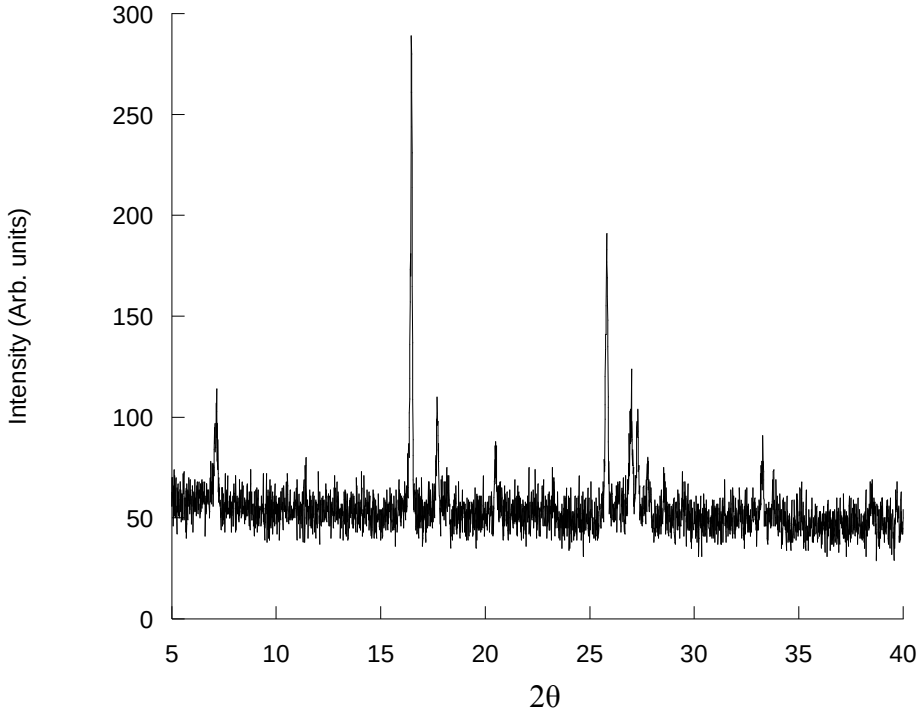

Figure 10 Powder X-ray diffraction pattern of $[Sm(B_6O_{13}H_3)][BO_3H_2]$.

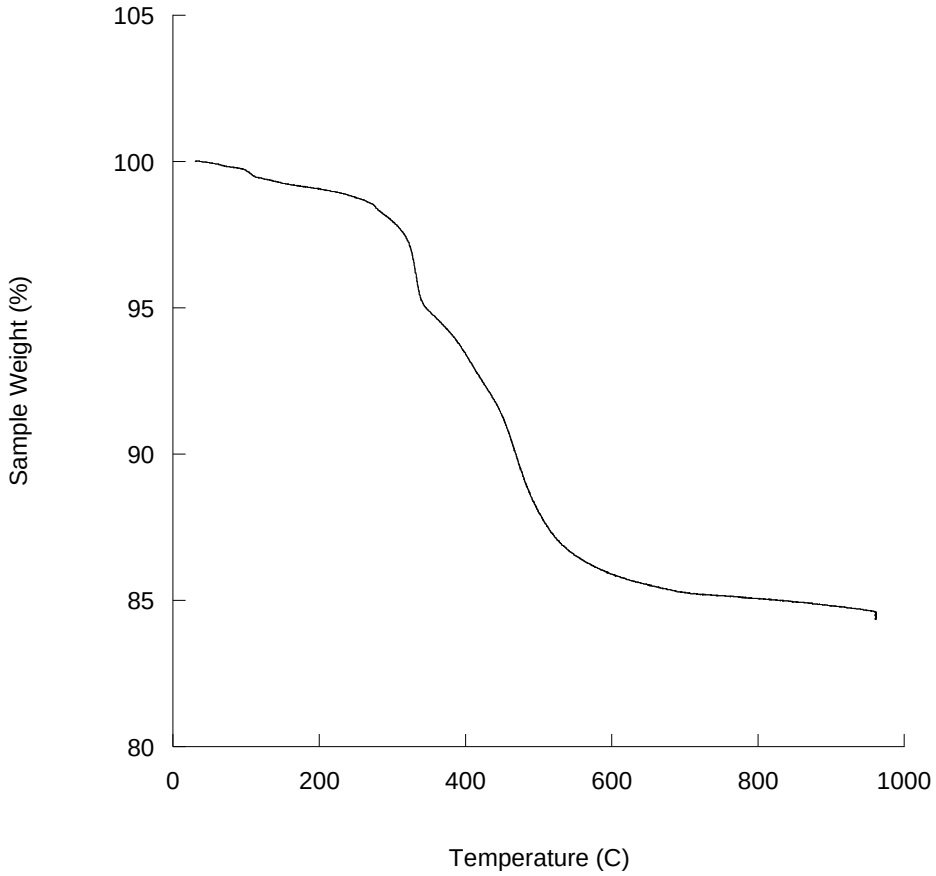

Figure 11 TGA trace of $[Sm(B_6O_{13}H_3)][BO_3H_2]$ showing two mass losses. First mass loss of 1.5 % below 275 °C and a second mass loss of 14.0 % below 995°C. End product $Sm(BO_2)_3$.

Figure 12 FTIR spectra of $[Sm(B_6O_{13}H_3)][BO_3H_2]$.

$[Eu(B_6O_{13}H_3)][BO_3H_2]$

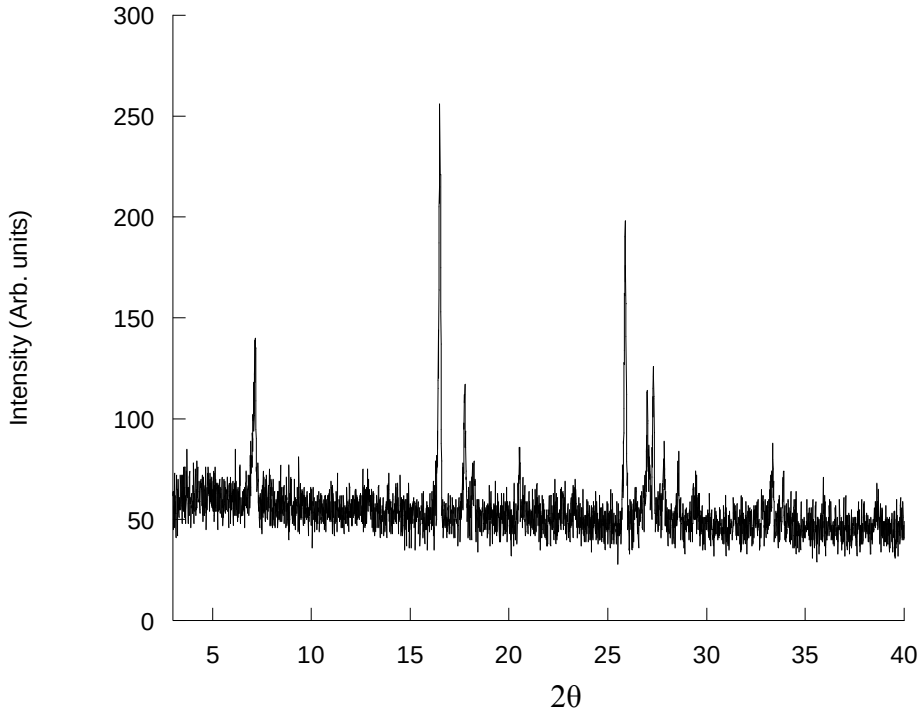

Figure 13 Powder X-ray diffraction pattern of $[Eu(B_6O_{13}H_3)][BO_3H_2]$.

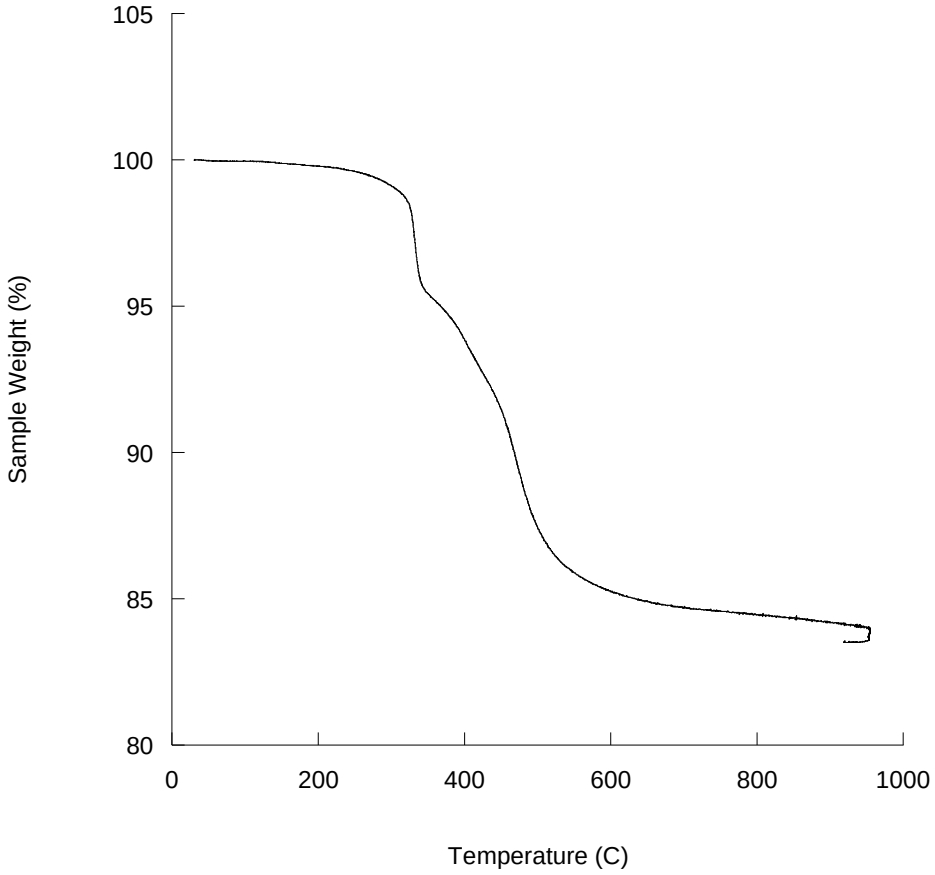

Figure 14 TGA trace of $[Eu(B_6O_{13}H_3)][BO_3H_2]$ showing two mass losses. First mass loss of 4.6 % below 350 °C and a second mass loss of 11.8 % below 995°C. End product $Eu(BO_2)_3$.

Table 12 Elemental analysis of $[Ln(B_6O_{13}H_3)][BO_3H_2]$ (Ln= Gd, Sm & Eu)

Lanthanide	Elemental Analysis	
	Observed (%)	Calculated (%)
Gd	H – 1.36	H - 1.02
Sm	H - 1.43	H - 1.03
Eu	H - 1.57	H - 1.03

Appendix E

Publications

Synthesis and Structure of Pillared Molybdates and Tungstates with Framework Layers

J. L. Nicholls, S. E. Hulse, S. K. Callear, G. J. Tizzard, R. A. Stephenson, M. B. Hursthouse, W. Clegg, R. W. Harrington and A. M. Fogg, *Inorganic Chemistry* 2010, *49*, 8545-8551;

Synthesis and Crystal Structure of a Neodymium Coordination Polymer with 2,6-Anthraquinonedisulfonate

J. L. Nicholls, J. Bacsa and A. M. Fogg, *Particuology* 2010, *8*, 221-224.

Oral Presentations

Beijing University of Chemical Technology: Materials Chemistry Conference, 2010- Beijing

Poster Presentations

Royal Society of Chemistry, Solid State Group Christmas Meeting, 2011- University of Liverpool

SSC 2011: 9th Solid State Chemistry Conference, 2010- Prague, Czech Republic

University of Liverpool Poster Day, 2010- Liverpool

Dalton One-Day Conference: Northwest regional meeting, 2009- Manchester